Finite Element Analysis of the Application of Synthetic Fiber Ropes to Reduce Seismic Response of Simply Supported Single Span Bridges

By

Robert Paul Taylor

Thesis Submitted to the Faculty of the

Virginia Polytechnic Institute and State University

In Partial Fulfillment of the Requirements for the Degree of

MASTER OF SCIENCE

IN

CIVIL ENGINEERING

Approved by:

Raymond H. Plaut, Chairman

Thomas E. Cousins

Carin L. Roberts-Wollmann

July 2005

Blacksburg, Virginia

Keywords: Bridge, Cable Restrainer, Seismic, Springs, Synthetic Fiber Ropes

Finite Element Analysis of the Application of Synthetic Fiber Ropes to Reduce Seismic Response of Simply Supported Single Span Bridges

by

Robert Paul Taylor
Raymond H. Plaut, Committee Chairman
Civil Engineering

(ABSTRACT)

Movement of a bridge superstructure during a seismic event can result in damage to the bridge or even collapse of the span. An incapacitated bridge is a life-safety issue due directly to the damaged bridge and the possible loss of a life-line. A lost bridge can be expensive to repair at a time when a region's resources are most strained and a compromised commercial route could result in losses to the regional economy. This thesis investigates the use of Snapping-Cable Energy Dissipators (SCEDs) to restrain a simply supported single span bridge subjected to three-dimensional seismic loads. SCEDs are synthetic fiber ropes that undergo a slack to taut transition when loaded.

Finite element models of six simply supported spans were developed in the commercial finite element program ABAQUS. Two seismic records of the 1940 Imperial Valley and 1994 Northridge earthquakes were scaled to 0.7g PGA and applied at the boundaries of the structure. The SCEDs were modeled as nonlinear springs with an initial slackness of 12.7mm. Comparisons of analyses without SCEDs were made to determine how one-dimensional, axial ground motion and three-dimensional ground motion affect bridge response. Analysis were then run to determine the effectiveness of the SCEDs at restraining bridge motion during strong ground motion. The SCEDs were found to be effective at restraining the spans during strong three-dimensional ground motion.

Acknowledgements

First and foremost I would like to thank my committee chair and advisor, Dr. Raymond H. Plaut. His help and guidance over the past several years has been vital to the completion of two research projects and the development of my ability as a researcher. Second, I would like to thank my committee members, Dr. Carin L. Roberts-Wollmann and Dr. Thomas E. Cousins, for their participation on this committee and instruction concerning bridges and concrete.

I would like to thank the other SCED researchers, Nick Pearson, Chris Hennessey, John Ryan, Mike Motley, and Greg Hensley, with whom I have collaborated over the past several years. Their help and teaching ability were invaluable. Of course, I would still be getting started without the help of Tim Tomlin, Steve Greenfield, and some patient folks at 4Help who had solutions for repeated complications between my system and ABAQUS or the Inferno supercluster. Additional thanks go to Dhaval Makhecha for his willingness to repeatedly help a total stranger with a multitude of ABAQUS questions.

I would like to thank the people who hold the keys in my life. A special thanks to Greg Hensley for his friendship and willingness to give a helping hand over the past three years. Without him, I would still be locked out of my office. Repeated thanks are due to Matt Lytton for four years of being the best roommate that I could imagine; I would still be locked out of my car and apartment if it were not for Matt. I would also like to thank Kara for keeping me motivated and fed in a few key moments during the past year.

Of course, most importantly, a special thanks to my family. They have always given me the encouragement to succeed. Mom, Dad, and Sarah, as well as my grandparents have always been there for guidance and support.

This research was funded by a National Science Foundation Grant, No. CMS-0114709. The support of the NSF made this research possible.

Table of Contents

List of Figures

List of Tables

Chapter One
Introduction and Literature Review

1.1 Introduction

Unrestrained displacements and excessive excitation of bridge segments during seismic events can result in structural failure or the total loss of a bridge span. The failure of a bridge section during an earthquake can be a serious threat to human life as well as an expensive and time consuming repair at a time when the resources of the community will be strained. The indirect life-safety and economic impacts due to the loss of routes vital to commerce and emergency services are also significant reasons to ensure that simple spans do not significantly displace from their bearings. Therefore, various passive and active control systems have been investigated and utilized in order to mitigate the effects of earthquakes on bridge superstructures.

The goal of this thesis is to discuss the application of snapping-cable energy dissipators (SCEDs) as an inexpensive passive control system between bridge sections. The potential use of SCEDs between bridge sections will have two functions. First, SCEDs are synthetic fiber ropes that are installed slightly slack between bridge sections. In a significant seismic event, the movement of the structure will force the slack ropes into a taut state, producing a dynamic snap load. The friction between the fibers of the rope resulting from the snap load will dampen the excitation of the superstructure. The research to develop the appropriate damping within the ropes is ongoing, therefore the ropes are modeled as nonlinear springs in this thesis and the effect of the friction in the ropes is only considered by the use of global damping parameters. Second, the ropes will serve as restrainers to minimize the relative displacement between bridge sections through added stiffness. This research focuses on the snap loads developed in the restraining cables and the appropriate stiffness to limit displacement for the various models.

The research uses the finite-element analysis program ABAQUS to model six single-span bridge models subjected to past seismic events. The seismic recording of the 1940 Imperial Valley earthquake measured at El Centro and the record of the 1994 Northridge event measured at Newhall are applied to each model. Each model is subjected to a scaled earthquake load without SCEDs and then the models are tested with SCEDs in order to determine the effectiveness of the restrainers. Relative displacement of the deck from the abutment was the benchmark used to determine the success of the restrainers.

This thesis also investigates the effects of applying three-dimensional earthquake motions to the models. Many studies ignore lateral or even vertical components of earthquakes in their analysis and this thesis seeks to demonstrate the effect of this omission. Again, relative displacement was used as the point of reference.

This research is part of a multiple-stage research project investigating the response and application of synthetic rope SCEDs. Previous research performed by Pearson (2002) and by Hennessey (2003) provides the initial response model on which analysis is based. Analysis of SCEDs for bracing moment frames subjected to blast loads was completed by Motley (2004). Analyses of SCEDs as inexpensive damping members for building structures and to model guy wires supporting masts are being conducted by fellow researchers.

1.2 Literature Review

1.2.1 Past responses of bridge sections to seismic loading

Bridge span unseating and collapse during recent seismic events have shown that there is a continuing need to control bridge deck motion during earthquakes. Also, the history of restrainer cables breaking during severe earthquakes shows the need for a restrainer that is better suited for a dynamic environment.

Mitchell et al. (1994) discussed bridge failures due to seismic loading. Retrofits were required to many bridges after the magnitude 6.6, 1971 San Fernando earthquake due to the lack of restraint or inadequate movement allowances between sections. Many simply supported spans had seat widths that only allowed for small movements due to temperature and shrinkage. Some other older designs had bearings that did not allow for adequate movement or did not consider lateral loading that can occur during earthquakes. The seismic load often caused the bearings to jump or the bearing supports to yield. As a result, steel bar or cable restrainers were added between bridge sections. In California, 1250 bridges received restrainers in the years following the San Fernando earthquake. The 1986 Palm Springs Earthquake induced the failure of restrainers in the Whitewater Overcrossing. The magnitude 7.1, 1989 Loma Prieta earthquake induced little damage to bridges designed to more recent code standards such as AASHTO 1983 and ATC 1981. However, 13 older bridges experienced severe damage and a total of 91 bridges had major damage. The famous collapse of a relatively short section of the San Francisco-Oakland Bay Bridge broke the restrainer cables and displaced the span from its five-inch seats. The failure resulted in the death of one motorist and the delay of millions more during the month of repairs to the structure (Housner 1990).

Mitchell (1995) investigated the collapse of the Gavin Canyon Undercrossing during the 1994 Northridge Earthquake in the San Fernando Valley. This was another example of loss of span during a seismic event. Although the failure of this structure can be partly blamed on an unusual skew, the ineffectiveness of the restrainer cables to control a problem 23 years after first being utilized due to failures in the same valley refocused some attention on how to retrofit bridges to prevent loss of span.

Seismic performance of steel bridges in the Central and South-Eastern United States (CSUS) was examined by DesRoches et al. (2004a, b) in a two-part study. The first half of the study investigated the response of typical bridges in three CSUS locations subjected to artificial strong ground motions from the New Madrid fault for the 475 and 2475 year events. These relate to the 10% and 2% probability of exceedance in 50 years, respectively. The study found that the 2475 earthquake could lead to significant failures and damage in both simply supported bridges and continuous decks. Pounding of the superstructure and failure of rocker bearings were the primary sources of damage, with limited damage to the columns. The second half of the study investigated steel bridge retrofit methods with regards to the CSUS. Elastomeric bearing pads, lead-rubber bearing pads, and restrainer cables were investigated. The study found that the retrofit measures often lead to simply transferring the load from one bridge component to another.

1.2.2 Restraint-type devices

Cable restrainer retrofits were developed in response to the numerous cases of loss of support in the 1971 San Fernando earthquake. These devices basically lash together the structural elements of a bridge so that relative displacements are limited to planned quantities during a seismic event.

The introduction of an improved design method for cable hinge restrainers was presented by DesRoches and Fenves (2000). The required stiffness for cable restrainers at hinges, or at gaps between 'continuous' bridge decks, was determined by modeling the frame on each side of the hinge and the restrainer in question as a two-degree-of-freedom system. Each frame, or set of frames, was modeled as a single-degree-of-freedom system with a mass linked to the ground motion by a single spring. The two systems were then linked by a third spring representing the restrainer stiffness. This model takes into account the period of the frames and the relative displacement between the frames, however the slack to taut transition was linearized.

Retrofits of concrete superstructure and piers were discussed by Spyrakos and Vlassis (2003). Many superstructure retrofits related to limited seat widths at movement joints can be accomplished by adding additional length to the seats or limiting displacement with cable restrainers. A cable restrainer in a concrete bridge is usually connected to a girder web or a diaphragm. Spyrakos and Vlassis also included an indication of the necessary stiffness for limiting displacement using dynamic analysis. They concluded that "restrainer stiffness should be at least equal to that of the more flexible of the two frames connected by the restrainers."

Caner et al. (2002) investigated the effectiveness of link slabs for retrofitting simple span bridges. Link slabs are reinforced deck sections that span a bridge expansion joint and resist excessive motion by the superstructure. These components were found to be effective in the 1999 Izmit Earthquake in Turkey. The installation of a link slab retrofit, when compared to the installation of restrainer cables, would likely be more time consuming, more expensive, and more challenging on roadways with heavy traffic. However, the research showed that link spans were effective in limiting displacements of the girders.

DesRoches et al. (2003) discussed cable restrainer retrofits for simply supported bridges typical to the Central and South-Eastern United States (CSUS). CSUS transportation departments, in states such as Tennessee, South Carolina, Indiana, Illinois, and Missouri, have installed, or are considering the installation of, cable restrainers to limit the displacement of bridge sections in a seismic event. A typical design of the Tennessee Department of Transportation (TDOT) was used as the example for full-scale testing. The tests showed that the connections were considerably weaker than desired and failed in a brittle manner at only 17.8kN. This was less than 11% of the designed cable capacity. Alternative connections were considered and tested, with some improvement in load capacity. However, yielding and prying of the connections was still an issue.

1.2.3 Damping devices for bridge superstructures

Traditional elastic steel cable restrainers do little to dissipate energy during a seismic event. Often, a large number of restrainers is required to limit the motion of bridge components, and the large resulting force on bridge diaphragms, bearings, and other components can still result in failure of the structure (DesRoches and Fenves 2000). Therefore, damping components to replace or to be used in addition to restrainers have been developed that would reduce the force caused by the restrainers. The list of isolator and damper technology available for use in bridge structures is diverse; examples are elastomeric bearing pads, lead core rubber bearings, steel-PTFE slide bearings, friction pendulum isolation (FPI) bearings, hydraulic piston dampers, viscoelastic dampers, metallic yield dampers, friction dampers, and tuned mass dampers (Zhang 2000). A good damping system must be robust, cost-effective, operational without outside power, and generally simple to design (Hiemenz and Werely 1999).

Magnetorheological (MR) and electrorheological (ER) dampers were discussed by Hiemenz and Wereley (1999) as semi-active control systems in civil engineering structures. Goals of control strategies were to increase the fundamental period of structures beyond that of an earthquake and to add damping. MR and ER dampers were found to reduce vibrations in a simulation of the El Centro event.

The use of seismic isolators and metallic yield dampers in bridges was discussed by Feng (1999). Lead core isolators and rubber bearings were discussed. For most motions, bearings allow the deck to become isolated from the earthquake-induced displacement of the piers. However, when small seat widths and large motions are considered, isolation may aggravate the problem of unseating. This is because laminated rubber bearings have little resistance to horizontal movement. Lead core isolators may also allow excessive horizontal movement if plasticity is reached. Therefore steel, preferably mild steel with high ductility, was introduced in "seismic displacement restrainers" to act as a final stop-block in case of extreme displacements. With the restrainers, the deck was then more integrated with the movements of the substructure and the relative movement of each superstructure section was reduced before sectional failure occurred.

Viscoelastic dampers at expansion joints in a continuous superstructure were analyzed by Kim et al. (2000) and Feng et al. (2000). The authors used two five-span bridge models to examine the effect of the dampers. The first bridge had a single expansion joint; the second had two joints. Both bridges had four columns of equal height. The horizontal peak ground accelerations (PGAs) of four seismic events were scaled to 0.7g to meet Caltran's maximum PGA in the seismic design spectra. The vertical component of ground acceleration was also applied to the model. A spring and damper with various magnitudes and configurations were applied in the model. For both linear and nonlinear analysis, the viscous damper appeared to be the component that contributed the most to reduced displacements. The authors found that viscous dampers for seismic retrofits would benefit expansion joints with narrow seat widths.

DesRoches and Delemont (2002) proposed using stress-induced phase change shape memory alloy (SMA) in restrainers. SMA materials have two or more chemical structures that occur during loading and unloading. As the material grains rearrange, yielding or yield recovery occurs, which creates a hysteresis loop and damps the system. The proposed bars could undergo a strain of about 8% elongation with a permanent deformation of 1%. The models showed efficiency in reducing maximum displacements, and a resiliency when compared to the current steel restrainers.

1.2.4 Restrainer response with a slack to taut transition

The restraining cables modeled in this thesis consider a slack to taut transition with dynamic effects. Most retrofit restrainer cables are designed for static control of the deck section (Kim et al. 2000). Previous research in the fields of mooring lines subjected to wave action and electrical conduits subjected to seismic loads has been conducted which encountered snap loads. Preliminary research has also been conducted to determine the response of the SCEDs so that the large forces can be adequately considered and used to reduce the motions of structures.

The study discussed briefly in part 1.2.1 by DesRoches et al. (2004b) considered the seismic response of retrofitted multispan bridges with steel girders. A slack of 12.7mm was assumed. Results showed that when restrainer cables are used jointly with elastomeric or lead-rubber bearings, the isolation of the bridge deck created by the bearings through increased displacements is negated by the force transmitted by the restrainer cables. Therefore, additional slack was recommended for these designs. The research showed mixed results for restrainer cables in bridges utilizing steel bearings; often the cables were not able to reduce deformation on these bearings because the bearings would begin to yield before the cable became taut.

Plaut et al. (2000) investigated snap loads in mooring lines securing a cylindrical breakwater. The cables were modeled as both linear and bi-linear springs, and three-dimensional deflections and rotations of the breakwater were considered. The analysis of the breakwater with a slack to taut transition, using the bi-linear spring, found that snapping of the mooring cables occurred with significant forcing amplitude. The snap loads dramatically increased the motions of the breakwater and the response became somewhat chaotic compared to the linear mooring cables. The snap loads in the bi-linear springs were up to ten times larger than the forces in the linear springs.

Filiatrault and Stearns (2004) observed the effect of slackness on flexible conduits between electric substation components in response to a history of damage to this equipment during seismic events. The researchers found that little force was transmitted through the conduit, and the two components connected by the conduit had independent responses when the conduit was significantly slack. However, when the slackness was reduced so that the conduit would alternate between slack and taut states, the motions of the components became similar and the tension forces were about ten times larger than observed in the previous, always slack, configurations.

Pearson (2002) and Hennessey (2003) conducted research preliminary to this paper. Their tests developed the response of synthetic ropes to static loads and snap loads with various applied forces. The dynamic forces were applied by dropping a mass from various heights. The ropes were initially slack. The rope ends were respectively secured to a base point and to the falling mass. When the ropes became taut, the stiffness, damping, and changes of those properties were observed.

1.3 Objective and Scope

The objective of this thesis is to determine the effect of restrainer cables in controlling the displacement of simply-supported bridge sections to strong ground motion. This thesis does not include the hysteresis loop in the stress-strain curve of the ropes, which would provide a small amount of additional damping. However, it does consider the ropes as nonlinear springs that encounter dynamic snap loads as the cables transition from slack to taut. The analysis determines the magnitude of the restrainer cable loads, the cable stiffness required to limit the displacement of the deck, and the effect of three-dimensional analysis on this problem.

Chapter two discusses the assumptions and process to develop the model used in the finite element program ABAQUS. This discussion is divided into the six parts of the model: the span, bearing pads, the SCEDs, the strong ground motion records, damping, and the application of a gravity load.

Chapter three focuses on the data collected from the models. The model output is discussed with key nodes, references, and parameters identified. The results discussed in the final three chapters refer to points defined in the third chapter.

Chapter four examines the effect of the inclusion of lateral and vertical components of the earthquake records on the behavior of the spans. This chapter is independent of the results in chapter five, whereas no SCEDs were tested on spans with only motion in the axial direction of the span.

Chapter five discusses the effect of the SCEDs on the axial motion of the spans. Comparisons of displacements of spans with SCEDs to displacements of spans without SCEDs are discussed. Analysis of the stiffness required to limit displacement to an acceptable magnitude is also discussed.

Chapter six summarizes the results from chapters four and five, and a final analysis is provided. Suggestions for future research concerning SCEDs for bridge span restraint are also discussed.

Appendix A contains the calculations used to calculate the rectangular section dimensions and properties, and is referenced in chapter two. Appendix B is referenced in chapters two and three and contains the spectral response in tripartite plots, ground motion time histories, and spatial ground motion plots. Appendix C contains a sample input file for ABAQUS/Explicit and is referenced in chapters two and three. Appendix D contains plots of the results from the models and is referenced in chapter five.

Chapter Two
Development of Finite Element Computer Models

2.1 Introduction

The previous research regarding SCEDs by Pearson (2002) and Hennessey (2003) created and analyzed the data required to adequately model the dynamic stiffness and snap load in a finite element model. For the present research, the finite element program ABAQUS was used to develop a three-dimensional model of simple-span bridges, such as the span shown in Figure 2.1. The models utilize SCEDs to reduce the displacement of the spans when subjected to the scaled motions of two historic seismic records. The records used were the 1940 Imperial Valley at El Centro and the Newhall record of the 1994 Northridge earthquake. In order to efficiently accommodate the possibility of complex contact surfaces and the impact-like snap loads, the finite-element solver ABAQUS/Explicit was used. Table 2.1 shows the defining dimensions for the six spans tested. For the remainder of this thesis, the test span will be referred to by the designations presented in Table 2.1.

Table 2.1 – Table of tested spans. This table designates a name to the specific combination of parameters.

Designation	Girder Type	Span Length, m	Girder Spacing, m
Span1	PCBT-29	12.192	1.981
Span2	PCBT-45	24.384	1.981
Span3	PCBT-69	36.576	1.981
Span4	PCBT-93	48.768	1.981
Span5	PCBT-61	24.384	2.438
Span6	PCBT-69	24.384	2.896

Typically, the axes, as shown in the bottom left corner of Figure 2.1, will be referred to with the following syntax. Axis 1 is called the "axial direction" in reference to the longest dimension of the span. Axis 3 is termed the "lateral direction" and axis 2 is identified as the "vertical direction."

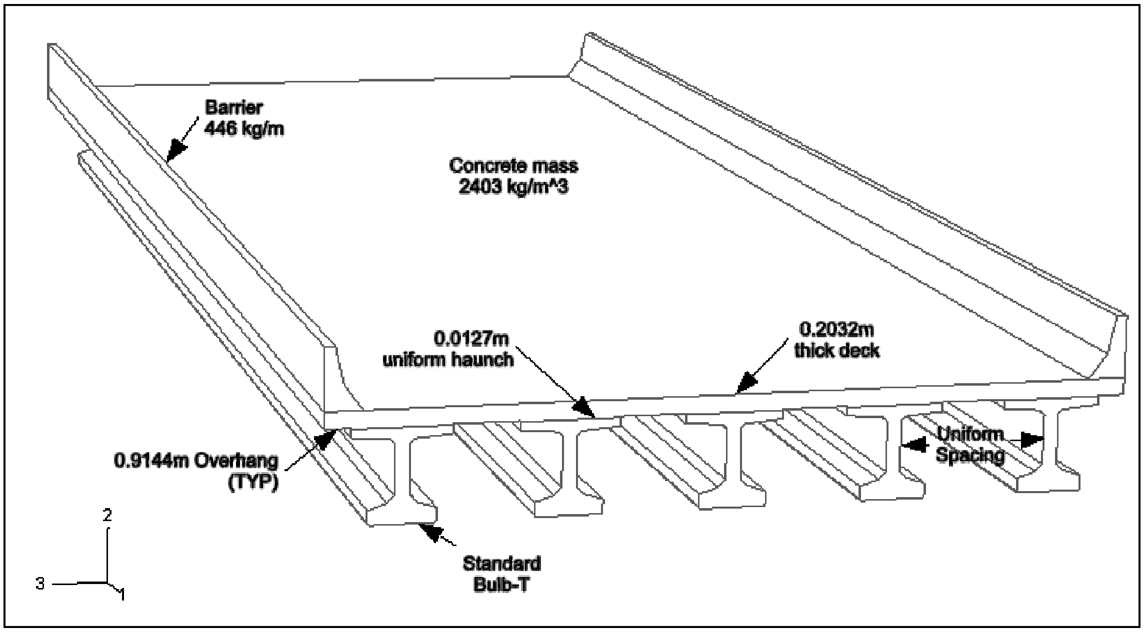

Figure 2.1 – Typical layout and considerations for span design.

The models have six parts that are described in depth in the sections below. First, section 2.2 describes the process used to develop the stiffness, density, dimensions, and node mesh used for the deck and girders. Second, section 2.3 describes the method used to model the bearings. Third, section 2.4 describes how the SCEDs were modeled. Fourth, the method used to select the input earthquake records is described in section 2.5. Fifth, the material and numerical damping is described in section 2.6. Finally, section 2.7 describes the process of applying dead load to the structure. The last part of each section references the applicable lines and keywords (ABAQUS 2003b) of the sample input file in Appendix C. Lists in Appendix C, such as node and element assignments, are compressed to save space.

2.2 Deck and Girder Models

This section is divided into three parts. Part 2.2.1 discusses the method used to create an equivalent rectangular section to mimic the behavior of a concrete deck and girder span. Part 2.2.2 discusses the convergence tests and philosophy used in meshing the span. Part 2.2.3 dissects the keywords in the input file related to this section.

2.2.1 Representative rectangular section

The research focused on modeling the behavior of a simple-span bridge using standard prestressed concrete bulb-T details. To use the exact dimensions and reinforcement for a three-dimensional model of a multi-span, multi-girder structure would have required too many elements to produce an efficient model with reasonable processing time. Therefore, several assumptions were made to simplify the geometry of a single span resting on narrow bearing pads. The deck was assumed to be initially designed for complete composite action with the girders. This assumption allowed the entire span to be considered as a single beam.

A set of calculations was performed to create a rectangular beam with similar behavior for normal bending. Axial stiffness and the lateral moment of inertia were considered to have negligible effects on the overall motion of the span. A verification of the procedure to represent the moment of inertia of an actual span with a rectangular section of similar proportions was performed by comparing the results of the MathCAD® routine. The verification routine is shown in section A.1 with the results of the routine highlighted in red. The results for the same section taken from section 9.4 of the PCI Bridge Design Manual (2003) are highlighted in blue. The variables that are changed to accommodate other sections are highlighted in green. The rectangular section properties of the test spans are also shown in Appendix A. Table 2.2 shows the results of the verification test using midspan deflections of the test span. The small disparity between the PCI values and the routine's estimation may be because the PCI values are based on a single interior girder, whereas the routine considers the section as a whole, including the exterior girders that have a slightly smaller composite moment of inertia.

Table 2.2– Deflection summary for accuracy of test section

Method	Deflection, m
PCI Design Manual	0.0422
Routine estimation	0.0397
ABAQUS test	0.0395

Camber was not applied to the sections to remove the initial dead load deflections, such as the deflections shown in Table 2.2. This assumption expedited and streamlined the model development process. The maximum dead load deflection was expected to only be 5.5cm, in Span4, therefore the geometry of the test sections was affected little by this assumption.

2.2.2 Convergence tests and node mesh

A convergence test was conducted to determine how many elements were required in the axial direction. The convergence test used Span2 with pin-pin conditions. The FREQUENCY keyword was used in ABAQUS/Standard to extract the first three modal frequencies with bending only about the lateral direction, as shown in Figure 2.2. As the number of elements increased, the tests became more accurate until increasing the number of elements had little effect on the extracted frequencies. Of course, minimizing the number of elements was desirable in order to minimize processing times. Therefore, finding the correct number of elements to produce accurate results with short processing times was imperative to efficient testing.

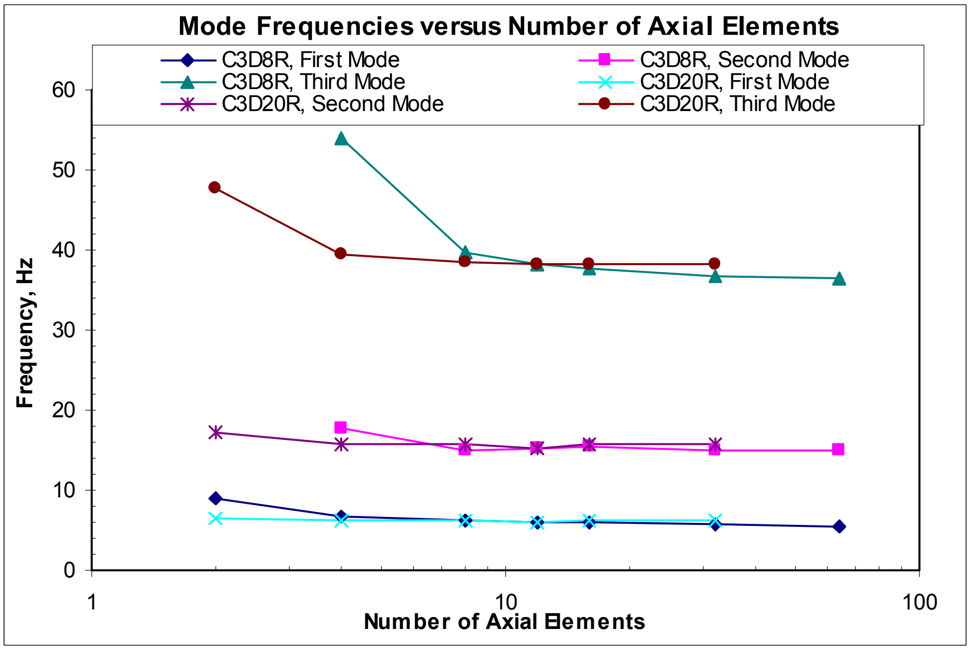

Figure 2.2 – Modal frequencies of a simply supported Span2 versus the number of axial elements considered.

ABAQUS/Explicit, used in the final dynamic tests, was not compatible with the quadratic C3D20R brick elements; however these elements gave the best estimation of the modal frequencies. Table 2.3 presents the mode shapes and frequencies for a selection of these tests. From this convergence test, a minimum of ten elements in the axial direction was required for an accurate representation of the section. As can be seen in Table 2.3, the quadratic elements better represent the mode shapes and were considered as the baseline for selecting the correct number of linear elements. The linear elements actually diverge from the quadratic trend as the number of elements increases beyond about 18 elements for the 24m span. For the final tests, 22 C3D8R elements were used in the axial direction. Three elements were used at each end of the span near the abutment to define contact stresses and displacements. The remaining 16 elements were distributed along the length of the span. The bending of the spans is probably best represented in the convergence test that used 16 C3D8R elements. The only exception is Span4, where an extra 4 C3D8R elements were used along the axial direction due to the extra length of the span.

Table 2.3 – Table of mode shapes and frequencies for a selection of element densities.

Axial Elements	Bending Mode 1, Hz	Bending Mode 2, Hz	Bending Mode 3, Hz
C3D8R , 2	 9.02	n/a	n/a
4	 6.76	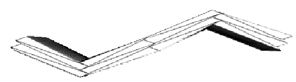 17.7	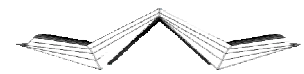 54.0
16	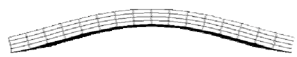 5.93	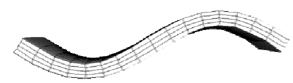 15.2	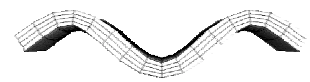 37.6
64	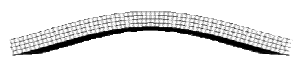 5.59	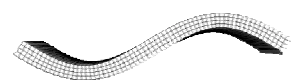 15.0	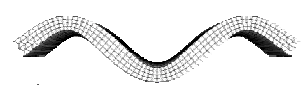 36.6
C3D20R, 2	 6.49	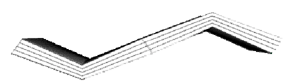 17.2	n/a
4	 6.25	 15.9	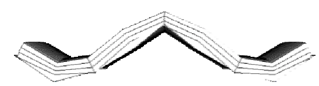 39.5
16	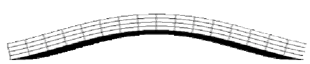 6.26	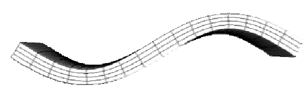 15.6	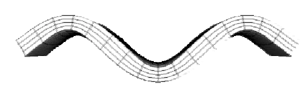 38.3
32	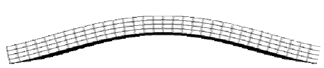 6.22	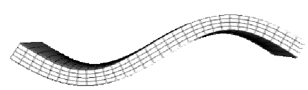 15.6	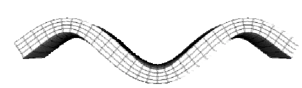 38.3

The density of elements in the lateral direction and in the vertical direction was also considered. Five girders were used for all tests. A minimum of six elements, one to the outside of the exterior girders and one between each girder, were required in the lateral direction. However, the stress concentrations created by the SCEDs required a finer mesh near those nodes in order to properly define the localized stress. Therefore, in the lateral direction three elements were used between each girder and one element outside of the exterior girder. Localized stress near the SCED nodes and proper span bending definition required four elements in the vertical direction. The only exception to this layout was Span6, where only one element was used in the lateral direction outside of the exterior girders. Figure 2.3 shows the layout of the final span mesh, where the black lines denote the element boundaries. The number of elements in all directions allowed for combination of both quick and accurate computations.

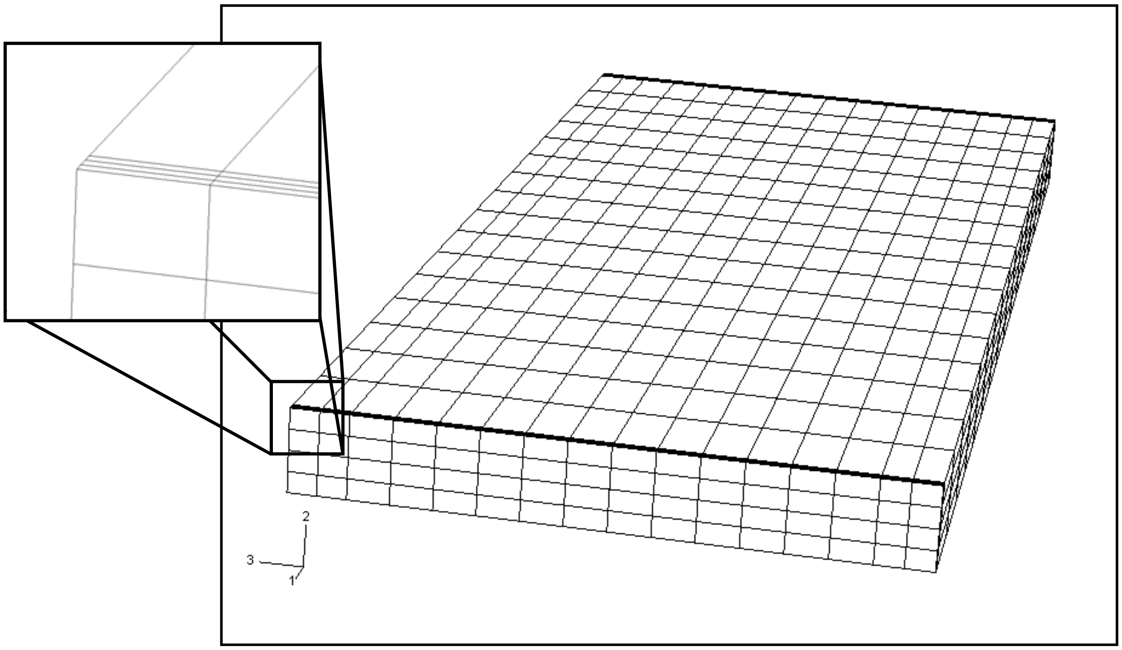

Figure 2.3 – Final layout of the span mesh.

2.2.3 Input file keywords

In Appendix C, under the keywords *Part and *Node in lines 50-51 the spatial node locations for the span are given on lines 52-60 with these nodes assigned to elements in lines 62-70 under the keyword *Element. The material property definitions are on lines 291-296 under the keyword *Material. Keywords *Elastic, *Damping, *Density, and *Elastic are utilized. The material definition is assigned to the span with the keyword *Solid Section on lines 168-169.

2.3 Bearing Models

2.3.1 Introduction

Elastomeric bearing pads were modeled in this analysis. Section 14.6.2 of the AASHTO LRFD Bridge Design Manual (2000) only recommends Plain Elastomeric Pads, Fiberglass-Reinforced Pads, and Steel-Reinforced Elastomeric Bearings as "suitable" or "suitable for limited applications" for movement and rotation in all degrees of freedom. All other bearing types were either "unsuitable" or "require special consideration". Seismic loading of a bearing not capable of limited motion in a degree of freedom can often lead to failure of the bearing. Failure includes undesirable yielding, fracture, or the uncoupling of mated surfaces. The main objective of this analysis was to understand the behavior of the SCEDs, therefore bearings that would require complex material definitions or mechanical motions were avoided. A plain elastomeric pad (PEP) was the basis of the definitions used.

The PEP considered was based on an approximation of values given by manufacturers and researchers. The thickness of the pad was set at 25mm. Seventy percent of the thickness was generally considered to be the limit of horizontal displacement – 17.5mm for this analysis. The approximate linear compression stiffness for a 0.127m by 0.127m pad was found to be 48.6MN/m from data collected by Aswad and Tulin (1986). Previous researchers, such as McDonald et al. (2000), DesRoches et al. (2004b), and Aswad and Tulin (1986), have considered the shear stiffness or friction coefficient common among elastomeric bearing pads. The approximate shear stiffness was set at 3.0MN/m. Generally, the friction coefficient is anticipated to be adequate to resist any relative displacement between the top surface of the bearing pad and the bottom of the girder. With this assumption, a bearing pad can be modeled as a spring. However, the friction coefficient between these components has been measured as high as 0.9 in inclined plane tests and as low as 0.2 in some field tests. Slippage, even under normal loading, has occurred between low quality-bearings and poorly-prepared girders

(McDonald et al. 2000). The friction coefficient of this pad was set at 0.5. A narrow length of 0.1524m was assumed. An axial slippage limit of 0.0762m was established to ensure the stability of the bearing and to ensure that the bridge remained open after a seismic event. Table 2.4 shows a summary of the properties and axial displacement limits for the bearing pad model.

Table 2.4 – Summary of PEP model properties and deflection limits

Parameter	Value	Parameter	Value
Thickness, mm	25	Length, mm	152
Coefficient of friction	0.5	Compression stiffness, MN/m	48.6
Shear stiffness, MN/m	3.0	Shear displacement limit, mm	17.5
Slip displacement limit, mm	76.2		

The difficulty of modeling a PEP was in finding an accurate and elegant way of defining compression stiffness, shear stiffness, damping, and friction simultaneously. Though many researchers simply define the shear stiffness, the sophistication of ABAQUS/Explicit allowed a relatively complete definition of the bearing pads. The *SURFACE INTERACTION keyword in ABAQUS/Explicit allowed for mechanical interaction definitions for behavior both tangential and normal to the contact surfaces.

2.3.2 Contact region

Tests showed early in the development process that more elements were required in the axial direction at the end region of the spans in order to properly define the shear stress, contact forces, and displacements in that region. Figure 2.4 qualitatively shows the difference of the calculated compressive stress in a span with a defined contact region to a span with uniform spacing of axial elements. In section 2.3.4, Figure 2.7 qualitatively reveals the distribution of contact force on the bearing pad between a span without contact regions and spans with contact regions.

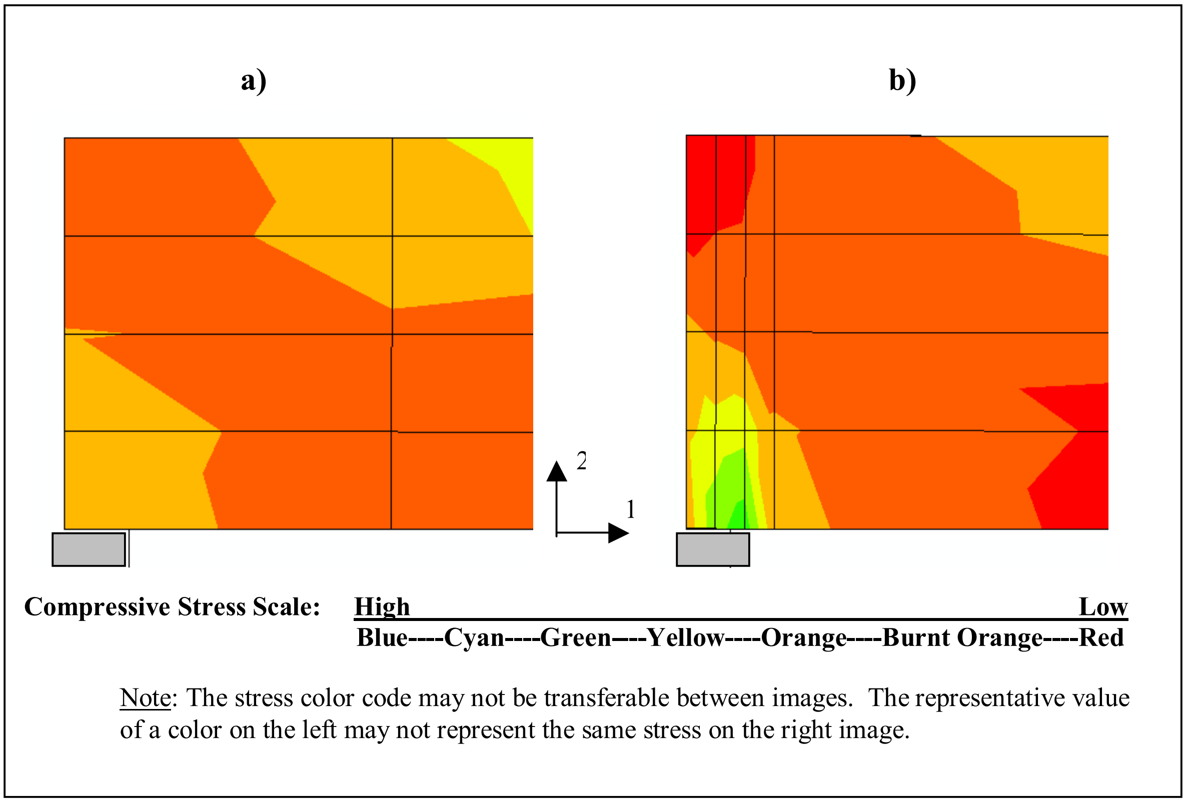

Figure 2.4 – Qualitative comparison of shear stress at the bearing with a hard contact definition
a) Span without contact regions. b) Span with contact regions.

2.3.3 Initial elastomeric bearing pad models in this research

The first model attempted to define the elastomeric bearing pads using three-dimensional continuum brick elements, as used for the span. The compressive strength, shear strength, and friction coefficient were defined. The General Contact algorithm was selected. This model created two problems. First, the mesh required to properly define the interaction between the contacting surfaces was computationally expensive. This cost may have been acceptable if the objective was to define the stresses in the bearing pad; however, the only goal of the bearing pad was to adequately restrict the movements of the span. The second problem was that large deformations in the bearing regions not in contact with the span often surpassed the angularity limits of ABAQUS and reality, and prematurely ended the analysis. Figure 2.5 shows the uneven deformation that occurred with a bearing pad one element thick. Therefore, the continuum elements were abandoned for a model that used springs to define the behavior of the bearing pads.

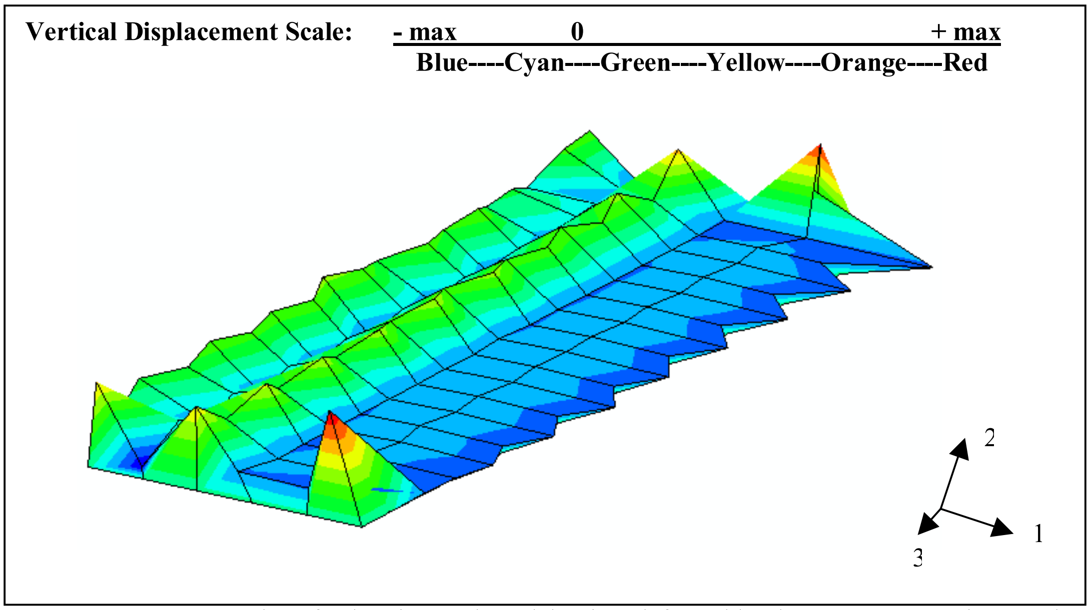

Figure 2.5 – Topography of a bearing pad model using deformable elements. A span is seated on the right half of the bearing. The span's depressed seat is outlined by unrealistic deformations.

The spring model was designed for ABAQUS/Standard. Springs equivalent to the average compression stiffness of a PEP were attached to nodes at the end of each girder line. The length of the spring was dependent on the approximate shear stiffness of a narrow seat pad with a depth of 0.025m. In theory, when the springs were vertical, the approximate shear stiffness was zero, and as the span displaced horizontally the equivalent shear stiffness increased due to the increasing horizontal component of the spring. With the proper spring length, the average shear stiffness between zero horizontal displacement and the horizontal deflection limit was approximated. The downside of this model was that it had extremely limited resistance to lateral motion for most deflections and that it completely ignored any slippage. Springs that had a line of action in only the vertical, axial, or lateral direction were also considered; however, the elements' configuration required to support this system was complex, computationally expensive, and still ignored slippage. In addition to the theoretical shortcomings mentioned above, the analysis of spring models proved to be very difficult - abrupt shutdown of ABAQUS always accompanied any attempt to start an analysis. Figure 2.6 shows the layout of the bearing pads represented by springs. Therefore, the spring models were abandoned for a discrete rigid body shell.

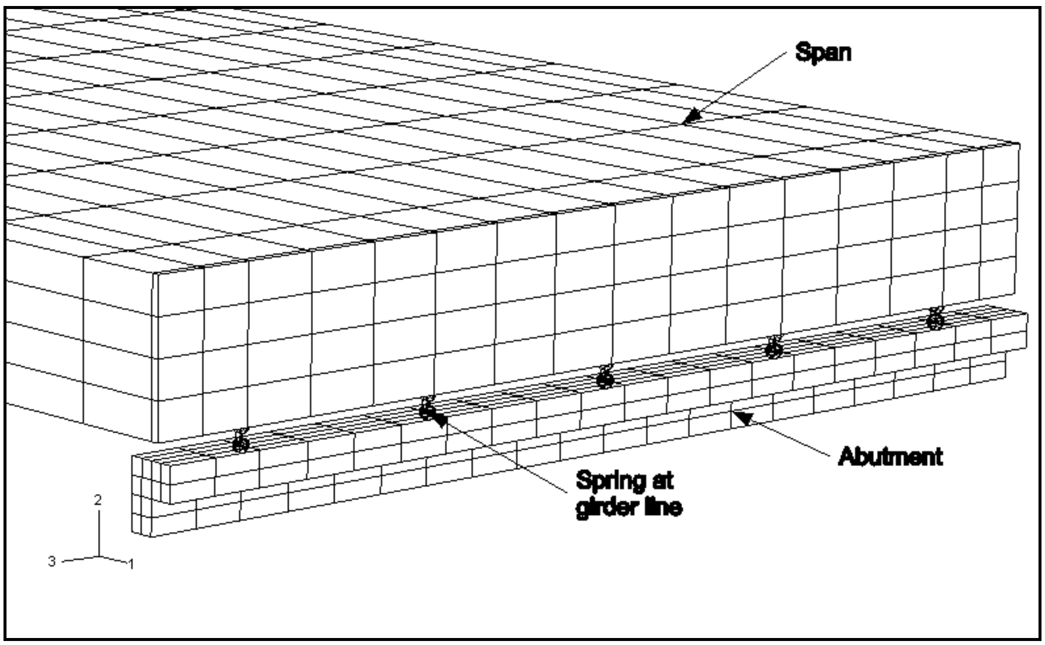

Figure 2.6 – Layout with model using springs to represent the bearing pads.

The original discrete rigid shell model of the PEP only defined friction. Though most movement allowed by a PEP is generally in shear, the friction coefficient that was chosen attempted to mimic the movement allowed by shear. In comparison to another analysis (DesRoches and Delemont 2002), the maximum movement allowed with a friction coefficient of 0.2 was reasonable. However, it was a very vague definition; vertical force was transmitted through the hard contact definition without the cushion of the bearing pad, and the recovery, or recentering, of the girder that would normally be allowed by the elastic PEP was missing from the model.

2.3.4 Final bearing model

The final model used more advanced contact definitions in the rigid shell model described in the previous section. The tangential behavior of the PEP contact definition was modified using the penalty type friction definition. The friction coefficient was set to 0.5 and the elastic slip stiffness was placed at 3,000kN/m. Contact damping was set at 10% of critical. Additionally, a definition for behavior normal to the contacting surfaces was added to the contact properties so that "soft contact" between the surfaces was allowed.

The effect of a soft contact distribution was shown with the vertical deflection of a point at the end of Span1 subject to dead load. In the case of hard contact, the end of the span deflected slightly away from the bearing, whereas with the soft contact case, the end of the span compressed the bearing. A summary of the results is shown in Table 2.5.

Table 2.5 – Summary of dead load deflections at the end of Span1 with hard and soft contact definitions.

Behavior normal to contact surface (stiffness)	Vertical deflection with no gravity load, mm	Vertical deflection with full gravity load, mm
Hard $k_n = \infty$	0	+0.0965
Soft, k_n = 48,000kN/m	0	-6.95

An approximate normal deformation of 30-40% engineering strain was used to calculate the normal stiffness behavior when in contact. The justification for this method is that PEPs come in many shapes, so the length of the pad can be set at 0.1524m and the width can be varied in order to accommodate more massive structures. The stiffness found from Aswad and Tulin (1986) was used for Span1; for the remaining spans, that stiffness was scaled equal to the mass of the span divided by the mass of Span1. A change in normal stiffness does not reflect a change in material properties, only in dimensions. Table 2.6 shows the normal stiffnesses used for each span.

Table 2.6 – Normal bearing stiffness used for each span.

Span Designation	Mass, kg	Stiffness Scaling Factor	Stiffness, MN/m
Span1	131,986	1	48.64
Span2	283,438	2.15	104.6
Span3	472,783	3.58	174.1
Span4	650,510	4.93	239.8
Span5	326,375	2.47	120.1
Span6	358,729	2.72	132.3

Finally, the contact formulation method was changed from general contact to surface-to-surface contact. This change smeared the stress that was previously localized near the span nodes over the entire contact area, creating a more uniform stress across the contact surface. Figure 2.7 qualitatively reveals the distribution of contact force on the bearing pad for various models.

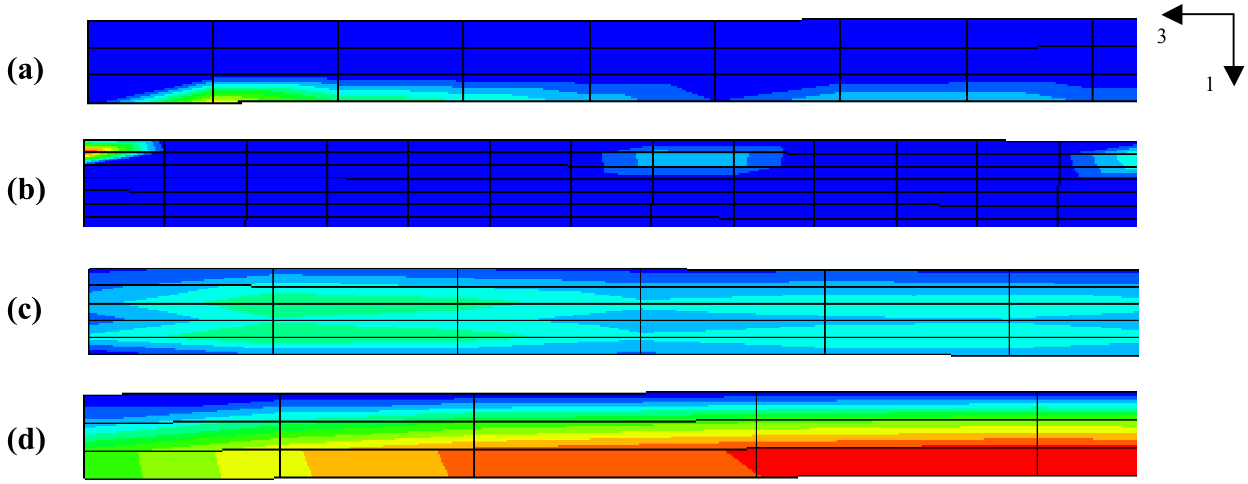

Pressure Scale: **Low ____ High**
Blue----Cyan----Green----Yellow----Orange----Burnt Orange---Red

Note: Pressure color code is not transferable between images. The maximum contact for each model is red and the minimum is blue. The maximum contact pressure in image (d) is equivalent to cyan or green in the other three images.

Figure 2.7 – Qualitative comparison of contact pressure on part of a bearing model for a variety of contact definitions. These are plan views of different bearing pads under gravity load. a) Hard contact in the normal direction with general contact algorithm; all stress along leading edge and near span nodes. b) Soft contact in the normal direction without contact region with general contact algorithm; all stress near the few span nodes. c) Soft contact in the normal direction with contact region and general contact algorithm; all stress near span nodes. d) Final model with soft contact in the normal direction, contact regions, and surface-to-surface contact algorithm; stress distributed across bearing but generally increases closer to the leading edge.

2.3.5 Input file keywords

Under the keyword *Part on line 7 of Appendix C the nodes of the bearing pad surface are defined in three-dimensional space with the keyword *Node in lines 8-18. The assignment of these nodes to elements occurs in lines 19-27 under the keyword *Element. The contact surfaces used are defined with the keyword *Surface in lines 40-45 and 132-163. The surfaces are then assigned a mate for surface-to-surface contact with the keyword *Contact Pair in lines 340-345. The properties of the contact interaction are defined with keywords *Surface Interaction and *Friction in lines 300-306.

2.4 Rope Models

The primary objective of this thesis is to accurately portray the behavior of the SCED ropes and their ability to restrain the span. The theses of Pearson (2002) and Hennessey (2003) were focused on properly modeling the behavior of the polymer ropes. That research showed that the ropes were unable to sustain any compressive force and could be modeled as springs when in tension. The ABAQUS keyword *SPRING was used to model the springs.

2.4.1 Nonlinear stiffness definition

Parallel research, also cited in Motley (2005), has concluded that the best approximation of the force in the ropes is found using the following equation:

$$F = kx^{1.3} \tag{2.1}$$

where F = the force in the rope (N)
k = spring stiffness ($N/m^{1.3}$)
x = the axial lengthening of the spring when taut (m)

The ropes were considered to be slightly slack, the usual configuration with restraining cables. The initial slackness was assumed to be 12.5mm; this distance was also used in the analysis by DesRoches et al. (2004b). Combining Equation 2.1 with the initial slackness, a piecewise equation was constructed to define the force in a rope at any displacement:

$$F = \begin{cases} 0 & \text{if } x \leq 0.0125m \\ k(x-0.0125)^{1.3} & \text{if } x > 0.0125m \end{cases} \tag{2.2}$$

The stiffness plot for a rope configuration with k=52,700 kN/m$^{1.3}$ is shown in Figure 2.8.

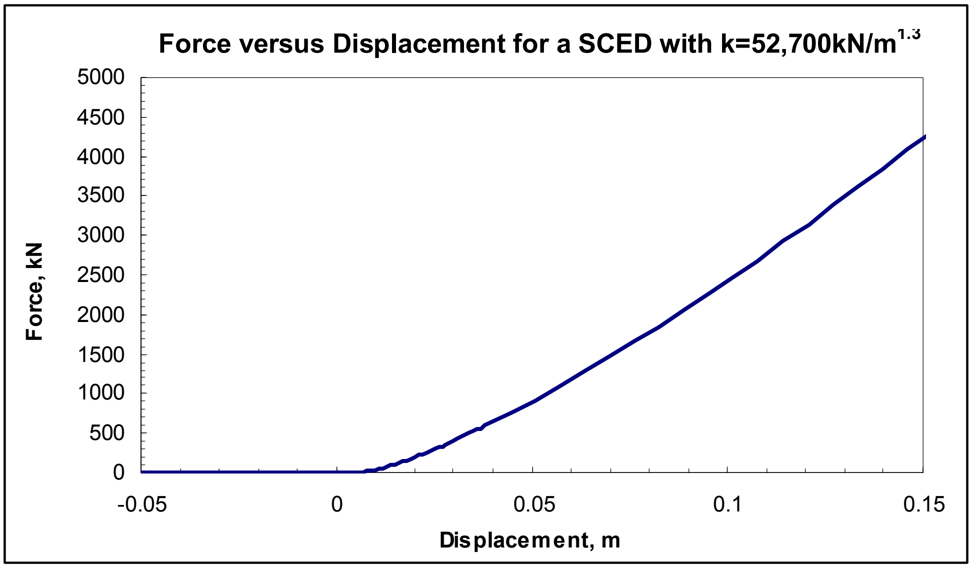

Figure 2.8 - An example of nonlinear SCED stiffness used for this analysis.

2.4.2 Bilinear equivalent

Rarely is the stiffness unit of any material supplied in units of force per length to the 1.3 power, therefore a bilinear equivalent of that stiffness for this application is important in utilizing the proper material. Motley (2004) used two methods to approximate the nonlinear curve over a length of 0.8382m. The first method qualitatively created a bilinear stiffness relationship with an average slope of the nonlinear relationship and the second method created a stiffness tangent to the nonlinear slope with little displacement. Both methods added slack to the initial conditions of the rope.

In this thesis, a more direct method is proposed using the same slackness as the nonlinear rope. For any given expected displacement length, the work done by the bilinear and nonlinear springs are set equal and then the equation is solved for the linear spring coefficient. The initial equations are:

$$Work_l = \int F_l dx = \int_0^d k_l (x-s) dx \quad (2.3)$$

$$Work_n = \int F_n dx = \int_0^d k_n (x-s)^{1.3} dx \quad (2.4)$$

where $Work_l$ = Work done by the bilinear stiffness relationship (J)

$Work_n$ = Work done by the nonlinear stiffness relationship (J)

F_l = Force in the bilinear spring for any displacement (N)

F_n = Force in the nonlinear spring for any displacement (N)

d = expected displacement range (m)

k_l = bilinear stiffness coefficient (N/m)

k_n = nonlinear stiffness coefficient (N/m$^{1.3}$)

x = spring displacement (m)

s = initial slack in the spring (m)

When $Work_l$ is set equal to $Work_n$ and the equation is reduced and solved for k_l, the resulting formula is:

$$k_l = 0.8696 * k_n \frac{(d-s)^{2.3} - s^{2.3}}{d(d-2s)} \quad (2.5)$$

For this application, the displacement range, d, is 0.1016m, the combined axial displacement limit in this analysis, and the initial slack is 0.0127m. The resulting relationship between k_l and k_n for this application is:

$$k_l = 0.42 k_n \quad (2.6)$$

Linear springs are not used in this analysis; however, this mathematical exercise shows that a linear spring coefficient, with approximately the same effect and initial conditions as the nonlinear springs used in this analysis, is approximately 42% of the specified value for nonlinear stiffness. Figure 2.9 shows the comparison of bilinear and nonlinear springs for this application.

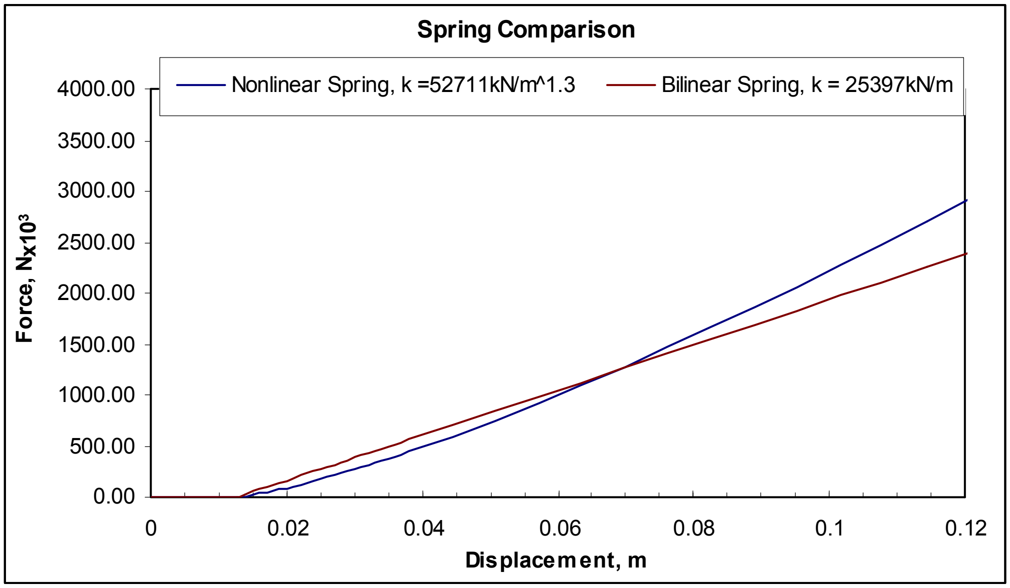

Figure 2.9 – Comparison of nonlinear to bilinear spring with equivalent work.

2.4.3 Location of SCEDs in model

The SCEDs were modeled as being attached to one end of each girder at half of the depth. The opposite end of the SCED was connected to a node on the abutment at the same elevation and lateral location but an axial offset of 0.2286m. In this configuration, the SCEDs are most effective in limiting axial movement but have limited resistance to transverse and vertical movement. This is the general configuration used for concrete bridges (Spyrakos and Vlassis 2003). However, connections would be made to brackets at an appropriate development length on one or both sides of the web. Figure 2.10 shows the typical layout of the SCEDs for this research.

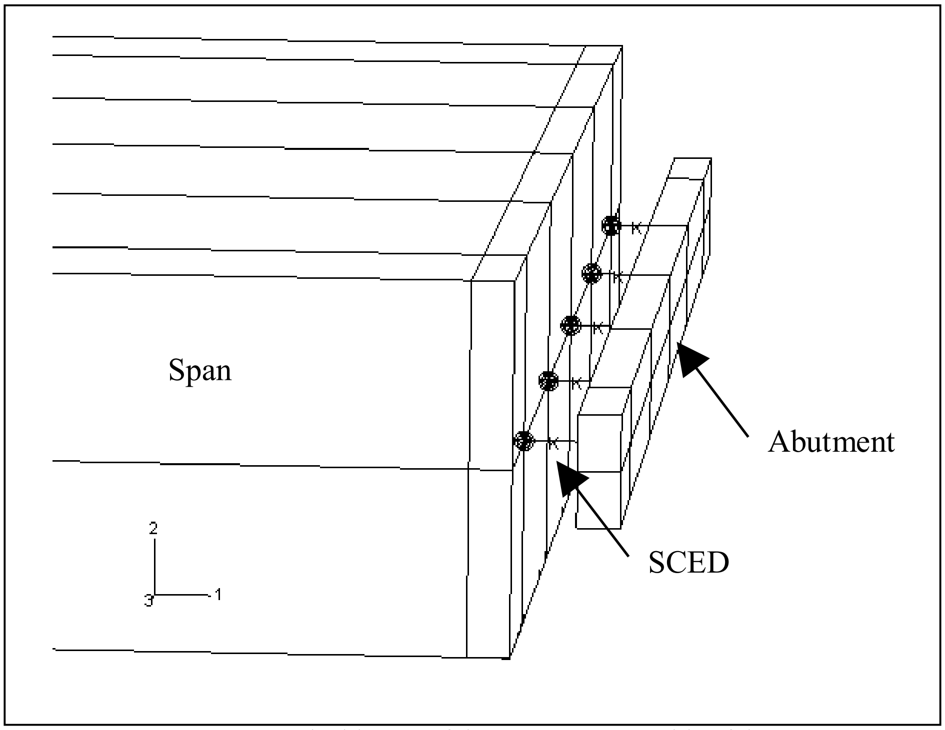

Figure 2.10 – Typical layout of the SCEDs on one side of the span.

2.4.4 Input file keywords

The nodes of the span geometry are assigned with the keyword *Element to ends of the springs in lines 170-180 of Appendix C. These elements are then assigned the force-displacement relationship with the keyword *Spring in lines 181-229.

2.5 Seismic Input Records

The earthquake records were selected to cover the broadest range of spectral excitation with only two earthquake records. The records were both scaled so that they had approximately the same magnitude of response. The earthquake recordings used were the Newhall record of the 1994 Northridge earthquake and the El Centro record of the 1940 Imperial Valley event. At least one of these records was included in the analyses by Kim et al. (2000), Filiatrault and Stearns (2004), DesRoches and Delemont (2002), and Caner et al. (2002). The seismic time histories and spectra were obtained from the Pacific Earthquake Engineering Research (PEER) Center Strong Motion Database (2005).

2.5.1 Orientation of seismic inputs

All three orthogonal components of the records were applied to boundaries of the finite-element models. The component with the largest PGA was applied in the axial direction. In the case of Northridge, the East-West (90) component was applied in the axial direction, with the North-South (360) component forcing the structure in the lateral direction. The Imperial Valley North-South (180) component was applied to the boundaries in the axial direction and the East-West (270) component was applied in the lateral direction. Of course, for both records the Up-Down component was applied at the vertical boundaries of the models.

It is important to note that the PGA does not also imply peak ground displacement. For both earthquake records the largest displacement was in the lateral direction. However, to ensure that the spans had some relative horizontal deflection, the strongest acceleration was applied in the axial direction. The Imperial Valley and Northridge earthquakes' acceleration time histories are provided in Figure 2.11 and displacement time histories are shown in Figure 2.12. The displacement records were shifted to an initial displacement of zero so that a jump would not occur in the first increment of the analysis. Also, only the first 20 seconds were used in the analysis, since limited span displacements occur with either record after that duration.

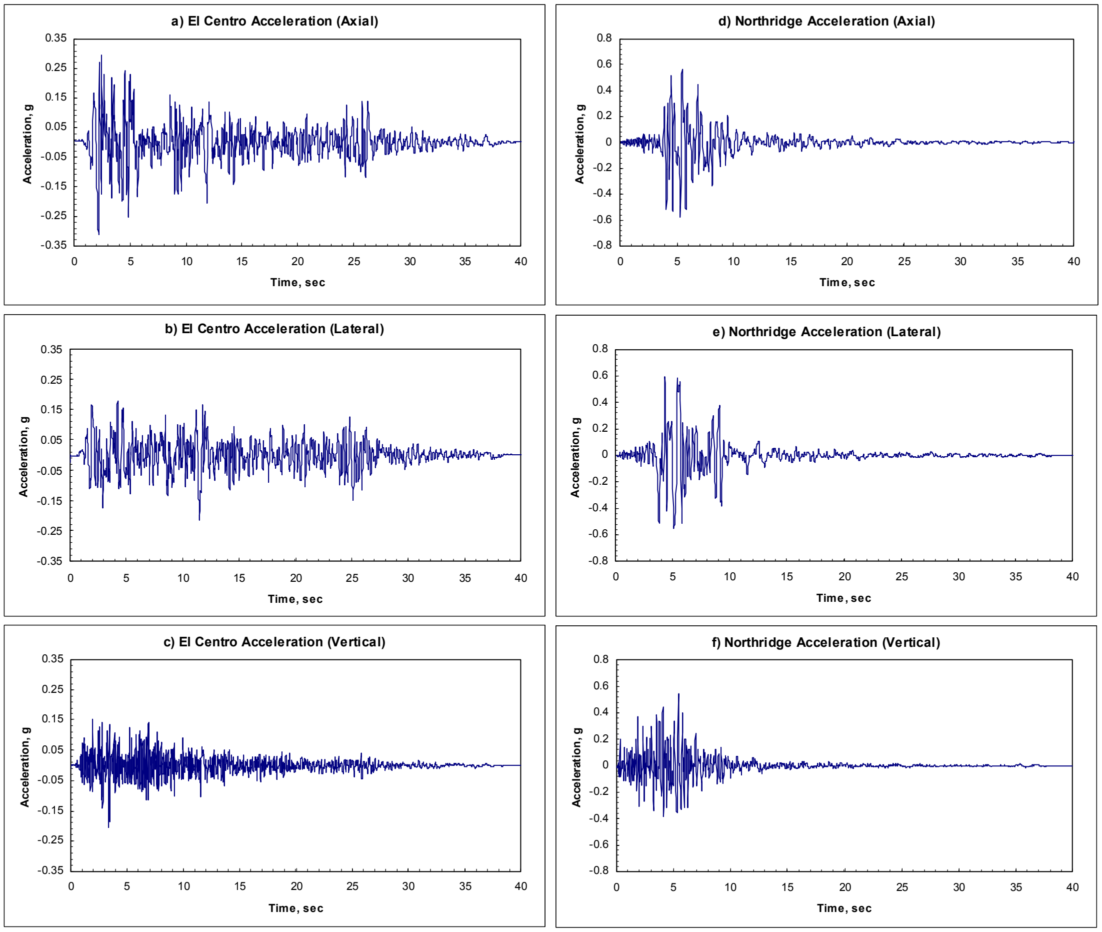

Figure 2.11 – Acceleration time histories of the 1940 Imperial Valley - El Centro and the 1994 Northridge - Newhall earthquake records. a) Imperial Valley axial acceleration. b) Imperial Valley lateral acceleration. c) Imperial Valley vertical acceleration. d) Northridge axial acceleration. e) Northridge lateral acceleration. f) Northridge vertical acceleration.

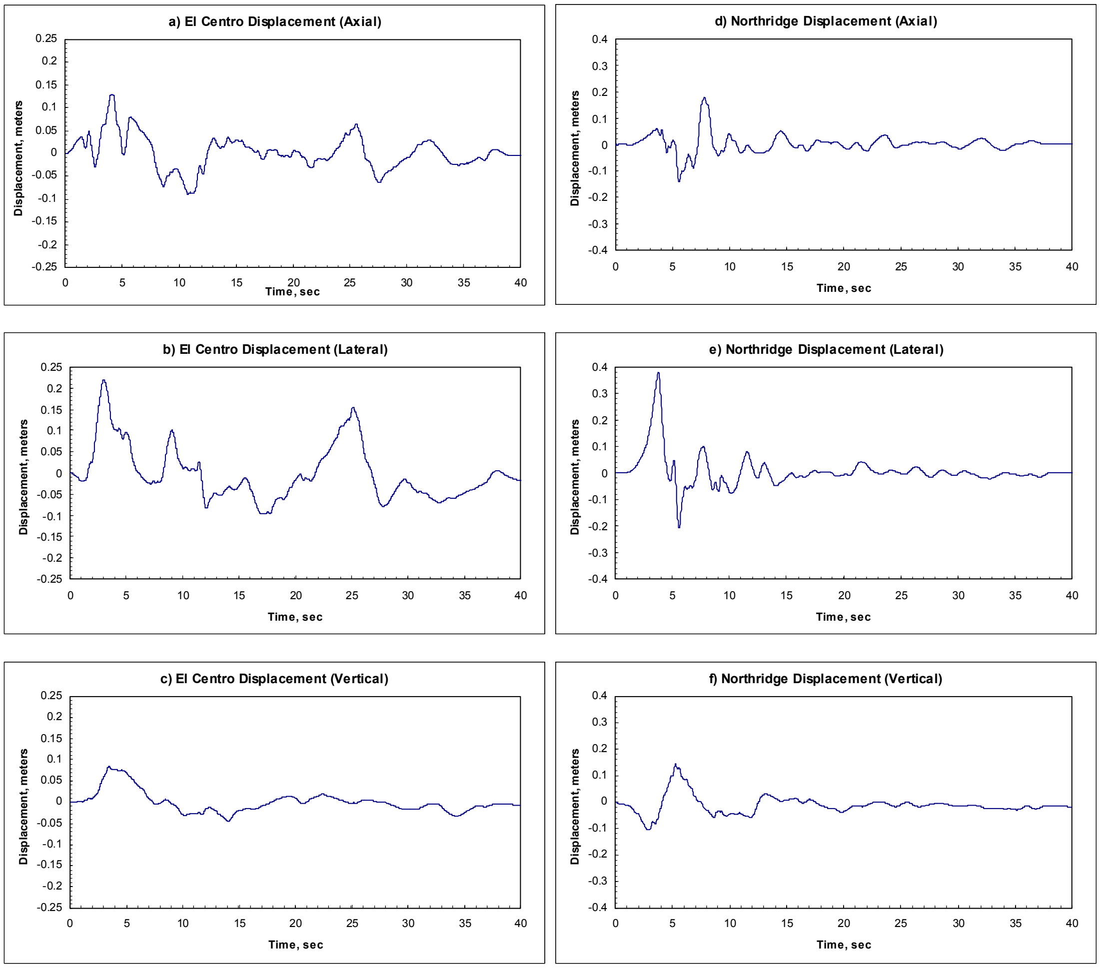

Figure 2.12 – Displacement time histories of the 1940 Imperial Valley - El Centro and the 1994 Northridge - Newhall earthquake records. a) Imperial Valley axial displacement. b) Imperial Valley lateral displacement. c) Imperial Valley vertical displacement. d) Northridge axial displacement. e) Northridge lateral displacement. f) Northridge vertical displacement.

2.5.2 Scaling of seismic records

The Northridge and Imperial Valley records were both linearly scaled to a PGA of 0.7g in the axial direction and applied as a forced displacement at the boundary of the model. The scaling factor was 1.187 for the Northridge record and 2.237 for the Imperial Valley record. The 2.237 factor for the Imperial Valley record stretches the approximate limit of 2.0 for magnifying earthquakes' time histories and spectra. This limit is a ballpark figure to bind the amplification of earthquake records to realistic magnitudes with realistic frequencies. The Northridge record at Newhall exhibits some characteristics of a near-field event with a few pulse-like velocity cycles with larger amplitudes and periods. Conversely, the Imperial Valley record used was a far-field event, with a log of many small velocity cycles at somewhat lower periods (Liao et al. 2004, Manfredi et al. 2003). The upshot is that by amplifying the time history and spectra of an earthquake by more than 100%, the scaled record may represent an event that could not be reproduced with simply a larger earthquake. The Imperial Valley record was scaled to a PGA of 0.7g in the axial direction of the structure by both DesRoches and Delemont (2002) and Kim et al. (2000), therefore the same procedure was used in this thesis. The vertical and lateral records were scaled by the same factors.

The advantage of scaling was that the magnitude of response from both records would be approximately the same, as can be seen by comparing Figure 2.13, where the magnitude of the response of the smaller Imperial Valley event was less for most of the spectrum, with Figure 2.14, where the magnitude of the responses were approximately the same. Both 3% and 5% of critical damping are shown because the material damping of the models was selected to be 4%, as described in section 2.6; a response spectrum of this damping was not provided by PEER (2005).

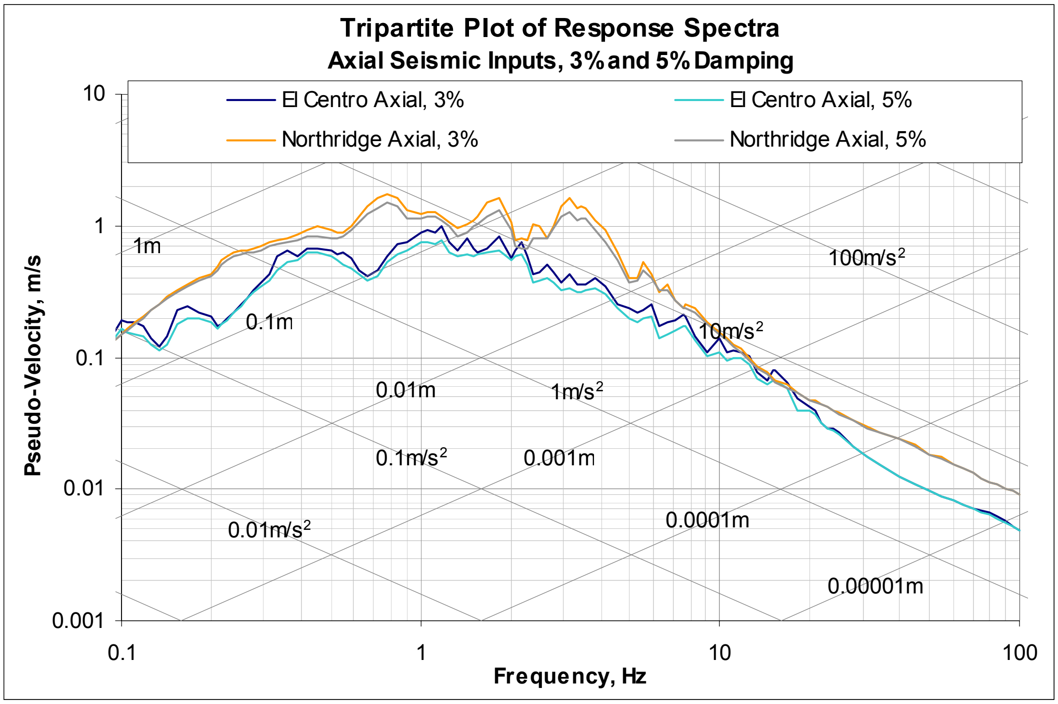

Figure 2.13 - Response spectra of original axial seismic inputs.

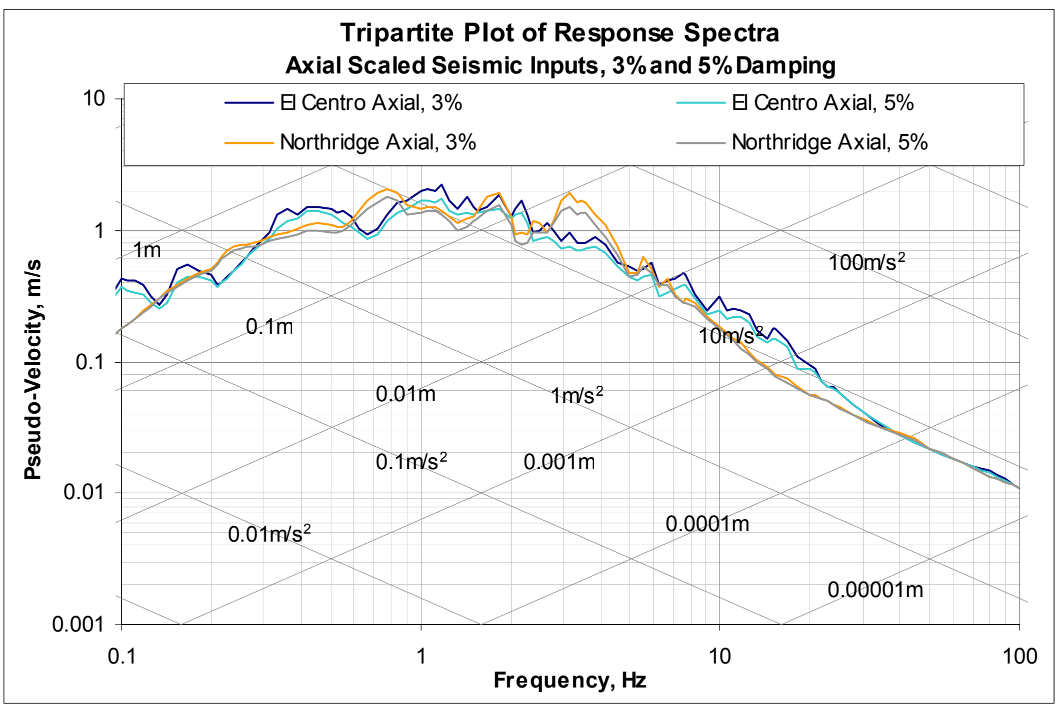

Figure 2.14 – Response spectra with axial seismic inputs scaled to 0.7g PGA.

Additional acceleration and displacement time histories, spatial acceleration and displacement plots, and tripartite plots of spectral response are provided in Appendix B.

2.5.3 Input file keywords

The Earthquake step was defined in lines 390-468 in Appendix C. The displacement time histories of the three orthogonal components of the seismic record are scripted unscaled under the keyword *Amplitude. The axial, lateral, and vertical component of the record are scripted in lines 245-255, lines 266-276, and lines 277-287, respectively. With the keyword *Boundary in the Earthquake step, the amplitudes are then assigned to the proper nodes in lines 400-426.

2.6 Damping

Three types of damping were provided. First, material damping was used to accurately model the response of a prestressed girder bridge. Second, default numerical damping was manipulated to reduce the oscillations of the structure before the introduction of seismic loading. Third, contact damping was defined to complete the definition of the bearing material.

2.6.1 Material damping

Damping in ABAQUS/Explicit was defined using Rayleigh damping parameters, α and β, in the equation modified from Chopra (1995):

$$\xi_i = \frac{\pi\alpha}{f_i} + \frac{\beta f_i}{4\pi} \qquad (2.7)$$

where ξ_i = fraction of critical damping for a given mode i

α = mass proportional Rayleigh damping parameter (Hz)

β = stiffness proportional Rayleigh damping parameter (sec)

f_i = natural frequency for mode i (Hz)

Rayleigh damping allows two frequencies to be damped at a given critical level. However, there was great computational cost to use the stiffness proportional parameter. When this parameter was used in this analysis, increment times decreased from $2\text{x}10^{-5}$sec to $5\text{x}10^{-8}$sec. Therefore, damping a single low frequency with only mass proportional damping was preferable. For this analysis the frequencies most excited by the vertical input ground motions were between about 0.05Hz and 30Hz, as seen in Figure 2.14, with most excitation between 0.2 and 10Hz. The first modal frequency of the test spans, shown in Table 2.7 without material damping in an ABAQUS/Standard test with pin-pin conditions, were generally between the same bounds. Therefore, the damping parameter, α, was selected to damp the structure at 4% of critical for the first mode only. Four percent damping was the median of damping recommended by other researchers for prestressed concrete spans (Caner et al. 2002; Zhang 2000; DesRoches and Fenves 2000). Simplifying Equation 2.7 for this analysis results in the following equation:

$$\alpha = \frac{0.04 f_1}{\pi} \tag{2.8}$$

The damping parameters used and first three natural frequencies of the test spans are presented in Table 2.7.

Table 2.7 – Natural frequencies and the Rayleigh damping parameters for the six test spans.

Span Designation	1st Natural Frequency, Hz	2nd Natural Frequency, Hz	3rd Natural Frequency, Hz	Rayleigh Parameter, α, Hz	Rayleigh Parameter, β, sec
Span1	16.1	39.0	94.6	0.2054	0
Span2	6.26	15.7	38.3	0.0797	0
Span3	4.36	10.9	26.6	0.0555	0
Span4	3.67	9.11	22.3	0.0467	0
Span5	8.37	20.4	49.6	0.1066	0
Span6	9.29	22.2	54.0	0.1183	0

2.6.2 Numerical damping

Numerical damping is a default setting for ABAQUS/Explicit in the form of linear bulk viscosity and quadratic bulk viscosity. These parameters were provided to damp the highest element frequency and to prevent the collapse of an element under extremely high changes in velocity, such as an impact condition. The formula for the fraction of critical damping for this mode was (ABAQUS 2003a):

$$\xi = b_1 - b_2^2 \frac{L_e}{c_d} \min(0, \dot{\varepsilon}_{vol})^2 \tag{2.9}$$

where ξ = fraction of critical damping for highest dilatational mode of each element

b_1 = linear bulk viscosity coefficient

b_2 = quadratic bulk viscosity coefficient

L_e = element characteristic length

c_d = dilatation wave speed

The linear bulk viscosity was raised from the default of 0.06 to 1.00 to help damp the initial gravity application, but these parameters were returned to the default settings during the earthquake input, as discussed in section 2.7.

2.6.3 Contact damping

Stiffness related damping is available for soft contact definitions in ABAQUS/Explicit. The formula used to calculate the contact damping force was (ABAQUS 2003a):

$$f_{vd} = \mu_0 \sqrt{4mk_c}\, v_{rel} \tag{2.10}$$

f_{vd} = damping force (N)

μ_0 = fraction of critical damping associated with the contact stiffness

m = nodal mass (kg)

k_c = contact stiffness (N/m)

v_{rel} = relative velocity between contact surfaces (m/s)

A critical damping fraction of 0.10 was used to damp the motion of the bearing pad interaction.

2.6.4 Input file keywords

The keywords and line numbers referenced are in Appendix C. Material damping is applied with the *Damping keyword in line 292. Numerical damping is applied to gravity step in lines 329-330 and to the earthquake step in lines 395-396. *Contact damping is found on lines 305 and 306.

2.7 Gravity Step

The proper implementation of the gravity step was essential to creating the proper initial conditions for seismic loading. ABAQUS does not allow any loading during the initial step, therefore an intermediate step must be used to apply gravity to the structure. Also, in ABAQUS/Explicit, a static step cannot be used to apply gravity and other pre-existing loads. The GRAV option for the *DLOAD keyword was used to apply a downward acceleration of $9.81 m/s^2$ to the entire model. Span4, without material damping, was used to determine the best way to quickly apply the gravity load to the structure without residual oscillations. This setup was considered a worst case scenario for this research. Palm (2000) was referenced for development of the loading ramps.

2.7.1 Development of the gravity step

First, as seen in Figure 2.15, the gravity load was applied instantaneously, creating large oscillations for many seconds after application. Next, a linear deflection ramp was applied to the midspan of the structure that was released at the expected midspan deflection, calculated in Appendix A as 0.055m, and replaced by the full gravity load.

The span still had oscillations from the inertia of the two shorter spans, so large oscillations at midspan still occurred when this forced deflection was released. Two more tests were conducted that allowed more time and a smoother transition to lessen the amount of energy in the system through the small amount of default numerical damping. However, in all three tests using deflection ramps, as seen in Figure 2.16, the small difference between the expected and the model static deflection, as well as the energy from the rest of the span, created an unacceptable amount of oscillations in the span.

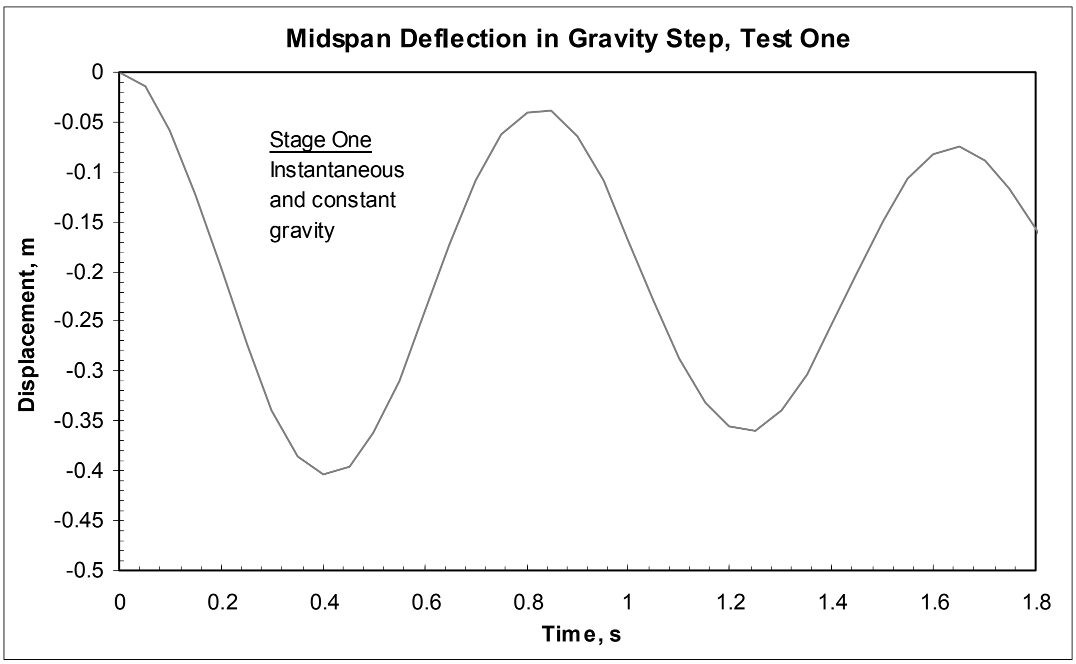

Figure 2.15 – Mid-span deflection of instantaneous, undamped gravity load

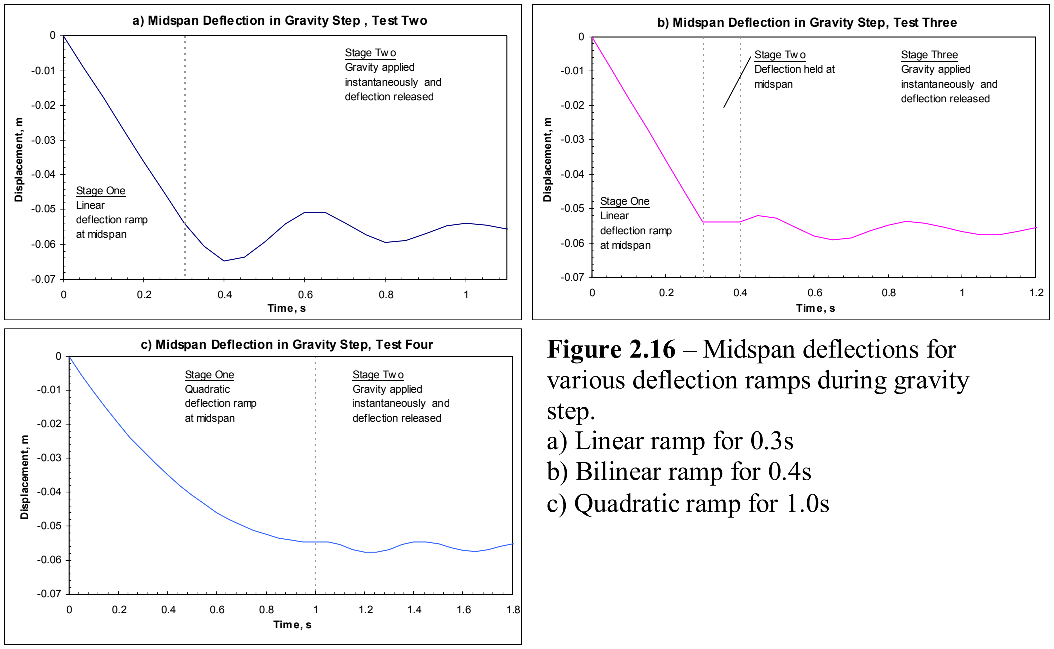

Figure 2.16 – Midspan deflections for various deflection ramps during gravity step.
a) Linear ramp for 0.3s
b) Bilinear ramp for 0.4s
c) Quadratic ramp for 1.0s

A quadratic gravity ramp, such as the one illustrated in Figure 2.17, was then applied to the model. In the sixth test, the linear bulk viscosity, a numerical damping parameter, b_1, as described in section 2.6.2, was increased to 0.40 for the duration of the first step.

2.7.2 Final gravity step

By the eighth test, the gravity ramp was lengthened to 1.5sec with a b_1 value of 1.00 for the entirety of the gravity step. With this procedure, the gravity load on the longest span without material damping was applied in two seconds with a resulting oscillation at the end of the step of approximately 3mm. Therefore, a two-second step was executed to apply gravity and damp any motion at the beginning of all tests. The results of the final four gravity step tests are presented in Figure 2.18.

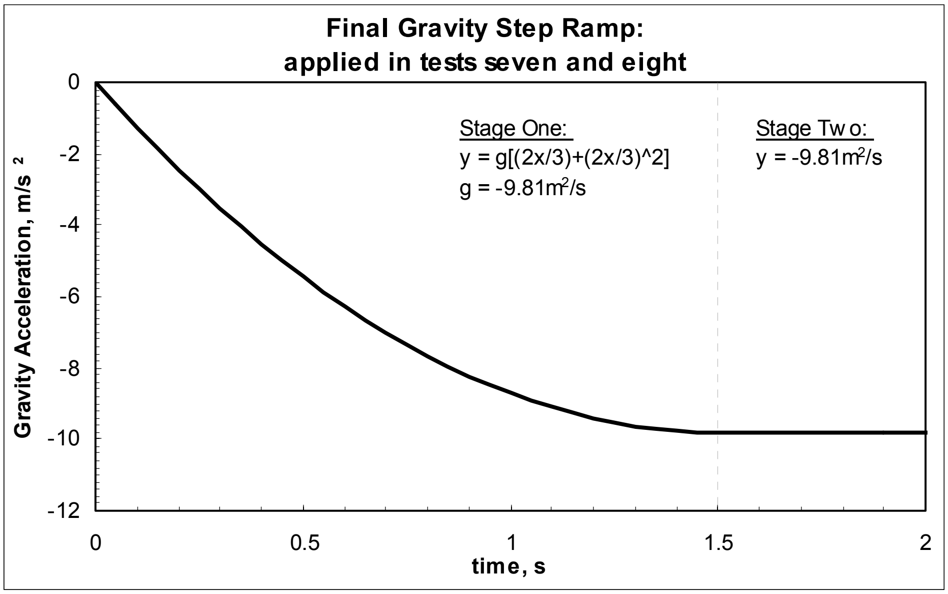

Figure 2.17 – Quadratic ramp used to smoothly apply gravity load.

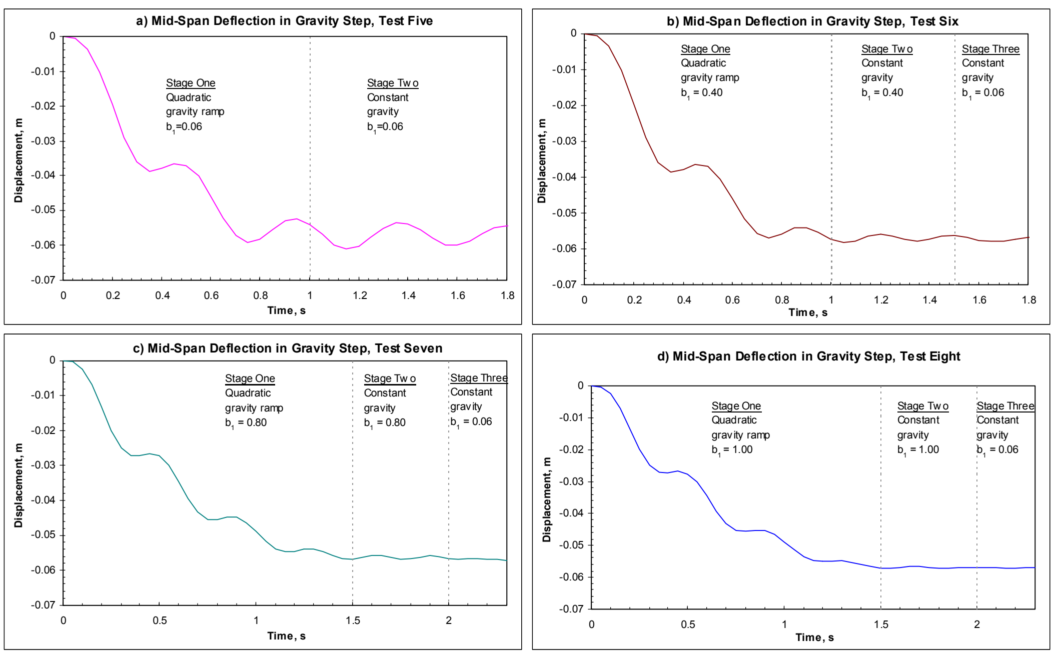

Figure 2.18 – Midspan deflections for various gravity ramps and linear bulk viscosity values during gravity step. a) Quadratic ramp for 1.0s with b_1=0.06. b) Quadratic ramp for 1.0s with b_1=0.40. c) Quadratic ramp for 1.5s with b_1=0.80. d) Quadratic ramp for 1.5s with b_1=1.00.

2.7.3 Input file keywords

The keywords and line numbers referenced are in Appendix C. The gravity step is defined in lines 323-387. The keyword *Amplitude is used to define points on the quadratic gravity ramp in lines 256-265. As mentioned in previous sections, numerical damping for the gravity step is defined in lines 329-330 and the magnitude and direction of gravity is defined with the keyword *Dload in lines 335-336.

Chapter Three
Variables, Measurements, and Limitations

3.1 Introduction

The previous chapter explained the process of constructing a model to mimic the behavior of a simple-span bridge subjected to seismic events. However, many of the properties and components discussed, for example bending stiffness of the span and bearing pad compression stiffness, are only the framework and background behaviors that shape the true focus of this thesis: measurement and mitigation of axial span displacement. Therefore, the success of a test is measured by evaluating the movement of a few key nodes and the force levels in the SCEDs. This chapter contains the methodology regarding the input variables, a description of the nodes and elements where output data was collected, and a discussion on assumptions and limitations of the models. The goal of this chapter is to articulate the exact scope and limitations of the data in the following chapters so that erroneous extrapolations are avoided.

3.2 Input Variables

3.2.1 Span dimensions

The length of the span was varied between 12.2, 24.4, 36.8, and 45.7m. Half of the tests focused on spans of 24.4m. The two shorter spans are much more common for simple-span construction. The longer spans were included to understand the response of a full range of frequencies and length to width ratios. However, with use of the longer, more massive spans comes the danger of encountering properties not included in this analysis, such as concrete cracking, nonlinear stiffness, and higher-mode excitation.

Girder spacings of 1.981, 2.438, and 2.896m were considered, with four of the six spans utilizing the 1.981m spacing. As with longer span lengths, the wider spacings are included in the analysis to explore the possible effect of changing this variable. However, with the approximate rectangular section, the moment of inertia of the span about the axial direction is ignored. For a dense spacing of short girders, especially spacings with minimal clear spacing between the top girder flanges, the bending stiffness would remain relatively large and in the range of this analysis. But for the wider spacings and deeper girders, large lateral loads at the base of a girder could result in bending about the axial direction and crack development in the deck between the girders, which this analysis does not consider. Figure 3.1 shows the plan dimensions of the six spans considered.

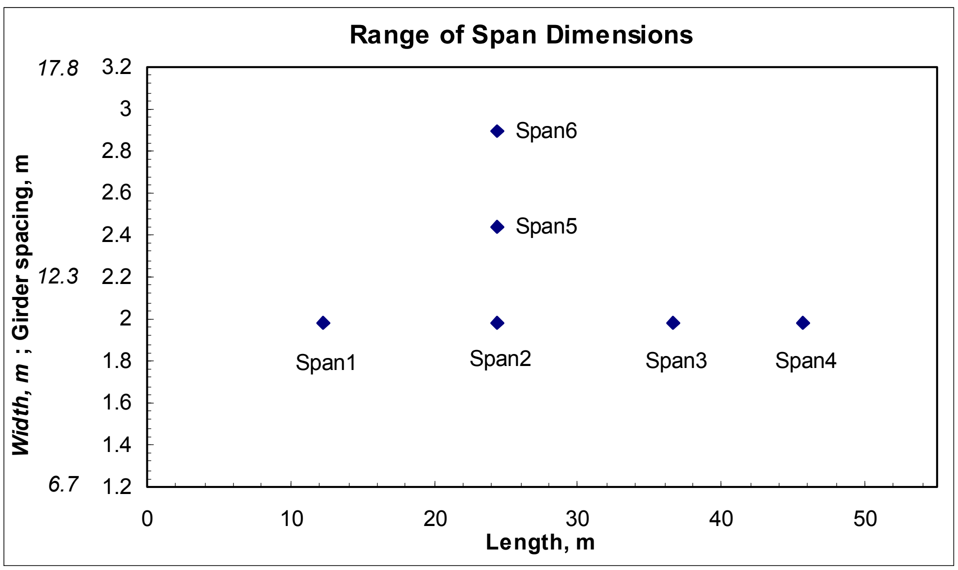

Figure 3.1 – Range of span dimensions, width or girder spacing versus length.

Composite depths of 0.927, 1.333, 1.740, and 1.943m were used. The same concerns apply with the depth as with length and width: as the dimension increases in magnitude, the stiffness of components at a local or global scale may become a concern. Figure 3.2 shows the relationship between composite depth and length for the spans considered.

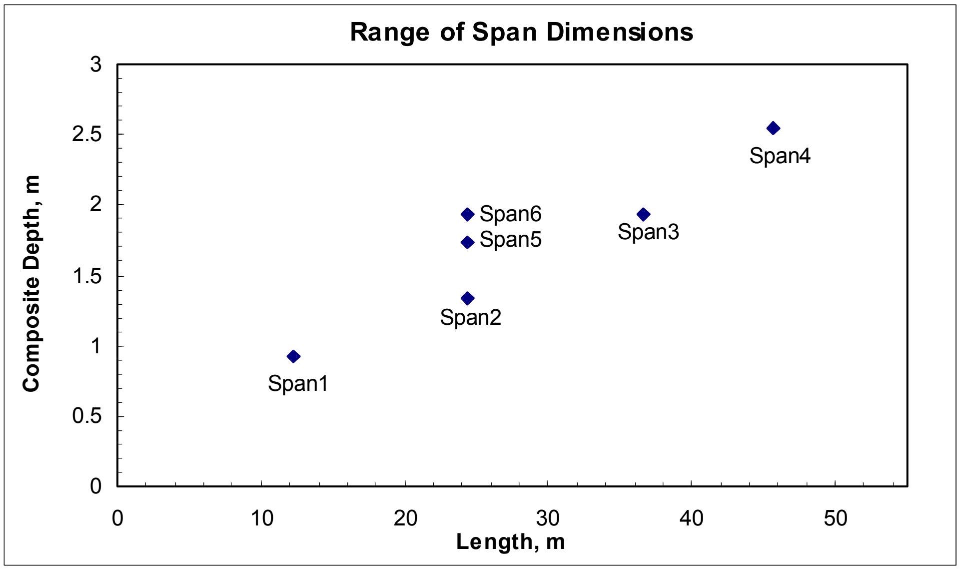

Figure 3.2 – Range of span dimensions, depth and length.

Concluding, the analysis method used here best represents spans that are wholly composite and are relatively rigid for longitudinal and transverse loading. Therefore, the tests of shorter spans with a close girder spacing are probably best suited for this analysis.

3.2.2 SCED stiffness

Initial tests were conducted to estimate the range of SCED stiffnesses that were required to restrain the spans for these strong ground motions. The first tests then applied SCEDs with the estimated stiffness levels. The success of these tests was then evaluated and a second stiffness was selected for a second round of tests. Table 3.1 presents the stiffness used in each test.

Table 3.1 – SCED stiffness for each test. "No SCED" tests had a linear stiffness of 1N/m so that the geometry of the models could be maintained.

Test	Stiffness of SCED			
Earthquake/ Span Designation	**Axial EQ only, no SCED, kN/m**	**No SCED test, kN/m**	**First SCED test, kN/m^1.3**	**Second SCED test, kN/m^1.3**
Imperial Valley/Span1	0.001	0.001	52,700	36,900
Imperial Valley/Span2	0.001	0.001	79,100	58,000
Imperial Valley/Span3	0.001	0.001	105,400	89,600
Imperial Valley/Span4	0.001	0.001	131,800	179,200
Imperial Valley/Span5	0.001	0.001	79,100	63,300
Imperial Valley/Span6	0.001	0.001	105,400	84,300
Northridge/Span1	0.001	0.001	52,700	42,200
Northridge/Span2	0.001	0.001	79,100	63,300
Northridge/Span3	0.001	0.001	105,400	147,600
Northridge/Span4	0.001	0.001	131,800	179,200
Northridge/Span5	0.001	0.001	79,100	68,500
Northridge/Span6	0.001	0.001	105,400	84,300

3.3 Output Measurements - Key Nodes and Elements

3.3.1 Corner nodes

Three-dimensional displacement of key nodes was recorded and used to judge the success of SCED tests to control the span. Figure 3.3 shows the node names that are referred to in future chapters. Due to the generally rigid body motion, the maximum three-dimensional displacement in the span occurs at one of the four corner nodes marked Nodes 98, 104, 141, and 143, so these are of primary focus.

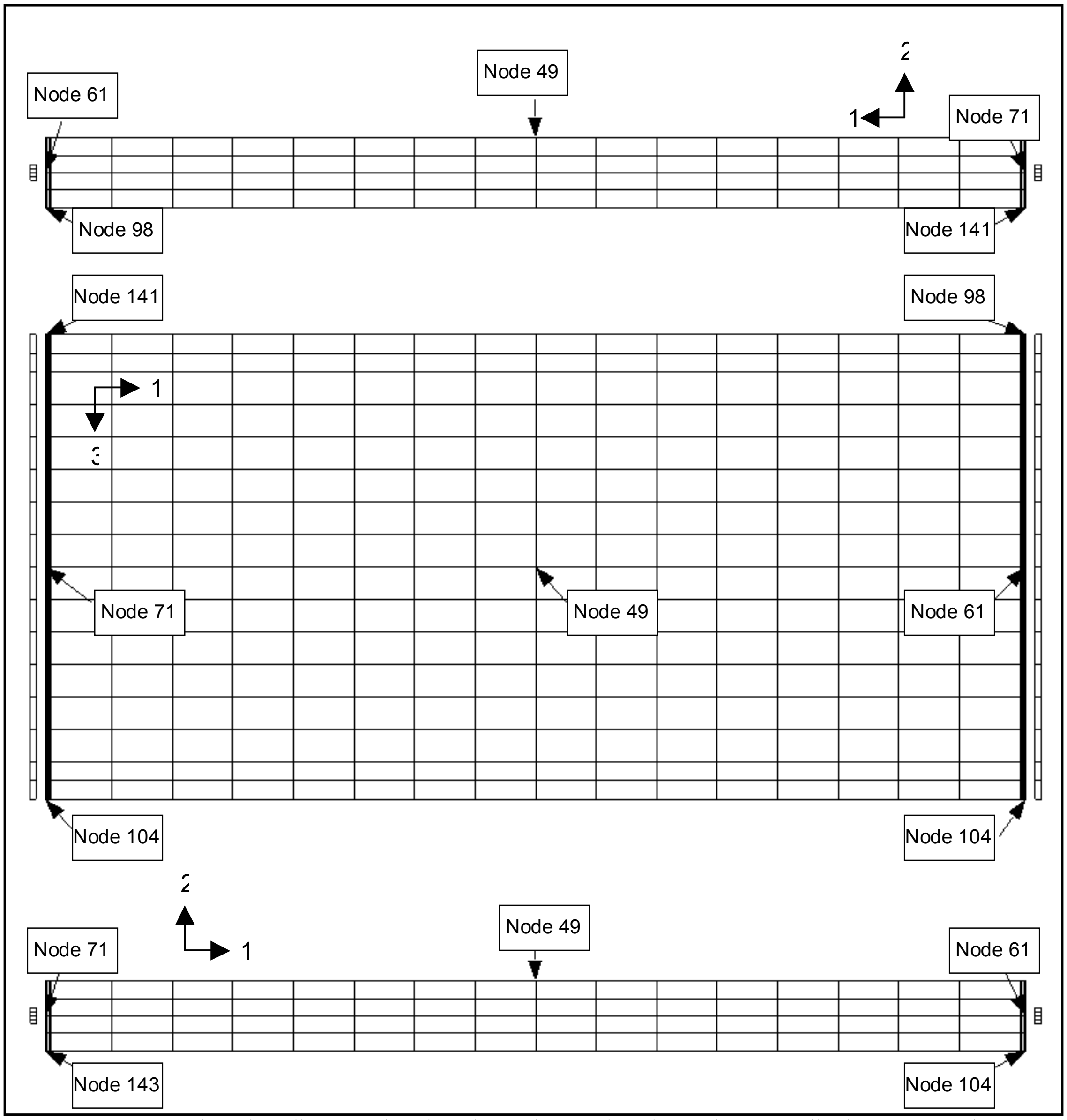

Figure 3.3 – Node location diagram showing the nodes used to determine span displacement and behavior.

A test was considered a success if, for the entire test, the axial displacement of all of the corner nodes was less than the sum of the shear displacement limit, 17.5mm, and the slip displacement limit, 76.2mm, a total of 93.7mm.

Tests were stopped after they had an axial deflection of two-thirds of the bearing width, 101.6mm. The remaining width, 50.8mm, would likely not have an effective compressive stiffness similar to the values used. By placing the span near the edge of the pad, the plain elastometric pad would severely bulge and possibly even ‘walk’ out from under the span. If it did not walk from under the span, conditions of increased stiffness, or strain hardening, could exist and cracking of the bearing pad could occur after being compressed approximately 16mm or more. Also, after severe axial displacement, the span would probably experience some pounding against one of the abutment faces, which is not supported by this analysis.

Pounding and opening of a joint would be a worst case scenario for these models. In multi-span bridges the columns or frames have movements that are unique from the abutment motion because of the fundamental frequency of the column or frame. In this analysis, the abutments are both assigned to follow the recorded ground motion, so relative displacement is caused by the inertial force of the span. However, since there is no differential movement between the two abutments, a span would never be able to completely collapse, only collide with the abutment since the opening is never wider than the span itself. Worst case scenarios are pounding of the girders against the abutment and unseating from the bearings.

No hard limits were imposed on lateral motion, though the lateral motion is observed and discussed in the following chapters.

3.3.2 Midspan measurements

The vertical displacement of Node 49, at the center of midspan, provides a check of the dead load displacement at the end of the gravity step and is the best location to measure vertical excitation. Large amplitudes in the vertical displacement of Node 49 can be followed by axial slip at the bearings due to the reduction of normal force and the resulting reduction in axial resistance from friction.

Excessive vertical displacement of Node 49 could indicate that cracking would occur, which is not considered in this analysis. Significant cracking would primarily affect the bending stiffness of the structure and could have an effect on the accuracy of remaining measurements in that test. In multi-span bridges, cracking must be analyzed because cracks in a column of a simply supported bridge, or anywhere in a continuous bridge, can create a plastic hinge that alters the period of the structure and the amplitude of what would be the input motion for the setup used in this thesis. However, for a single simple span, as analyzed here, cracks would affect the bending stiffness and the periods of the bending mode frequencies discussed in Chapter Two. This may have secondary effects on the bearing resistance and inertia of the span, but the effects on axial and lateral motion would remain limited.

No hard limits were imposed on vertical motion, though the vertical motion is observed and discussed in the following chapters.

3.3.3 SCED connection nodes and measurements

The forces in the spring elements were observed. A test with pulse-like load cycles in the springs was desired. Pulses indicate that the force generated by the snap of the SCED was sufficient to reverse the motion of the span back towards the initial position of the span. The force records also indicate if the load in the SCEDs was distributed uniformly across the span in the lateral direction or if the span undergoes rigid body rotation that disproportionately loads the SCEDs at the exterior girders. As shown in Figure 3.4, the spring elements are labeled “SCED 1” through “SCED 10”.

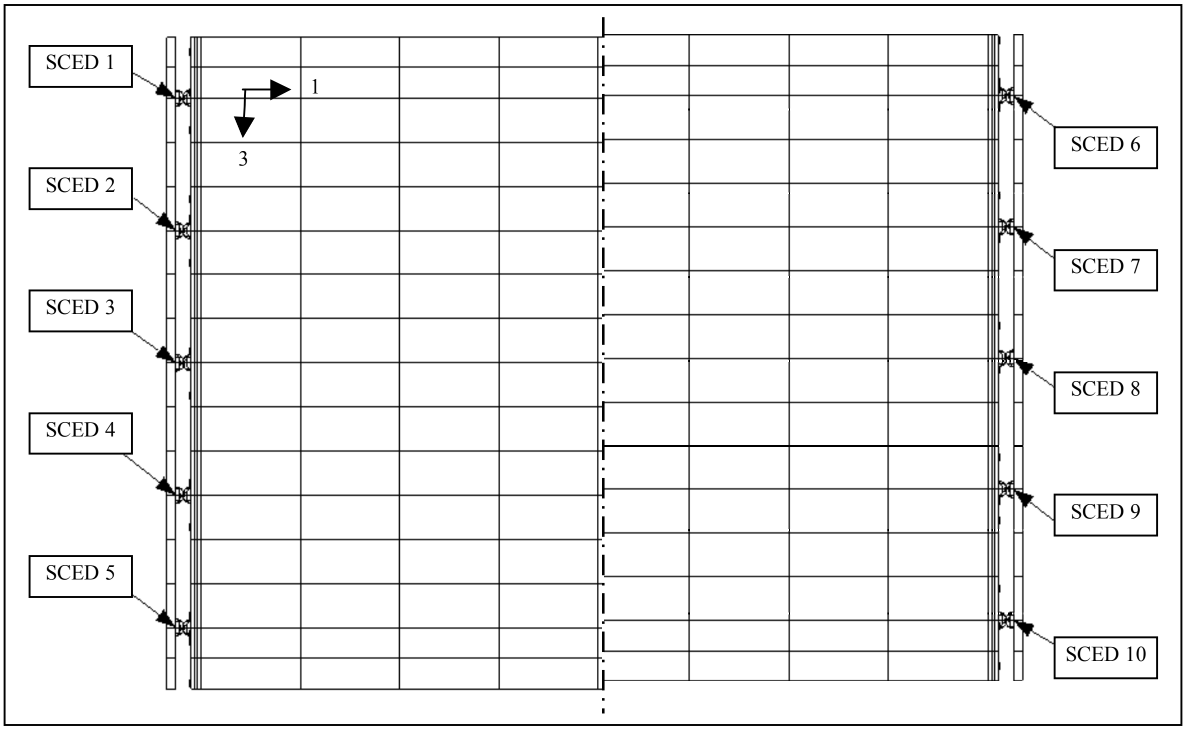

Figure 3.4 – Locations and names assigned to SCEDs in the model.

Nodes 71 and 61 are located in the center of the end-faces of the span. They are the connection nodes for the centermost spring on each end of the span. The nodal displacements, particularly when the springs became taut, were observed to ensure that the springs, not the span, undergo the vast majority of deformation when loaded. Modest deformations would occur in any connection scheme. However, this thesis does not in any way attempt to model the connection of the SCEDs to the girder or abutment. Past research (DesRoches et al. 2003), has indicated that the connections of retrofits can often be the weakest component in the assembly. As implied in section 2.5, the stiffness specified assumes that the connection would be at least as stiff as the SCED.

A sample history output request is shown in Appendix C. Acceleration and displacement are requested in the principal directions for the nodes described above and the load on the springs is requested in lines 361-385 for the gravity step and lines 442-467 for the earthquake step.

Chapter Four
Effect of Three-Dimensional Seismic Records

4.1 Introduction

The purpose of this chapter is to compare the response of unrestrained bridge spans using only the axial seismic input record to the response of bridge spans using all components of the three-dimensional seismic record. Previous researchers often used only the axial or only the axial and vertical components of the seismic record. The general practice to ignore one or both of the non-axial components raised the question of whether or not these earthquake components were necessary to understand the axial response of the simple span structures in this research.

These two types of seismic input records were analyzed by comparing the axial displacement of the corner nodes, Nodes 98, 104, 141 and 143. The four corners were compared simultaneously by determining the most severe displacement at any corner for any given time. Test data past the "terminal limit" of 0.1016m was removed because the compression stiffness and bearing behavior was not modeled for displacement past this limit. Without SCEDs, data for the Imperial Valley tests and the Northridge tests were generally terminated at approximately 2.0s and 5.3s, respectively. The displacement of a typical corner subjected to the Imperial Valley Earthquake is shown in Figure 4.1. The typical displacement of a corner subjected to the Northridge Earthquake is shown in Figure 4.2. All graphs are shown full-size in Appendix D.

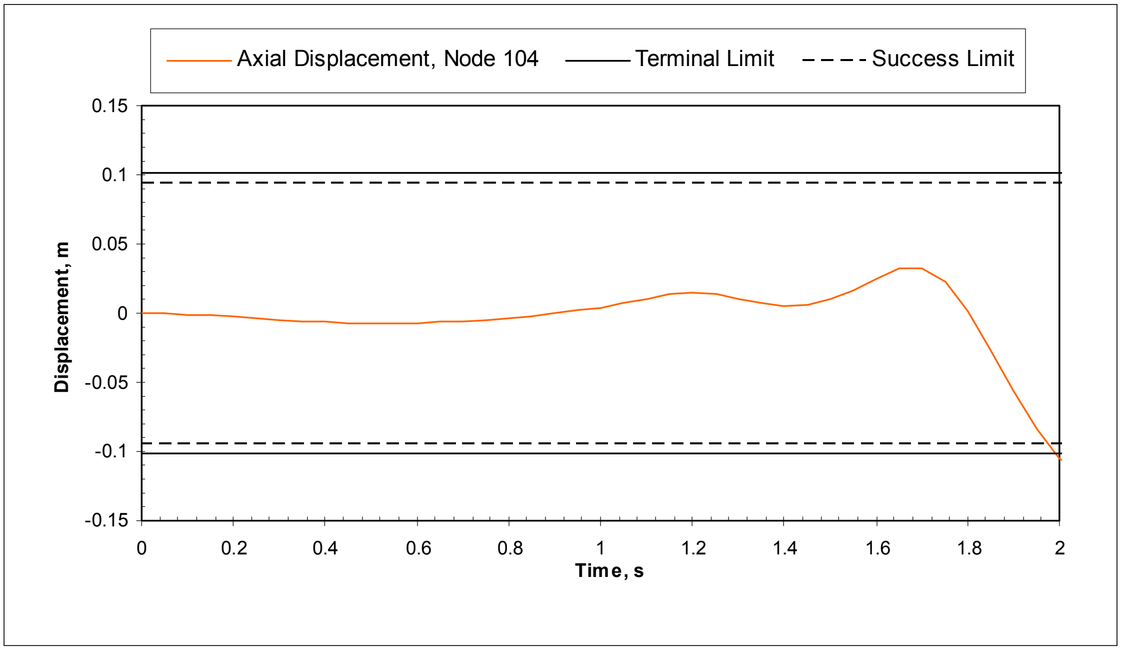

Figure 4.1 – Typical corner axial displacement of an Imperial Valley test. Example is from Node 104 of Span2 with a full three-dimensional seismic record.

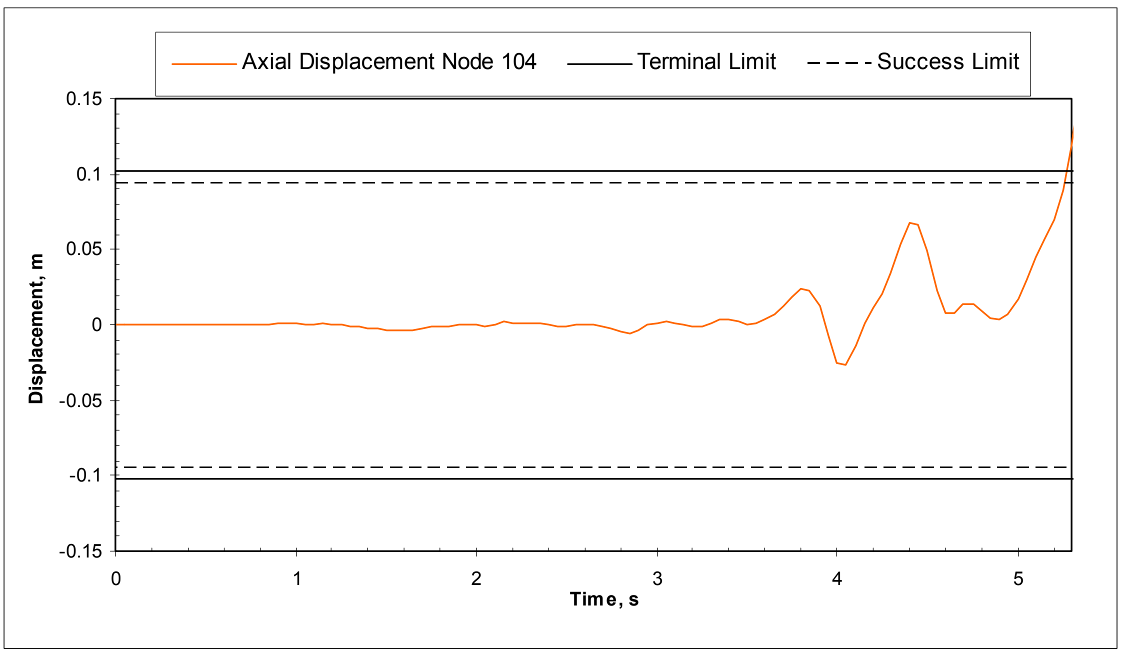

Figure 4.2 - Typical corner axial displacement of a Northridge test. Example is from Node 104 of Span2 with a full three-dimensional seismic record.

The maximum absolute value of the displacement of the four corners is then plotted versus time to create a record of the most severe axial displacement, as shown in Figure 4.3.

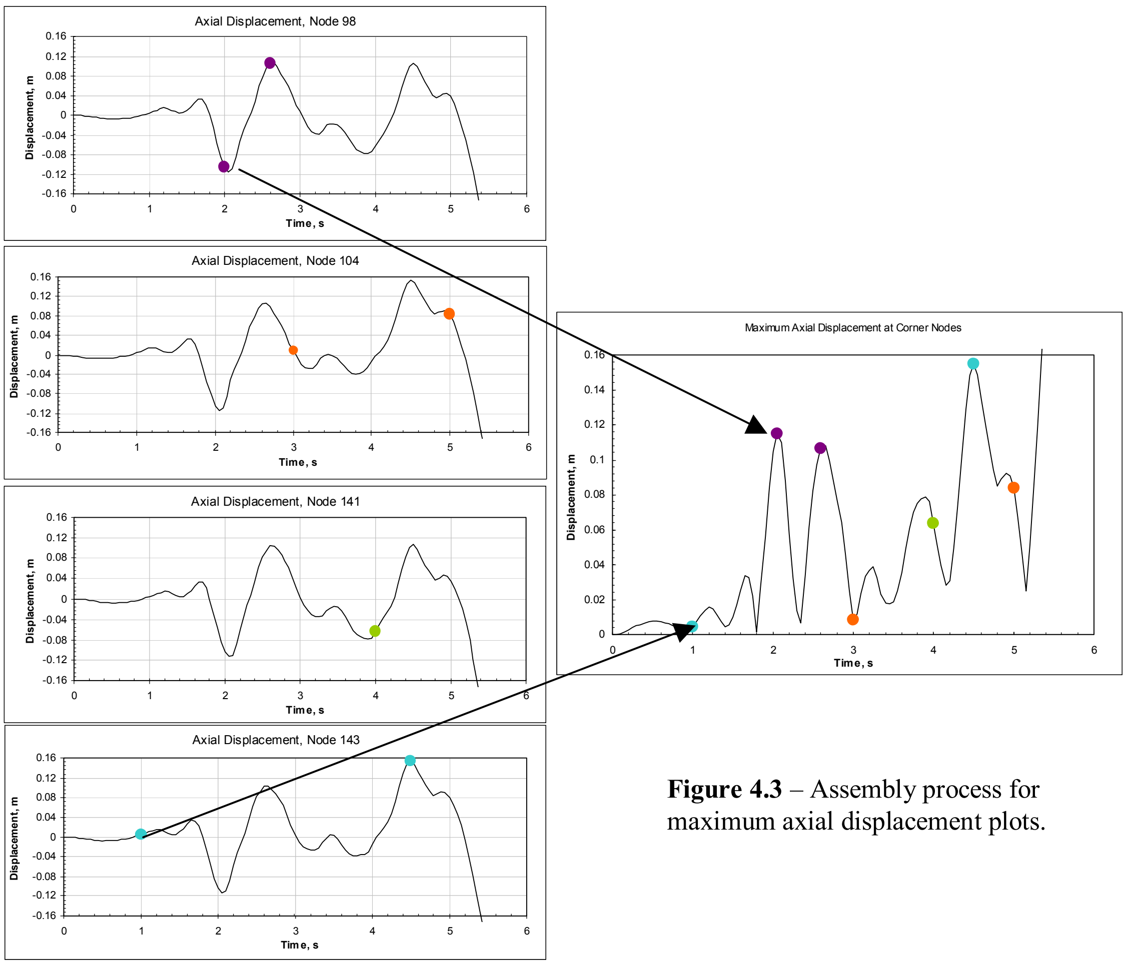

Figure 4.3 – Assembly process for maximum axial displacement plots.

The advantage of maximum displacement plots is that, if a span rotates about the vertical axis, measuring only the displacements of a single node may produce results that appear to have no displacement. In reality, another location of the span could have already displaced off of the bearing. Such is the case with Nodes 143 and 141 in the example shown in Figure 4.3. At 4.5s, Node 143 displaced from the bearing while Node 141 is almost within the acceptable limit. The disadvantage of the maximum axial displacement plots is that only magnitude is measured. Therefore the displacement direction, positive or negative, is lost. Two typical maximum axial displacement plots are shown in Figures 4.4 and 4.5. This chapter uses the maximum axial displacement plots and single corner displacement plots to understand the relationship between the axial displacement and seismic input records orthogonal to the axial direction.

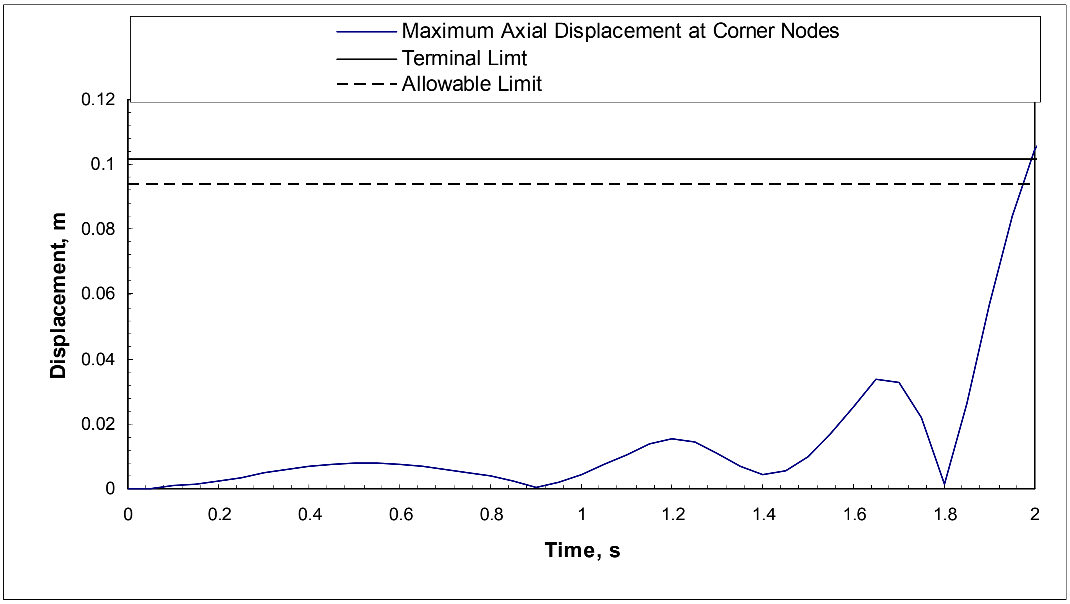

Figure 4.4 - Typical maximum axial displacement of any corner node for an Imperial Valley test. Example is from Span2 with a full three-dimensional seismic record.

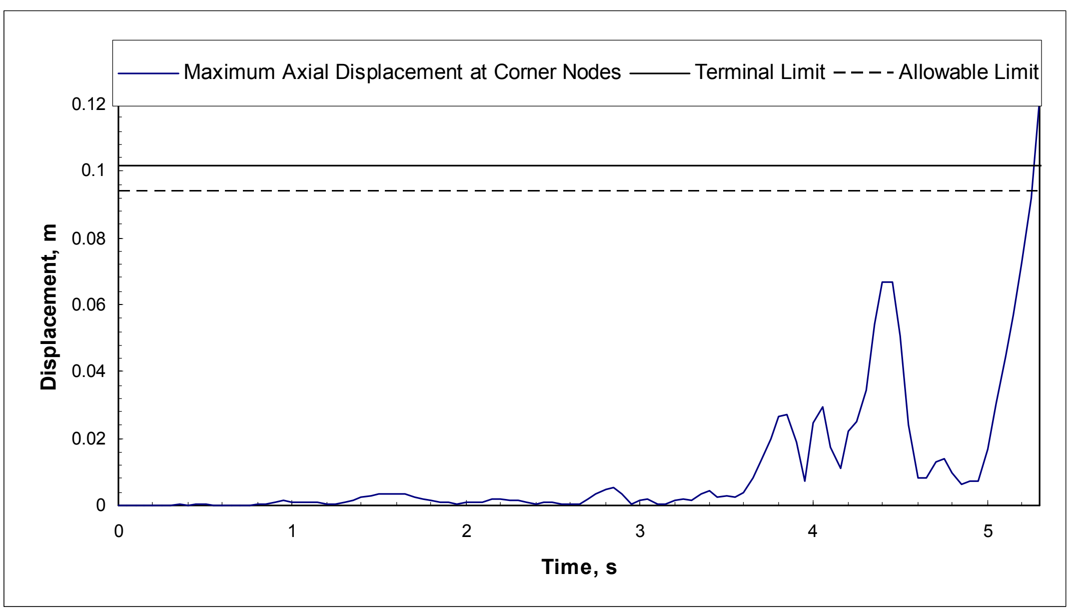

Figure 4.5 - Typical maximum axial displacement of any corner node for a Northridge test. Example is from Span2 with a full three-dimensional seismic record.

4.2 Data and Analysis

4.2.1 Data and analysis from Imperial Valley tests

Figures 4.6-4.12 show the maximum axial displacement from the Imperial Valley tests. Figures on the left are from tests that only used axial seismic input records. Tests on the right used all seismic components.

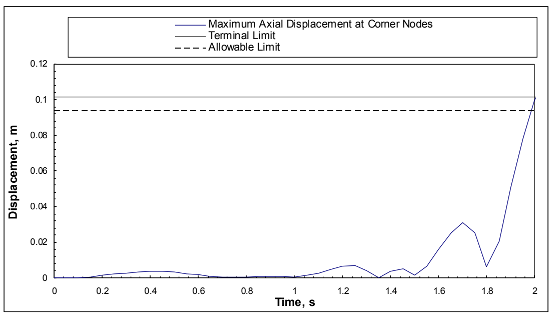

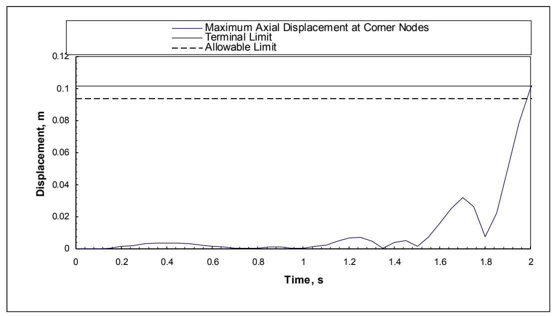

Figure 4.6 – Maximum corner node displacements for Span1 subjected to the Imperial Valley event. (a) Response for axial seismic input only. (b) Response for three-dimensional seismic input.

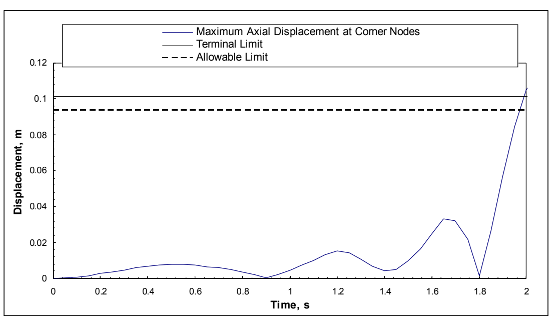

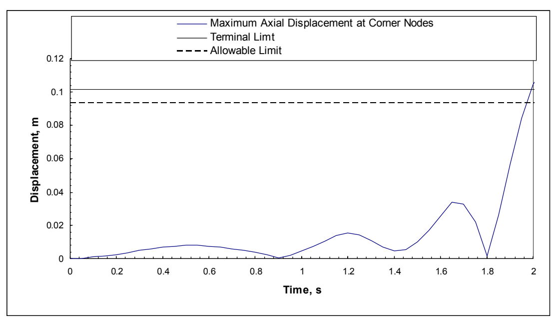

Figure 4.7 – Maximum corner node displacements for Span2 subjected to the Imperial Valley event. (a) Response for axial seismic input only. (b) Response for three-dimensional seismic input.

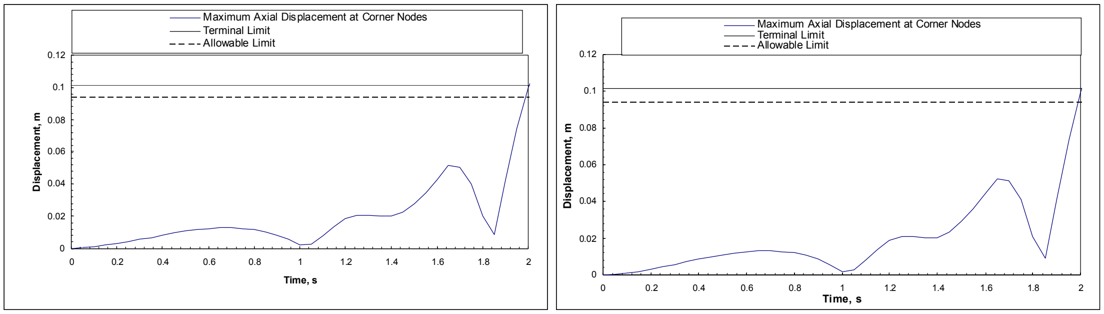

Figure 4.8 – Maximum corner node displacements for Span3 subjected to the Imperial Valley event. (a) Response for axial seismic input only. (b) Response for three-dimensional seismic input.

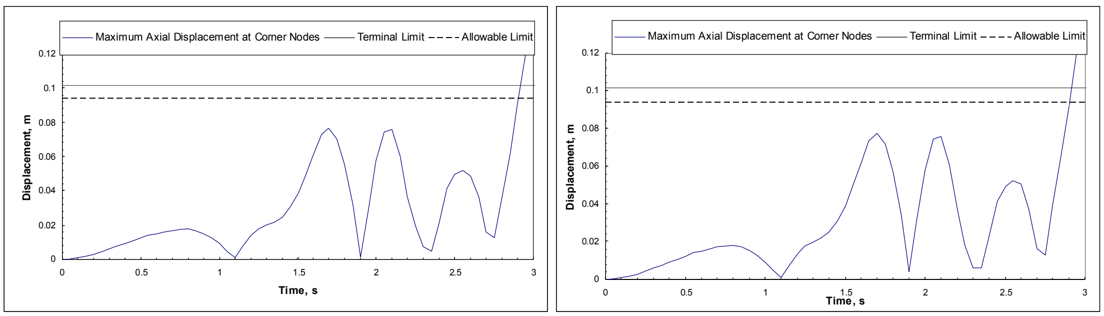

Figure 4.9 – Maximum corner node displacements for Span4 subjected to the Imperial Valley event. (a) Response for axial seismic input only. (b) Response for three-dimensional seismic input.

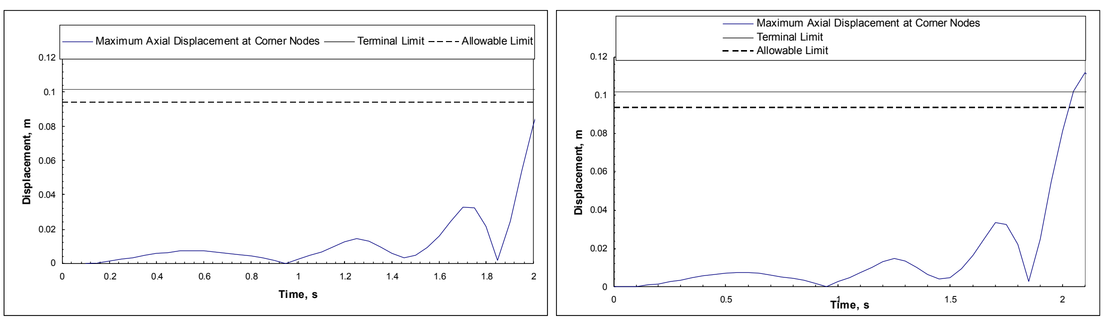

Figure 4.10 – Maximum corner node displacements for Span5 subjected to the Imperial Valley event. (a) Response for axial seismic input only. (b) Response for three-dimensional seismic input.

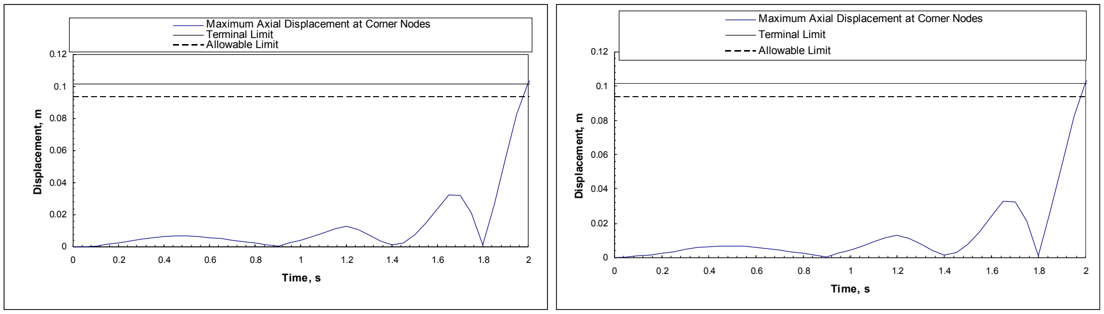

Figure 4.11 – Maximum corner node displacements for Span6 subjected to the Imperial Valley event. (a) Response for axial seismic input only. (b) Response for three-dimensional seismic input.

It is important to note from these plots that there is little change between the two types of tests. Most of the tests have only one large displacement cycle, between approximately 1.6s and 1.8s, before reaching the terminal limit. It is possible that the displacements would eventually diverge. However, the one test that contained three complete displacement cycles, Span4, had little change between the axial input tests and the three-dimensional input tests. Therefore, it may be concluded from the Imperial Valley tests that including lateral and vertical seismic input components has little effect on axial displacement.

4.2.2 Data and analysis from the Northridge tests

The Northridge record has the largest axial and vertical displacements at approximately 5.0s. Therefore several displacement cycles can be observed before a test is terminated. Unlike the Imperial Valley tests, the three-dimensional record has an effect on the maximum displacement of the Northridge tests, as shown in Figures 4.12-4.17.

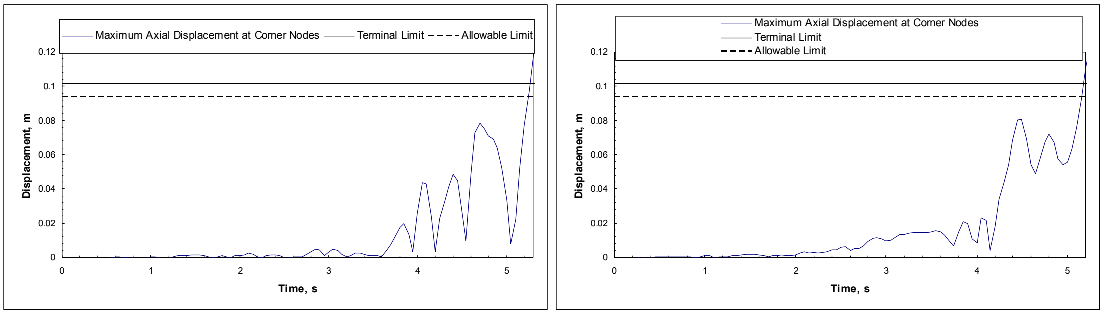

Figure 4.12 – Maximum corner node displacements for Span1 subjected to the Northridge event. (a) Response for axial seismic input only. (b) Response for three-dimensional seismic input.

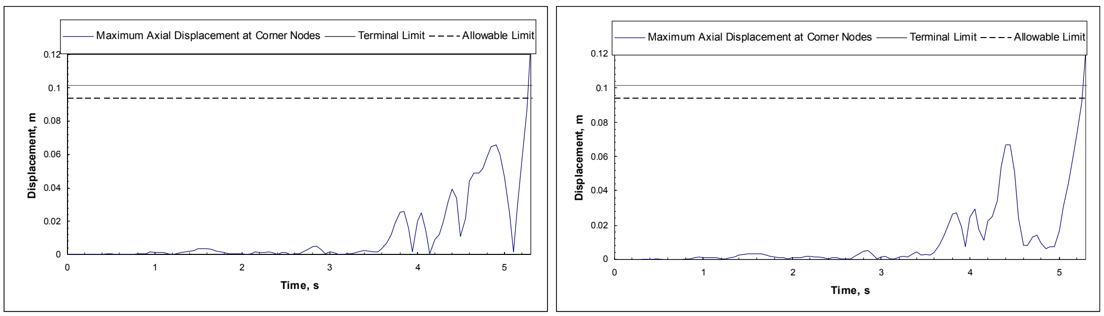

Figure 4.13 – Maximum corner node displacements for Span2 subjected to the Northridge event. (a) Response for axial seismic input only. (b) Response for three-dimensional seismic input.

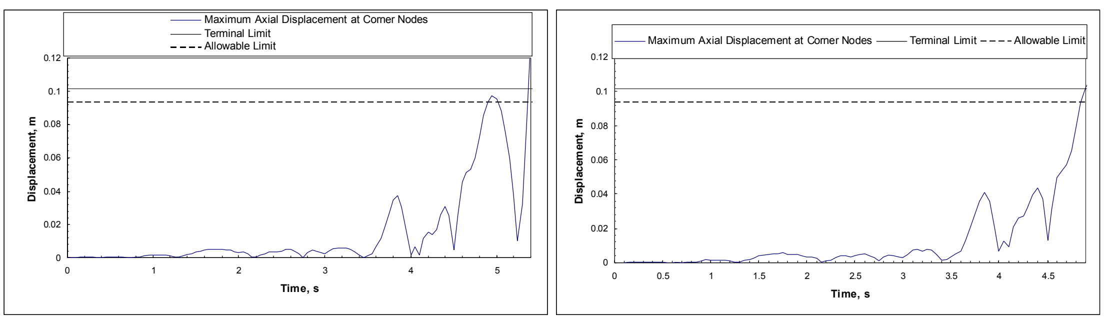

Figure 4.14 – Maximum corner node displacements for Span3 subjected to the Northridge event. (a) Response for axial seismic input only. (b) Response for three-dimensional seismic input.

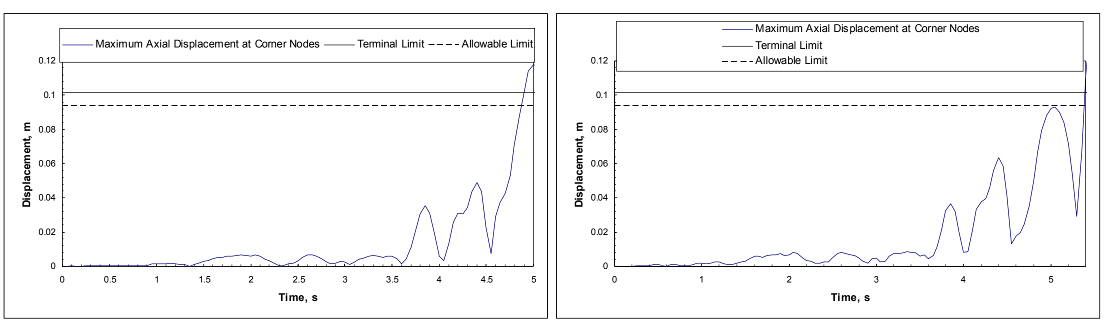

Figure 4.15 – Maximum corner node displacements for Span4 subjected to the Northridge event. (a) Response for axial seismic input only. (b) Response for three-dimensional seismic input.

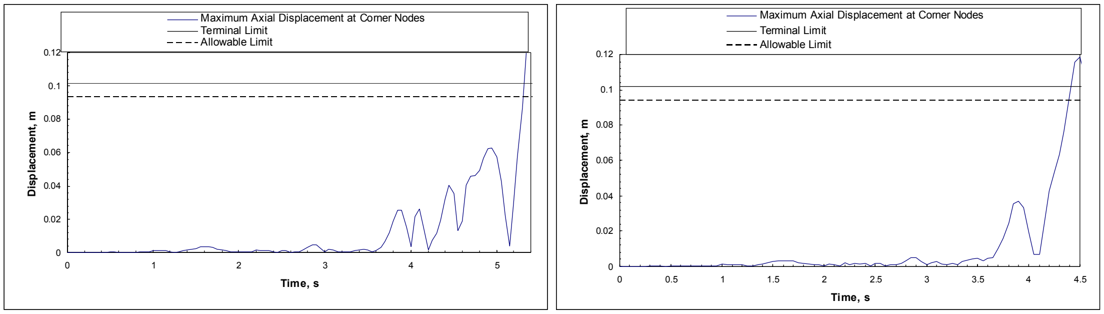

Figure 4.16 – Maximum corner node displacements for Span5 subjected to the Northridge event. (a) Response for axial seismic input only. (b) Response for three-dimensional seismic input.

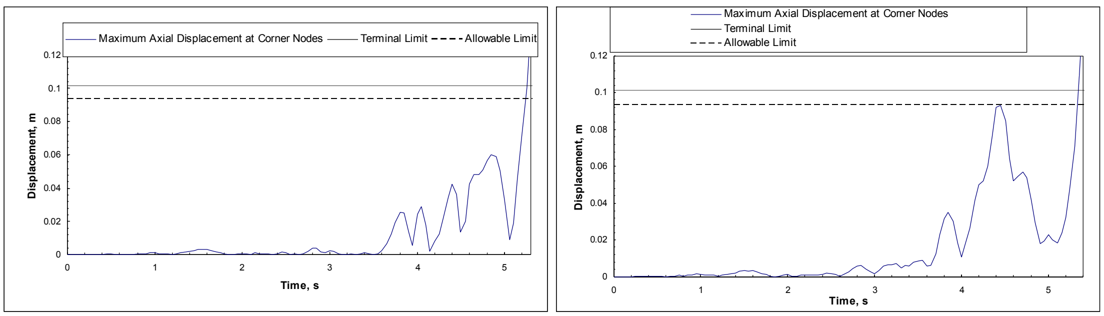

Figure 4.17 – Maximum corner node displacements for Span6 subjected to the Northridge event. (a) Response for axial seismic input only. (b) Response for three-dimensional seismic input.

From this comparison, it is evident that there is a large difference in the maximum displacement when all three components of the Northridge record are applied. The difference in displacement at only Node 104 was investigated with the plots shown in Figure 4.18.

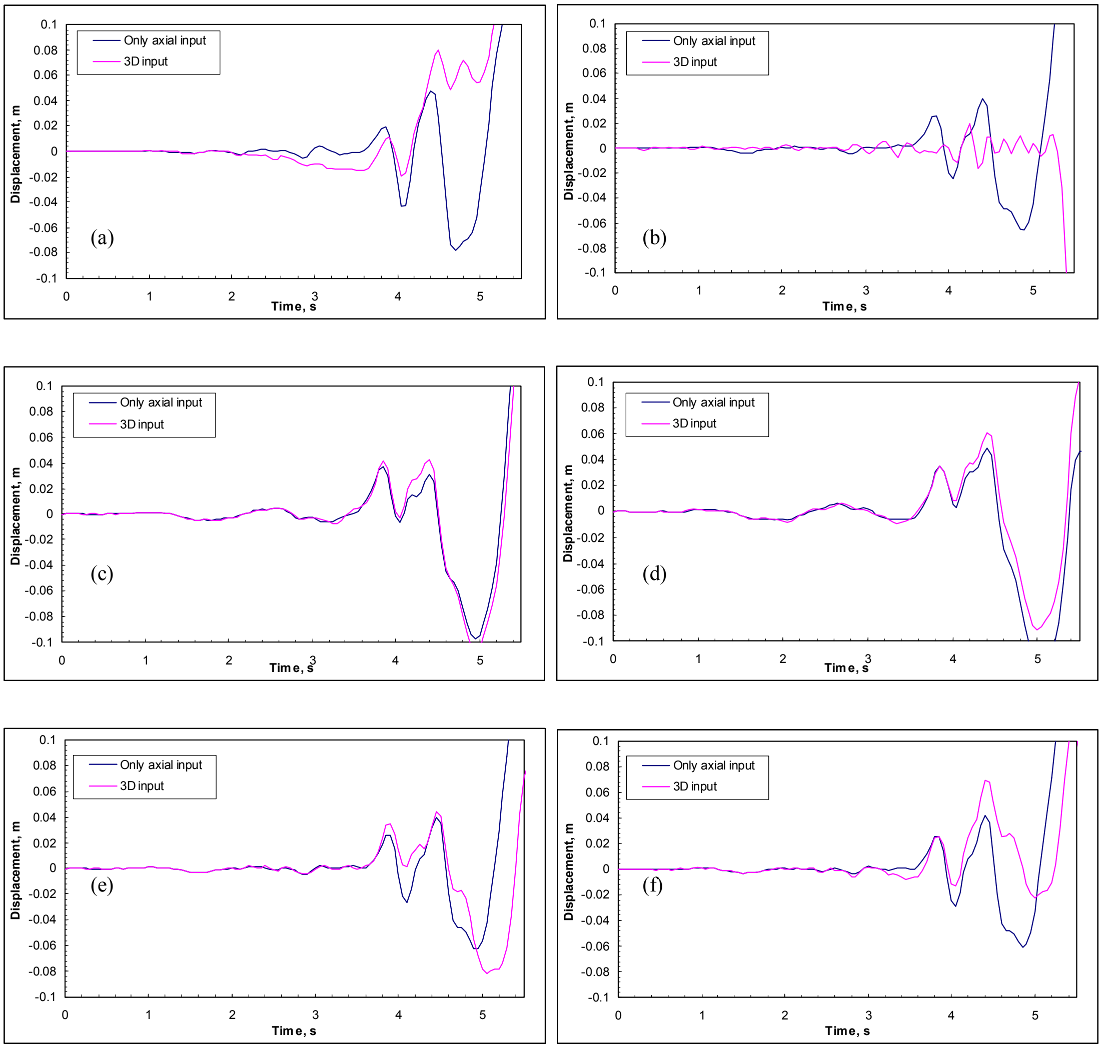

Figure 4.18 – Corner Node 104 displacements for spans subjected to axial only inputs and complete three-dimensional inputs from the Northridge event. (a) Response of Span1. (b) Response of Span2. (c) Response of Span3. (d) Response of Span4. (e) Response of Span5. (f) Response of Span6.

The displacements of Node 104 leave little doubt that three-dimensional seismic records have a significant influence on the axial response of the spans when subjected to the Northridge event. The axial tests and the three-dimensional tests of Span2 terminated while moving in opposite directions. The effect of three-dimensional input was most evident for the two lightest spans, Span1 and Span2.

4.3 Summary

In conclusion, the three-dimensional record has a significant effect on the axial response of some of the spans when compared to the response with only the axial seismic input. The effect of the lateral or of the vertical component was not conducted, so a direct correlation between one of these inputs and the change in axial response cannot be made; however, some conjecture on the influence of each component is made from the data in the following paragraphs. From the comparisons in this chapter, it was concluded that using the complete three-dimensional record was proper for tests utilizing SCEDs, as discussed in Chapter 5.

The vertical component appears to have a significant influence on the response of a span. An upward acceleration of the bearing can directly increase the compression stress at the contact surface, reducing the likelihood of slippage. Likewise, a downward acceleration of the bearing relieves some of the stress at the contact surface and increases the chance of slip. Bending that occurs in the span due to a vertical acceleration at the bearings can propagate throughout the length of the test with alternating periods of lessened compression stress and larger compression stress on the bearing, influencing the likelihood of slippage. For example, a large vertical acceleration just after 5s, as seen in Appendix B, appears to be the cause of the reversed direction at the end of the Northridge record on Span2. Inspection of the divergence of the three-dimensional responses from the axial responses during the Northridge tests, as well as consideration of the acceleration magnitudes at these times, indicates there is a strong likelihood that the vertical component could induce or reduce slip.

Determining the effect of the lateral component on the response of the spans is more difficult. There are very large lateral displacements with significant accelerations after 3.5s for the Northridge record; however, it is more complicated to directly link the divergence of any three-dimensional record to the lateral component without further tests.

Chapter Five
Evaluation of SCED Performance

5.1 Introduction

This chapter presents and analyzes the results from the finite-element tests that included nonlinear SCED definitions in the models. The data in the previous chapter was divided by which seismic input was used because there was a distinct difference in the results from the Imperial Valley and Northridge tests. However, in this chapter the tests are divided by span designation. Two tests with SCEDs were performed with each earthquake, as described in Chapter Three.

The next section of this chapter is divided into six subsections, one for each span. Generally, each subsection has summary plots of the maximum axial displacements for the four tests performed with that span and plots of the maximum SCED load distribution for all tests with a short discussion of the results. The subsection on Span1 also contains snap load time-histories for two of the trials, as well as single node displacement plots for axial and lateral motion at corner Node 104 and vertical motion at midspan Node 49. The subsection on Span5 also contains a discussion on the data sampling rate.

The final section of this chapter includes summary plots of maximum axial displacement versus a mass scaled SCED stiffness for all spans and a summary of maximum SCED load distribution. Appendix D contains a complete collection of full-size displacement and load time-histories.

Data and Analyses

5.2.1 Results from Span1 tests

Four tests were conducted for Span1. Two tests with SCED stiffnesses of 36,900 and 52,700kN/m$^{1.3}$ were completed with the Imperial Valley ground motions. Two tests with SCED stiffnesses of 42,200 and 52,700kN/m$^{1.3}$ were completed with the Northridge ground motions. Typical corner node responses for the two earthquakes are shown in Figures 5.1 and 5.2.

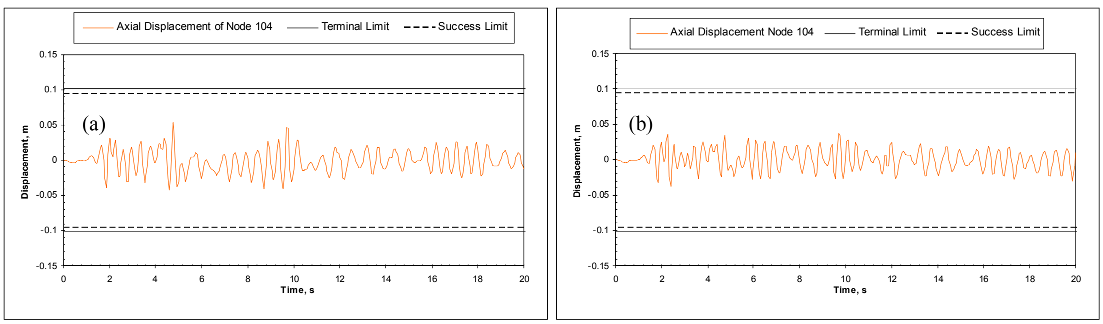

Figure 5.1 - Typical node response for an Imperial Valley test. Example from Span1 test with stiffnesses of (a) 36,900kN/m$^{1.3}$ and (b) 52,700kN/m$^{1.3}$

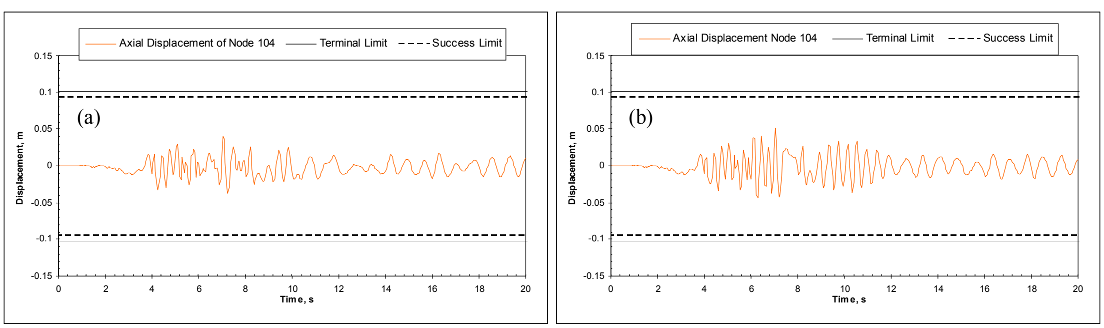

Figure 5.2 - Typical node response for a Northridge test. Example from Span1 test with stiffnesses of (a) 42,200kN/m$^{1.3}$ and (b) 52,700kN/m$^{1.3}$

Figure 5.2 also shows how the response frequency of the structure changes as the SCEDs become stiff. Note that during the most energetic part of the earthquake record, between 5s and 8s the displacement cycle frequency was significantly shorter. During the strongest portions of the input record, the natural frequency of the structure for axial displacement was controlled by the stiffness of the SCEDs, whereas during the weaker portion of the record, after 12s, when axial displacement did not engage the SCEDs, the response frequency was controlled by the stiffness of the bearings. Furthermore, Figure 5.1 shows less notable changes in response frequency because the earthquake was relatively strong throughout the 20s test period.

The maximum axial displacement plots in Figure 5.3 are much more reliable than the single node displacement plots in Figures 5.1 and 5.2 for distinguishing the worst-case displacement of the span. Therefore, maximum axial displacement plots are used to distinguish the success of a test. Single node displacement plots for Node 104 are available in Appendix D for the remainder of the tests.

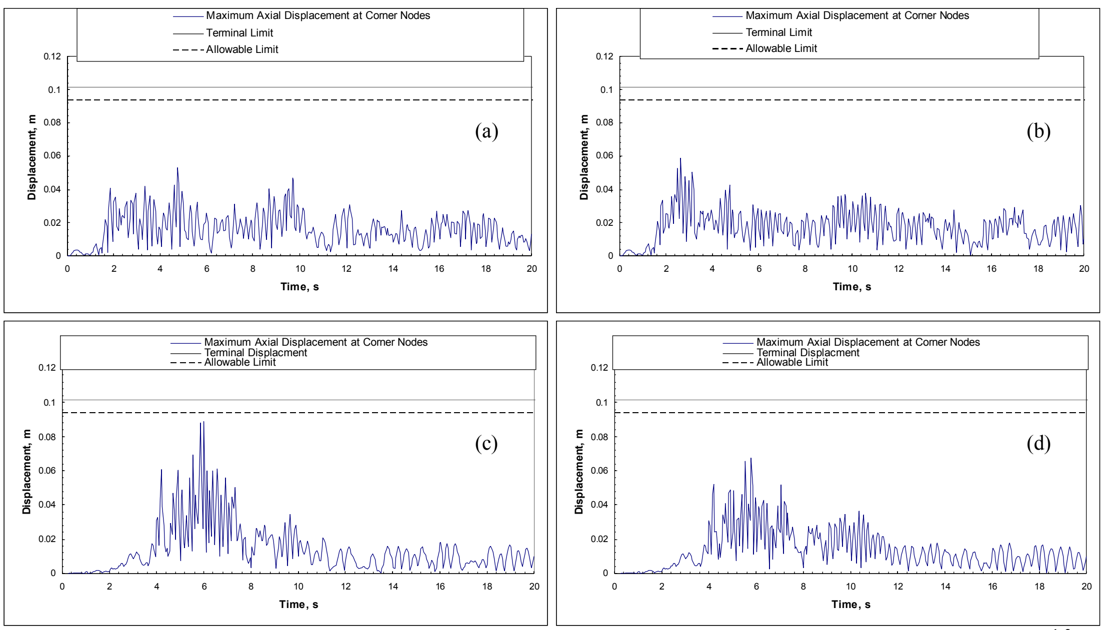

Figure 5.3 – Maximum axial displacements for Span1. (a) SCED stiffness of 36,900kN/m$^{1.3}$ with Imperial Valley ground motion. (b) SCED stiffness of 52,700kN/m$^{1.3}$ with Imperial Valley ground motion. (c) SCED stiffness of 42,200kN/m$^{1.3}$ with Northridge ground motion. (d) SCED stiffness of 52,700kN/m$^{1.3}$ with Northridge ground motion.

The load time-histories for the SCEDs in the Span1 test with a stiffness of 52,700kN/m$^{1.3}$ subject to the Imperial Valley record are shown in Figure 5.5. It is important to note the distribution of SCED activity throughout the 20s test period and that the exterior SCED 1 and SCED 10 have a maximum load twice as large as the exterior SCEDs on the opposing side. The large discrepancy in load indicates some rotation of the span as a result of the lateral component. However, it was found that the large rotation was not inevitable when the maximum SCED load was plotted for all of the nodes. When the SCED stiffness was reduced 30% from 52,700kN/m$^{1.3}$ to 36,900kN/m$^{1.3}$, the maximum load, and even the maximum displacement, was reduced. As can be seen in Figure 5.4, a reduced stiffness produced an almost even distribution of maximum load across all of the SCEDs. Therefore, in some cases there may be a performance penalty for a large SCED stiffness.

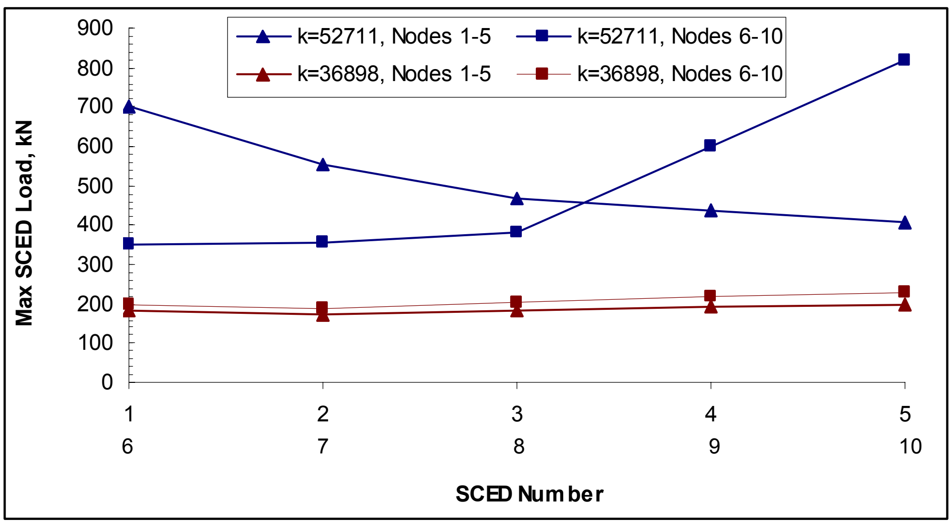

Figure 5.4 – Distribution of maximum SCED load for Span1 with Imperial Valley seismic input.

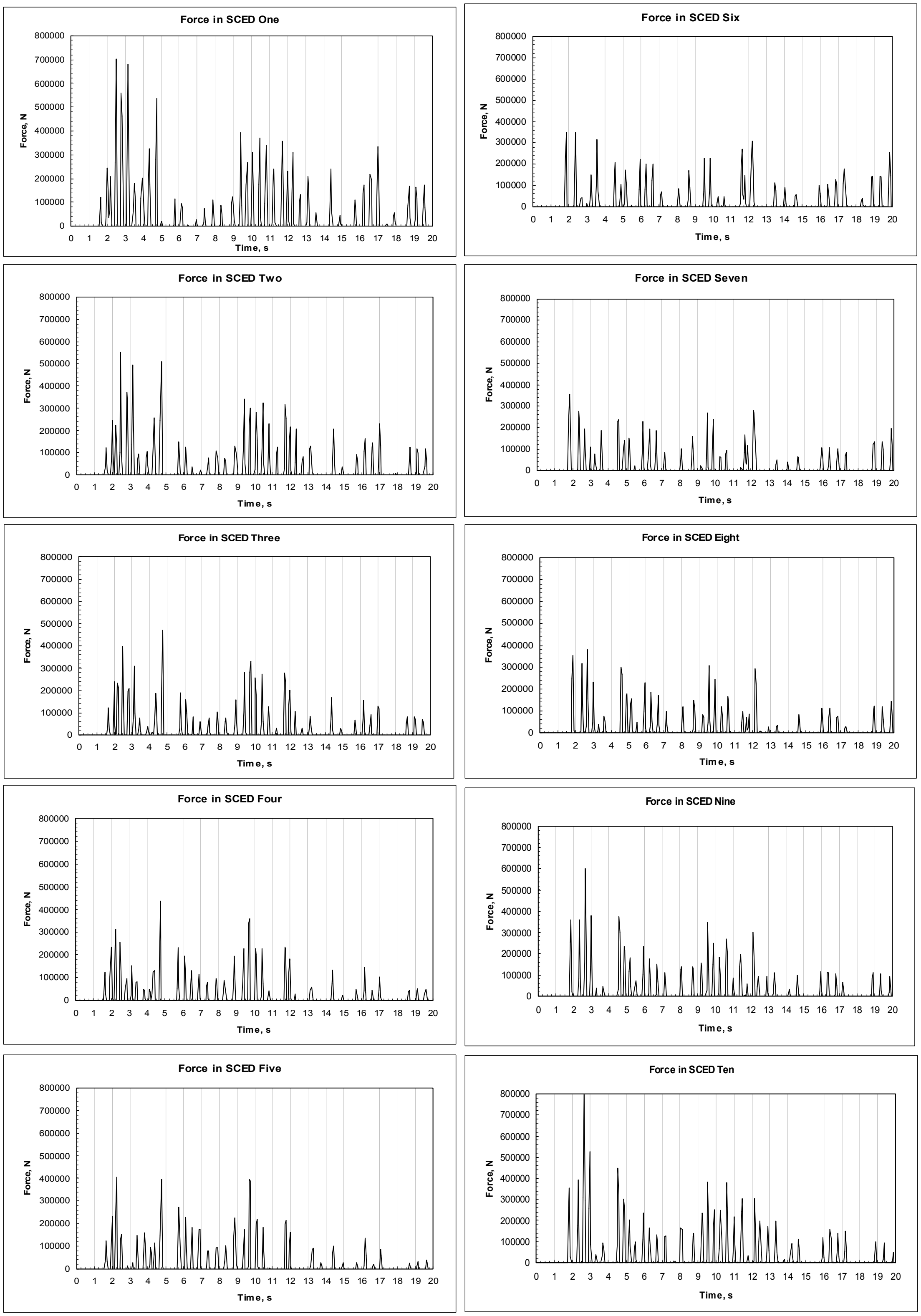

Figure 5.5 - Typical SCED load distribution for an Imperial Valley test. Load distribution from test with SCED stiffness of 52,700kN/m$^{1.3}$. Note a distribution of loading throughout the test period, and the alternating loading between SCEDs in the left column and SCEDs in the right column.

The differences between the remaining tests of the same span designation and seismic input motion are not as defined as with the previous example. The next two tests, Span1 with Northridge inputs, have limited separation between their maximum loads. As seen in Figure 5.6, both tests show signs of rotation, though in opposite directions. The individual SCED load time-histories for the 52,700kN/m$^{1.3}$ test are shown in Figure 5.7. The individual SCED load time-histories for the remaining tests are shown in Appendix D.

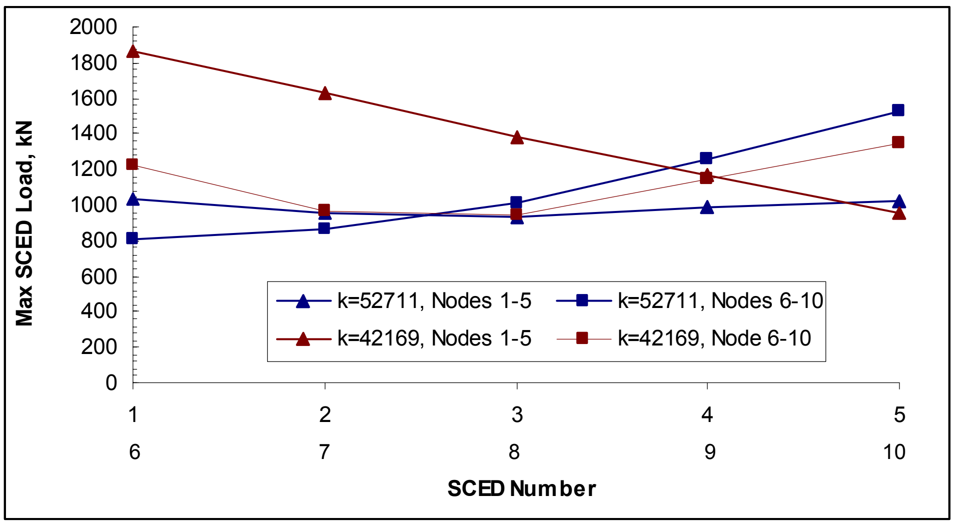

Figure 5.6 – Distribution of maximum SCED load for Span1 with Northridge seismic input.

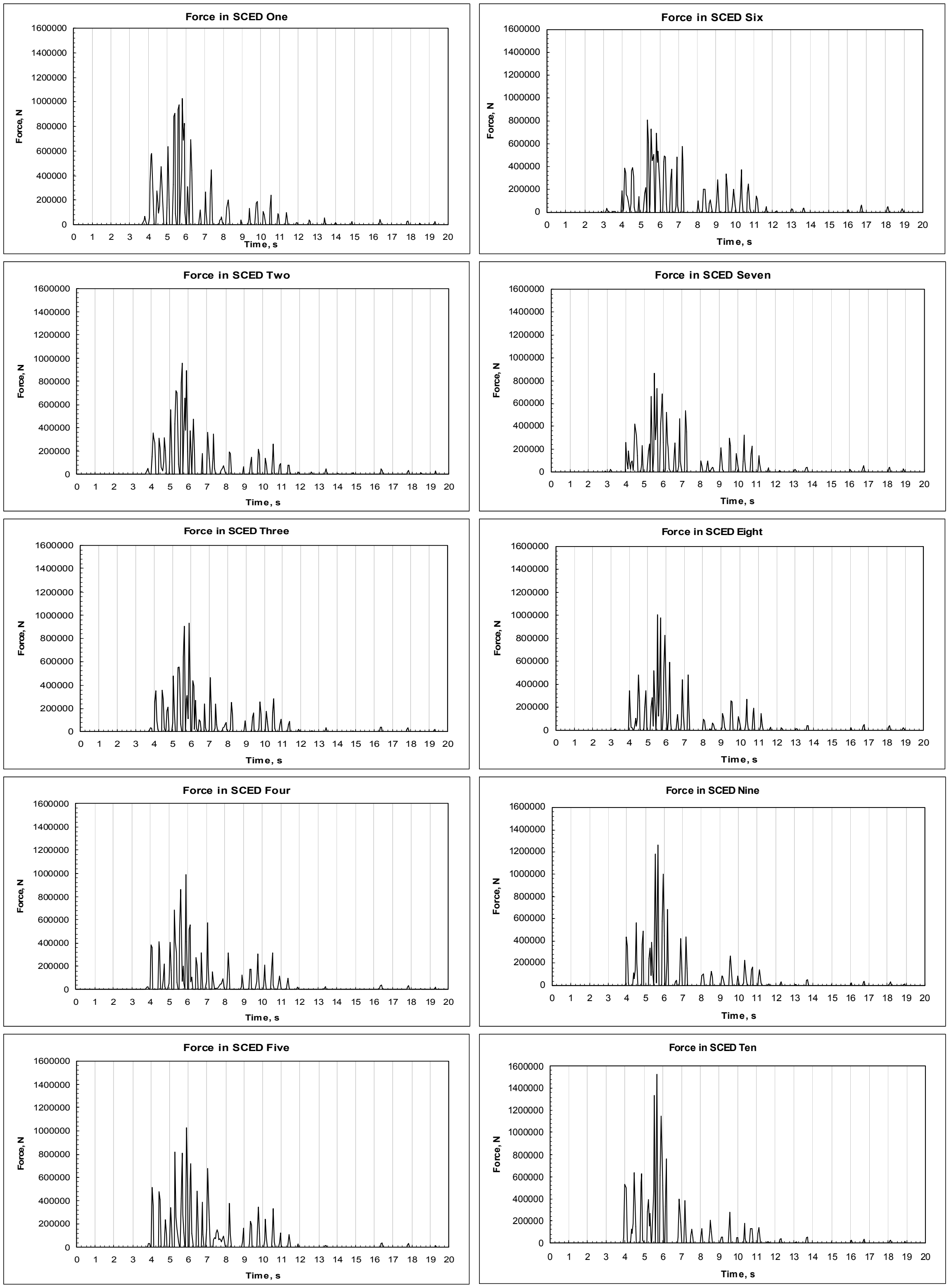

Figure 5.7 - Typical SCED load distribution for a Northridge test. Load distribution from test with SCED stiffness of 52,700kN/m$^{1.3}$. Note a distribution of loading through only a portion of the time period when compared to the Imperial Valley example.

Vertical displacement at midspan, Node 49, is shown below in Figure 5.8 for the four tests of Span1. The motions shown are typical for all of the spans, though the magnitude of the displacement increases with span length. The axial components of the earthquakes were scaled to similar magnitudes, but the vertical components were scaled to be proportional to the axial components. Imperial Valley has a relatively small vertical component, which results in vertical displacements at midspan for Imperial Valley tests that are as much as five times smaller than those in the Northridge tests. The effect of the vertical component on axial displacement was discussed in Chapter 4. Vertical displacement plots for the remaining spans are shown in Appendix D.

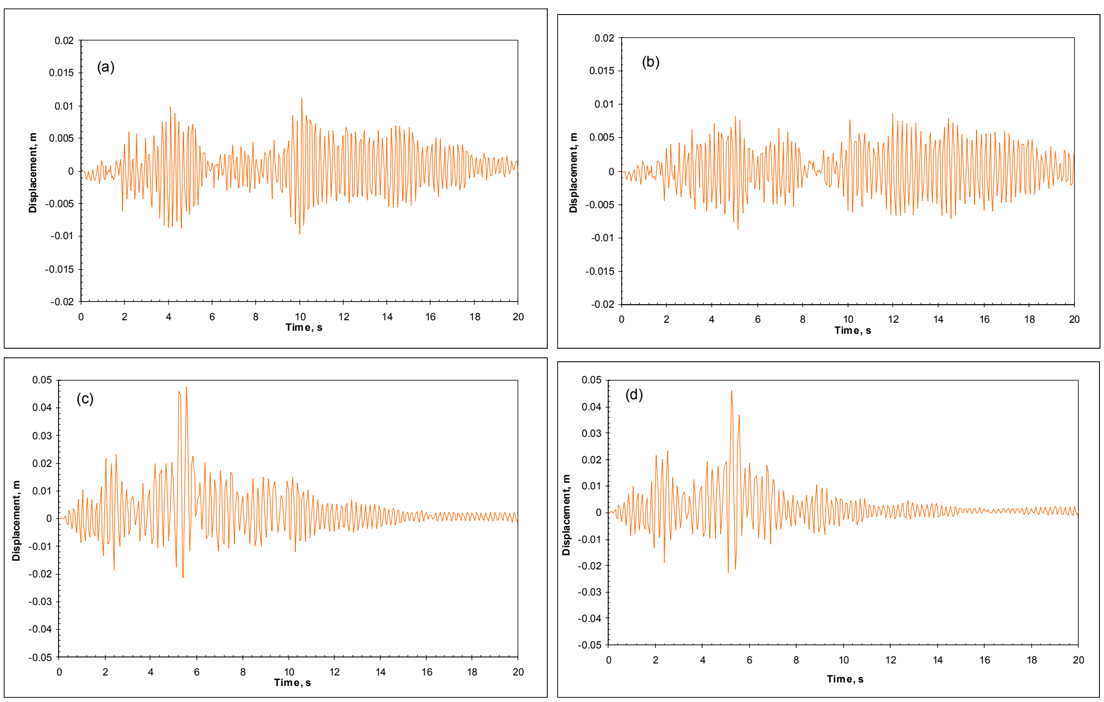

Figure 5.8 – Vertical displacement of midspan for Span1 tests. (a) SCED stiffness of 36,900kN/m$^{1.3}$ with Imperial Valley ground motion. (b) SCED stiffness of 52,700kN/m$^{1.3}$ with Imperial Valley ground motion. (c) SCED stiffness of 42,200kN/m$^{1.3}$ with Northridge ground motion. (d) SCED stiffness of 52,700kN/m$^{1.3}$ with Northridge ground motion.

Lateral displacements at a corner, Node 104, are shown in Figure 5.9 for the four tests of Span1. As with vertical motion at midspan, the magnitudes of the lateral motion for Northridge tests are much larger than those recorded in Imperial Valley tests. Lateral motion does seem to have some dependency on the stiffness of the SCEDs. However, since the lateral direction was initially orthogonal to the lines-of-action of the SCEDs, any significant effect is likely limited to larger displacements. The lateral motions of additional tests are shown in Appendix D.

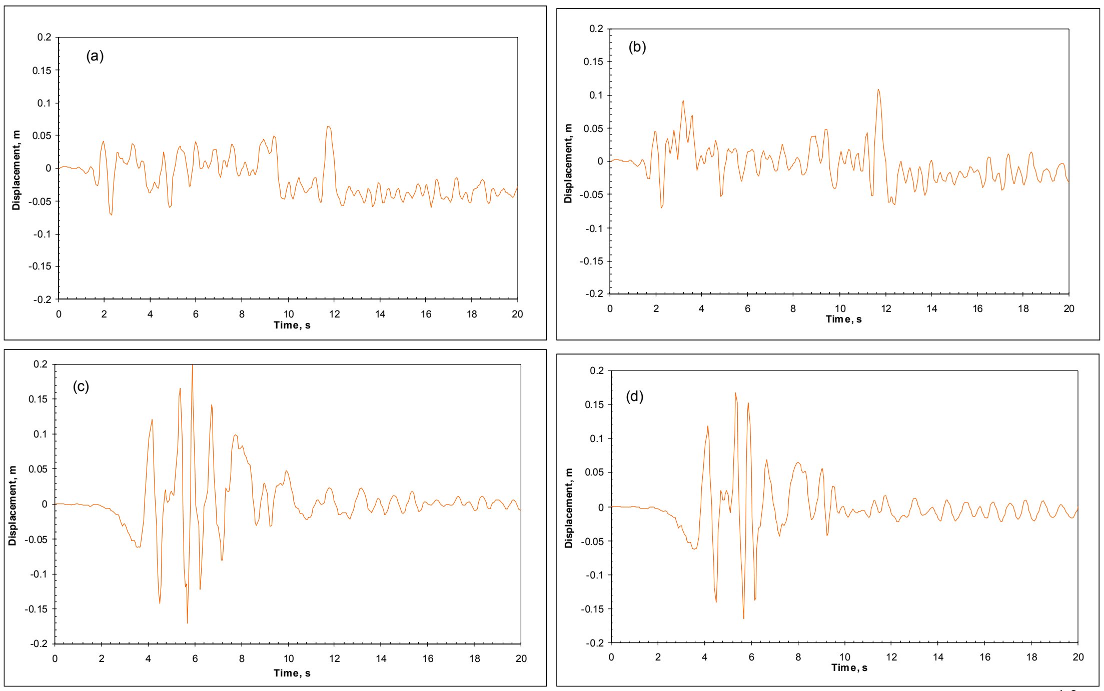

Figure 5.9 – Lateral displacement of midspan for Span1 tests. (a) SCED stiffness of 36,900kN/m$^{1.3}$ with Imperial Valley ground motion. (b) SCED stiffness of 52,700kN/m$^{1.3}$ with Imperial Valley ground motion. (c) SCED stiffness of 42,200kN/m$^{1.3}$ with Northridge ground motion. (d) SCED stiffness of 52,700kN/m$^{1.3}$ with Northridge ground motion.

The axial responses of Nodes 61 and 71 were inspected and the axial response was minimal when snap load occurred at those nodes. Plots of the responses at these nodes are also available in Appendix D for all tests.

5.2.2 Results from Span2 tests

Four tests were conducted for Span2. Two tests with SCED stiffnesses of 58,000 and 79,100kN/m$^{1.3}$ were completed with the Imperial Valley ground motions. Two tests with SCED stiffnesses of 63,300 and 79,100kN/m$^{1.3}$ were completed with the Northridge ground motions. The maximum axial displacements in those tests are presented in Figure 5.10. The relationship between maximum displacement and SCED stiffness, decreased displacements with increased stiffness, was more like the expected relationship than what was observed in the Span1 tests.

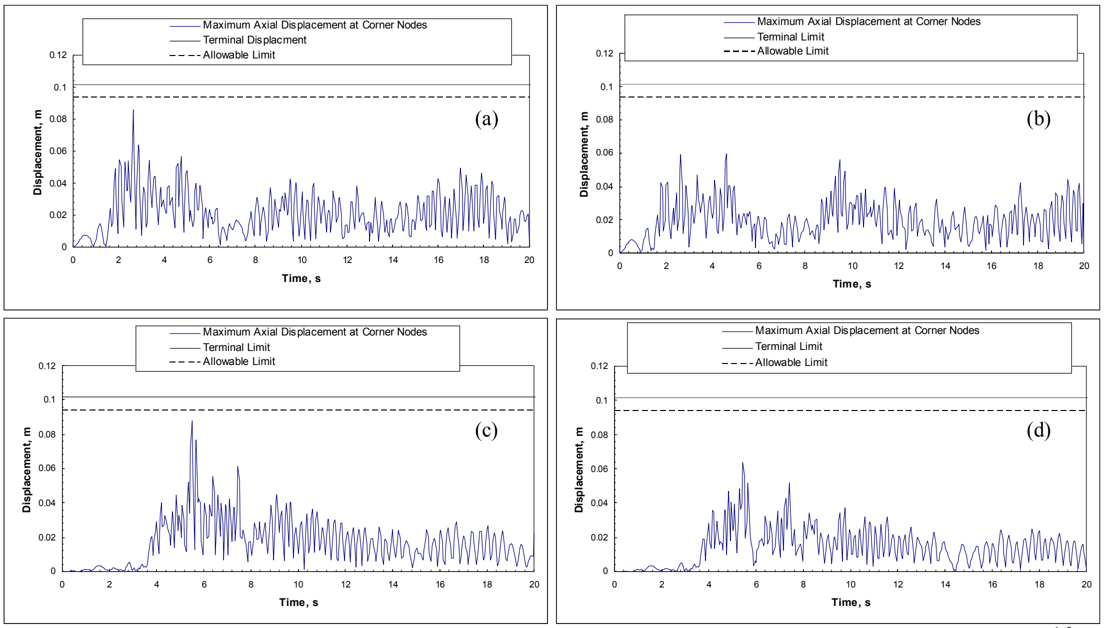

Figure 5.10 – Maximum axial displacements for Span2. (a) SCED stiffness of 58,000kN/m$^{1.3}$ with Imperial Valley ground motion. (b) SCED stiffness of 79,100kN/m$^{1.3}$ with Imperial Valley ground motion. (c) SCED stiffness of 63,300kN/m$^{1.3}$ with Northridge ground motion. (d) SCED stiffness of 79,100kN/m$^{1.3}$ with Northridge ground motion.

The maximum SCED load was increased approximately 200kN for both Imperial Valley and Northridge events by increasing the SCED stiffness, as seen in Figure 5.11 and Figure 5.12. However, for the Span2 tests there was little effect on the load distribution, unlike for the Span1 tests. In both Imperial Valley tests, the load on one set of SCEDs is relatively uniform while the load in the other set of SCEDs increases approximately 650kN from one exterior SCED to the other; however, the side of the span on which the behavior occurs changes when the stiffness increases. During the Northridge tests, changes are even more similar. The only noticeable change in maximum load distribution is an increase in load on one side of the span. The load is slightly lower on one exterior SCED than on the other side of the same set for the Northridge tests.

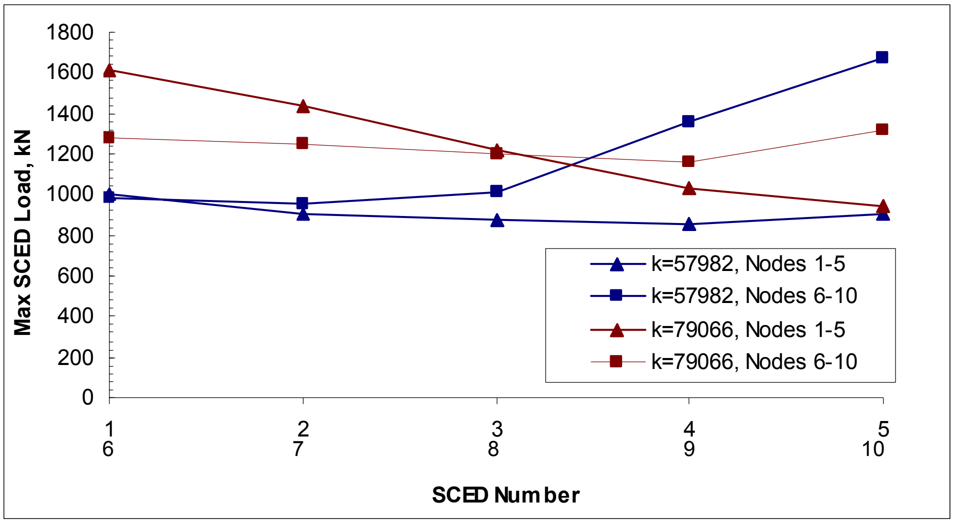

Figure 5.11 – Distribution of maximum SCED load for Span2 with Imperial Valley seismic input.

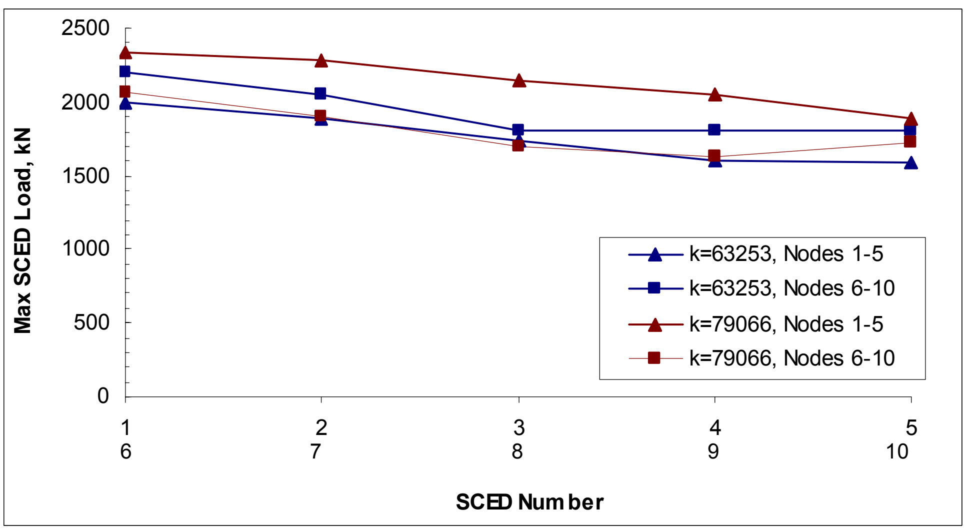

Figure 5.12 – Distribution of maximum SCED load for Span2 with Northridge seismic input.

5.2.3 Results from Span3 tests

Four tests were conducted for Span3. Two tests with SCED stiffnesses of 89,600 and 105,400kN/m$^{1.3}$ were completed with the Imperial Valley ground motions. Two tests with SCED stiffnesses of 105,400 and 147,600kN/m$^{1.3}$ were completed with the Northridge ground motions. The maximum axial displacements in those tests are presented in Figure 5.13. This is the only span where there were significant differences in the maximum displacement of the Northridge and Imperial Valley tests with the same SCED stiffness.

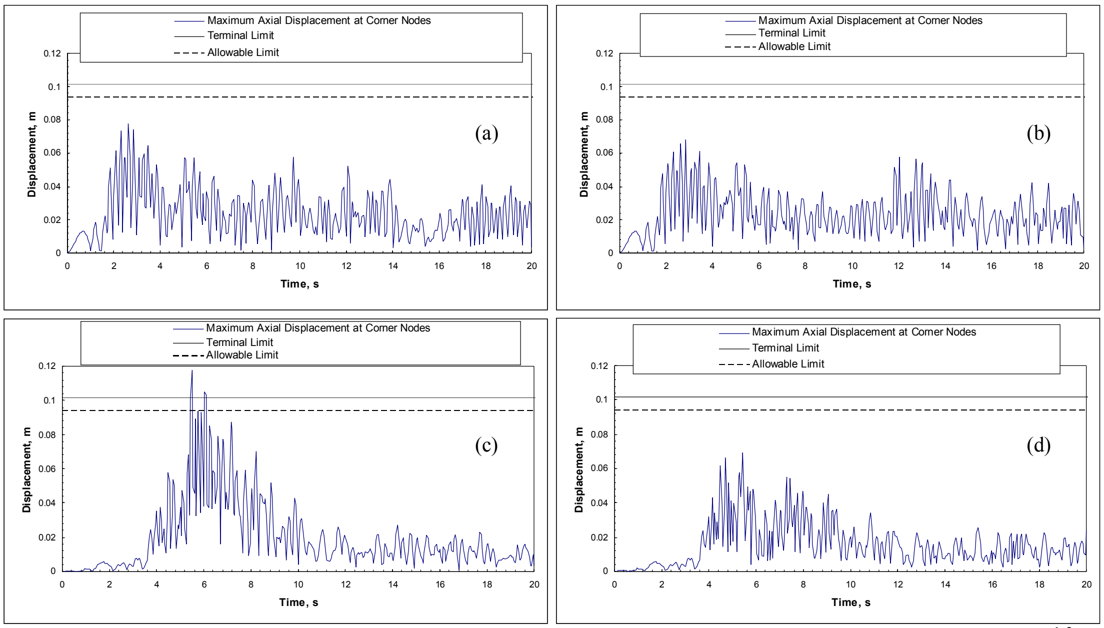

Figure 5.13 – Maximum axial displacements for Span3. (a) SCED stiffness of 89,600kN/m$^{1.3}$ with Imperial Valley ground motion. (b) SCED stiffness of 105,400kN/m$^{1.3}$ with Imperial Valley ground motion. (c) SCED stiffness of 105,400kN/m$^{1.3}$ with Northridge ground motion. (d) SCED stiffness of 147,600kN/m$^{1.3}$ with Northridge ground motion.

The distribution of maximum loads for Span3 was relatively nondescript. The trends for both SCED sets for the stiffer Imperial Valley and Northridge tests decreased slightly from one exterior SCED to the other. The other two tests were slightly less uniform. The less stiff Imperial Valley decreased slightly from one side to the other as well, but the two sets did so from opposite directions, resulting in equal displacements at the center SCED. The most notable test was the Northridge test with a SCED stiffness of 105,400kN/m$^{1.3}$, where the maximum SCED load at one end of an exterior girder was 7500kN and the maximum SCED load at the other end of that girder was approximately 3500kN. However, this test had data points beyond the terminal limit, so the results should be taken with some reservations.

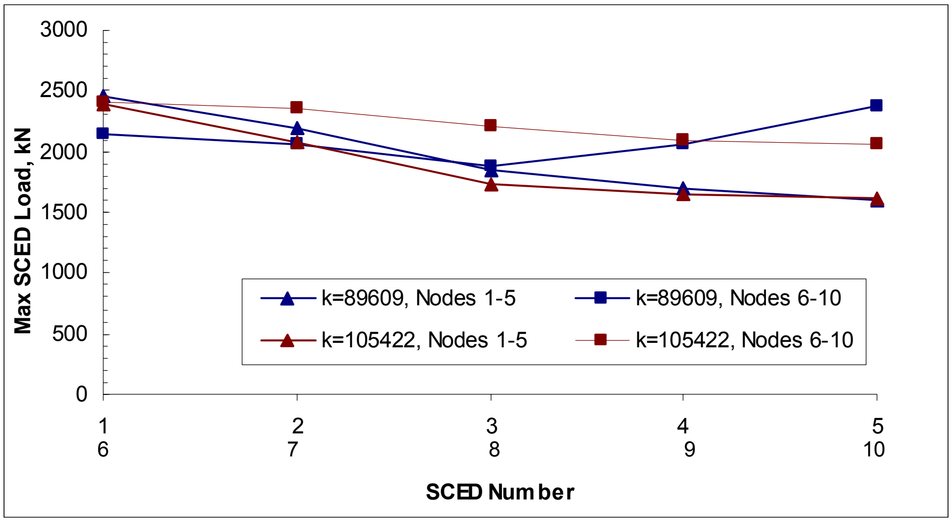

Figure 5.14 – Distribution of maximum SCED load for Span3 with Imperial Valley seismic input.

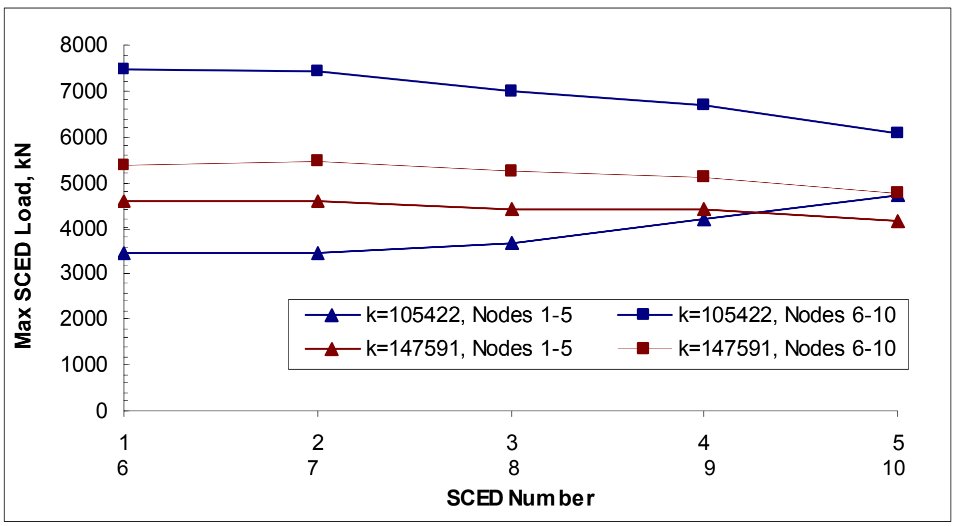

Figure 5.15 – Distribution of maximum SCED load for Span3 with Northridge seismic input.

5.2.4 Results from Span4 tests

Four tests were conducted for Span4. Two tests with SCED stiffnesses of 131,800 and 179,200kN/m$^{1.3}$ were completed with the Imperial Valley ground motions. Two tests with SCED stiffnesses of 131,800 and 179,200kN/m$^{1.3}$ were also completed with the Northridge ground motions. Span4 was the longest and most massive span tested, and therefore the largest stiffness values were assumed. The Northridge tests of this span were the only tests of the SCEDs that did not meet the acceptable limit with either test stiffness. Note the point that crosses the limit in the stiffer test is slightly later in the test period than in the test utilizing a less stiff SCED. The maximum axial displacements in the Span4 tests are presented in Figure 5.16.

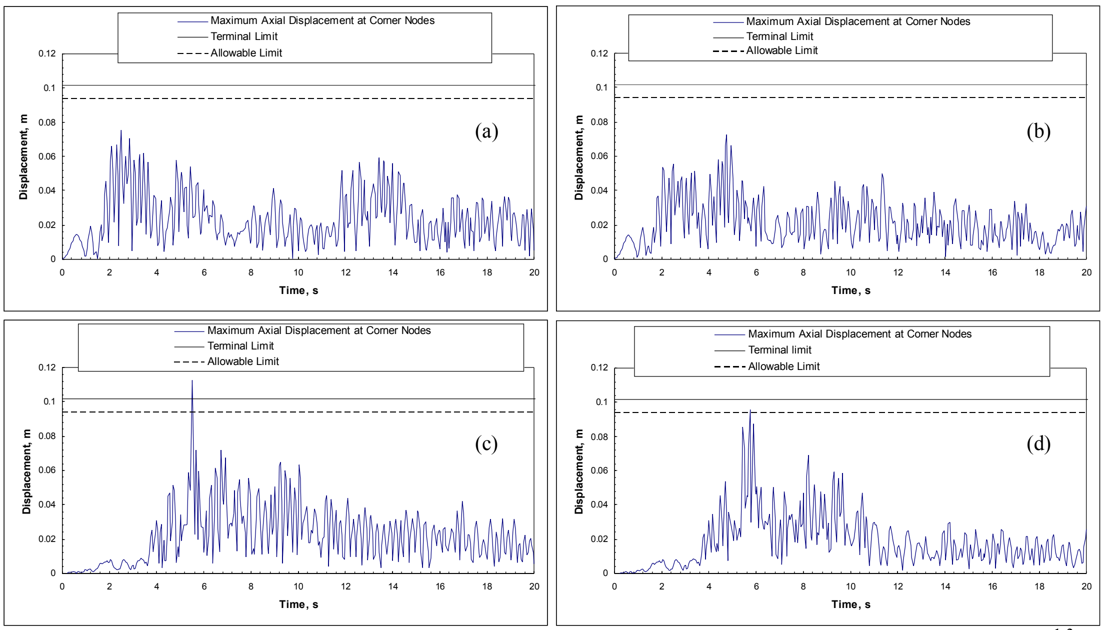

Figure 5.16 – Maximum axial displacements for Span4. (a) SCED stiffness of 131,800kN/m$^{1.3}$ with Imperial Valley ground motion. (b) SCED stiffness of 179,200kN/m$^{1.3}$ with Imperial Valley ground motion. (c) SCED stiffness of 131,800kN/m$^{1.3}$ with Northridge ground motion. (d) SCED stiffness of 179,200kN/m$^{1.3}$ with Northridge ground motion.

The generally uniform maximum SCED load distribution of Span4 is the best case to discuss issues concerning the resolution of results. Test data was recorded at intervals of 0.05s for both displacement and load. In one SCED set in the Imperial Valley maximum load data, and in three SCED sets for the Northridge data, the intermediate SCEDs, SCEDs 2, 4, 7, and 9, appear to have maximum loads greater than both the center and exterior SCEDs. However, the rigid body rotation that allows for different maximum loads to occur would dictate that the maximum load of a set of SCEDs would always be at an exterior SCED. Therefore, the reason that the intermediate SCEDs have a greater load may be a result of data sampling at a rate that does not always determine the maximum load. In fact, the loading time-histories of the pulse-like snap loads indicate that there could be as many as five or six loading cycles per second, or only 3 or 4 data points per cycle. Figure 5.17 shows the data points for the load time-history between 4s and 7s for the exterior SCED 6 with a stiffness of 179,200kN/m$^{1.3}$. With an increase in load from 0kN to 8000kN or greater occurring within thousandths of a second, "in a snap", the data sampling rate required to have a load time-history that does not underestimate some of the peak loads by a sizeable amount is extraordinarily small. The maximum SCED load distribution for the two Imperial Valley and two Northridge tests are shown in Figure 5.18 and 5.19, respectively.

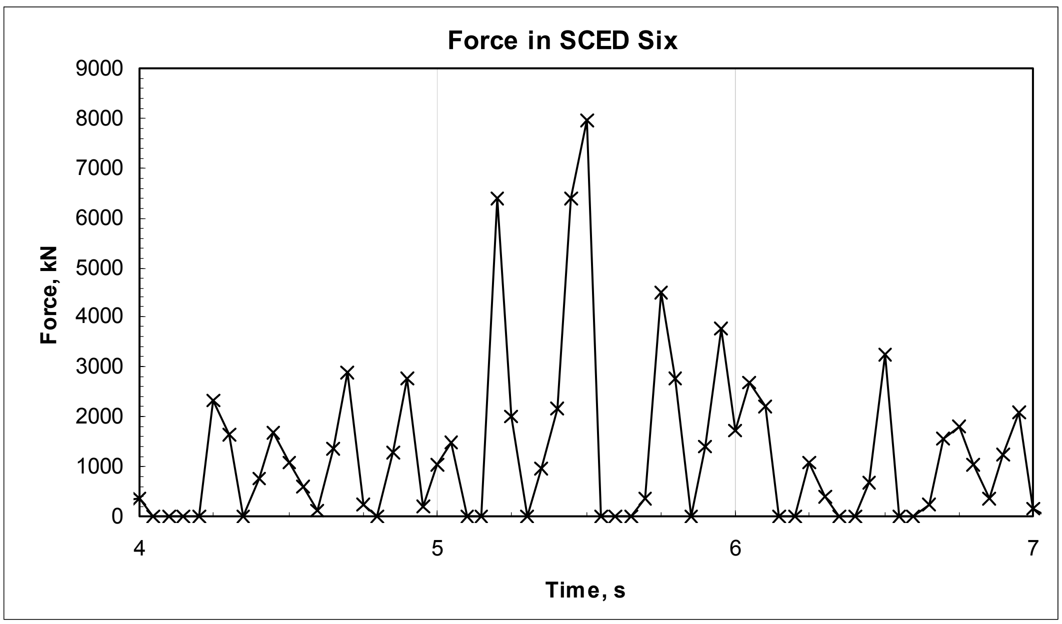

Figure 5.17 – Example of sampling rate and data resolution for SCED snap loading. SCED 6 subject to the Northridge event with a SCED stiffness of 179,200kN/m$^{1.3}$.

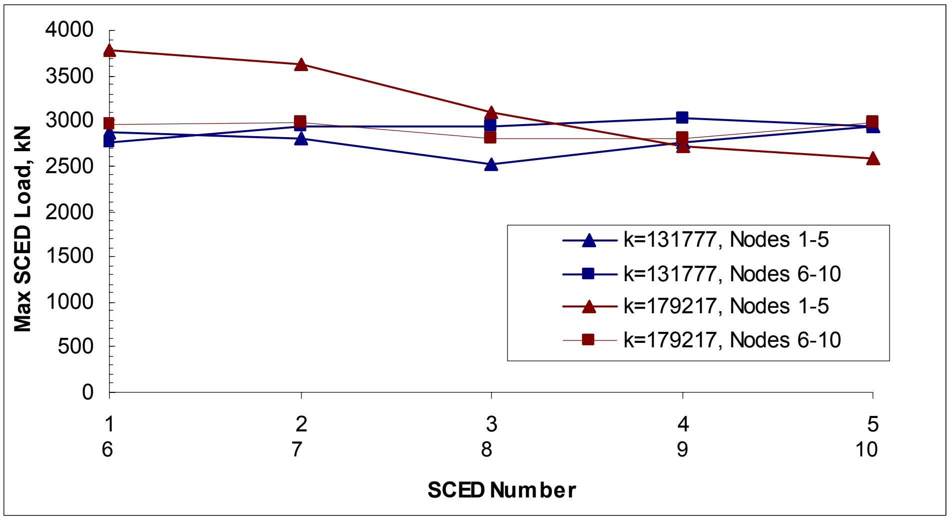

Figure 5.18 – Distribution of maximum SCED load for Span4 with Imperial Valley seismic input.

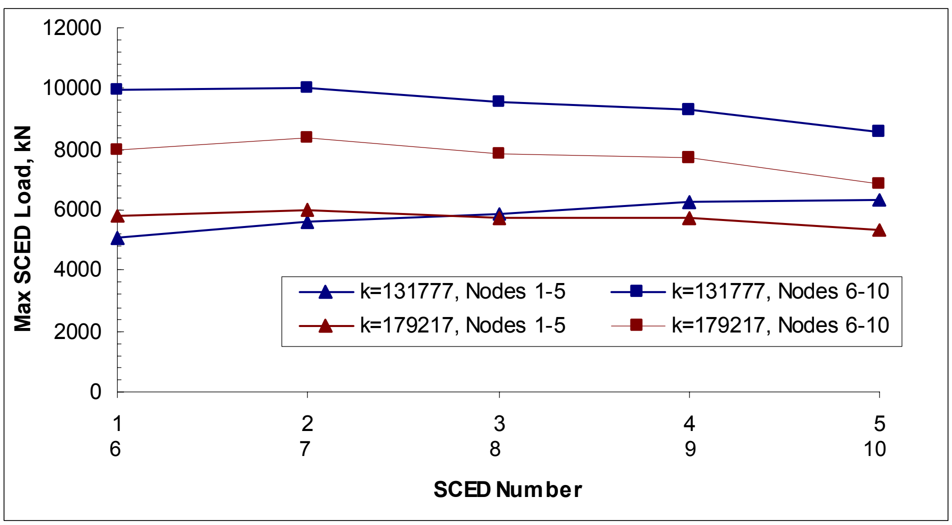

Figure 5.19 – Distribution of maximum SCED load for Span4 with Northridge seismic input.

5.2.5 Results from Span5 tests

Four tests were conducted for Span5. Two tests with SCED stiffnesses of 63,300 and 79,100kN/m$^{1.3}$ were completed with the Imperial Valley ground motions. Two tests with SCED stiffnesses of 68,500 and 79,100kN/m$^{1.3}$ were completed with the Northridge ground motions. The maximum axial displacements in those tests are presented in Figure 5.20.

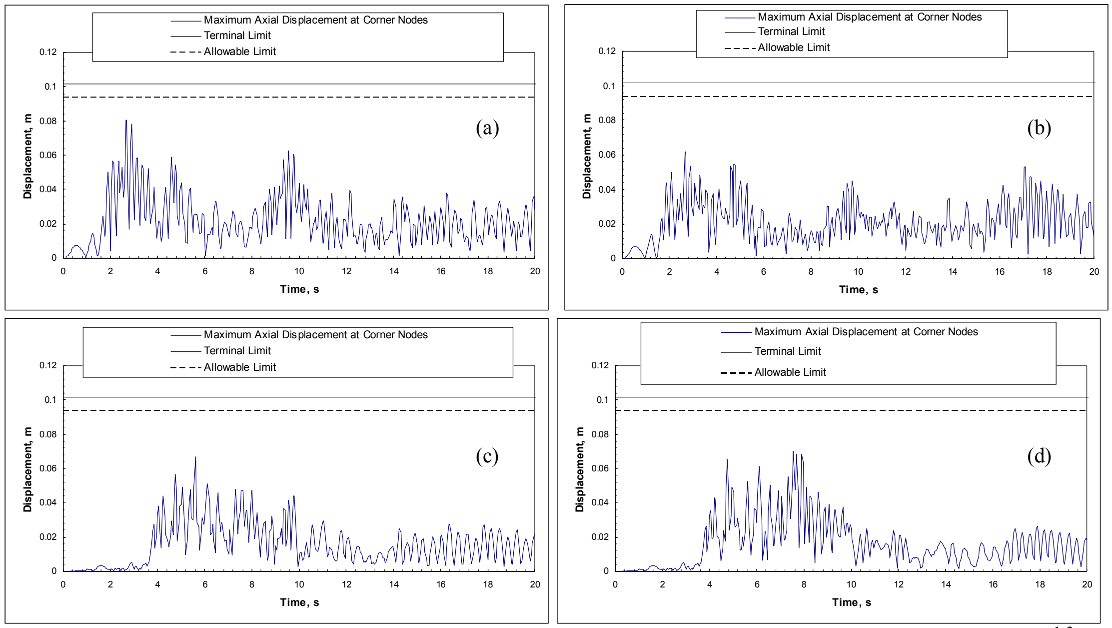

Figure 5.20 – Maximum axial displacements for Span5. (a) SCED stiffness of 63,300kN/m$^{1.3}$ with Imperial Valley ground motion. (b) SCED stiffness of 79,100kN/m$^{1.3}$ with Imperial Valley ground motion. (c) SCED stiffness of 68,500kN/m$^{1.3}$ with Northridge ground motion. (d) SCED stiffness of 79,100kN/m$^{1.3}$ with Northridge ground motion.

The maximum load distributions for the two Imperial Valley tests, as seen in Figure 5.21, have an average maximum load of similar proportions. However, the test with stiffer SCEDs has a more uniform load distribution than the less stiff SCED test that has large load concentrations at the exterior SCEDs. The Northridge tests are almost opposite of that statement with a more uniform maximum load distribution for the less stiff SCED test.

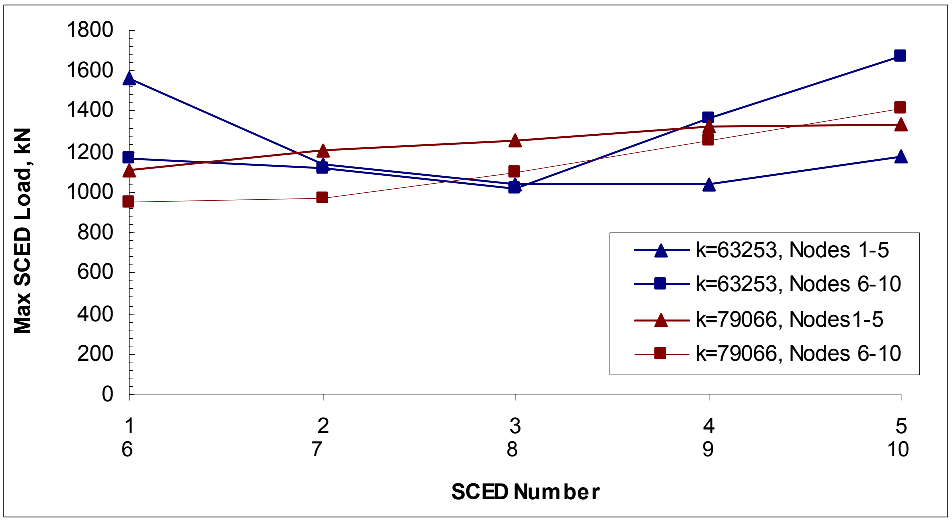

Figure 5.21 – Distribution of maximum SCED load for Span5 with Imperial Valley seismic input.

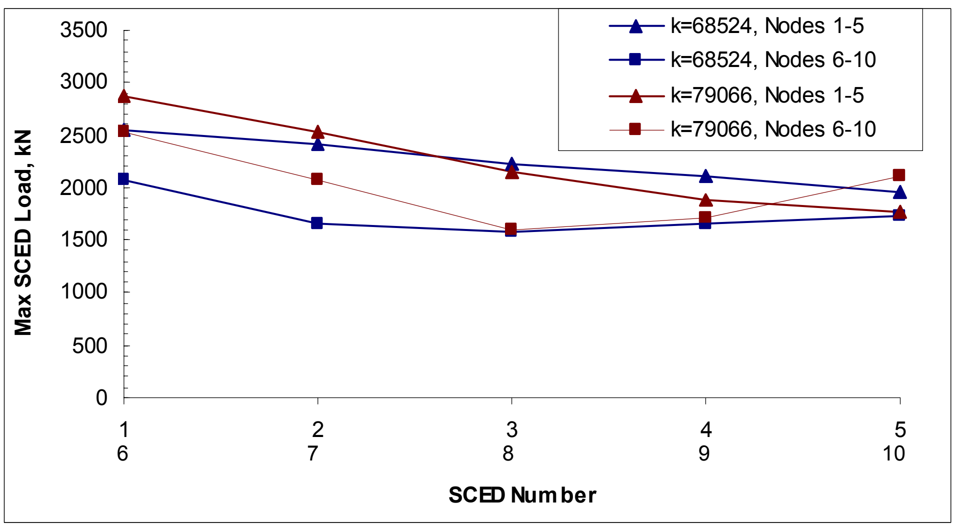

Figure 5.22 – Distribution of maximum SCED load for Span5 with Northridge seismic input.

5.2.6 Results from Span6 tests

Four tests were conducted for Span6. Two tests with SCED stiffnesses of 84,300 and 105,400kN/m$^{1.3}$ were completed with the Imperial Valley ground motions. Two tests with SCED stiffnesses of 84,300 and 105,400kN/m$^{1.3}$ were completed with the

Northridge ground motions. The maximum axial displacements in those tests are presented in Figure 5.23.

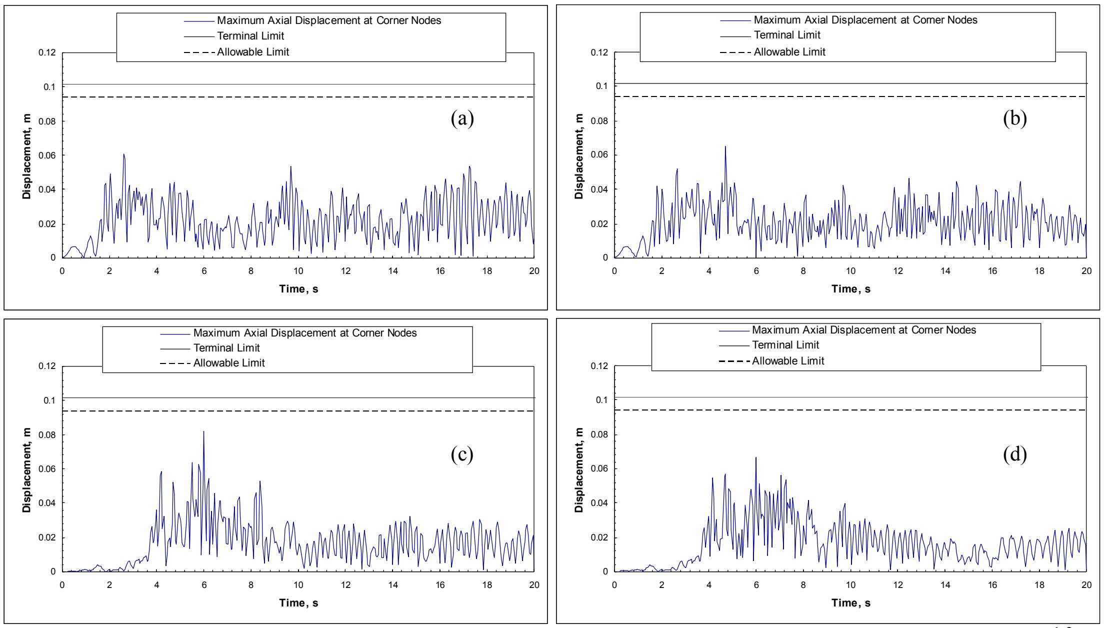

Figure 5.23 – Maximum axial displacements for Span6. (a) SCED stiffness of 84,300kN/m$^{1.3}$ with Imperial Valley ground motion. (b) SCED stiffness of 105,400kN/m$^{1.3}$ with Imperial Valley ground motion. (c) SCED stiffness of 84,300kN/m$^{1.3}$ with Northridge ground motion. (d) SCED stiffness of 105,400kN/m$^{1.3}$ with Northridge ground motion.

The maximum SCED load for Span 6 had more correlation to SCED stiffness than any of the previous tests. In both the Imperial Valley and Northridge tests the distribution of load across the span was remarkably similar. The maximum load distribution was basically scaled up to a slightly higher loading for the stiffer SCEDs with only a few slight changes in the gradient of the distribution.

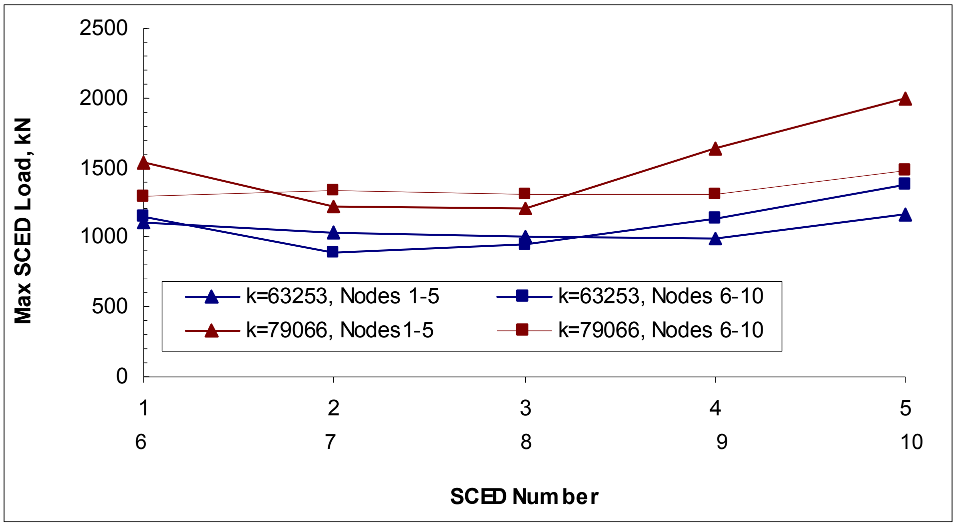

Figure 5.24 – Distribution of maximum SCED load for Span6 with Imperial Valley seismic input.

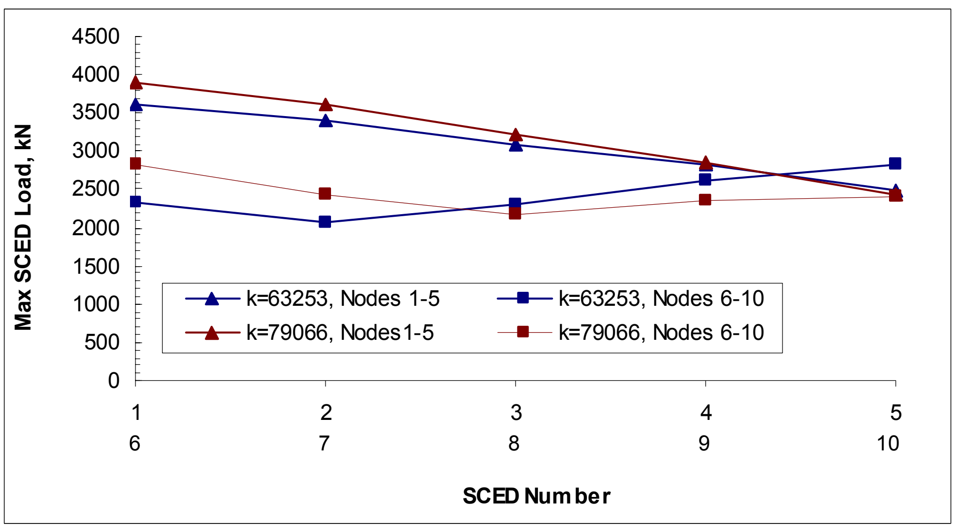

Figure 5.25 – Distribution of maximum SCED load for Span6 with Northridge seismic input.

5.3 Summary

In summary, the nonlinearity of the spans introduced by contact conditions, the SCEDs' stiffness, and the seismic input records produce a complex response that is difficult to condense without significant oversights. However, the results for all of the tests were compiled into Figure 5.26 with maximum axial displacement of each test plotted versus the SCED stiffness divided by the total weight of the each span. Of course, each span had its own unique response to the earthquakes and it was found that even after scaling the records the Northridge tests generally created a larger displacement in the spans. However, the data appears to have the general downward trend that would be expected and with copious data points a more definite trend, or lack thereof, could be established.

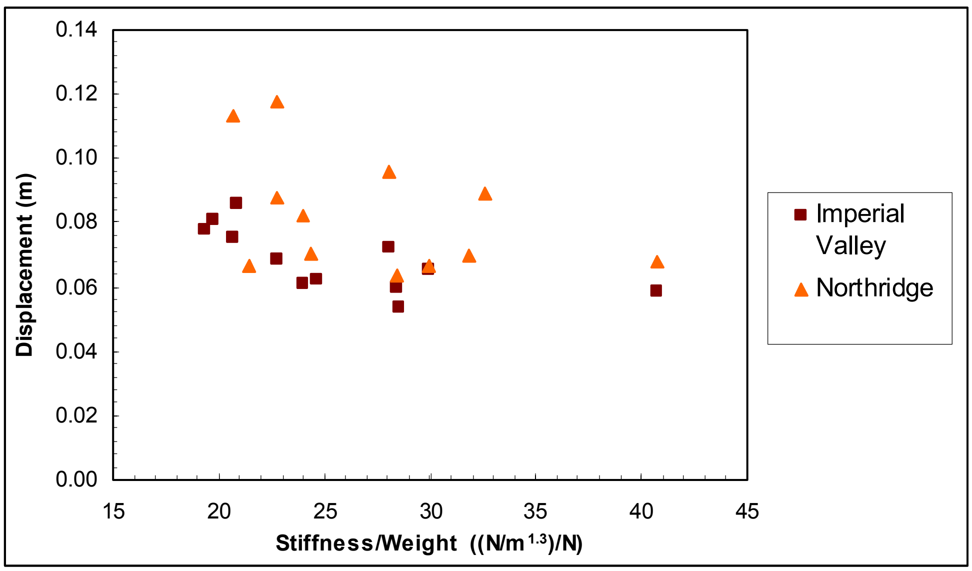

Figure 5.26 – Displacement versus scaled SCED stiffness for all tests.

There was a trend for the maximum load in the ropes versus the bearing force. The R^2 value for a linear trend was near 0.9 for both records. The trend was different for each seismic input record. The slope of the trend for the Imperial Valley tests was 5.53. The upward slope for Northridge tests was approximately three times larger at 16.18. Both trends have a negative intercept indicating that smaller spans may not require SCEDs. These trends are shown in Figure 5.27.

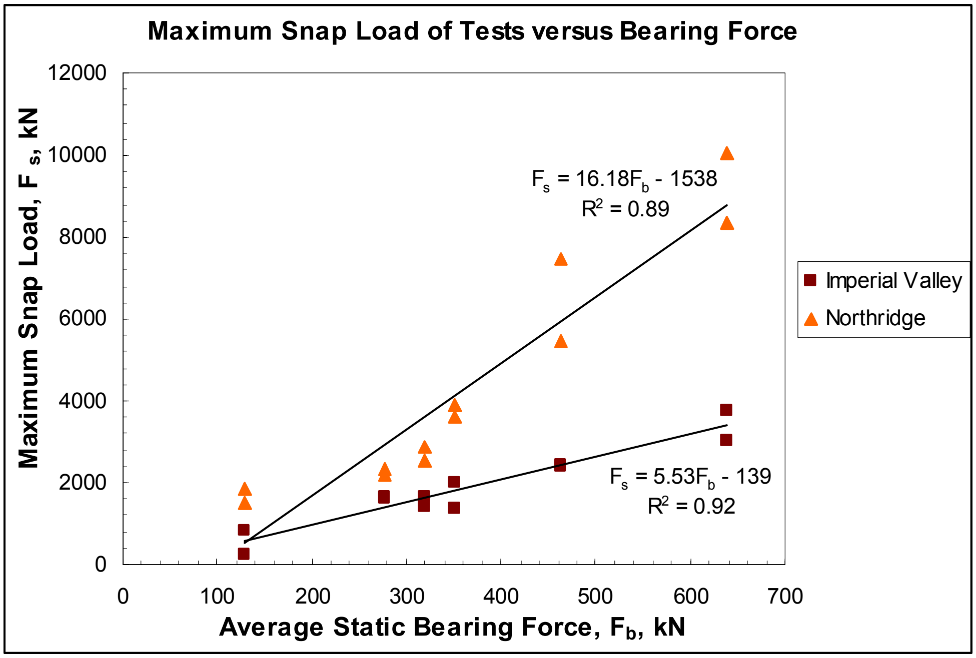

Figure 5.27 – Load versus static bearing force for all tests.

Another that was statistically significant was the distribution of load toward the exterior SCEDs (SCEDs 1, 5, 6, and 10). This was expected due to small span rotations but it was unclear what fraction of the maximum load the center (SCEDs 3 and 8) and intermediate SCEDs (SCEDs 2, 4, 7, and 9) would encounter. Figure 5.28 combines the maximum SCED load data into a single plot which distinctly shows the slightly "bow-tie" shaped distribution of loading across the spans. The distributions are normalized by dividing the maximum load of each SCED by the average load encountered by the corresponding set of SCEDs in the same test. The statistical distribution of this data is presented in Figure 5.29, where the mean and standard deviation of the data are plotted.

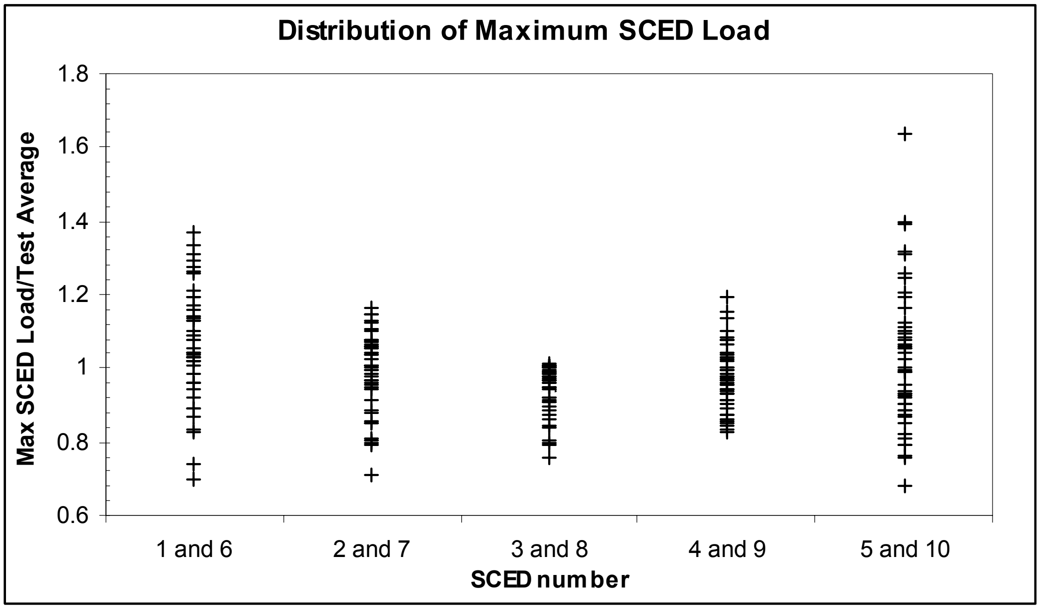

Figure 5.28 – Distribution of maximum SCED load for all tests. Note the larger possible loads at the exterior girders.

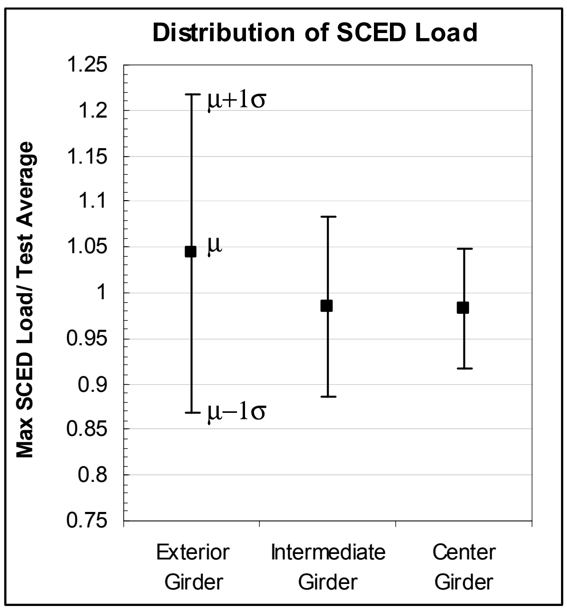

Figure 5.29 – Statistical distribution of SCED loading.

Additional accuracy could be added to these statistics by increasing the data sampling rate in a study focused on this distribution. The upshot of the data is that it may be more efficient to require stiffer SCEDs or all of the SCED capacity at the exterior girder lines. This would impose maximum displacement on the greatest SCED capacity and possibly require a configuration with a lower stiffness.

Generally for advocating the use of SCEDs, the simple fact that the tests lasted beyond 2.1s for the Imperial Valley trials and 5.3s for the Northridge trials to the full 20s test period shows marked success of the SCEDs in restraining simply supported single span bridge motion to within acceptable limits. Establishing a good relationship for what stiffness is required for any given bridge was reached by the data.

Chapter Six

Conclusions and Recommendations for Future Research

6.1 Summary and Conclusions

This thesis examined a method of reducing seismic load induced displacements of simply supported single span bridges. Movement of a bridge superstructure during a seismic event can result in damage to the bridge or even collapse of the span. An incapacitated bridge is a life-safety issue due directly to the damaged bridge and indirectly due the possible loss of a life-line. A lost bridge can be expensive to repair at a time when a region's resources are most strained, and a compromised commercial route could result in losses to the regional economy. Therefore, a retrofit method that is simple, reliable, and does not rely on outside power would be beneficial to seismic bridge design.

Six simply supported single spans were modeled using the commercial finite element program ABAQUS. Prestressed concrete girders with poured concrete decks were considered and rectangular sections with equivalent bending stiffnesses were developed to mimic the behavior of composite spans. Elastomeric bearing pads were modeled to consider friction, elastic horizontal stiffness, and damping. Vertical stiffness of the bearings was also considered.

Snapping-Cable Energy Dissipators (SCEDs) were modeled as nonlinear springs with stiffness units of $kN/m^{1.3}$ under tension. The SCEDs were modeled to have an initial slackness of 12.7mm. Therefore as the spans displaced, the SCEDs would only influence the response of the structure after 12.7mm displacement had occurred. At this point, the horizontal stiffness of the SCEDs, as well as the entire structure, increased. It was determined that for the range of motion encountered in these tests, the equivalent bilinear spring (kN/m) would have a stiffness coefficient of 42% or less than what was specified for the nonlinear spring. The SCEDs were modeled as being connected to the centroids of the girders.

The seismic records of the 1940 Imperial Valley earthquake and the 1994 Northridge earthquake were applied to the boundaries of the structures. The records were scaled to have peak ground accelerations (PGAs) of 0.7g. The orthogonal components were linearly scaled by the same factor.

Key nodes and elements on the models were then selected. During each test, the nodes were primarily monitored for displacement and the loads in the spring elements were recorded.

Tests were conducted to determine how a span's response was influenced by the orthogonal ground motion components. Twelve spans without SCEDs were subjected to only axial ground motion and an additional 12 spans were subjected to the full three-dimensional strong ground motion. The results showed that the response varied depending on the span and which earthquake record was used. Little change in response occurred in the Imperial Valley tests. However, some of the Northridge tests had extreme changes in response which was attributed mainly to the strong vertical component of this earthquake record. Heavier spans, such as span3 and span4, had limited variation in response when either of the three-dimensional records was used.

The final tests compared the response of spans with varying SCED stiffness. SCEDs of equal stiffness were connected between the ground and the girder ends. Acceptable axial displacement was confined to 0.1016m. Two tests of each span with each of the ground motions were conducted with various stiffnesses. In general, the SCEDs tested confined the axial motion of the spans within the acceptable displacement limits. However, the exact relationship between maximum displacement and a spans length, mass, and SCED stiffness was not determined. Trends relating the maximum snap load and the bearing weight were discovered for each earthquake. The tests showed loads as high as 10,000 kN in the SCEDs with the complete loading and unloading of the SCED occurring in a fraction of a second. The tests also showed that the demand on SCEDs connected to the exterior girders could be significantly larger than the demand on the other SCEDs.

In conclusion, the analysis showed that the SCEDs were effective in restraining the motion of the spans to within an acceptable limit when subjected to strong ground motions of up to 0.7g PGA in the axial direction. In only three tests with SCEDs did the motion of the span exceed the acceptable limit; even in these tests the exceedance was restricted to only a fraction of a second. In most cases, the maximum displacements of SCED tests were between 50% and 75% of the allowable limit.

6.2 Recommendations for Future Research

The next stage in the development of SCEDs for application as bridge restrainers would be to continue to develop finite element models. Further research to develop exact SCED properties for large diameter ropes and determining what, if any, damping should be applied in the models when the SCED ropes are taut would be beneficial to constructing finite element models utilizing SCEDs. For simply supported single span bridges, alternative bearing properties and SCED orientations, such as placing additional stiffness at the exterior girders and lateral restrainers, should be considered. Additional research to determine a practical relationship between maximum axial displacement and SCED stiffness for credible strong ground motions could create a quick and reliable way to size SCEDs for bridge applications.

Expanding the research into applications for steel girders, multispan simply supported bridges, and hinge restrainers in continuous decks creates a large number of variables worthy of investigation. Furthermore, development of a practical retrofit connection scheme for SCEDs is vital so that the snap loads can be fully developed.

Beyond finite element models, connections and verification of the SCEDs performance should be considered with full-scale models of bridge spans. The difficulty of applying a three-dimensional earthquake input to a full-scale model may necessitate a scaled model. In summary, the nonlinear effect of the SCEDs on a bridge span response and the numerous bridge parameters that can be modified require numerous more tests to be conducted in order to develop a robust but efficient stiffness requirement for any span.

References

AASHTO (2000). *2000 Interim AASHTO LRFD Bridge Design Specifications, SI Units, 2nd Ed.*, Washington, DC, Section 14.

ABAQUS (2003a). *Analysis User's Manual, v.6.4*, ABAQUS, Inc., Pawtucket, RI.

ABAQUS (2003b). *Keywords Reference Manual, v.6.4*, ABAQUS, Inc., Pawtucket, RI.

Aswad, A., Tulin, L.G. (1986). "Responses of random-oriented-fiber and neoprene bearing pads under selected loading conditions." Second World Congress on Joint Sealing and Bearing Systems for Concrete Structures, San Antonio, TX.

Caner, A., Dogan, E., Zia, P. (2002). "Seismic performance of multisimple-span bridges retrofitted with link slabs." *Journal of Bridge Engineering*, 7(2), 85-93.

Chopra, A.K. (1995). *Dynamics of Structures: Theory and Applications to Earthquake Engineering*, Prentice Hall, Upper Saddle River, NJ, 417-425.

DesRoches, R., Delemont, M. (2002). "Seismic retrofit of simply supported bridges using shape memory alloys." *Engineering Structures*, 24(3), 325-332.

DesRoches, R., Fenves, G.L. (2000). "Design of seismic cable hinge restrainers for bridges." *Journal of Structural Engineering*, 126(4), 500-509.

DesRoches, R., Choi, E., Leon, R.T., Dyke, S.J., Aschheim, M. (2004a). "Seismic response of multispan bridges in central and southeastern United States. I: as built." *Journal of Bridge Engineering*, 9(5), 464-472.

DesRoches, R., Choi, E., Leon, R.T., Pfeifer, T.A. (2004b). "Seismic response of multispan bridges in central and southeastern United States. II: retrofitted." *Journal of Bridge Engineering*, 9(5), 473-479.

DesRoches, R., Pfeifer, T., Leon, R.T., Lam, T. (2003). "Full-scale tests of seismic cable restrainer retrofits for simply supported bridges." *Journal of Bridge Engineering*, 8(4), 191-198.

Feng, M.Q. Kim, J.-M., Shinozuka, M., Purasinghe, R. (2000). "Viscoelastic dampers at expansion joints for seismic protection of bridges." *Journal of Bridge Engineering*, 5(1), 67-74.

Feng, X. (1999). "Bridge earthquake protection with seismic isolation." *Optimizing Post-Earthquake Lifeline System Reliability: Proceedings of the 5th U.S. Conference on Lifeline Earthquake Engineering*, ASCE, Reston, VA, 267-275.

Filiatrault, A., Stearns, C. (2004). "Seismic response of electrical substation equipment interconnected by flexible conductors." *Journal of Structural Engineering*, 130(5), 769-778.

Hennessey, C.M. (2003). "Analysis and modeling of snap loads on synthetic fiber ropes." M.S. Thesis. Virginia Polytechnic Institute and State University, Blacksburg, VA. http://scholar.lib.vt.edu/theses/available/etd-11092003-135228/.

Hiemenz, G.J., Wereley, N.M. (1999). "Seismic response of civil engineering structures utilizing semi-active MR and ER bracing systems." *Journal of Intelligent Material Systems and Structures*, 10(8), 646-651.

Housner, G. W., Thiel, C. C. (1990). “Competing against time: report of the Governor’s Board of Inquiry on the 1989 Loma Prieta earthquake.” *Earthquake Spectra*, 6(4), 681-711.

Kim, J.-M., Feng, M.Q., Shinozuka, M. (2000). “Energy dissipating restrainers for highway bridges.” *Soil Dynamics and Earthquake Engineering*, 19(1), 65-69.

Liao, W.-I., Loh, C.-H., Lee, B.-H. (2004). “Comparison of dynamic response of isolated and no-isolated continuous girder bridges subjected to near-fault ground motions.” *Engineering Structures*, 26(14), 2173-2183.

Manfredi, G., Polese, M., Cosenza, E. (2003). “Cumulative demand of the earthquake ground motions in the near source.” *Earthquake Engineering and Structural Dynamics*, 32(12), 1853-1865.

McDonald, J., Heymsfield, E., Avent, R.R. (2000). “Slippage of neoprene bridge bearings.” *Journal of Bridge Engineering*, 5(3), 216-223.

Mitchell, D., Bruneau, M., Williams, M., Anderson, D., Saatcioglu, M., Sexsmith, R. (1995). “Performance of bridges in the 1994 Northridge earthquake.” *Canadian Journal of Civil Engineering*, 22(2), 415-427.

Mitchell, D., Sexsmith, R., Tinawi, R. (1994). “Seismic retrofitting techniques for bridges – a state-of-the-art report.” *Canadian Journal of Civil Engineering*, 21(5), 823-835.

Motley, M.R. (2004). “Finite element analysis of the application of synthetic fiber ropes to reduce blast response of frames.” M.S. Thesis. Virginia Polytechnic Institute and State University, Blacksburg, VA. http://scholar.lib.vt.edu/theses/available/ etd-12152004-102556.

Pacific Earthquake Engineering Research Center (2005). "PEER Strong Motion Database". Regents of the University of California, Berkeley, CA. http://peer.berkeley.edu/smcat/.

Palm III, W.J. (2000). *Modeling, Analysis, and Control of Dynamic Systems, 2nd Ed.*, John Wiley & Sons, Inc., New York, NY, 83-97, 245-262.

Precast/Prestressed Concrete Institute (2003). *PCI Bridge Design Manual*, Chicago, IL, Section 9.4.

Pearson, N.J. (2002). "Experimental snap loading of synthetic fiber ropes," M.S. Thesis. Virginia Polytechnic Institute and State University, Blacksburg, VA. http://scholar.lib.vt.edu/theses/available/etd-01132003-105300/.

Plaut, R.H., Archilla, J.C., Mays, T.W. (2000). "Snap loads in mooring lines during large three-dimensional motions of a cylinder." *Nonlinear Dynamics*, 23(3), 271-284.

Spyrakos, C.C., Vlassis, A.G. (2003) "Seismic retrofit of reinforced concrete bridges." *Earthquake Resistant Engineering Structures IV*, WIT Press, Boston, MA, 79-88.

Zhang, R. (2000). "Seismic isolation and supplemental energy dissipation." *Bridge Engineering Handbook*, Chen, W.F., and Duan, L., eds., CRC Press, Boca Raton, FL, 41/1-41/36.

Appendix A

Approximate Rectangular Section Calculations

A.1 Verification Routine

Name: Verification

Matching results from Section 9.4 of
PCI Bridge Design Manual, Jul 03

Input Variables:

Span length, m
$L = 36.576$

Girder spacing, m
$S = 2.743$

Girder depth, m
$d = 1.829$

Girder cross-sectional area, m^2
$A = 0.495$

Girder moment of inertia, m^4
$Ig = 0.227$

Girder centroid from base, m
$Yg = 0.93$

Deck structural thickness, m
$t = 0.191$

Deck actual thickness, m
$tm = 0.203$

Deck width, m
$w := (N-1)\cdot S + 6$
$w = 15.545$

Unit mass, kg/m^3
$m = 2402.535$

Other dead weight, kg/m
$dc = 892.8$

Web thickness, m
$tw = 0.152$

Flange width, m
$wf = 1.067$

Average haunch depth, m
$dh = 0.013$

Girder f'c, psi
Fc = 6500

Deck f'c, psi
Fcd = 4000

New Total Cross-Section

New width, m	$wnew := w$	$wnew = 15.545$
New height, m	$dnew := d + t$	$dnew = 2.019$
New cross-sectional area, m	$Anew := dnew \cdot wnew$	$Anew = 31.39$

Moduli of Elasticity

Girder Concrete Modulus, Pa

$$Eg := 33\cdot 6895\cdot\left(\frac{m}{16.0169}\right)^{1.5}\cdot fc^{0.5} \qquad Eg = 33.701\times 10^{9}$$

Strand Modulus, Pa

$$Es := 195000000000 \qquad Es = 195\times 10^{9}$$

Deck Modulus of Elasticity, Pa

$$Ed := 33\cdot 6895\cdot\left(\frac{m}{16.0169}\right)^{1.5}\cdot fcd^{0.5} \qquad Ed = 26.437\times 10^{9}$$

Total Mass:

1. Old C-S area, m^2 $\quad Atotal := N\cdot A + t\cdot w \qquad Atotal = 5.93$
2. Total mass, kg $\quad Mtotal := m\cdot L\cdot(N\cdot A + tm\cdot w + N\cdot dh\cdot wf) + dc\cdot L \qquad Mtotal = 578289.593$
3. New unit mass, kg/m^3 $\quad mnew := \dfrac{Mtotal}{Anew\cdot L} \qquad mnew = 503.69$

Bending Stiffness:

1. New Moment of Inertia, m^4 $\quad Inew := \frac{(dnew)^3 \cdot (wnew)}{12}$ $\quad Inew = 10.666$

2. Actual moment of inertia, m^4

A. Interior Girder

i. Effective interior deck width, m $\quad wdei := \min\left(\frac{L}{4}, 12 \cdot t + \max(tw, 0.5 \cdot wf), S\right)$ $\quad wdei = 2.743$

ii. Modular ratio, Pa/Pa $\quad n := \frac{Ed}{Eg}$ $\quad n = 0.784$

iii. Interior transformed deck and haunch areas, m^2

$Adti := n \cdot wdei \cdot t$ $\quad Adti = 0.41$

$Ahti := n \cdot wf \cdot dh$ $\quad Ahti = 0.011$

iv. Composite centroid distance from bottom, m

$$Ybi := \frac{A \cdot Yg + Ahti \cdot (d + 0.5 \cdot dh) + (Adti) \cdot (d + dh + .5 \cdot t)}{A + Adti + Ahti} \qquad Ybi = 1.391$$

v. Composite moment of inertia, m^4

$$Iint := Ig + A \cdot (Ybi - Yg)^2 + \frac{Ahti \cdot dh^2}{12} + Ahti \cdot (Ybi - d + 0.5 \cdot dh)^2 + \frac{wdei \cdot t^3}{12} + Adti \cdot [Ybi - (d + dh + .5t)]^2$$

$\boxed{Iint = 0.458}$ $\quad \boxed{IintfromPCI := 0.45799}$

B. Exterior Girder

i. Effective exterior deck width, m

$$wdee := \min\left(\frac{L}{4}, 12 \cdot t + \max(tw, 0.5 \cdot wf), .5S + 3 \cdot .3048\right) \qquad wdee = 2.286$$

ii. Modular ratio, Pa/Pa $\quad n := \frac{Ed}{Eg}$ $\quad n = 0.784$

iii. Exterior transformed deck and haunch areas, m^2

$Adte := n \cdot wdee \cdot t$ $\quad Adte = 0.342$

$Ahte := n \cdot wf \cdot dh$ $\quad Ahte = 0.011$

iv. Composite centroid distance from bottom, m

$$Ybe := \frac{A \cdot Yg + Ahte \cdot (d + 0.5 \cdot dh) + (Adte) \cdot (d + dh + .5 \cdot t)}{A + Adte + Ahte} \qquad Ybe = 1.347$$

v. Composite moment of inertia, m^4

$$Iext := Ig + A\cdot(Ybe - Yg)^2 + \frac{Ahte\cdot dh^2}{12} + Ahte\cdot(Ybe - d + 0.5\cdot dh)^2 + \frac{wdee\cdot t^3}{12} + Adte\cdot[Ybe - (d + dh + .5t)]^2$$

$Iext = 0.436$

C. Combined Composite moment of inertia, m^4 $\quad Iold := (N - 2)\cdot Iint + 2Iext \quad Iold = 2.705$

3. Bending Stiffness, $N.m^2$

$EIold := Iold\cdot Eg \quad EIold = 91.153\times 10^9$

Determination of new modulus:

1. From Bending, Pa $\quad Ebend := \frac{EIold}{Inew} \quad Ebend = 8.546\times 10^9$

2. New Modulus, Pa $\quad Enew := Ebend \quad Enew = 8.546\times 10^9$

Dead load deflection:

$$\delta := \frac{5(9.81mnew\cdot wnew\cdot dnew)\cdot L^4}{384\cdot Enew\cdot Inew}$$

$\delta = 0.03965$ m

Deflections expected at 6% of PCI values

Deflection of interior beam at full strength using PCI's values:

$0.7343 + 0.7988 + 0.130 = 1.663$ in.

$\delta pci := 1.663\cdot 0.0254 \quad \delta pci = 0.0422$ m

$$1 - \frac{\delta}{\delta pci} = 0.061$$

Summary of new span section:

1. Depth, m	$dnew = 2.019$
2. Width, m	$wnew = 15.545$
3. Length, m	$L = 36.576$
4. Unit mass, kg/m^3	$mnew = 503.69$
5. Young's modulus, Pa	$Enew = 8.546\times 10^9$
6. Mid-span deflection, m	$\delta = 0.0397$
7. Girder spacing, m	$S = 2.743$
8. Interior moment of Inertia, m^4	$Iint = 0.458$

A.2 Summary of Span1 Calculations

Input Variables:

Span length, m
$L = 12.192$

Girder spacing, m
$S = 1.981$

Girder depth, m
$d = 0.737$

Girder cross-sectional area, m^2
$A = 0.415$

Girder moment of inertia, m^4
$Ig = 0.028$

Girder centroid from base, m
$Yg = 0.372$

Deck structural thickness, m
$t = 0.191$

Deck actual thickness, m
$tm = 0.203$

Deck width, m
$w := (N - 1) \cdot S + 6$
$w = 9.754$

Unit mass, kg/m^3
$m = 2402.535$

Other dead weight, kg/m
$dc = 892.8$

Web thickness, m
$tw = 0.178$

Flange width, m
$wf = 1.194$

Average haunch depth, m
$dh = 0.013$

Girder f'c, psi
Fc = 6000

Deck f'c, psi
Fcd = 4000

Summary of new span section:

1. Depth, m	$dnew = 0.927$
2. Width, m	$wnew = 9.754$
3. Length, m	$L = 12.192$
4. Unit mass, kg/m^3	$mnew = 1197.187$
5. Young's Modulus, Pa	$Enew = 17.078 \times 10^9$
6. Mid-span deflection, m	$\delta = 0.002762$
7. Girder spacing, m	$S = 1.981$
8. Interior moment of Inertia, m^4	$Iint = 0.069$
9. Span total mass, kg	$M = 131986$

A.3 Summary of Span2 Calculations

Input Variables:

Span length, m
$L = 24.384$

Girder spacing, m
$S = 1.981$

Girder depth, m
$d = 1.143$

Girder cross-sectional area, m^2
$A = 0.482$

Girder moment of inertia, m^4
$Ig = 0.086$

Girder centroid from base, m
$Yg = 0.565$

Deck structural thickness, m
$t = 0.191$

Deck actual thickness, m
$tm = 0.203$

Deck width, m
$w := (N - 1) \cdot S + 6$
$w = 9.754$

Unit mass, kg/m^3
$m = 2402.535$

Other dead weight, kg/m
$dc = 892.8$

Web thickness, m
$tw = 0.178$

Flange width, m
$wf = 1.194$

Average haunch depth, m
$dh = 0.013$

Girder f'c, psi
Fc = 6000

Deck f'c, psi
Fcd = 4000

Summary of new span section:

1. Depth, m — $dnew = 1.333$
2. Width, m — $wnew = 9.754$
3. Length, m — $L = 24.384$
4. Unit mass, kg/m^3 — $mnew = 893.708$
5. Young's Modulus, Pa — $Enew = 14.804 \times 10^9$
6. Mid-span deflection, m — $\delta = 0.0184$
7. Girder spacing, m — $S = 1.981$
8. Interior moment of Inertia, m^4 — $Iint = 0.177$
9 Span total mass, kg — $M = 283438$

A.4 Summary of Span3 Calculations

Input Variables:

Span length, m
$L = 36.576$

Girder spacing, m
$S = 1.981$

Girder depth, m
$d = 1.753$

Girder cross-sectional area, m^2
$A = 0.59$

Girder moment of inertia, m^4
$Ig = 0.25$

Girder centroid from base, m
$Yg = 0.858$

Deck structural thickness, m
$t = 0.191$

Deck actual thickness, m
$tm = 0.203$

Deck width, m
$w := (N - 1) \cdot S + 6$
$w = 9.754$

Unit mass, kg/m^3
$m = 2402.535$

Other dead weight, kg/m
$dc = 892.8$

Web thickness, m
$tw = 0.178$

Flange width, m
$wf = 1.194$

Average haunch depth, m
$dh = 0.013$

Girder f'c, psi
Fc = 6000

Deck f'c, psi
Fcd = 4000

Summary of new span section:

1. Depth, m	$dnew = 1.943$
2. Width, m	$wnew = 9.754$
3. Length, m	$L = 36.576$
4. Unit mass, kg/m^3	$mnew = 682.033$
5. Young's Modulus, Pa	$Enew = 12.746 \times 10^9$
6. Mid-span deflection, m	$\delta = 0.039$
7. Girder spacing, m	$S = 1.981$
8. Interior moment of Inertia, m^4	$Iint = 0.453$
9 Span total mass, kg	$M = 472783$

A.5 Summary of Span4 Calculations

Input Variables:

Span length, m
$L = 45.72$

Girder spacing, m
$S = 1.981$

Girder depth, m
$d = 2.362$

Girder cross-sectional area, m^2
$A = 0.699$

Girder moment of inertia, m^4
$Ig = 0.524$

Girder centroid from base, m
$Yg = 1.155$

Deck structural thickness, m
$t = 0.191$

Deck actual thickness, m
$tm = 0.203$

Deck width, m
$w := (N - 1)\cdot S + 6$
$w = 9.754$

Unit mass, kg/m^3
$m = 2402.535$

Other dead weight, kg/m
$dc = 892.8$

Web thickness, m
$tw = 0.178$

Flange width, m
$wf = 1.194$

Average haunch depth, m
$dh = 0.013$

Girder f'c, psi
Fc = 6000

Deck f'c, psi
Fcd = 4000

Summary of new span section:

1. Depth, m	$dnew = 2.553$
2. Width, m	$wnew = 9.754$
3. Length, m	$L = 45.72$
4. Unit mass, kg/m^3	$mnew = 571.457$
5. Young's Modulus, Pa	$Enew = 10.76\times 10^9$
6. Mid-span deflection, m	$\delta = 0.0546$
7. Girder spacing, m	$S = 1.981$
8. Interior moment of Inertia, m^4	$Iint = 0.902$
9 Span total mass, kg	$M = 650510$

A.6 Summary of Span5 Calculations

Input Variables:

Span length, m
$L = 24.384$

Girder spacing, m
$S = 2.438$

Girder depth, m
$d = 1.549$

Girder cross-sectional area, m^2
$A = 0.554$

Girder moment of inertia, m^4
$Ig = 0.184$

Girder centroid from base, m
$Yg = 0.76$

Deck structural thickness, m
$t = 0.191$

Deck actual thickness, m
$tm = 0.203$

Deck width, m
$w := (N - 1) \cdot S + 6$
$w = 11.582$

Unit mass, kg/m^3
$m = 2402.535$

Other dead weight, kg/m
$dc = 892.8$

Web thickness, m
$tw = 0.178$

Flange width, m
$wf = 1.194$

Average haunch depth, m
$dh = 0.013$

Girder f'c, psi
Fc = 6000

Deck f'c, psi
Fcd = 4000

Summary of new span section:

1. Depth, m	$d = 1.549$
2. Width, m	$wnew = 11.582$
3. Length, m	$L = 24.384$
4. Unit mass, kg/m^3	$mnew = 664.186$
5. Young's Modulus, Pa	$Enew = 11.581 \times 10^9$
6. Mid-span deflection, m	$\delta = 0.01027$
7. Girder spacing, m	$S = 2.438$
8. Interior moment of Inertia, m^4	$Iint = 0.369$
9 Span total mass, kg	$M = 326375$

A.7 Summary of Span6 Calculations

Input Variables:

Span length, m
$L = 24.384$

Girder spacing, m
$S = 2.896$

Girder depth, m
$d = 1.753$

Girder cross-sectional area, m^2
$A = 0.59$

Girder moment of inertia, m^4
$Ig = 0.25$

Girder centroid from base, m
$Yg = 0.858$

Deck structural thickness, m
$t = 0.191$

Deck actual thickness, m
$tm = 0.203$

Deck width, m
$w := (N - 1) \cdot S + 6$
$w = 13.411$

Unit mass, kg/m^3
$m = 2402.535$

Other dead weight, kg/m
$dc = 892.8$

Web thickness, m
$tw = 0.178$

Flange width, m
$wf = 1.194$

Average haunch depth, m
$dh = 0.013$

Girder f'c, psi
Fc = 6000

Deck f'c, psi
Fcd = 4000

Summary of new span section:

1. Depth, m	$dnew = 1.943$
2. Width, m	$wnew = 13.411$
3. Length, m	$L = 24.384$
4. Unit mass, kg/m^3	$mnew = 564.546$
5. Young's Modulus, Pa	$Enew = 9.856 \times 10^9$
6. Mid-span deflection, m	$\delta = 0.00822$
7. Girder spacing, m	$S = 2.896$
8. Interior moment of Inertia, m^4	$Iint = 0.51$
9 Span total mass, kg	$M = 358729$

Appendix B

Ground Motion Figures

B.1 1940 Imperial Valley – El Centro record

B.1.1 Ground acceleration time-history

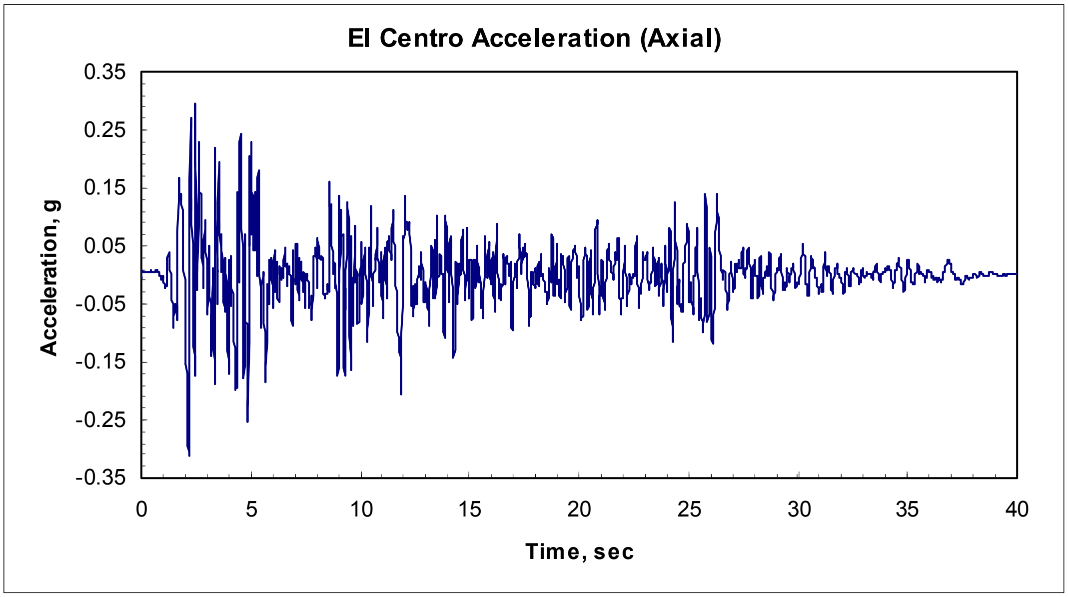

Figure B.1– 1940 Imperial Valley (El Centro 180, North-South)

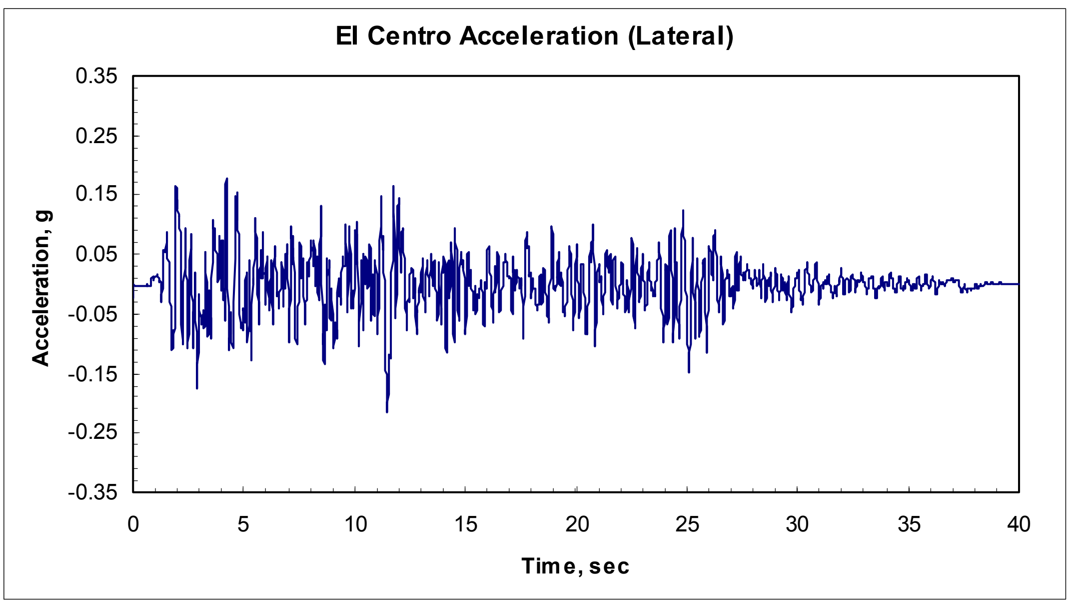

Figure B.2 – 1940 Imperial Valley (El Centro 270, East-West)

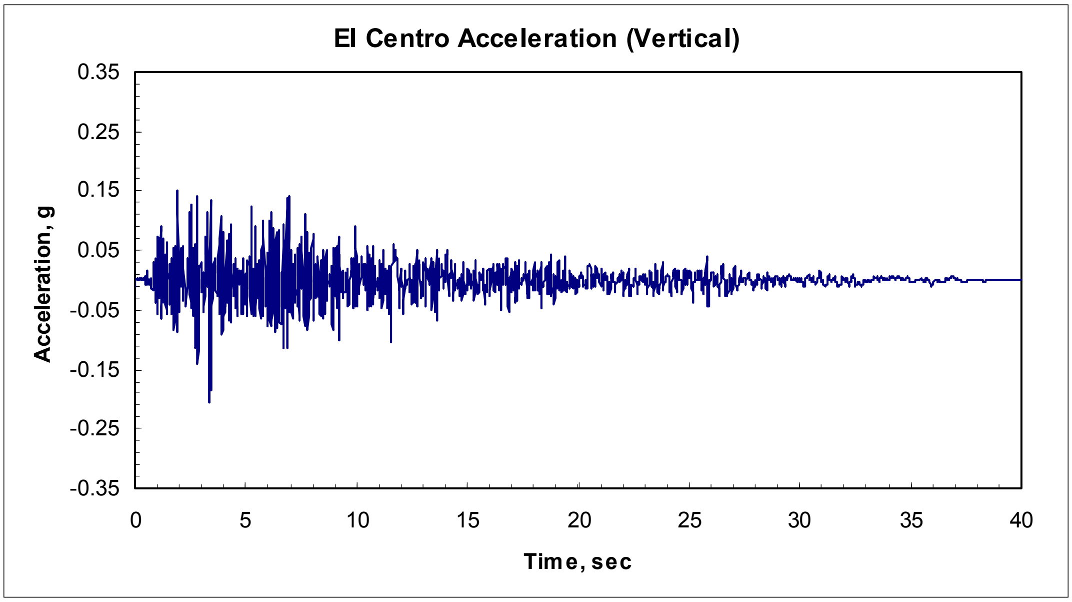

Figure B.3 – 1940 Imperial Valley (El Centro, Up-Down)

B.1.2 Ground displacement time-history

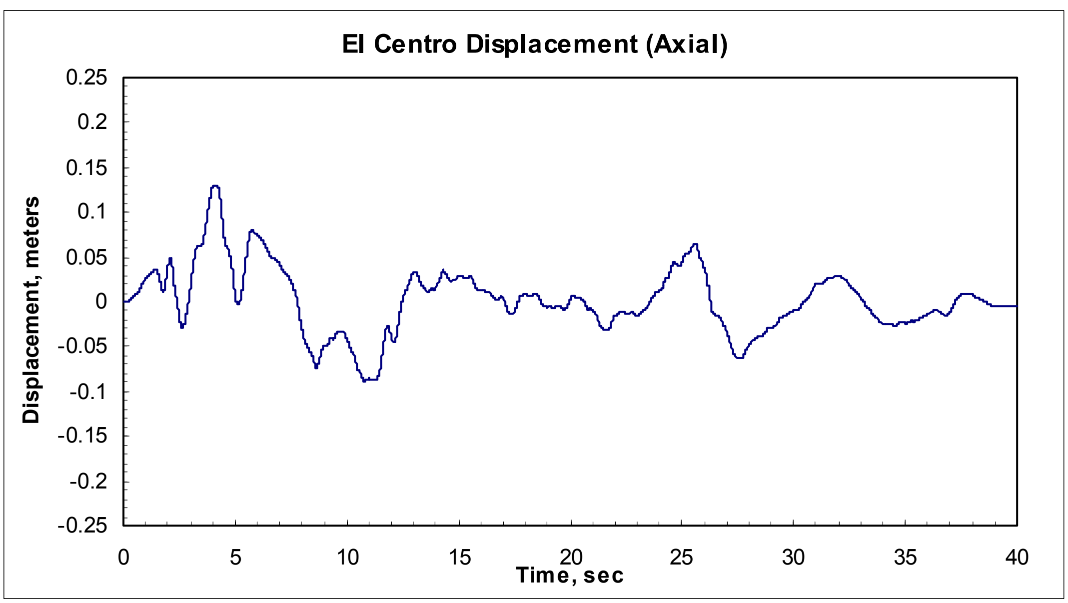

Figure B.4 – 1940 Imperial Valley (El Centro 180, North-South)

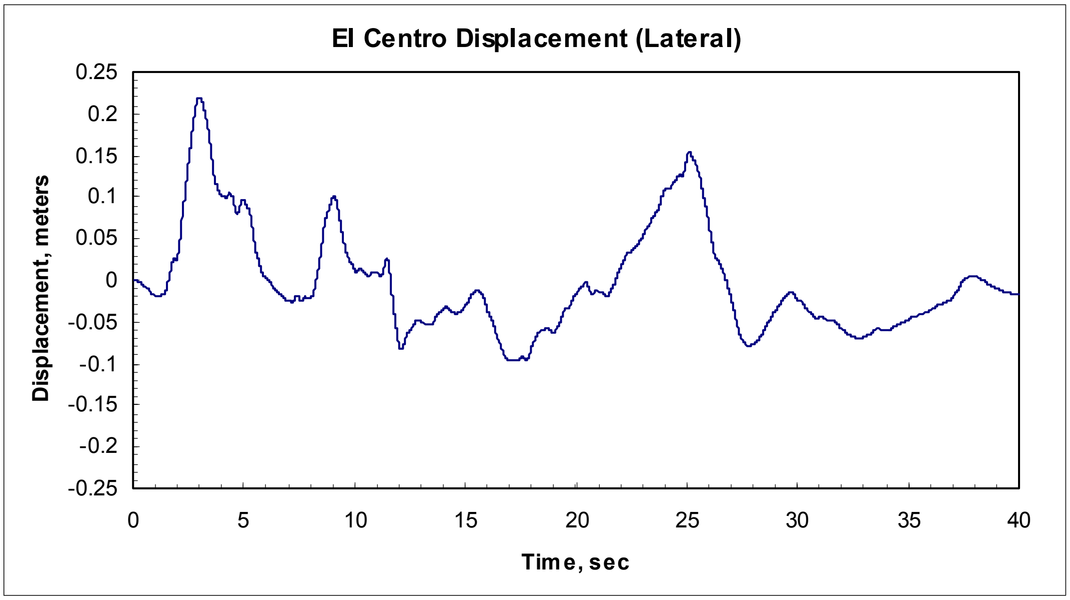

Figure B.5 – 1940 Imperial Valley (El Centro 270, East-West)

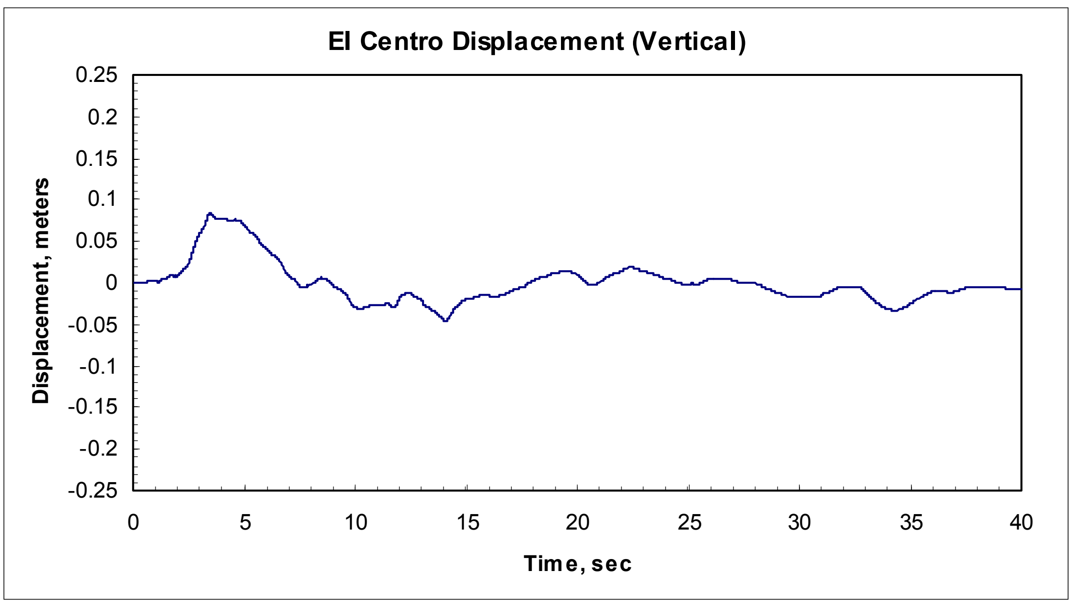

Figure B.6 – 1940 Imperial Valley (El Centro, Up-Down)

B.1.3 Spatial acceleration history

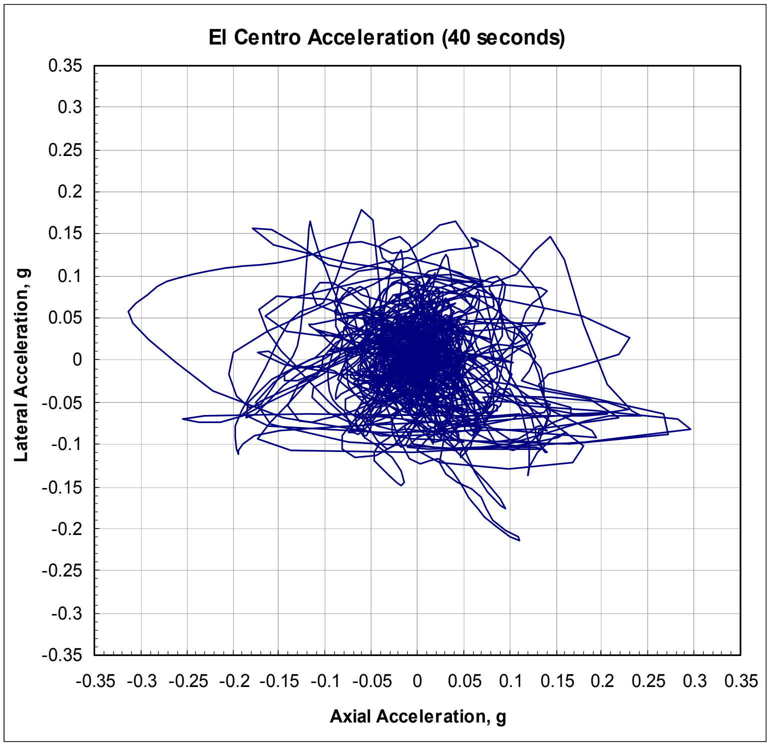

Figure B.7 – Horizontal spatial ground acceleration record.

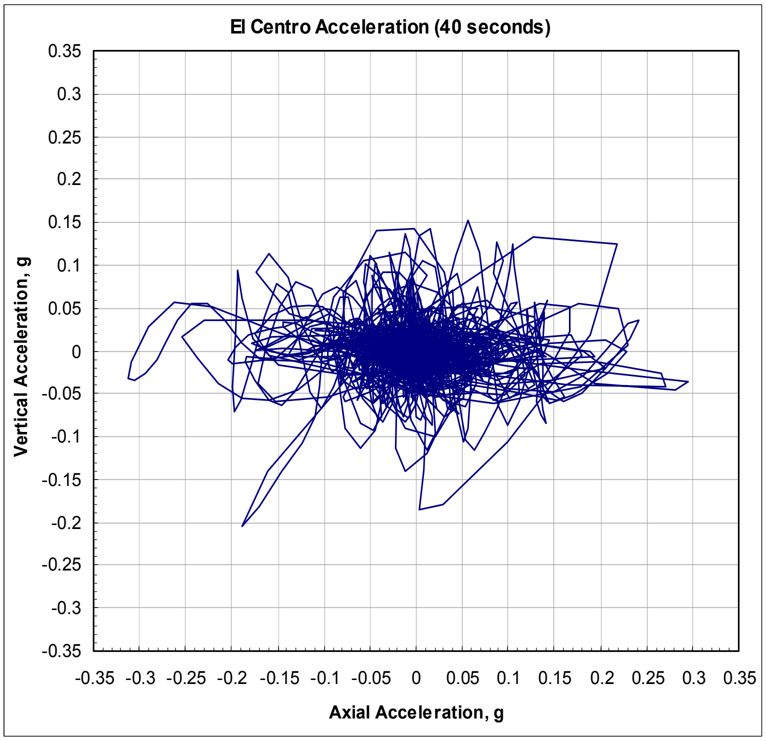

Figure B.8 – Up-Down vs. N-S spatial ground acceleration record.

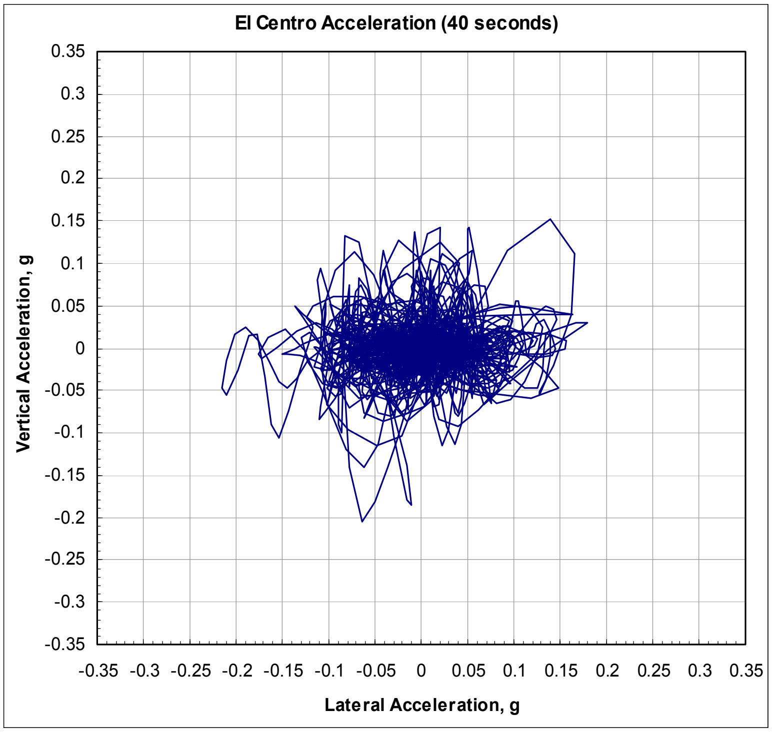

Figure B.9 – Up-Down vs. E-W spatial ground acceleration record.

B.1.4 Spatial displacement history

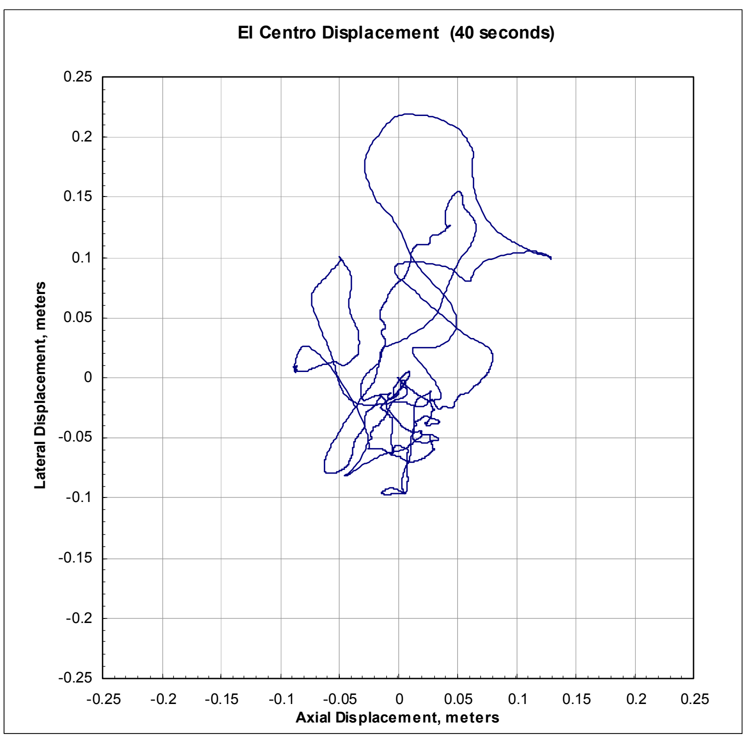

Figure B.10 – Horizontal spatial ground acceleration record.

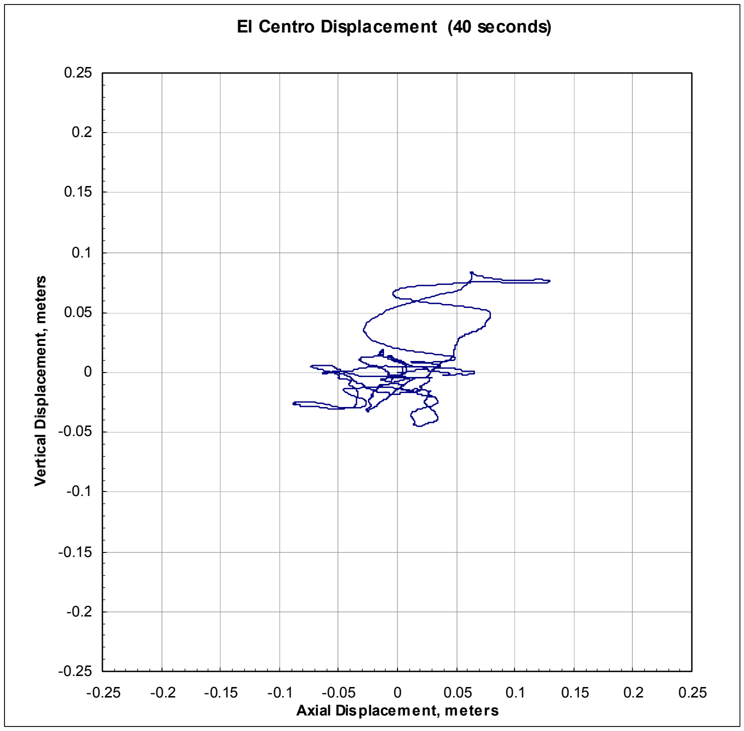

Figure B.11 – Up-Down vs. N-S spatial ground acceleration record.

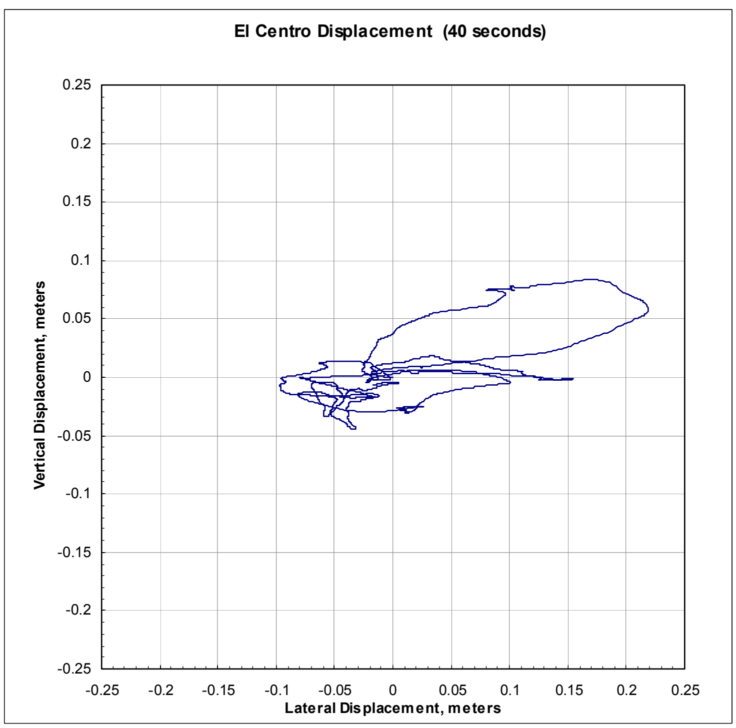

Figure B.12 – Up-Down vs. E-W spatial ground acceleration record.

B.2 1994 Northridge – Newhall record

B.2.1 Ground acceleration time-history

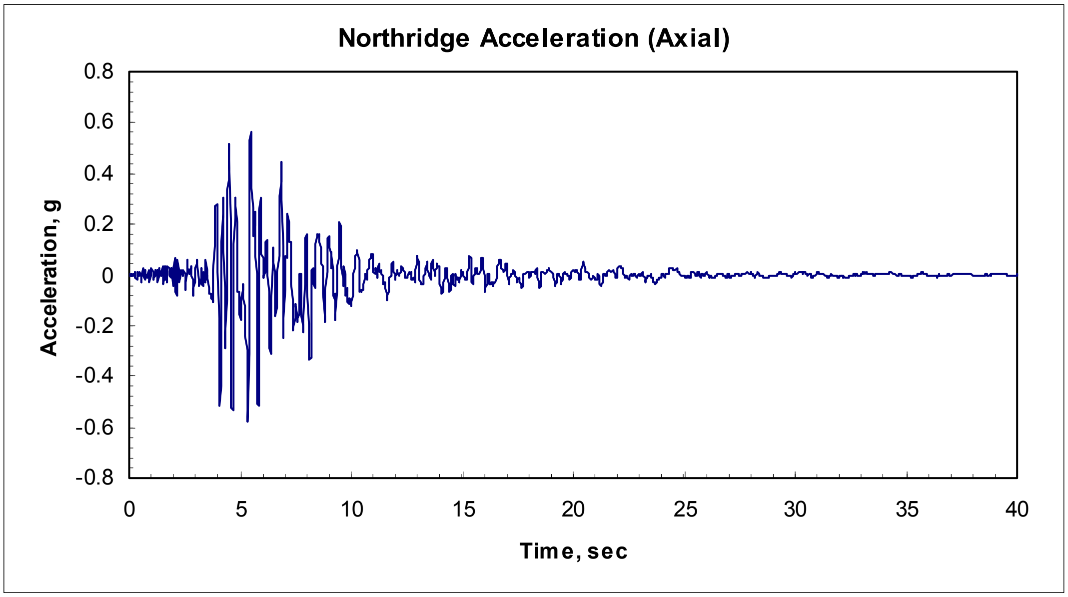

Figure B.13 – 1994 Northridge (Newhall 90, East-West)

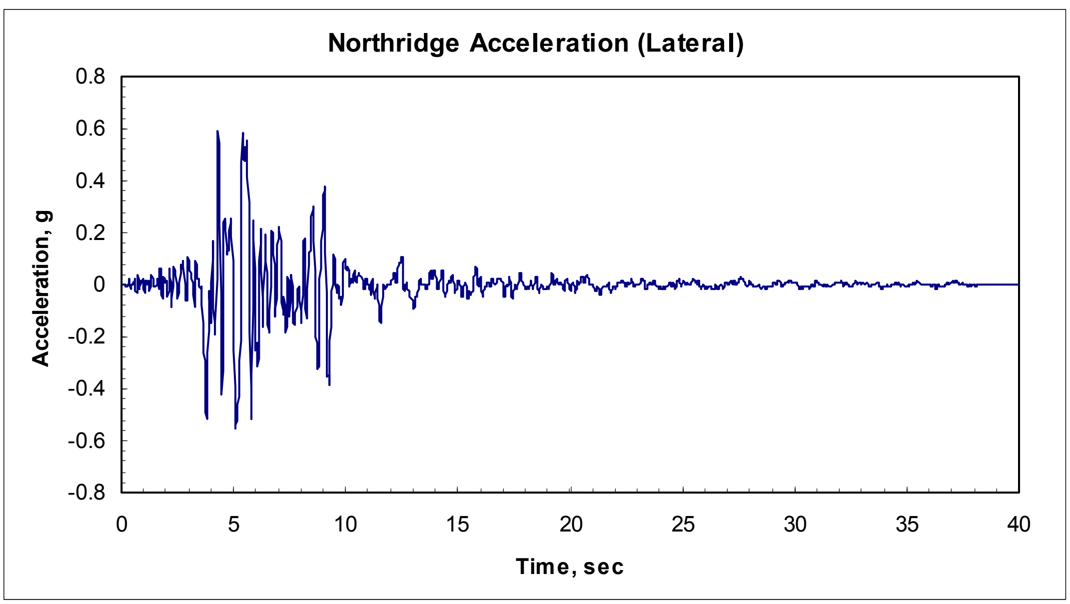

Figure B.14 - 1994 Northridge (Newhall 360, North-South)

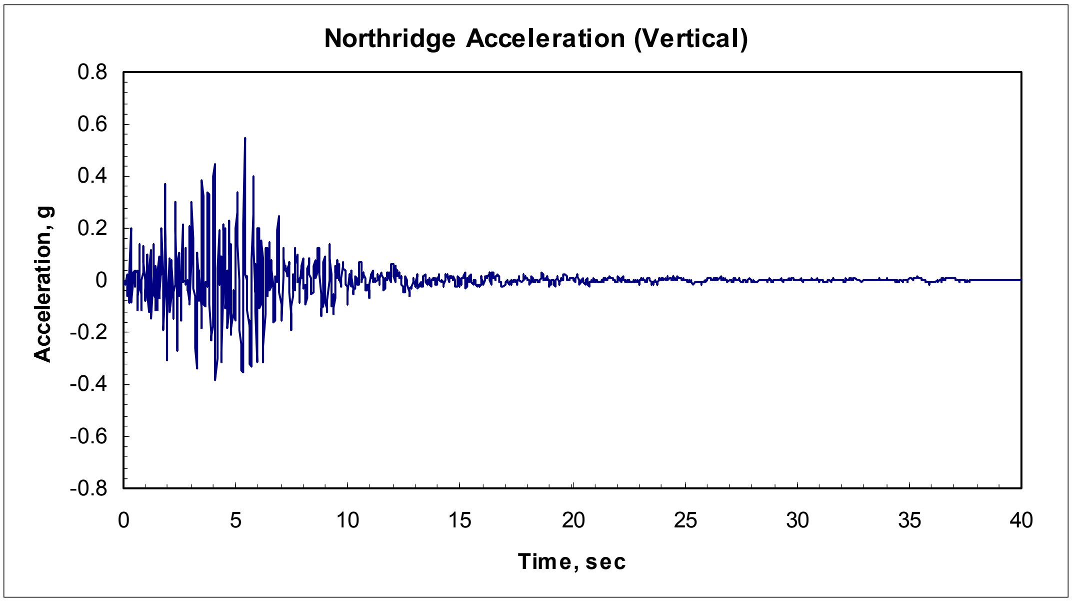

Figure B.15 - 1994 Northridge (Newhall, Up-Down)

B.2.2 Ground displacement time-history

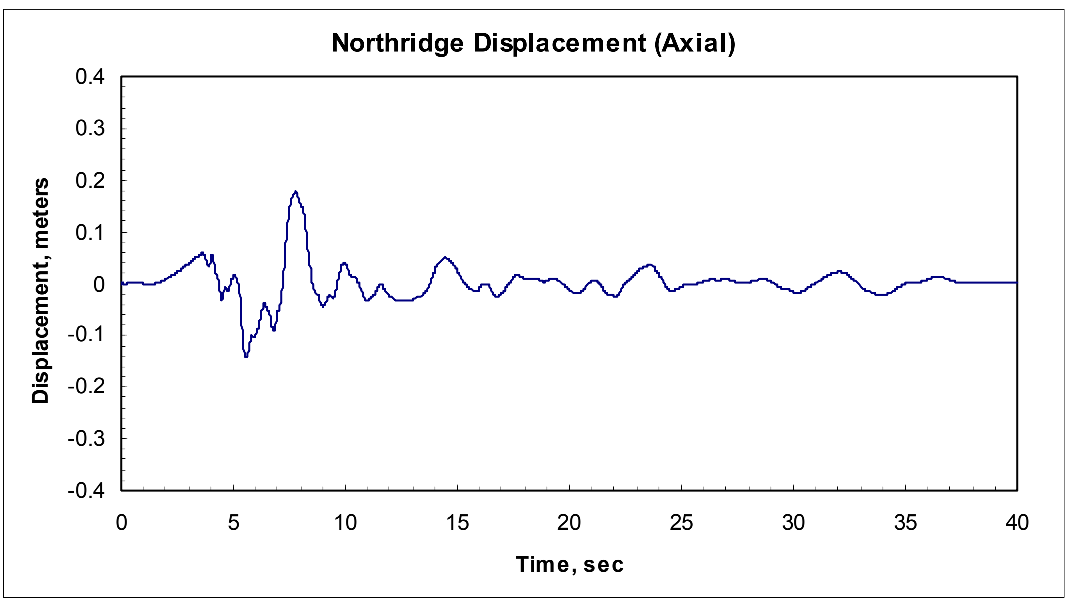

Figure B.16 – 1994 Northridge (Newhall 90, East-West)

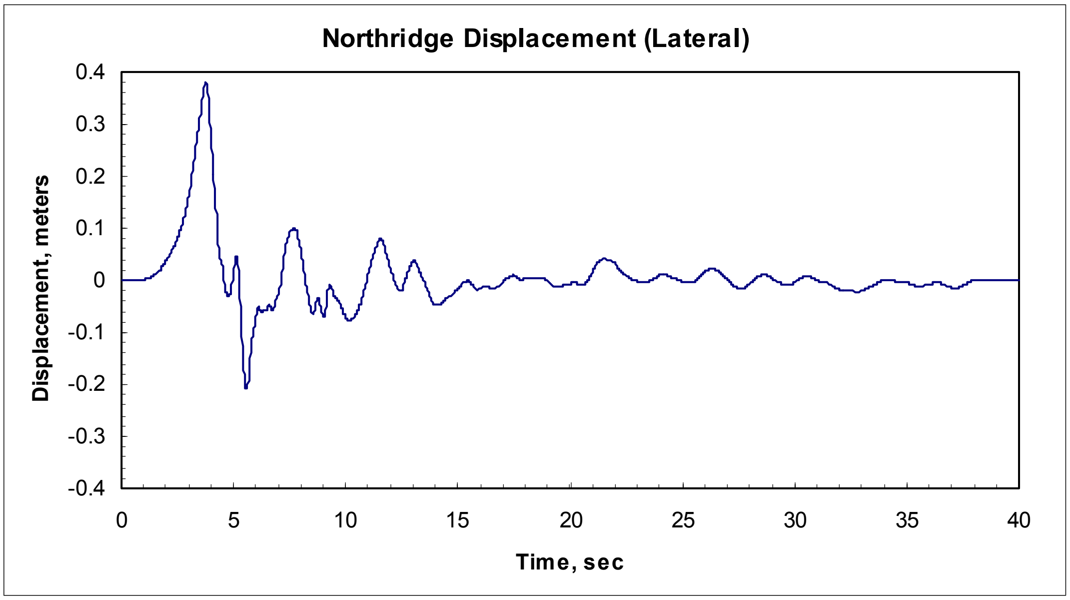

Figure B.17 - 1994 Northridge (Newhall 360, North-South)

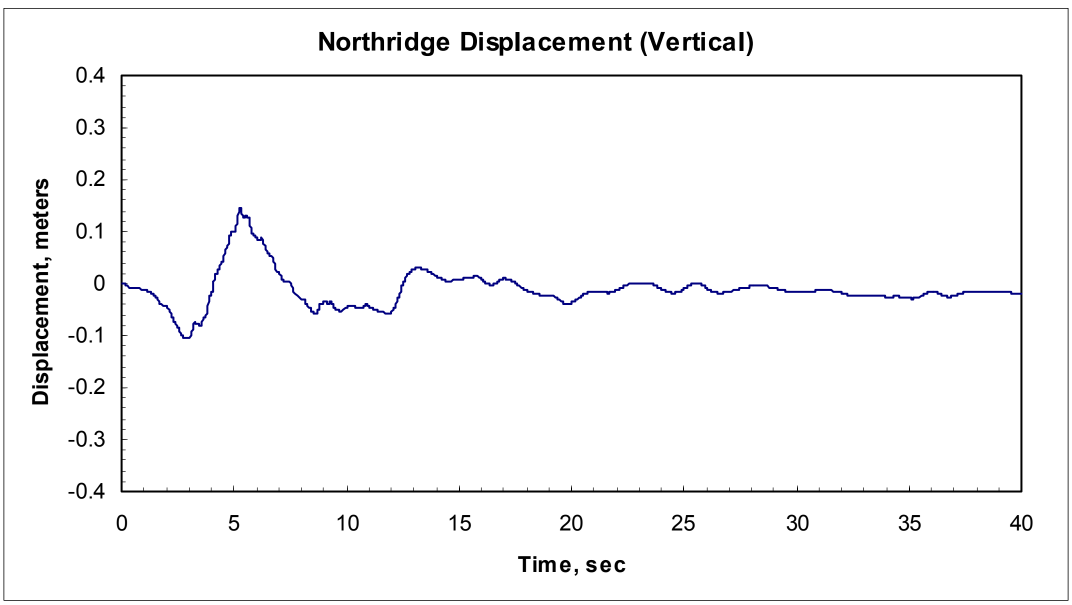

Figure B.18 – 1994 Northridge (Newhall, Up – Down)

B.2.3 Spatial acceleration history

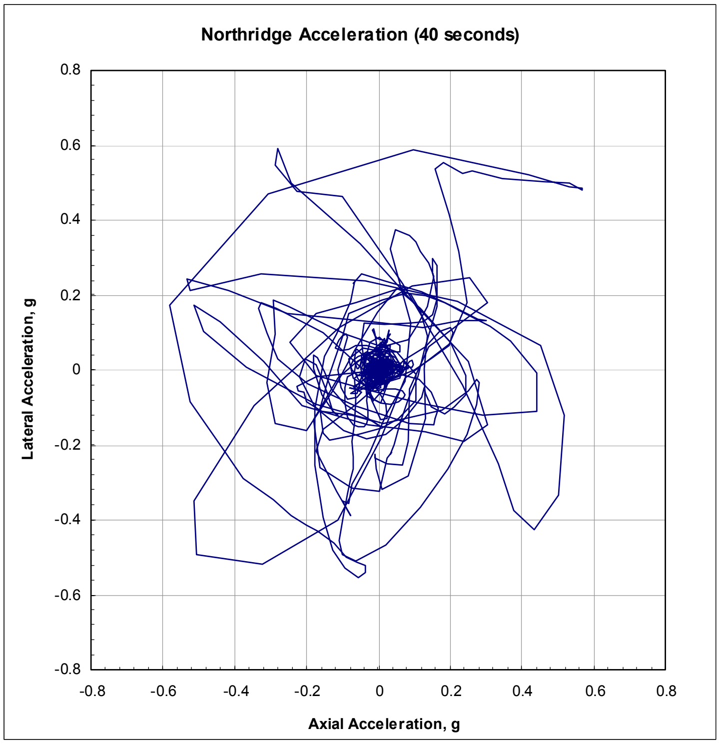

Figure B.19 – Horizontal spatial ground acceleration record**.**

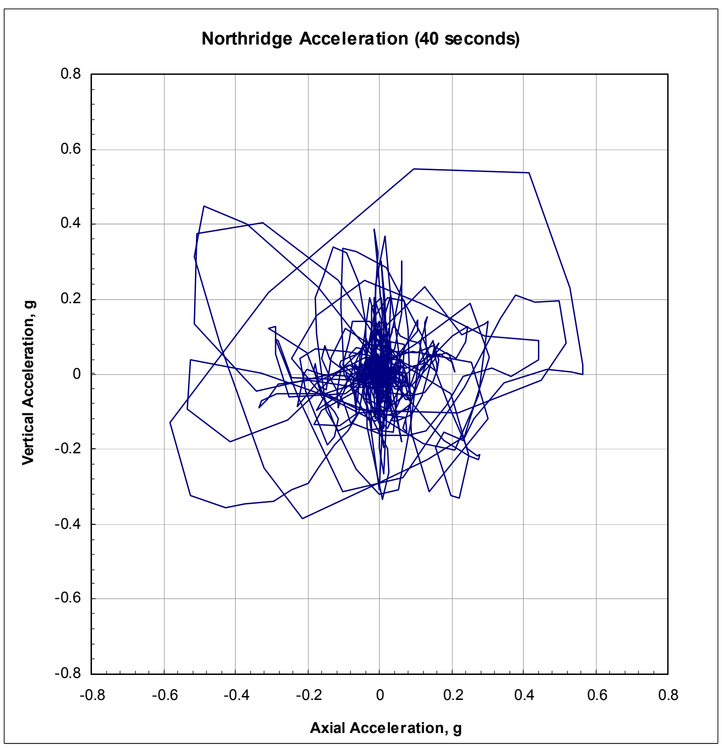

Figure B.20 – Up-Down vs. E-W spatial ground acceleration record.

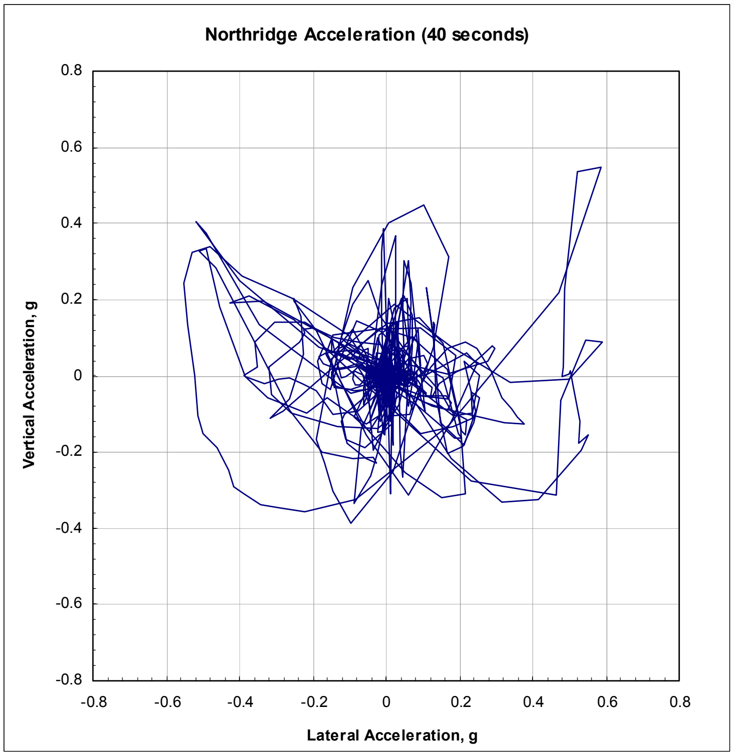

Figure B.21 – Up-Down vs. N-S spatial ground acceleration record.

B.2.4 Spatial displacement history

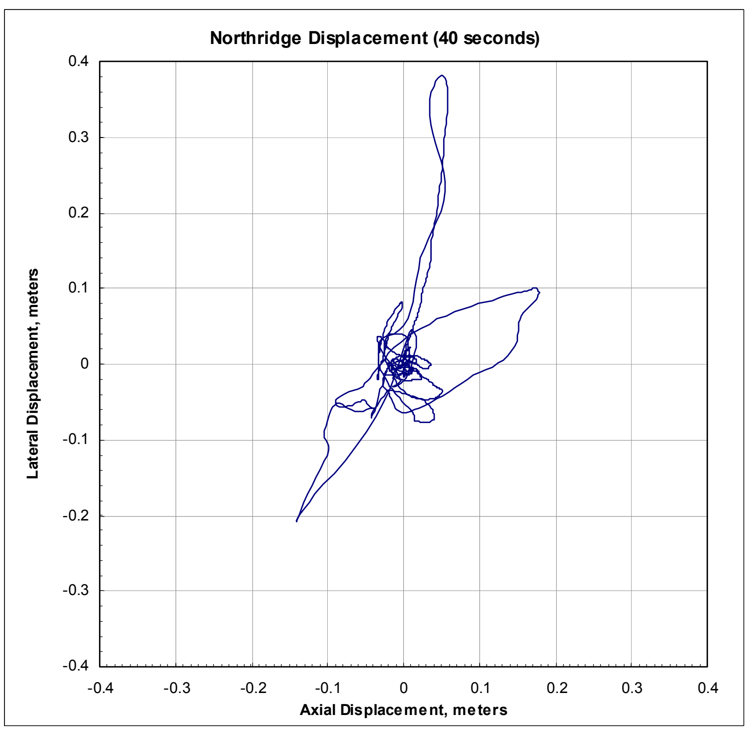

Figure B.22 – Horizontal spatial ground displacement record.

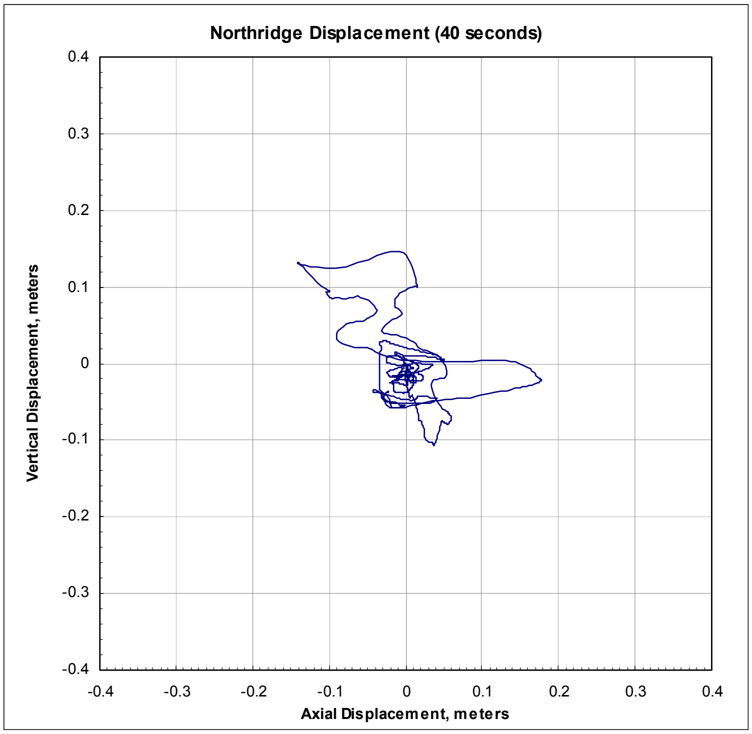

Figure B.23 – Up-Down vs. E-W spatial ground displacement record.

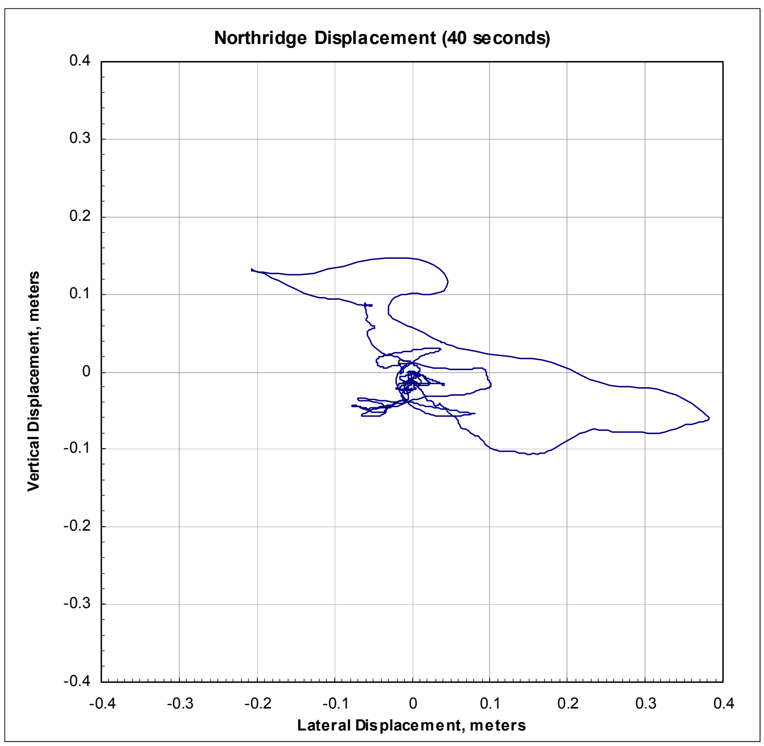

Figure B.24 – Up-Down vs. N-S spatial ground displacement record.

B.3 Scaled Spectral Response

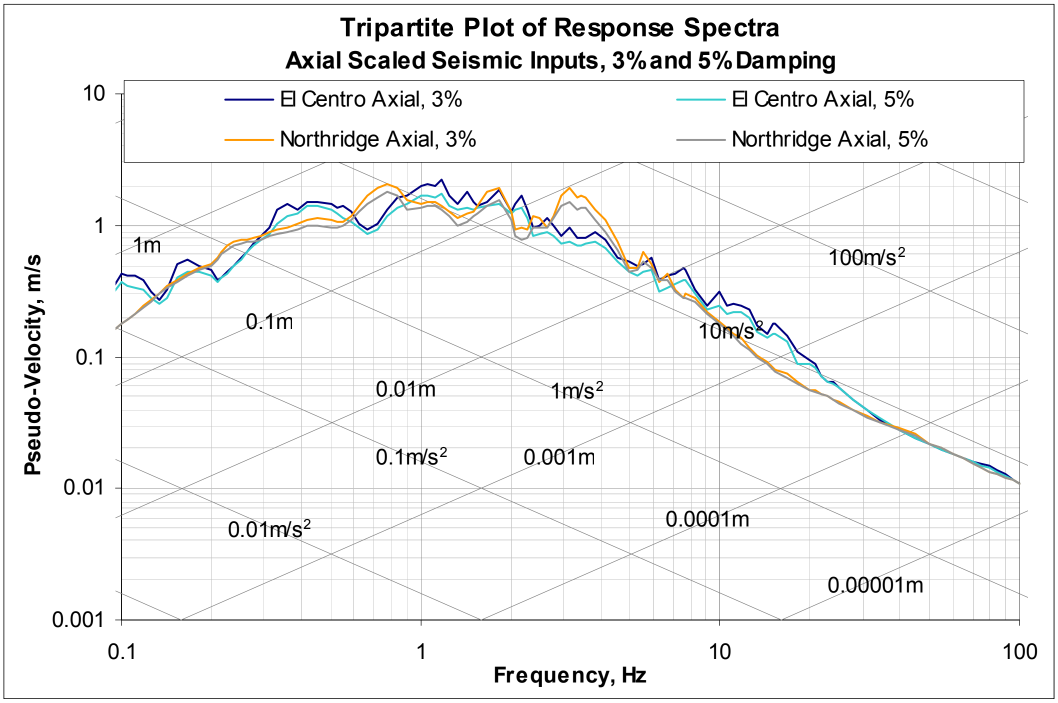

Figure B.25 – Axial scaled response spectra

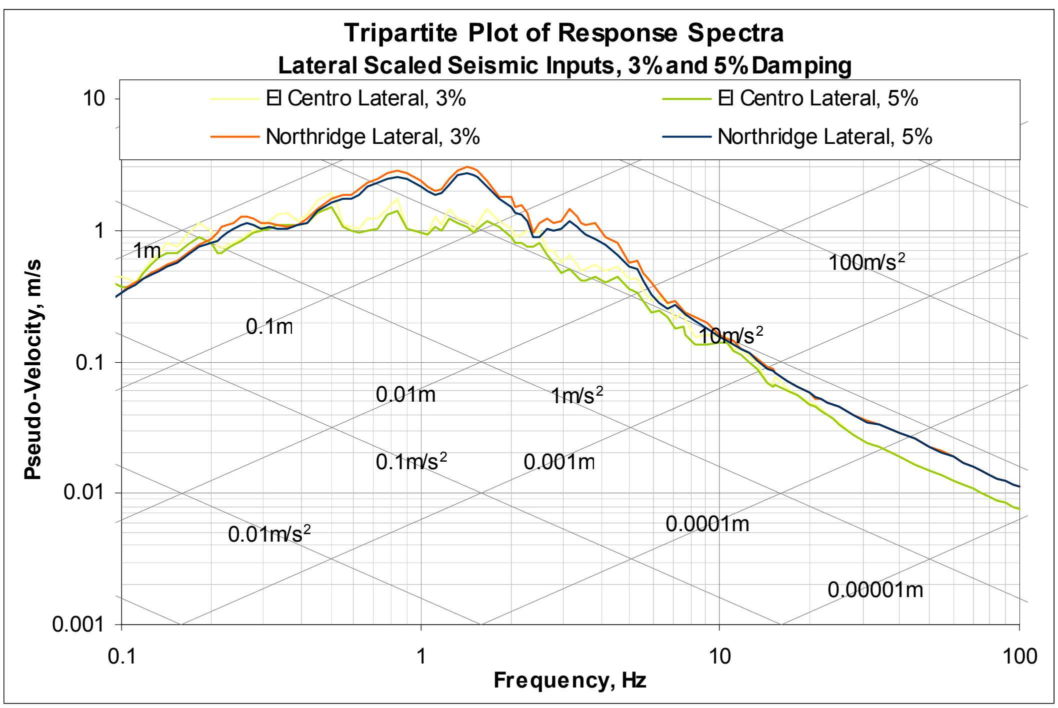

Figure B.26 – Lateral scaled response spectra

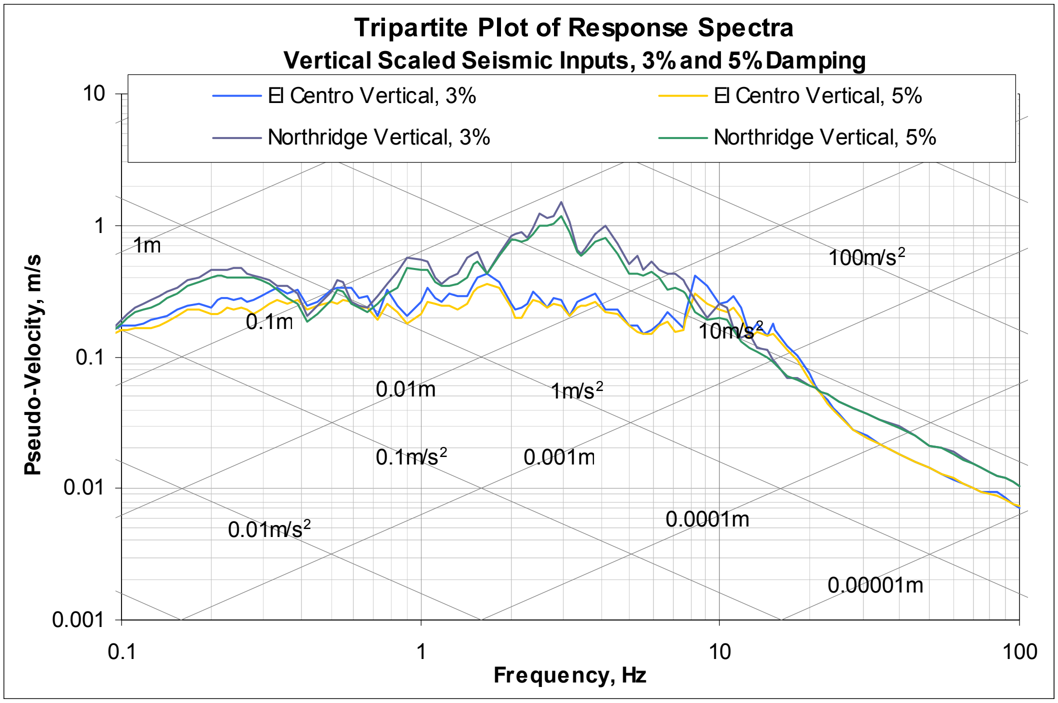

Figure B.27 - Vertical scaled response spectra

Appendix C

Sample ABAQUS\Explicit Input File

Input file for Span1 with a spring stiffness of 52711kN/$m^{1.3}$ and Imperial Valley seismic input.

```
*Heading
** Job name: ECs1k0 Model name: Simple Span
*Preprint, echo=NO, model=NO, history=NO, contact=NO
**
** PARTS
**
*Part, name=Abutment
*Node
     1,   12.2680998,           0.,   9.75399971
     2,   12.1156998,           0.,   9.75399971
     3,   12.1156998,           0.,           0.
            .
            .
            .
   274, 0.0152399996,           0.,  0.443363637
   275, -0.0152399996,           0.,  0.443363637
   276, -0.0457199998,           0.,  0.443363637
*Element, type=R3D4
  1,   1,   9, 109,  58
  2,   9,  10, 110, 109
  3,  10,  11, 111, 110
            .
            .
            .
218, 274, 275,  85,  86
219, 275, 276,  84,  85
220, 276,  83,   7,  84
*Node
   277,           0.,           0.,           0.
*Nset, nset=Abutment-RefPt_, internal
277,
*Nset, nset=AbutmentSet, generate
   1,  276,    1
*Elset, elset=AbutmentSet, generate
   1,  220,    1
*Nset, nset=RP
 277,
*Elset, elset=_BPorigin_SNEG, internal, generate
 111,  220,    1
*Surface, type=ELEMENT, name=BPorigin
_BPorigin_SNEG, SNEG
*Elset, elset=_BPaway_SNEG, internal, generate
   1,  110,    1
*Surface, type=ELEMENT, name=BPaway
_BPaway_SNEG, SNEG
*Elset, elset=Abutment, generate
   1,  220,    1
*End Part
**
*Part, name=Deck
*Node
```

```
      1, -0.304800004,  0.663500011,    6.8579998
      2, -0.304800004,  0.463499993,    6.8579998
      3, -0.304800004,  0.463499993,   4.87699986
              .
              .
              .
   2293,    8.3536253,  0.695249975,   9.29650021
   2294,   7.60115004,  0.695249975,   9.29650021
   2295,   6.84867477,  0.695249975,   9.29650021
*Element, type=C3D8R
1,   8, 196, 966, 200,   1, 190, 964, 195
2, 196,   5, 198, 966, 190,   2, 191, 964
3, 200, 966, 967, 201, 195, 964, 965, 194
              .
              .
              .
1534, 1934, 1935,  963,  962,  951,  955,  187,  184
1535,  160,  159,  960,  961,  896,  898, 1935, 1934
1536,  961,  960,  188,  189, 1934, 1935,  963,  962
*Nset, nset="Deck Corners"
  98, 104, 141, 143
*Nset, nset=Endmid
 61, 71
*Nset, nset=BC
    5,    6,    7,    8,    9,   11,   12,   16,   17,   19,   20,   24,   25,   28,   29,   30
   33,   38,   39,   40,   41,  148,  149,  150,  151,  157,  160,  161,  162,  165,  168,  169
  170,  173,  174,  178,  179,  181,  182,  183,  184,  189,  196,  197,  198,  199,  200,  201
  202,  203,  206,  207,  212,  213,  214,  215,  218,  219,  224,  225,  231,  232,  233,  234
  235,  236,  237,  238,  244,  245,  246,  248,  249,  250,  254,  257,  258,  259,  266,  267
  268,  269,  272,  273,  274,  277,  876,  877,  878,  879,  880,  881,  890,  891,  894,  895
  896,  897,  902,  903,  906,  907,  908,  909,  912,  913,  914,  915,  916,  925,  926,  927
  928,  929,  933,  937,  938,  939,  941,  942,  946,  947,  948,  949,  950,  951,  956,  957
  961,  962,  966,  967,  970,  971,  974,  975,  978,  979,  980,  981,  984,  985,  988,  991
  994,  995,  997, 1000, 1001, 1003, 1896, 1897, 1900, 1901, 1904, 1905, 1908, 1909, 1914, 1915
 1918, 1919, 1921, 1922, 1924, 1925, 1928, 1930, 1931, 1934
*Elset, elset=BC
    1,    2,    3,    4,    5,    6,    7,    8,    9,   10,   11,   12,   13,   14,   15,   16
   17,   18,   19,   20,   21,   22,   23,   24,   25,   26,   27,   28,   29,   30,   31,   32
   33,   34,   35,   36,   37,   38,   39,   40,   41,   42,   43,   44,   45,   46,   47,   48
   49,   50,   51,   52,   53,   54,   55,   56,   57,   58,   59,   60,   61,   62,   63,   64
 1473, 1474, 1475, 1476, 1477, 1478, 1479, 1480, 1481, 1482, 1483, 1484, 1485, 1486, 1487, 1488
 1489, 1490, 1491, 1492, 1493, 1494, 1495, 1496, 1497, 1498, 1499, 1500, 1501, 1502, 1503, 1504
 1505, 1506, 1507, 1508, 1509, 1510, 1511, 1512, 1513, 1514, 1515, 1516, 1517, 1518, 1519, 1520
 1521, 1522, 1523, 1524, 1525, 1526, 1527, 1528, 1529, 1530, 1531, 1532, 1533, 1534, 1535, 1536
*Nset, nset=_PickedSet232, internal, generate
    1,  2295,     1
*Elset, elset=_PickedSet232, internal, generate
    1,  1536,     1
*Nset, nset=_PickedSet245, internal
 21,
*Nset, nset=_PickedSet246, internal
 126,
*Nset, nset=_PickedSet247, internal
 22,
```

```
*Nset, nset=_PickedSet248, internal
 86,
*Nset, nset=_PickedSet249, internal
 3,
*Nset, nset=_PickedSet250, internal
 71,
*Nset, nset=_PickedSet251, internal
 2,
*Nset, nset=_PickedSet252, internal
 67,
*Nset, nset=_PickedSet253, internal
10,
*Nset, nset=_PickedSet254, internal
 68,
*Nset, nset=_PickedSet255, internal
 167,
*Nset, nset=_PickedSet256, internal
 96,
*Nset, nset=_PickedSet257, internal
 166,
*Nset, nset=_PickedSet258, internal
 121,
*Nset, nset=_PickedSet259, internal
 153,
*Nset, nset=_PickedSet260, internal
 61,
*Nset, nset=_PickedSet261, internal
 152,
*Nset, nset=_PickedSet262, internal
 62,
*Nset, nset=_PickedSet263, internal
 156,
*Nset, nset=_PickedSet264, internal
 75,
*Nset, nset=midpoint
 49,
*Elset, elset=_Deckaway_S2, internal
  161,  162,  163,  164,  165,  166,  167,  168,  169, 1147, 1148, 1149, 1150, 1151, 1152, 1153
 1154, 1155
*Elset, elset=_Deckaway_S5, internal
 413, 414, 417, 418, 421, 422, 425, 426, 429, 430, 433, 434, 610, 611, 612, 616
 617, 618, 622, 623, 624, 868, 869, 870, 874, 875, 876, 880, 881, 882
*Surface, type=ELEMENT, name=Deckaway
_Deckaway_S2, S2
_Deckaway_S5, S5
*Elset, elset=_Deckorigin_S4, internal, generate
 752,  768,    2
*Elset, elset=_Deckorigin_S2, internal
  901,  902,  903,  904,  905,  906,  907,  908,  909, 1165, 1166, 1167, 1168, 1169, 1170
*Elset, elset=_Deckorigin_S6, internal, generate
 197,  213,    2
*Elset, elset=_Deckorigin_S1, internal
 1329, 1330, 1331, 1332, 1333, 1334, 1432, 1433, 1434, 1435, 1436, 1437, 1438, 1439, 1440
*Surface, type=ELEMENT, name=Deckorigin
```

```
_Deckorigin_S4, S4
_Deckorigin_S2, S2
_Deckorigin_S6, S6
_Deckorigin_S1, S1
** Region: (Deck:Picked)
*Elset, elset=_PickedSet232, internal, generate
   1,  1536,     1
** Section: Deck
*Solid Section, elset=_PickedSet232, material=Deck
1.,
*Element, type=SpringA, elset=SCED-spring
1537, 21, 126
1538, 22, 86
1539, 3, 71
1540, 2, 67
1541, 10, 68
1542, 167, 96
1543, 166, 121
1544, 153, 61
1545, 152, 62
1546, 156, 75
*Spring, elset=SCED-spring, NONLINEAR

0, -1, ,
0, 0, ,
0, 0.0127, ,
1387.26077, 0.013, ,
9333.119621, 0.014, ,
19595.06286, 0.015, ,
31330.59163, 0.016, ,
44198.69701, 0.017, ,
58004.15503, 0.018, ,
72617.81687, 0.019, ,
87946.83044, 0.02, ,
103920.6834, 0.021, ,
120483.7031, 0.022, ,
137590.6322, 0.023, ,
155203.8359, 0.024, ,
173291.4434, 0.025, ,
191826.0603, 0.026, ,
210783.8452, 0.027, ,
230143.8289, 0.028, ,
249887.4009, 0.029, ,
269997.9136, 0.03, ,
290460.3731, 0.031, ,
311261.1917, 0.032, ,
332387.9901, 0.033, ,
353829.4347, 0.034, ,
375575.104, 0.035, ,
397615.377, 0.036, ,
419941.3401, 0.037, ,
444820, 0.0381, ,
594521.1685, 0.04445, ,
753534.1557, 0.0508, ,
```

```
920733.1274, 0.05715, ,
1095275.316, 0.0635, ,
1276502.234, 0.06985, ,
1463882.83, 0.0762, ,
1656978.25, 0.08255, ,
1855418.732, 0.0889, ,
2058887.776, 0.09525, ,
2267110.892, 0.1016, ,
2469698.477, 0.10765, ,
2696884.172, 0.1143, ,
2917679.688, 0.12064, ,
3143117.189, 0.127, ,
3371987.828, 0.13335, ,
3604502.337, 0.1397, ,
3840532.107, 0.14605, ,
4079959.031, 0.1524, ,
*End Part
**
**
** ASSEMBLY
**
*Assembly, name=Assembly
**
*Instance, name=Deck-1, part=Deck
*End Instance
**
*Instance, name=Abutment-1, part=Abutment
*End Instance
**
*Rigid Body, ref node=Abutment-1.Abutment-RefPt_, elset=Abutment-1.Abutment
*End Assembly
*Amplitude, name=Axial
0., 0., 0.01, 0., 0.02, -4.661e-06, 0.03, -1.4722e-05
0.04, -2.4176e-05, 0.05, -2.6758e-05, 0.06, -2.249e-05, 0.07, -1.1492e-05
0.08, 6.054e-06, 0.09, 3.0089e-05, 0.1, 6.0148e-05, 0.11, 9.6287e-05
            .
            .
            .
19.88, -0.00446683, 19.89, -0.00390602, 19.9, -0.00333095, 19.91, -0.00275043
19.92, -0.00217062, 19.93, -0.00159508, 19.94, -0.00102427, 19.95, -0.000455406
19.96, 0.0001161, 19.97, 0.000694682, 19.98, 0.00128384, 19.99, 0.00188647
20., 0.00250443
*Amplitude, name="Grav ramp", time=TOTAL TIME
0., 0., 0.05, 0.0655556, 0.1, 0.128889, 0.15, 0.19
0.2, 0.248889, 0.25, 0.305556, 0.3, 0.36, 0.35, 0.412222
0.4, 0.462222, 0.45, 0.51, 0.5, 0.555556, 0.55, 0.598889
0.6, 0.64, 0.65, 0.678889, 0.7, 0.715556, 0.75, 0.75
0.8, 0.782222, 0.85, 0.812222, 0.9, 0.84, 0.95, 0.865556
1., 0.888889, 1.05, 0.91, 1.1, 0.928889, 1.15, 0.945556
1.2, 0.96, 1.25, 0.972222, 1.3, 0.982222, 1.35, 0.99
1.4, 0.995556, 1.45, 0.998889, 1.5, 1., 1.6, 1.
1.7, 1., 1.8, 1., 1.9, 1., 22., 1.
*Amplitude, name=Lateral
0., 0., 0.01, 0., 0.02, -1.613e-05, 0.03, -5.594e-05
```

```
0.04, -0.00011125, 0.05, -0.00016983, 0.06, -0.00023166, 0.07, -0.00029712
0.08, -0.0003662, 0.09, -0.00043877, 0.1, -0.00051519, 0.11, -0.00059522
            .
            .
            .
19.88, -0.019393, 19.89, -0.0190091, 19.9, -0.0186952, 19.91, -0.0184388
19.92, -0.0182275, 19.93, -0.0180513, 19.94, -0.0179043, 19.95, -0.0177796
19.96, -0.0176687, 19.97, -0.01756, 19.98, -0.0174419, 19.99, -0.0173019
20., -0.0171287
*Amplitude, name=Vertical
0., 0., 0.01, 0., 0.02, -6.869e-06, 0.03, -2.3258e-05
0.04, -4.4554e-05, 0.05, -6.477e-05, 0.06, -8.3912e-05, 0.07, -0.000101924
0.08, -0.000118476, 0.09, -0.000133169, 0.1, -0.000146099, 0.11, -0.000157284
            .
            .
            .
19.88, 0.0121932, 19.89, 0.0120693, 19.9, 0.0119247, 19.91, 0.0117562
19.92, 0.0115669, 19.93, 0.0113641, 19.94, 0.0111557, 19.95, 0.0109469
19.96, 0.0107392, 19.97, 0.0105305, 19.98, 0.0103177, 19.99, 0.0100979
20., 0.00986992
**
** MATERIALS
**
*Material, name=Deck
*Damping, alpha=0.2054
*Density
 1197.19,
*Elastic
 1.7078e+10, 0.15
**
** INTERACTION PROPERTIES
**
*Surface Interaction, name=PEP
*Friction, shear traction slope=3e+06
 0.5,
*Surface Behavior, pressure-overclosure=LINEAR
4.86439e+07,
*Contact Damping, definition=CRITICAL DAMPING
0.1,
**
** BOUNDARY CONDITIONS
**
** Name: NoRotate Type: Displacement/Rotation
*Boundary
Abutment-1.RP, 4, 4
Abutment-1.RP, 5, 5
Abutment-1.RP, 6, 6
** Name: Pinned Type: Symmetry/Antisymmetry/Encastre
*Boundary
Abutment-1.RP, PINNED
** Name: Pinned2 Type: Symmetry/Antisymmetry/Encastre
*Boundary
Deck-1.BC, PINNED
** ----------------------------------------------------------------
```

```
**
** STEP: Gravity
**
*Step, name=Gravity
Gravity
*Dynamic, Explicit, element by element
, 2.
*Bulk Viscosity
1., 1.2
**
** LOADS
**
** Name: Gravity   Type: Gravity
*Dload, amplitude="Grav ramp"
, GRAV, 9.81, 0., -1., 0.
**
** INTERACTIONS
**
** Interaction: Int-1
*Contact Pair, interaction=PEP, mechanical constraint=PENALTY, cpset=Int-1
Abutment-1.BPorigin, Deck-1.Deckorigin
** Interaction: Int-2
*Contact Pair, interaction=PEP, mechanical constraint=PENALTY, cpset=Int-2
Abutment-1.BPaway, Deck-1.Deckaway
**
** OUTPUT REQUESTS
**
*Restart, write, number interval=1, time marks=NO
**
** FIELD OUTPUT: Model Output
**
*Output, field, time interval=0.05
*Node Output
A, RF, U, V
*Element Output, directions=YES
ENER, LE, S
*Contact Output
CSTRESS,
**
** HISTORY OUTPUT: Endmid
**
*Output, history
*Node Output, nset=Deck-1.Endmid
A1, A2, A3, U1, U2, U3
**
** HISTORY OUTPUT: Ropes
**
*Output, history, time interval=0.05
*Element Output, elset=Deck-1.SCED-spring
S11, S22, S33
**
** HISTORY OUTPUT: Corner History
**
*Node Output, nset=Deck-1."Deck Corners"
```

```
A1, A2, A3, U1, U2, U3
**
** HISTORY OUTPUT: Ground Motion
**
*Node Output, nset=Abutment-1.RP
A1, A2, A3, U1, U2, U3
**
** HISTORY OUTPUT: Midspan History
**
*Node Output, nset=Deck-1.midpoint
A1, A2, A3, U1, U2, U3
*End Step
** ----------------------------------------------------------------
**
** STEP: Earthquake
**
*Step, name=Earthquake
*Dynamic, Explicit, element by element
, 20.
*Bulk Viscosity
0.06, 1.2
**
** BOUNDARY CONDITIONS
**
** Name: Axial Type: Displacement/Rotation
*Boundary, op=NEW, amplitude=Axial
Abutment-1.RP, 1, 1, 2.237
** Name: Axial2 Type: Displacement/Rotation
*Boundary, op=NEW, amplitude=Axial
Deck-1.BC, 1, 1, 2.237
** Name: Lateral Type: Displacement/Rotation
*Boundary, op=NEW, amplitude=Lateral
Abutment-1.RP, 3, 3, 2.2373
** Name: Lateral2 Type: Displacement/Rotation
*Boundary, op=NEW, amplitude=Lateral
Deck-1.BC, 3, 3, 2.2373
** Name: NoRotate Type: Displacement/Rotation
*Boundary, op=NEW
Abutment-1.RP, 4, 4
Abutment-1.RP, 5, 5
Abutment-1.RP, 6, 6
** Name: Pinned Type: Symmetry/Antisymmetry/Encastre
*Boundary, op=NEW
** Name: Pinned2 Type: Symmetry/Antisymmetry/Encastre
*Boundary, op=NEW
** Name: Vertical Type: Displacement/Rotation
*Boundary, op=NEW, amplitude=Vertical
Abutment-1.RP, 2, 2, 2.2373
** Name: Vertical2 Type: Displacement/Rotation
*Boundary, op=NEW, amplitude=Vertical
Deck-1.BC, 2, 2, 2.2373
**
** OUTPUT REQUESTS
**
```

```
*Restart, write, number interval=1, time marks=NO
**
** FIELD OUTPUT: Model Output
**
*Output, field, time interval=0.05
*Node Output
A, RF, U, V
*Element Output, directions=YES
ENER, LE, S
*Contact Output
CSTRESS,
**
** HISTORY OUTPUT: Endmid
**
*Output, history
*Node Output, nset=Deck-1.Endmid
A1, A2, A3, U1, U2, U3
**
** HISTORY OUTPUT: Ropes
**
*Output, history, time interval=0.05
*Element Output, elset=Deck-1.SCED-spring
S11, S22, S33
**
** HISTORY OUTPUT: Corner History
**
*Node Output, nset=Deck-1."Deck Corners"
A1, A2, A3, U1, U2, U3
**
** HISTORY OUTPUT: Ground Motion
**
*Node Output, nset=Abutment-1.RP
A1, A2, A3, U1, U2, U3
**
** HISTORY OUTPUT: Midspan History
**
*Node Output, nset=Deck-1.midpoint
A1, A2, A3, U1, U2, U3
*End Step
```

Appendix D

Other Figures

D.1 Span1 Figures

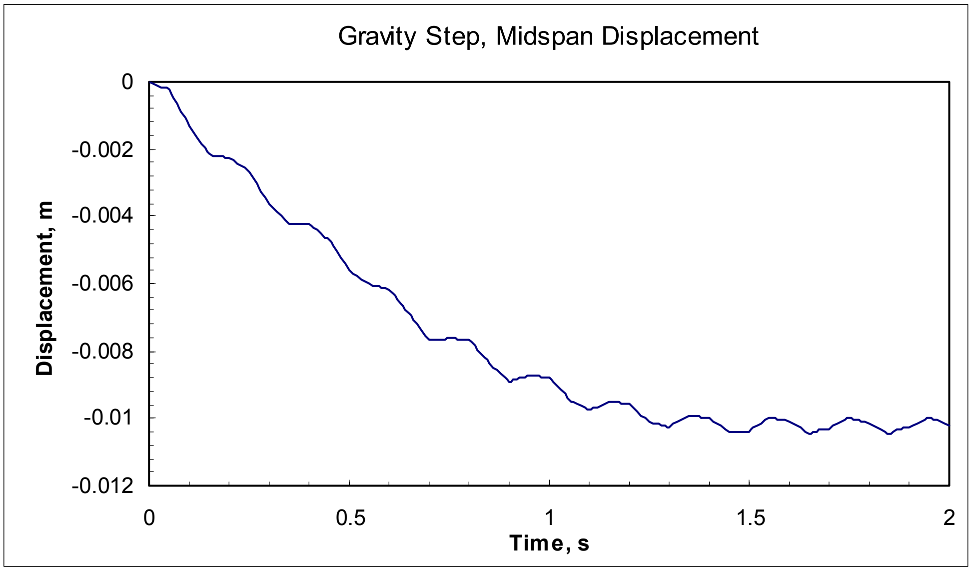

Figure D.1 - Span1, Imperial Valley input, gravity step response.

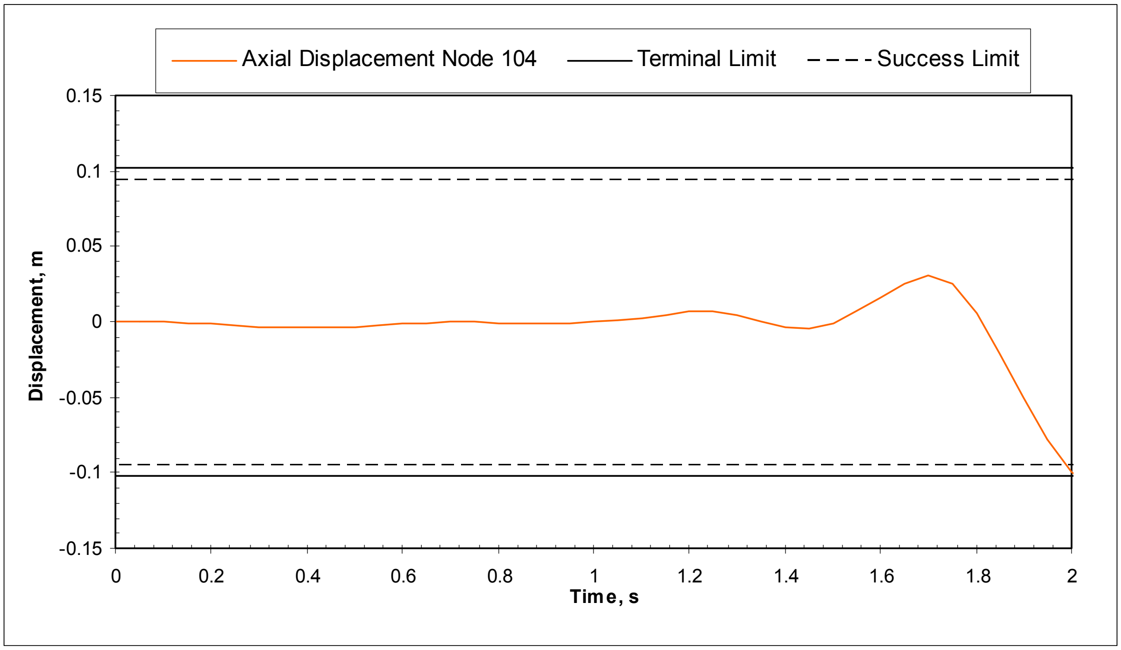

Figure D.2 - Span1, Imperial Valley axial input only, node 104 axial displacement

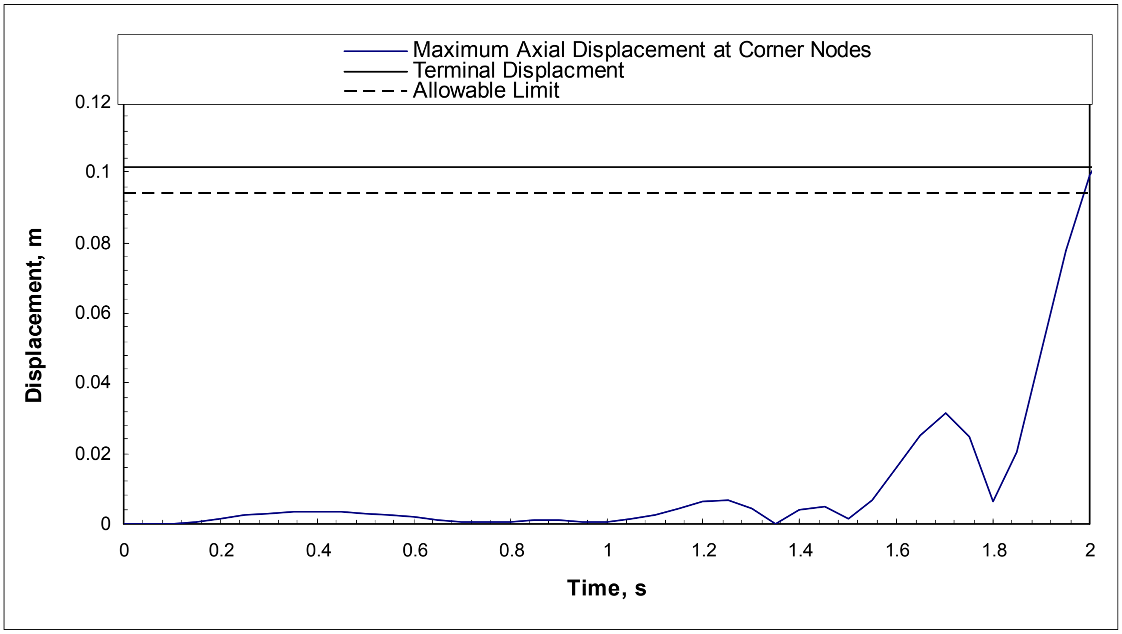

Figure D.3 - Span1, Imperial Valley axial input only, maximum axial displacement

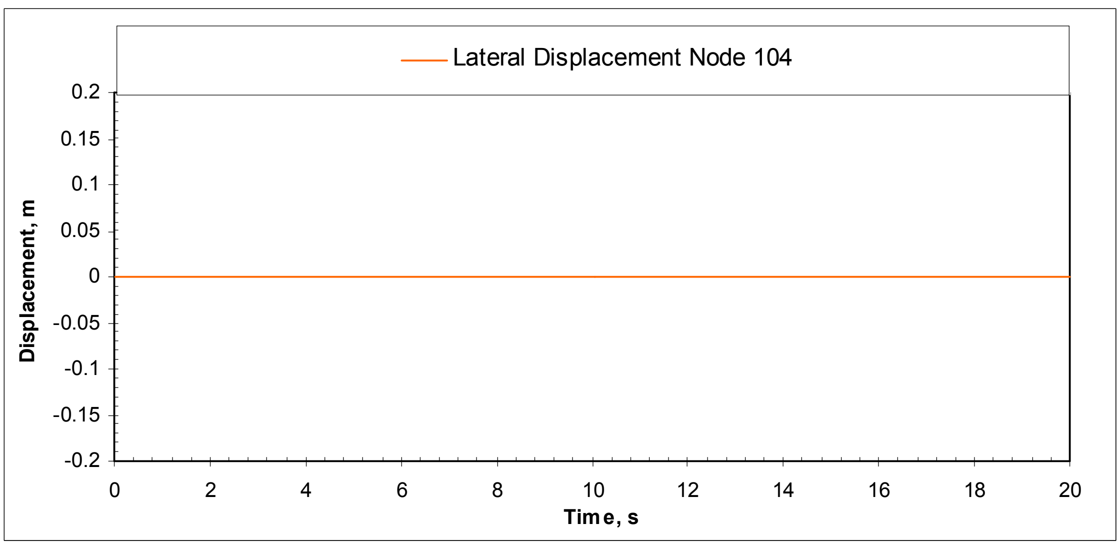

Figure D.4 - Span1, Imperial Valley axial input only, node 104 lateral displacement

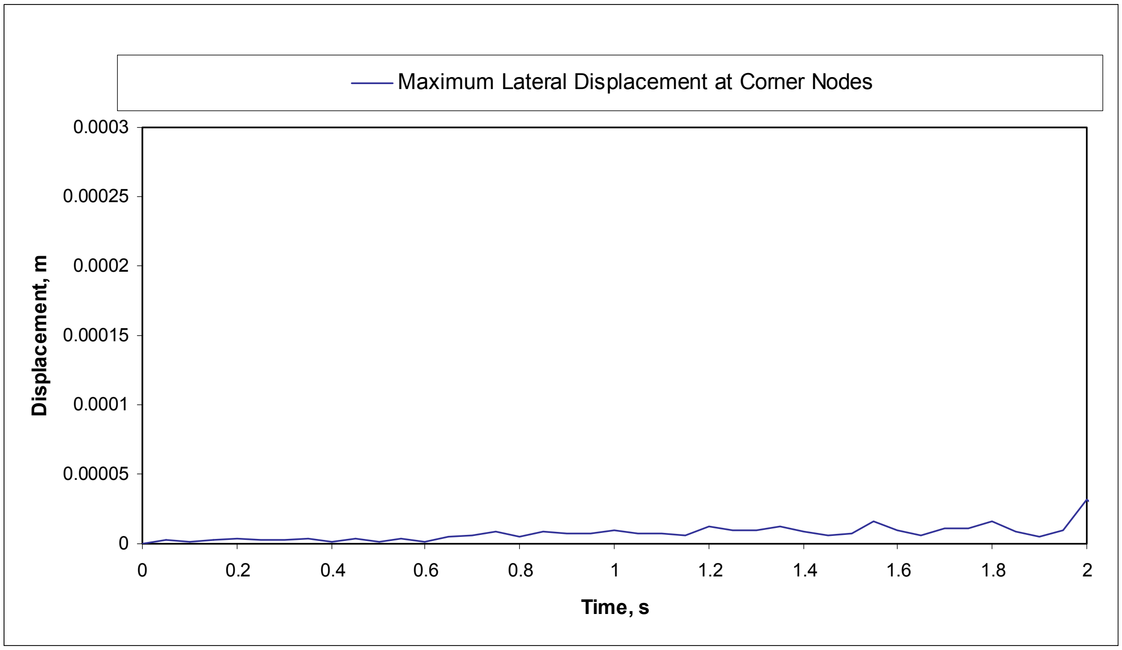

Figure D.5 - Span1, Imperial Valley axial input only, maximum lateral displacement

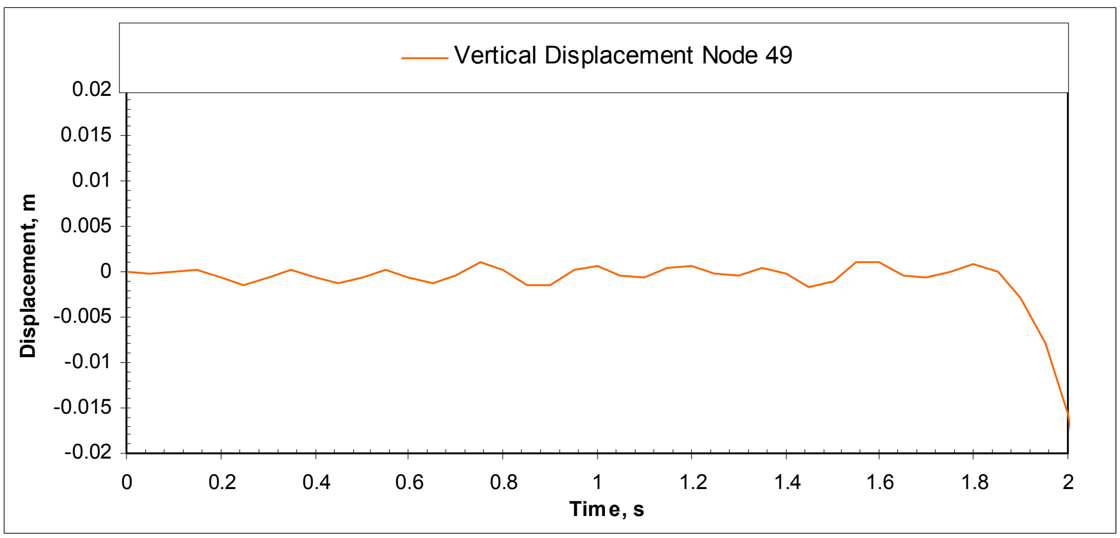

Figure D.6 - Span1, Imperial Valley axial input only, node 49 vertical displacement

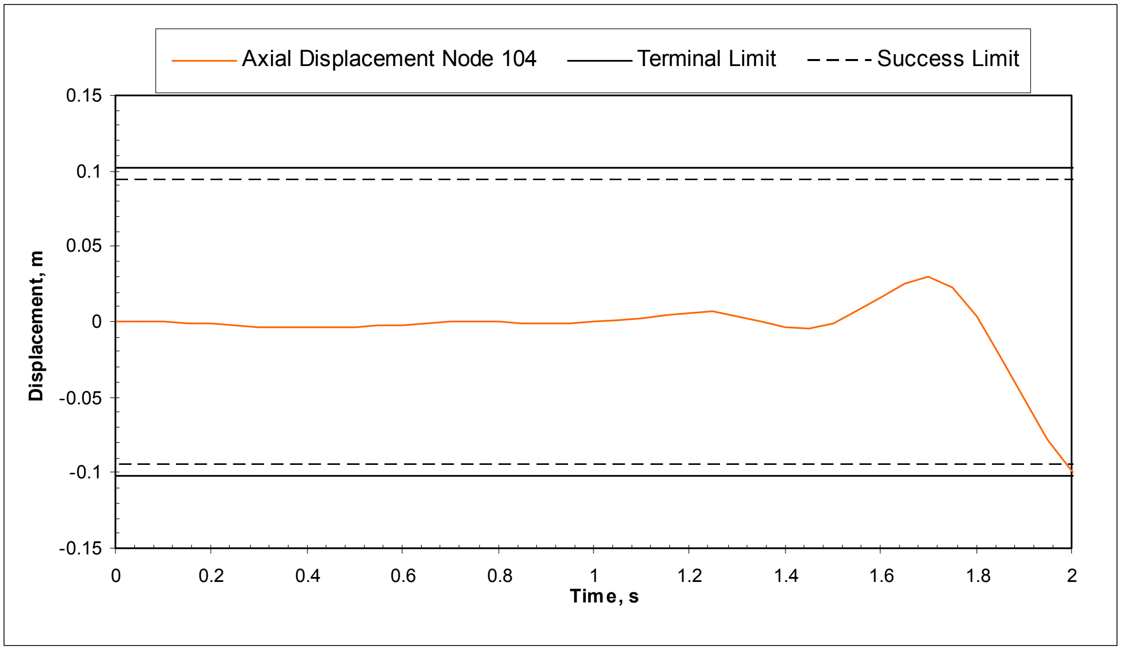

Figure D.7 - Span1, Imperial Valley three-dimensional input, no SCEDs, node 104 axial displacement

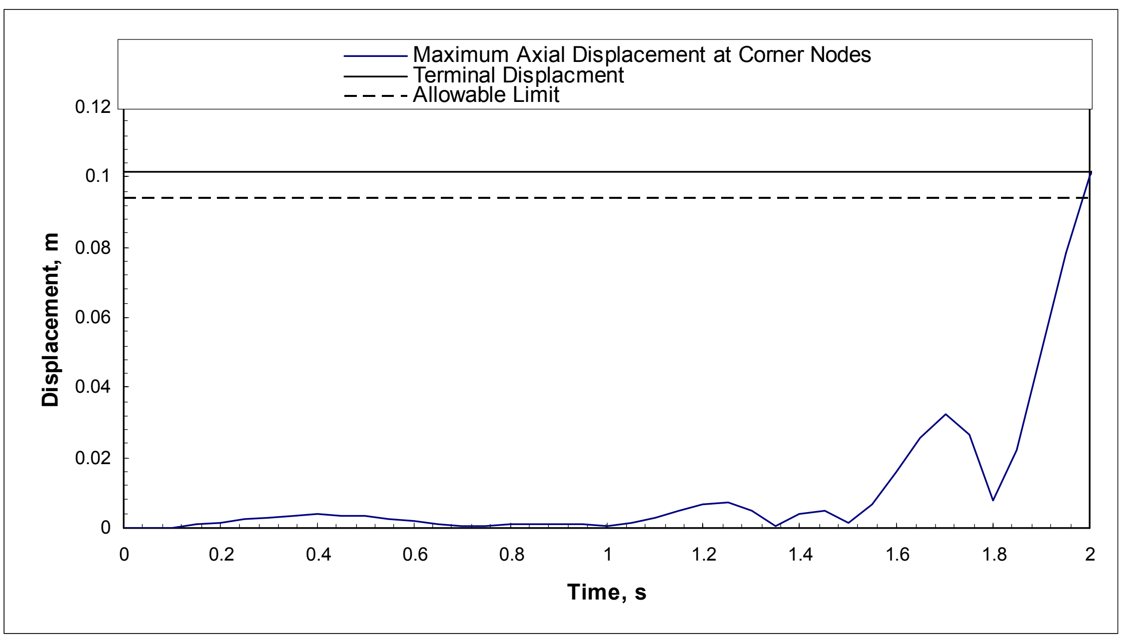

Figure D.8 - Span1, Imperial Valley three-dimensional input, no SCEDs, maximum axial displacement

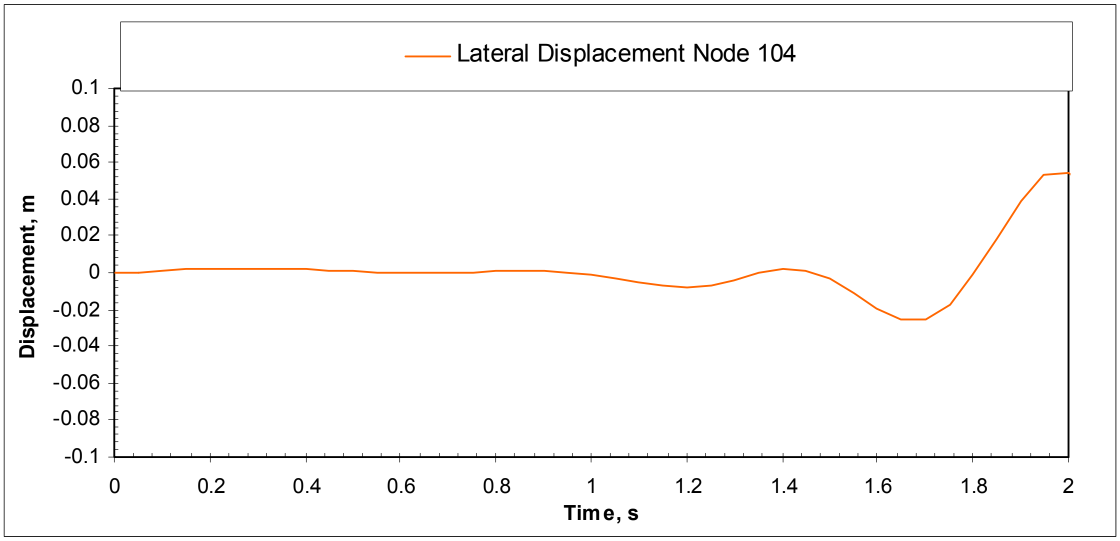

Figure D.9 - Span1, Imperial Valley three-dimensional input, no SCEDs, node 104 lateral displacement

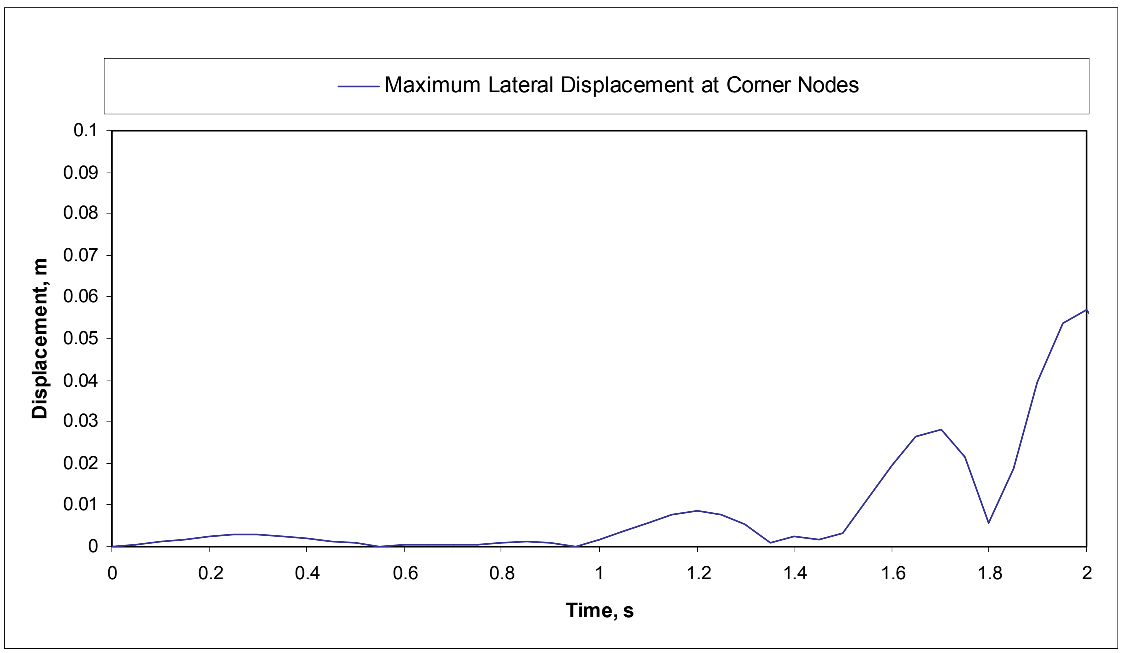

Figure D.10 - Span1, Imperial Valley three-dimensional input, no SCEDs, maximum lateral disp.

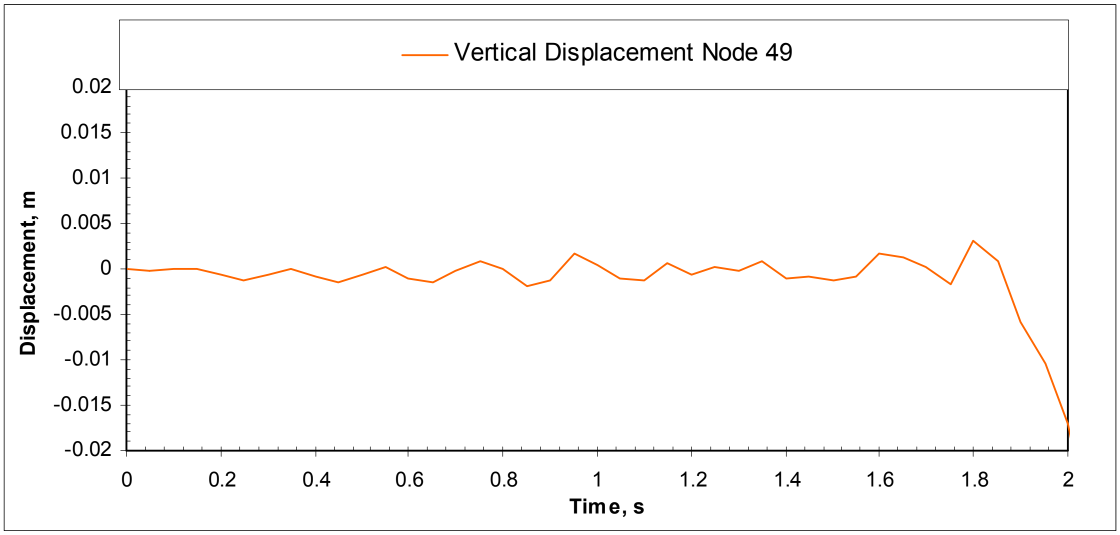

Figure D.11 - Span1, Imperial Valley three-dimensional input, no SCEDs, node 49 vertical displacement

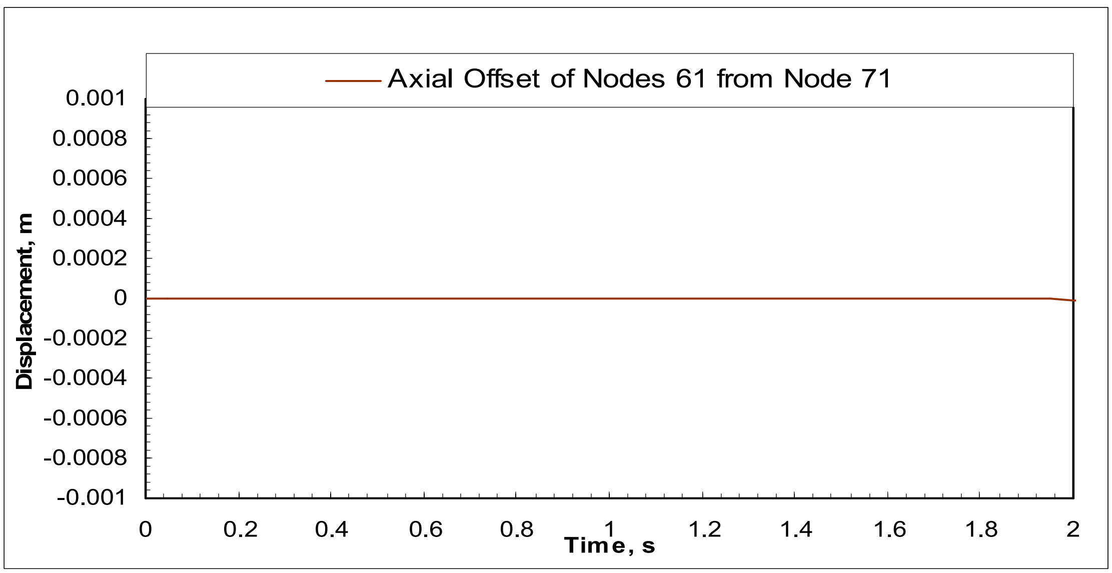

Figure D.12 - Span1, Imperial Valley three-dimensional input, no SCEDs, node 61 and 71 response

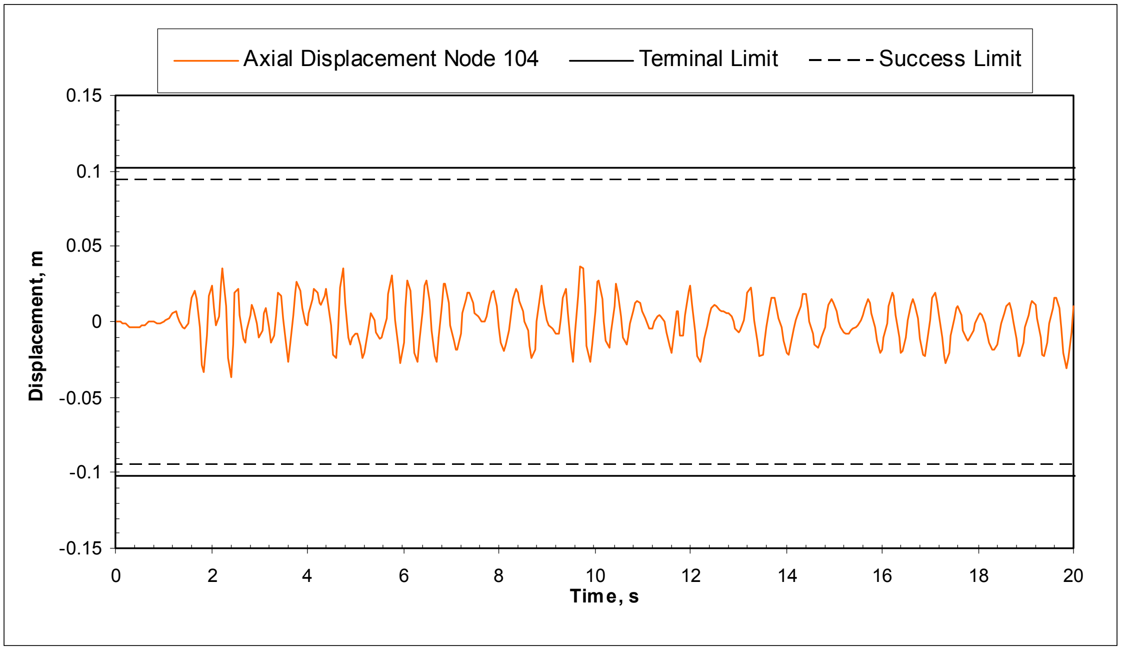

Figure D.13 - Span1, Imperial Valley 3D input, SCED k = 52.7MN/m$^{1.3}$, node 104 axial disp.

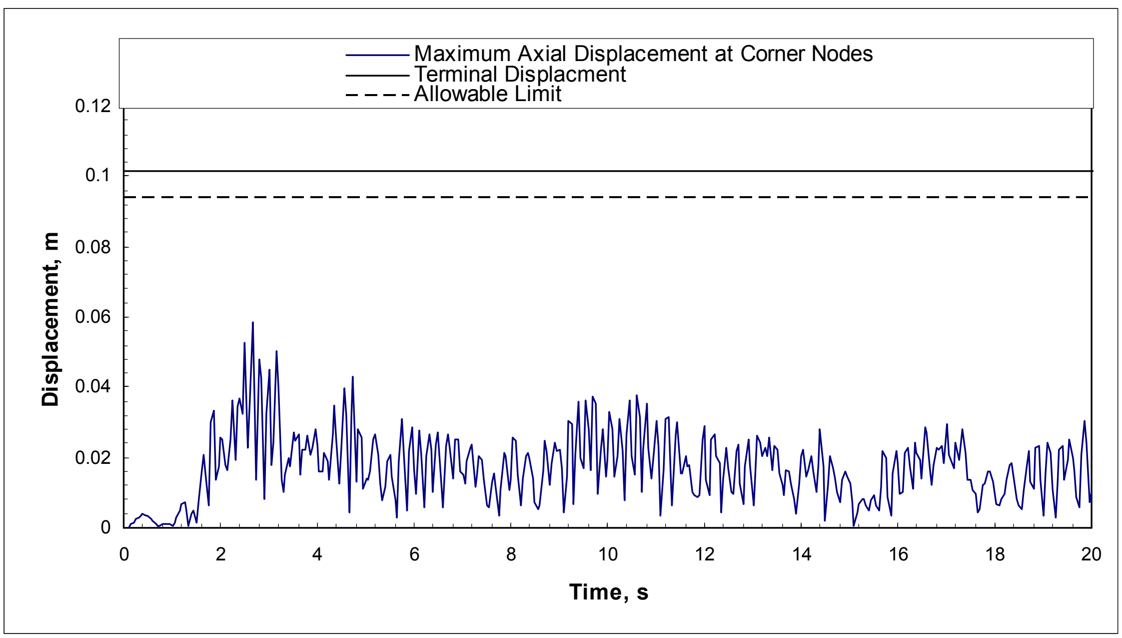

Figure D.14 - Span1, Imperial Valley 3D input, SCED k = 52.7MN/m$^{1.3}$, maximum axial disp.

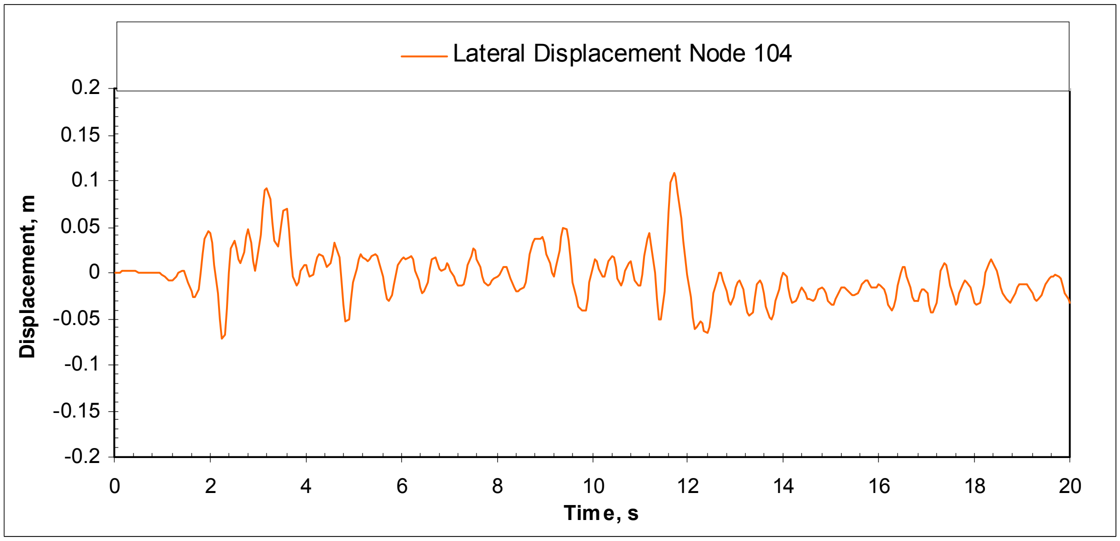

Figure D.15 - Span1, Imperial Valley 3D input, SCED k = 52.7MN/m$^{1.3}$, node 104 lateral disp.

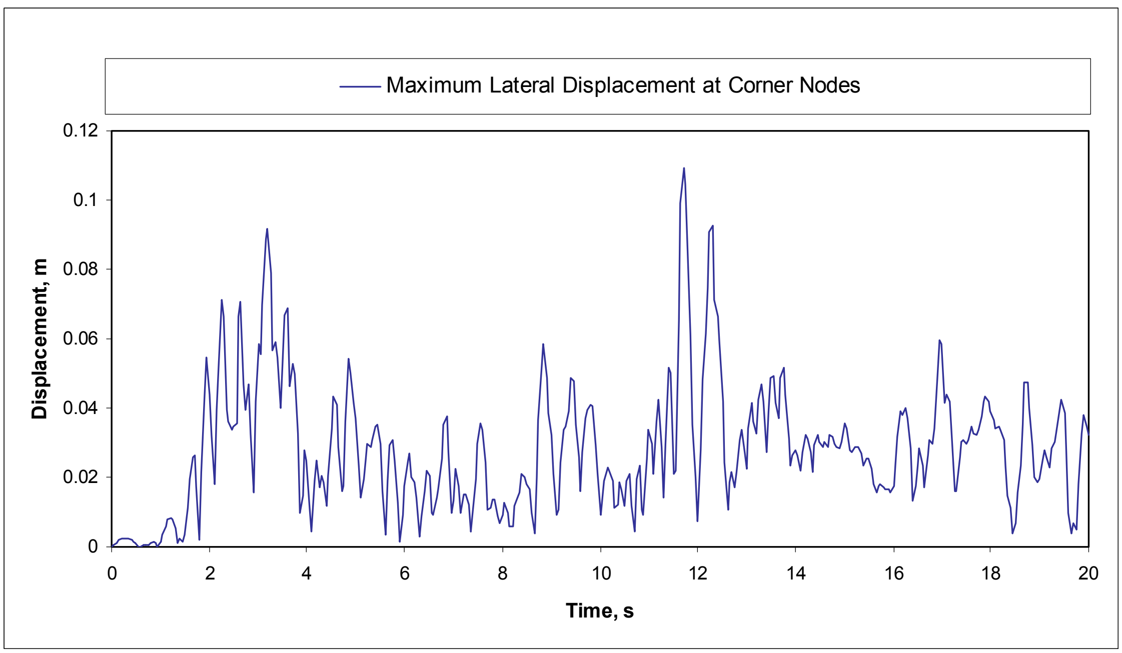

Figure D.16 - Span1, Imperial Valley 3D input, SCED k = 52.7MN/m$^{1.3}$, maximum lateral disp.

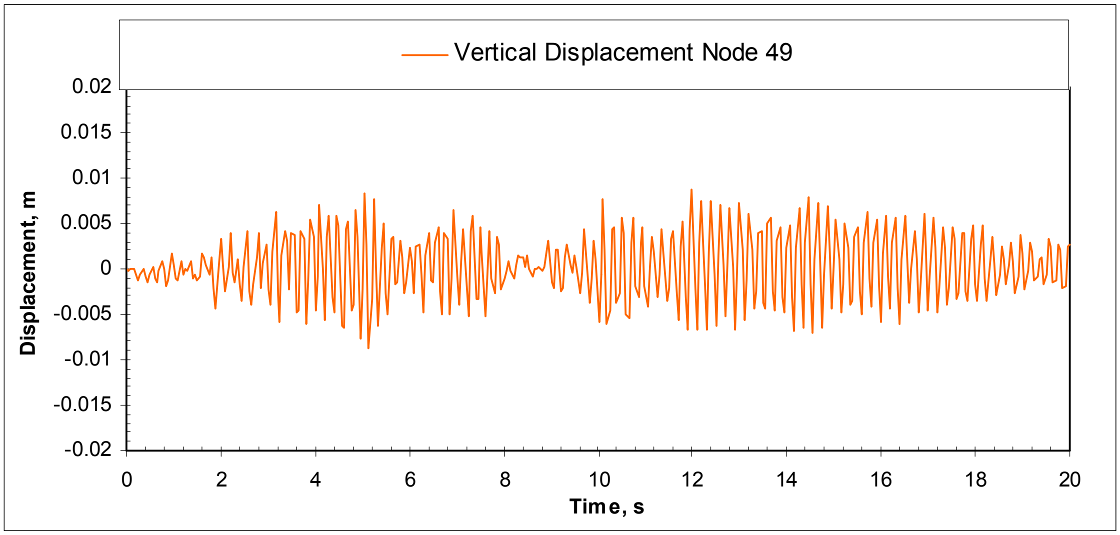

Figure D.17 - Span1, Imperial Valley 3D input, SCED k = 52.7MN/m$^{1.3}$, node 49 vertical disp.

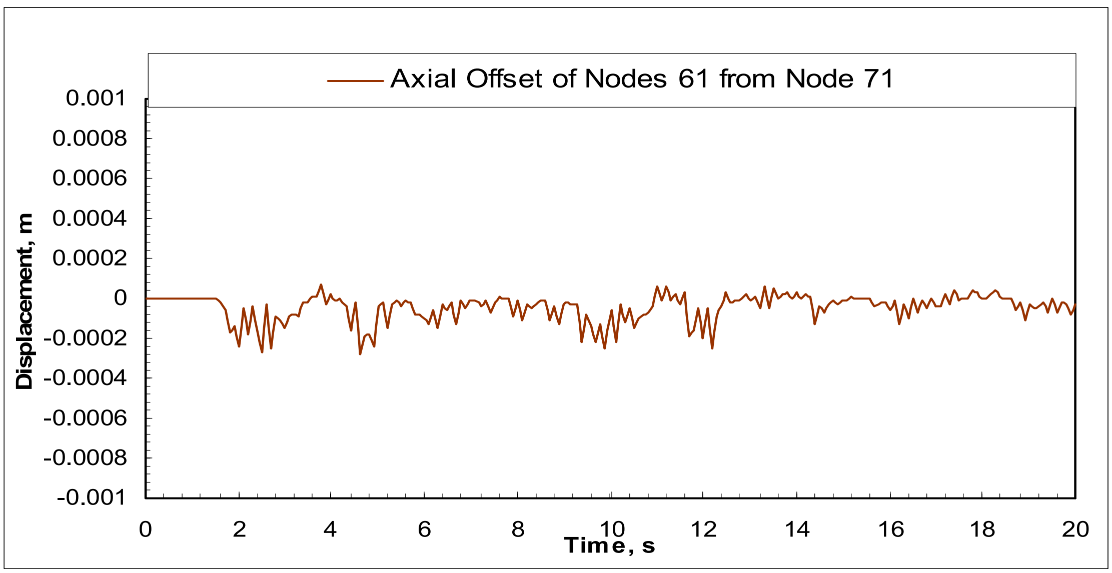

Figure D.18 - Span1, Imperial Valley 3D input, SCED k = 52.7MN/m$^{1.3}$, node 61 and 71 response

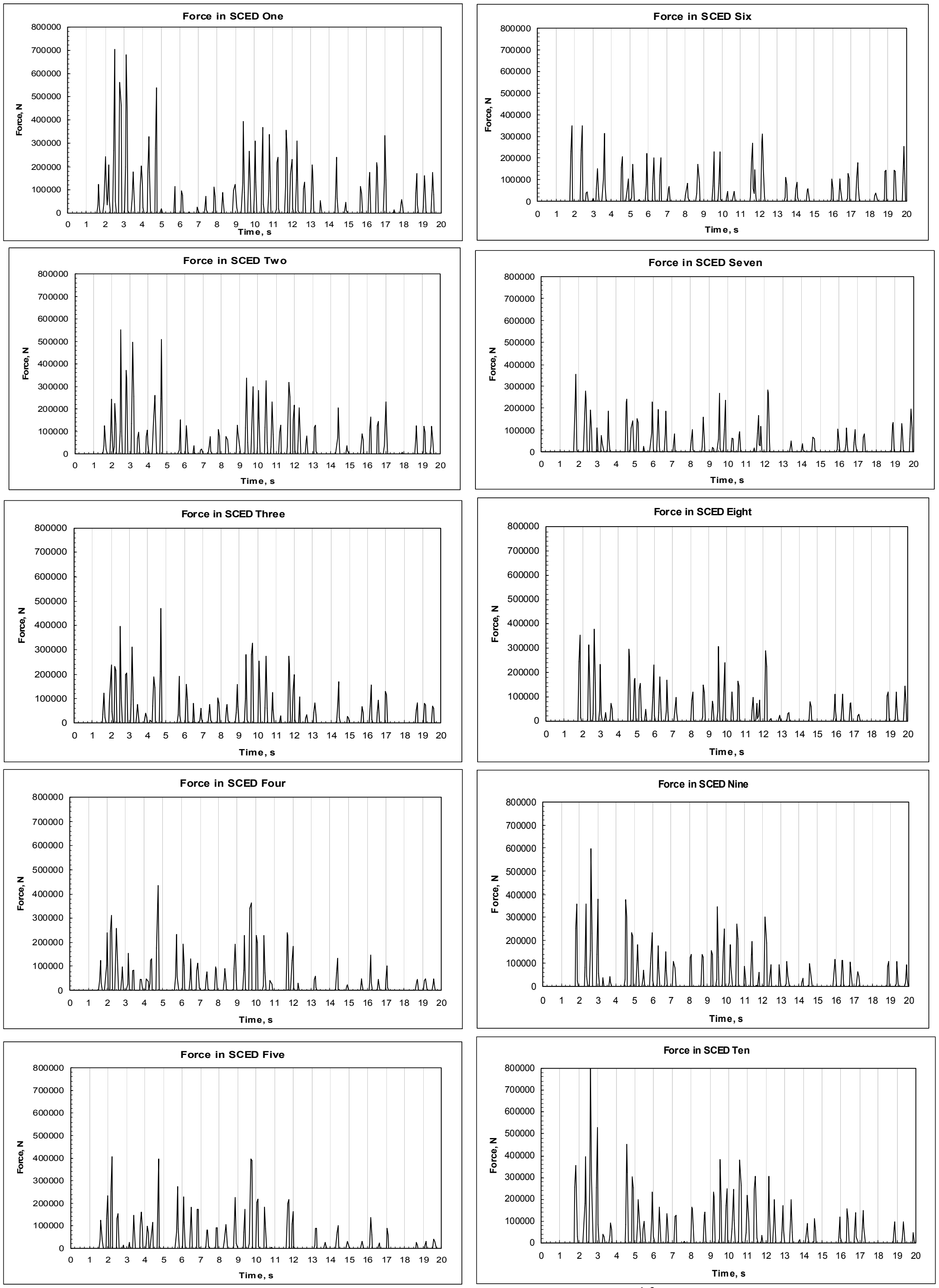

Figure D.19 - Span1, Imperial Valley 3D input, SCED k = 52.7MN/m$^{1.3}$, snap load histories

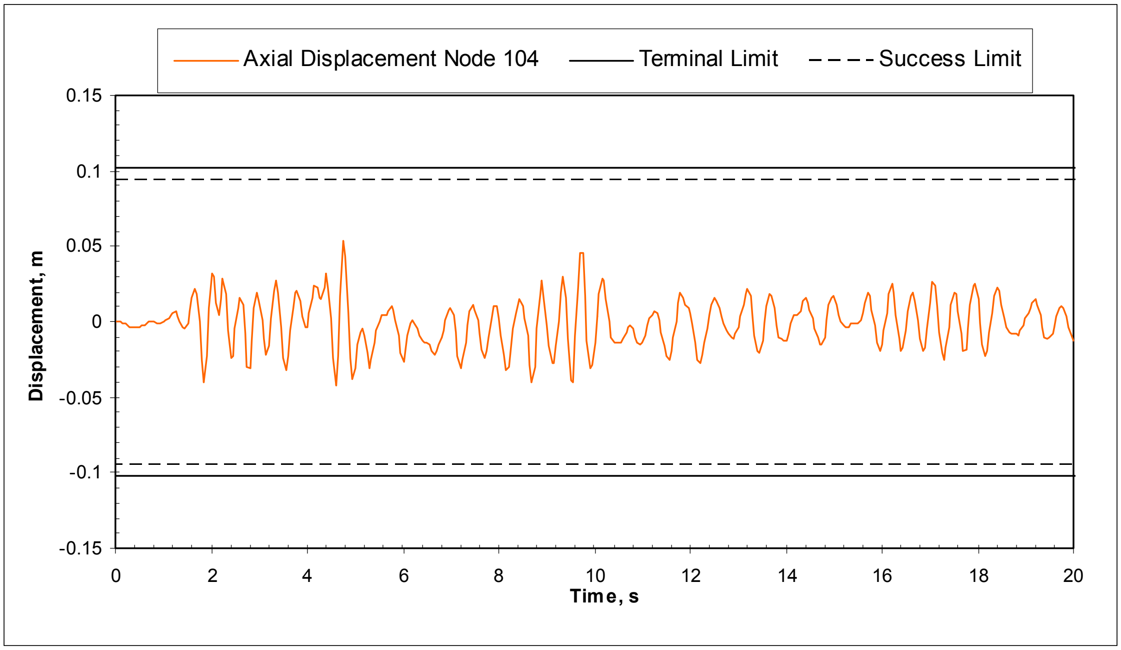

Figure D.20 - Span1, Imperial Valley 3D input, SCED k = 36.9MN/m$^{1.3}$, node 104 axial disp.

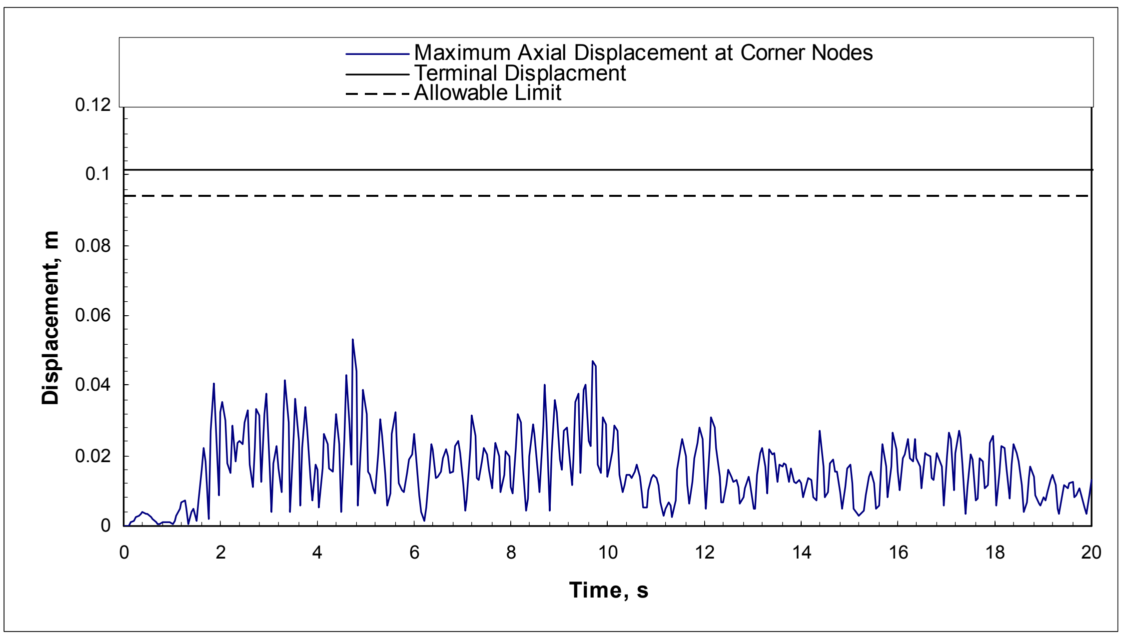

Figure D.21 - Span1, Imperial Valley 3D input, SCED k = 36.9MN/m$^{1.3}$, maximum axial displacement

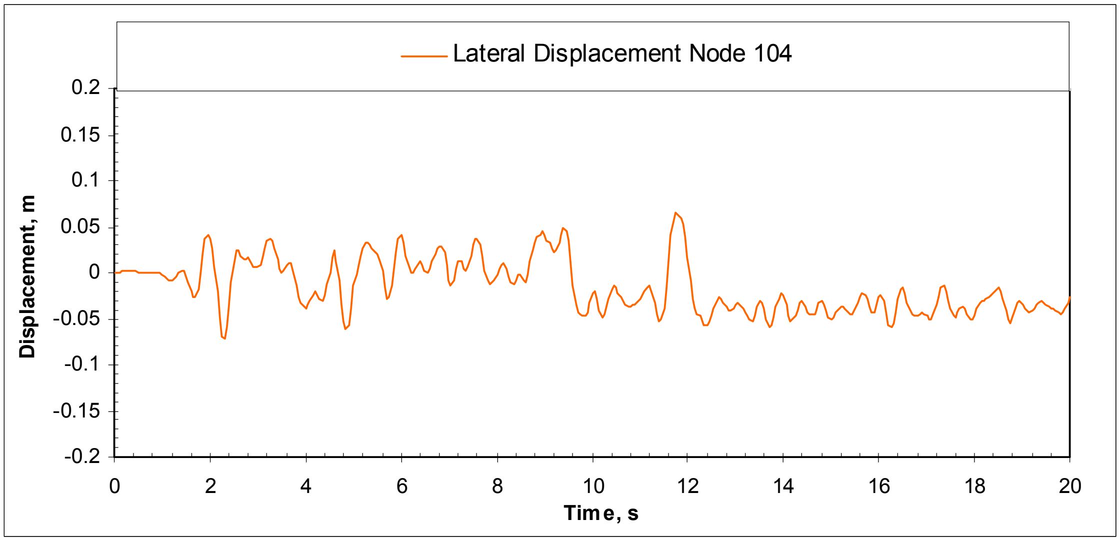

Figure D.22 - Span1, Imperial Valley 3D input, SCED k = 36.9MN/$m^{1.3}$, node 104 lateral displacement

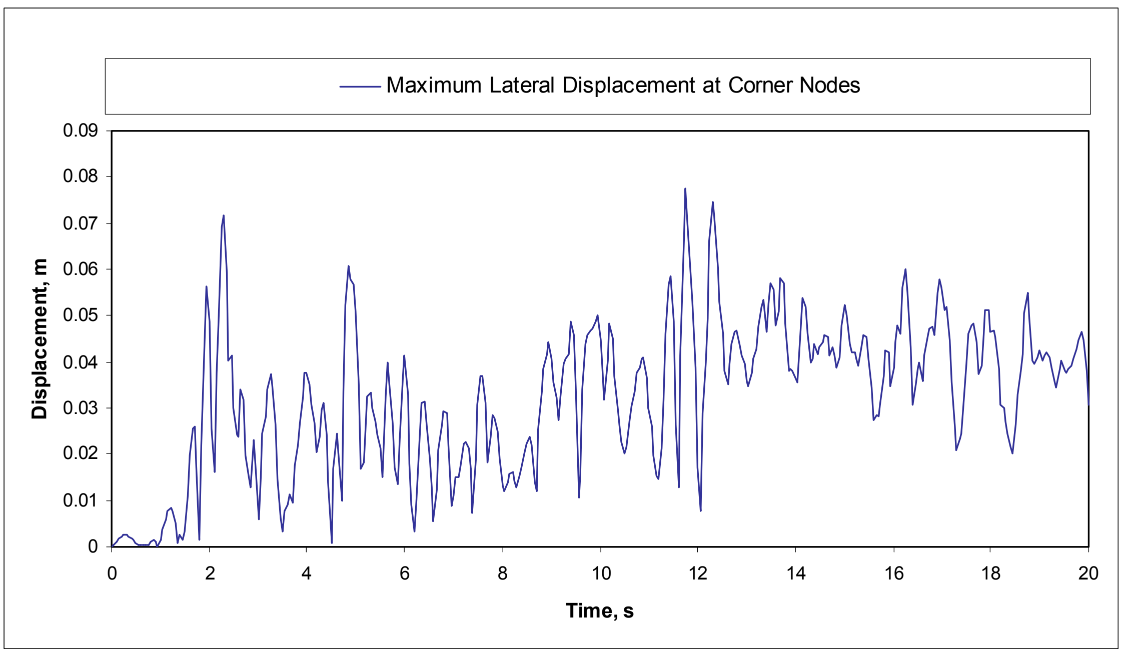

Figure D.23 - Span1, Imperial Valley 3D input, SCED k = 36.9MN/$m^{1.3}$, maximum lateral disp.

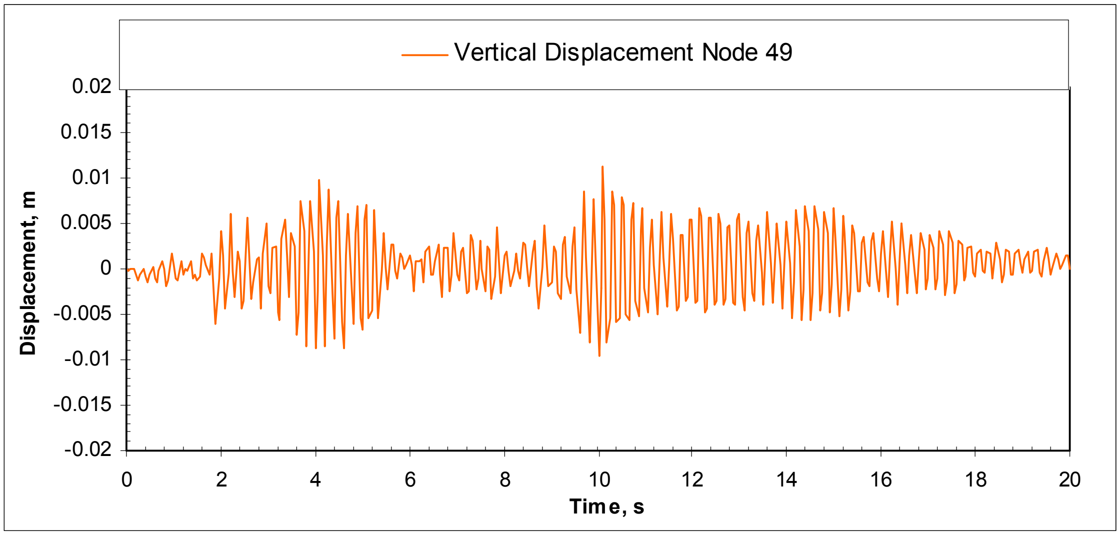

Figure D.24 - Span1, Imperial Valley 3D input, SCED k = 36.9MN/$m^{1.3}$, node 49 vertical displacement

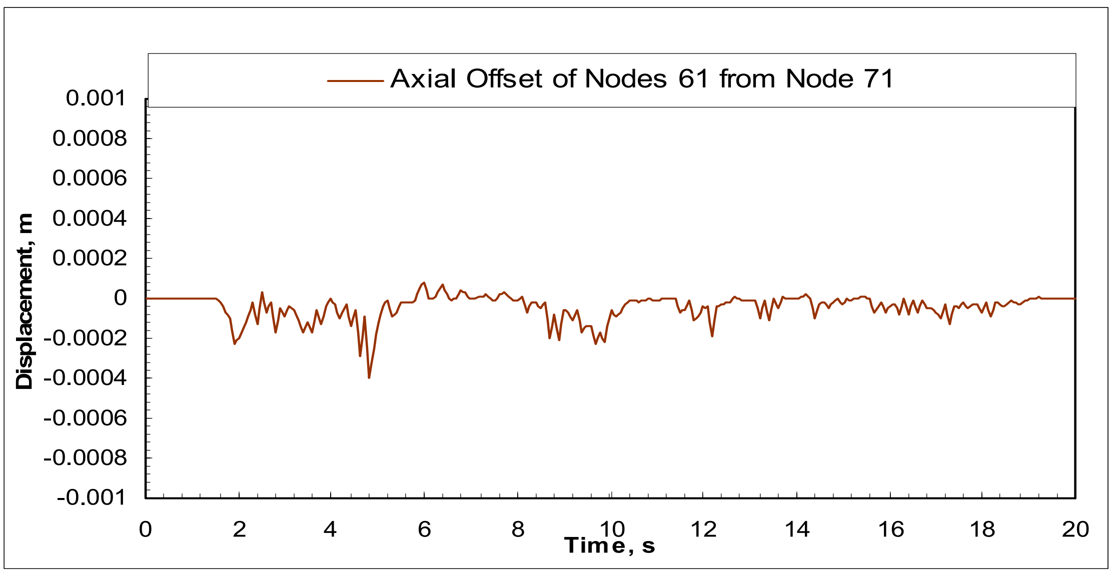

Figure D.25 - Span1, Imperial Valley 3D input, SCED k = 36.9MN/$m^{1.3}$, node 61 and 71 response

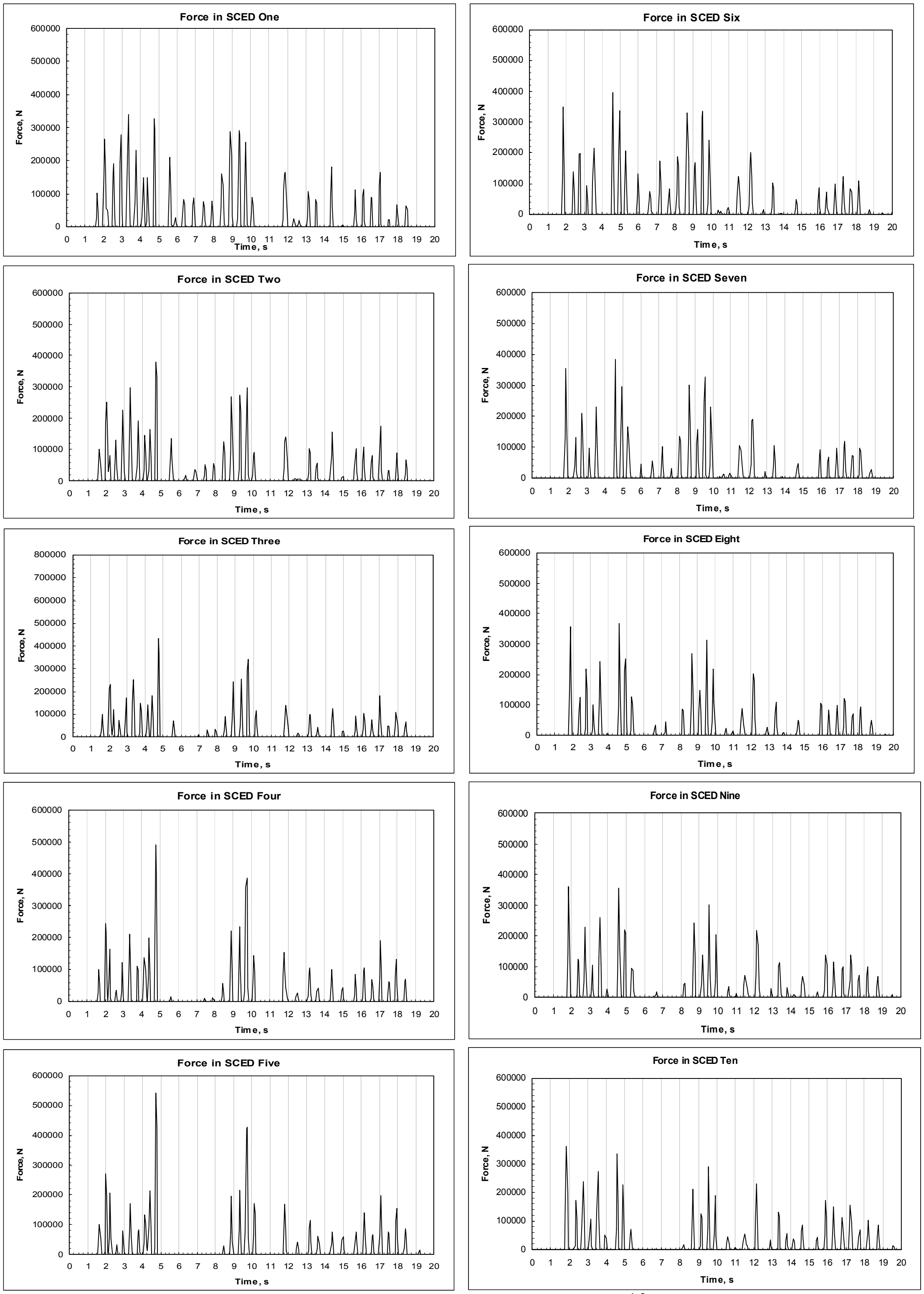

Figure D.26 - Span1, Imperial Valley 3D input, SCED k = 36.9MN/m$^{1.3}$, snap load histories

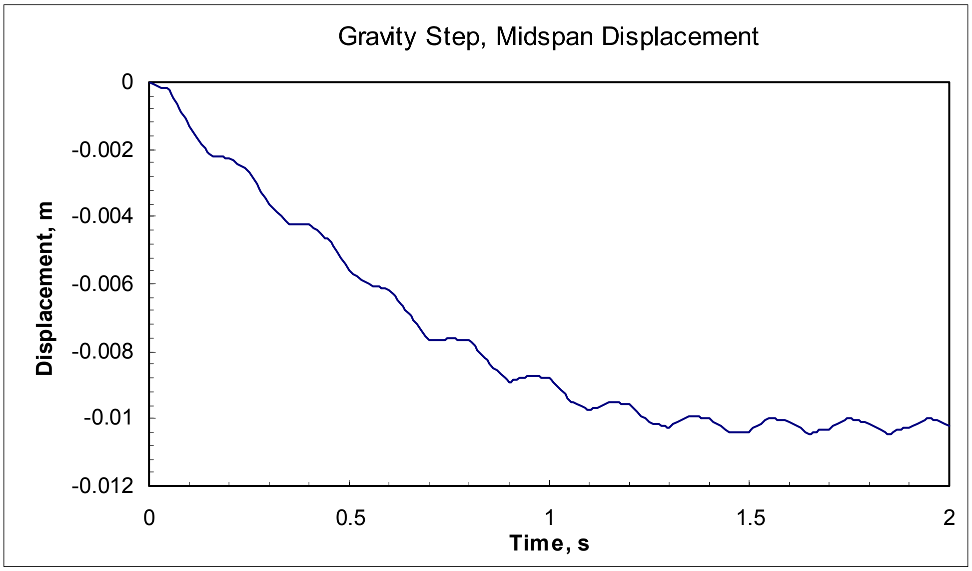

Figure D.27 - Span1, Northridge input, gravity step response

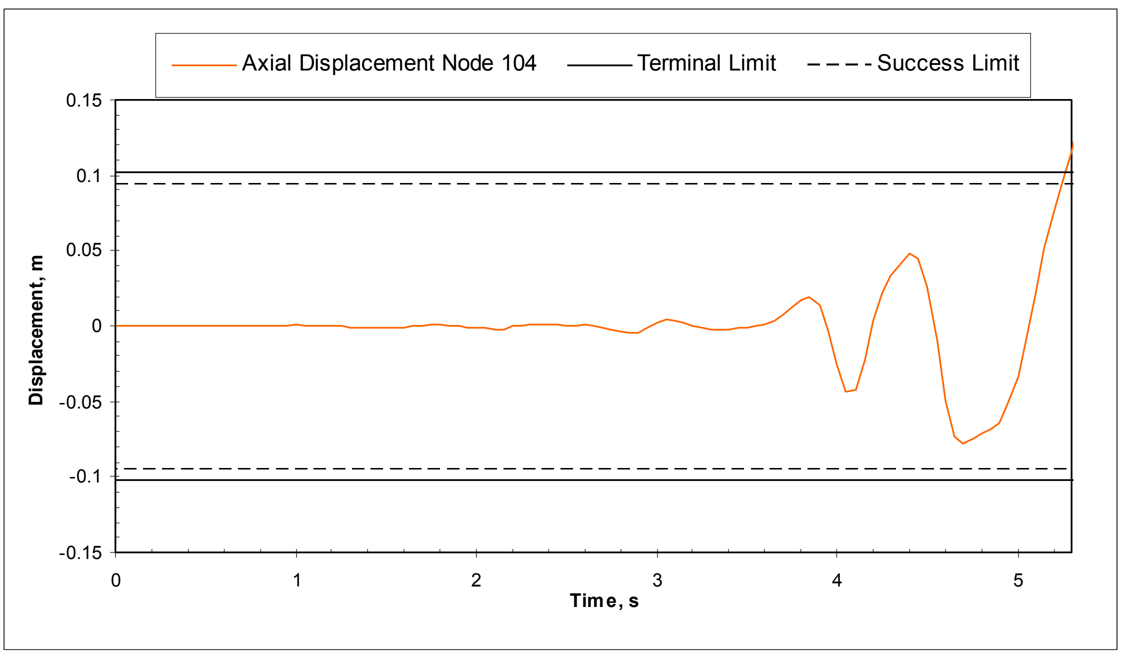

Figure D.28 - Span1, Northridge axial input only, node 104 axial displacement

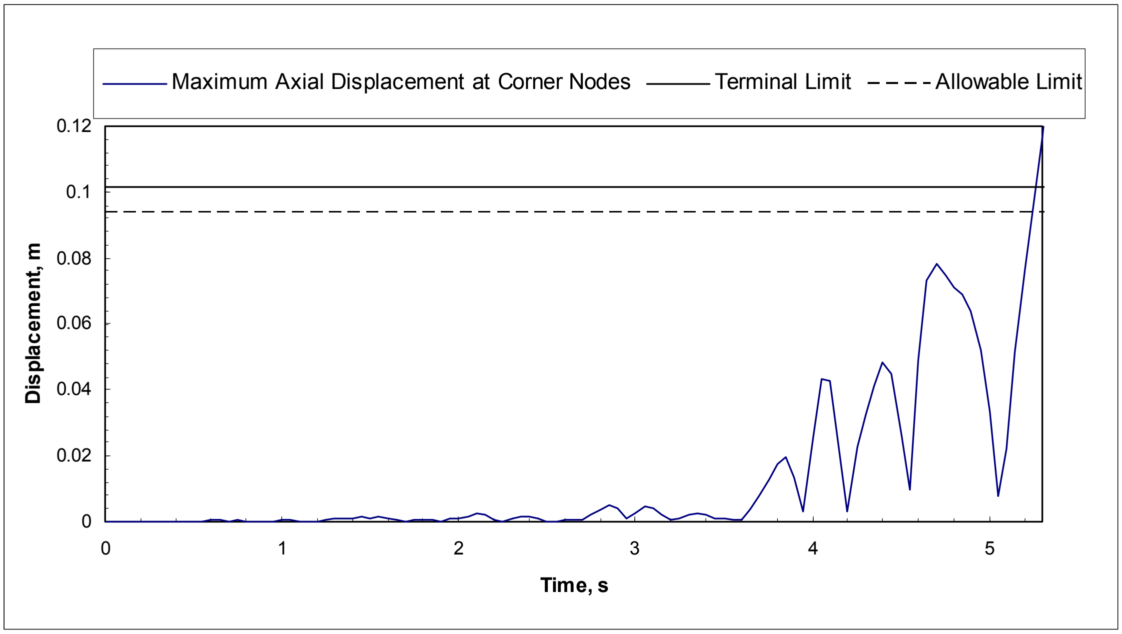

Figure D.29 - Span1, Northridge axial input only, maximum axial displacement

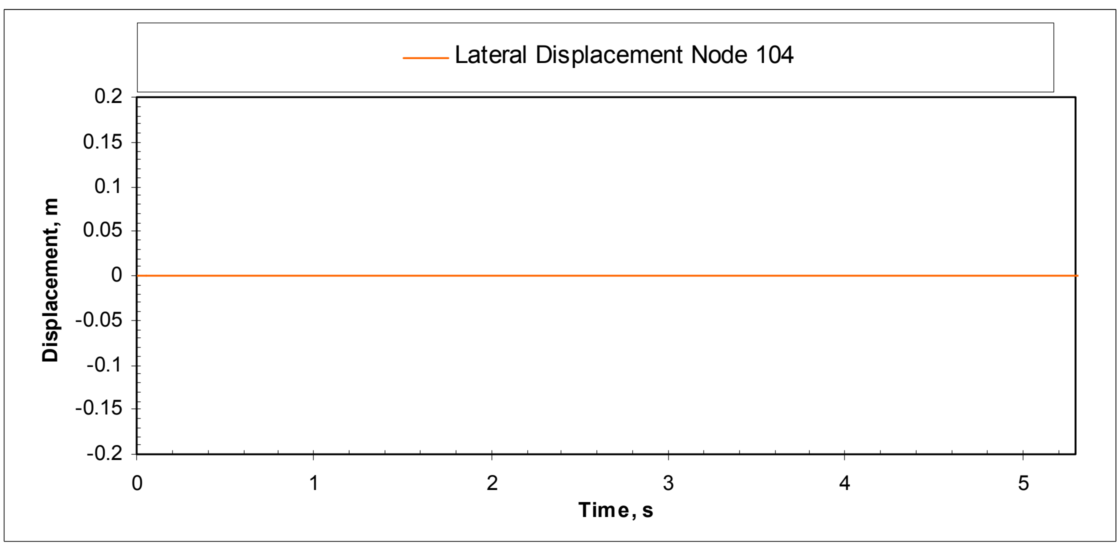

Figure D.30 - Span1, Northridge axial input only, node 104 lateral displacement

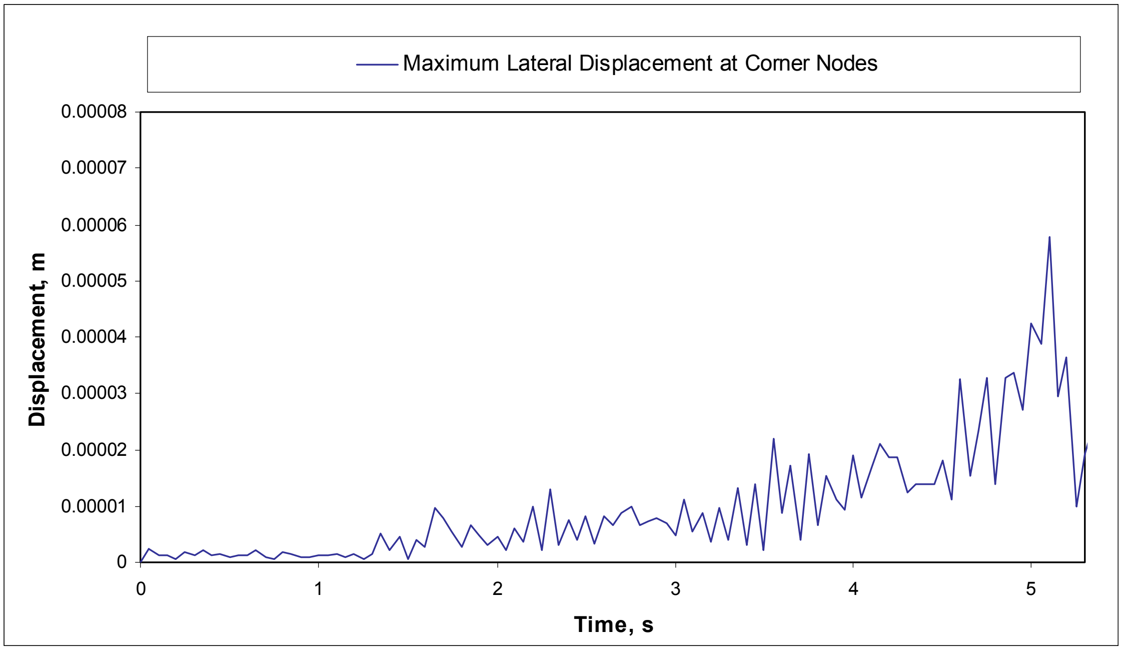

Figure D.31 - Span1, Northridge axial input only, maximum lateral displacement

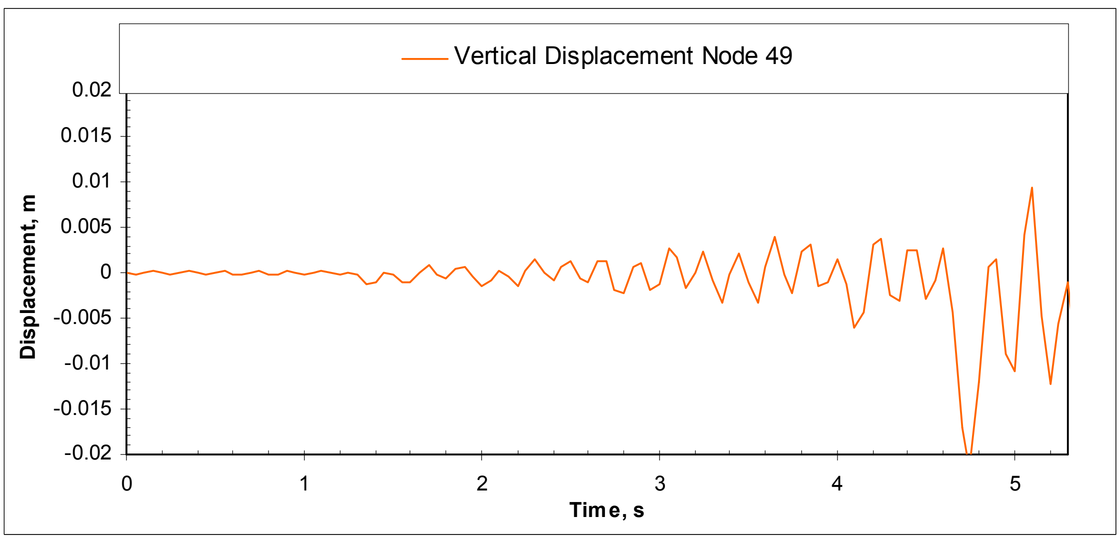

Figure D.32 - Span1, Northridge axial input only, node 49 vertical displacement

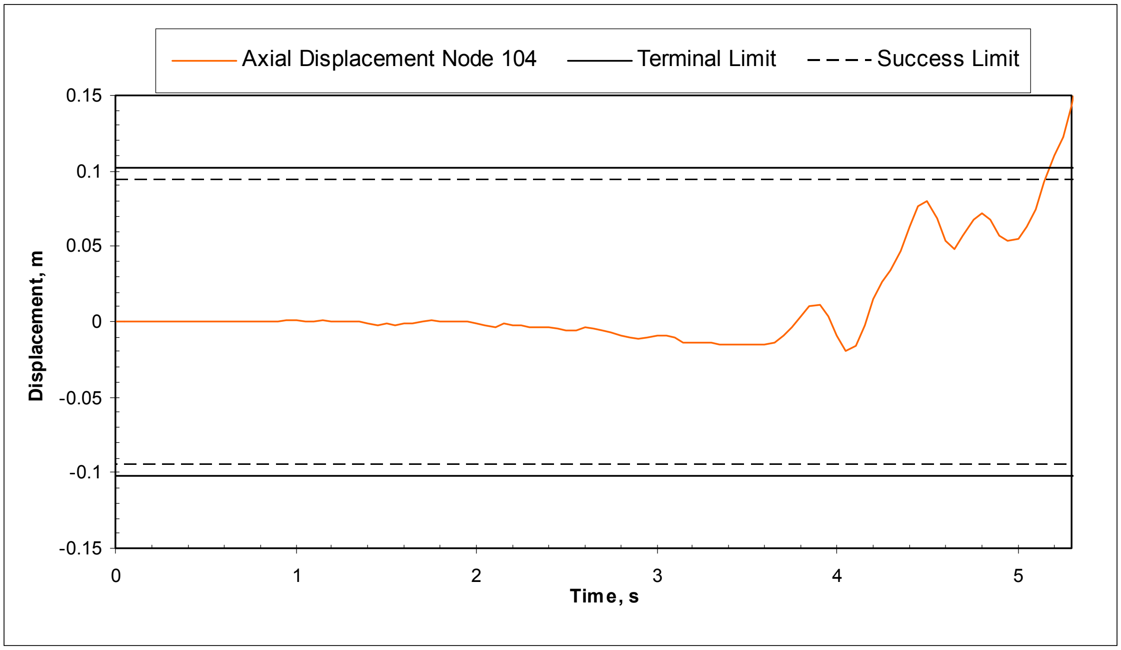

Figure D.33 - Span1, Northridge three-dimensional input, no SCEDs, node 104 axial displacement

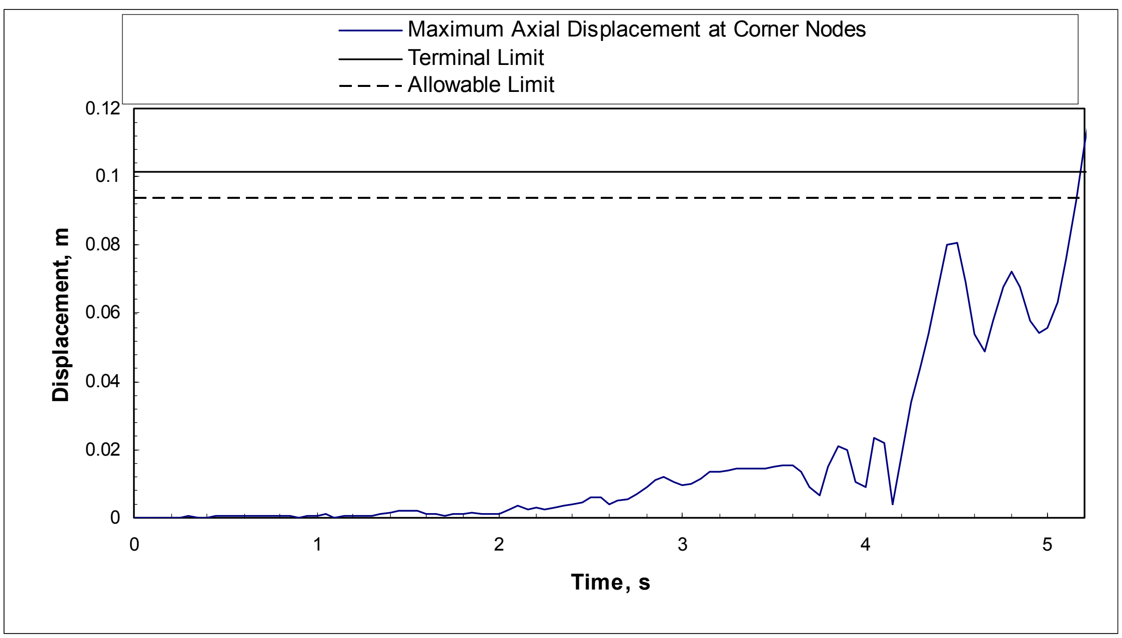

Figure D.34 - Span1, Northridge three-dimensional input, no SCEDs, maximum axial displacement

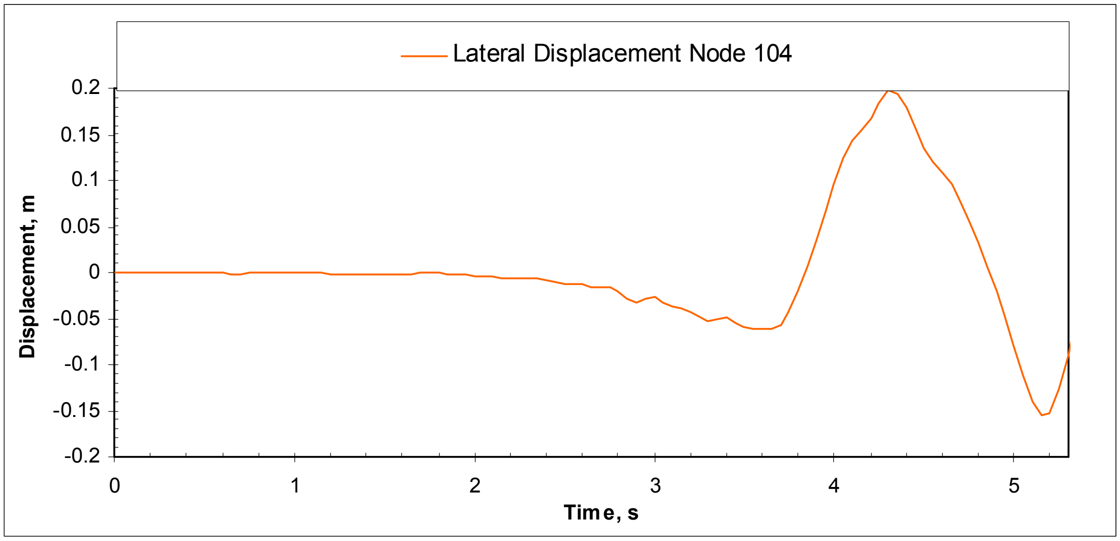

Figure D.35 - Span1, Northridge three-dimensional input, no SCEDs, node 104 lateral displacement

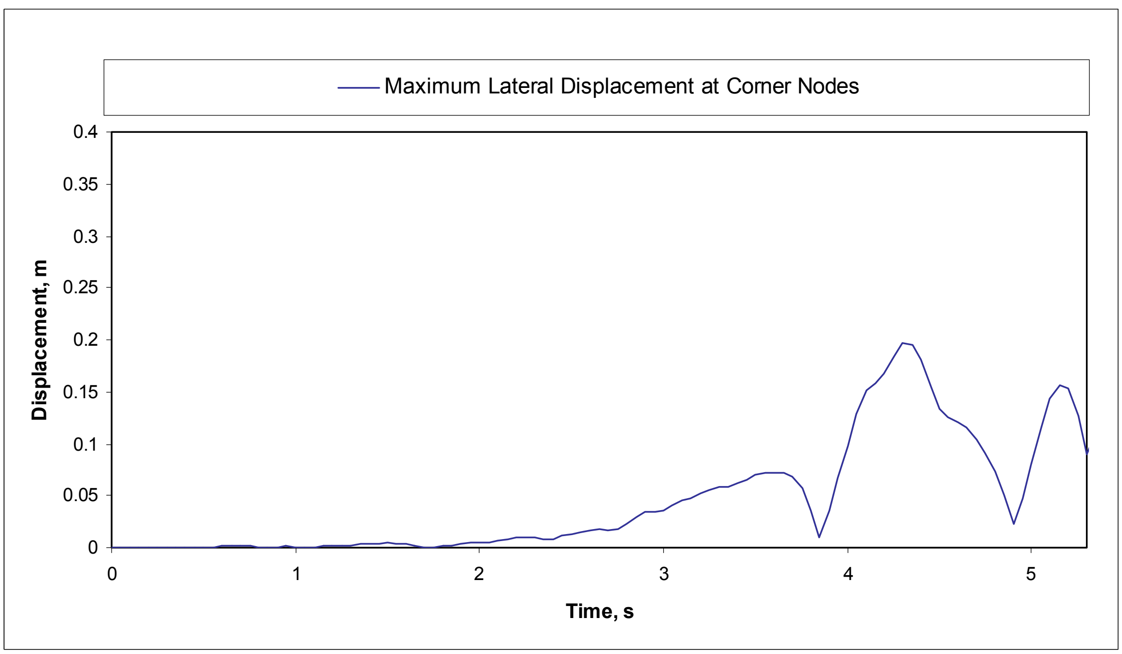

Figure D.36 - Span1, Northridge three-dimensional input, no SCEDs, maximum lateral displacement

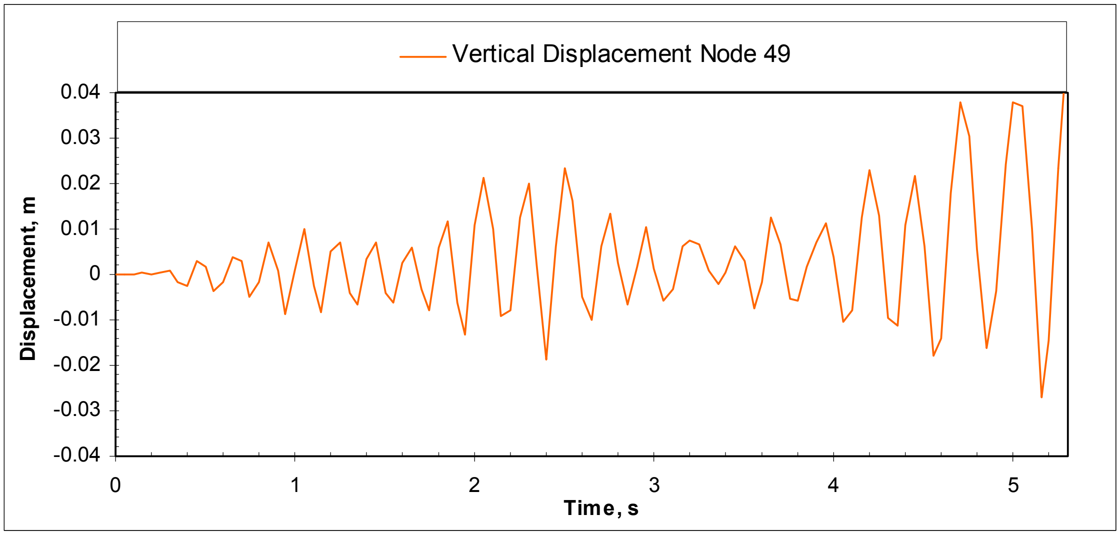

Figure D.37 - Span1, Northridge three-dimensional input, no SCEDs, node 49 vertical displacement

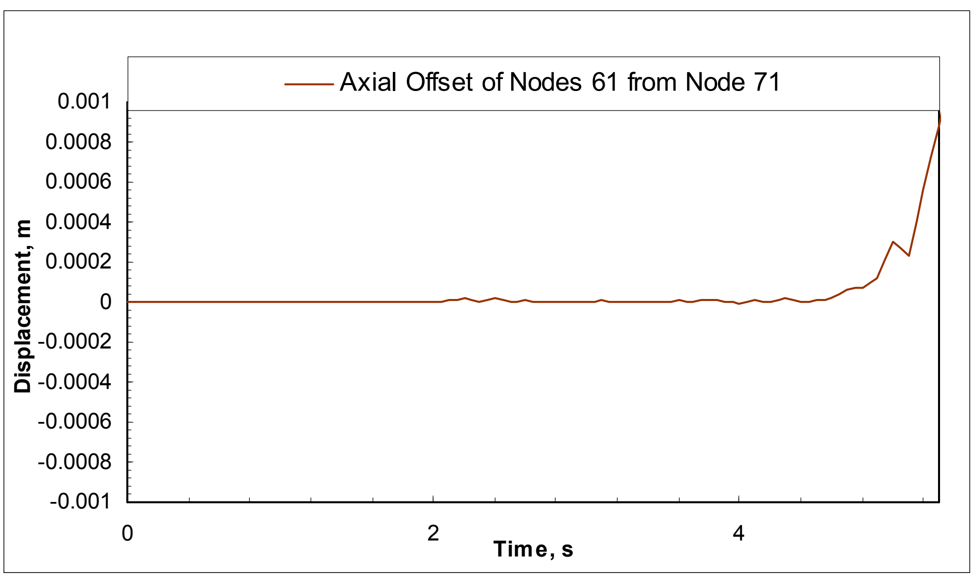

Figure D.38 - Span1, Northridge three-dimensional input, no SCEDs, node 61 and 71 response

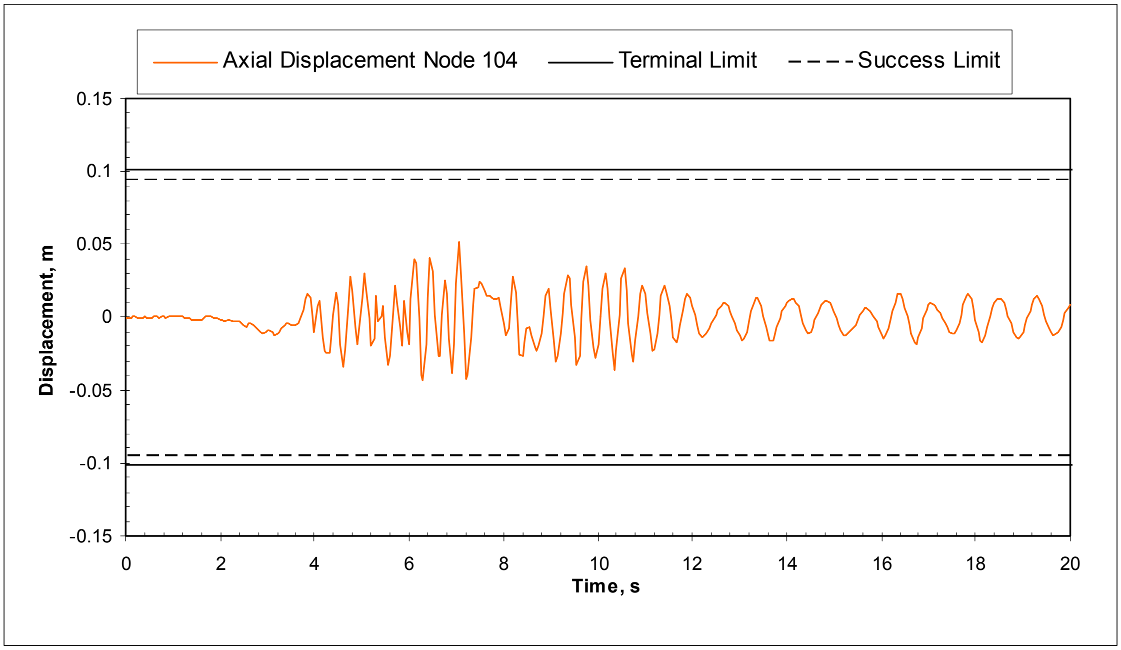

Figure D.39 - Span1, Northridge 3D input, SCED k = 52.7MN/$m^{1.3}$, node 104 axial displacement

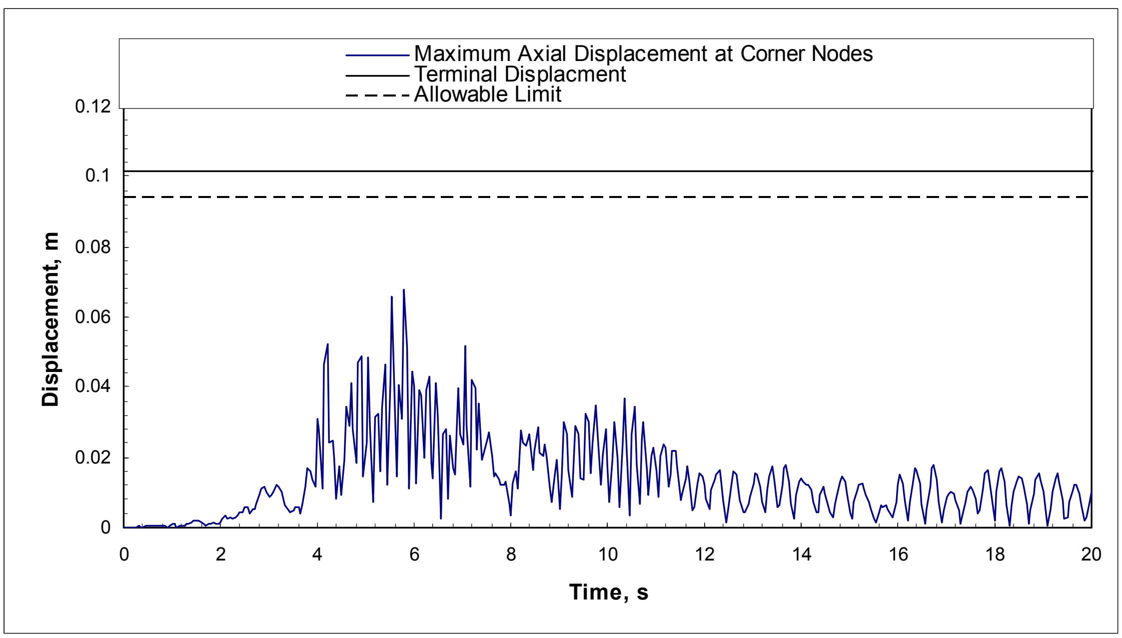

Figure D.40 - Span1, Northridge 3D input, SCED k = 52.7MN/$m^{1.3}$, maximum axial disp.

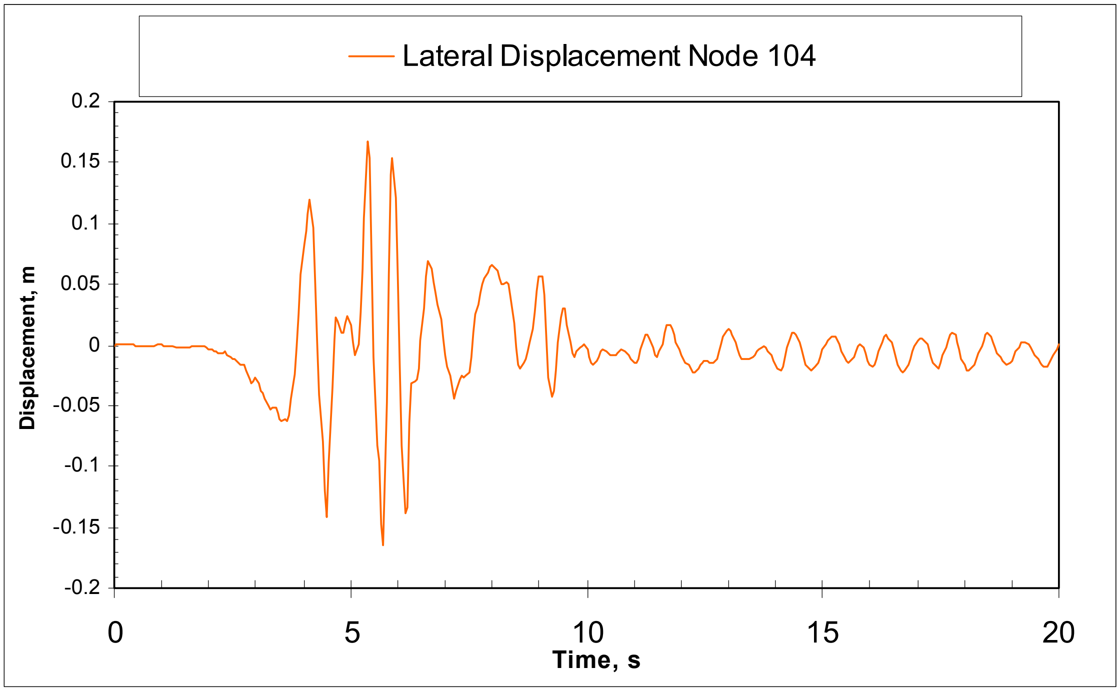

Figure D.41 - Span1, Northridge 3D input, SCED k = 52.7MN/m$^{1.3}$, node 104 lateral displacement

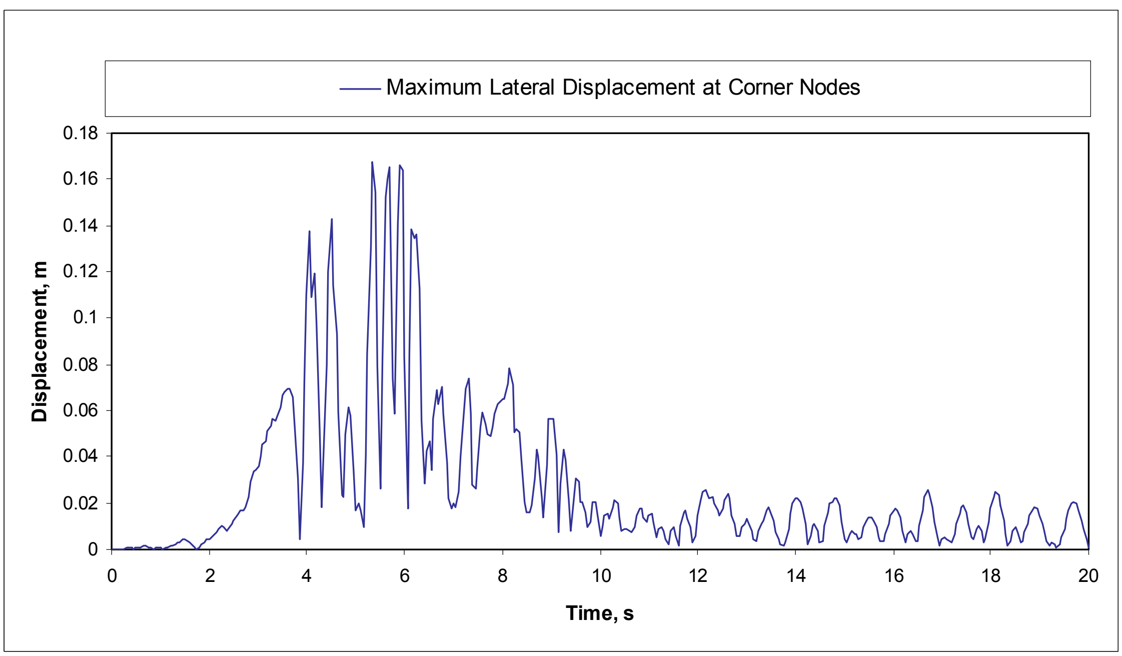

Figure D.42 - Span1, Northridge 3D input, SCED k = 52.7MN/m$^{1.3}$, maximum lateral displacement

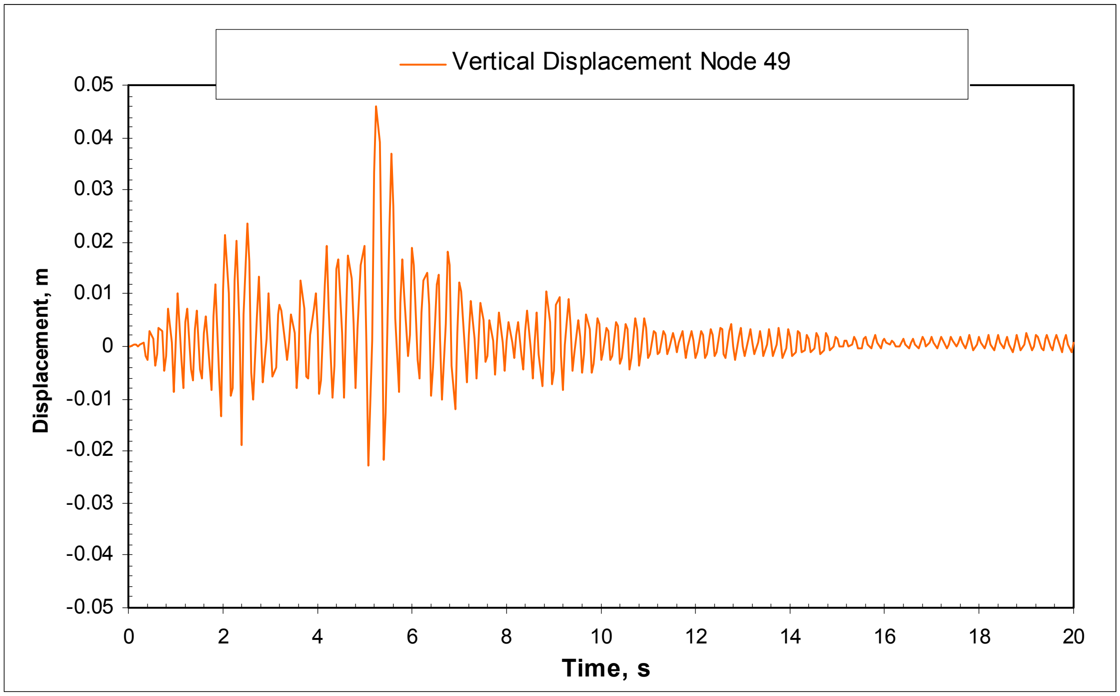

Figure D.43 - Span1, Northridge 3D input, SCED k = 52.7MN/m$^{1.3}$, node 49 vertical displacement

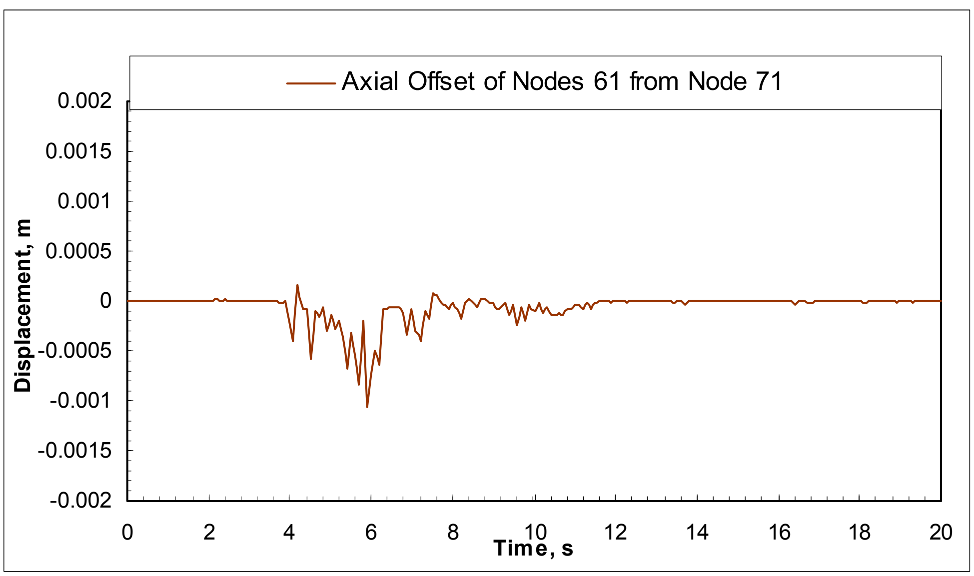

Figure D.44 - Span1, Northridge 3D input, SCED k = 52.7MN/m$^{1.3}$, node 61 and 71 response

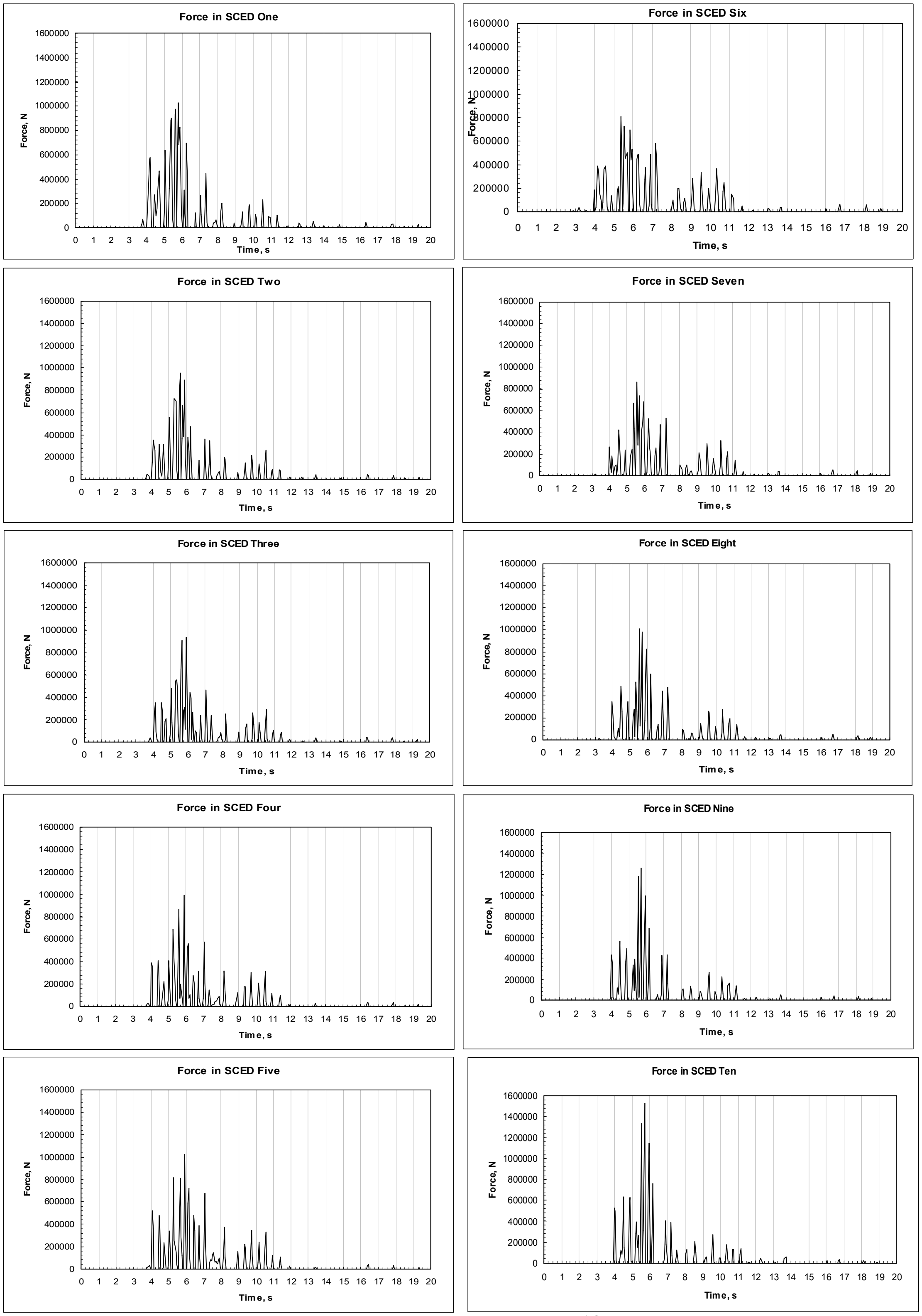

Figure D.45 - Span1, Northridge 3D input, SCED k = 52.7MN/$m^{1.3}$, snap load histories

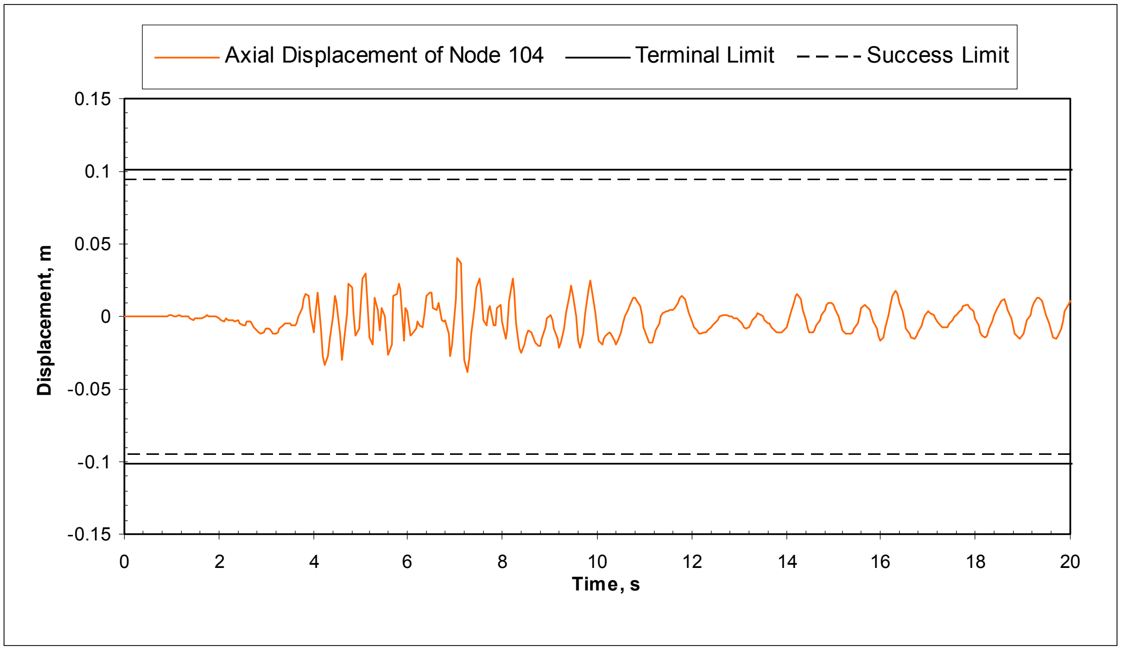

Figure D.46 - Span1, Northridge 3D input, SCED k = 42.2MN/m$^{1.3}$, node 104 axial displacement

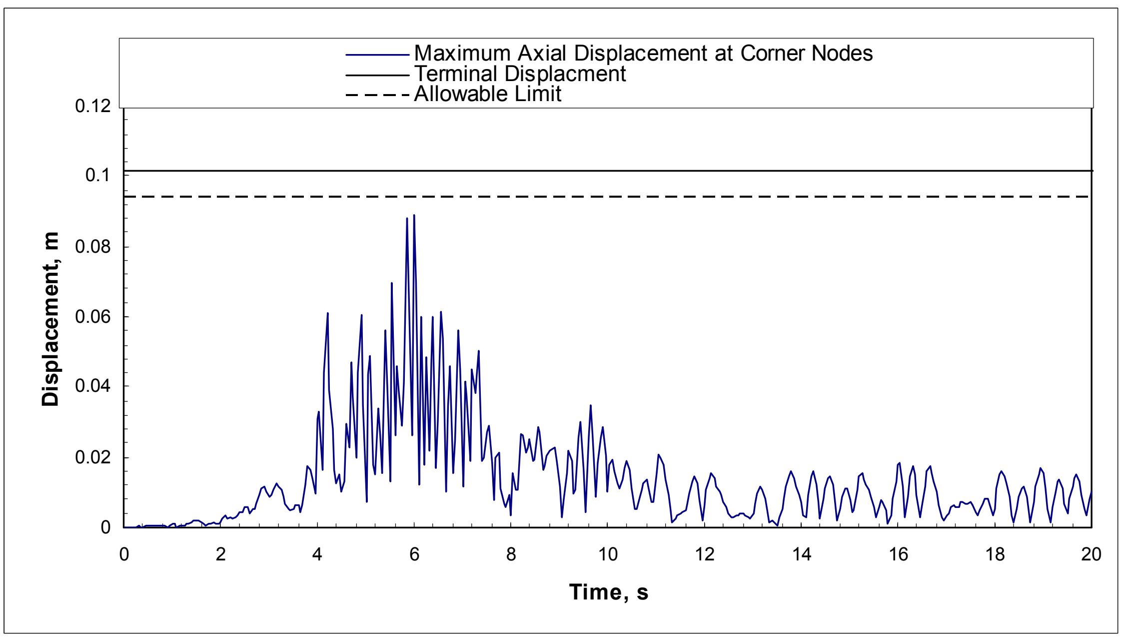

Figure D.47 - Span1, Northridge 3D input, SCED k = 42.2MN/m$^{1.3}$, maximum axial displacement

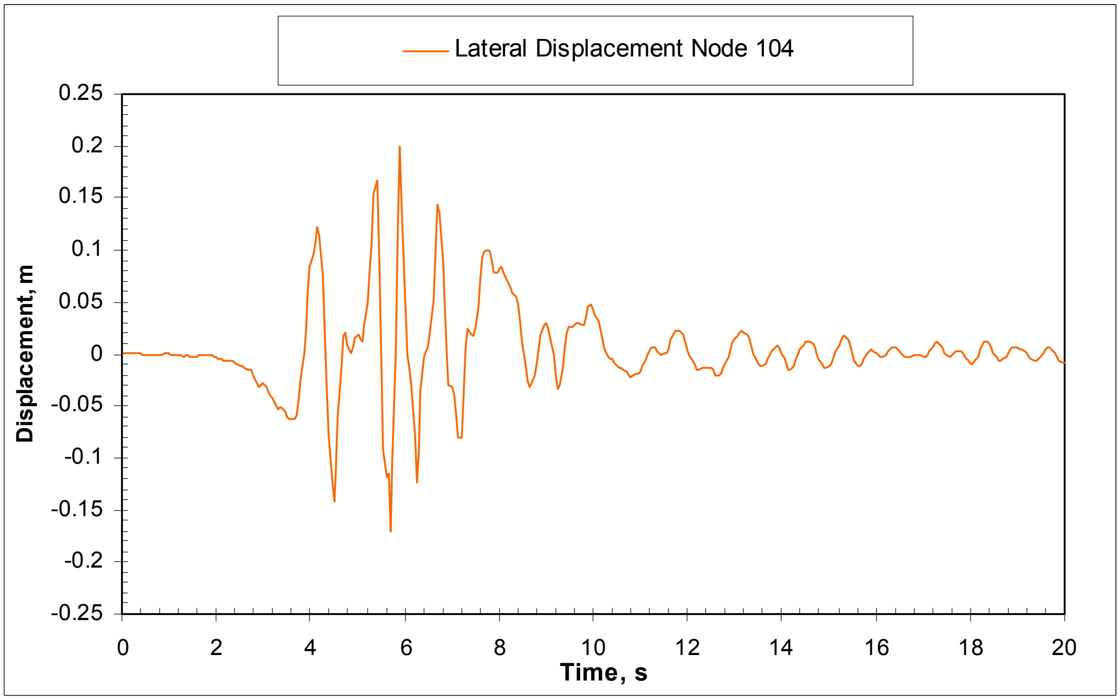

Figure D.48 - Span1, Northridge 3D input, SCED k = 42.2MN/m$^{1.3}$, node 104 lateral displacement

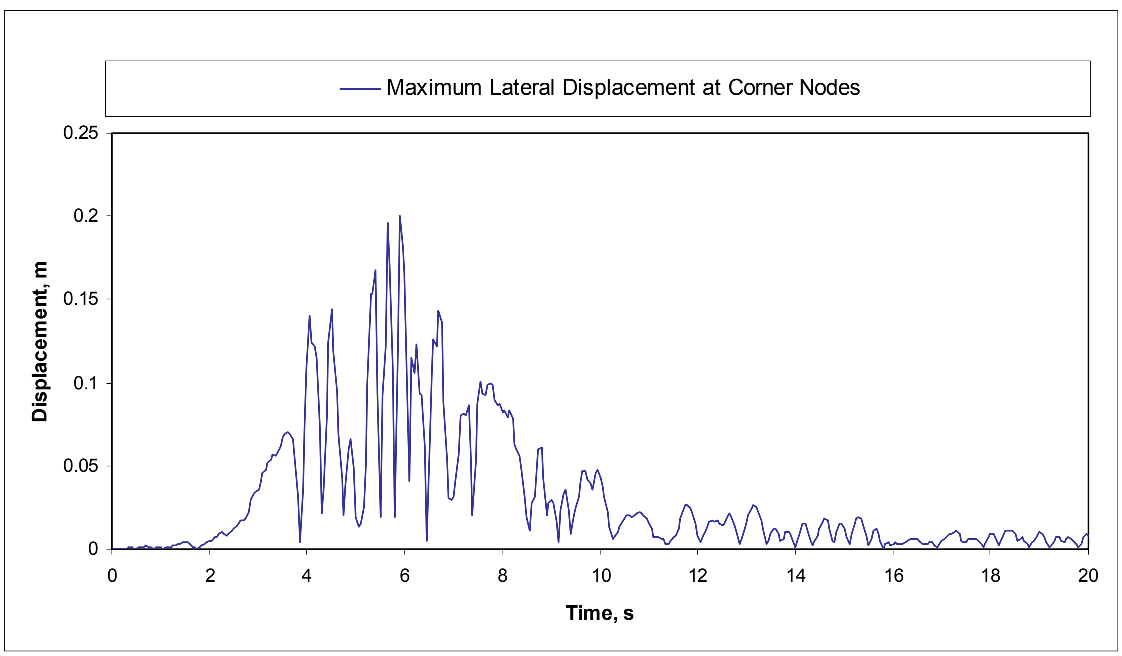

Figure D.49 - Span1, Northridge 3D input, SCED k = 42.2MN/m$^{1.3}$, maximum lateral displacement

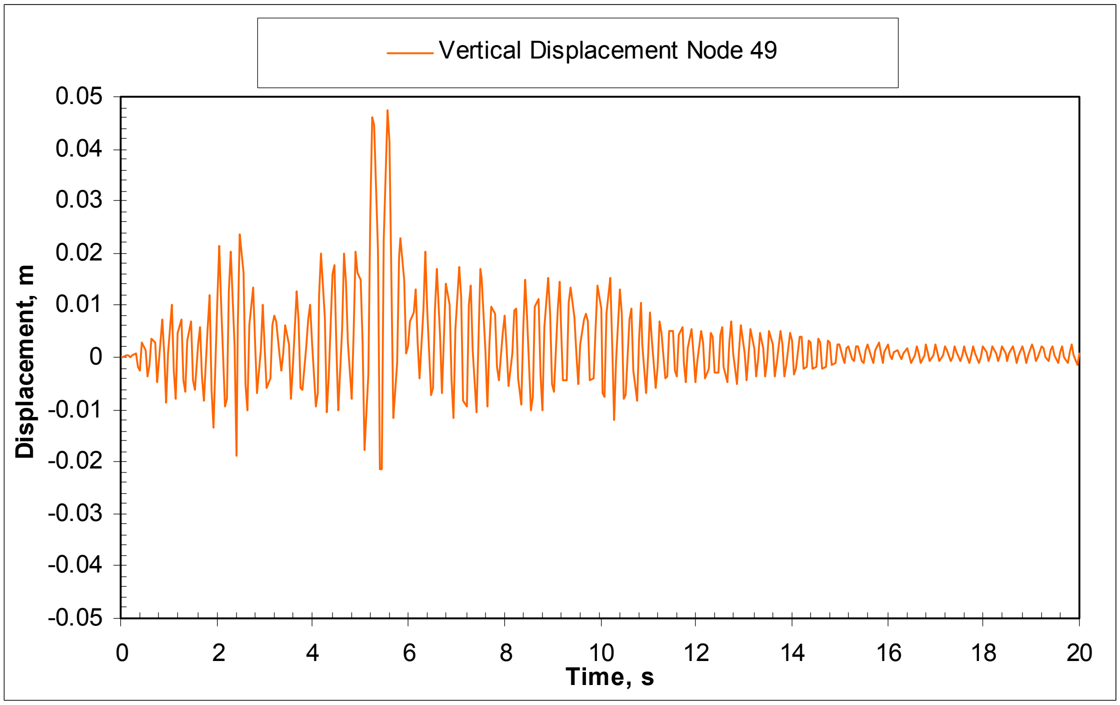

Figure D.50 - Span1, Northridge 3D input, SCED k = 42.2MN/m$^{1.3}$, node 49 vertical displacement

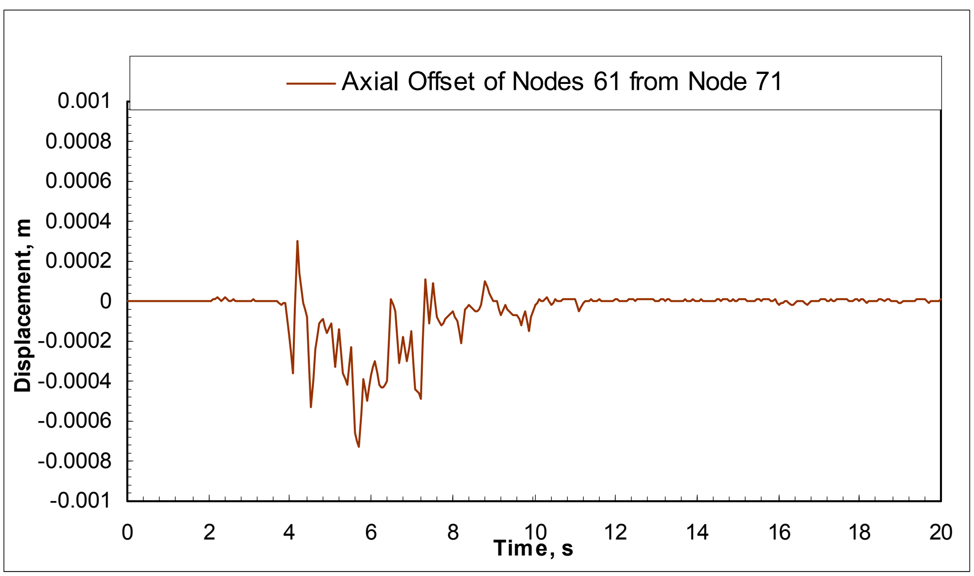

Figure D.51 - Span1, Northridge 3D input, SCED k = 42.2MN/m$^{1.3}$, node 61 and 71 response

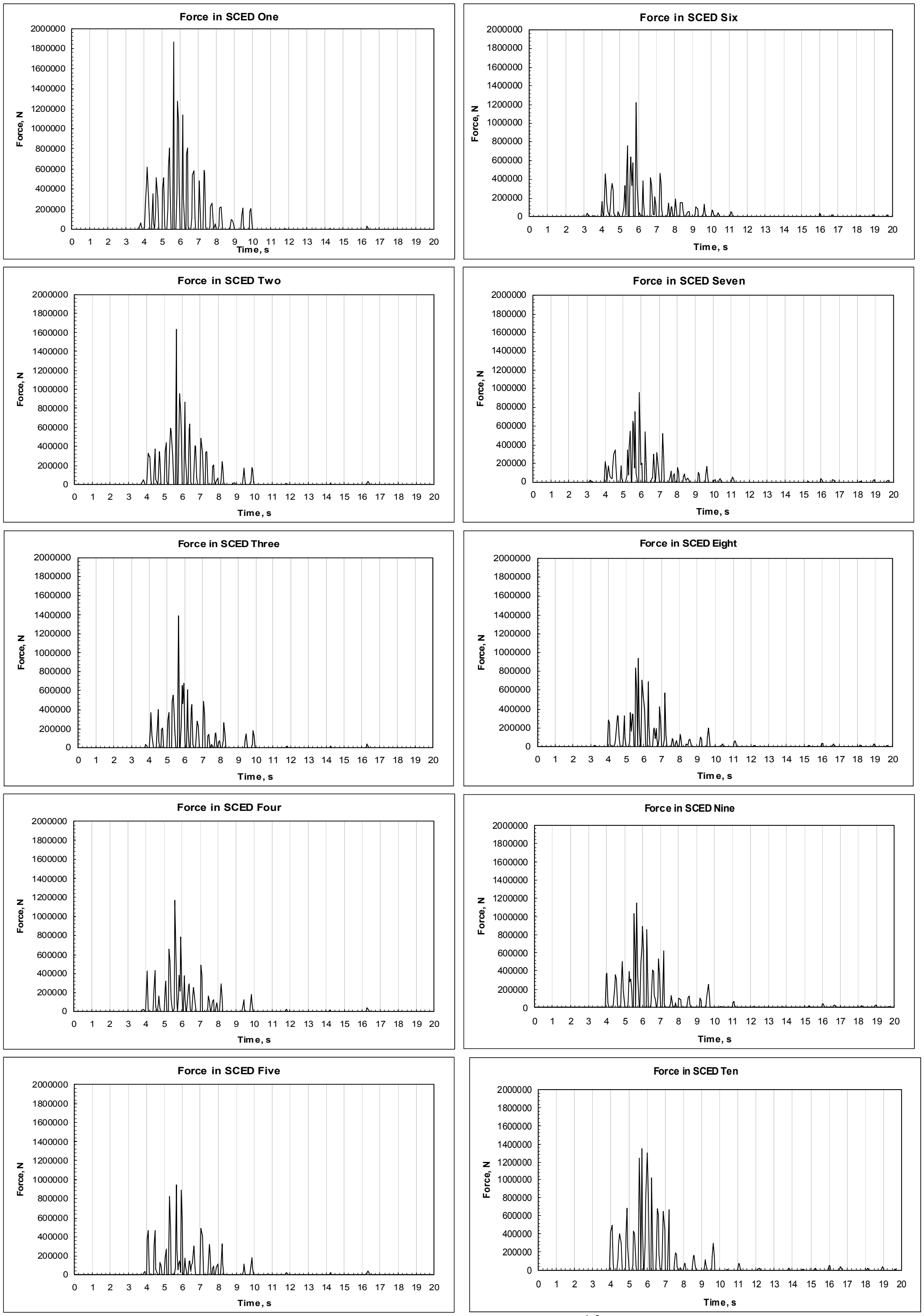

Figure D.52 - Span1, Northridge 3D input, SCED k = 42.2MN/m$^{1.3}$, snap load histories

D.2 Span2 Figures

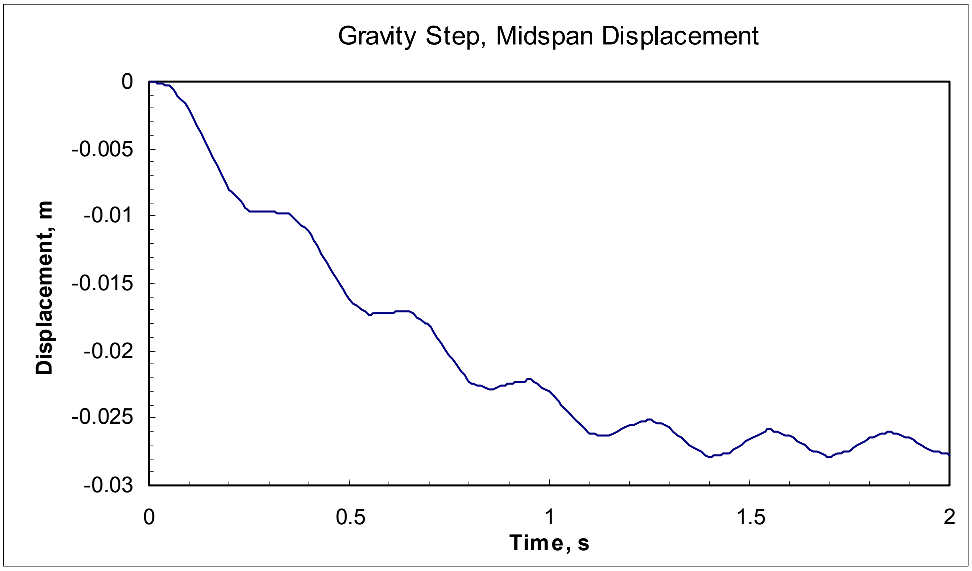

Figure D.53 - Span2, Imperial Valley input, gravity step response

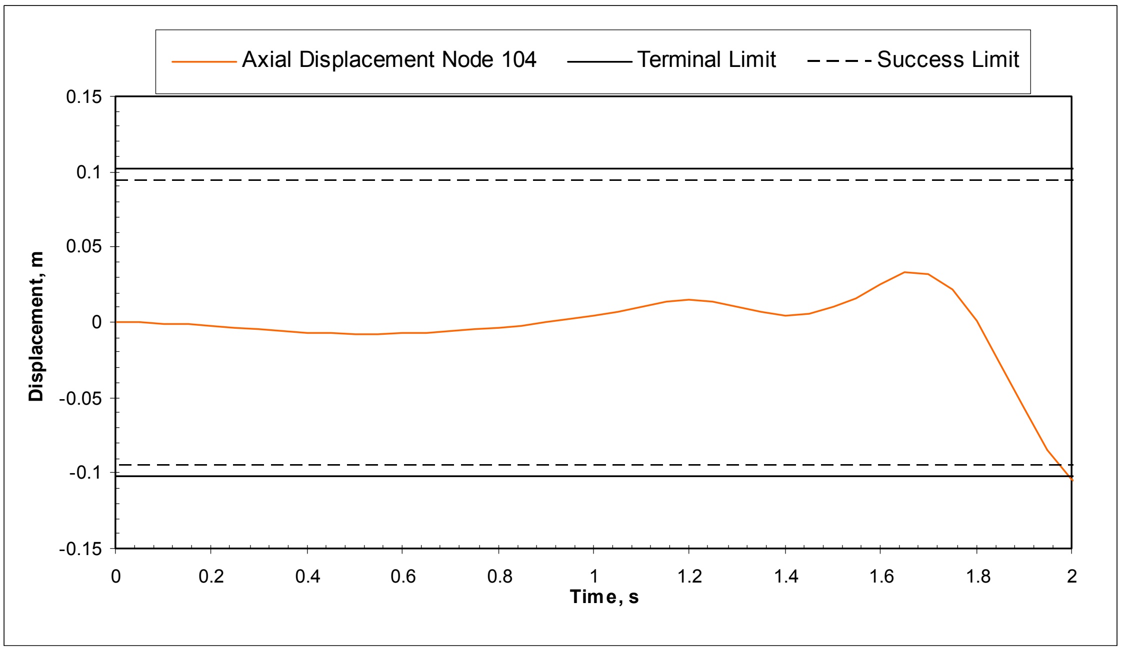

Figure D.54 - Span2, Imperial Valley axial input only, node 104 axial displacement

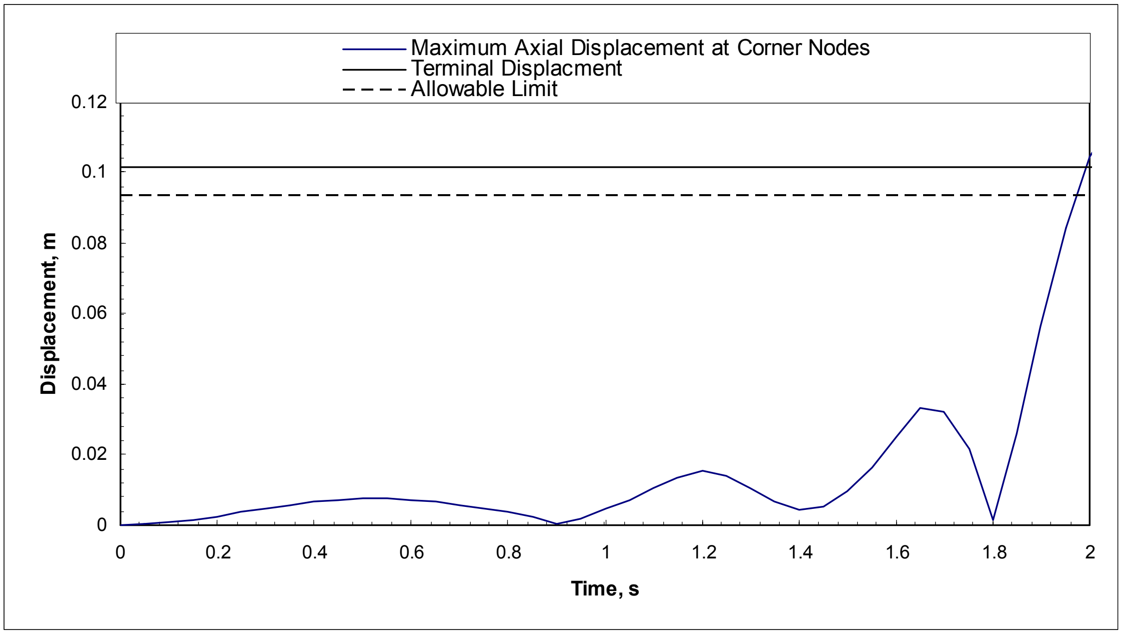

Figure D.55 - Span2, Imperial Valley axial input only, maximum axial displacement

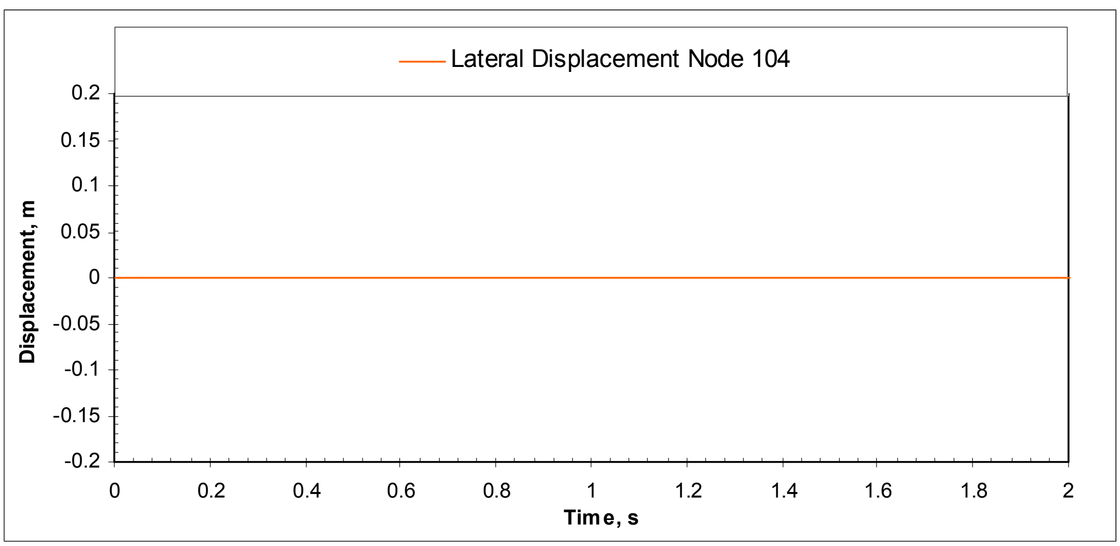

Figure D.56 - Span2, Imperial Valley axial input only, node 104 lateral displacement

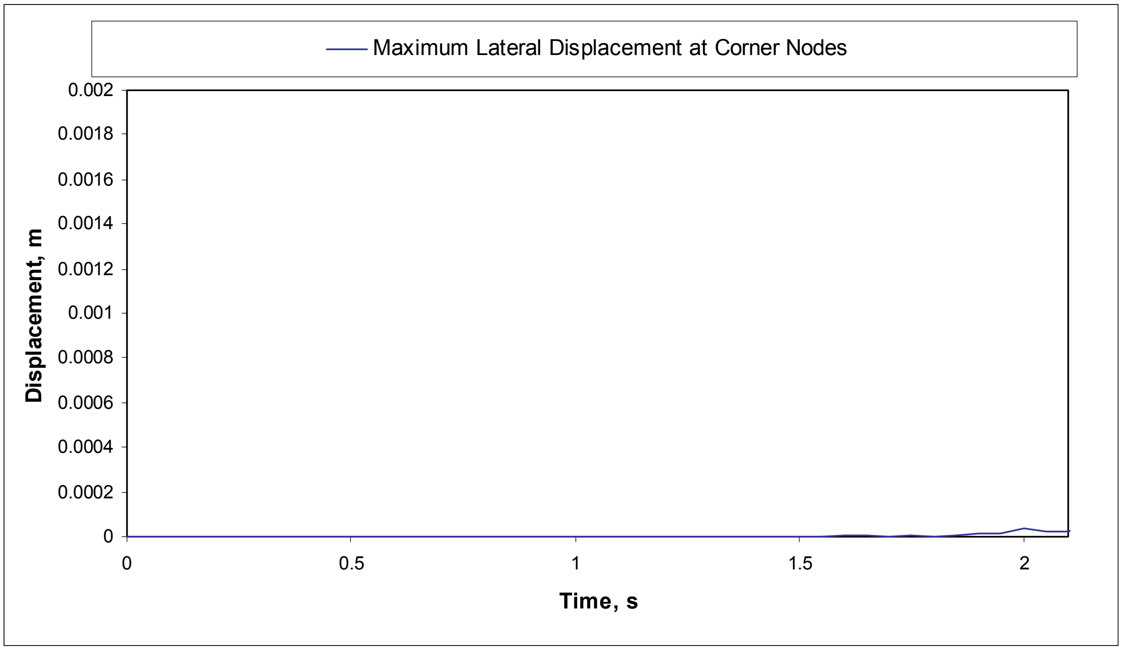

Figure D.57 - Span2, Imperial Valley axial input only, maximum lateral displacement

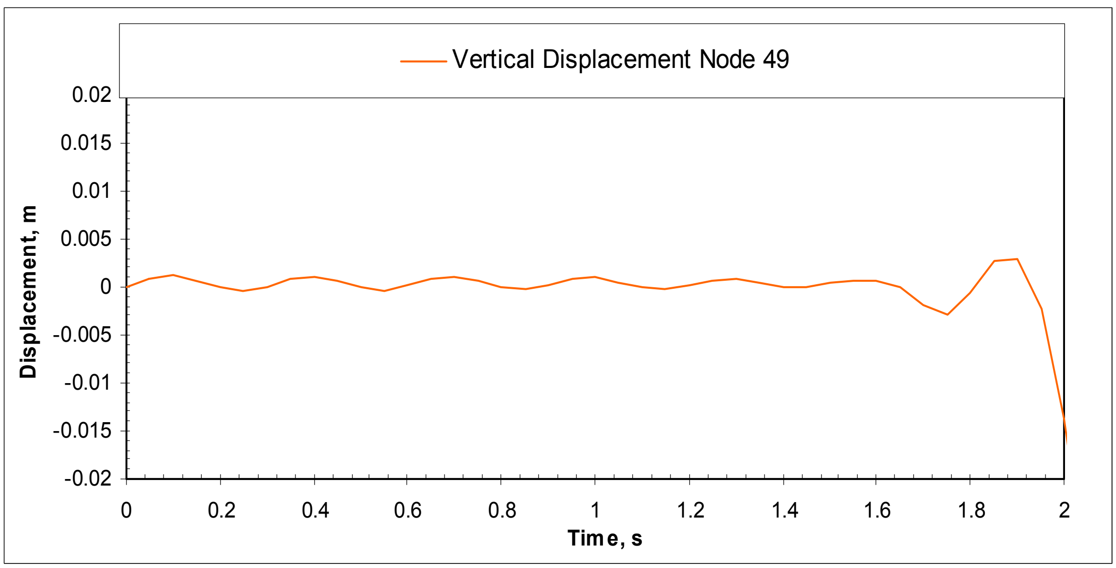

Figure D.58 - Span2, Imperial Valley axial input only, node 49 vertical displacement

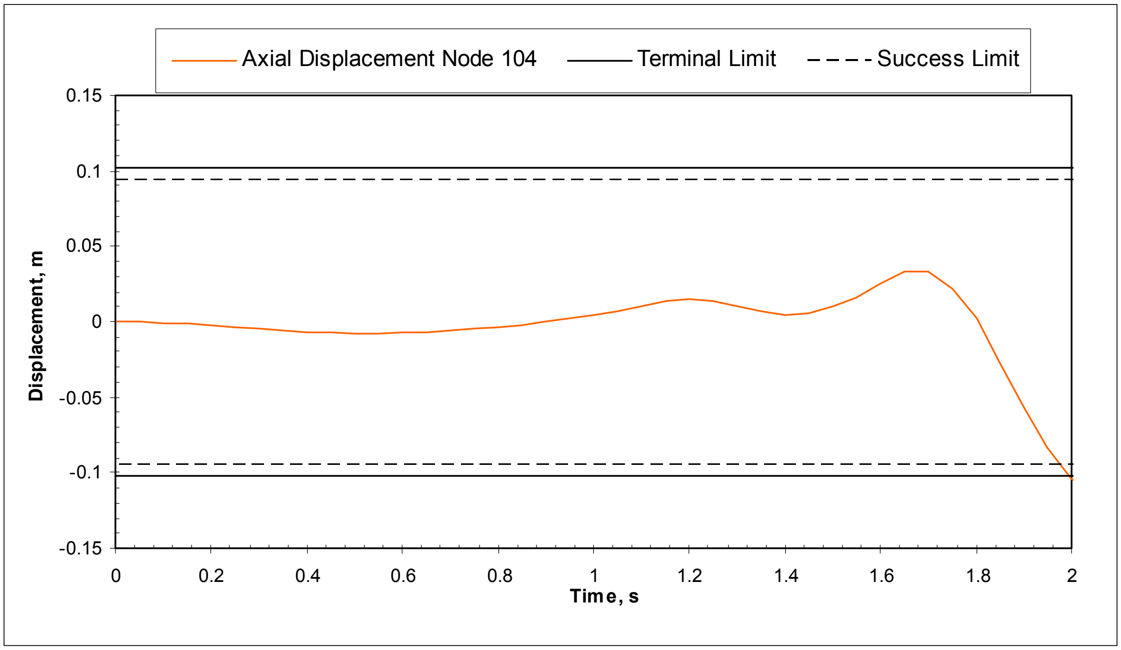

Figure D.59 - Span2, Imperial Valley 3D input, no SCEDs, node 104 axial displacement

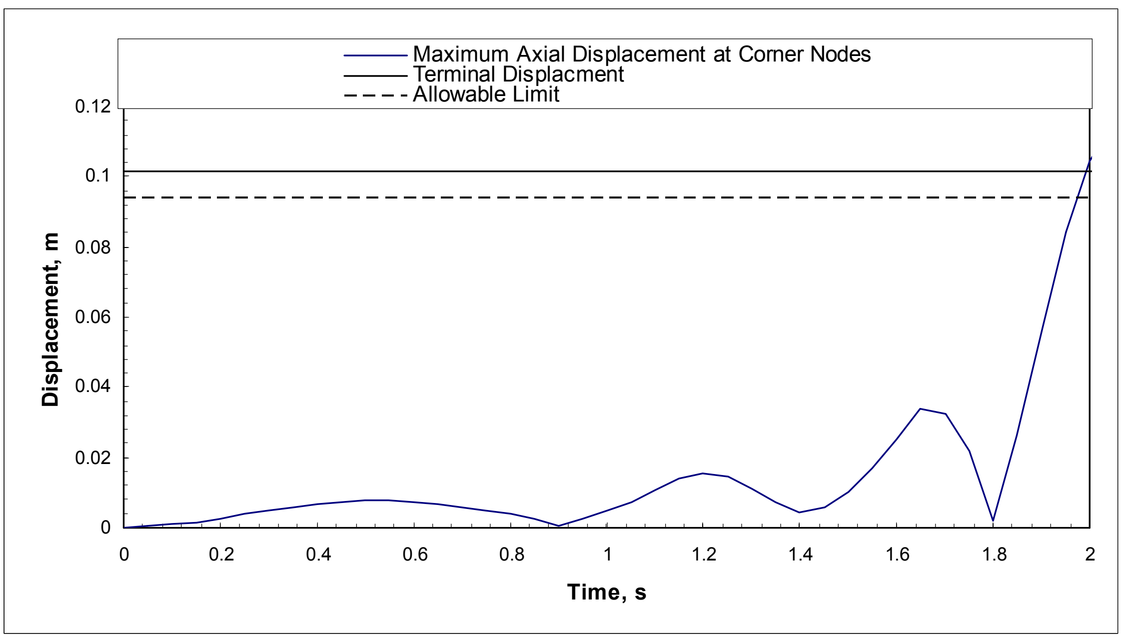

Figure D.60 - Span2, Imperial Valley 3D input, no SCEDs, maximum axial displacement

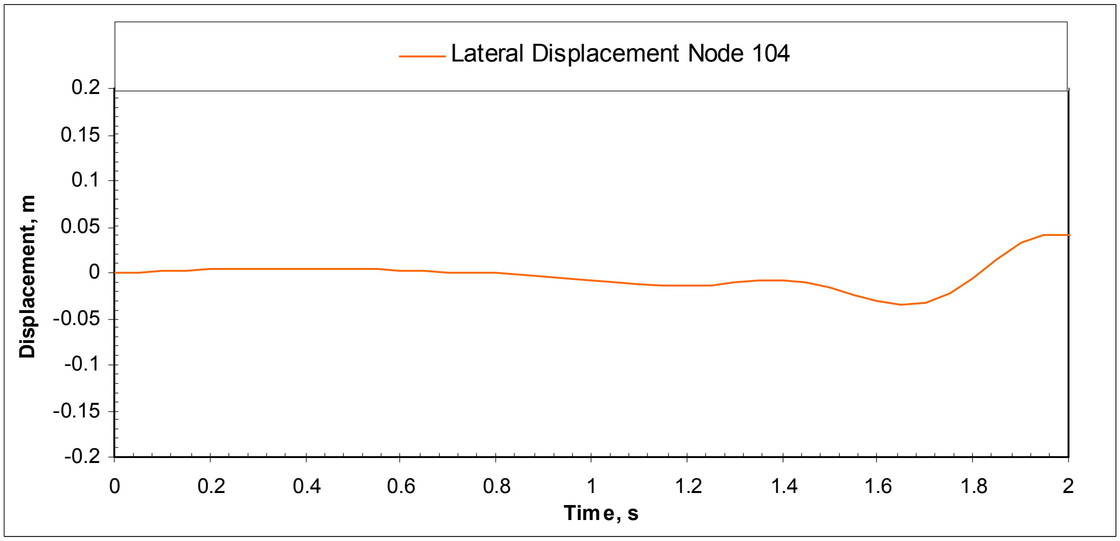

Figure D.61 - Span2, Imperial Valley 3D input, no SCEDs, node 104 lateral displacement

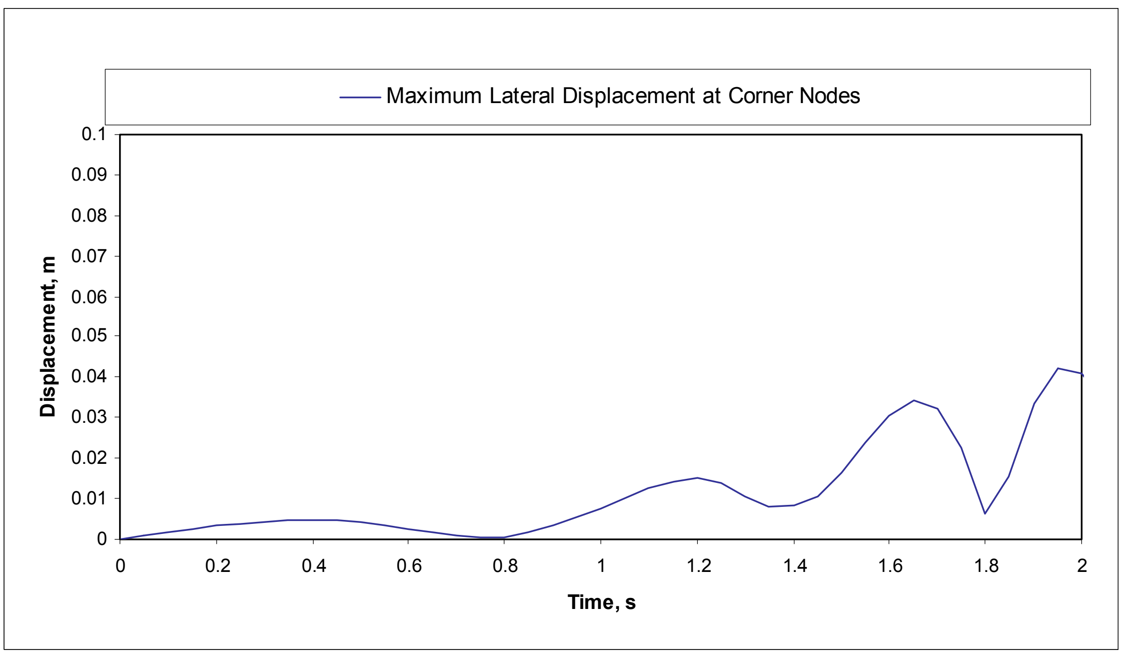

Figure D.62 - Span2, Imperial Valley 3D input, no SCEDs, maximum lateral displacement

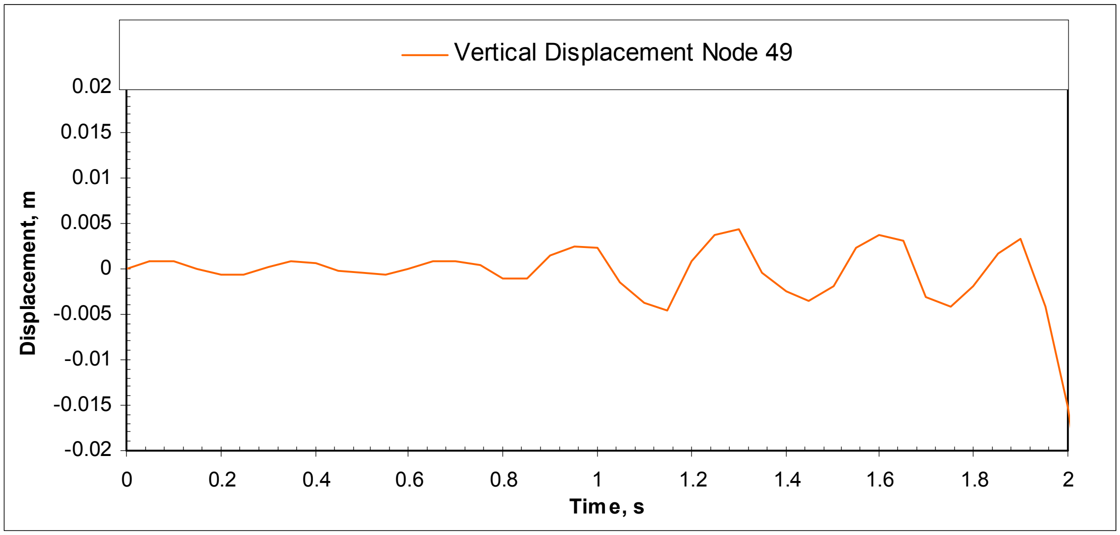

Figure D.63 - Span2, Imperial Valley 3D input, no SCEDs, node 49 vertical displacement

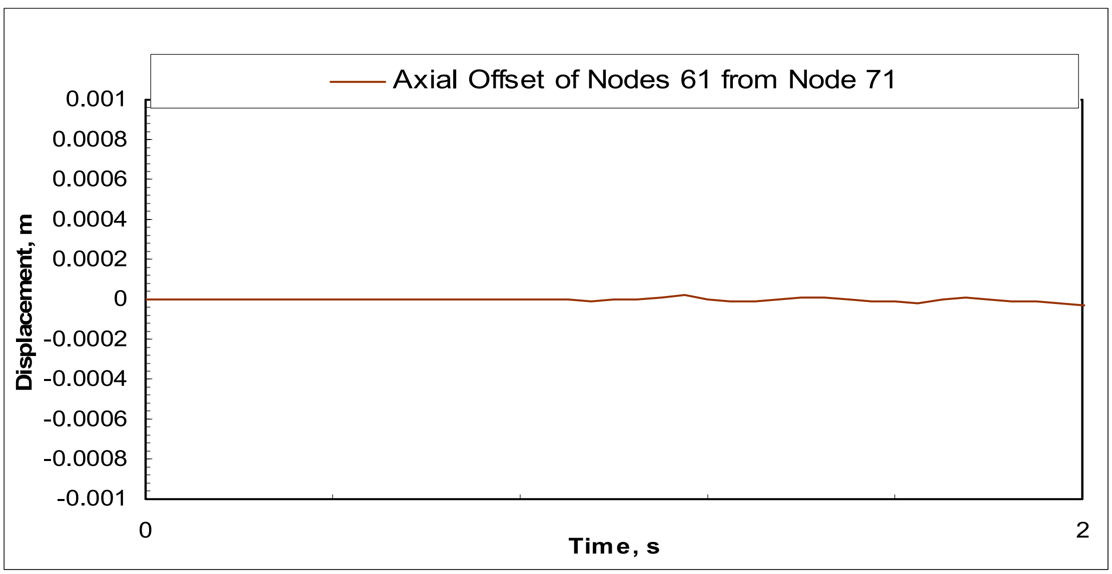

Figure D.64 - Span2, Imperial Valley 3D input, no SCEDs, node 61 and 71 response

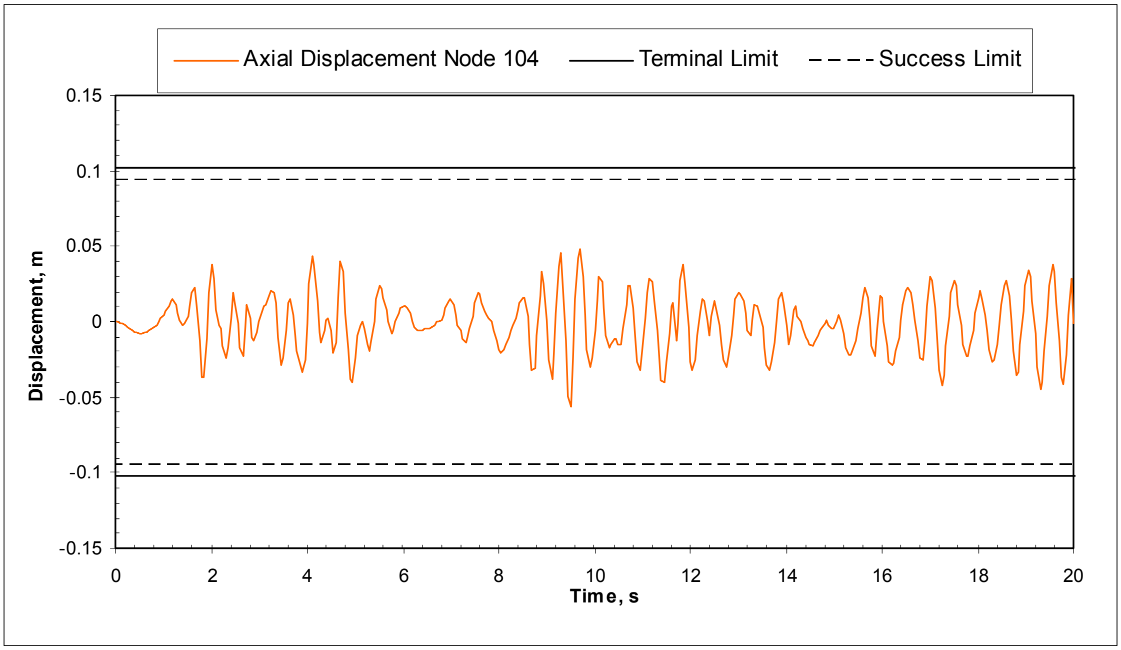

Figure D.65 - Span2, Imperial Valley 3D input, SCED k = 79.1MN/m$^{1.3}$, node 104 axial displacement

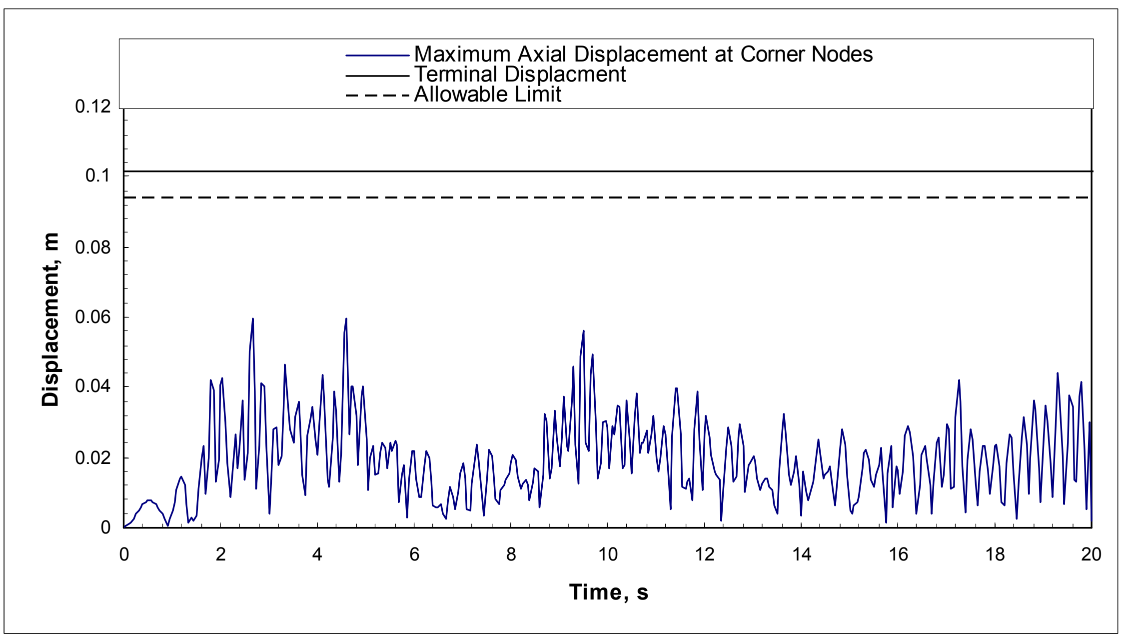

Figure D.66 - Span2, Imperial Valley 3D input, SCED k = 79.1MN/m$^{1.3}$, maximum axial displacement

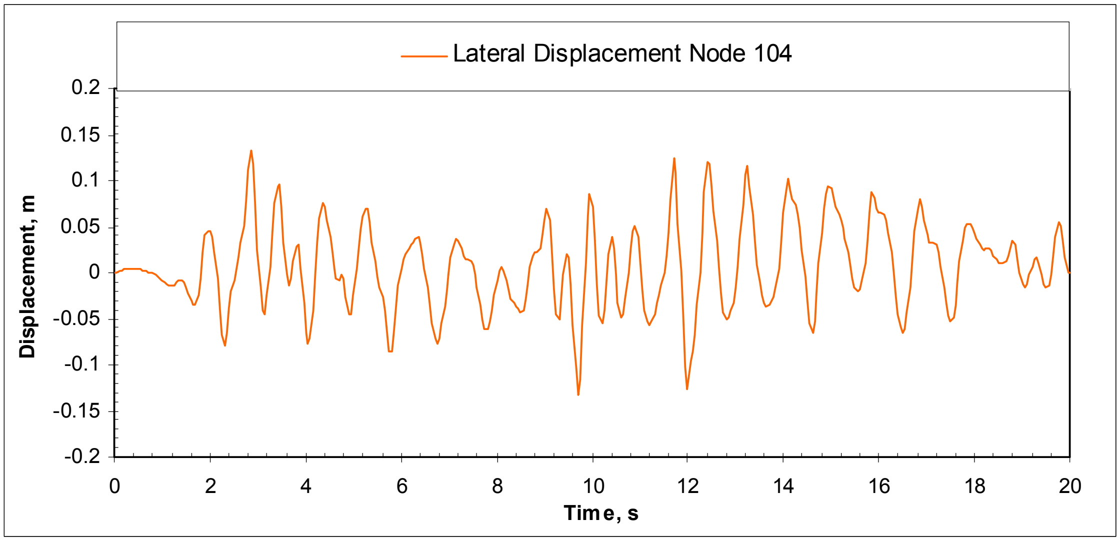

Figure D.67 - Span2, Imperial Valley 3D input, SCED k = 79.1MN/m$^{1.3}$, node 104 lateral displacement

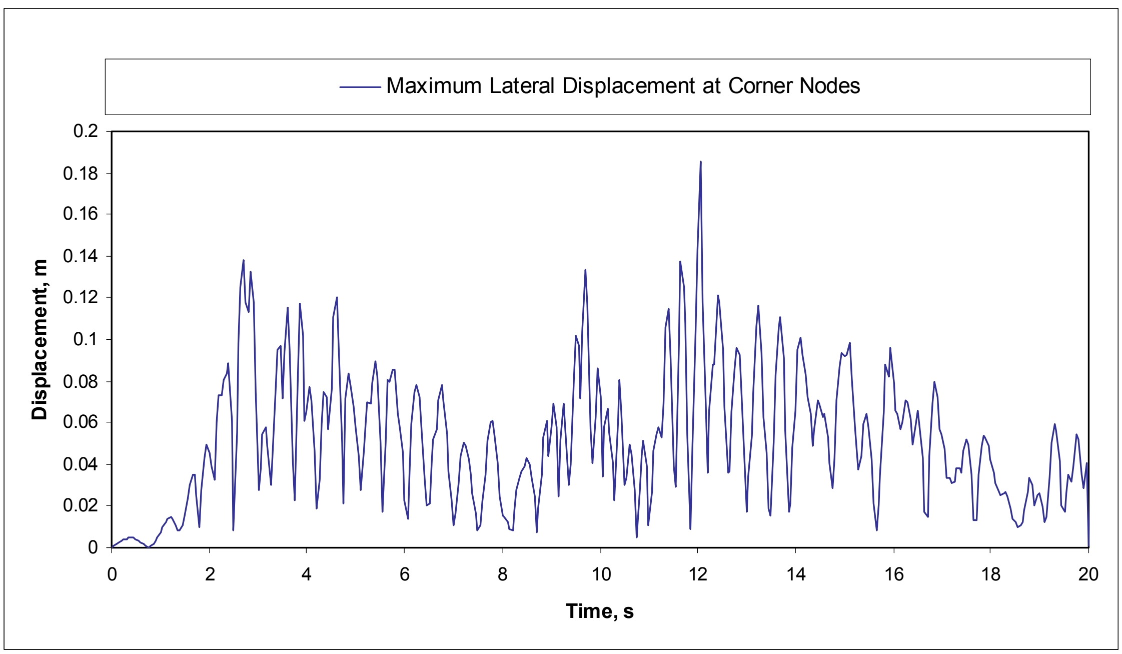

Figure D.68 - Span2, Imperial Valley 3D input, SCED k = 79.1MN/m$^{1.3}$, maximum lateral displacement

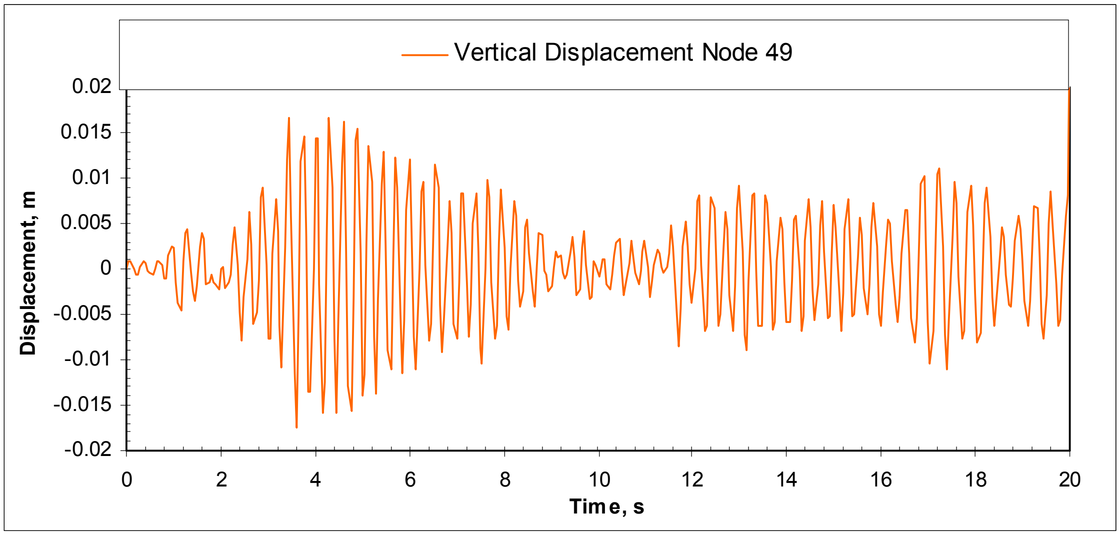

Figure D.69 - Span2, Imperial Valley 3D input, SCED k = 79.1MN/m$^{1.3}$, node 49 vertical displacement

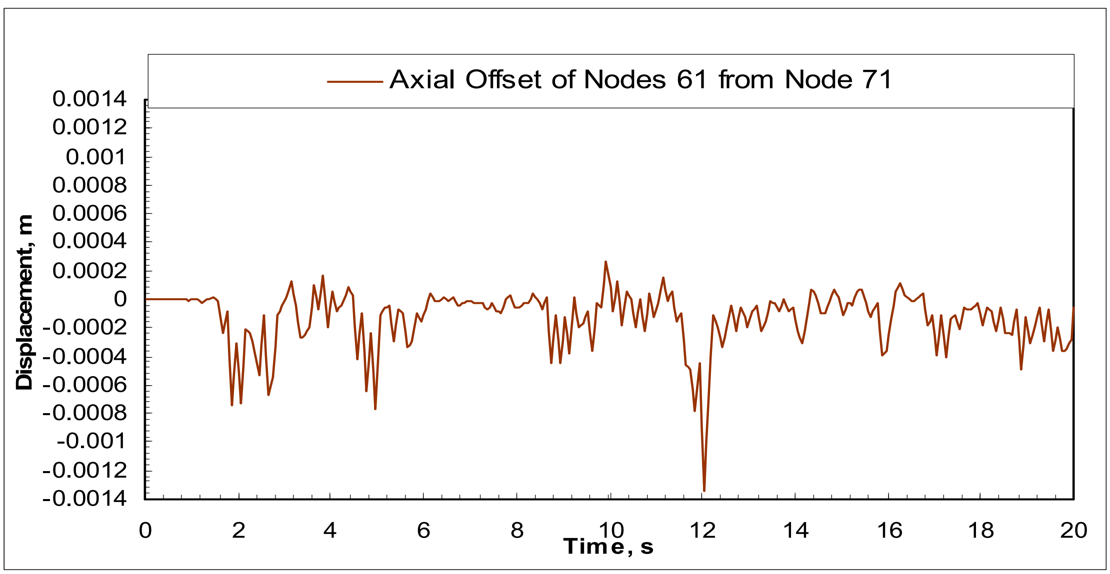

Figure D.70 - Span2, Imperial Valley 3D input, SCED k = 79.1MN/m$^{1.3}$, node 61 and 71 response

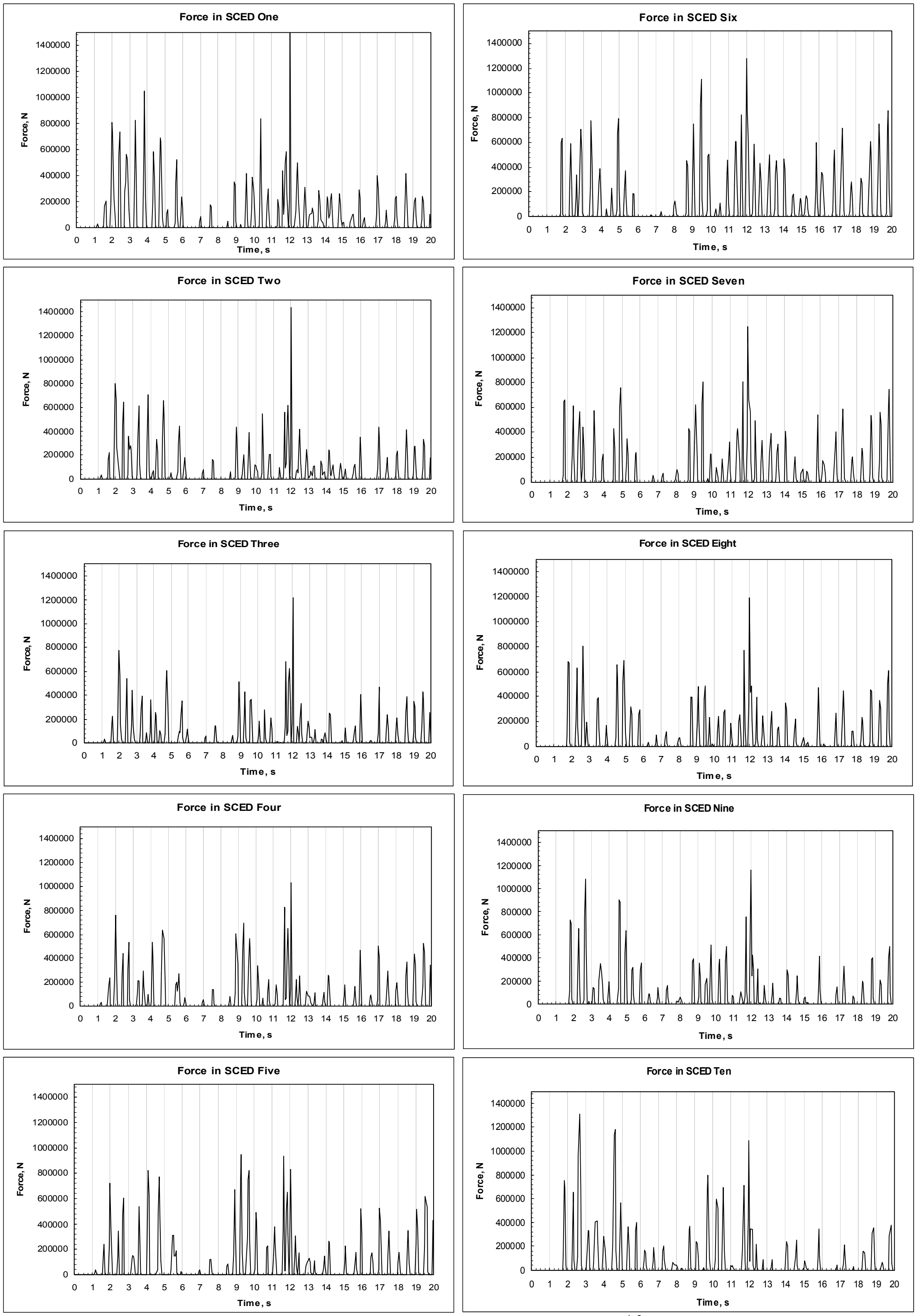

Figure D.71 - Span2, Imperial Valley 3D input, SCED k = 79.1MN/m$^{1.3}$, snap load histories

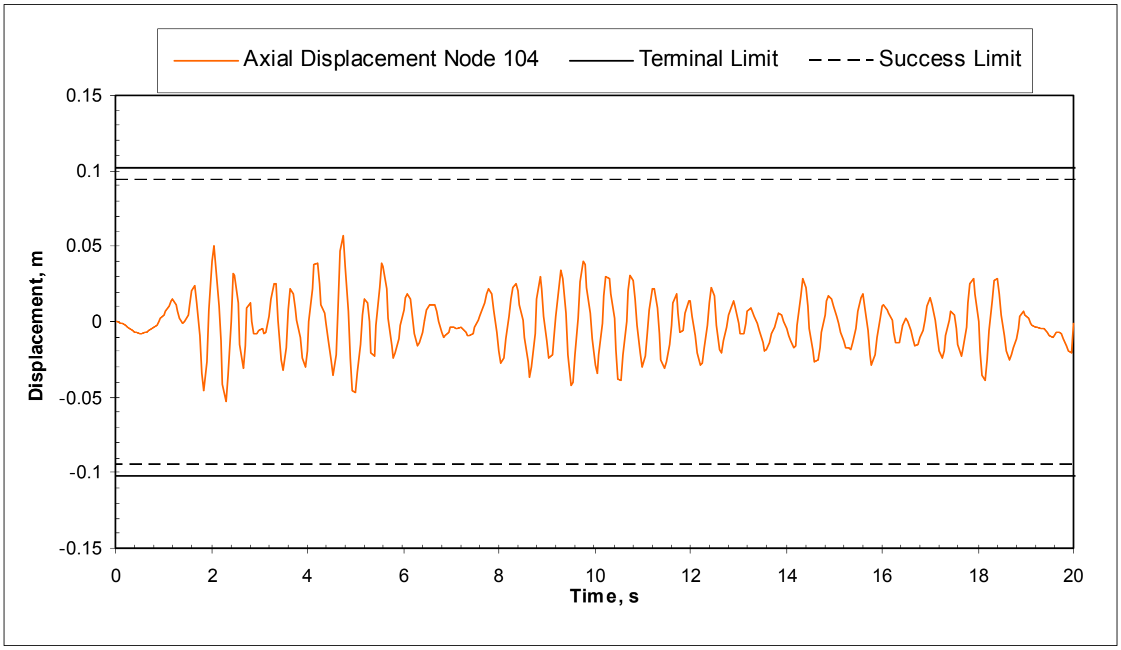

Figure D.72 - Span2, Imperial Valley 3D input, SCED k = 58.0MN/m$^{1.3}$, node 104 axial displacement

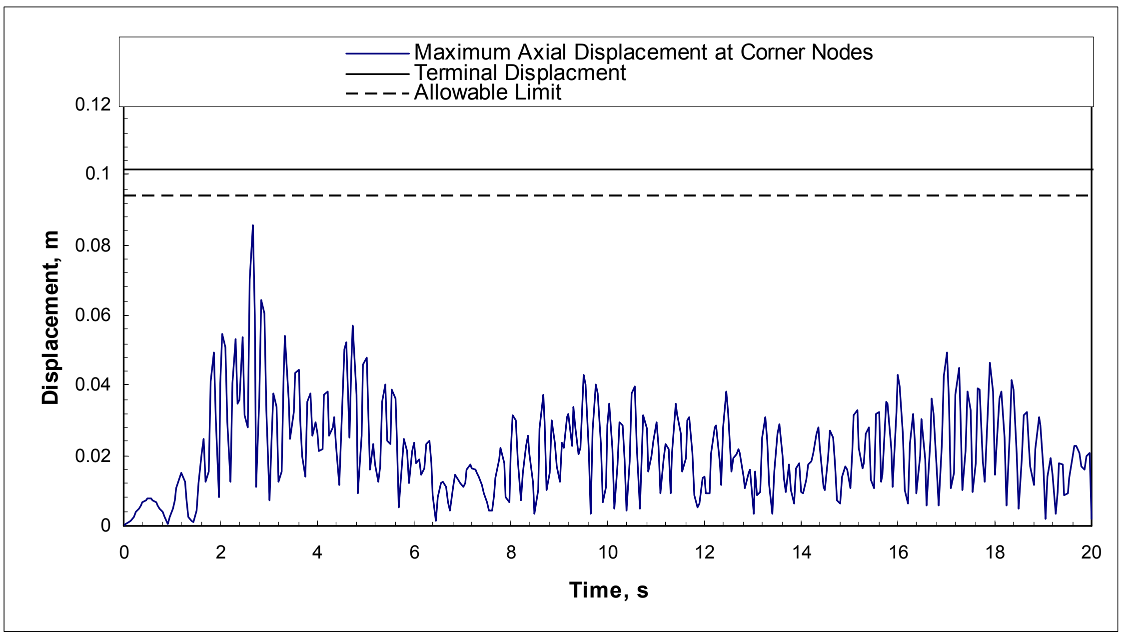

Figure D.73 - Span2, Imperial Valley 3D input, SCED k = 58.0MN/m$^{1.3}$, maximum axial displacement

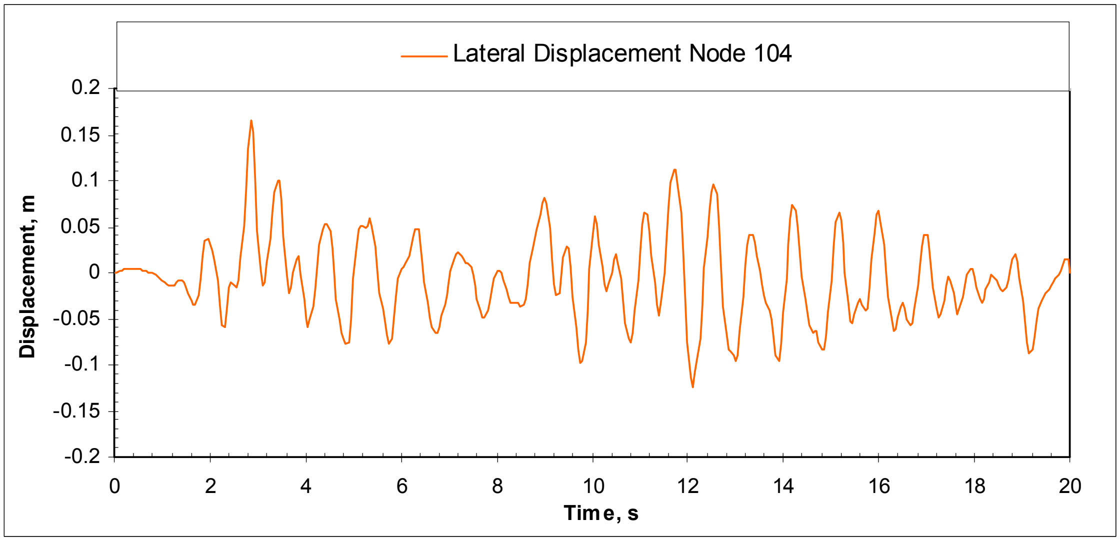

Figure D.74 - Span2, Imperial Valley 3D input, SCED k = 58.0MN/$m^{1.3}$, node 104 lateral displacement

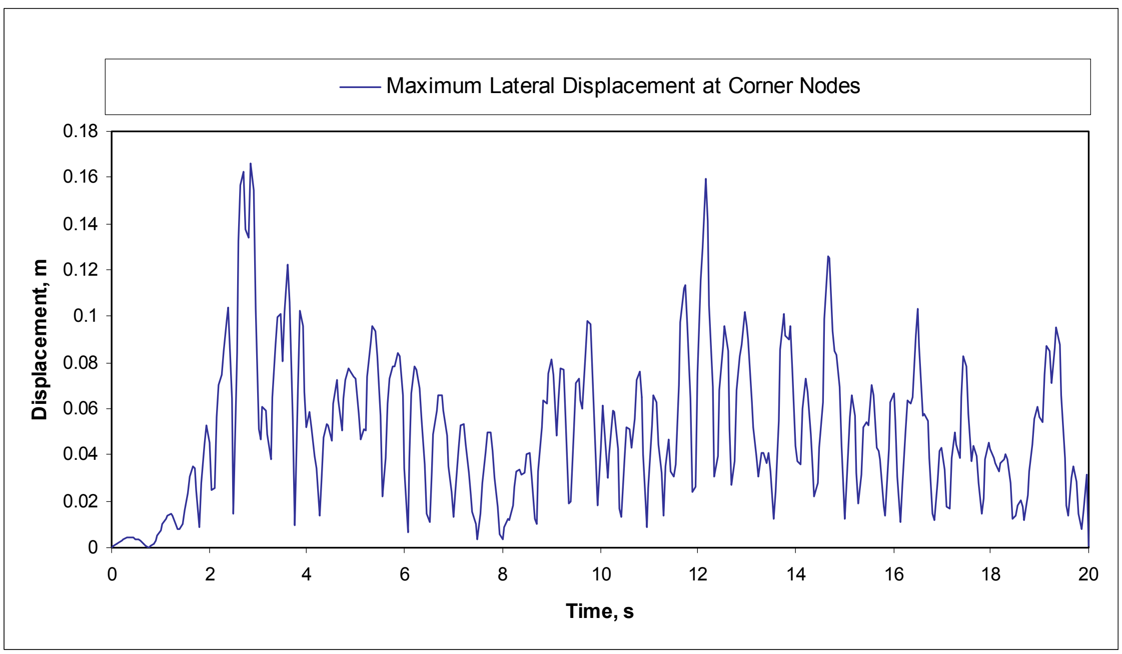

Figure D.75 - Span2, Imperial Valley 3D input, SCED k = 58.0MN/$m^{1.3}$, maximum lateral displacement

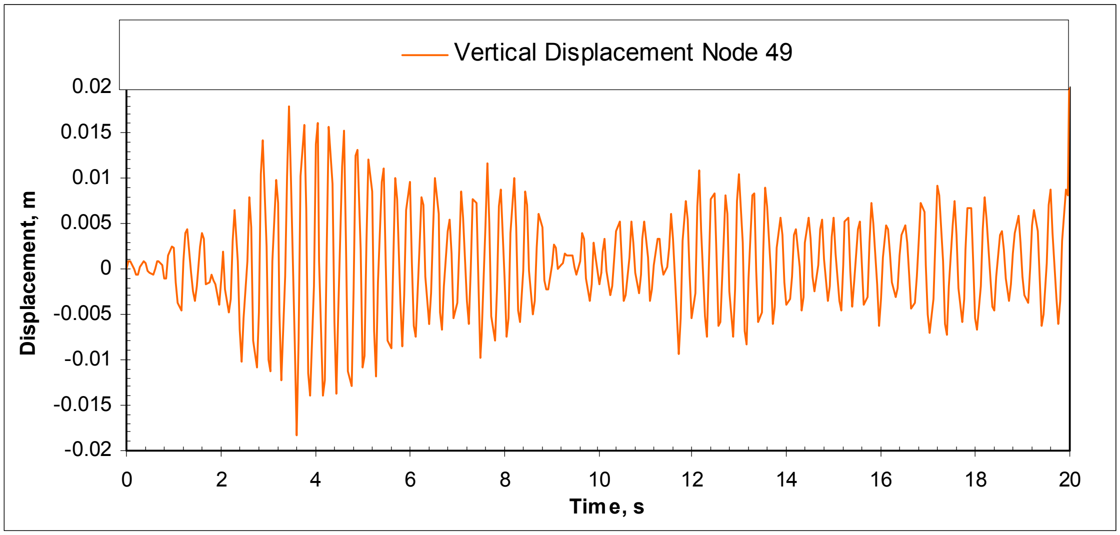

Figure D.76 - Span2, Imperial Valley 3D input, SCED k = 58.0MN/m$^{1.3}$, node 49 vertical displacement

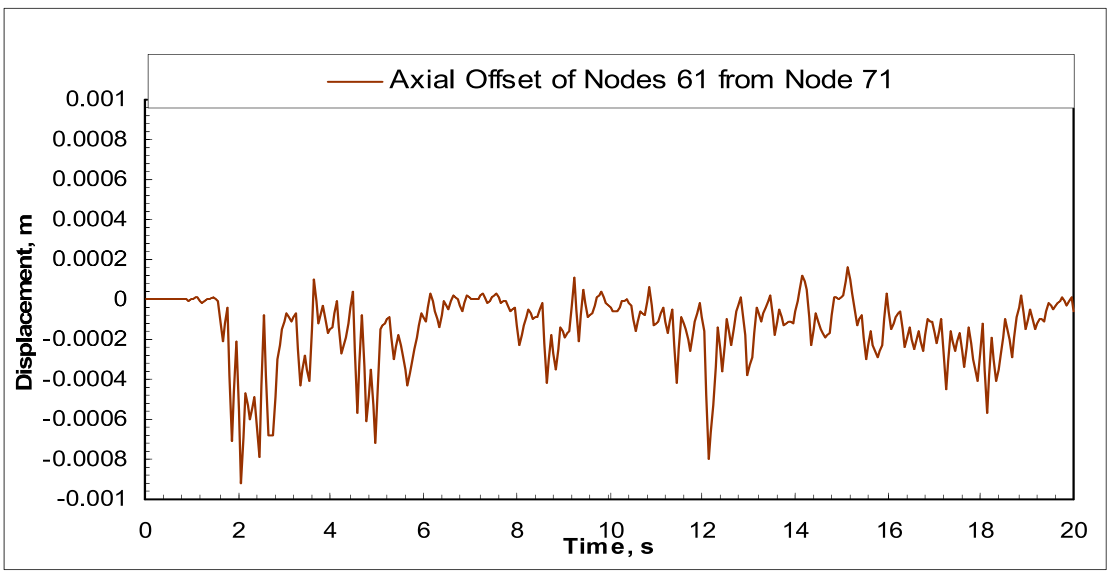

Figure D.77 - Span2, Imperial Valley 3D input, SCED k = 58.0MN/m$^{1.3}$, node 61 and 71 response

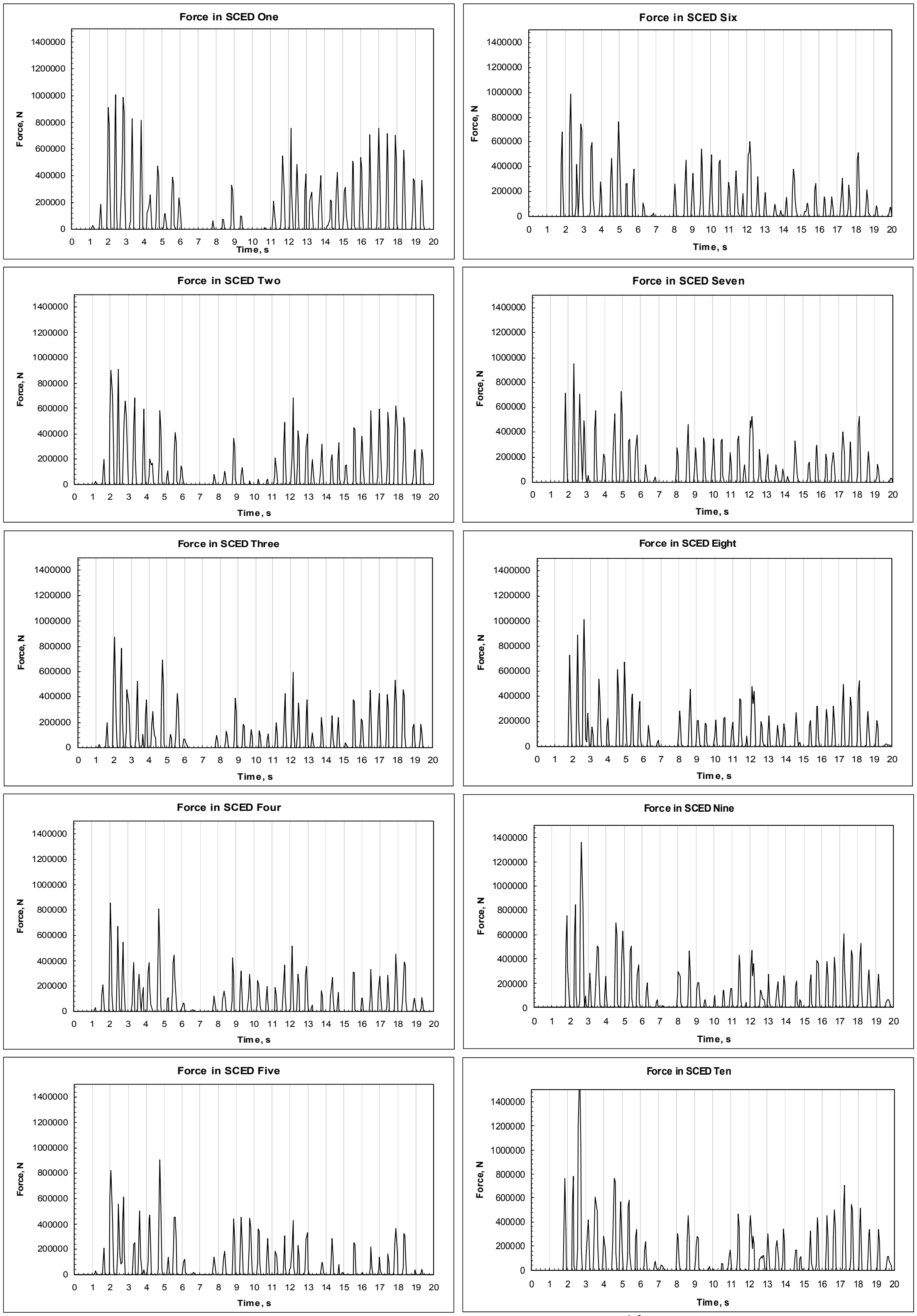

Figure D.78 - Span2, Imperial Valley 3D input, SCED k = 58.0MN/m$^{1.3}$, snap load histories

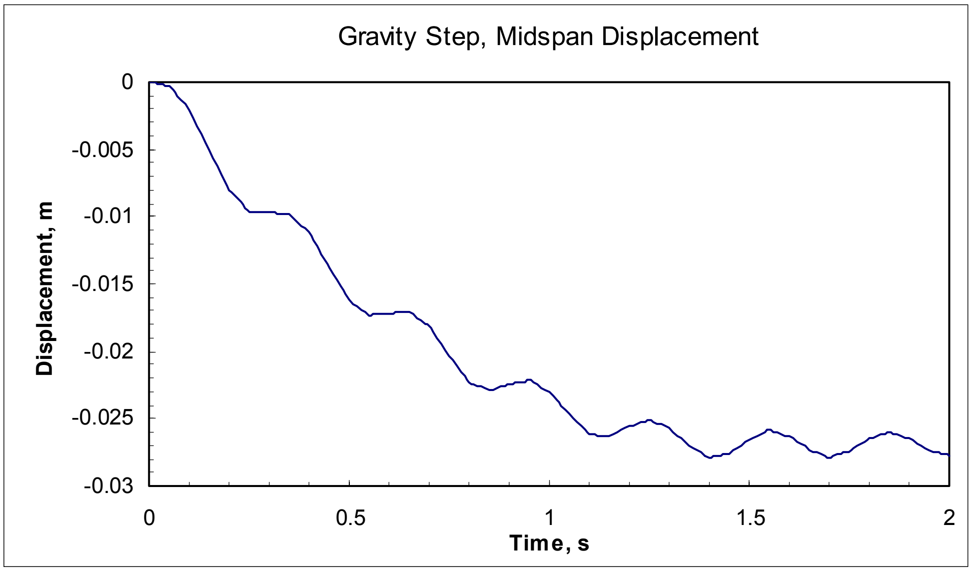

Figure D.79 - Span2, Northridge input, gravity step response

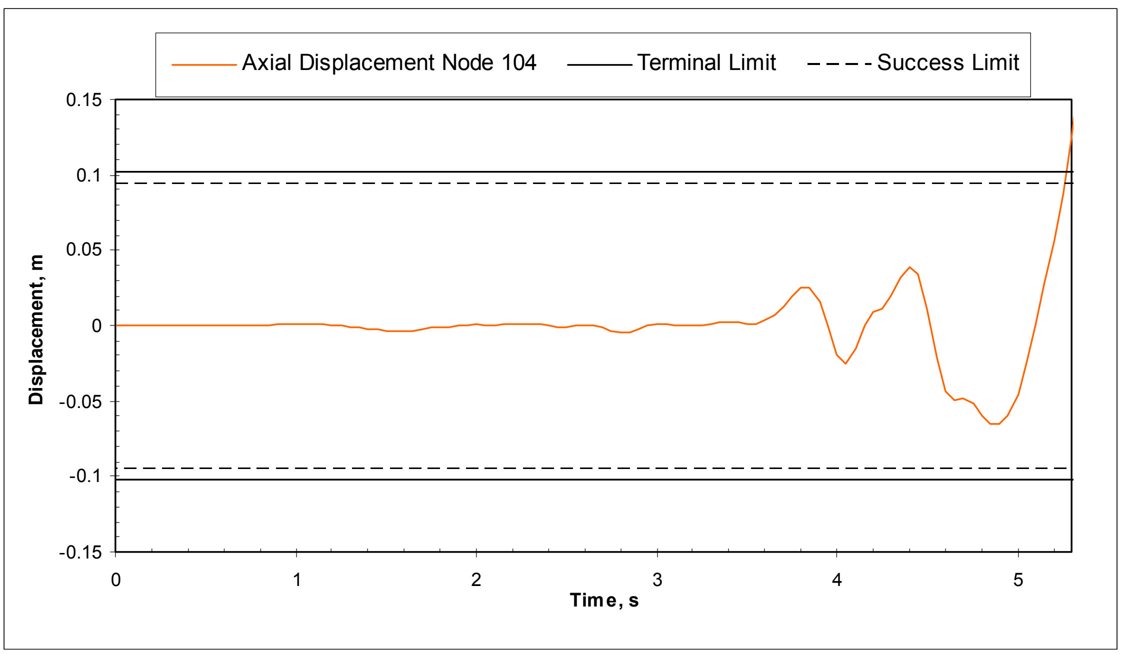

Figure D.80 - Span2, Northridge axial input only, node 104 axial displacement

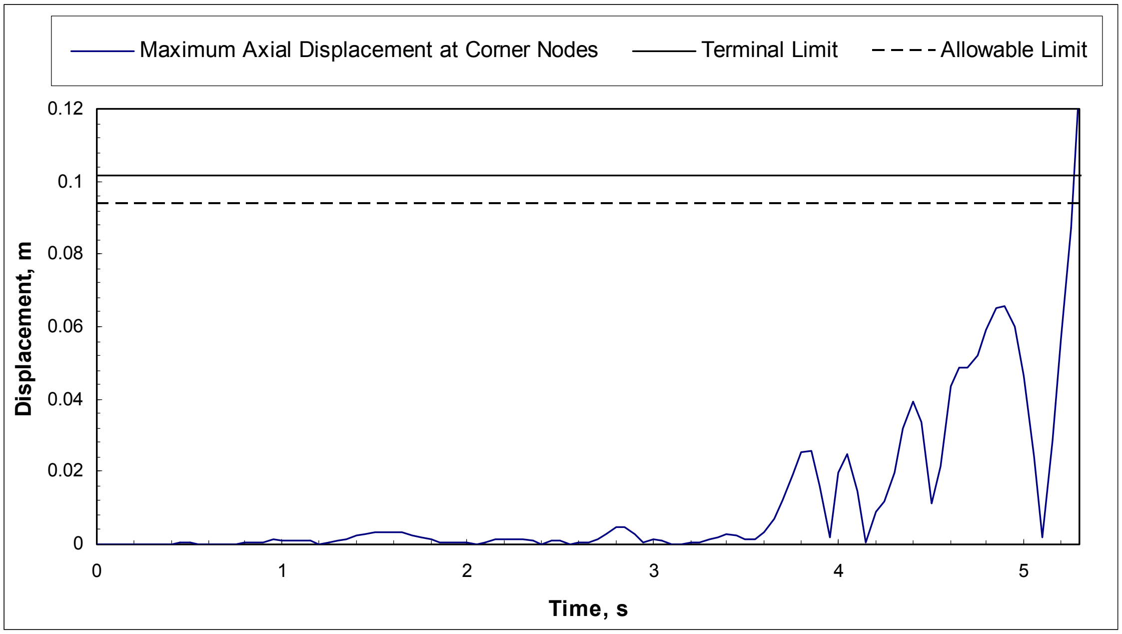

Figure D.81 - Span2, Northridge axial input only, maximum axial displacement

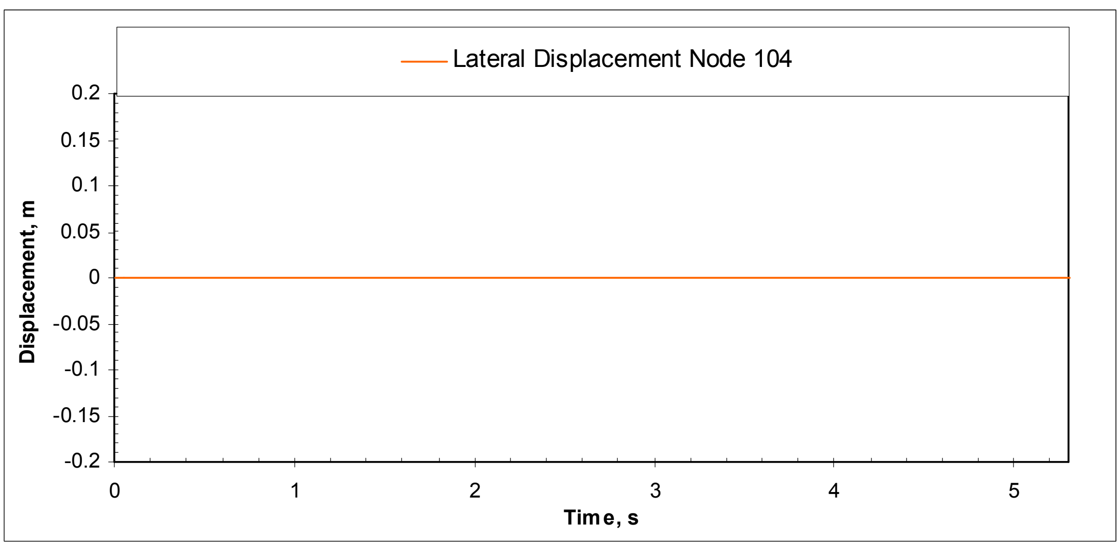

Figure D.82 - Span2, Northridge axial input only, node 104 lateral displacement

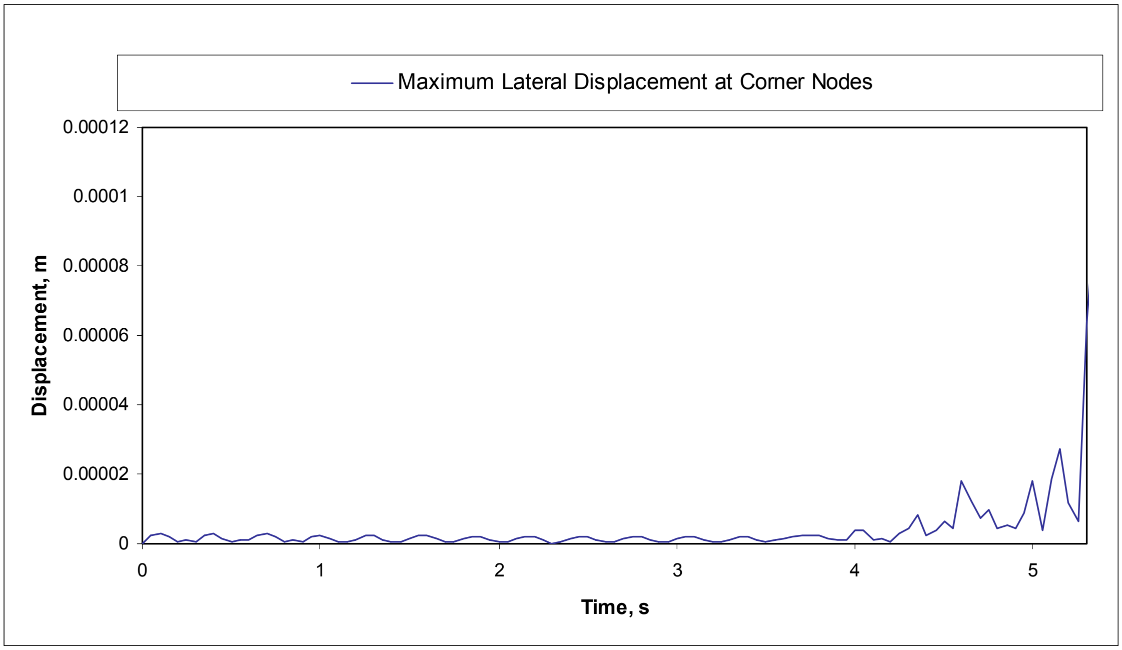

Figure D.83 - Span2, Northridge axial input only, maximum lateral displacement

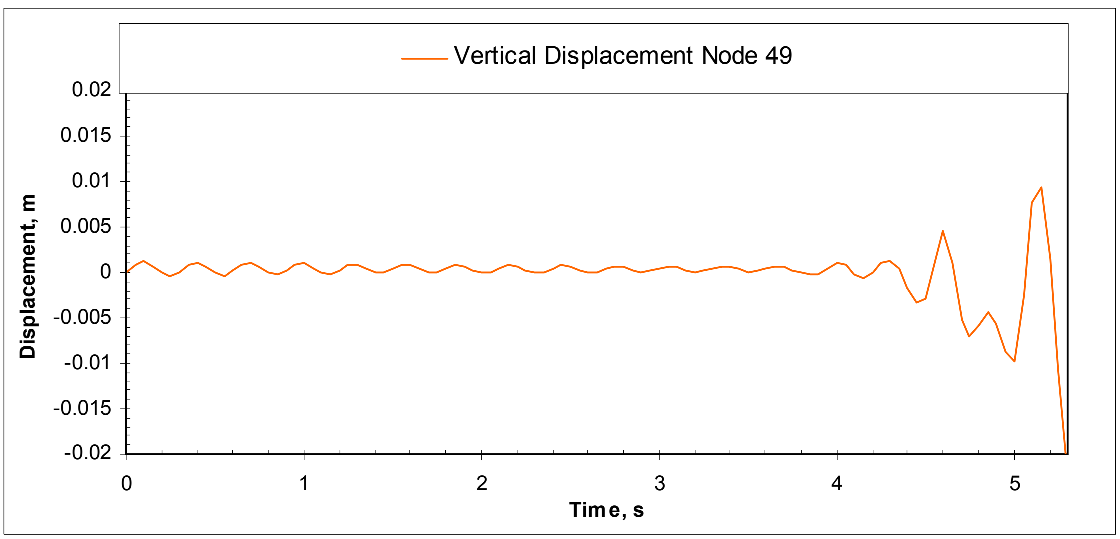

Figure D.84 - Span2, Northridge axial input only, node 49 vertical displacement

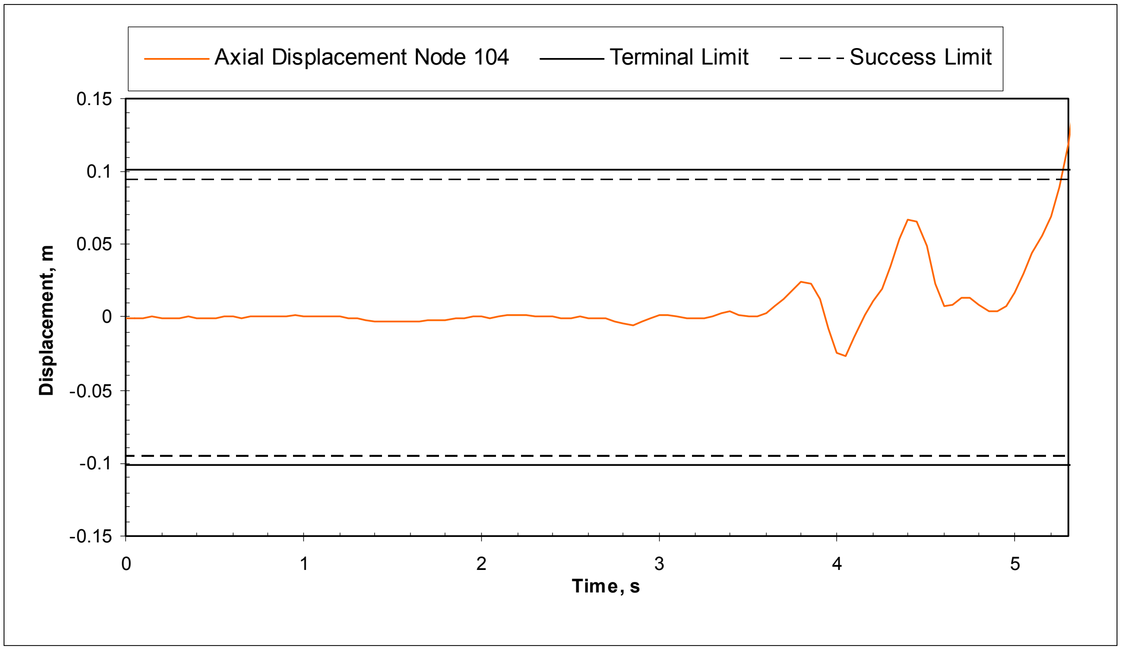

Figure D.85 - Span2, Northridge 3D input, no SCEDs, node 104 axial displacement

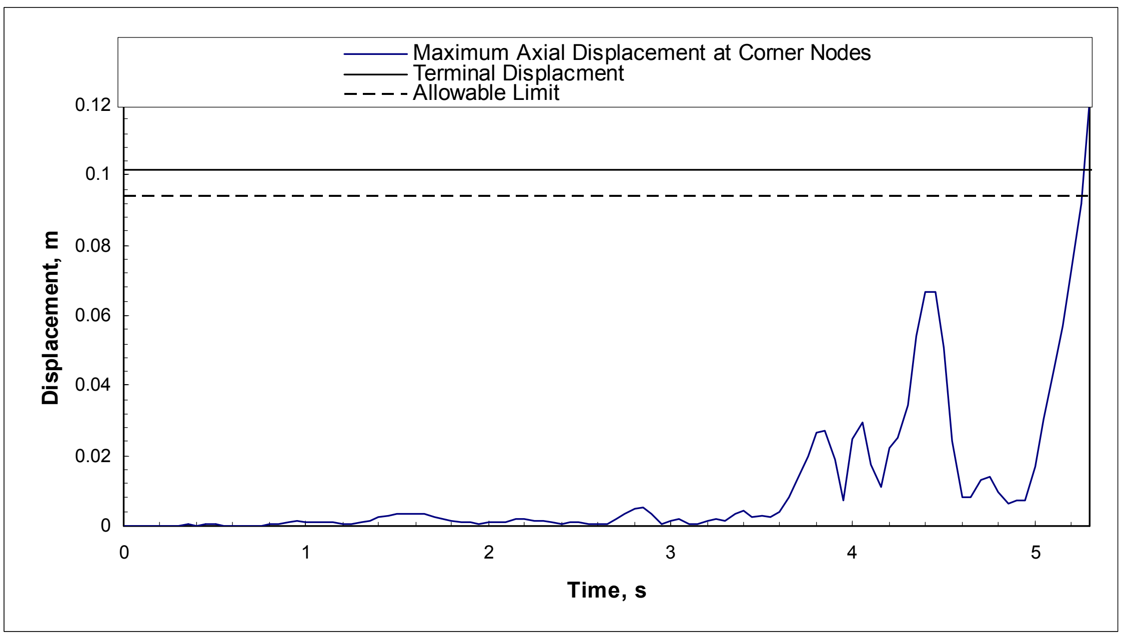

Figure D.86 - Span2, Northridge 3D input, no SCEDs, maximum axial displacement

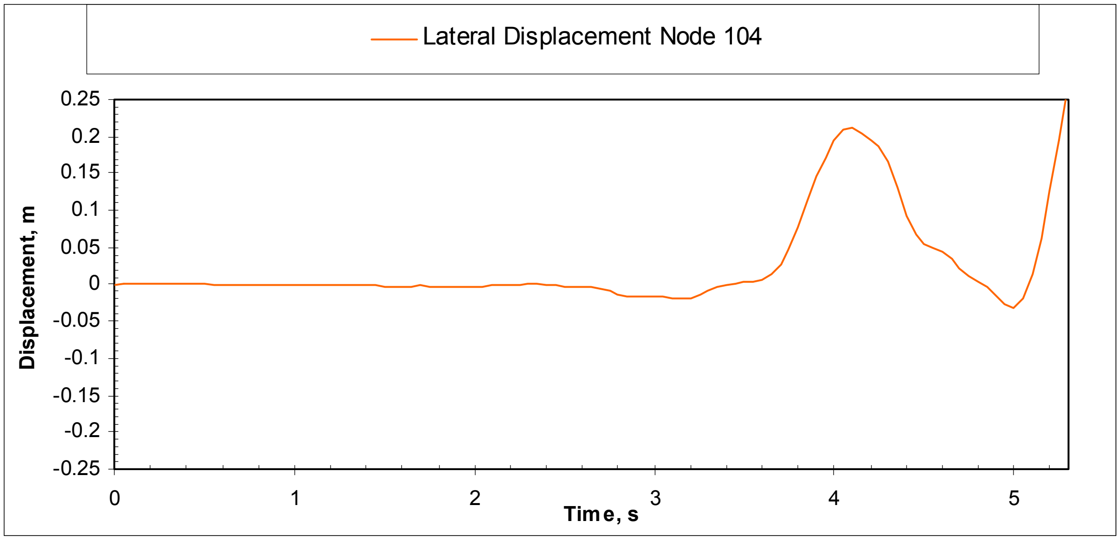

Figure D.87 - Span2, Northridge 3D input, no SCEDs, node 104 lateral displacement

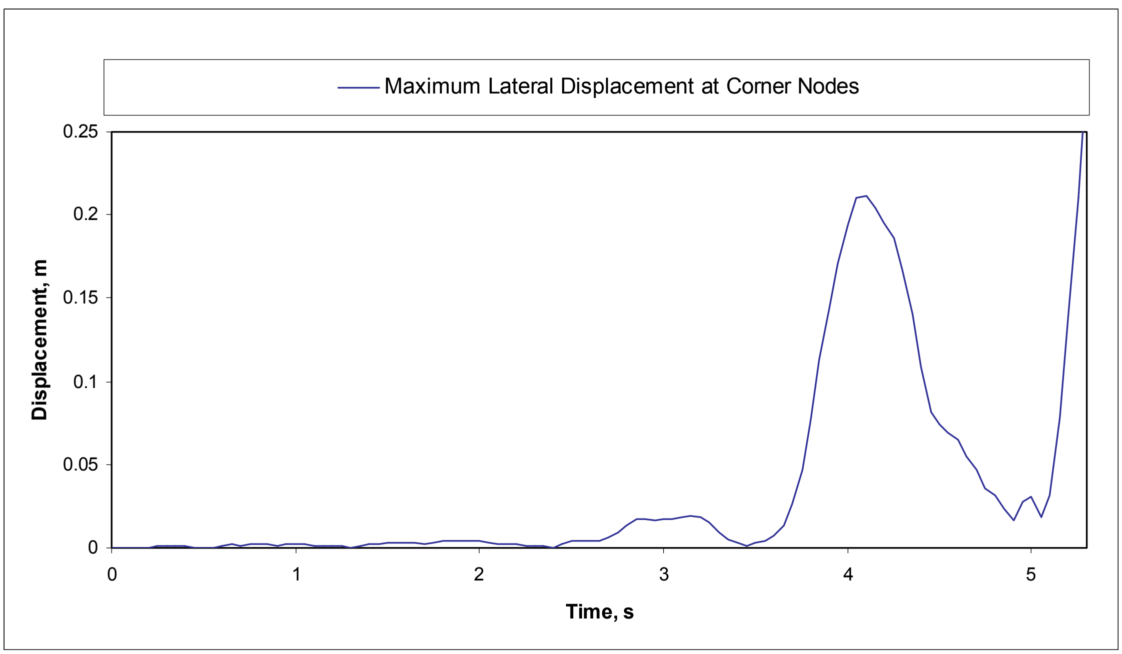

Figure D.88 - Span2, Northridge 3D input, no SCEDs, maximum lateral displacement

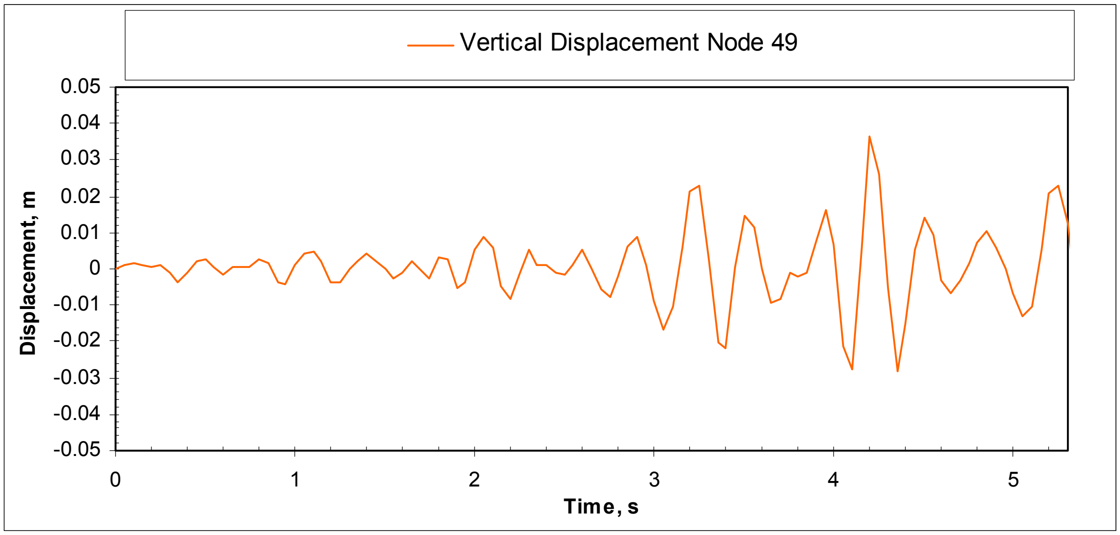

Figure D.89 - Span2, Northridge 3D input, no SCEDs, node 49 vertical displacement

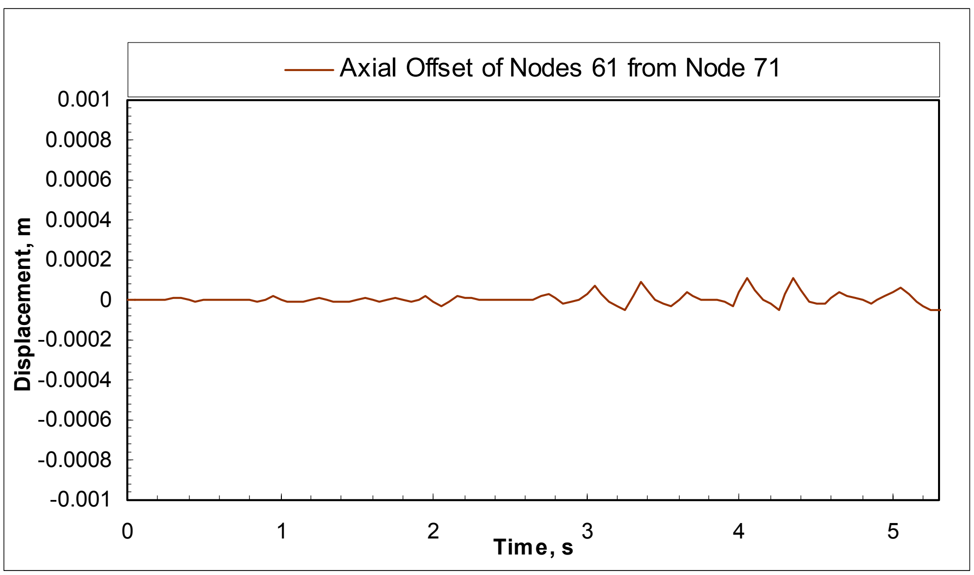

Figure D.90 - Span2, Northridge 3D input, no SCEDs, node 61 and 71 response

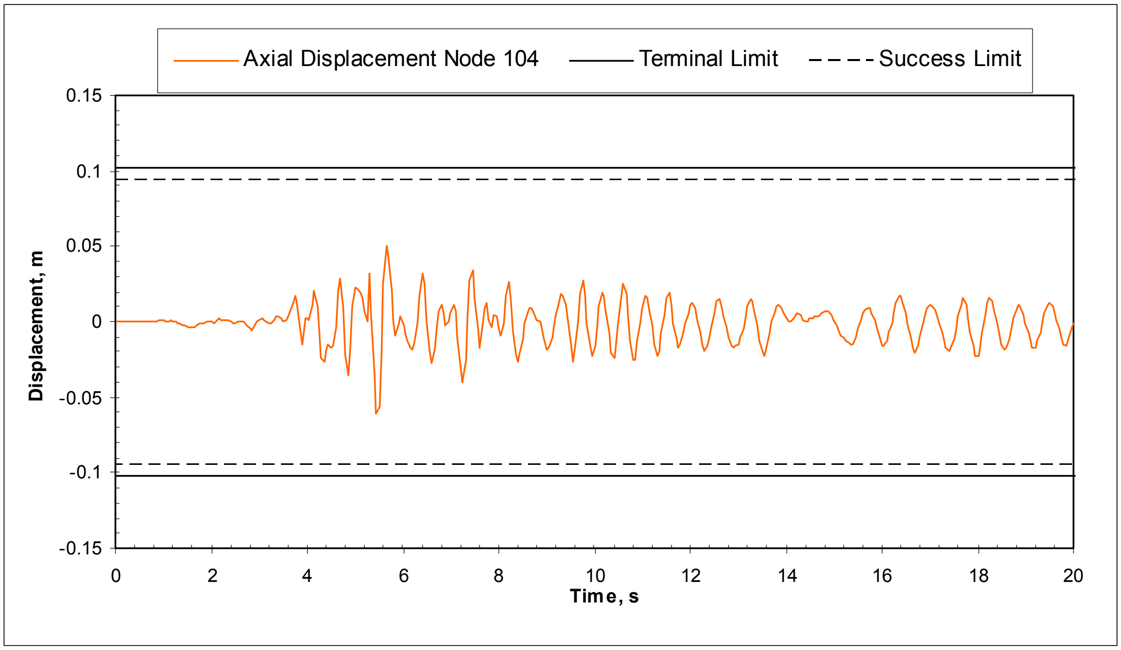

Figure D.91 - Span2, Northridge 3D input, SCED k = 79.1MN/m$^{1.3}$, node 104 axial displacement

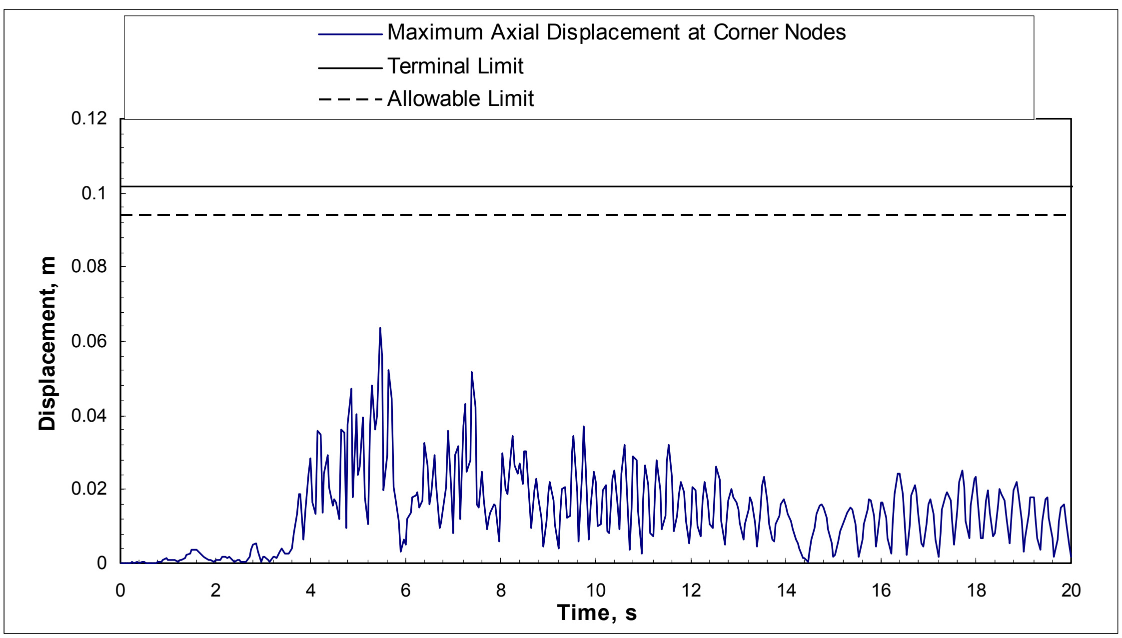

Figure D.92 - Span2, Northridge 3D input, SCED k = 79.1MN/m$^{1.3}$, maximum axial displacement

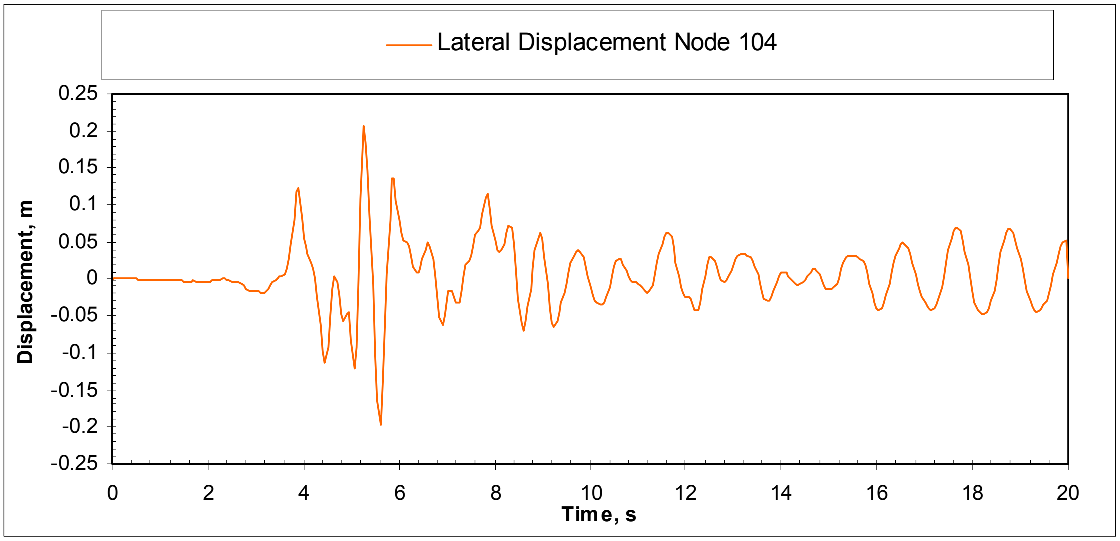

Figure D.93 - Span2, Northridge 3D input, SCED k = 79.1MN/m$^{1.3}$, node 104 lateral displacement

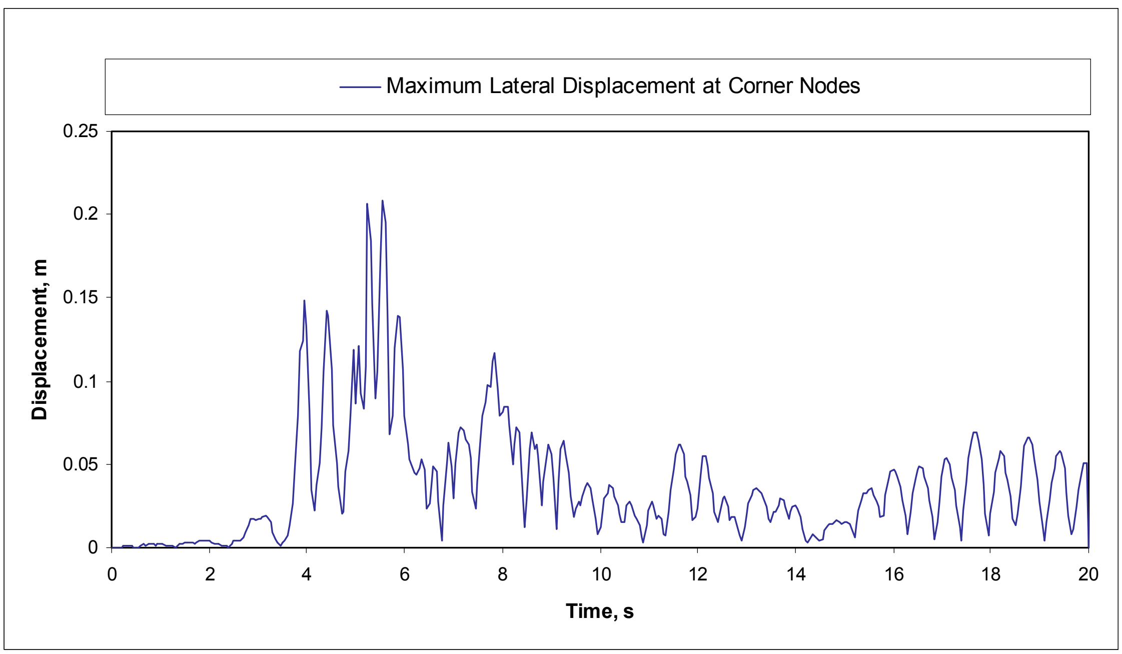

Figure D.94 - Span2, Northridge 3Dl input, SCED k = 79.1MN/m$^{1.3}$, maximum lateral displacement

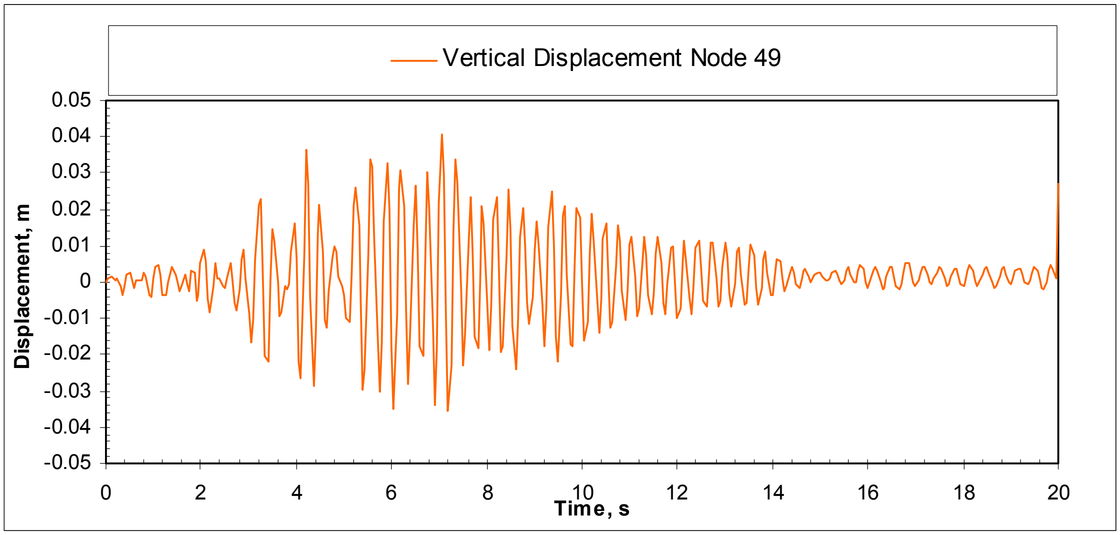

Figure D.95 - Span2, Northridge 3D input, SCED k = 79.1MN/m$^{1.3}$, node 49 vertical displacement

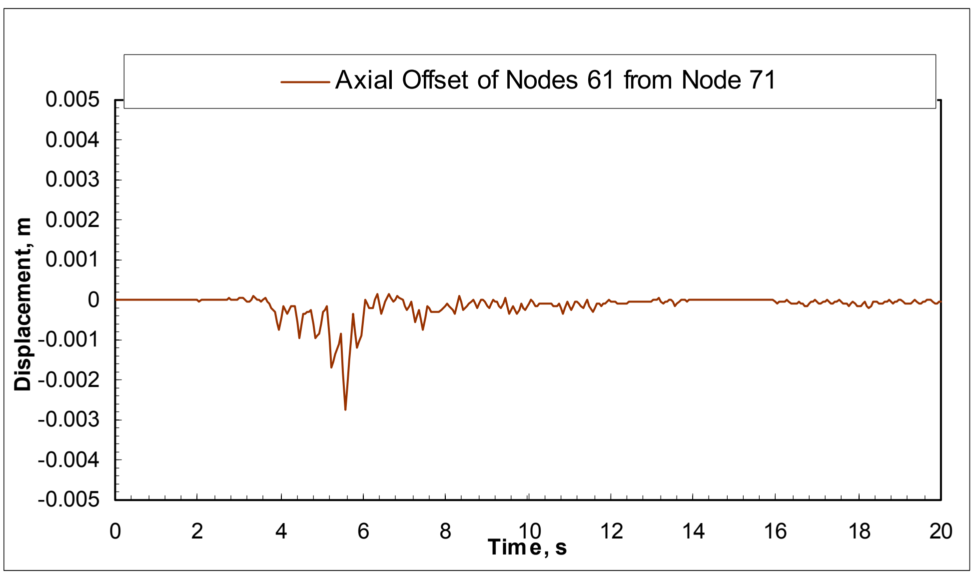

Figure D.96 - Span2, Northridge 3D input, SCED k = 79.1MN/m$^{1.3}$, node 61 and 71 response

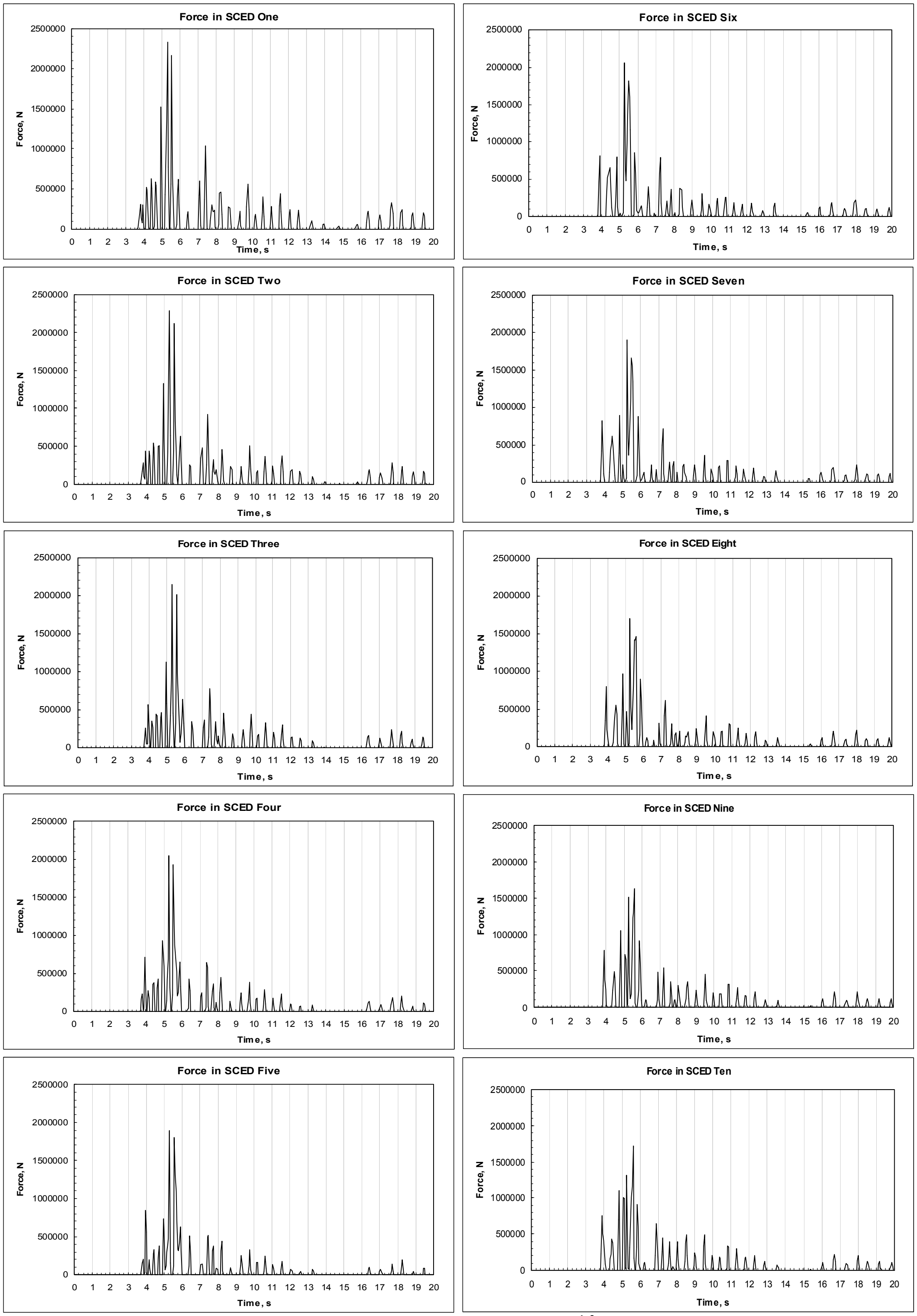

Figure D.97 - Span2, Northridge 3d input, SCED k = 79.1MN/m$^{1.3}$, snap load histories

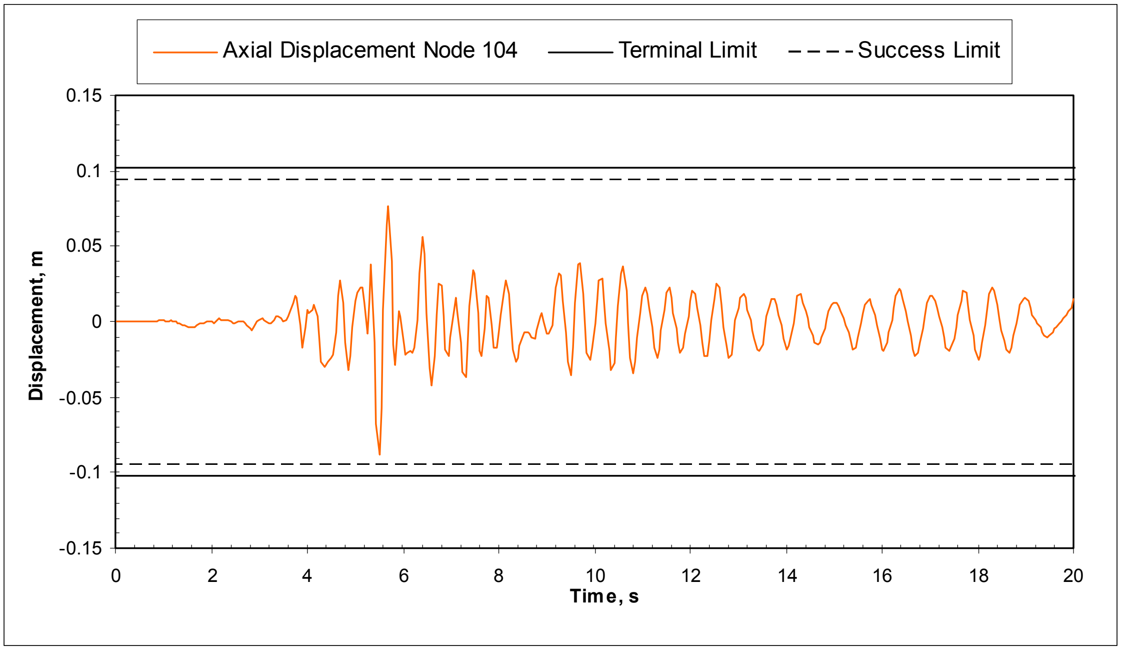

Figure D.98 - Span2, Northridge 3D input, SCED k = 63.3MN/m$^{1.3}$, node 104 axial displacement

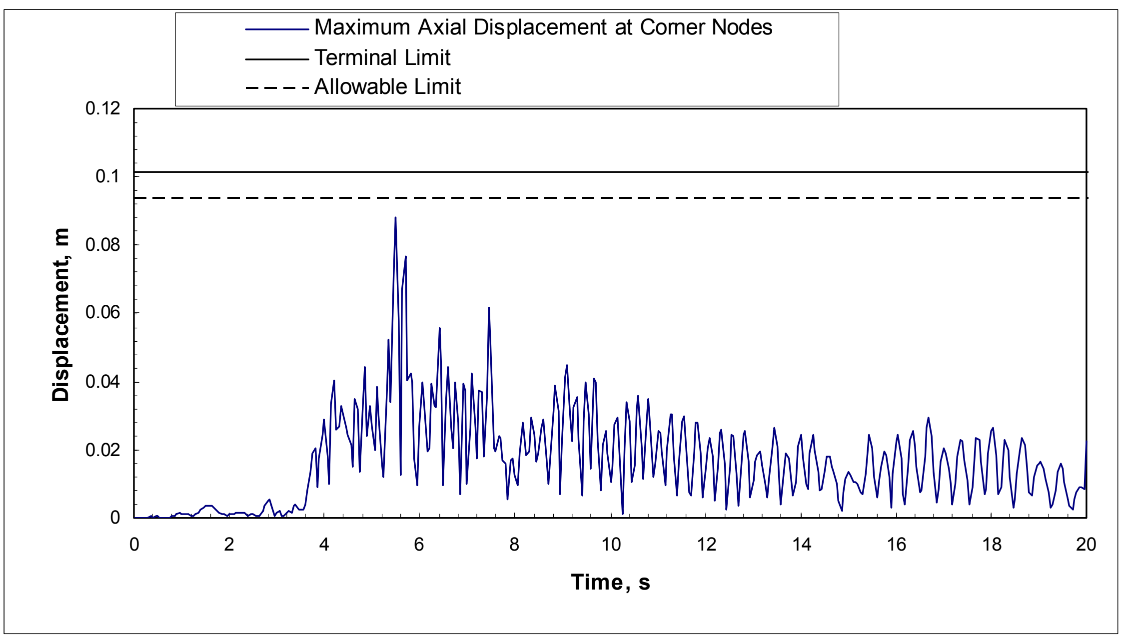

Figure D.99 - Span2, Northridge 3D input, SCED k = 63.3MN/m$^{1.3}$, maximum axial displacement

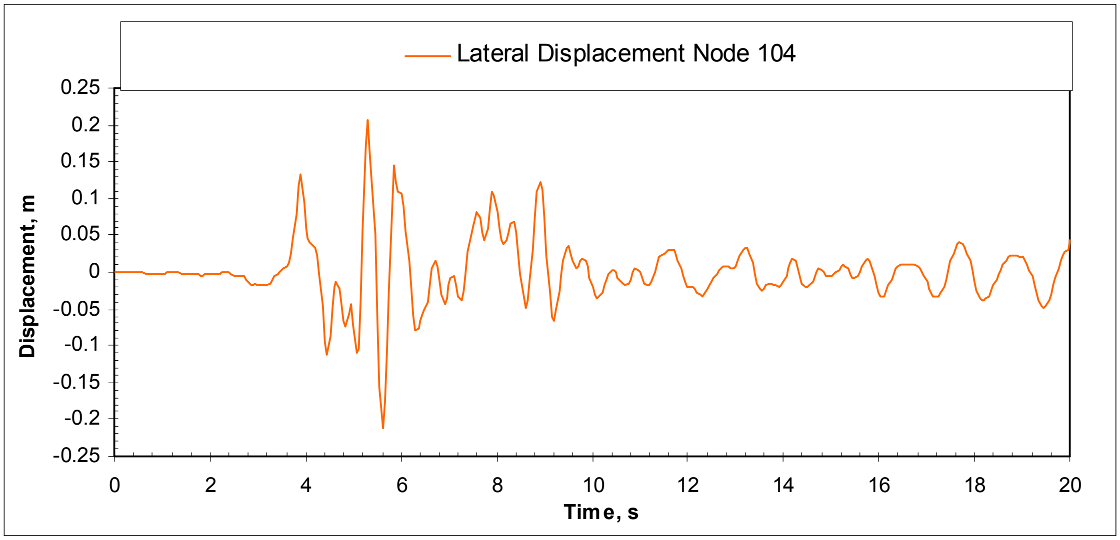

Figure D.100 - Span2, Northridge 3D input, SCED k = 63.3MN/m$^{1.3}$, node 104 lateral displacement

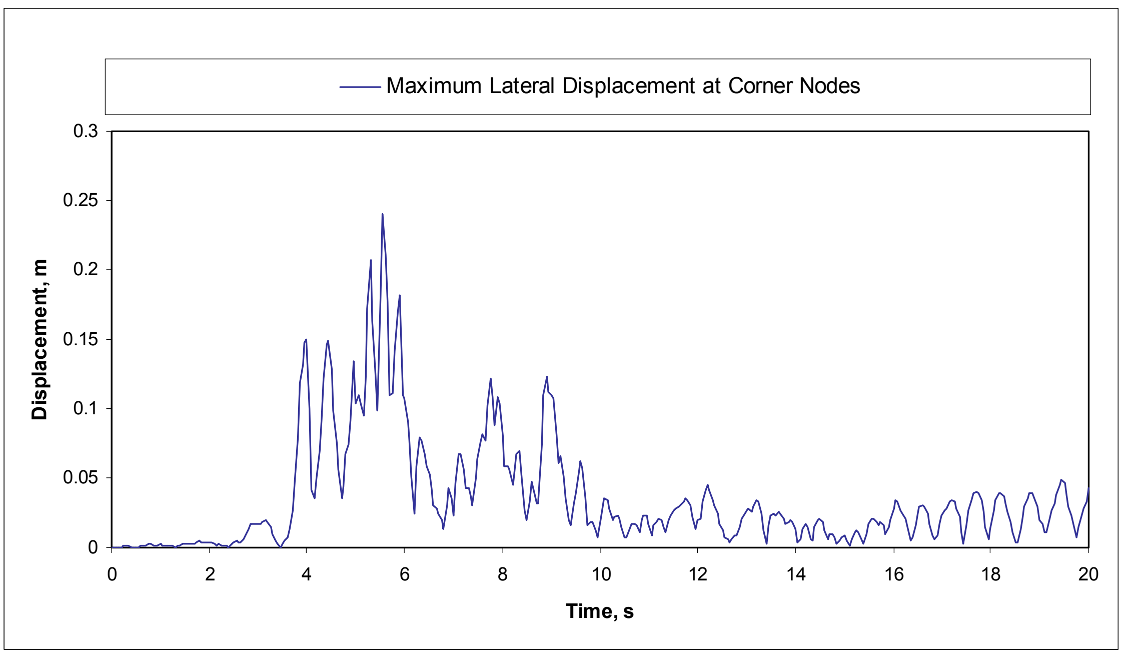

Figure D.101 - Span2, Northridge 3D input, SCED k = 63.3MN/m$^{1.3}$, maximum lateral displacement

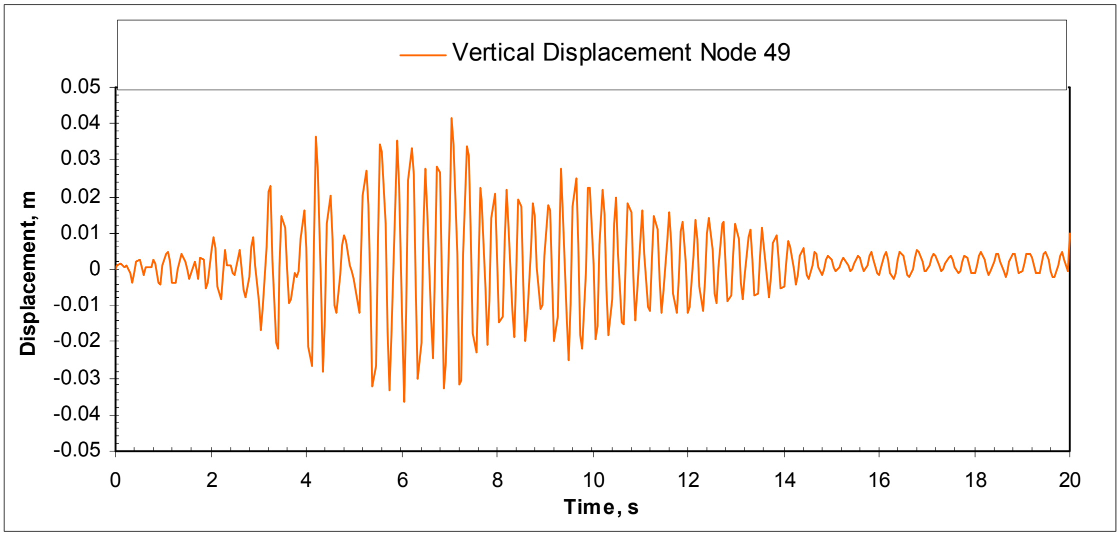

Figure D.102 - Span2, Northridge 3D input, SCED k = 63.3MN/m$^{1.3}$, node 49 vertical displacement

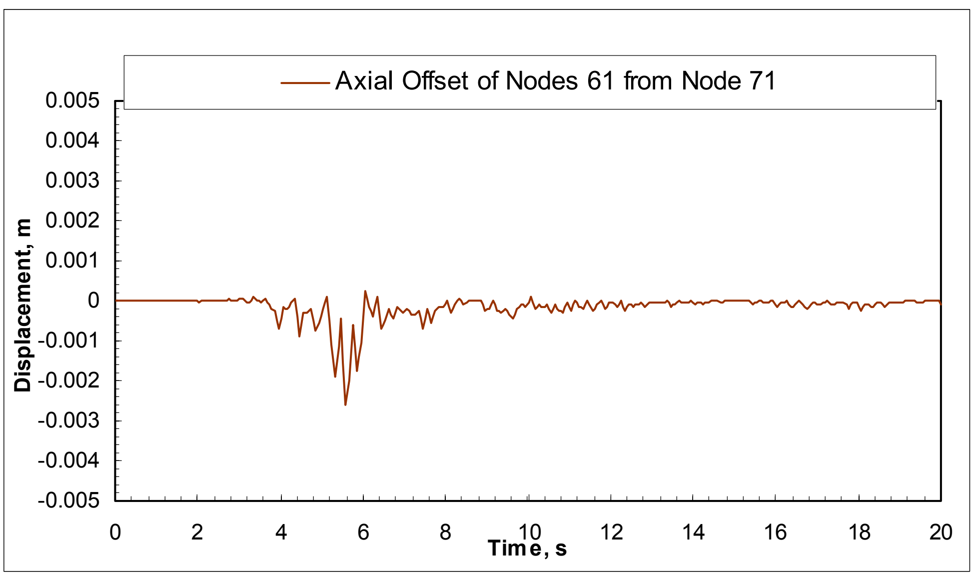

Figure D.103 - Span2, Northridge 3D input, SCED k = 63.3MN/m$^{1.3}$, node 61 and 71 response

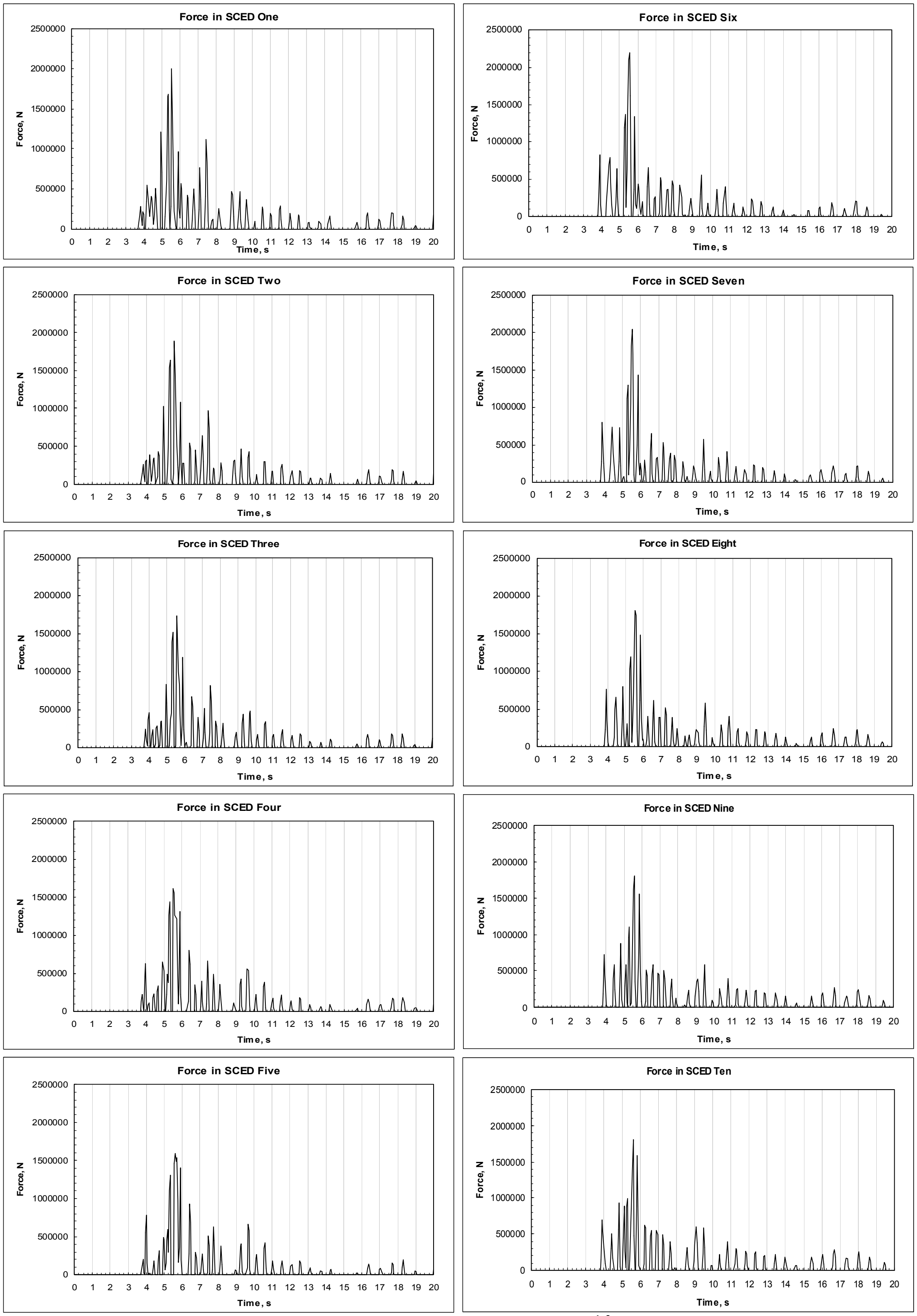

Figure D.104 - Span2, Northridge 3D input, SCED k = 63.3MN/m$^{1.3}$, snap load histories

D.3 Span3 Figures

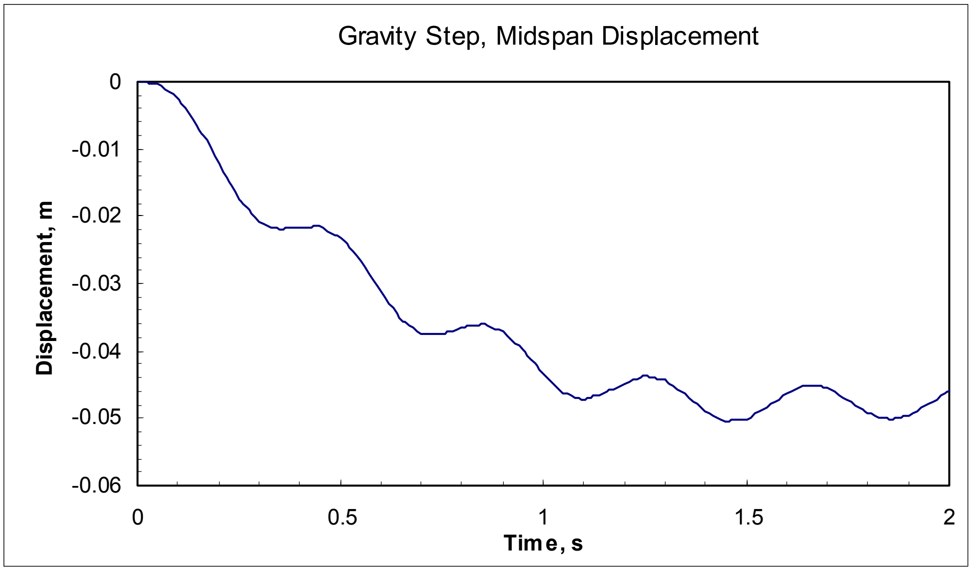

Figure D.105 - Span3, Imperial Valley input, gravity step response

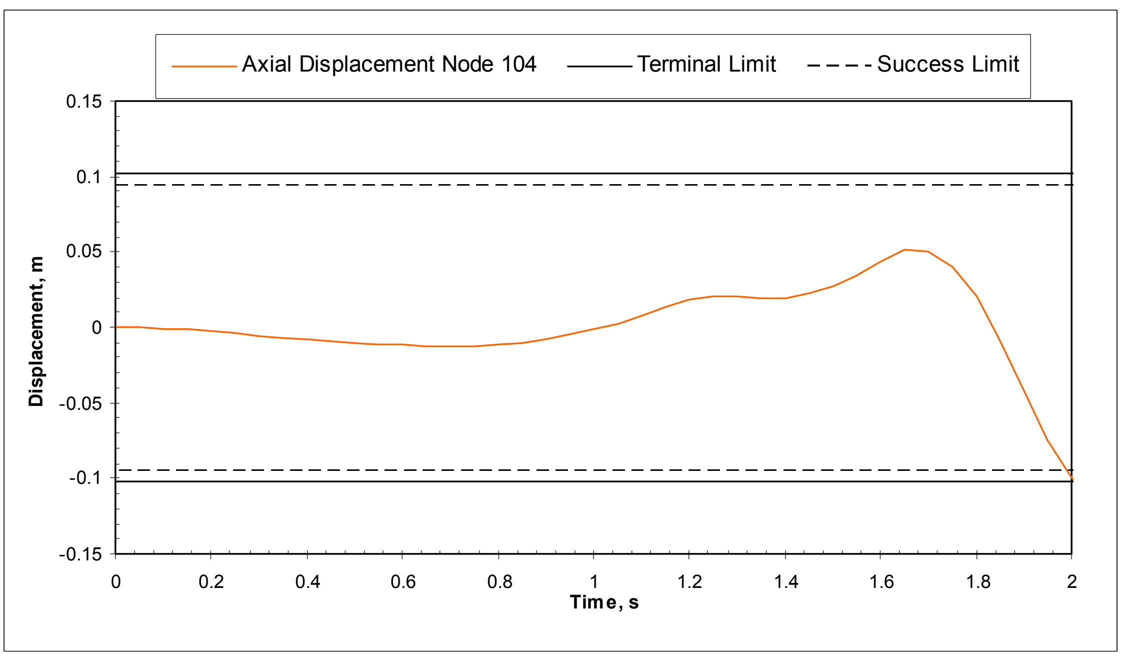

Figure D.106 - Span3, Imperial Valley axial input only, node 104 axial displacement

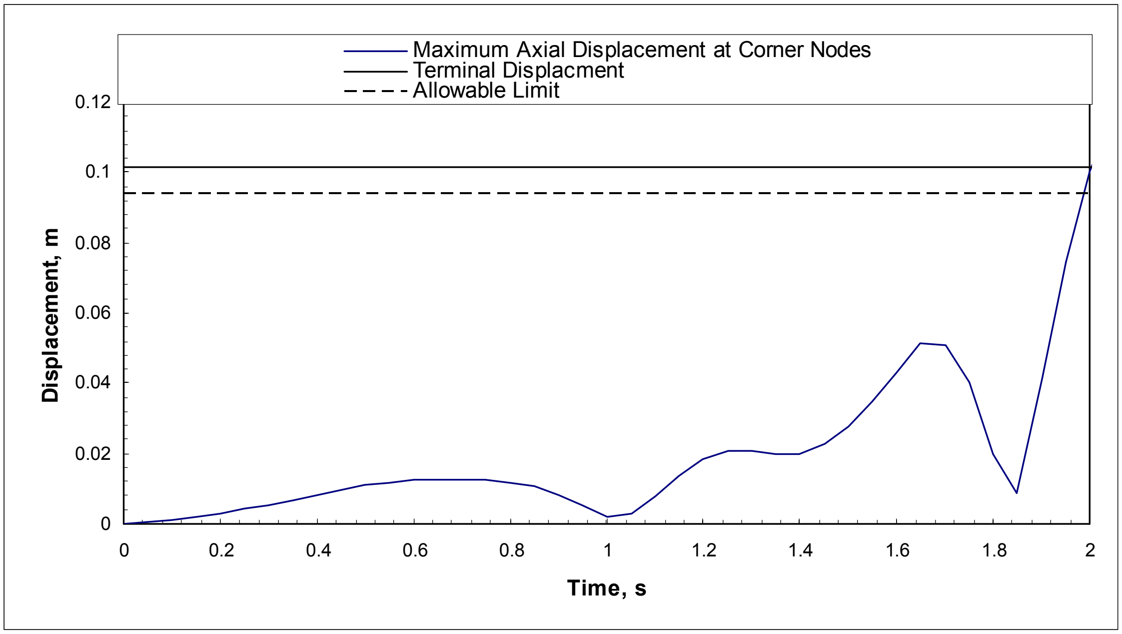

Figure D.107 - Span3, Imperial Valley axial input only, maximum axial displacement

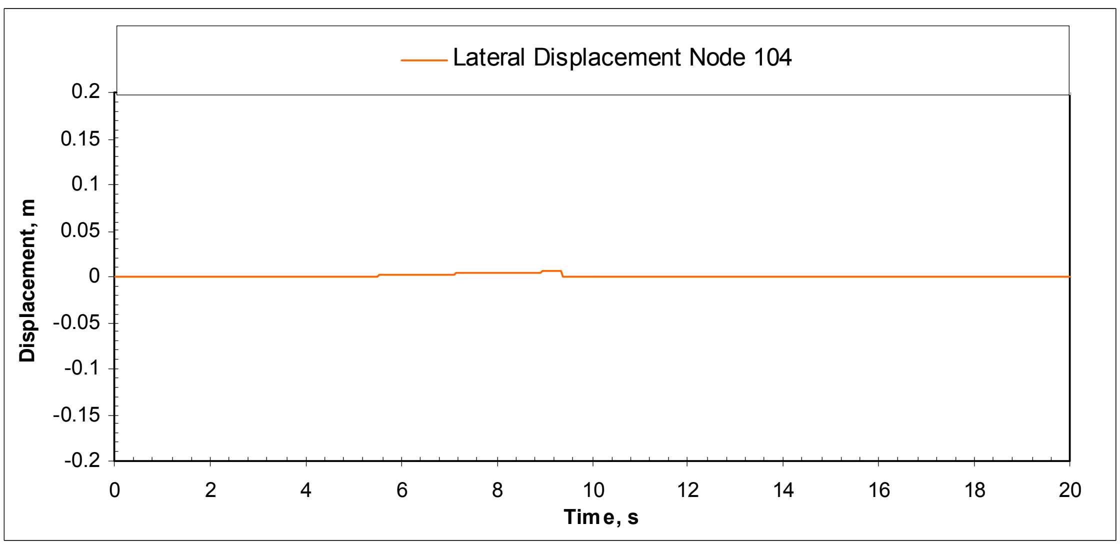

Figure D.108 - Span3, Imperial Valley axial input only, node 104 lateral displacement

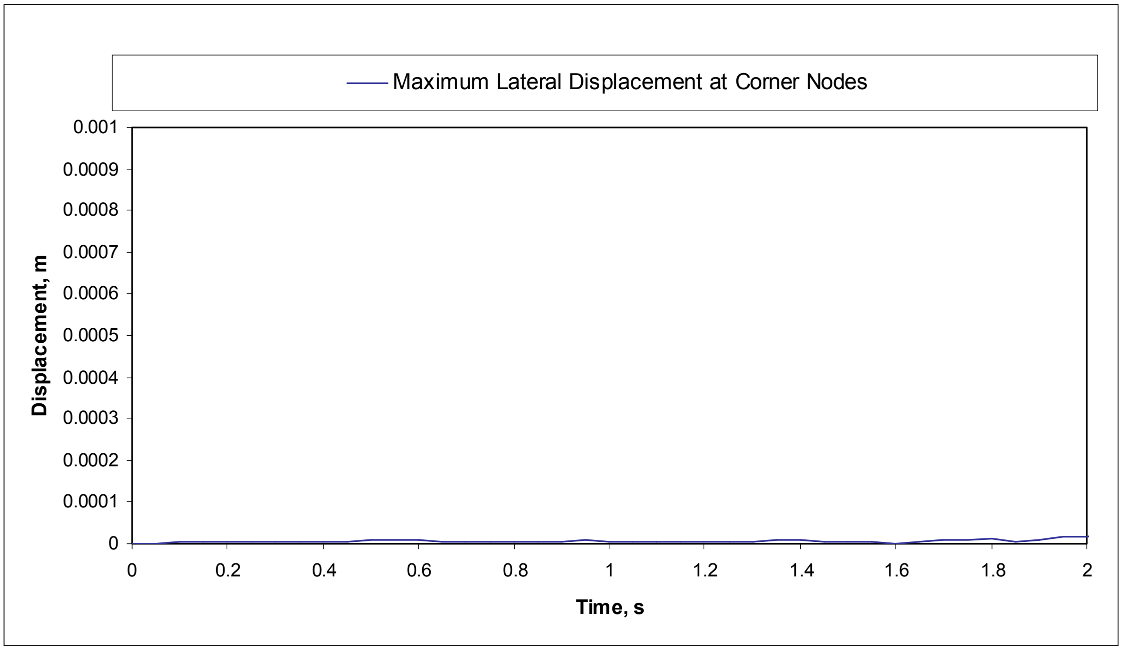

Figure D.109 - Span3, Imperial Valley axial input only, maximum lateral displacement

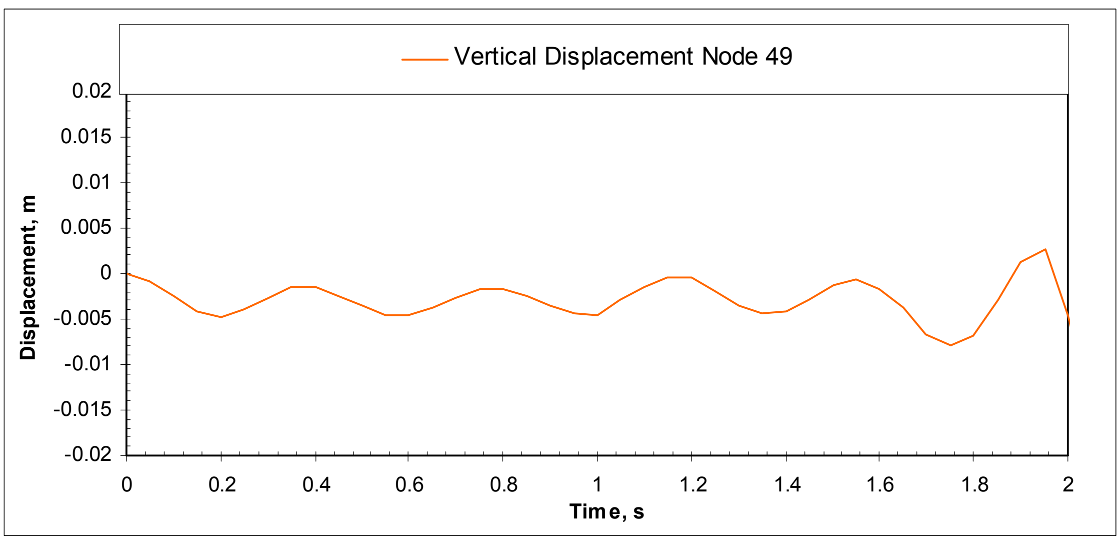

Figure D.110 - Span3, Imperial Valley axial input only, node 49 vertical displacement

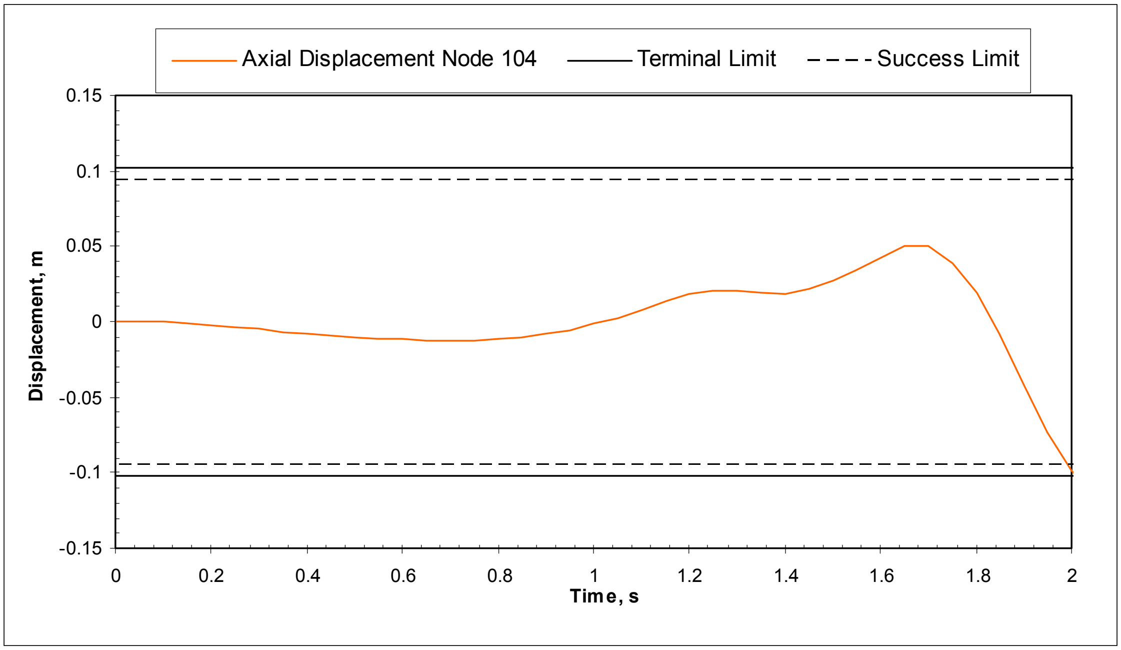

Figure D.111 - Span3, Imperial Valley 3D input, no SCEDs, node 104 axial displacement

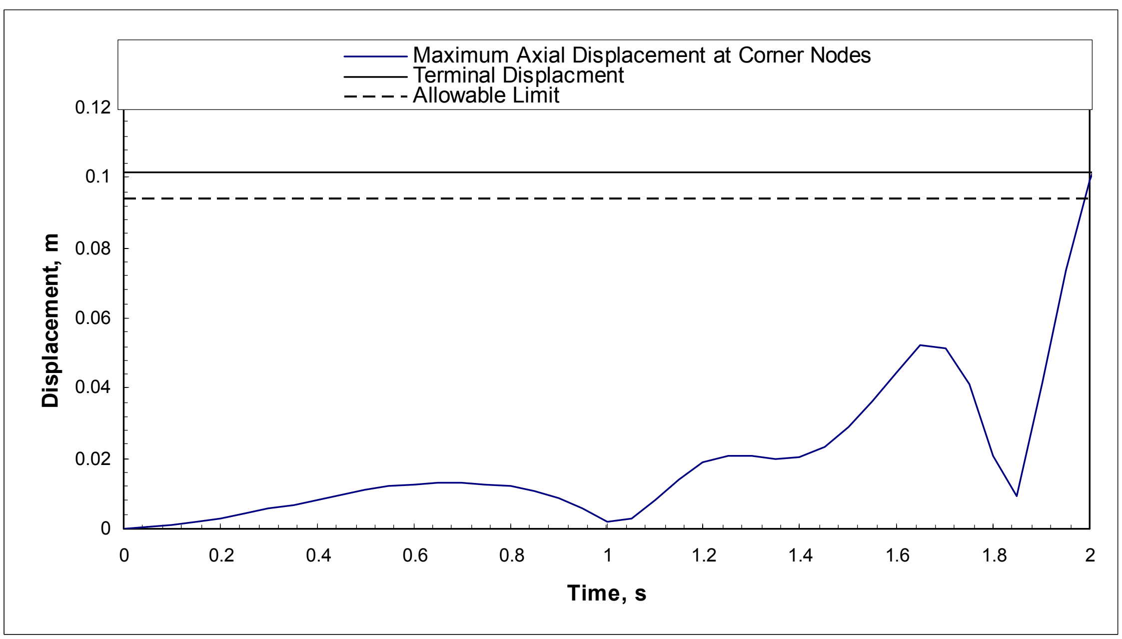

Figure D.112 - Span3, Imperial Valley 3D input, no SCEDs, maximum axial displacement

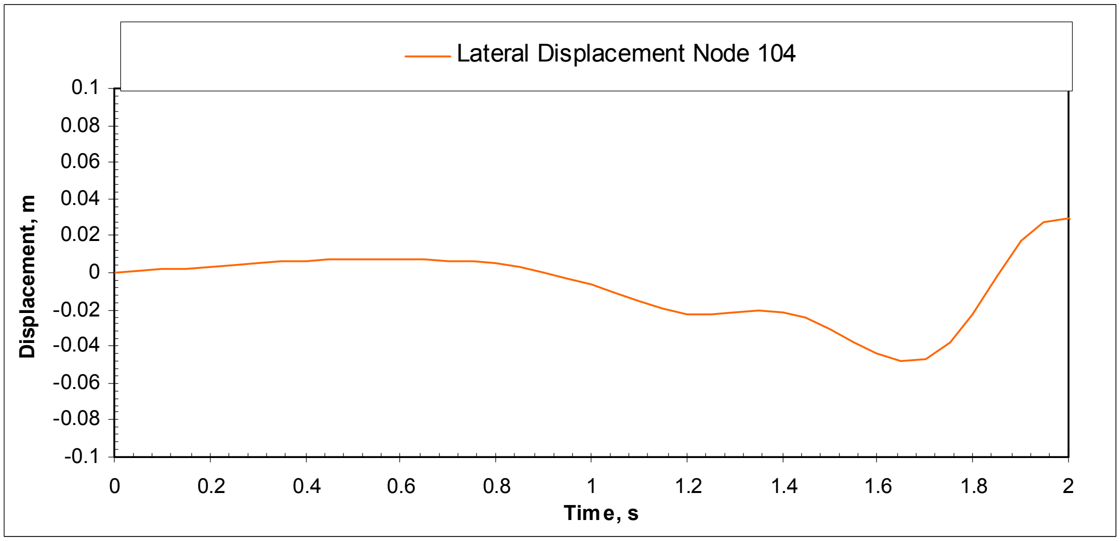

Figure D.113 - Span3, Imperial Valley 3D input, no SCEDs, node 104 lateral displacement

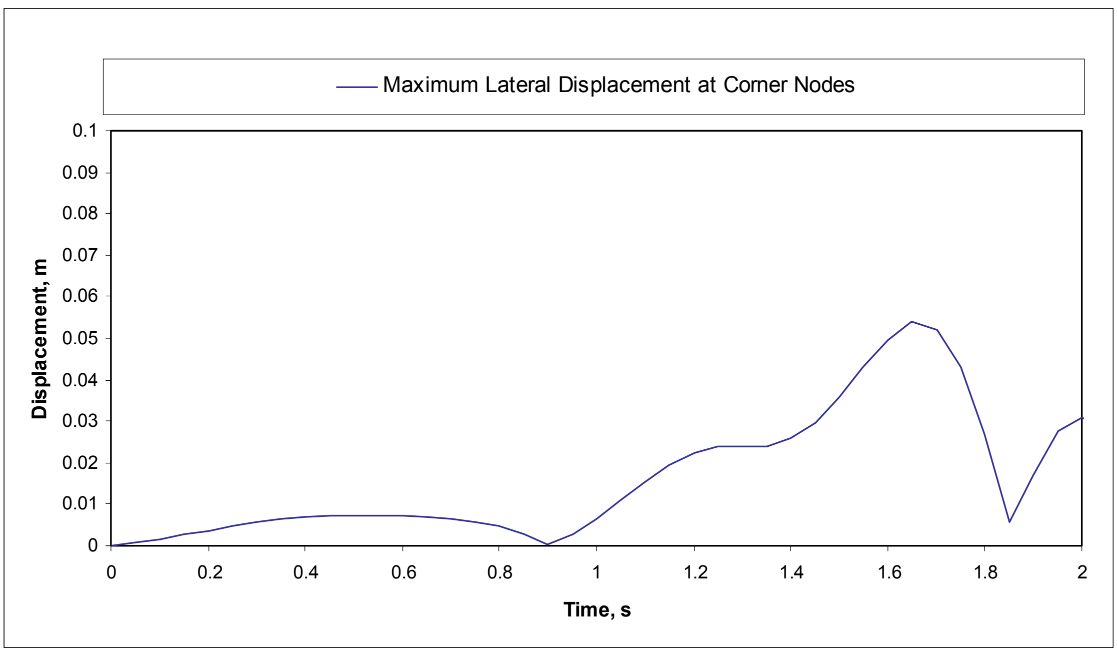

Figure D.114 - Span3, Imperial Valley 3D input, no SCEDs, maximum lateral displacement

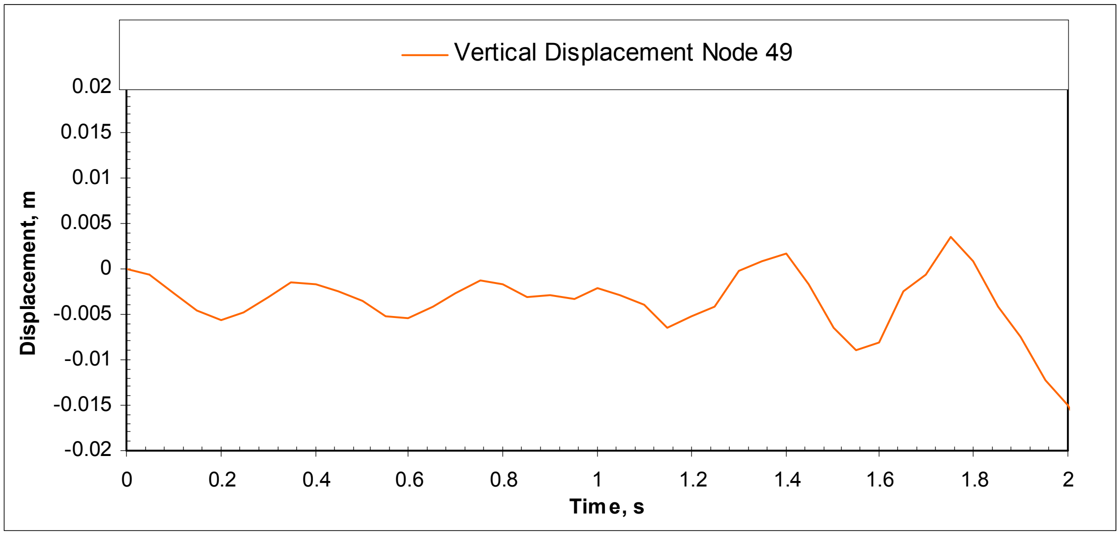

Figure D.115 - Span3, Imperial Valley 3D input, no SCEDs, node 49 vertical displacement

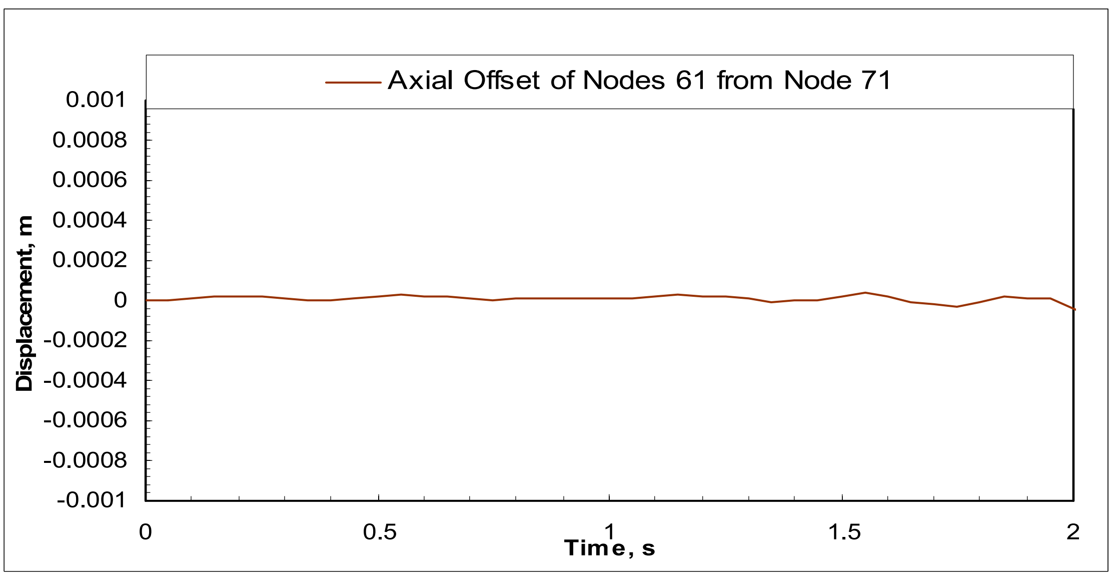

Figure D.116 - Span3, Imperial Valley 3D input, no SCEDs, node 61 and 71 response

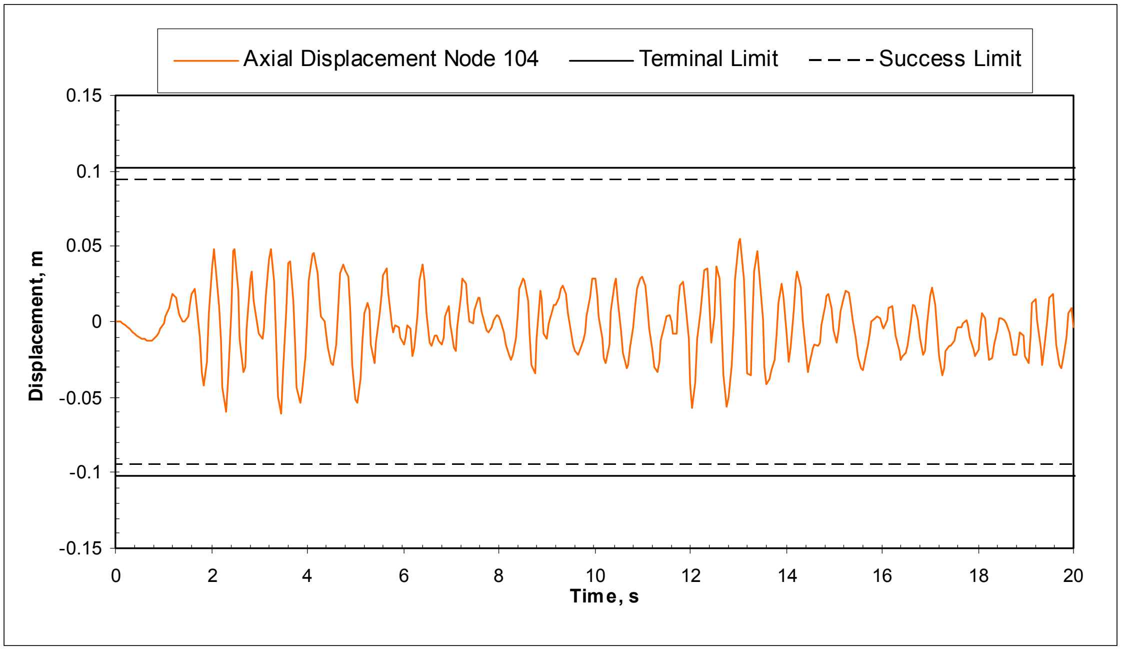

Figure D.117 - Span3, Imperial Valley 3D input, SCED k = 105.4MN/m$^{1.3}$, node 104 axial displacement

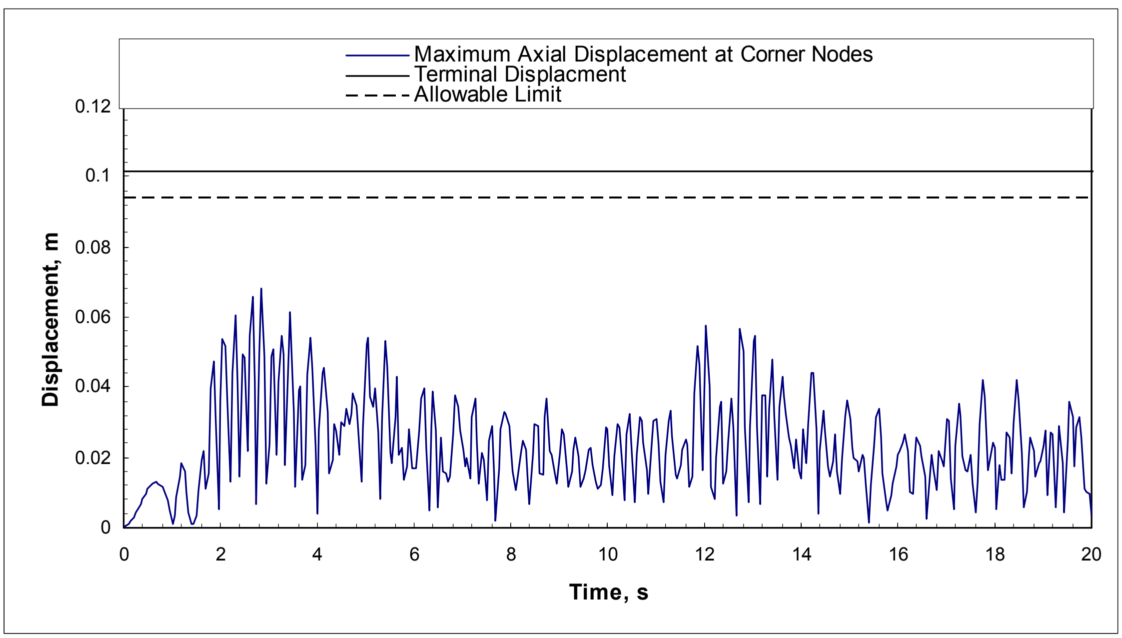

Figure D.118 - Span3, Imperial Valley 3D input, SCED k = 105.4MN/m$^{1.3}$, maximum axial displacement

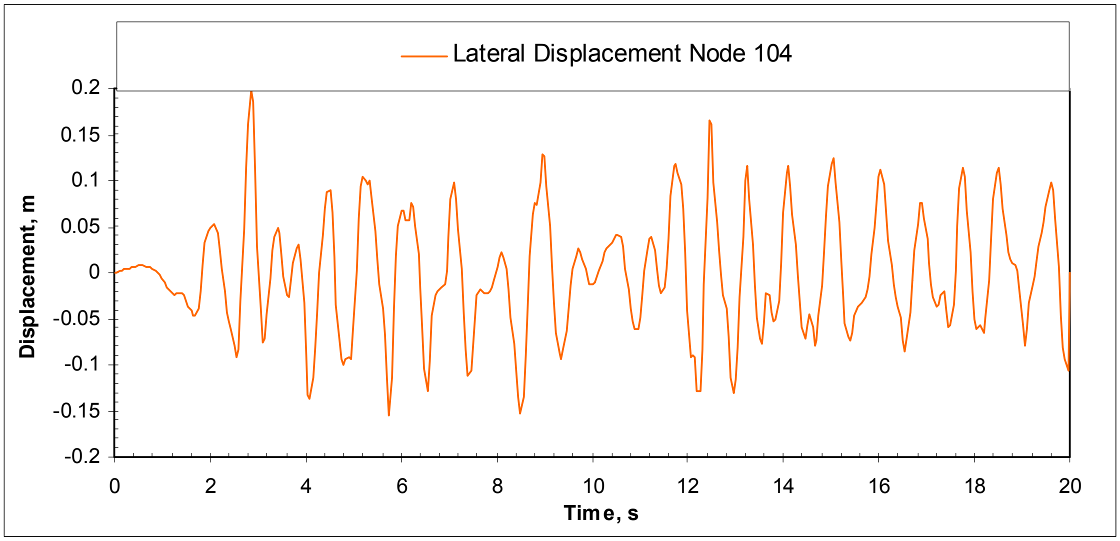

Figure D.119 - Span3, Imperial Valley 3D input, SCED k = 105.4MN/m$^{1.3}$, node 104 lateral disp.

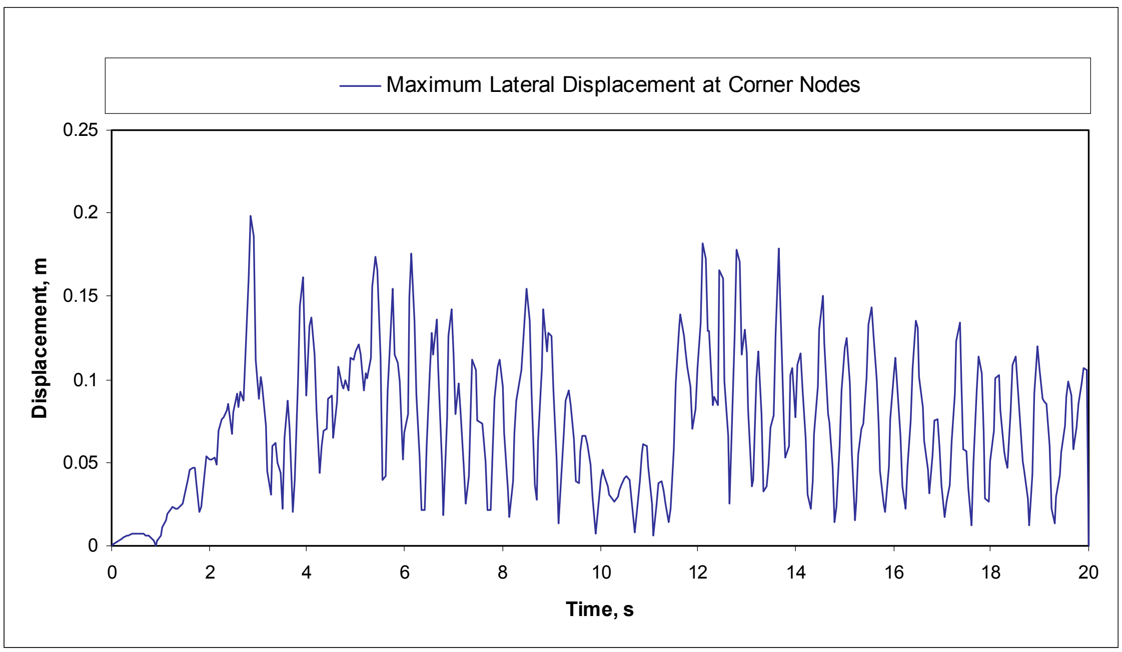

Figure D.120 - Span3, Imperial Valley 3D input, SCED k = 105.4MN/m$^{1.3}$, maximum lateral disp.

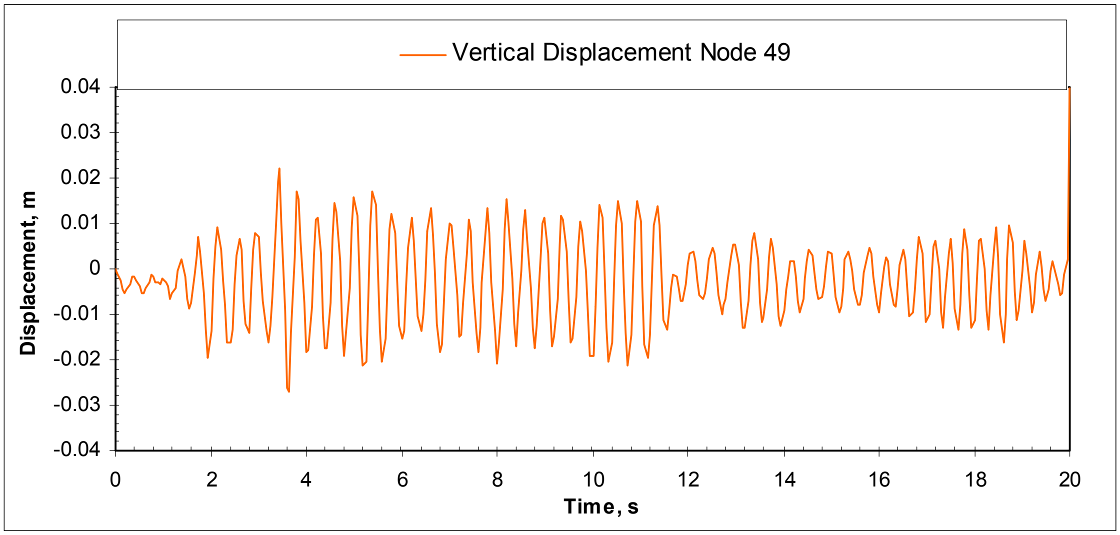

Figure D.121 - Span3, Imperial Valley 3D input, SCED k = 105.4MN/m$^{1.3}$, node 49 vertical disp.

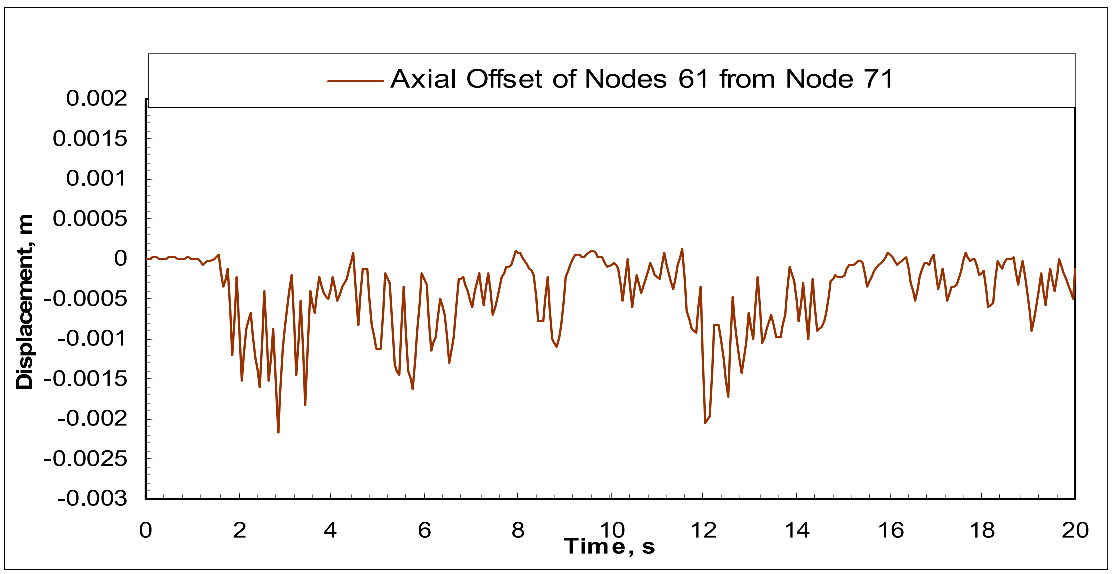

Figure D.122 - Span3, Imperial Valley 3D input, SCED k = 105.4MN/m$^{1.3}$, node 61 and 71 response

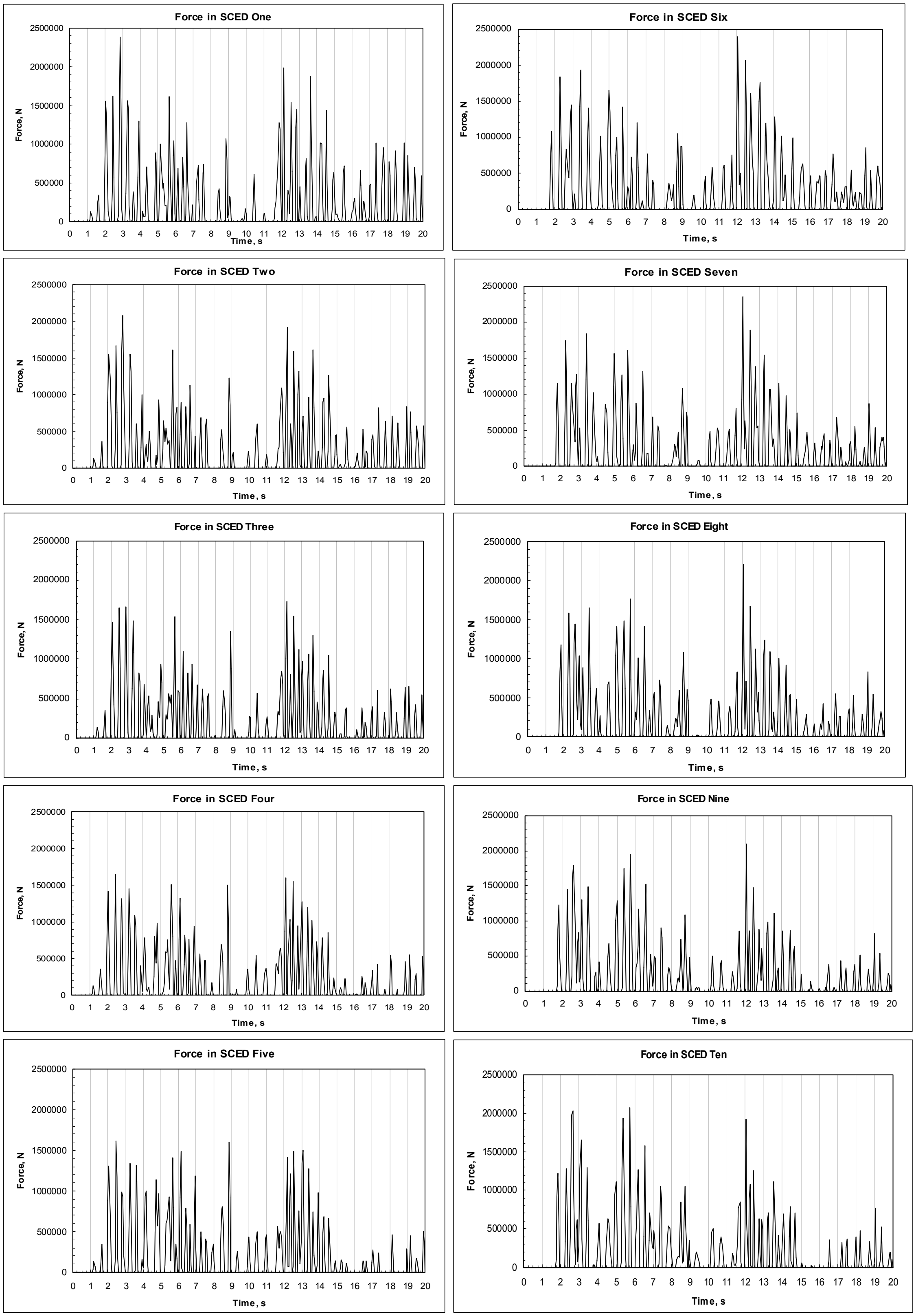

Figure D.123 - Span3, Imperial Valley 3D input, SCED k = 105.4MN/m$^{1.3}$, snap load histories

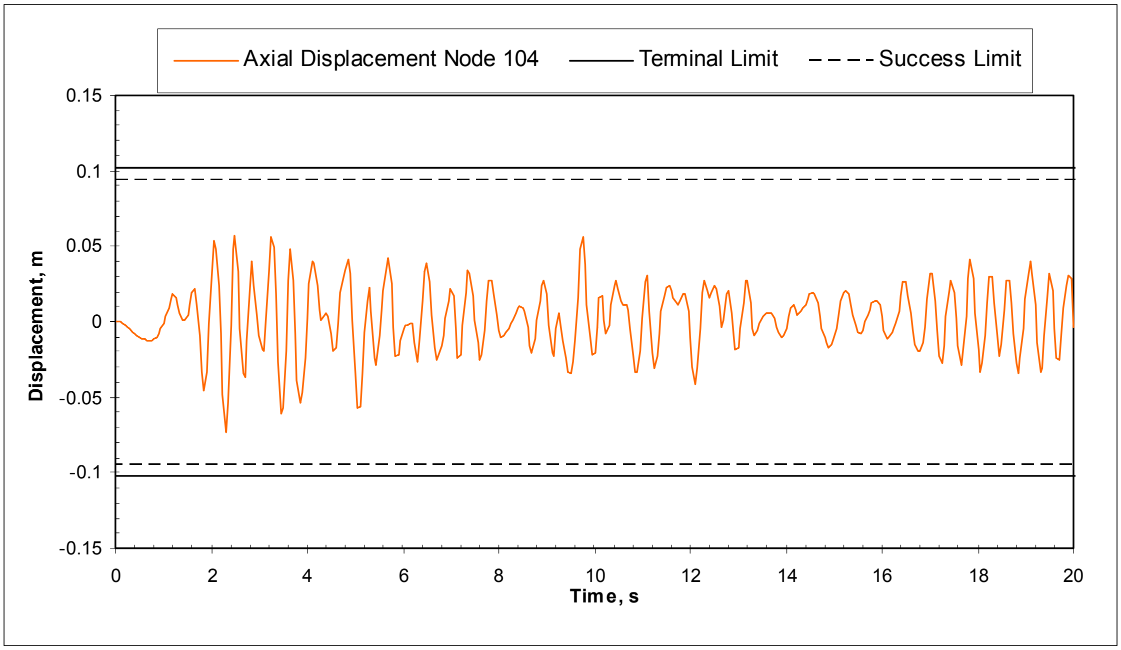

Figure D.124 - Span3, Imperial Valley 3D input, SCED k = 89.6MN/m$^{1.3}$, node 104 axial displacement

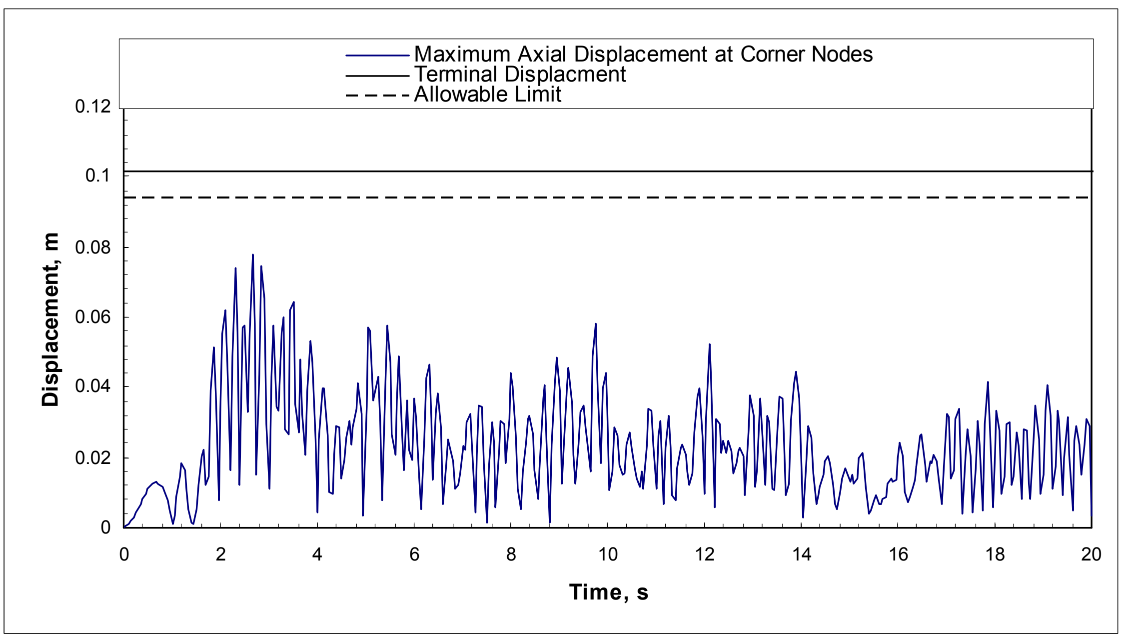

Figure D.125 - Span3, Imperial Valley 3D input, SCED k = 89.6MN/m$^{1.3}$, maximum axial displacement

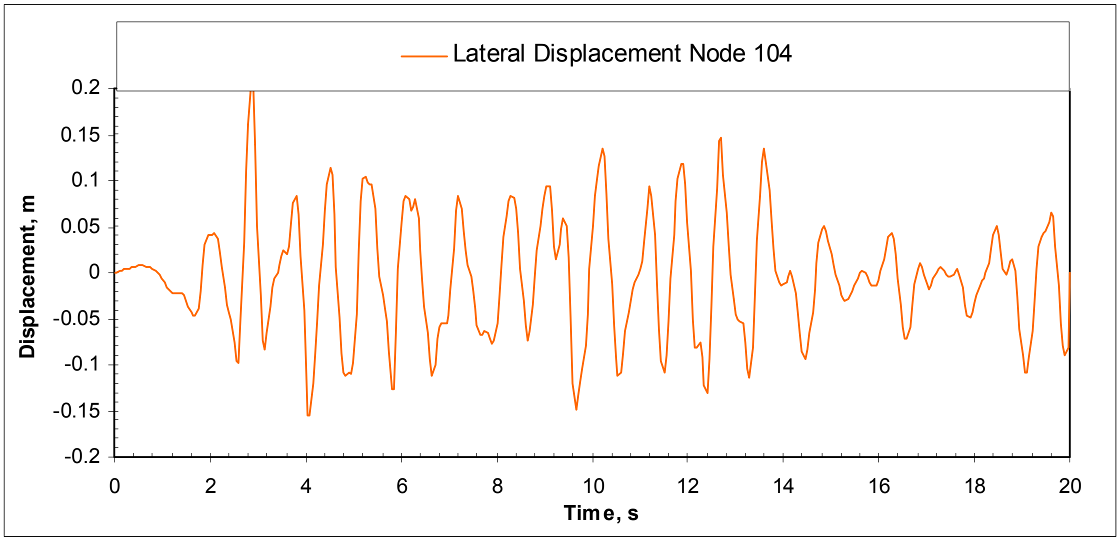

Figure D.126 - Span3, Imperial Valley 3D input, SCED k = 89.6MN/m$^{1.3}$, node 104 lateral displacement

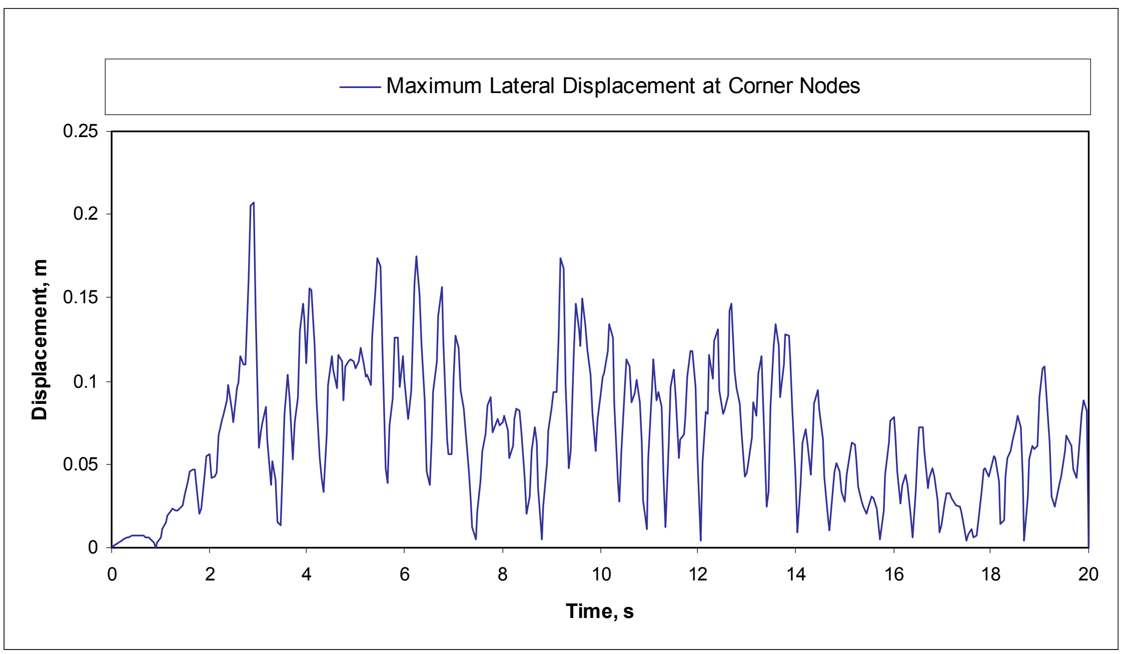

Figure D.127 - Span3, Imperial Valley 3D input, SCED k = 89.6MN/m$^{1.3}$, maximum lateral displacement

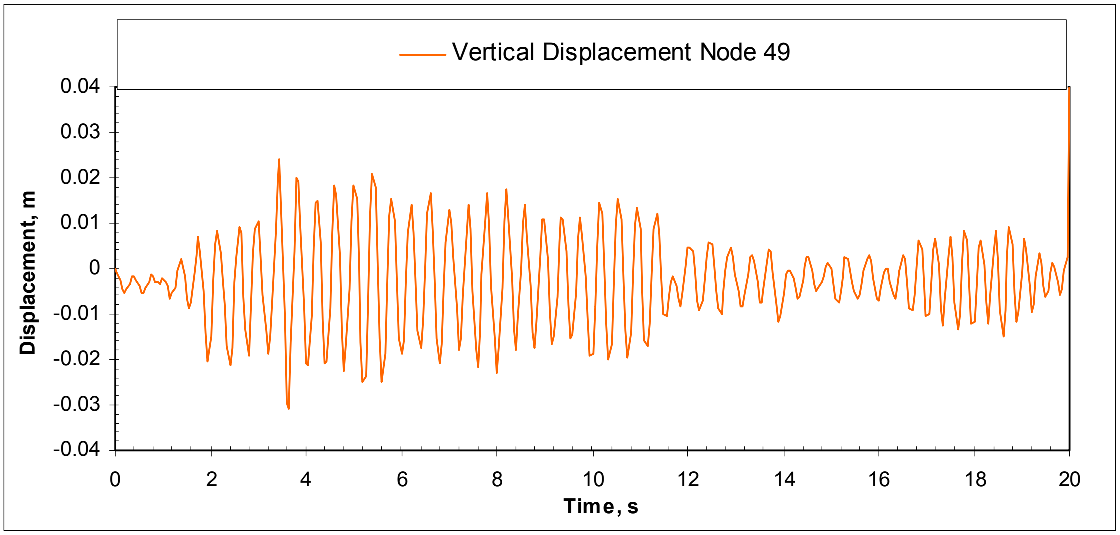

Figure D.128 - Span3, Imperial Valley 3D input, SCED k = 89.6MN/m$^{1.3}$, node 49 vertical displacement

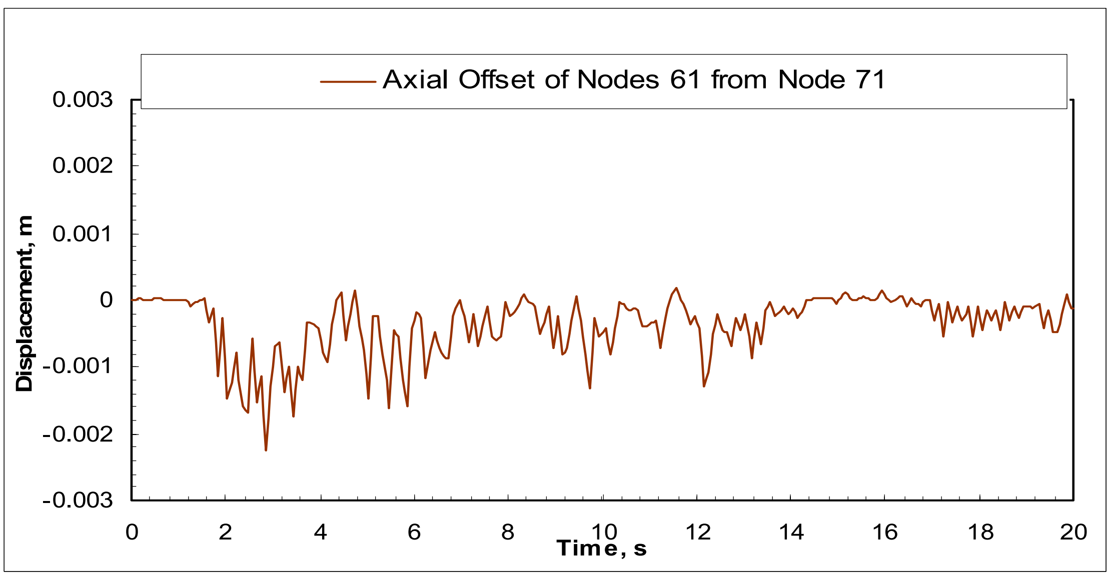

Figure D.129 - Span3, Imperial Valley 3D input, SCED k = 89.6MN/m$^{1.3}$, node 61 and 71 response

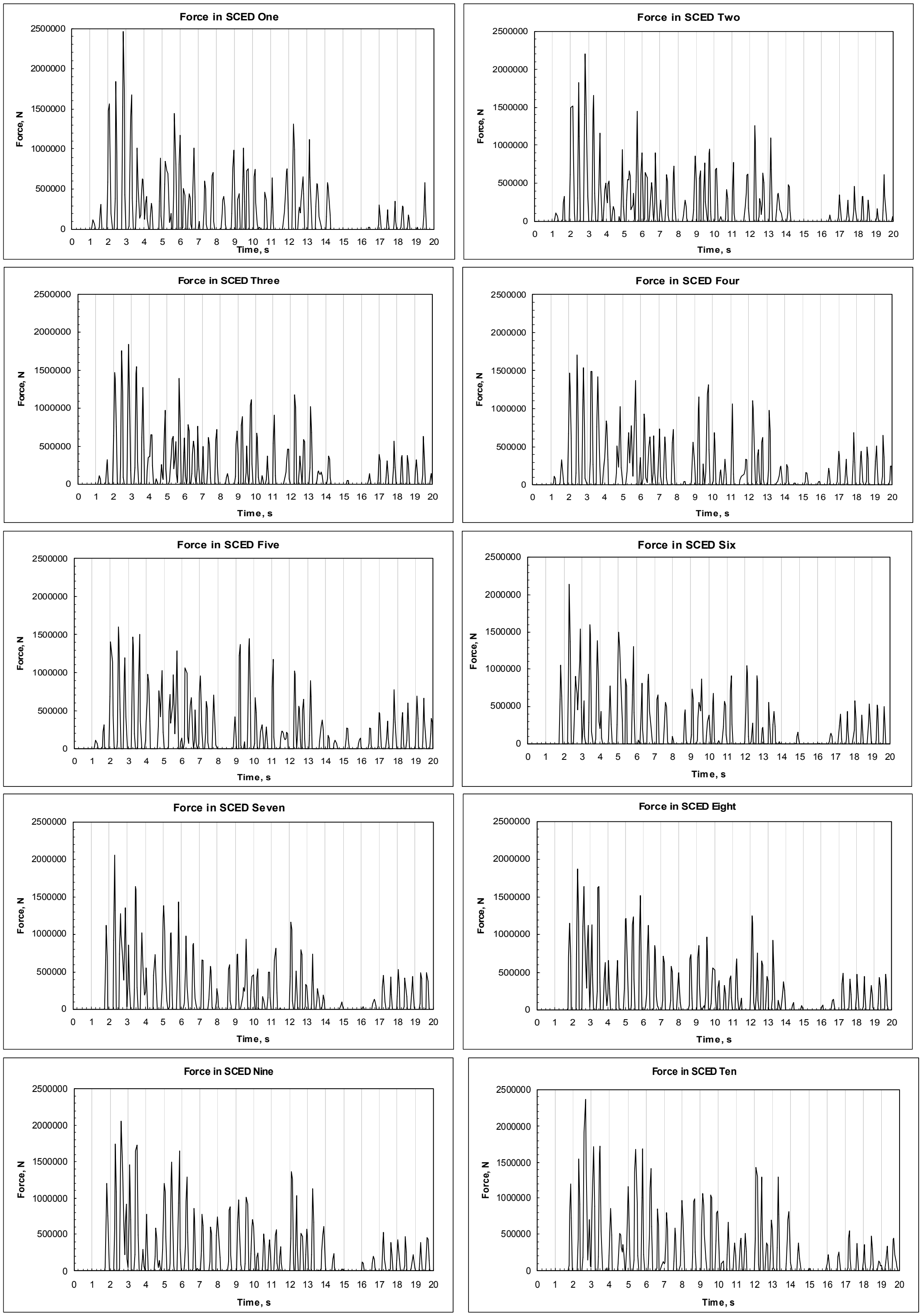

Figure D.130 - Span3, Imperial Valley 3D input, SCED k = 89.6MN/m$^{1.3}$, snap load histories

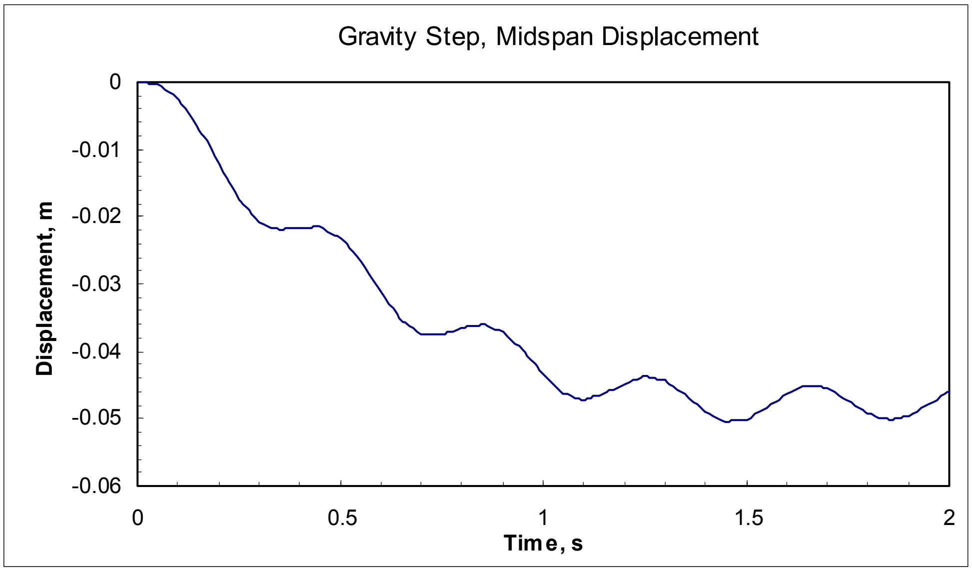

Figure D.131 - Span3, Northridge input, gravity step response

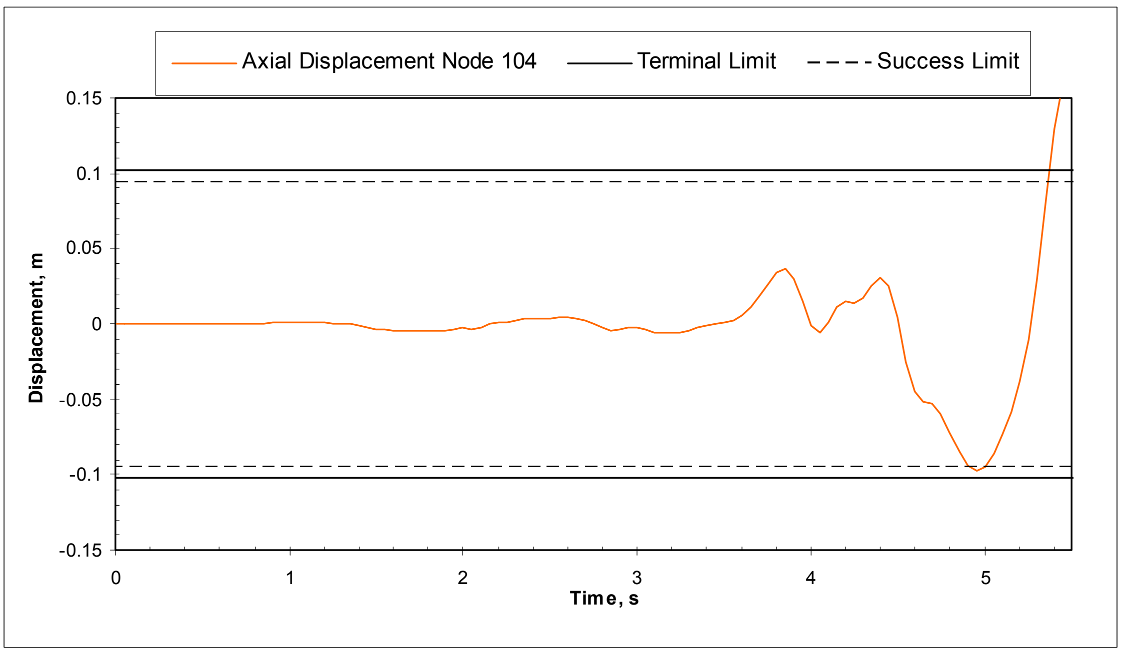

Figure D.132 - Span3, Northridge axial input only, node 104 axial displacement

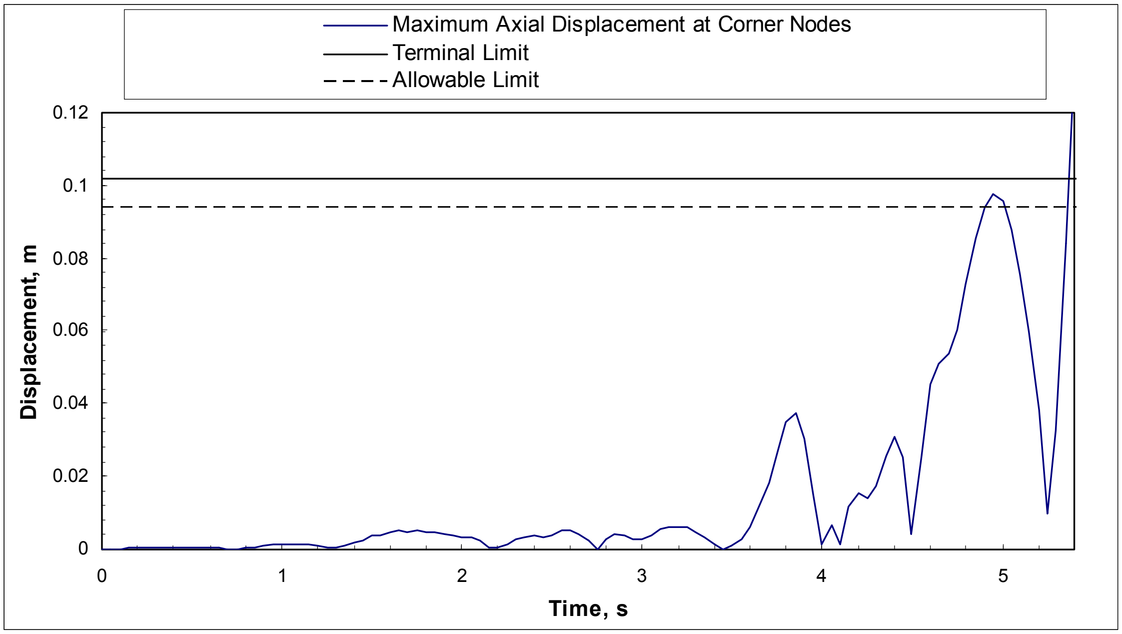

Figure D.133 - Span3, Northridge axial input only, maximum axial displacement

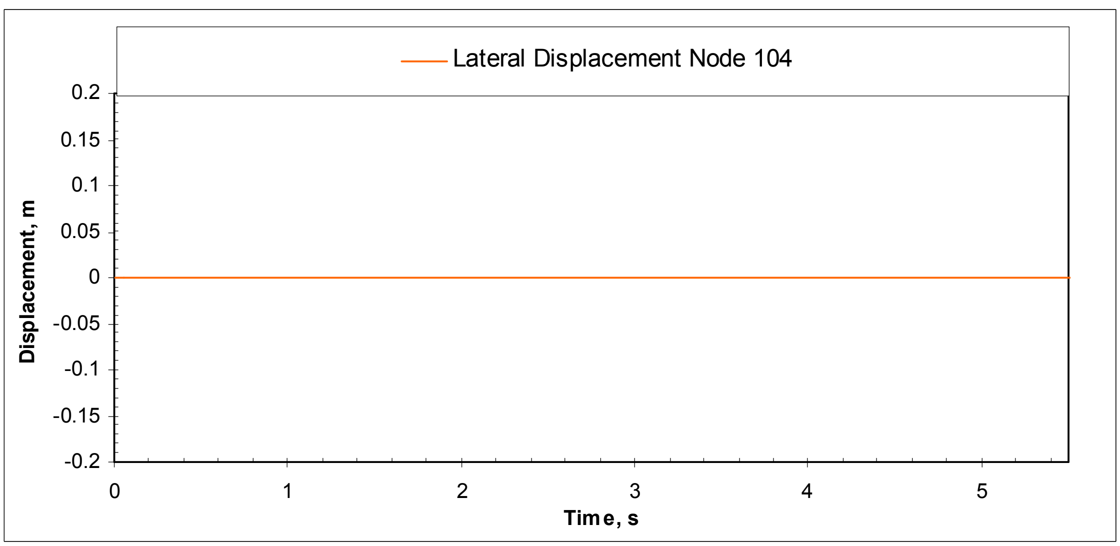

Figure D.134 - Span3, Northridge axial input only, node 104 lateral displacement

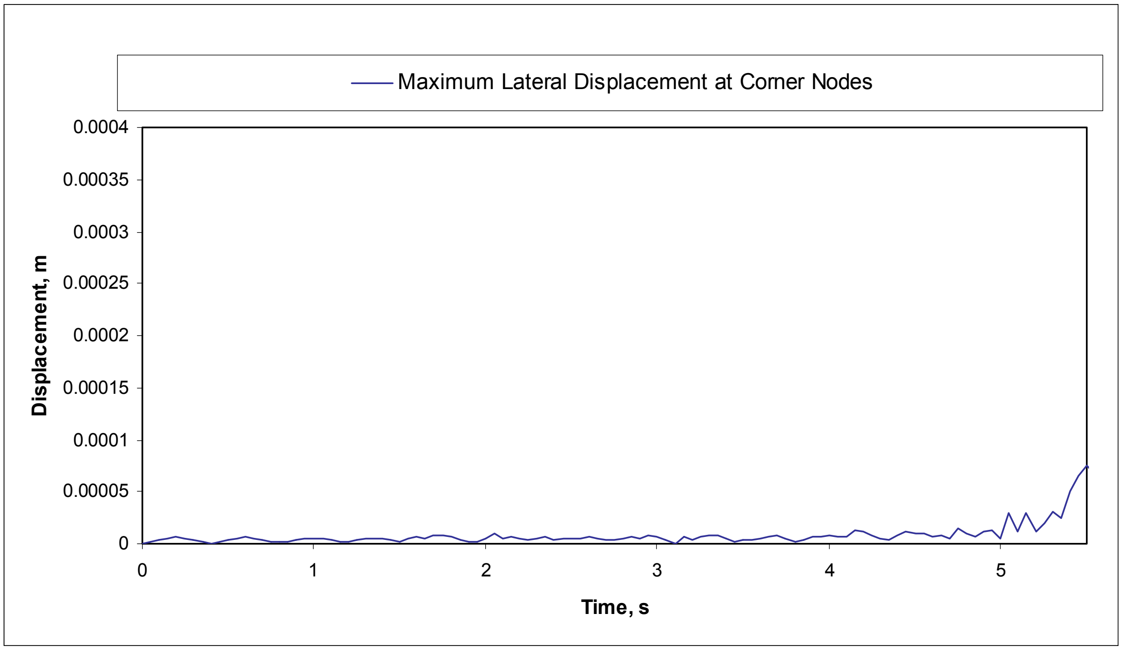

Figure D.135 - Span3, Northridge axial input only, maximum lateral displacement

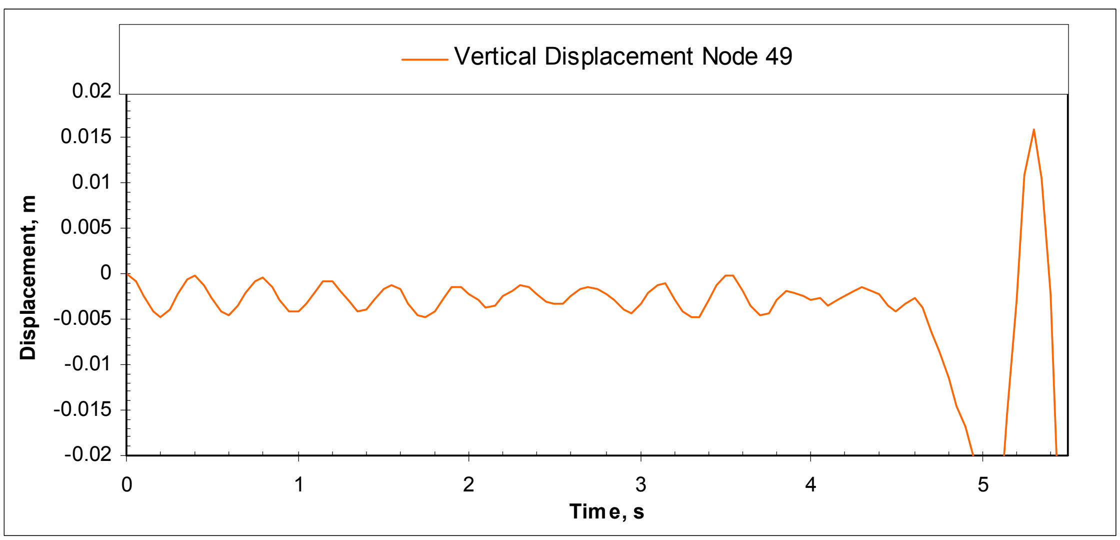

Figure D.136 - Span3, Northridge axial input only, node 49 vertical displacement

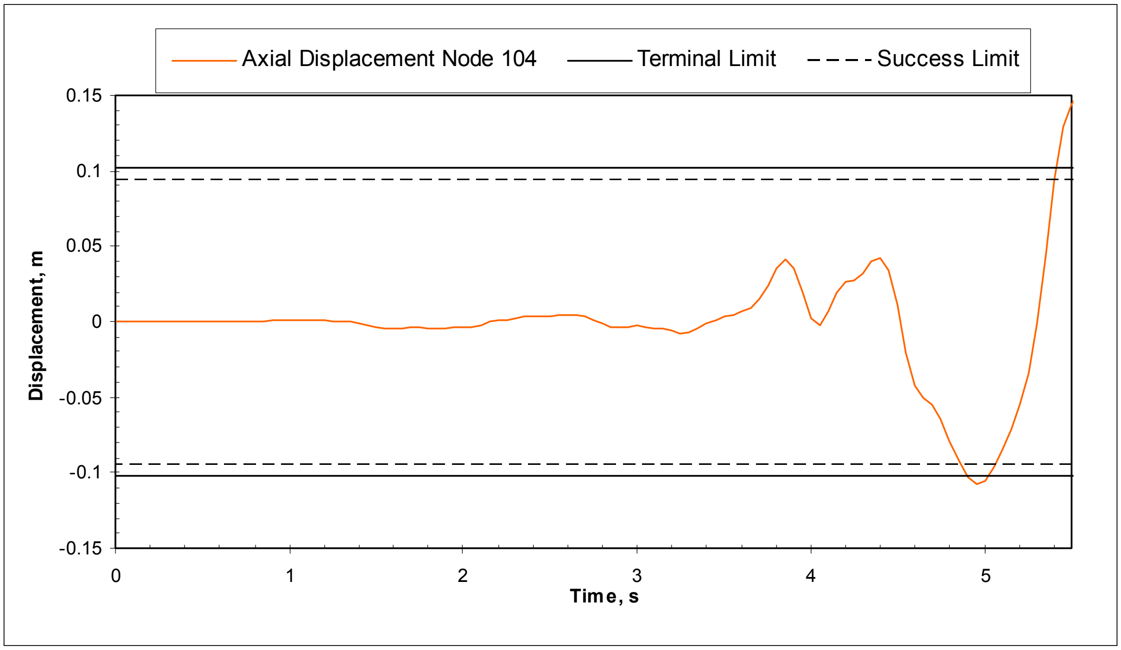

Figure D.137 - Span3, Northridge three-dimensional input, no SCEDs, node 104 axial displacement

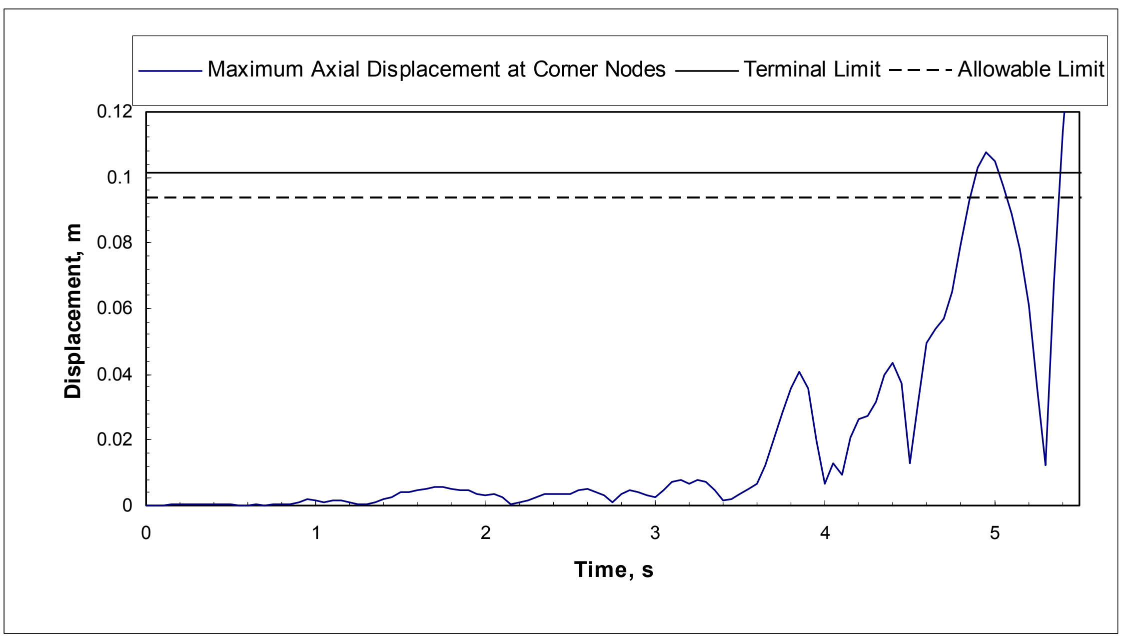

Figure D.138 - Span3, Northridge 3D input, no SCEDs, maximum axial displacement

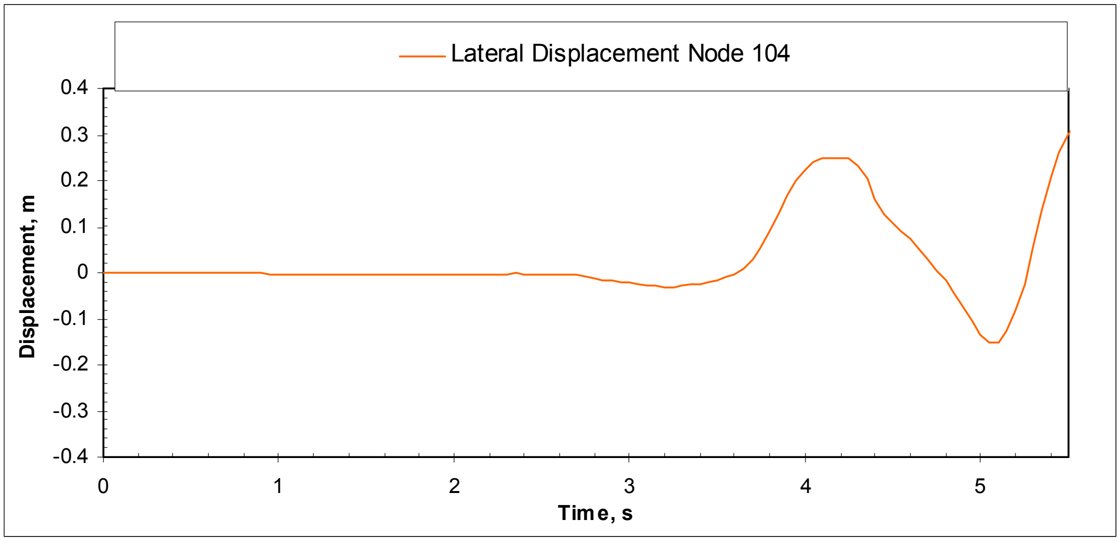

Figure D.139 - Span3, Northridge 3D input, no SCEDs, node 104 lateral displacement

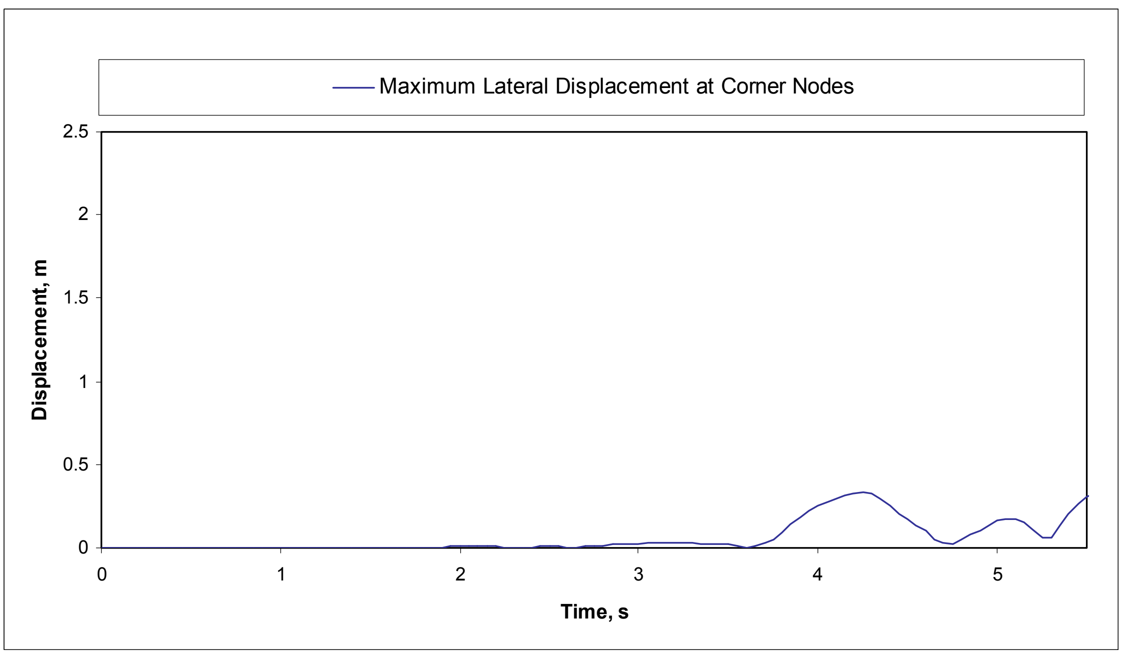

Figure D.140 - Span3, Northridge three-dimensional input, no SCEDs, maximum lateral displacement

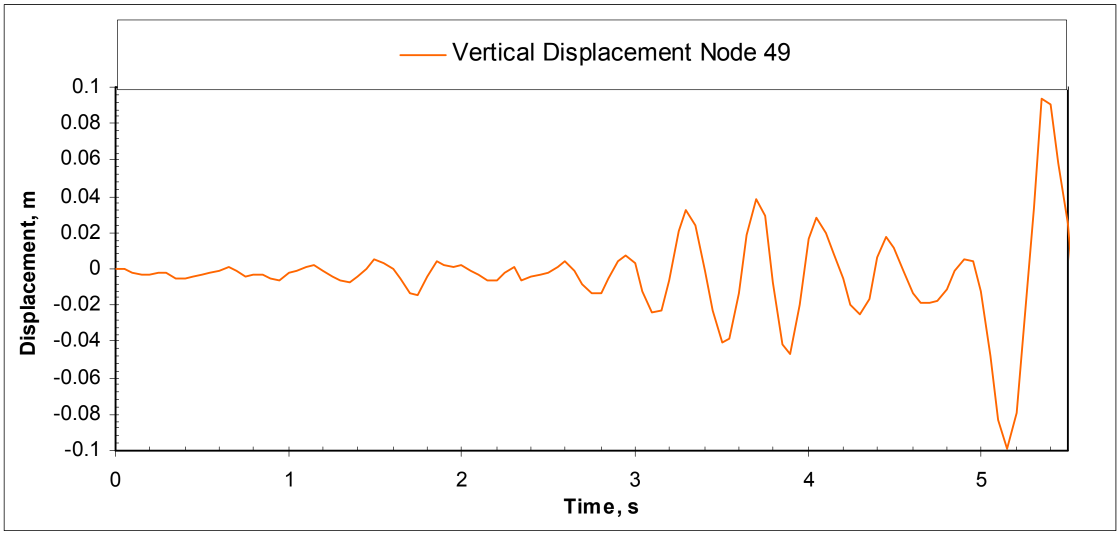

Figure D.141 - Span3, Northridge 3D input, no SCEDs, node 49 vertical displacement

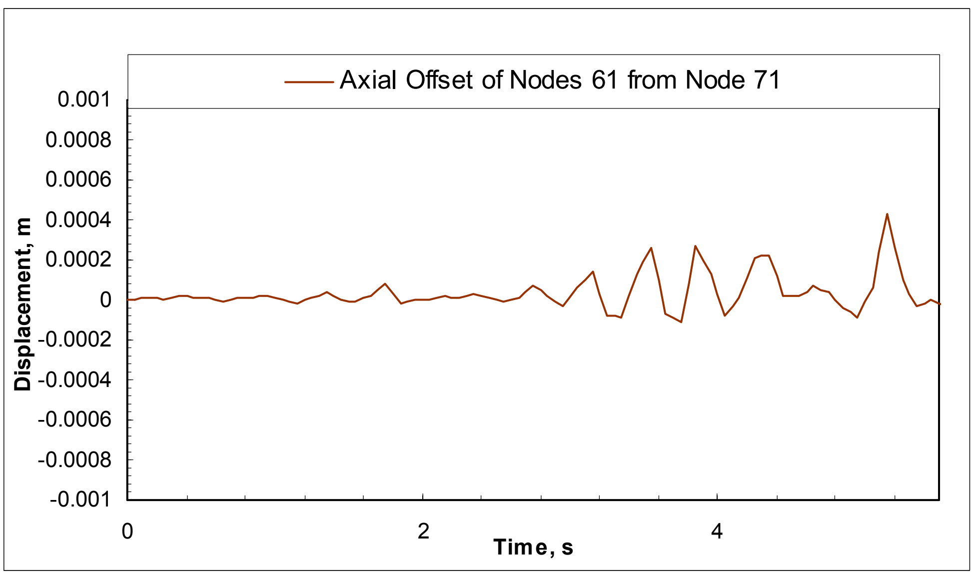

Figure D.142 - Span3, Northridge 3D input, no SCEDs, node 61 and 71 response

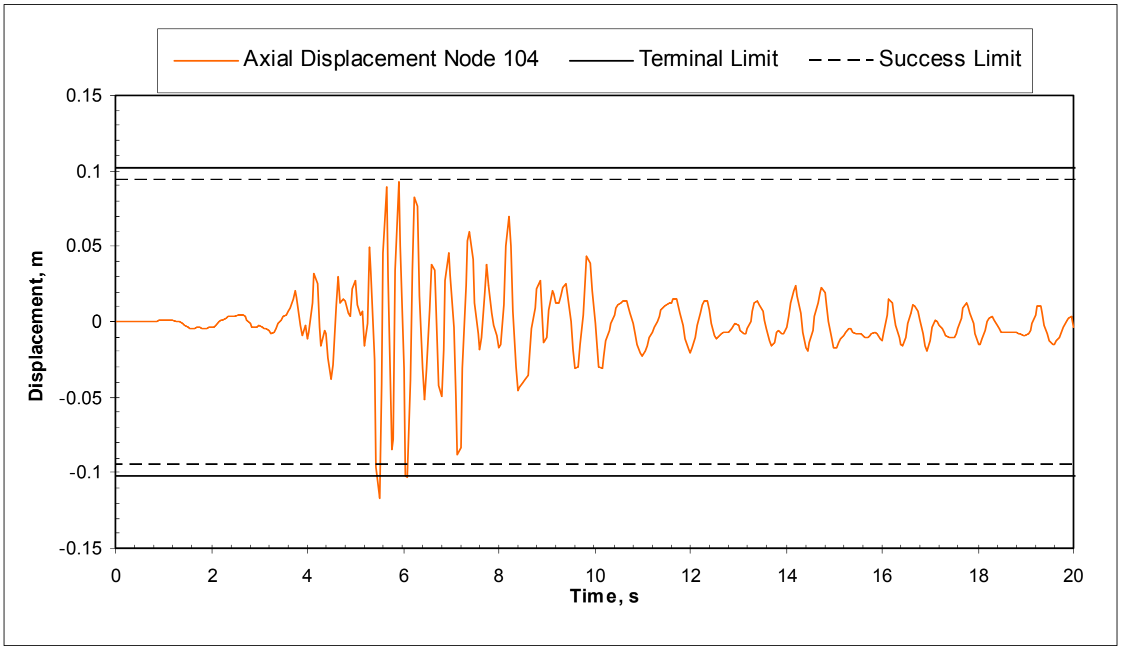

Figure D.143 - Span3, Northridge 3D input, SCED k = 105.4MN/m$^{1.3}$, node 104 axial displacement

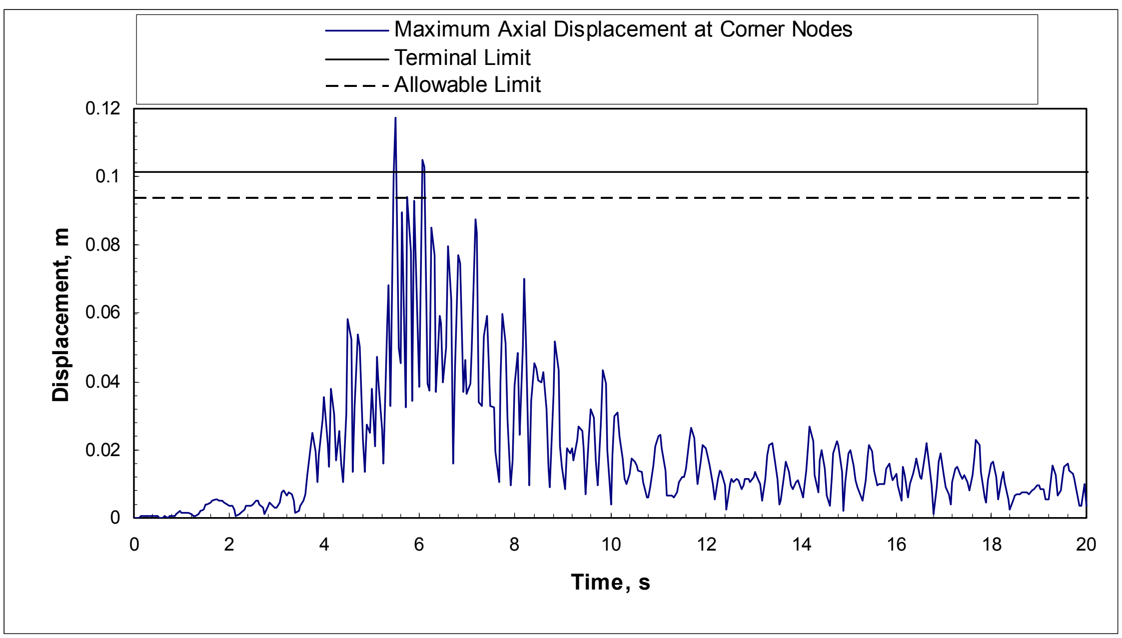

Figure D.144 - Span3, Northridge 3D input, SCED k = 105.4MN/m$^{1.3}$, maximum axial displacement

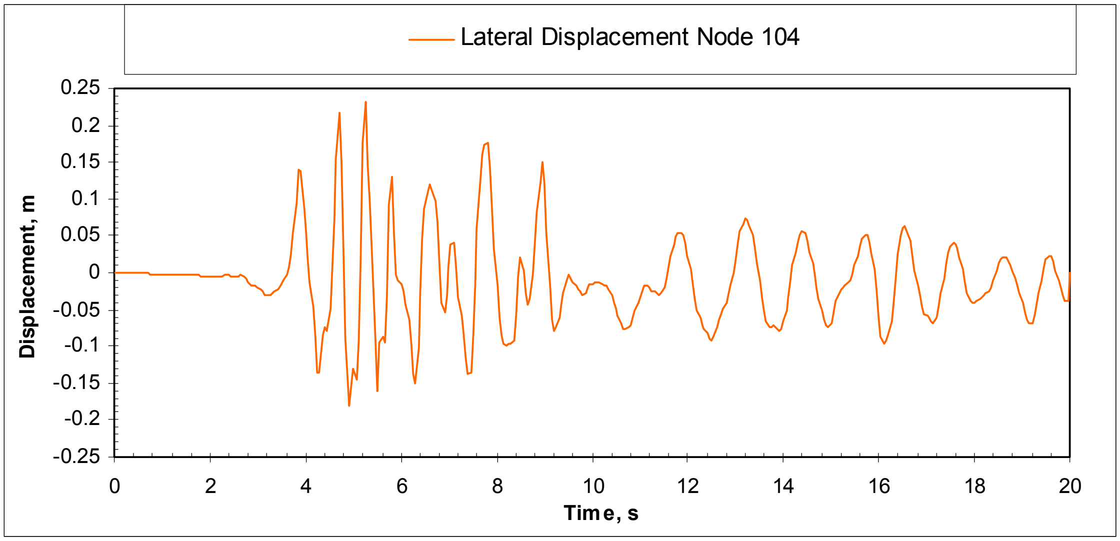

Figure D.145 - Span3, Northridge 3D input, SCED k = 105.4MN/m$^{1.3}$, node 104 lateral displacement

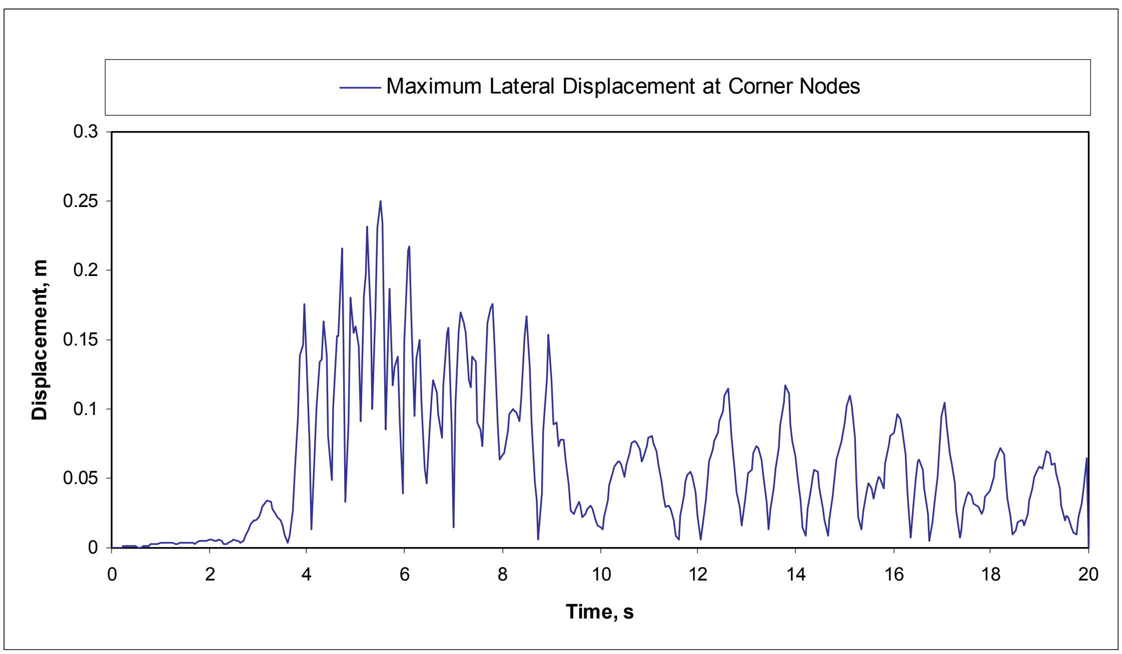

Figure D.146 - Span3, Northridge 3D input, SCED k = 105.4MN/m$^{1.3}$, maximum lateral displacement

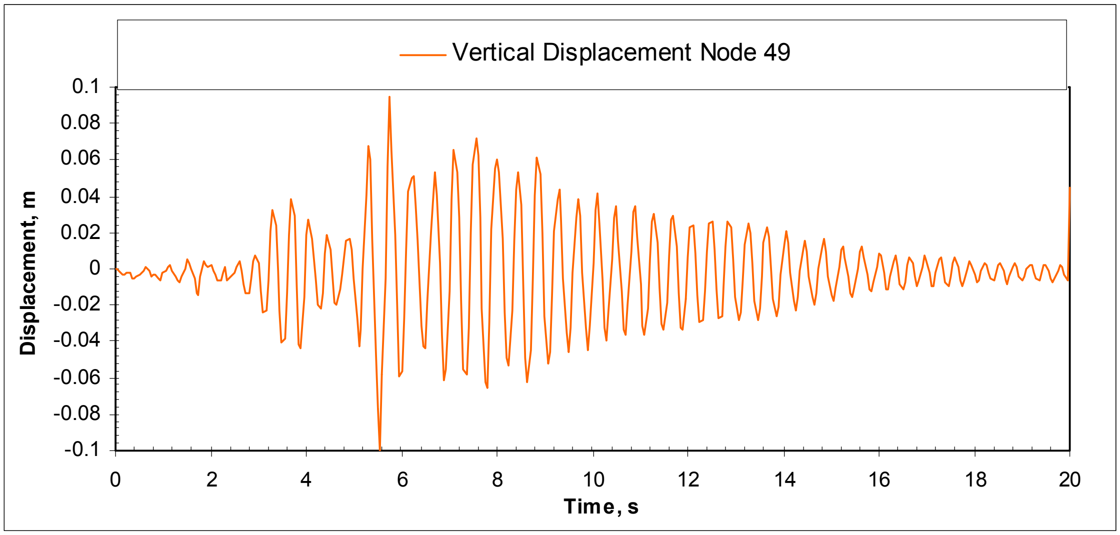

Figure D.147 - Span3, Northridge 3D input, SCED k = 105.4MN/m$^{1.3}$, node 49 vertical displacement

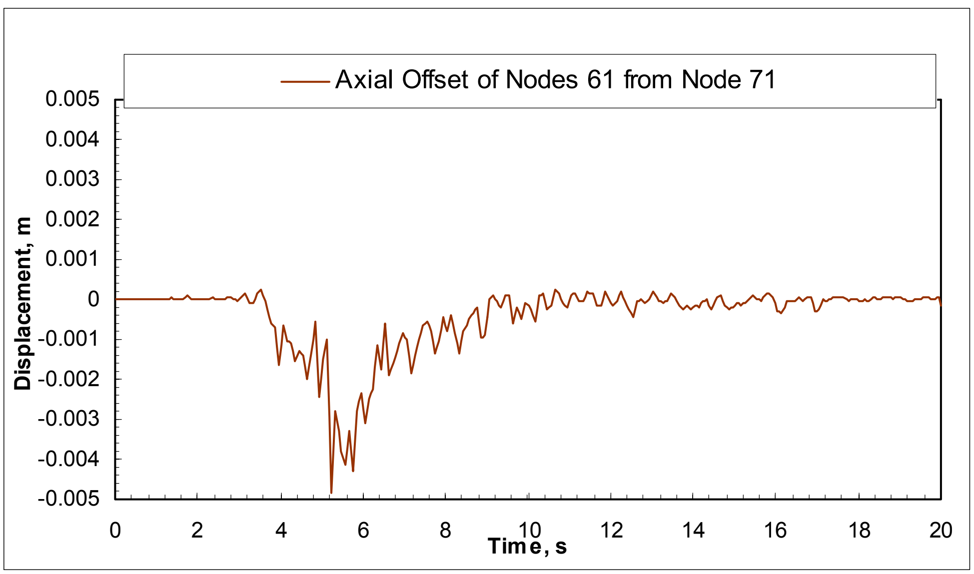

Figure D.148 - Span3, Northridge 3D input, SCED k = 105.4MN/m$^{1.3}$, node 61 and 71 response

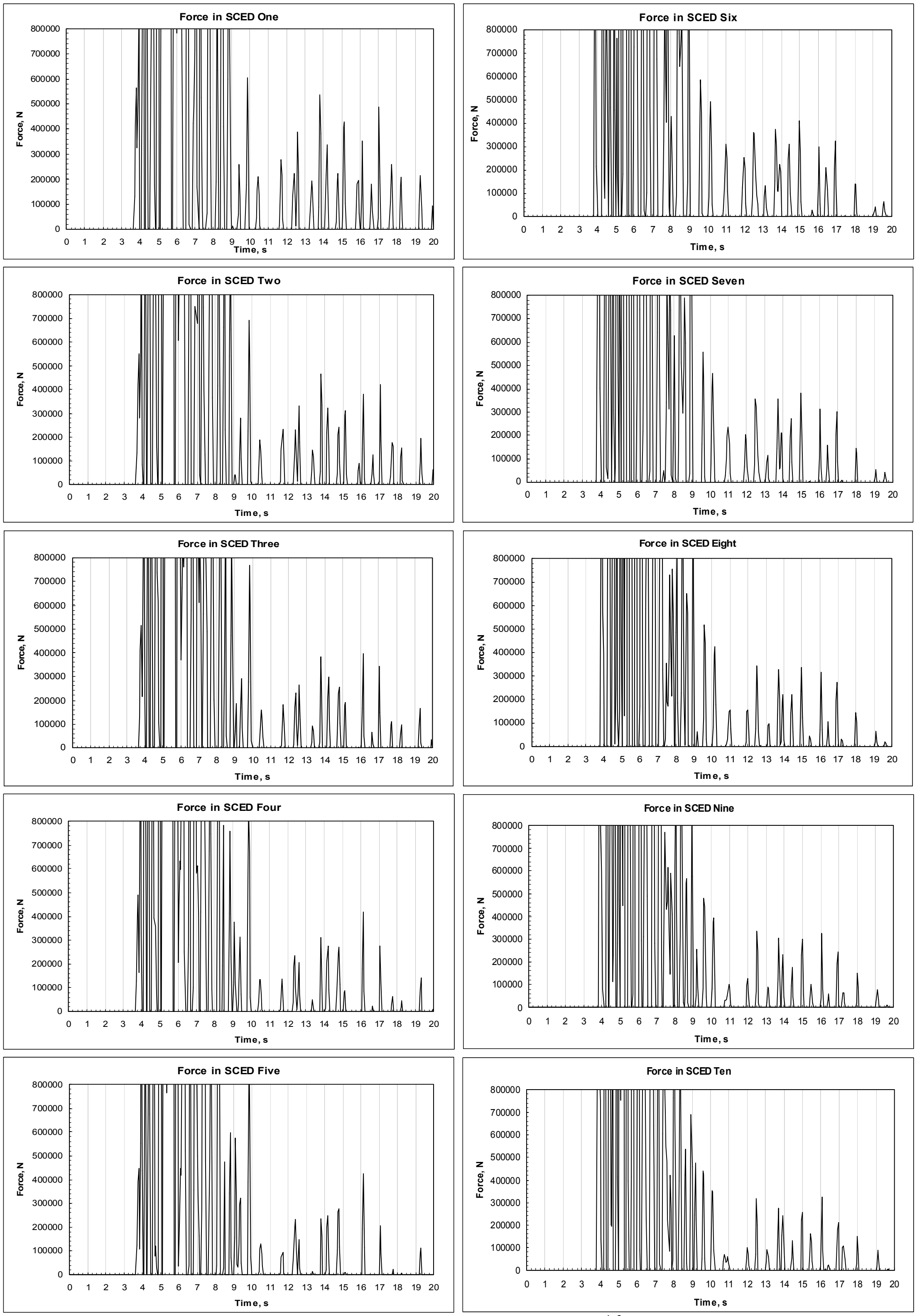

Figure D.149 - Span3, Northridge 3D input, SCED k = 105.4MN/m$^{1.3}$, snap load histories

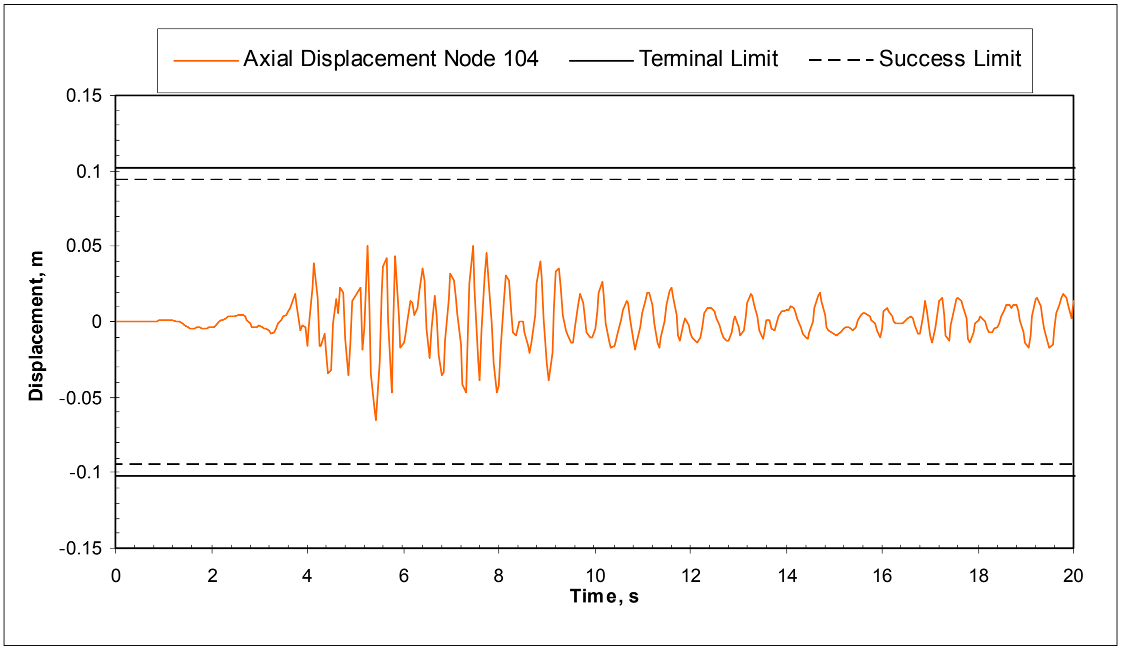

Figure D.150 - Span3, Northridge 3D input, SCED k = 147.6MN/m$^{1.3}$, node 104 axial displacement

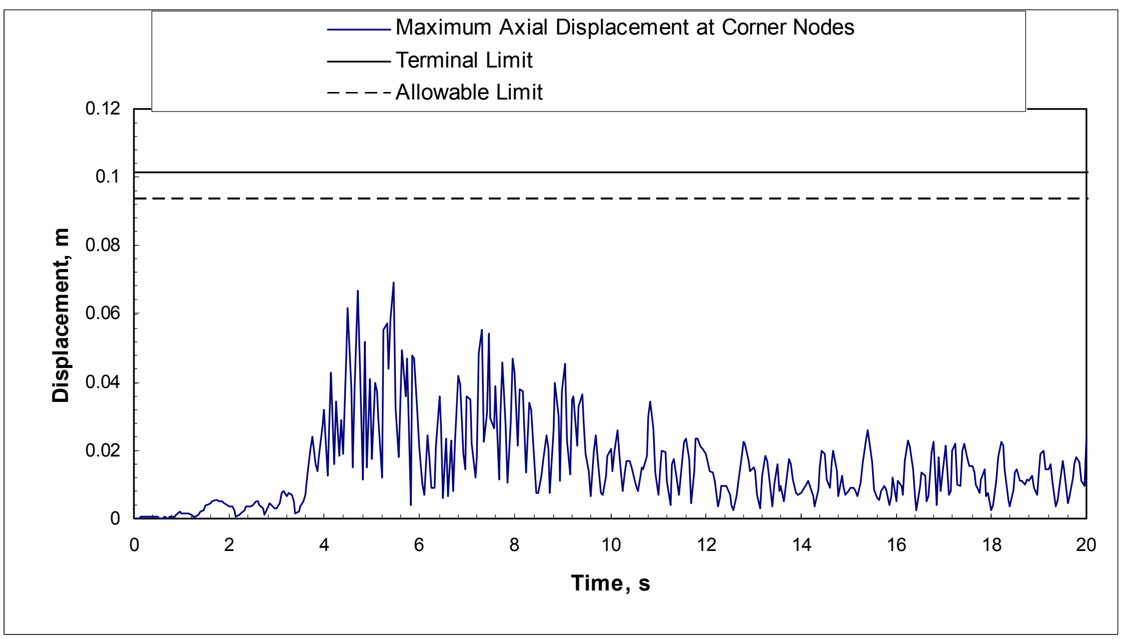

Figure D.151 - Span3, Northridge 3D input, SCED k = 147.6MN/m$^{1.3}$, maximum axial displacement

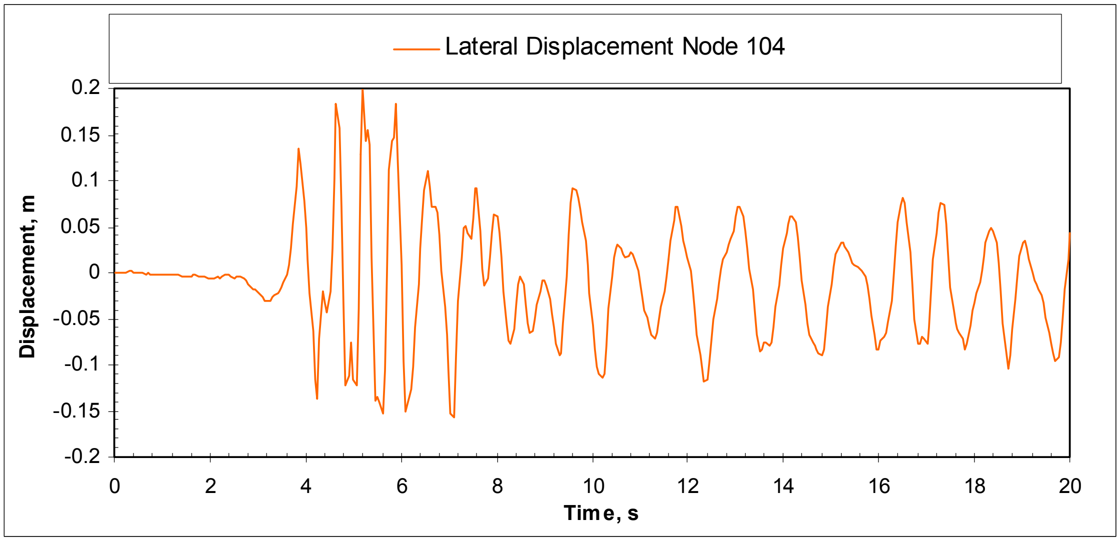

Figure D.152 - Span3, Northridge 3D input, SCED k = 147.6MN/$m^{1.3}$, node 104 lateral displacement

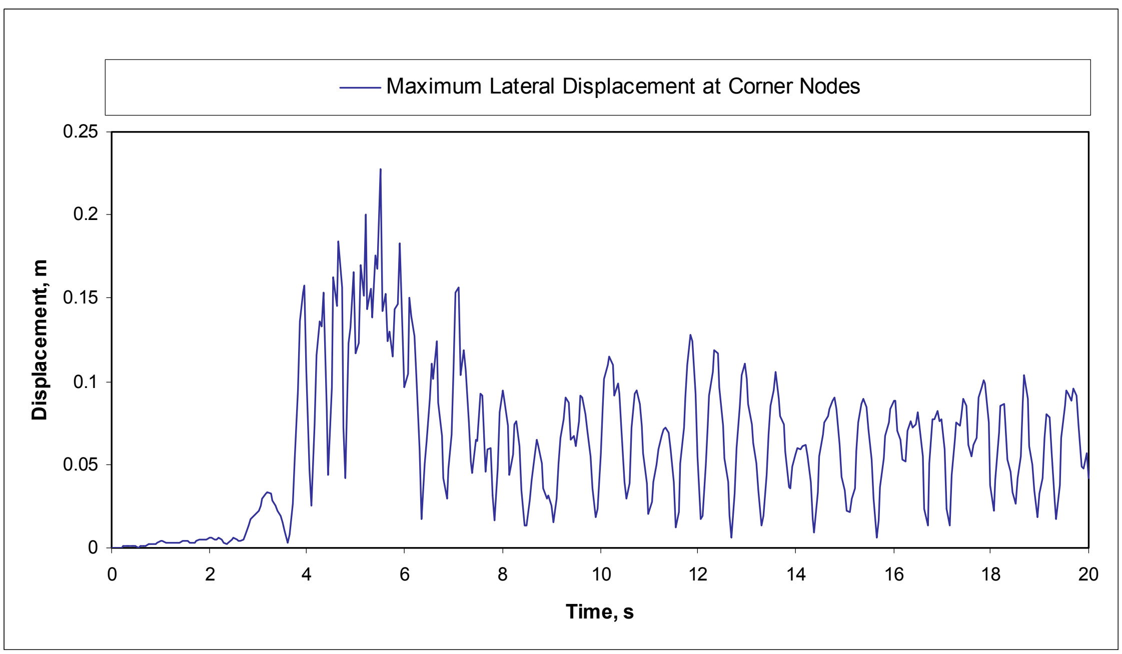

Figure D.153 - Span3, Northridge 3D input, SCED k = 147.6MN/$m^{1.3}$, maximum lateral displacement

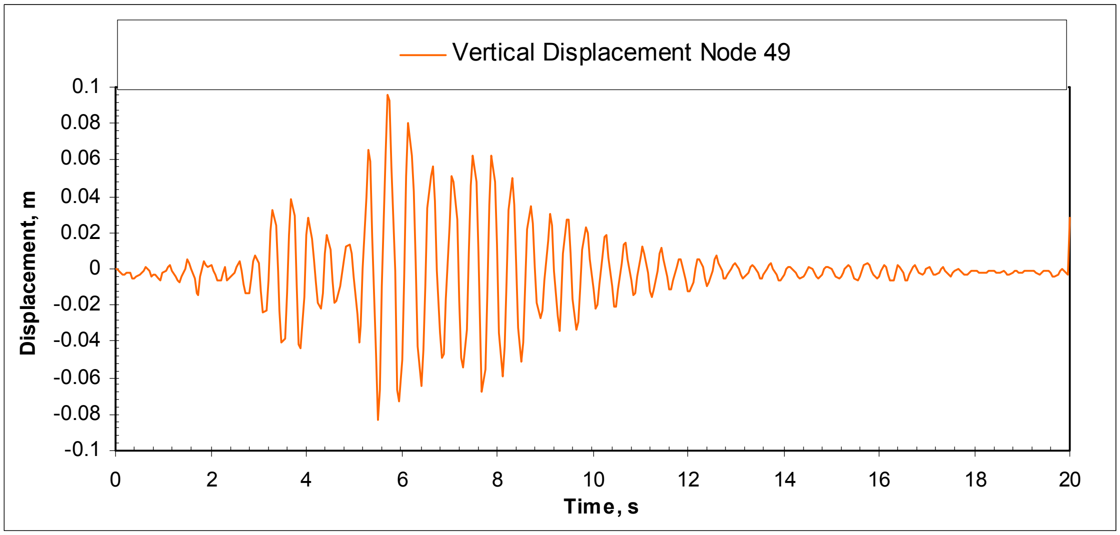

Figure D.154 - Span3, Northridge 3D input, SCED k = 147.6MN/m$^{1.3}$, node 49 vertical displacement

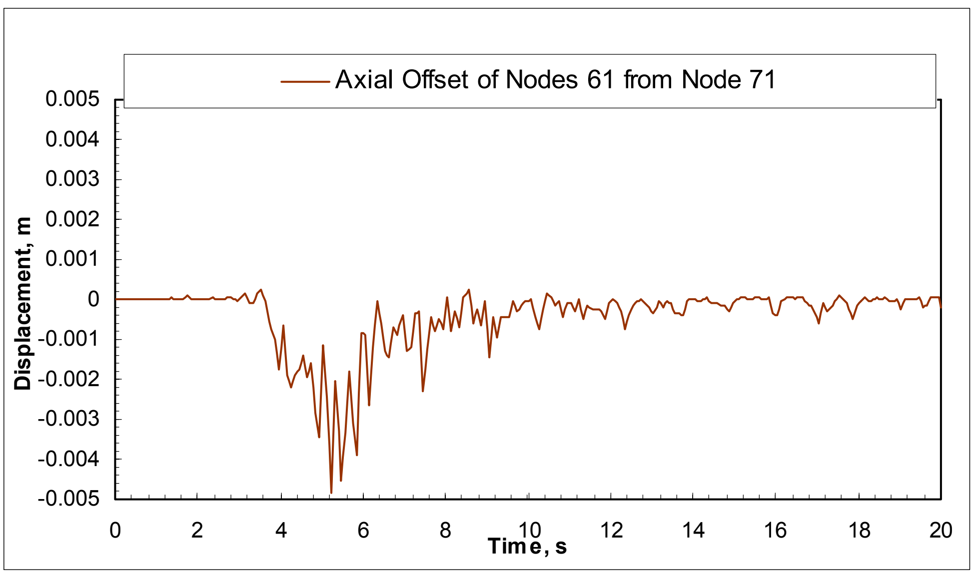

Figure D.155 - Span3, Northridge 3D input, SCED k = 147.6MN/m$^{1.3}$, node 61 and 71 response

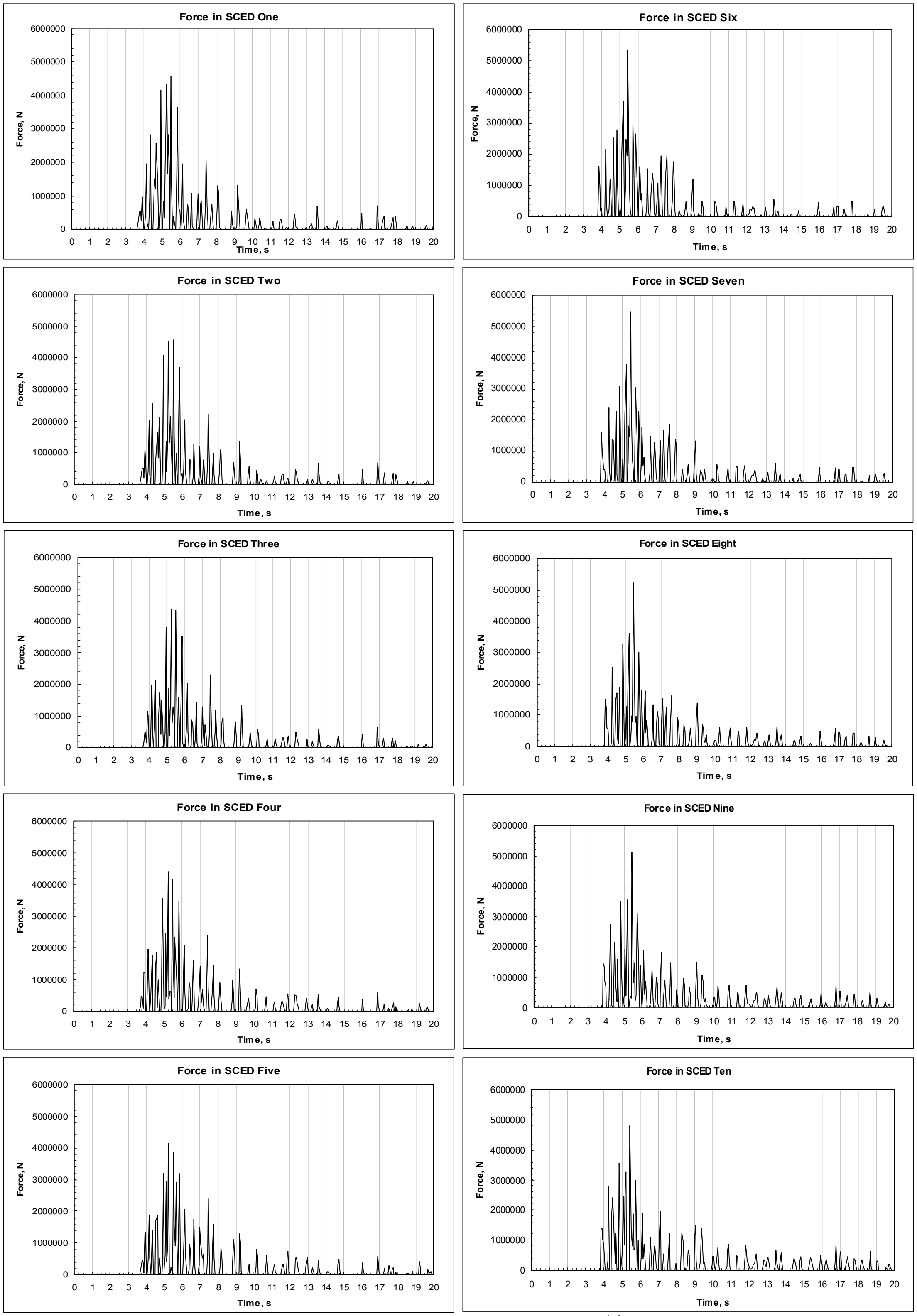

Figure D.156 - Span3, Northridge 3D input, SCED k = 147.6MN/m$^{1.3}$, snap load histories

D.4 Span4 Figures

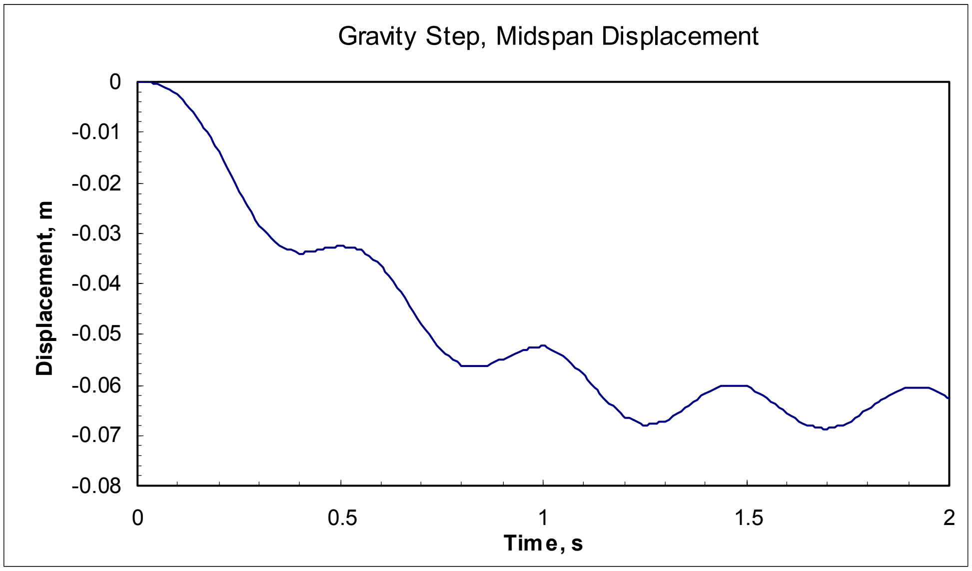

Figure D.157 - Span4, Imperial Valley input, gravity step response

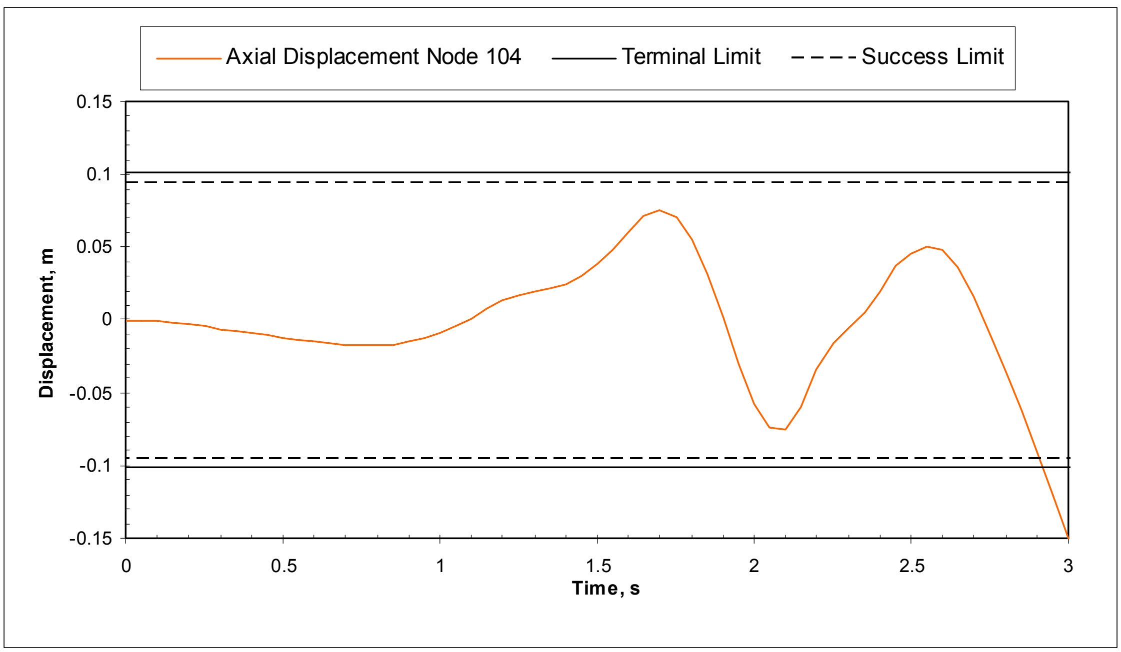

Figure D.158 - Span4, Imperial Valley axial input only, node 104 axial displacement

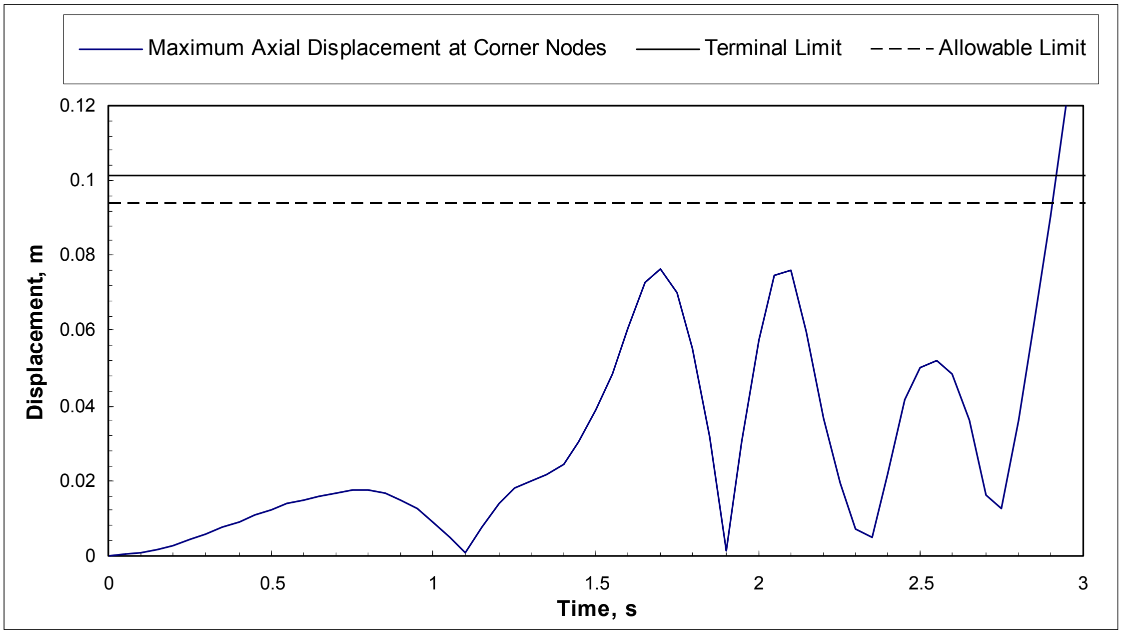

Figure D.159 - Span4, Imperial Valley axial input only, maximum axial displacement

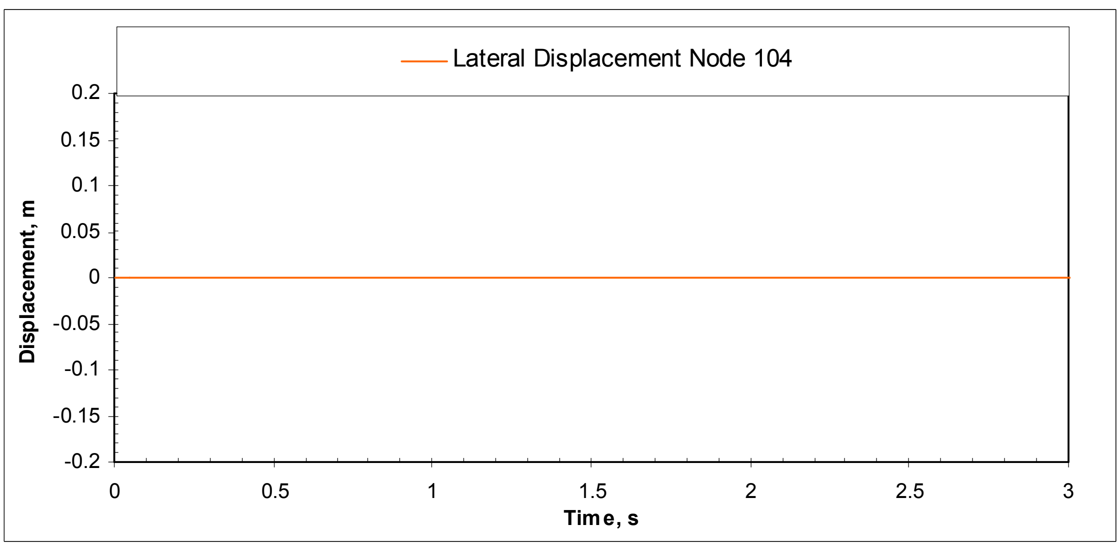

Figure D.160 - Span4, Imperial Valley axial input only, node 104 lateral displacement

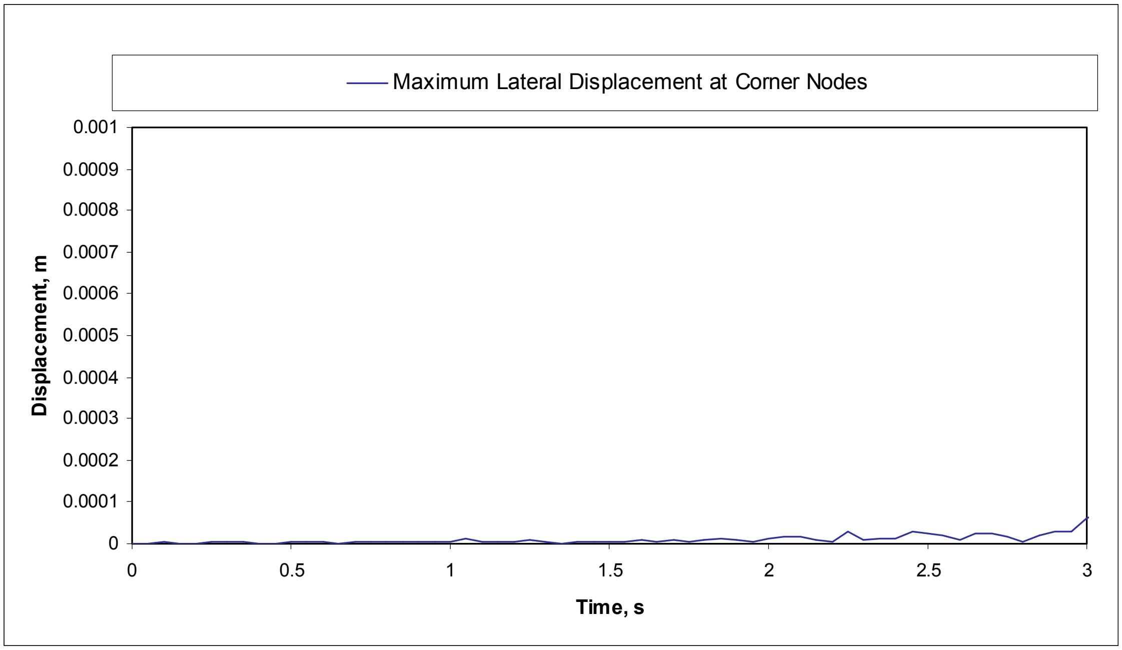

Figure D.161 - Span4, Imperial Valley axial input only, maximum lateral displacement

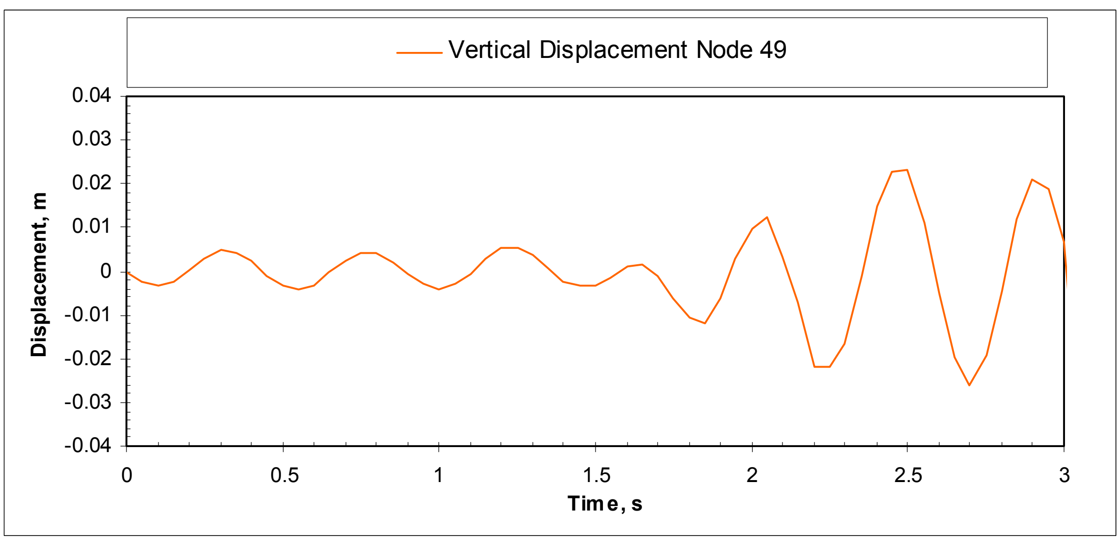

Figure D.162 - Span4, Imperial Valley axial input only, node 49 vertical displacement

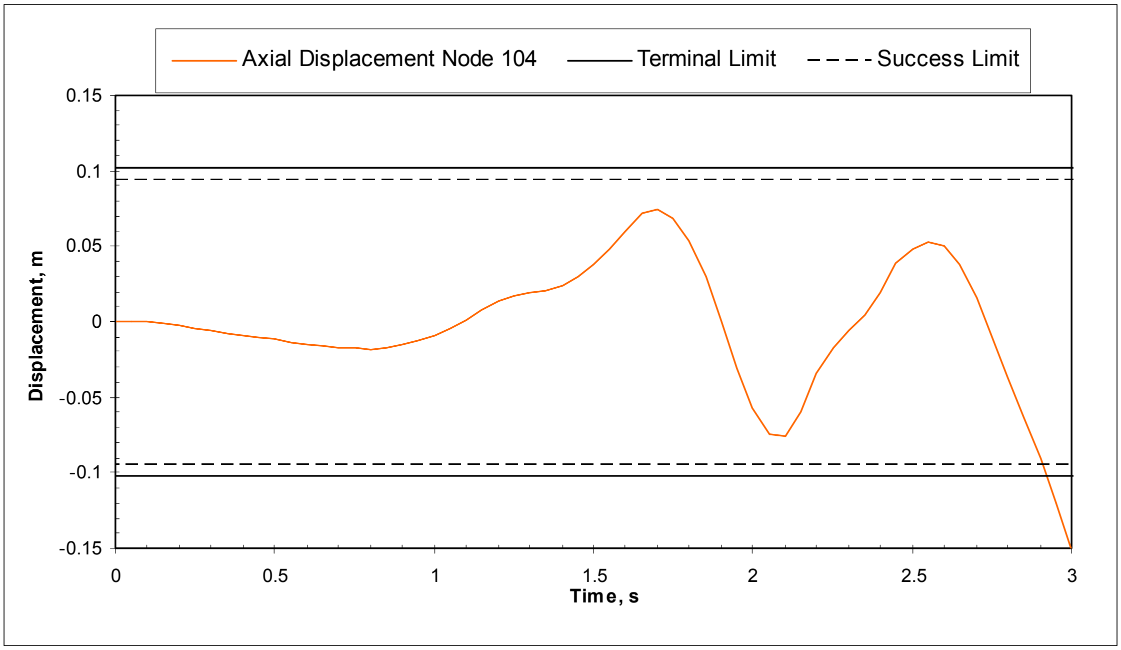

Figure D.163 - Span4, Imperial Valley 3D input, no SCEDs, node 104 axial displacement

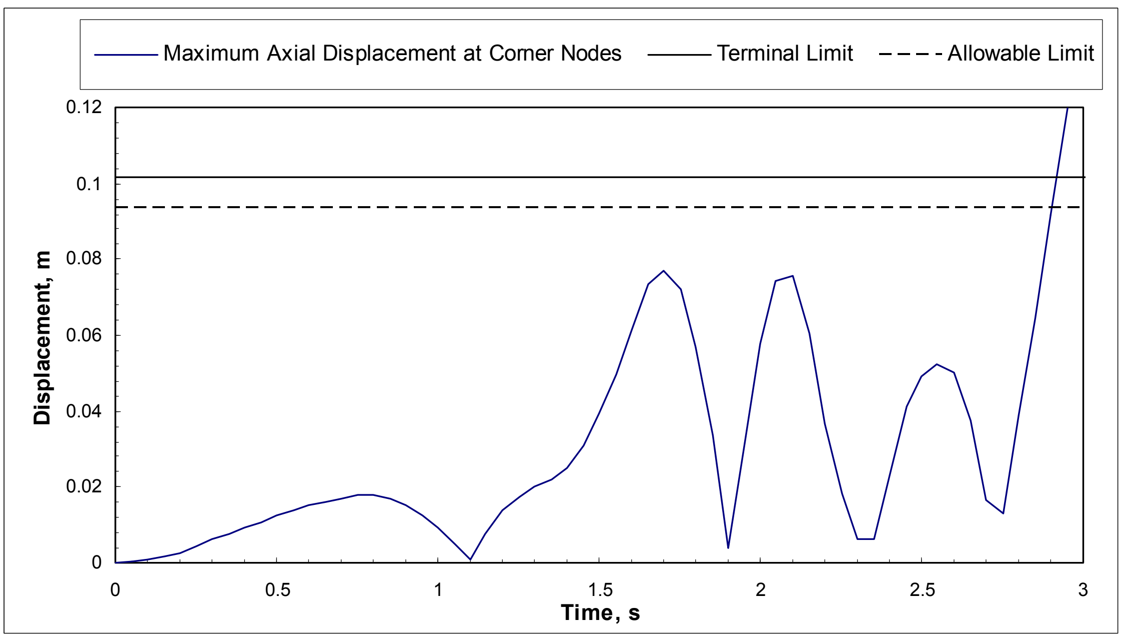

Figure D.164 - Span4, Imperial Valley 3D input, no SCEDs, maximum axial displacement

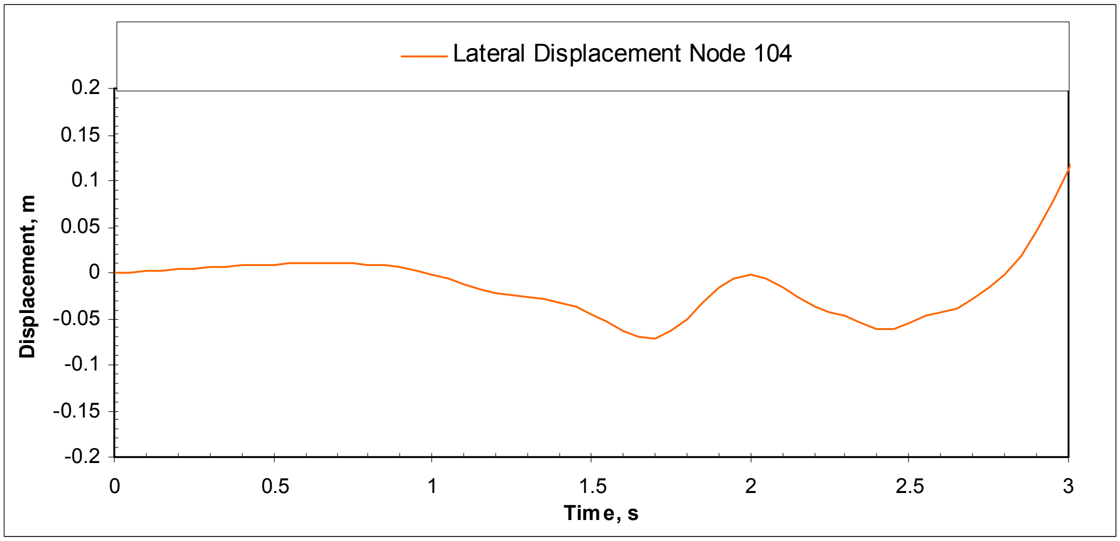

Figure D.165 - Span4, Imperial Valley 3D input, no SCEDs, node 104 lateral displacement

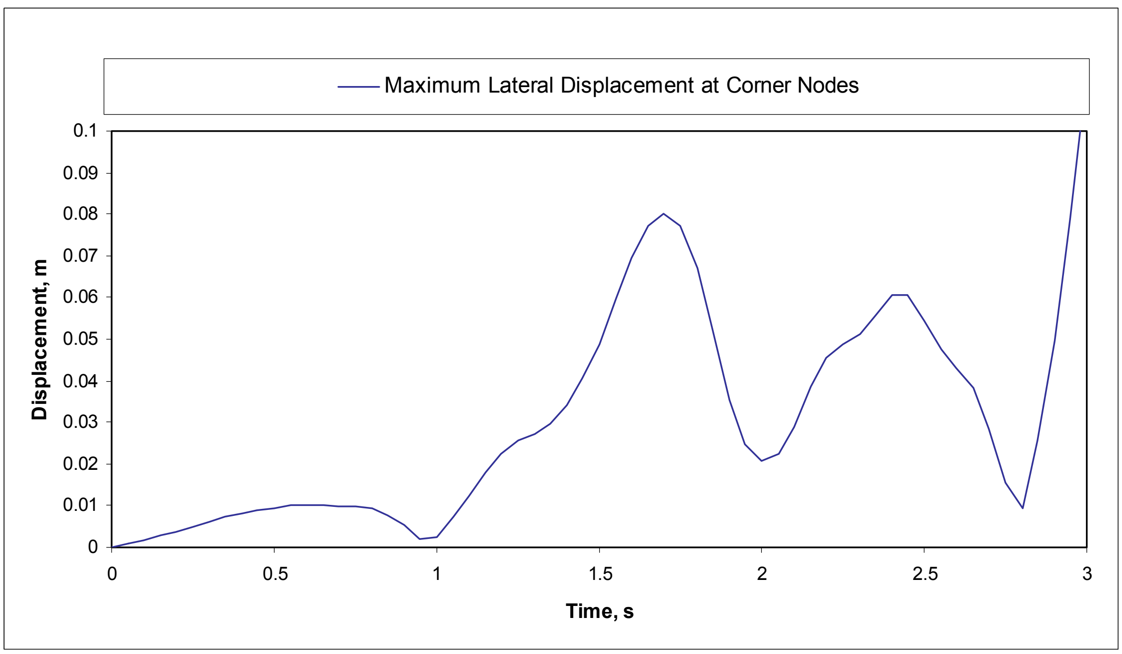

Figure D.166 - Span4, Imperial Valley 3D input, no SCEDs, maximum lateral displacement

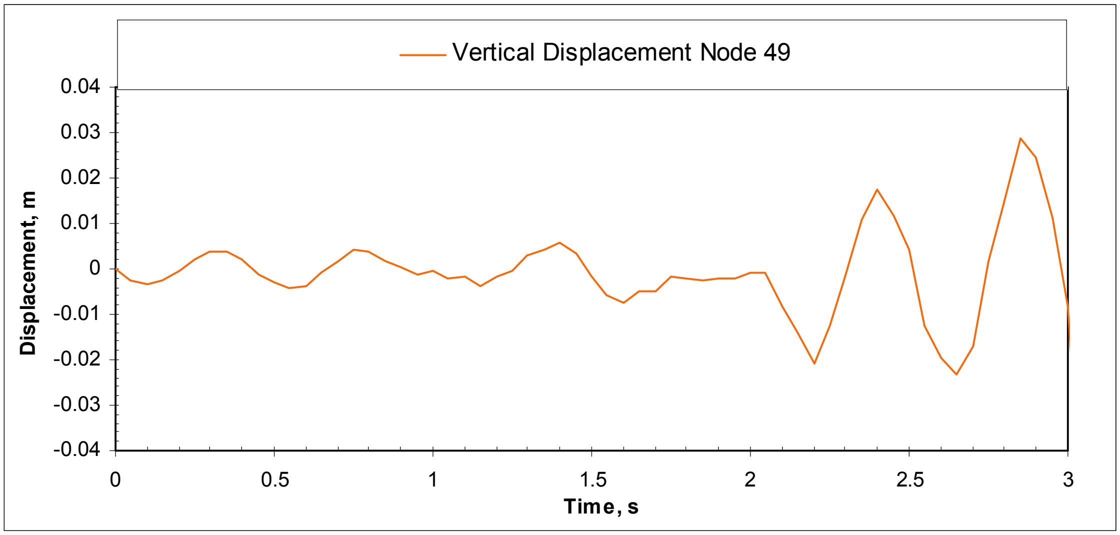

Figure D.167 - Span4, Imperial Valley 3D input, no SCEDs, node 49 vertical displacement

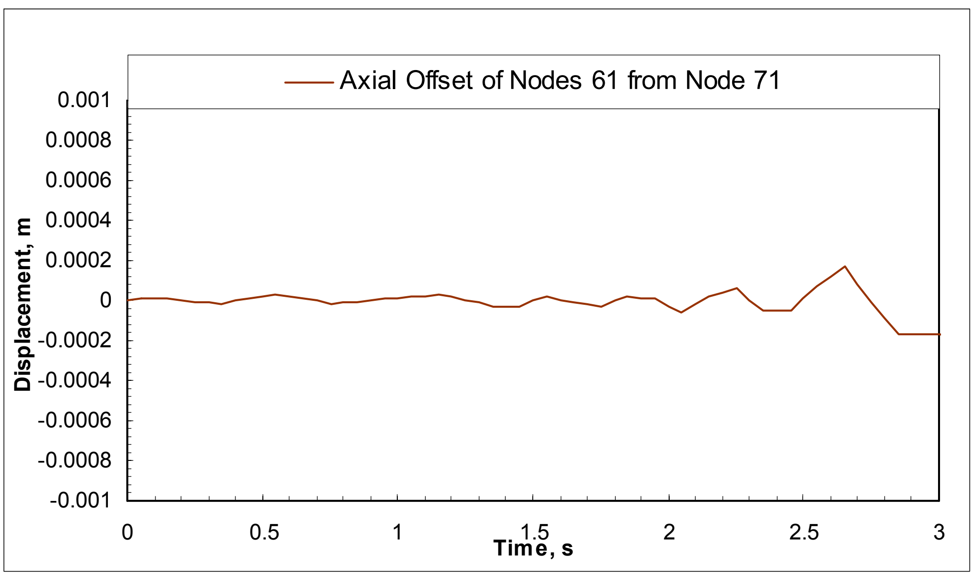

Figure D.168 - Span4, Imperial Valley 3D input, no SCEDs, node 61 and 71 response

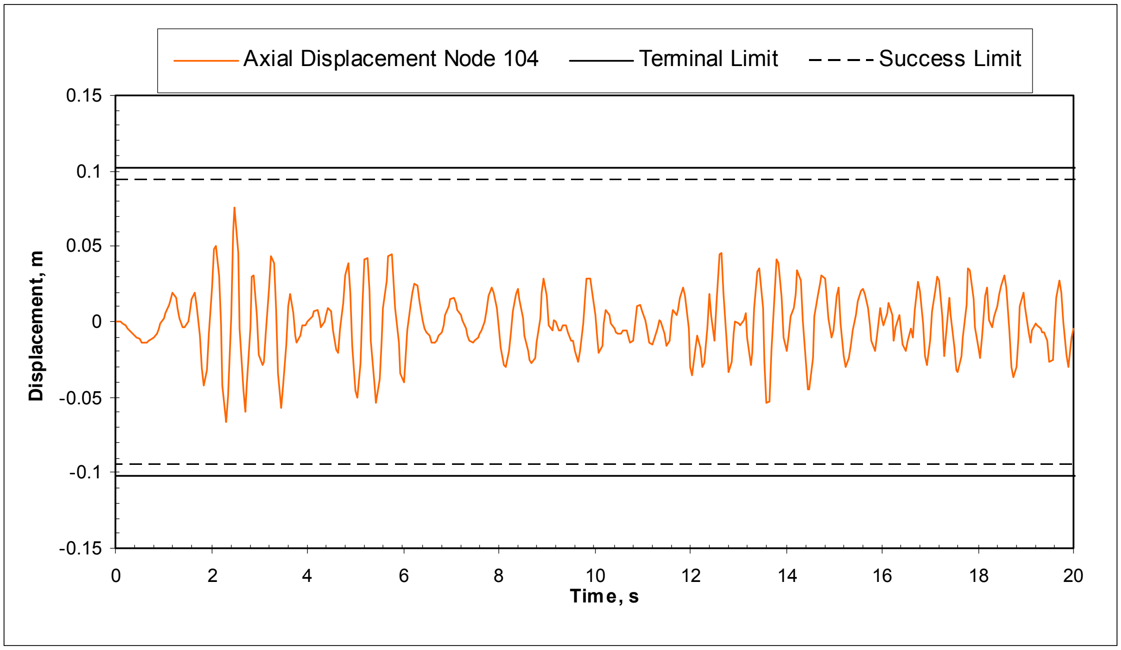

Figure D.169 - Span4, Imperial Valley 3D input, SCED k = 131.8MN/m$^{1.3}$, node 104 axial displacement

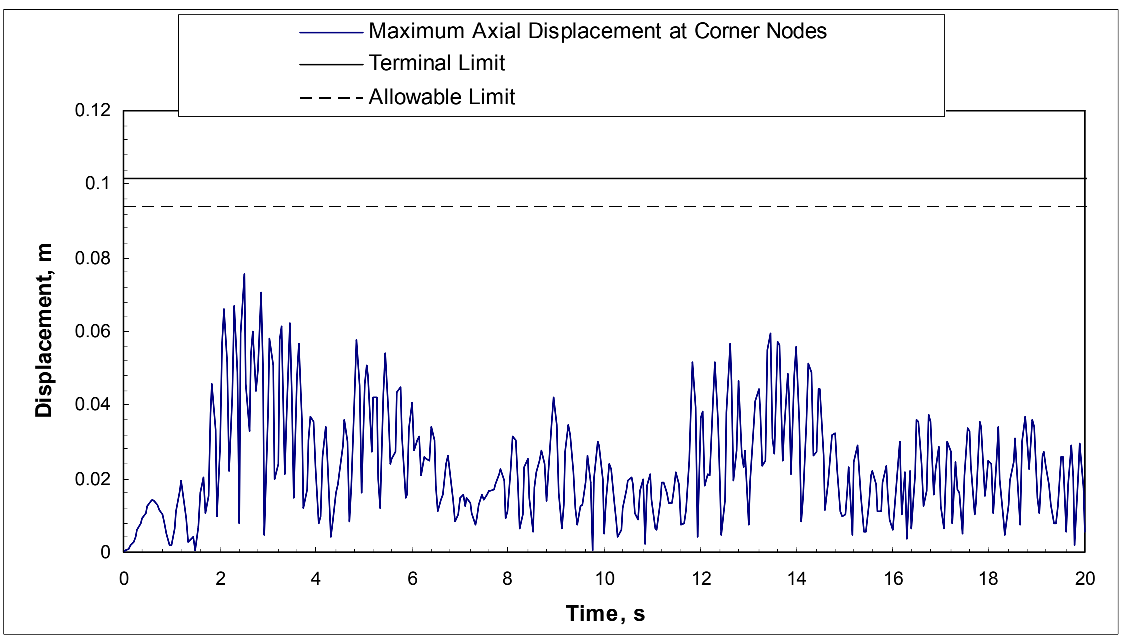

Figure D.170 - Span4, Imperial Valley 3D input, SCED k = 131.8MN/m$^{1.3}$, maximum axial displacement

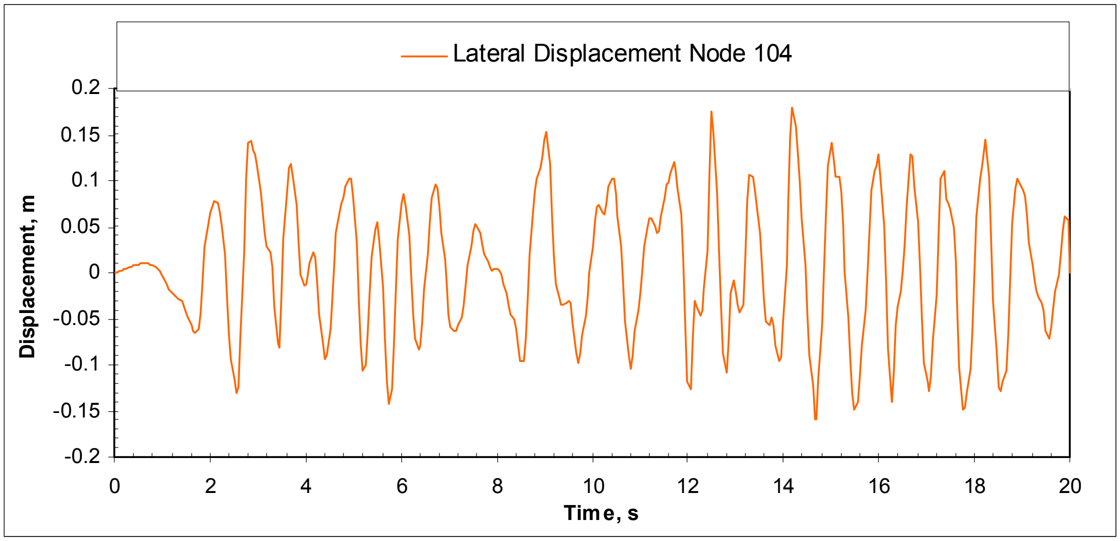

Figure D.171 - Span4, Imperial Valley 3D input, SCED k = 131.8MN/$m^{1.3}$, node 104 lateral disp.

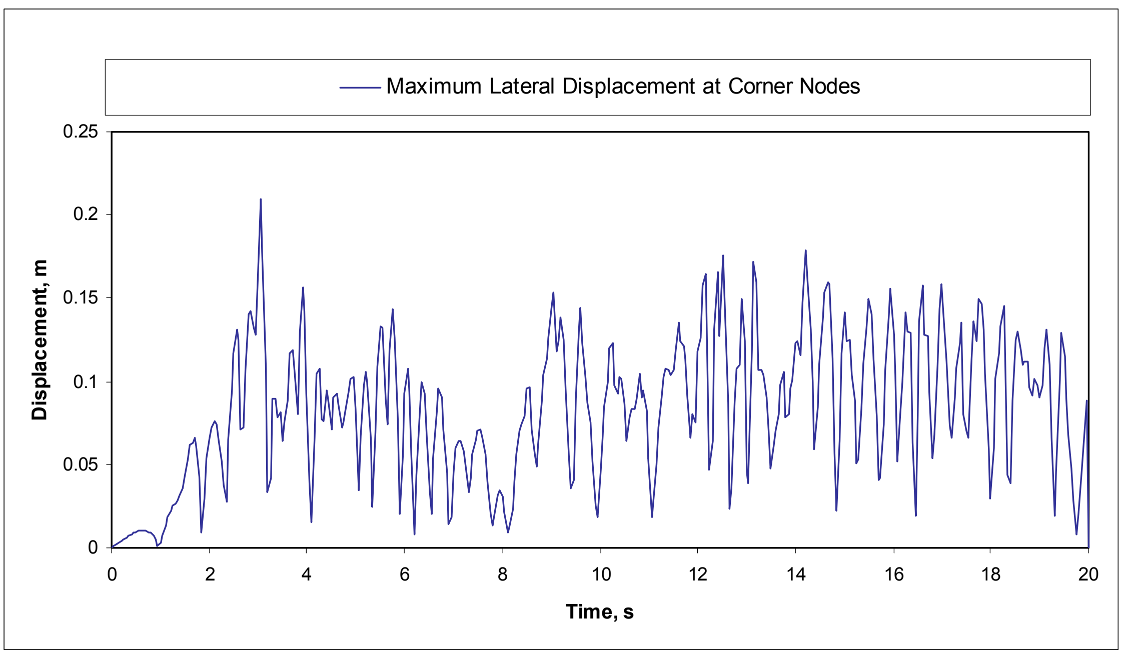

Figure D.172 - Span4, Imperial Valley 3D input, SCED k = 131.8MN/$m^{1.3}$, maximum lateral disp.

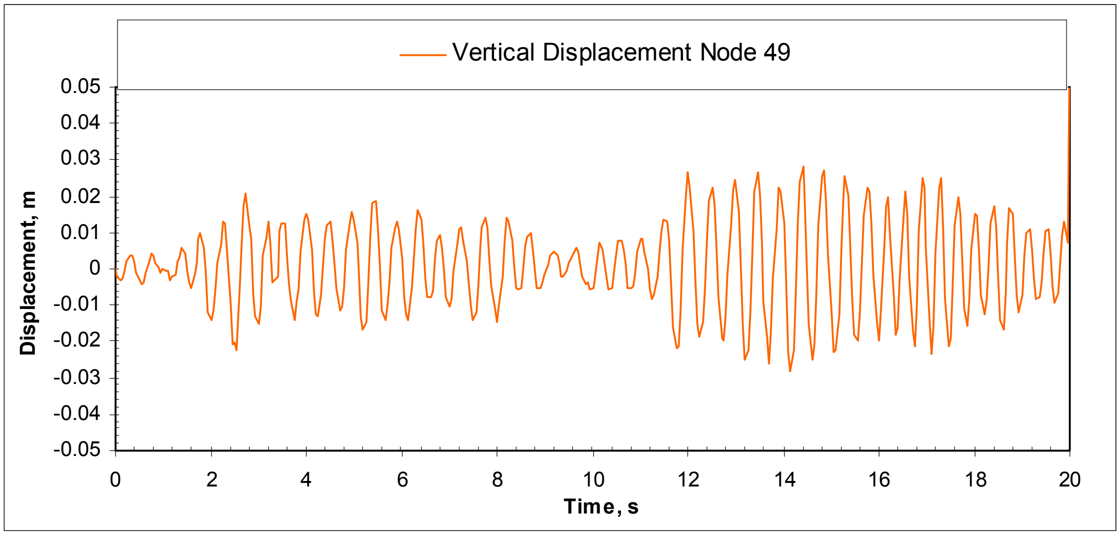

Figure D.173 - Span4, Imperial Valley 3D input, SCED k = 131.8MN/$m^{1.3}$, node 49 vertical disp.

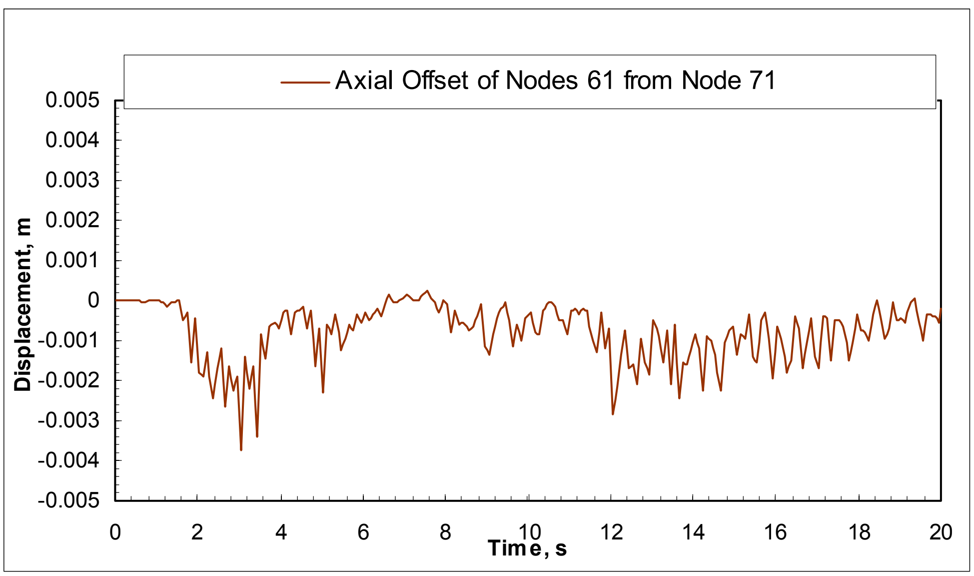

Figure D.174 - Span4, Imperial Valley 3D input, SCED k = 131.8MN/$m^{1.3}$, node 61 and 71 response

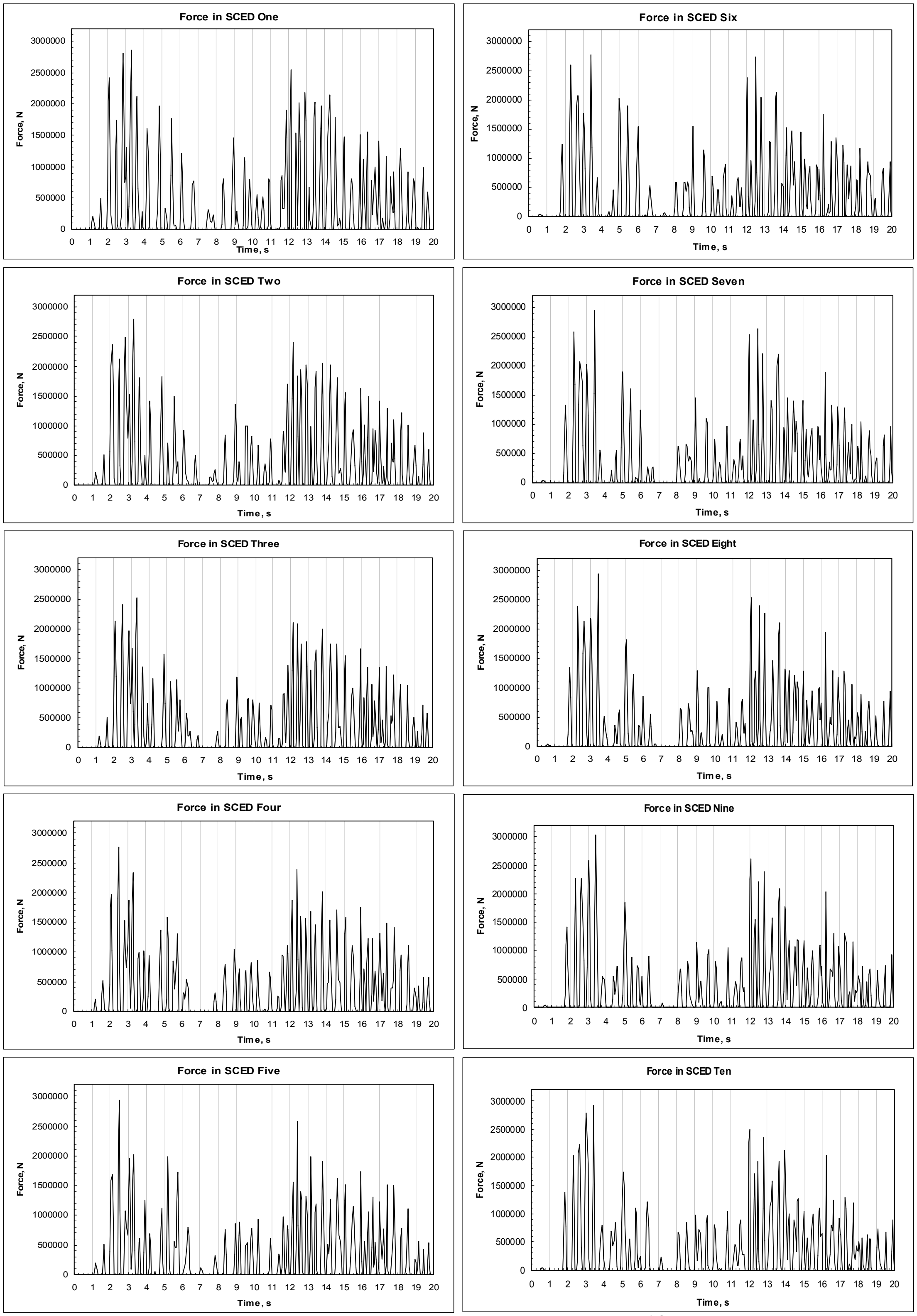

Figure D.175 - Span4, Imperial Valley 3D input, SCED k = 131.8MN/m$^{1.3}$, snap load histories

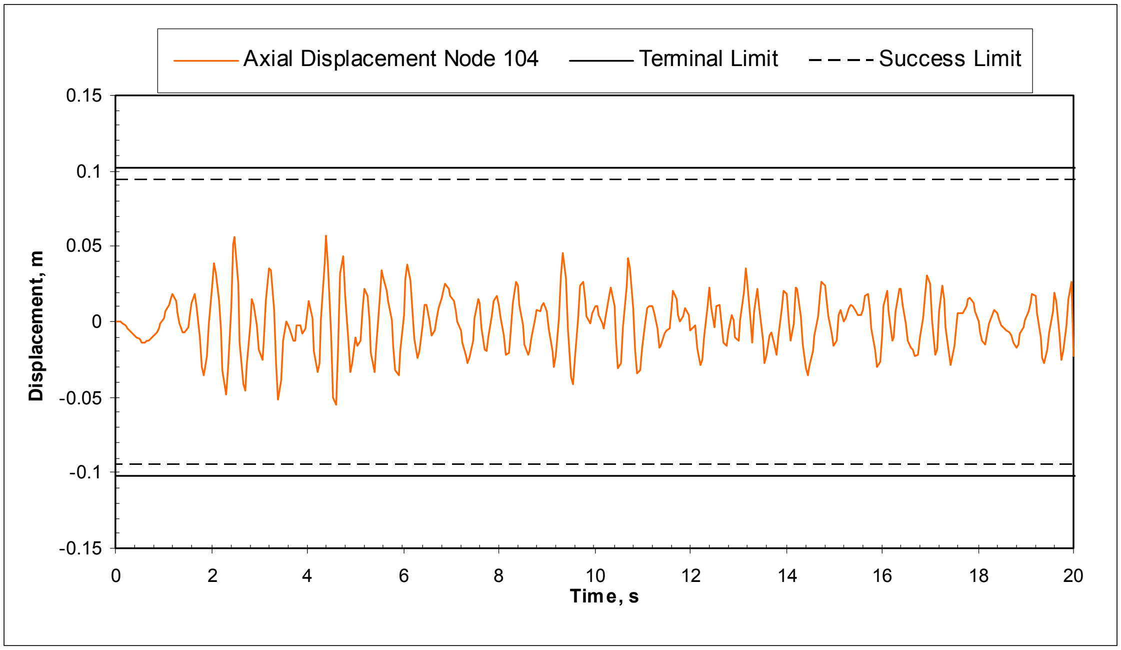

Figure D.176 - Span4, Imperial Valley 3D input, SCED k = 179.2MN/m$^{1.3}$, node 104 axial displacement

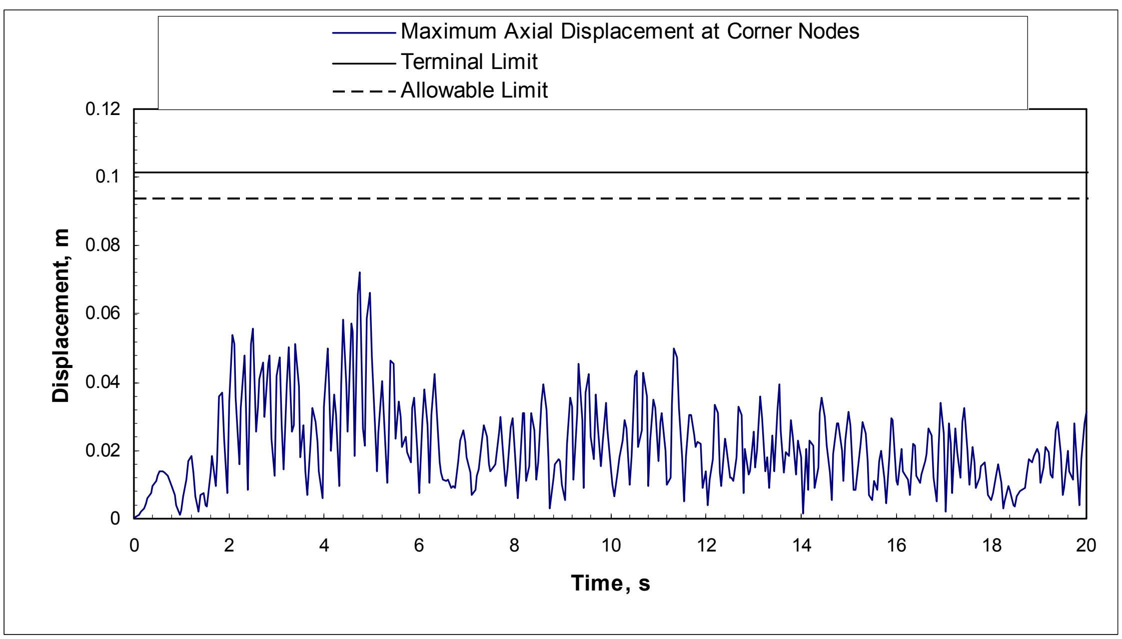

Figure D.177 - Span4, Imperial Valley 3D input, SCED k = 179.2MN/m$^{1.3}$, maximum axial displacement

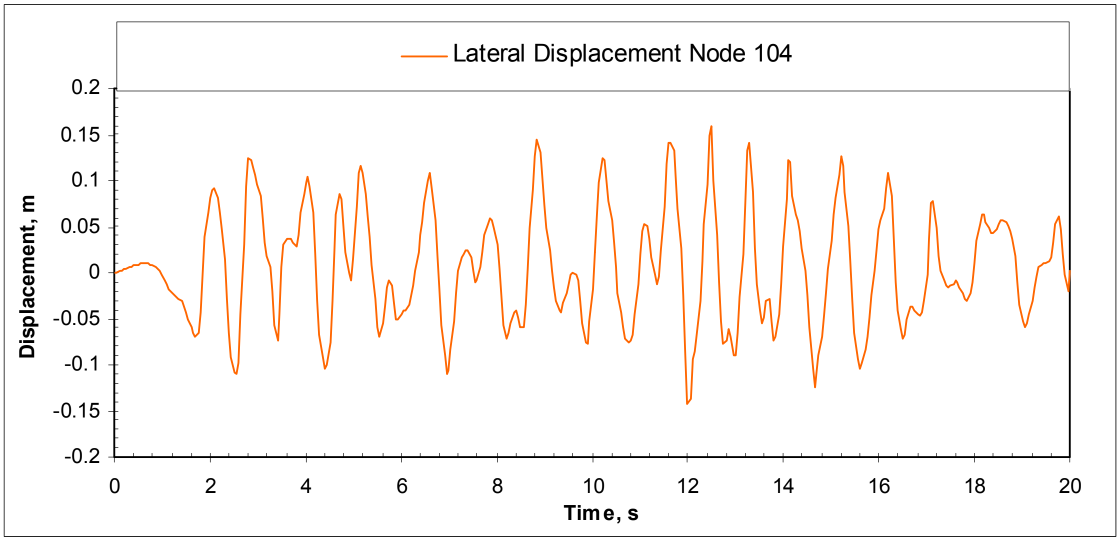

Figure D.178 - Span4, Imperial Valley 3D input, SCED k = 179.2MN/m$^{1.3}$, node 104 lateral disp.

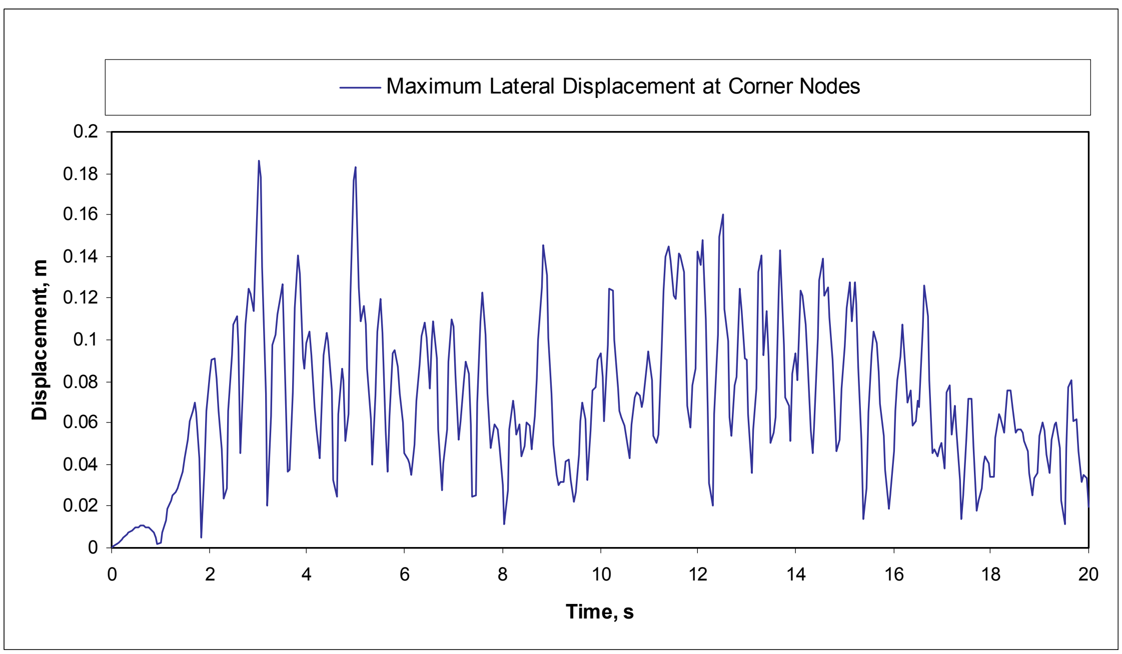

Figure D.179 - Span4, Imperial Valley 3D input, SCED k = 179.2MN/m$^{1.3}$, maximum lateral disp.

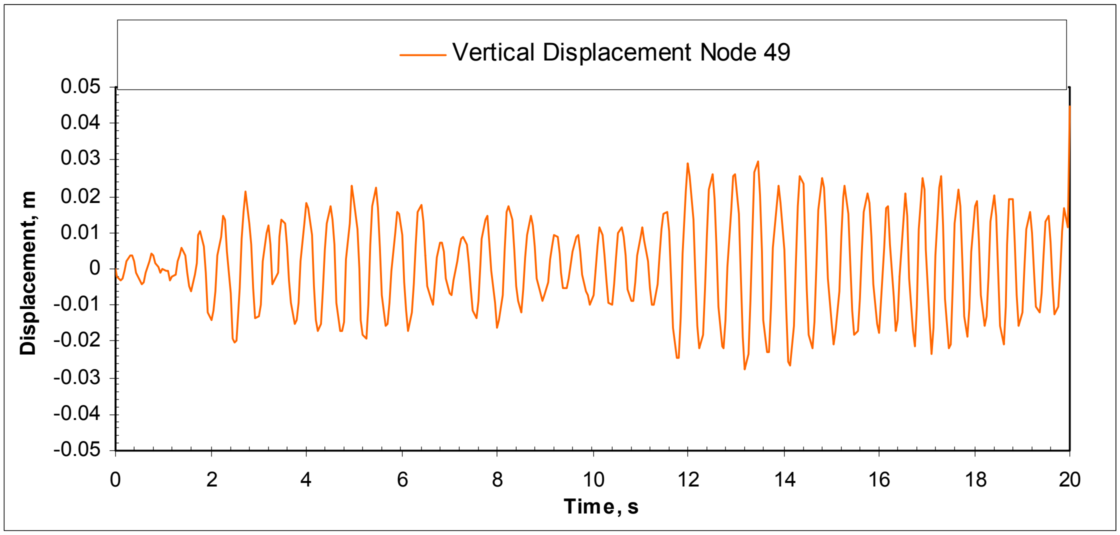

Figure D.180 - Span4, Imperial Valley 3D input, SCED k = 179.2MN/m$^{1.3}$, node 49 vertical disp.

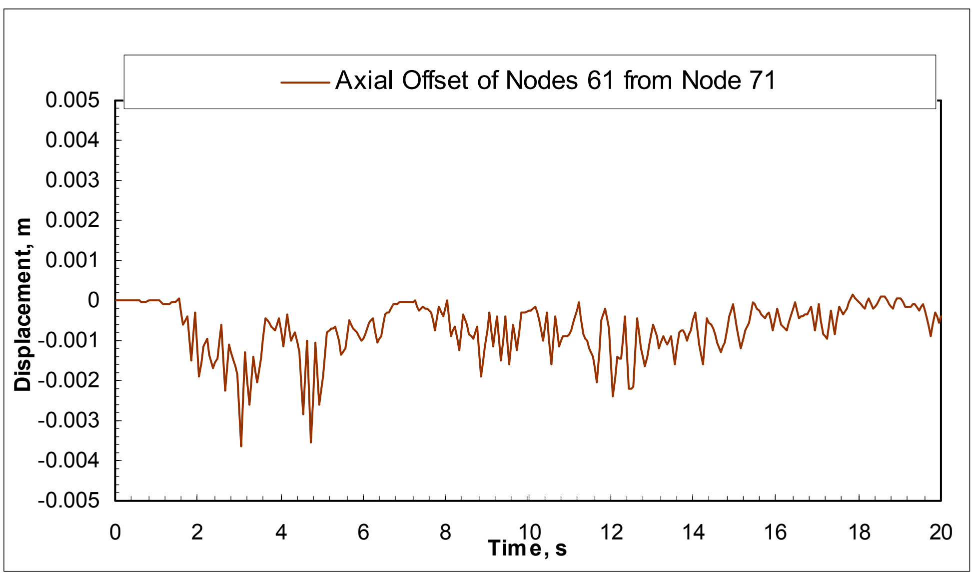

Figure D.181 - Span4, Imperial Valley 3D input, SCED k = 179.2MN/m$^{1.3}$, node 61 and 71 response

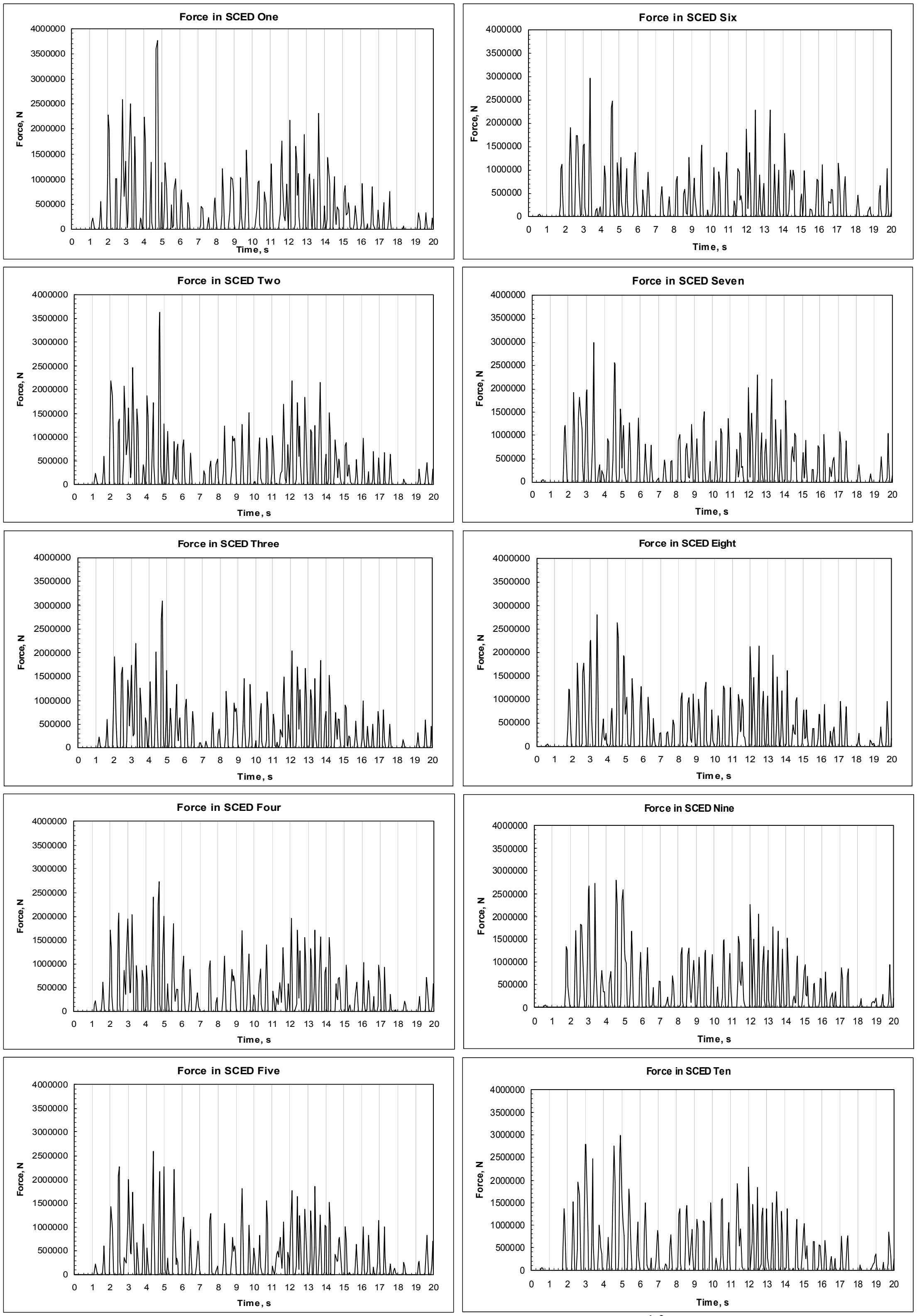

Figure D.182 - Span4, Imperial Valley 3D input, SCED k = 179.2MN/m$^{1.3}$, snap load histories

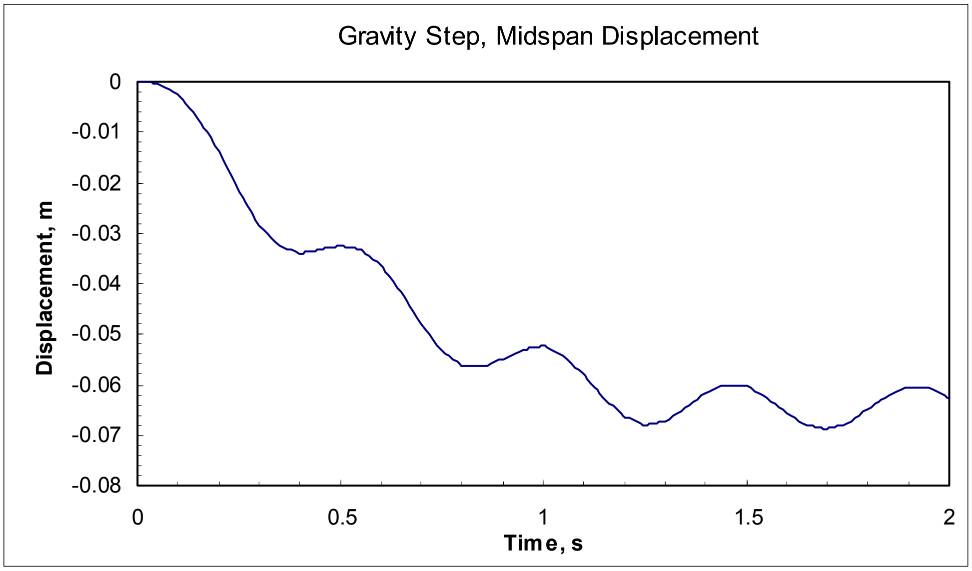

Figure D.183 - Span4, Northridge input, gravity step response

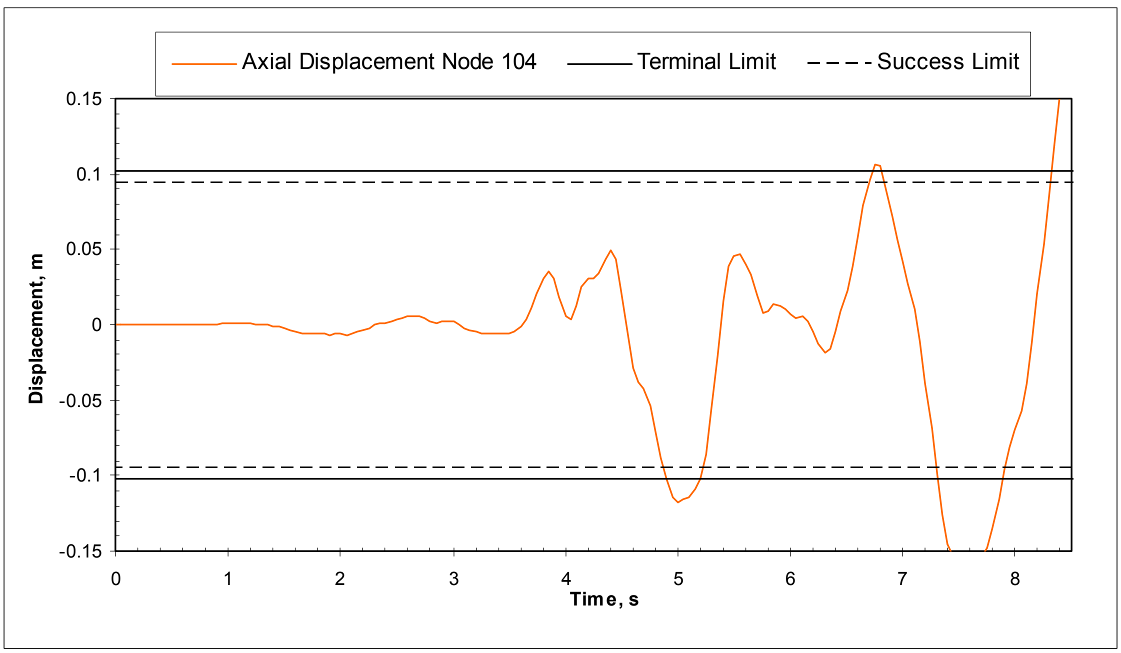

Figure D.184 - Span4, Northridge axial input only, node 104 axial displacement

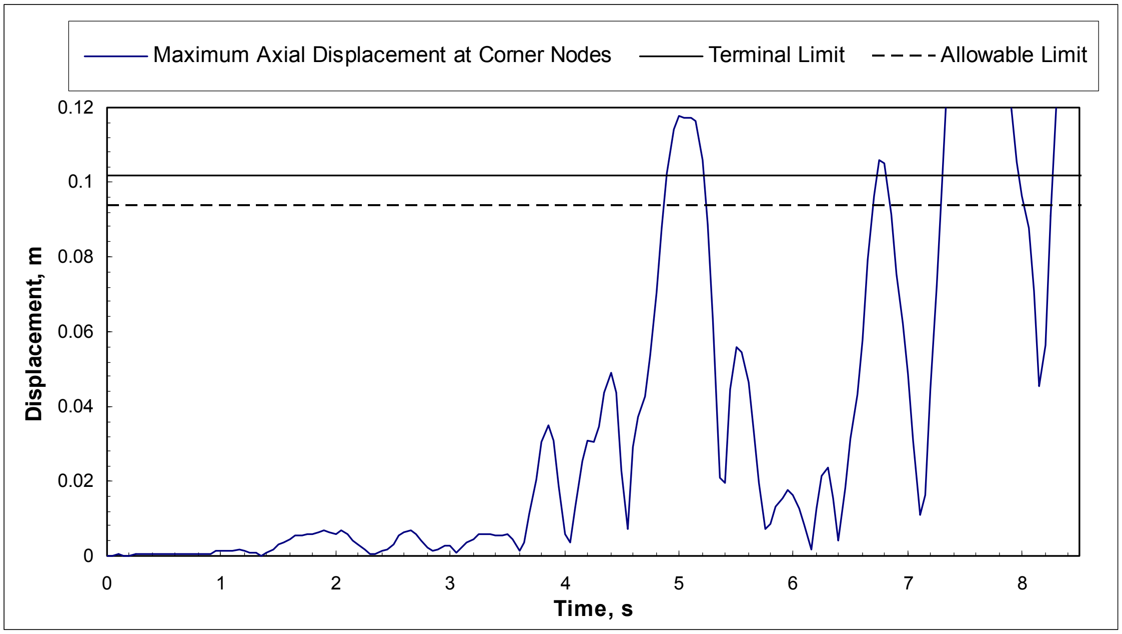

Figure D.185 - Span4, Northridge axial input only, maximum axial displacement

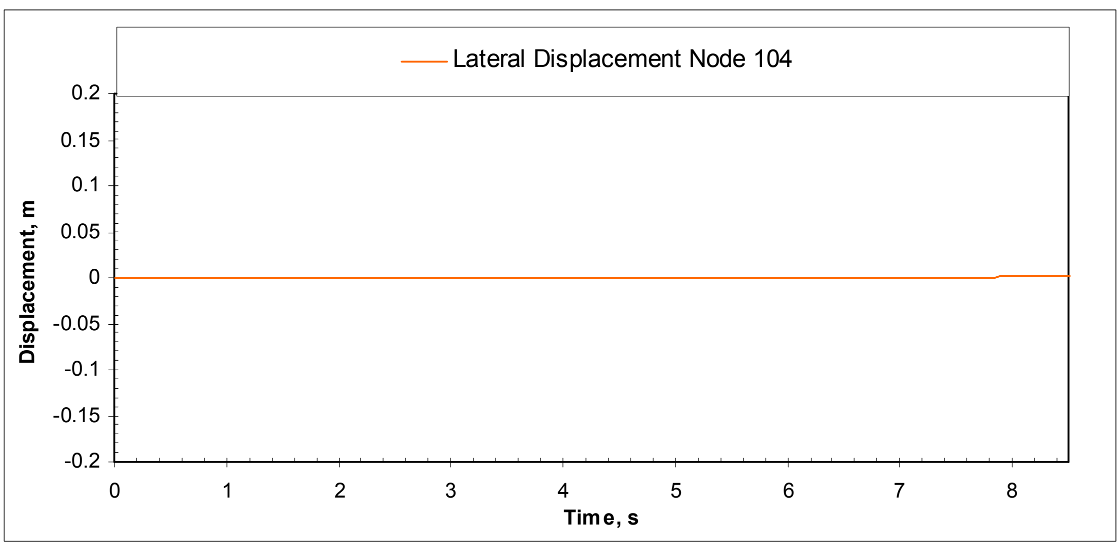

Figure D.186 - Span4, Northridge axial input only, node 104 lateral displacement

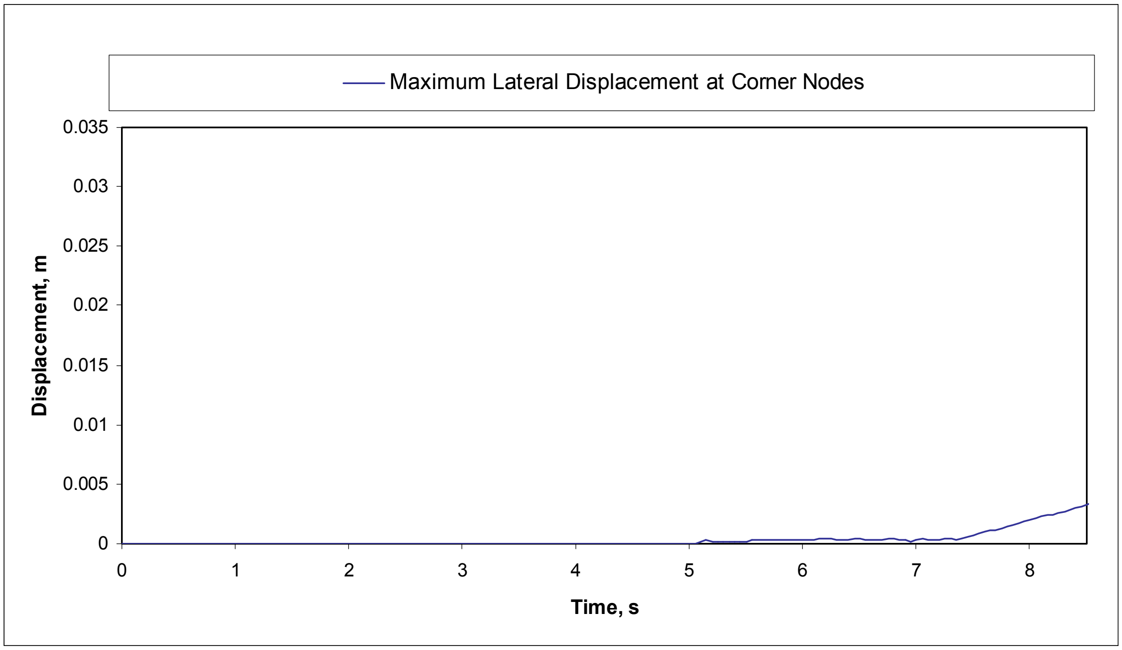

Figure D.187 - Span4, Northridge axial input only, maximum lateral displacement

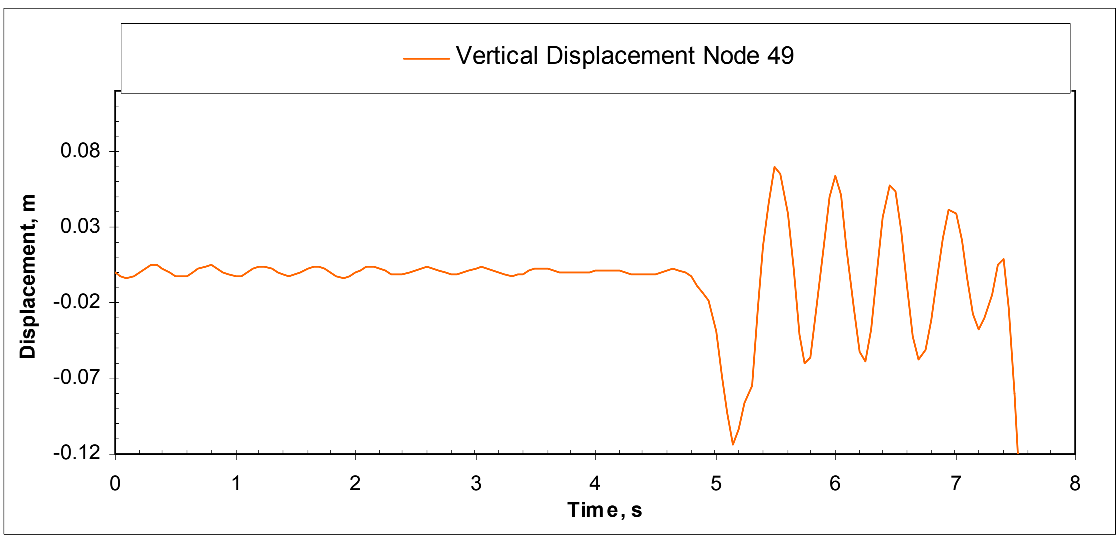

Figure D.188 - Span4, Northridge axial input only, node 49 vertical displacement

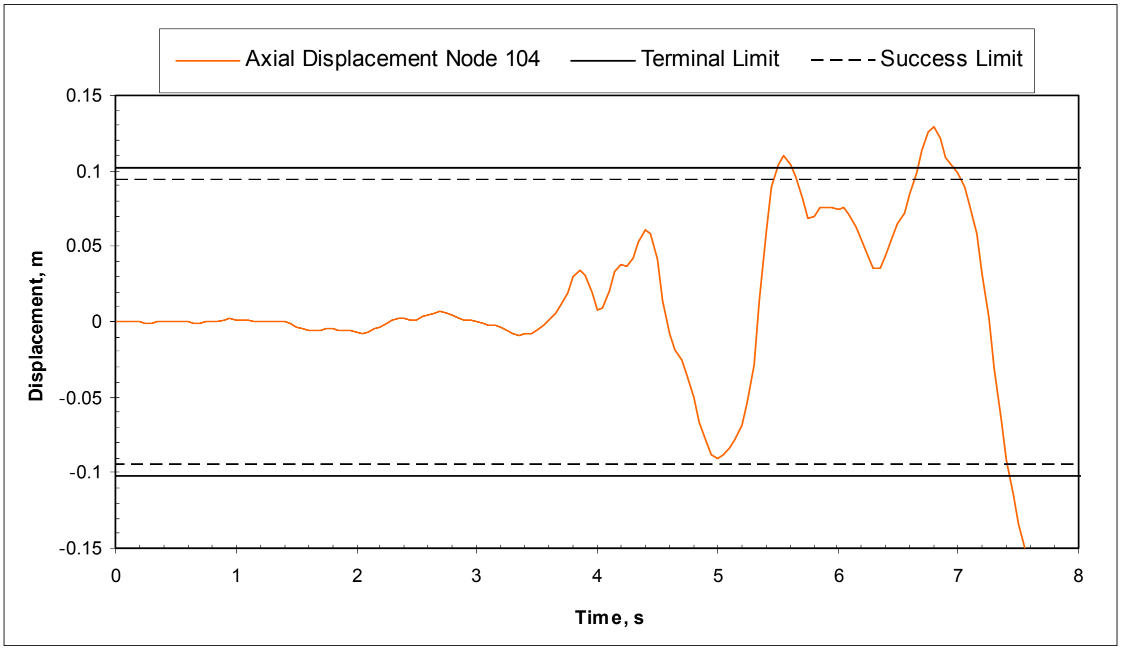

Figure D.189 - Span4, Northridge 3D input, no SCEDs, node 104 axial displacement

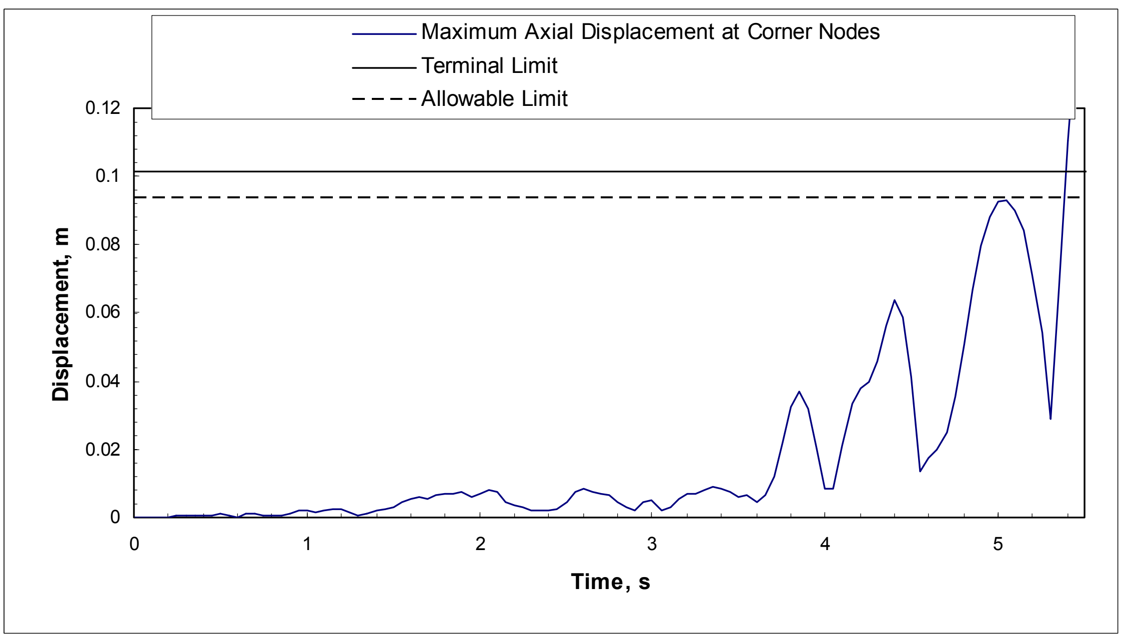

Figure D.190 - Span4, Northridge 3D input, no SCEDs, maximum axial displacement

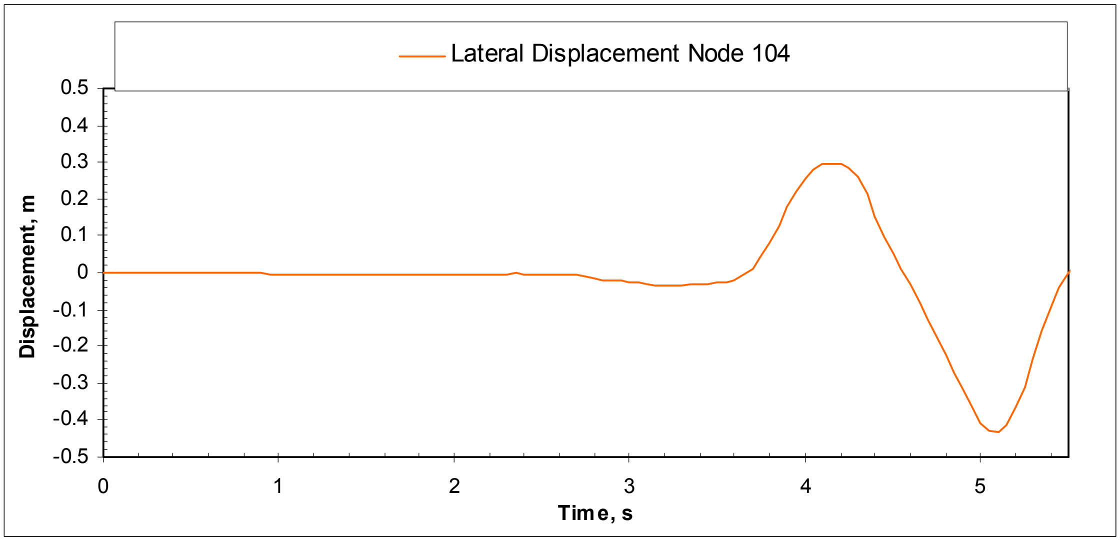

Figure D.191 - Span4, Northridge 3D input, no SCEDs, node 104 lateral displacement

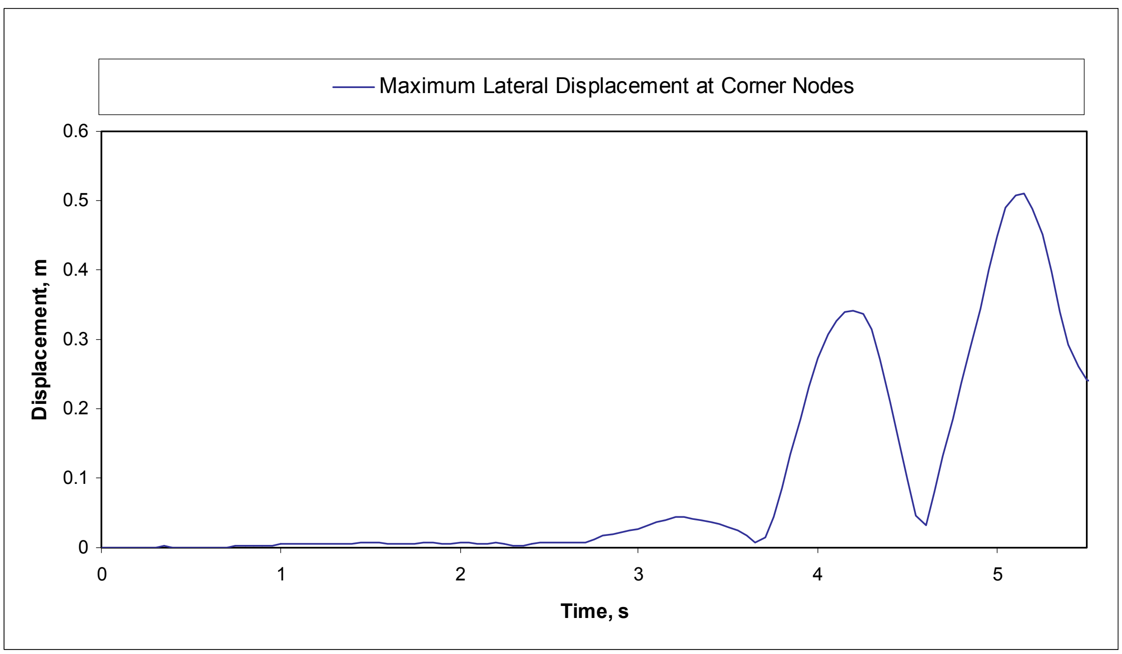

Figure D.192 - Span4, Northridge 3D input, no SCEDs, maximum lateral displacement

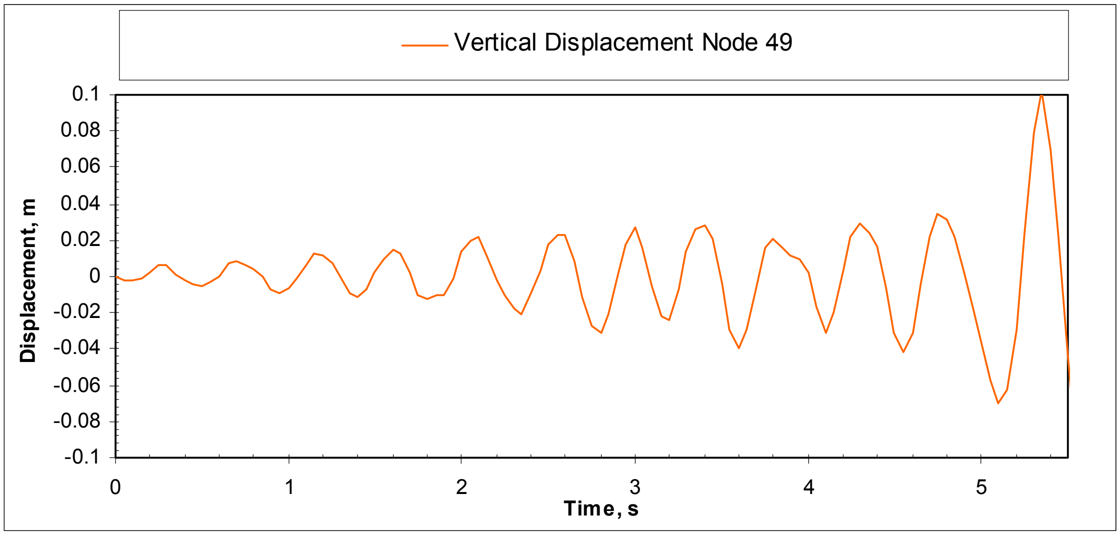

Figure D.193 - Span4, Northridge 3D input, no SCEDs, node 49 vertical displacement

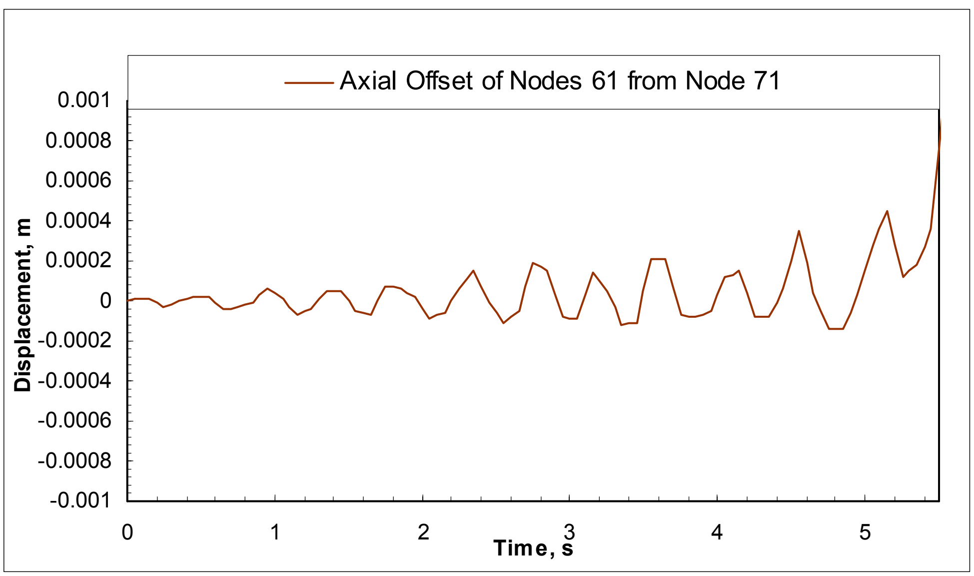

Figure D.194 - Span4, Northridge 3D input, no SCEDs, node 61 and 71 response

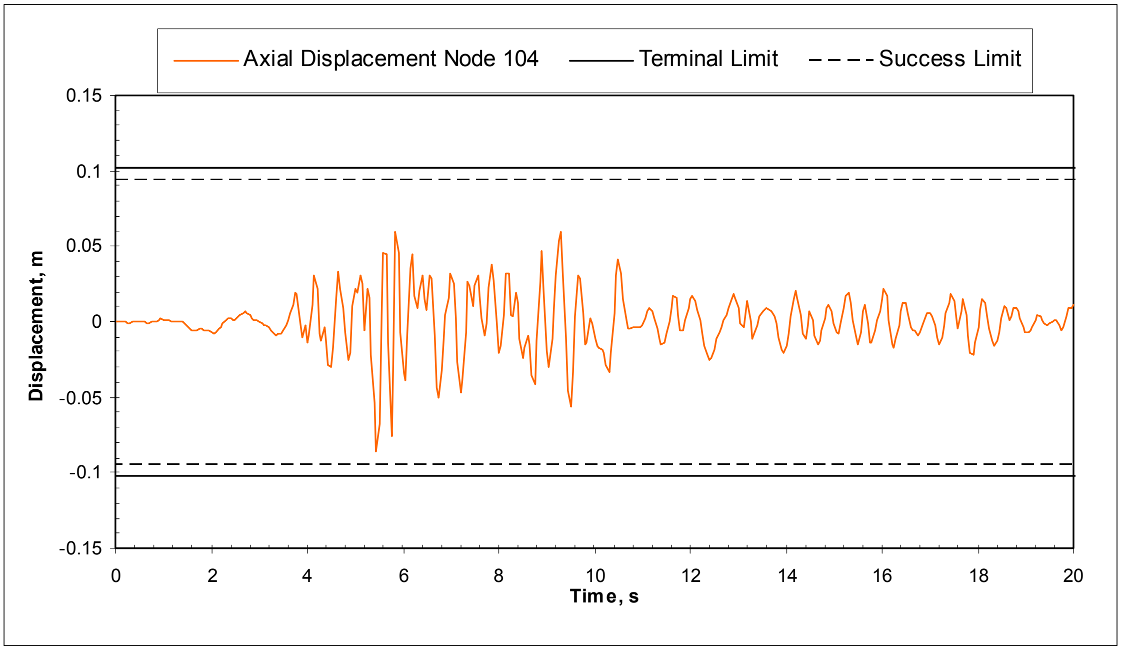

Figure D.195 - Span4, Northridge 3D input, SCED k = 131.8MN/m$^{1.3}$, node 104 axial displacement

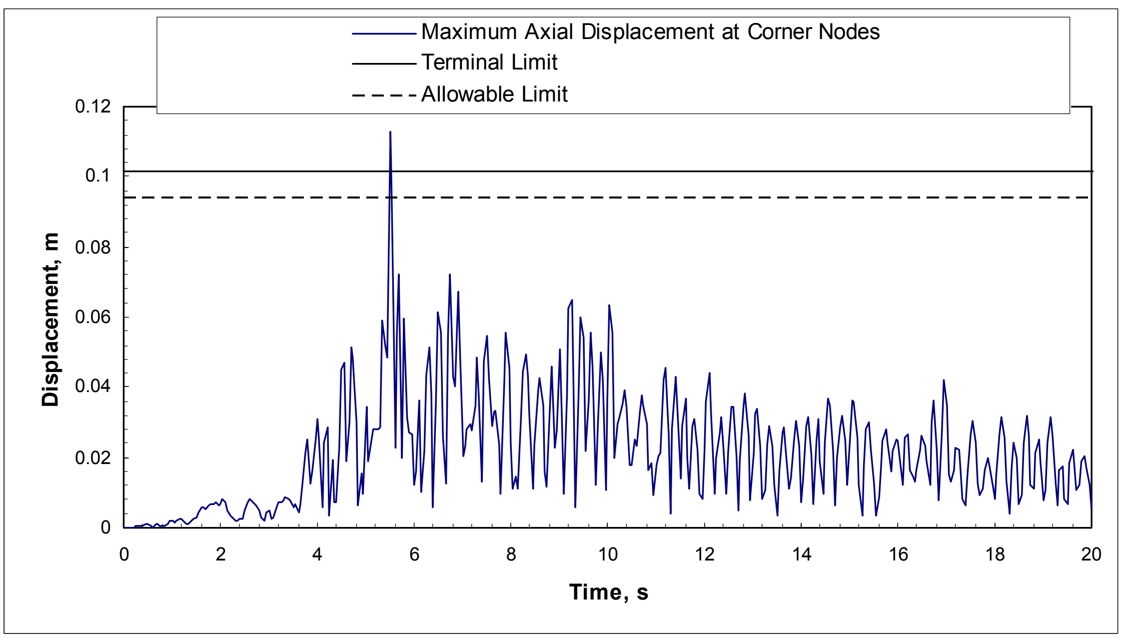

Figure D.196 - Span4, Northridge 3D input, SCED k = 131.8MN/m$^{1.3}$, maximum axial displacement

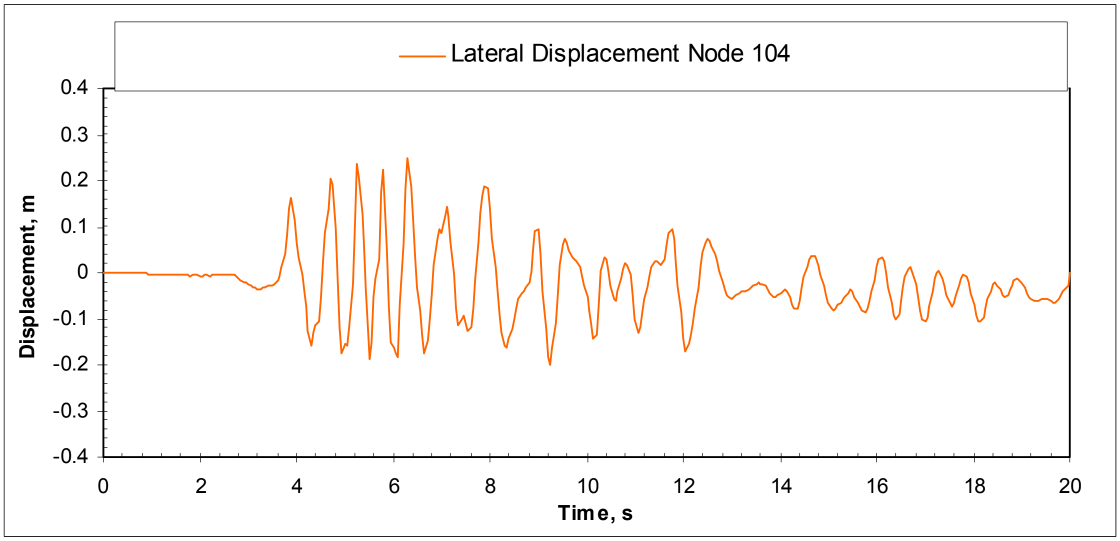

Figure D.197 - Span4, Northridge 3D input, SCED k = 131.8MN/m$^{1.3}$, node 104 lateral displacement

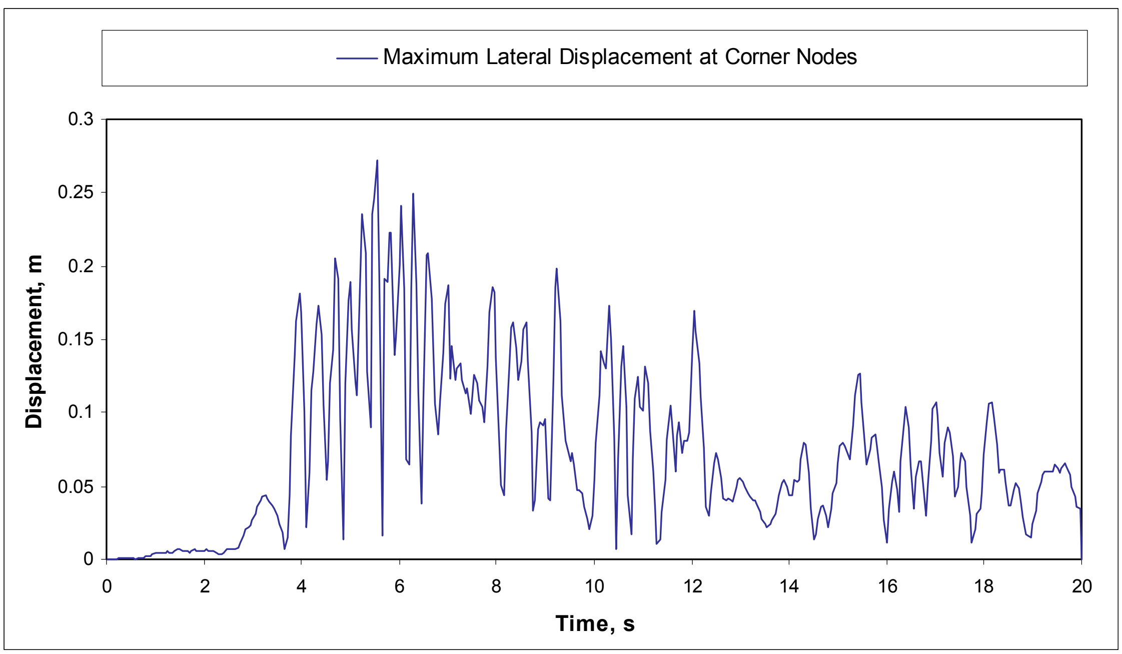

Figure D.198 - Span4, Northridge 3D input, SCED k = 131.8MN/m$^{1.3}$, maximum lateral displacement

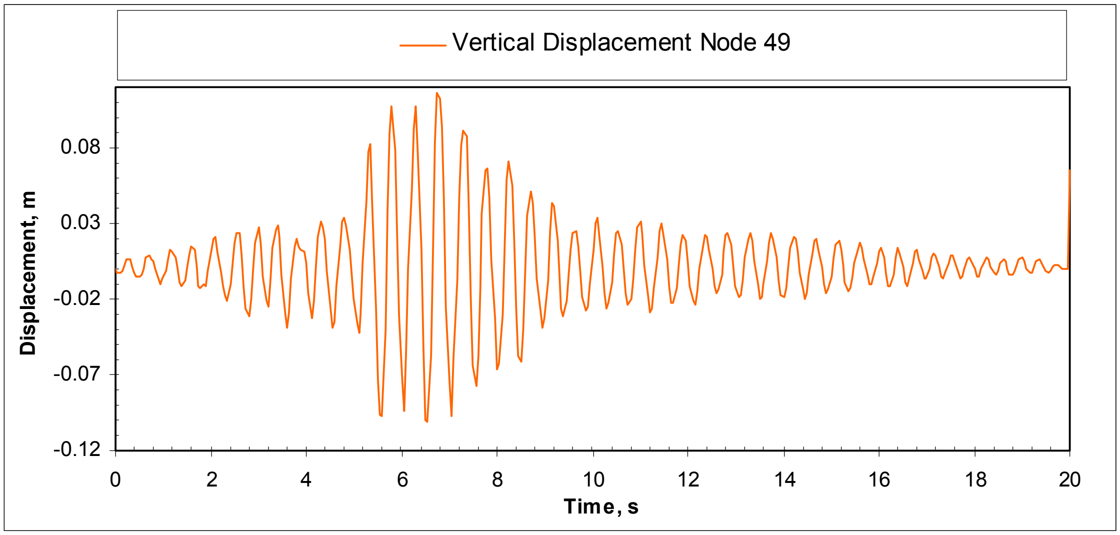

Figure D.199 - Span4, Northridge 3D input, SCED k = 131.8MN/$m^{1.3}$, node 49 vertical displacement

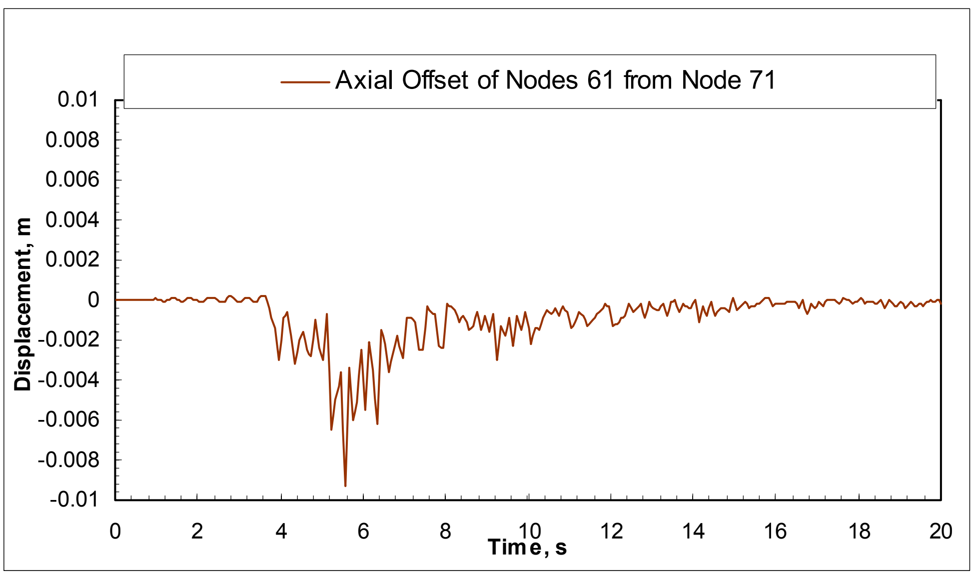

Figure D.200 - Span4, Northridge 3D input, SCED k = 131.8MN/$m^{1.3}$, node 61 and 71 response

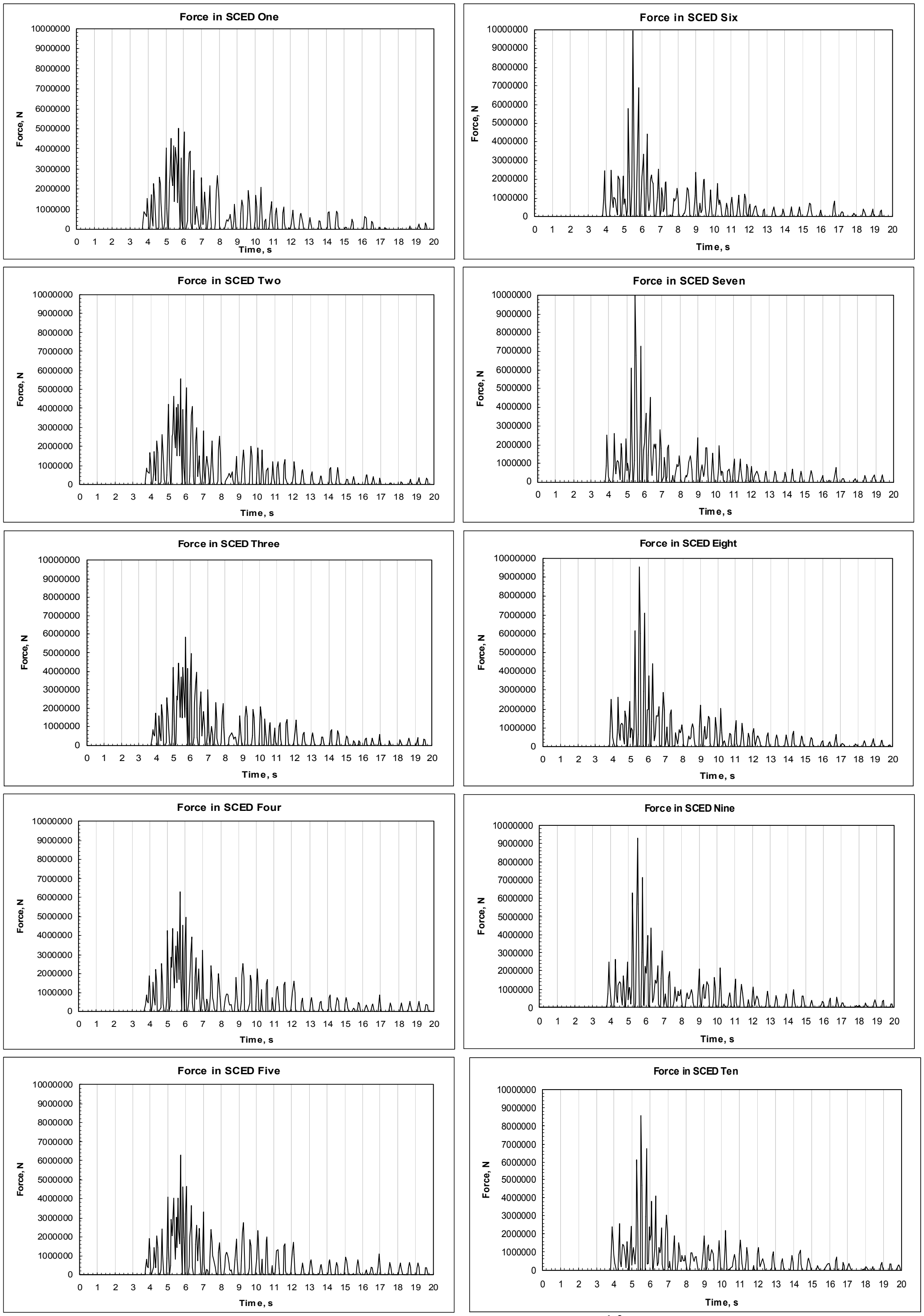

Figure D.201 - Span4, Northridge 3D input, SCED k = 131.8MN/m$^{1.3}$, snap load histories

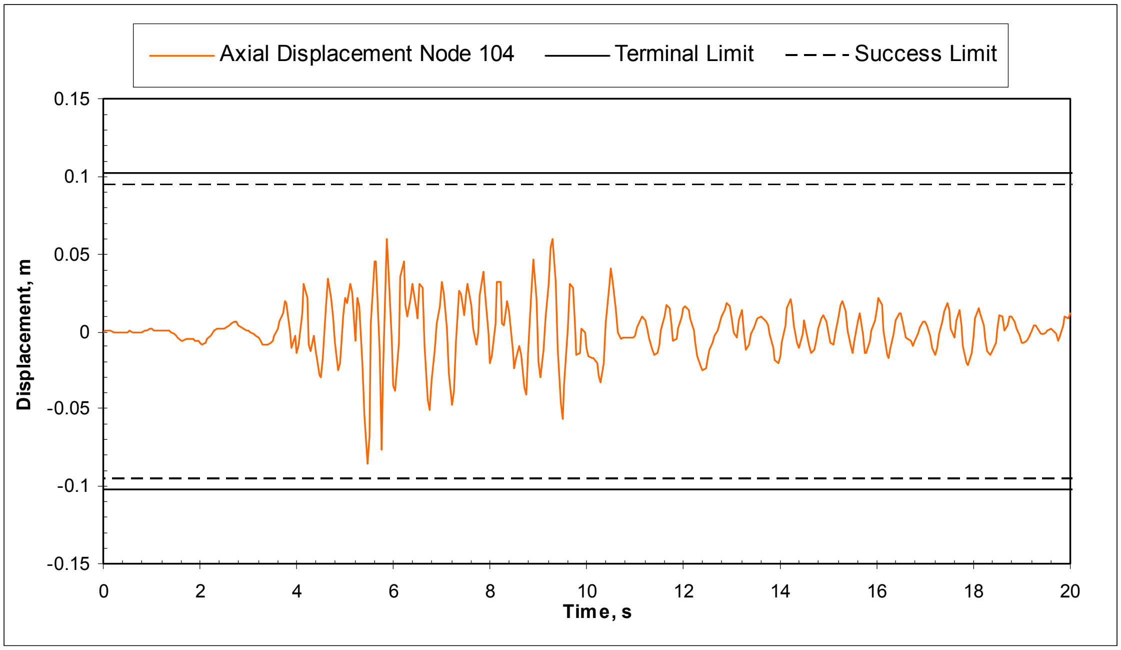

Figure D.202 - Span4, Northridge 3D input, SCED k = 179.2MN/m$^{1.3}$, node 104 axial displacement

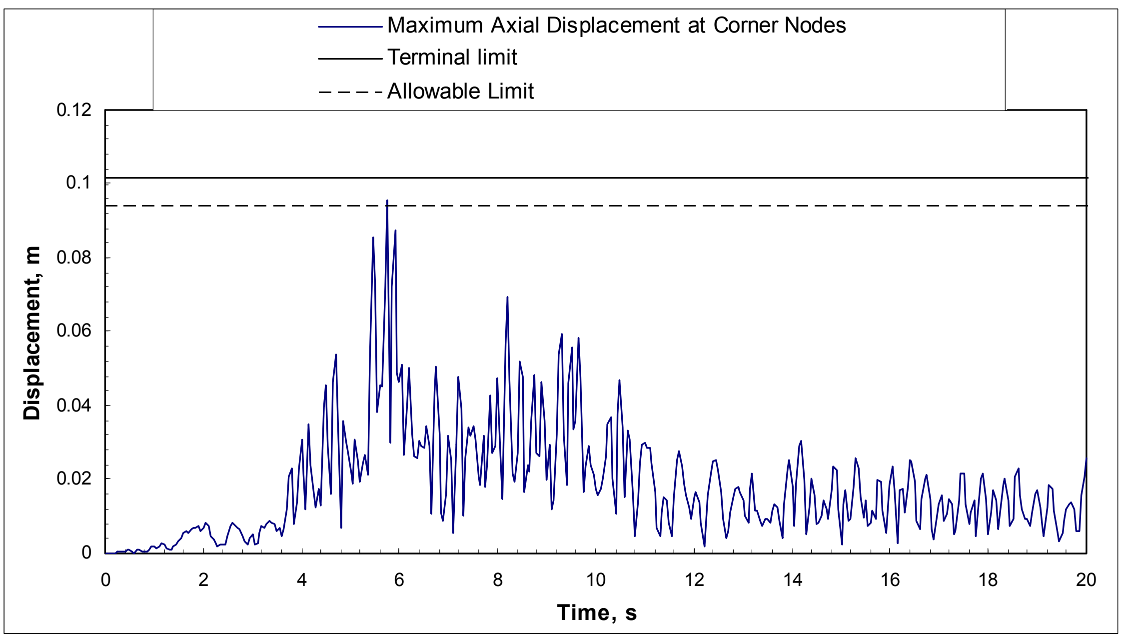

Figure D.203 - Span4, Northridge 3D input, SCED k = 179.2MN/m$^{1.3}$, maximum axial displacement

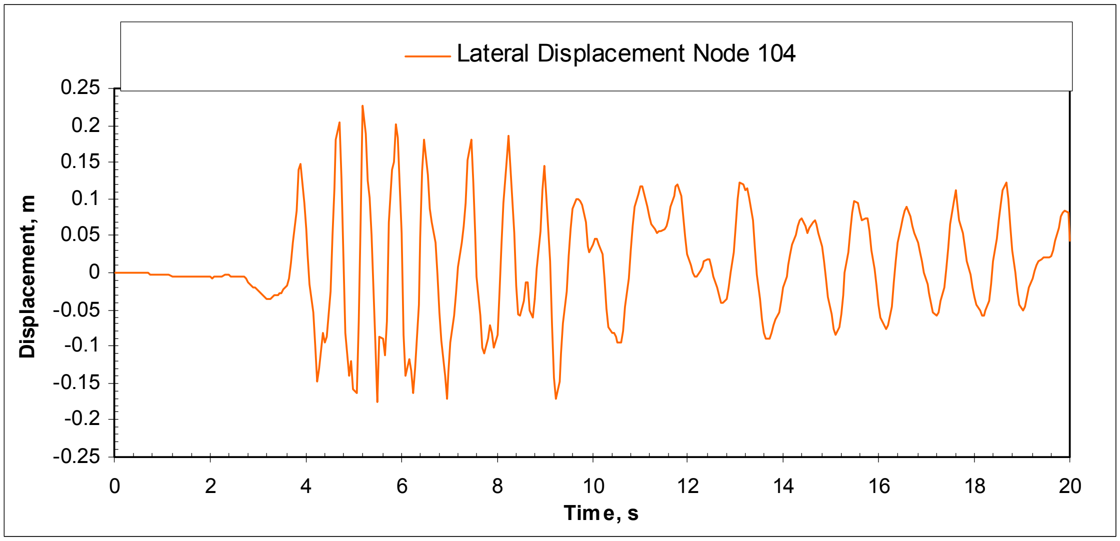

Figure D.204 - Span4, Northridge 3D input, SCED k = 179.2MN/m$^{1.3}$, node 104 lateral displacement

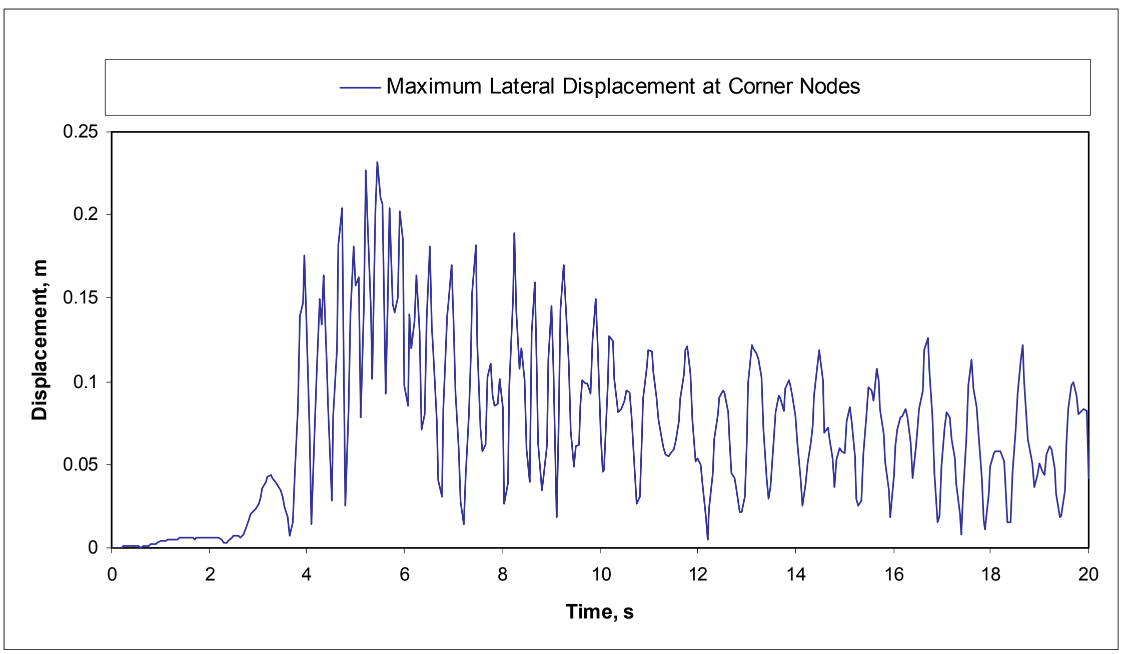

Figure D.205 - Span4, Northridge 3D input, SCED k = 179.2MN/m$^{1.3}$, maximum lateral displacement

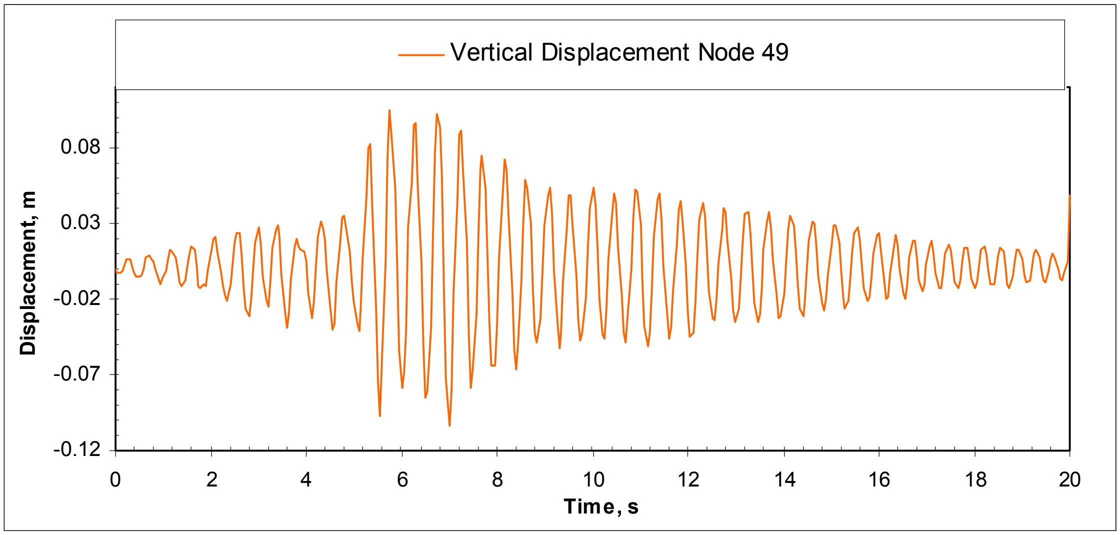

Figure D.206 - Span4, Northridge 3D input, SCED k = 179.2MN/$m^{1.3}$, node 49 vertical displacement

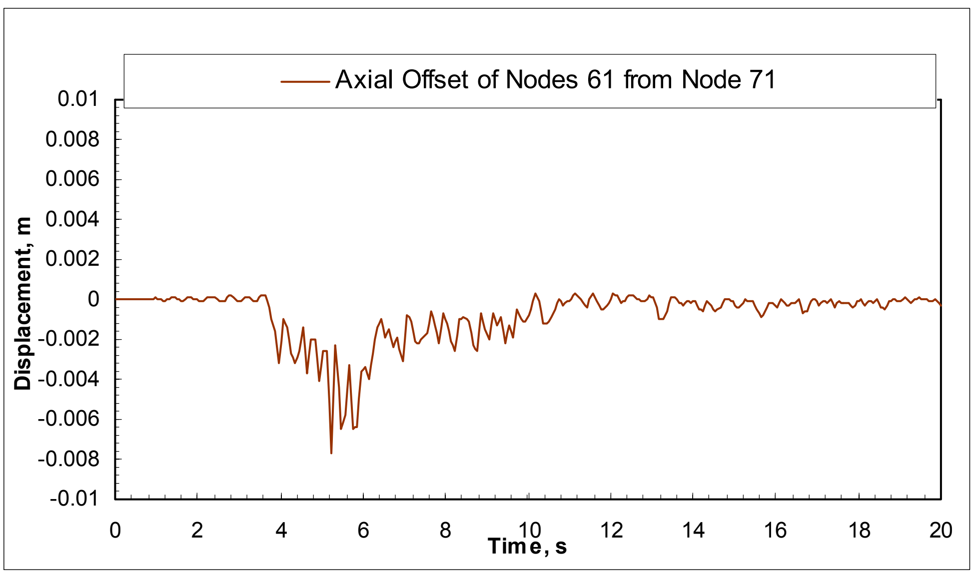

Figure D.207 - Span4, Northridge 3D input, SCED k = 179.2MN/$m^{1.3}$, node 61 and 71 response

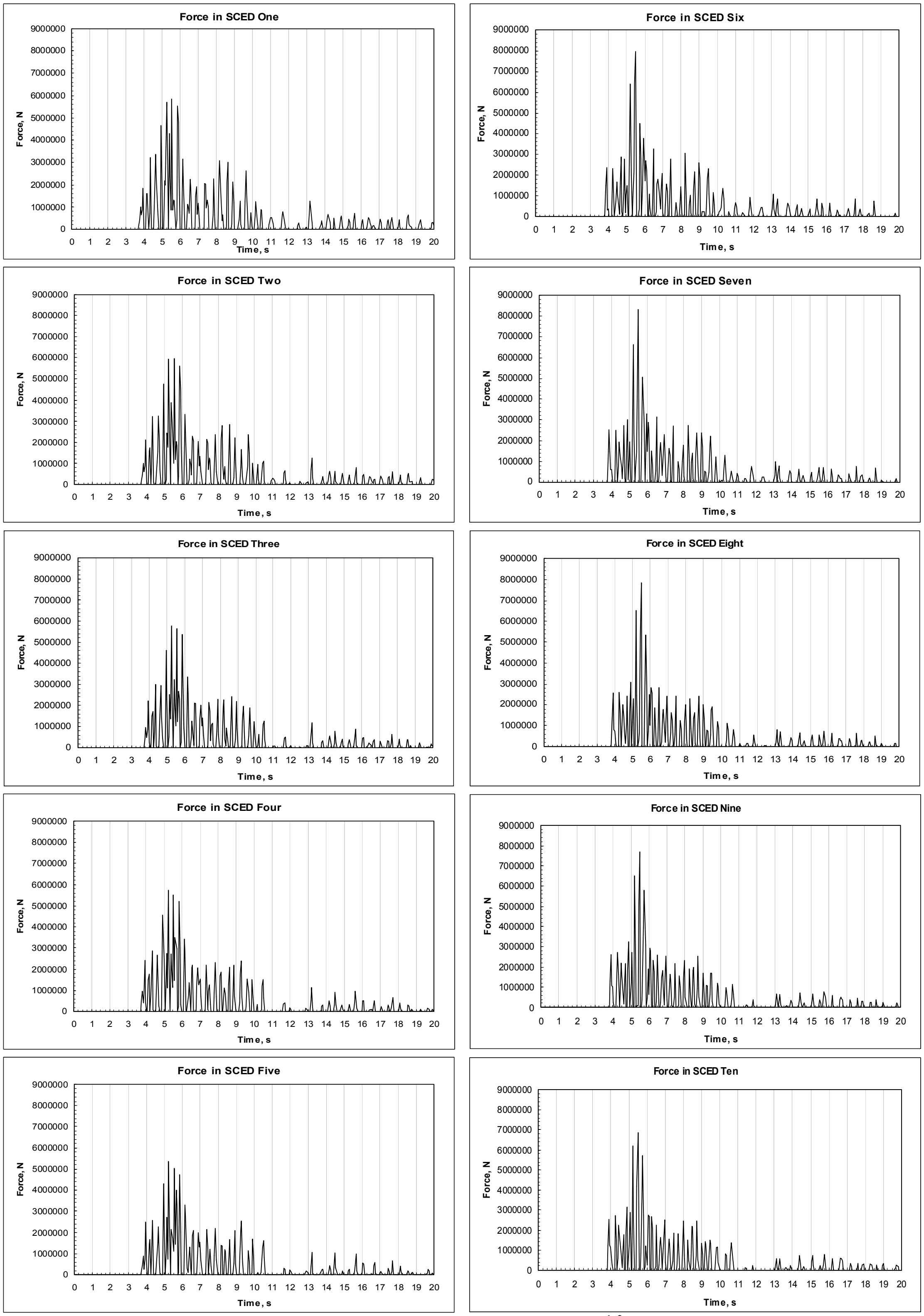

Figure D.208 - Span4, Northridge 3D input, SCED k = 179.2MN/m$^{1.3}$, snap load histories

D.5 Span5 Figures

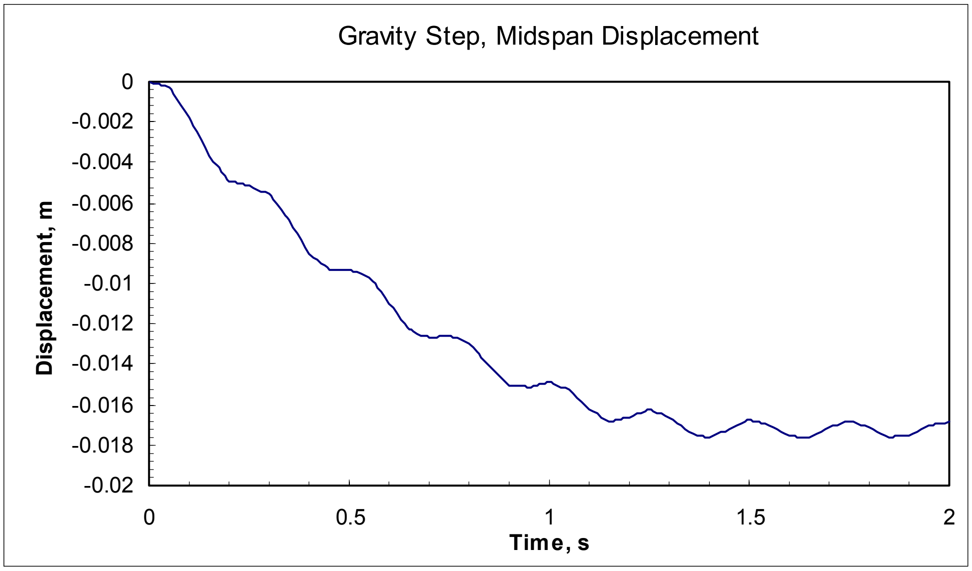

Figure D.209 - Span5, Imperial Valley input, gravity step response

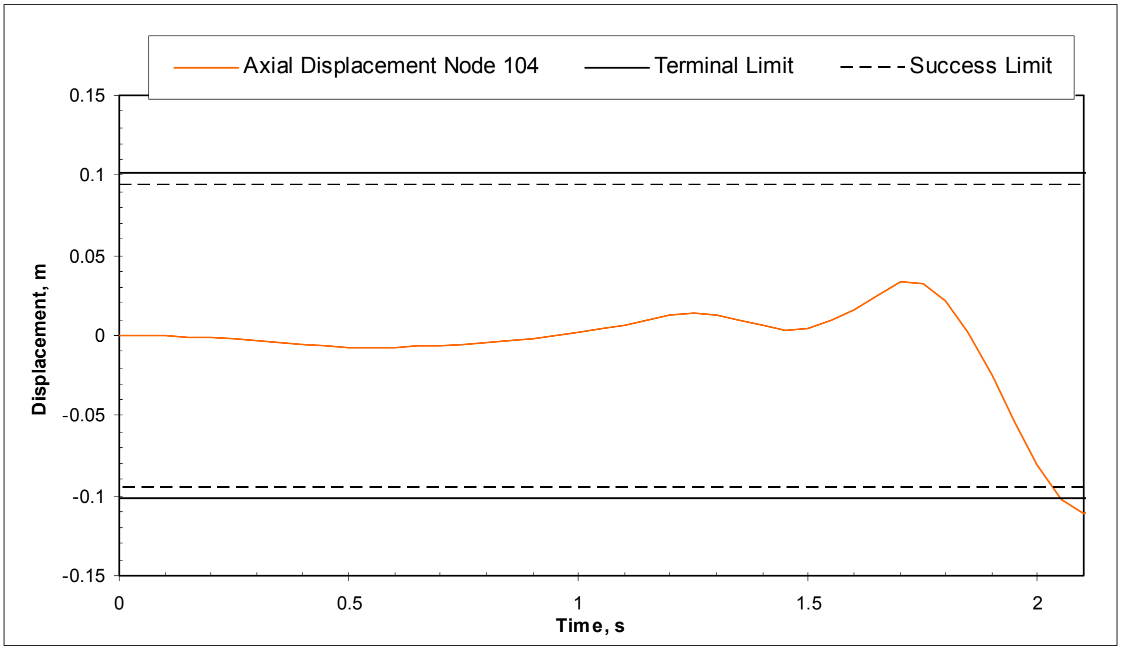

Figure D.210 - Span5, Imperial Valley axial input only, node 104 axial displacement

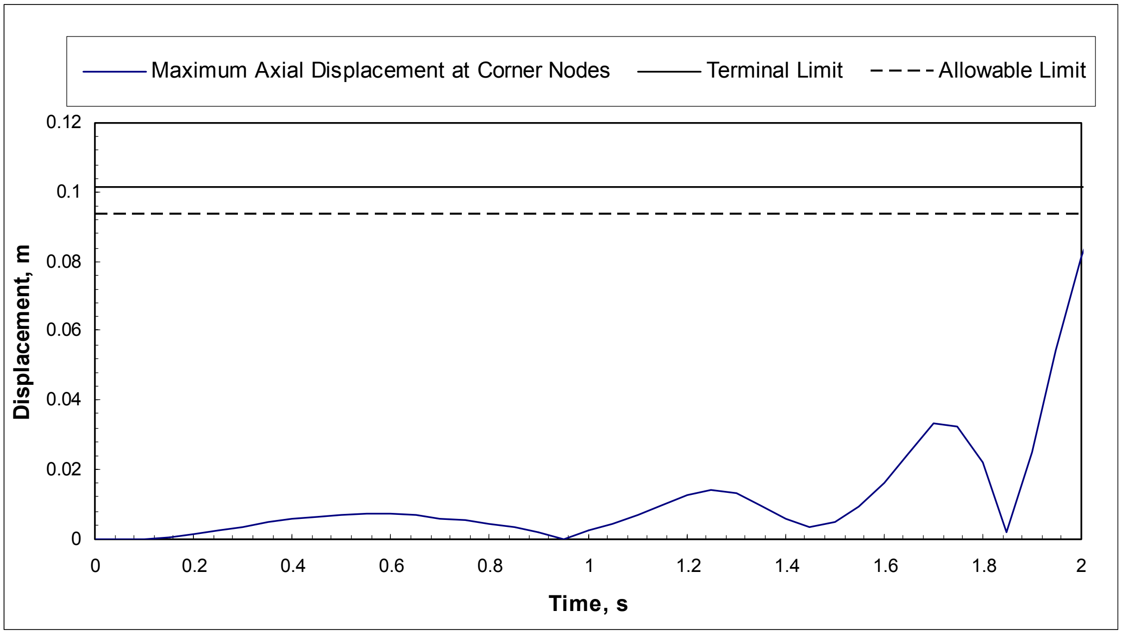

Figure D.211 - Span5, Imperial Valley axial input only, maximum axial displacement

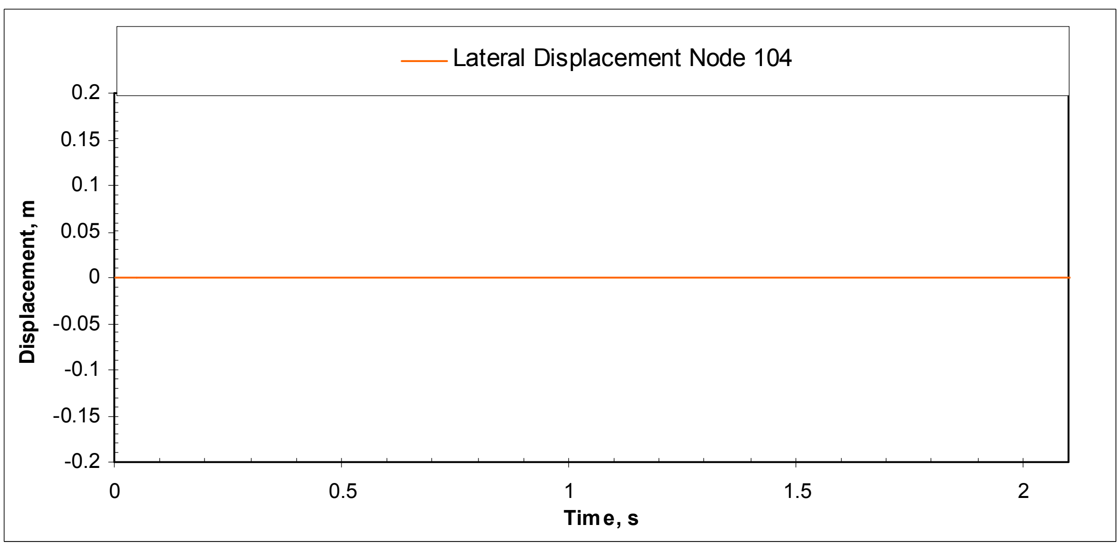

Figure D.212 - Span5, Imperial Valley axial input only, node 104 lateral displacement

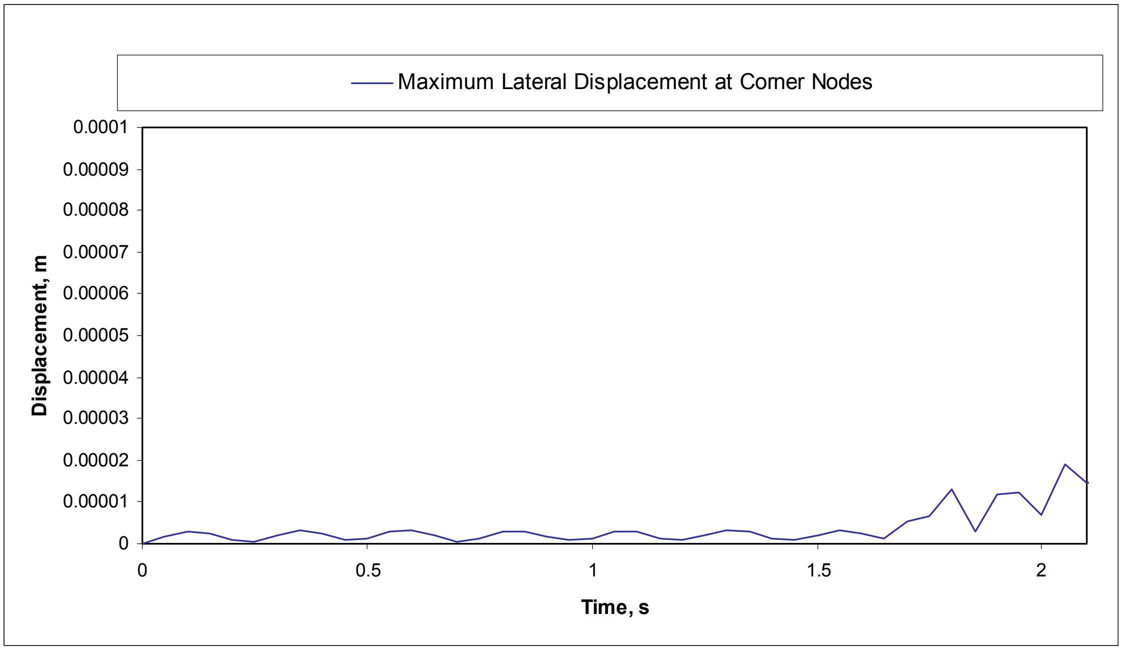

Figure D.213 - Span5, Imperial Valley axial input only, maximum lateral displacement

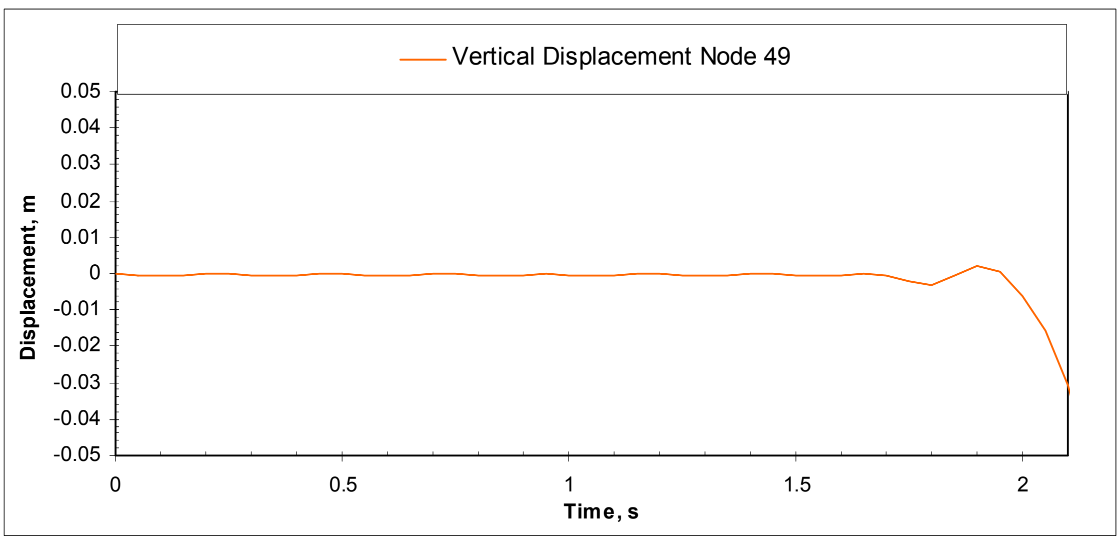

Figure D.214 - Span5, Imperial Valley axial input only, node 49 vertical displacement

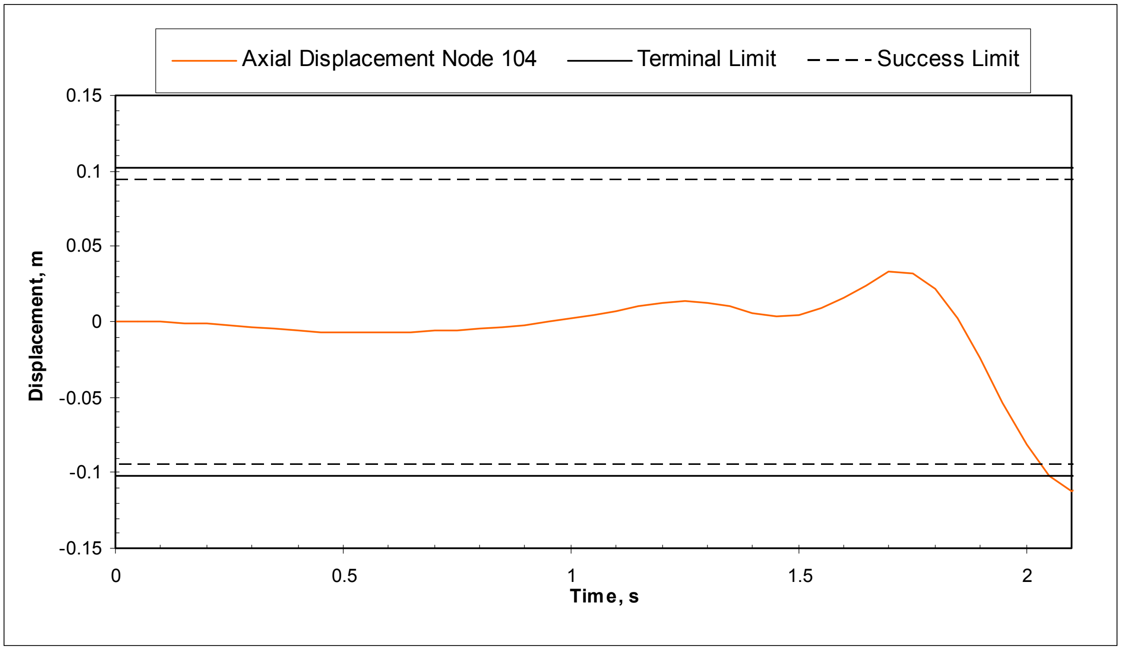

Figure D.215 - Span5, Imperial Valley three-dimensional input, no SCEDs, node 104 axial displacement

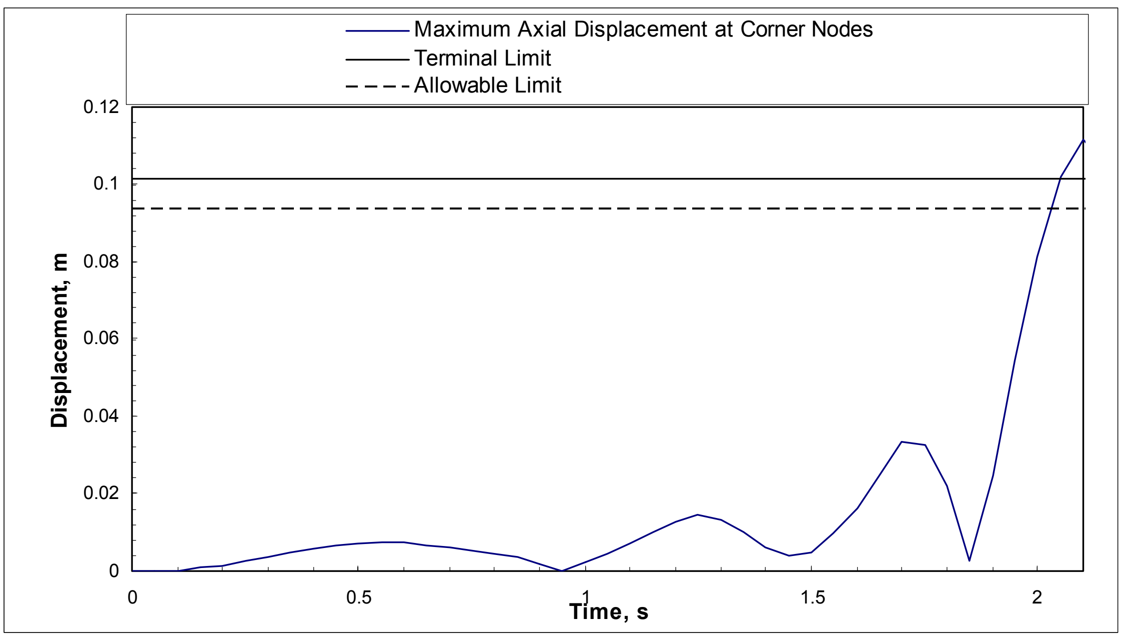

Figure D.216 - Span5, Imperial Valley 3D input, no SCEDs, maximum axial displacement

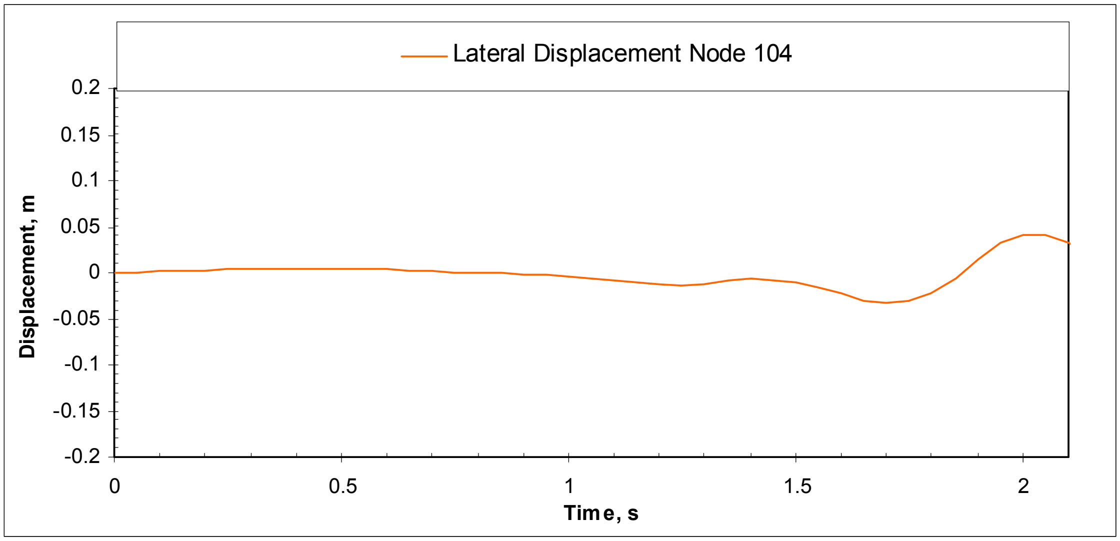

Figure D.217 - Span5, Imperial Valley 3D input, no SCEDs, node 104 lateral displacement

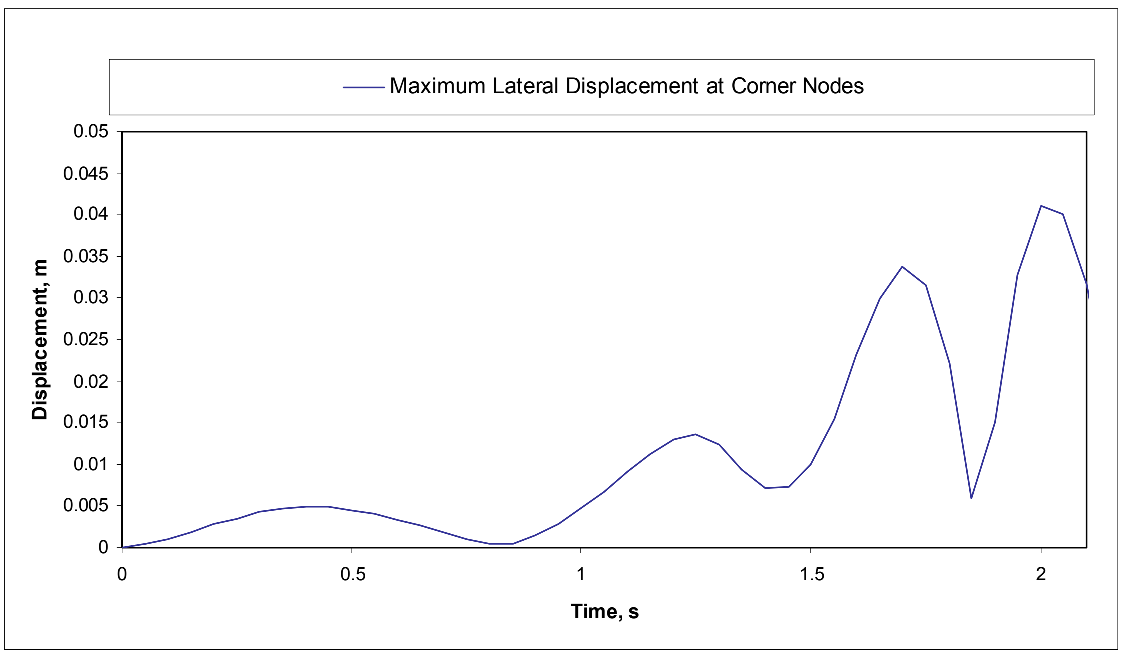

Figure D.218 - Span5, Imperial Valley 3D input, no SCEDs, maximum lateral displacement

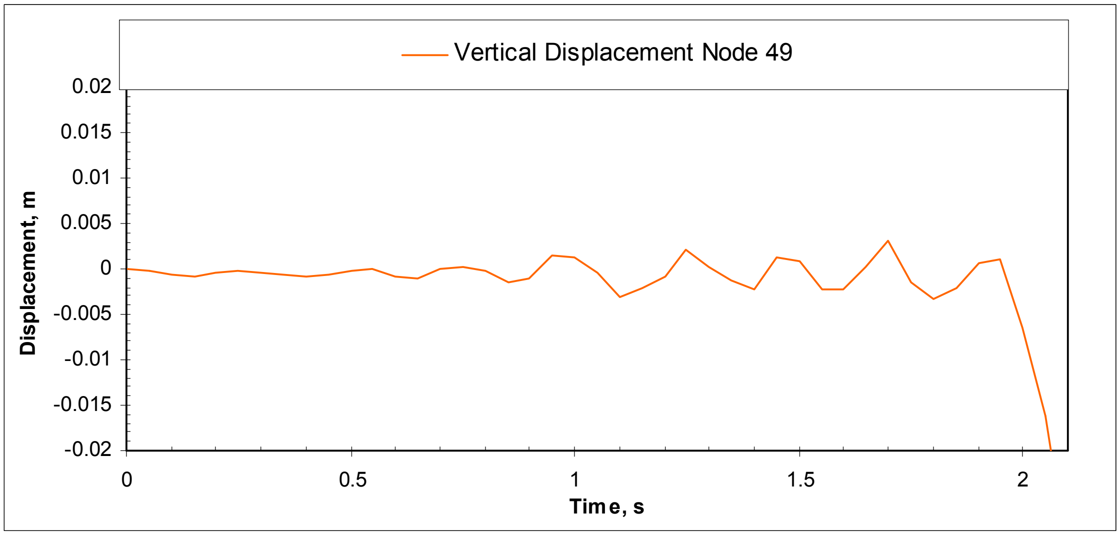

Figure D.219 - Span5, Imperial Valley 3D input, no SCEDs, node 49 vertical displacement

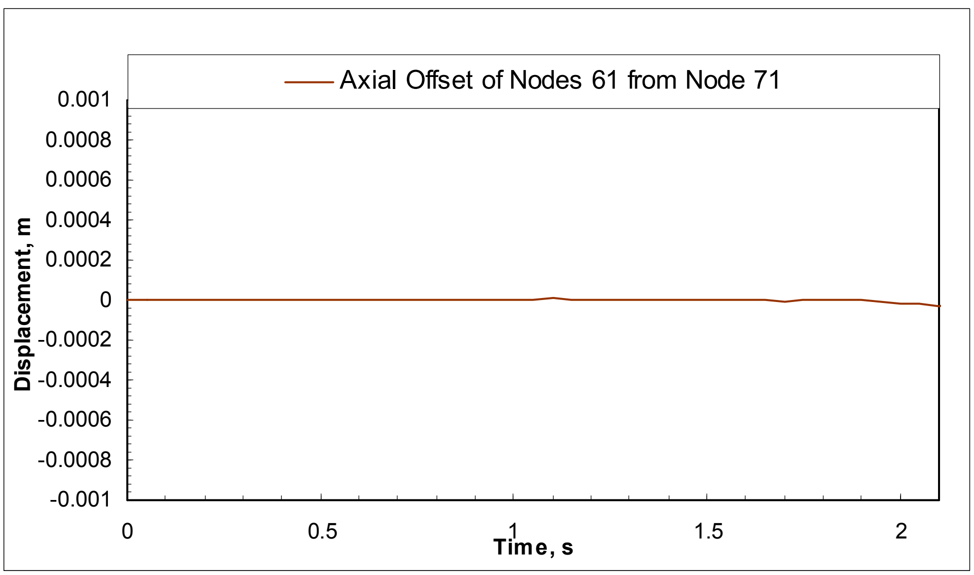

Figure D.220 - Span5, Imperial Valley 3D input, no SCEDs, node 61 and 71 response

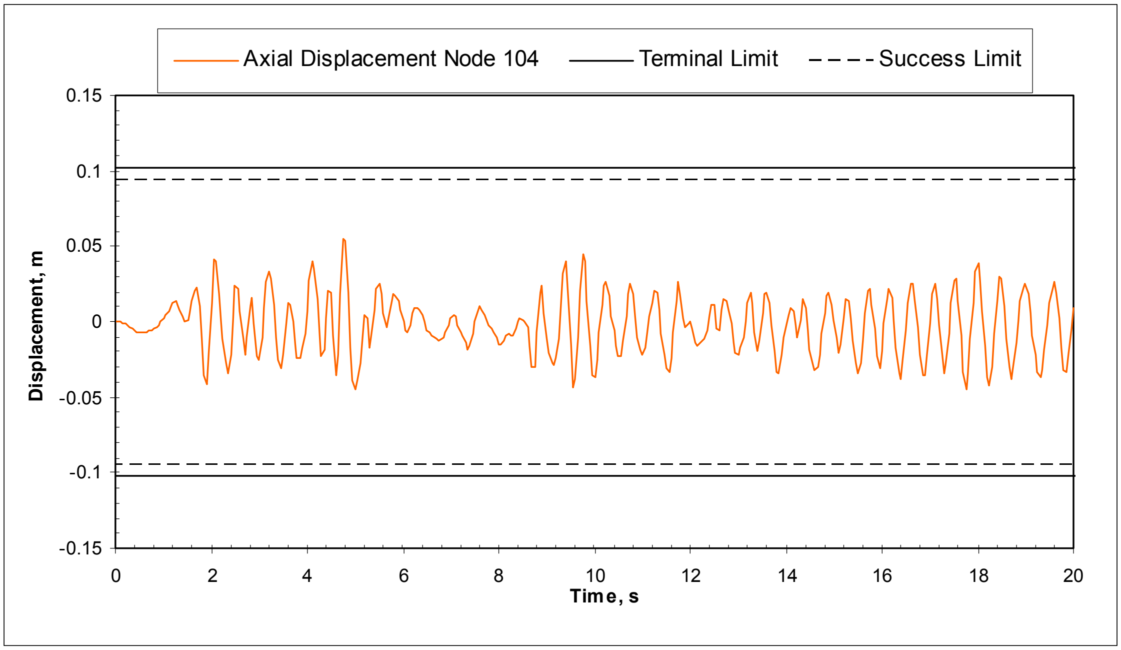

Figure D.221 - Span5, Imperial Valley 3D input, SCED k = 79.1MN/m$^{1.3}$, node 104 axial displacement

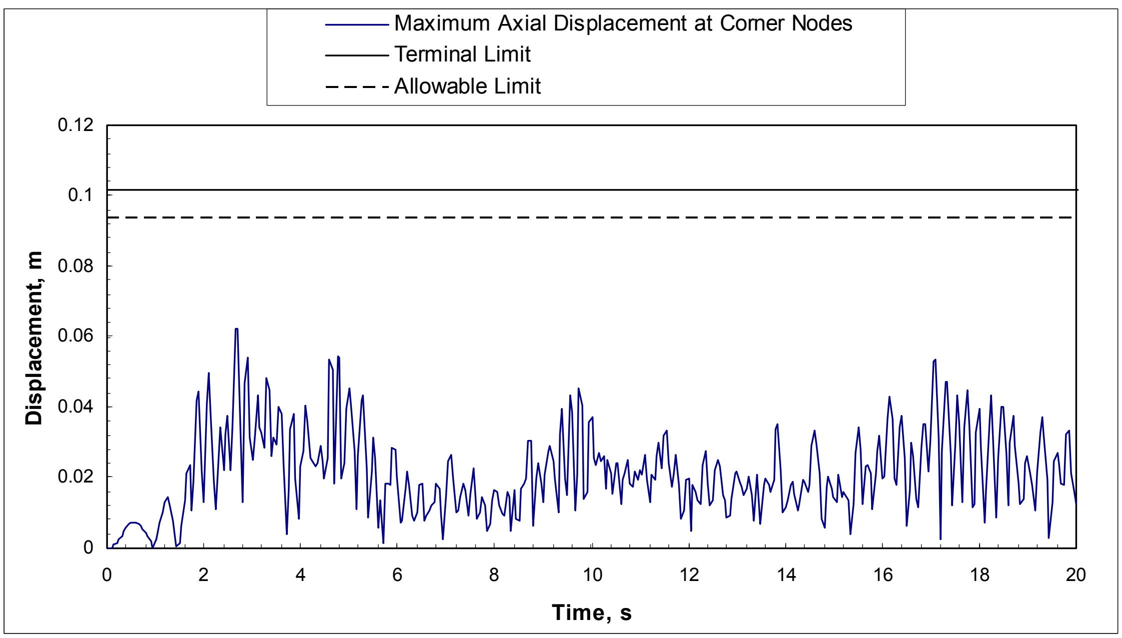

Figure D.222 - Span5, Imperial Valley 3D input, SCED k = 79.1MN/m$^{1.3}$, maximum axial displacement

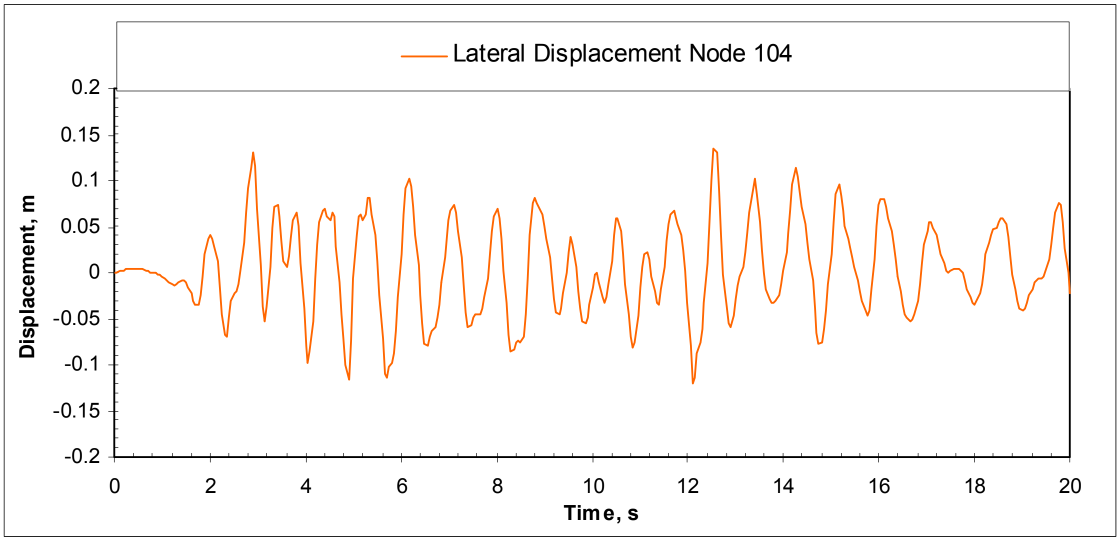

Figure D.223 - Span5, Imperial Valley 3D input, SCED k = 79.1MN/$m^{1.3}$, node 104 lateral displacement

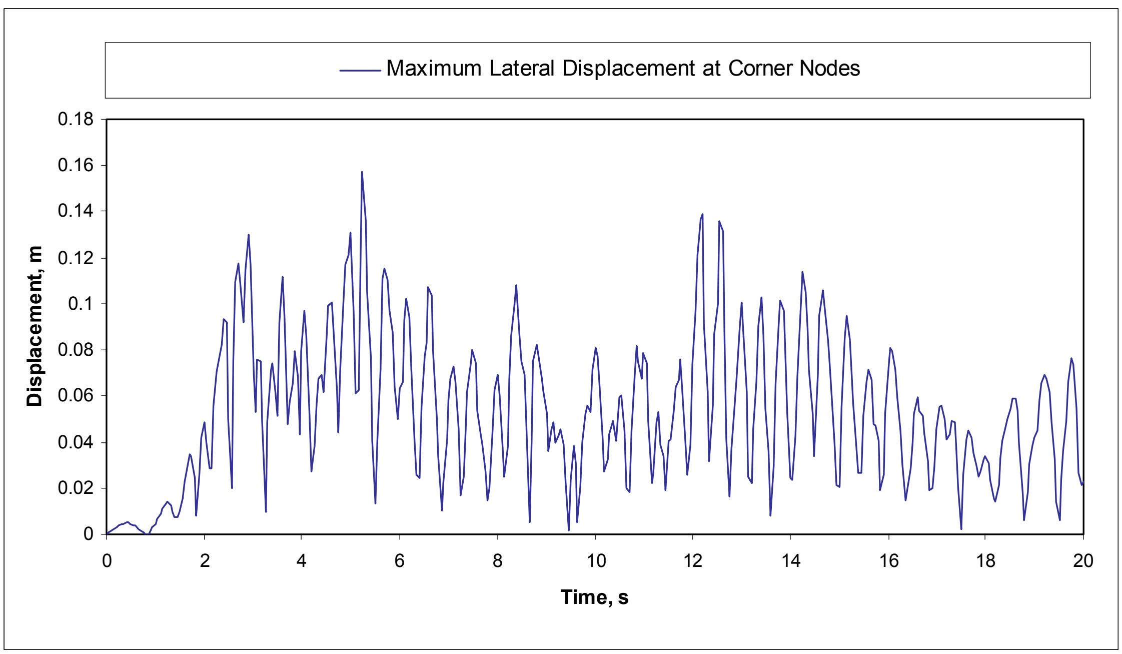

Figure D.224 - Span5, Imperial Valley 3D input, SCED k = 79.1MN/$m^{1.3}$, maximum lateral displacement

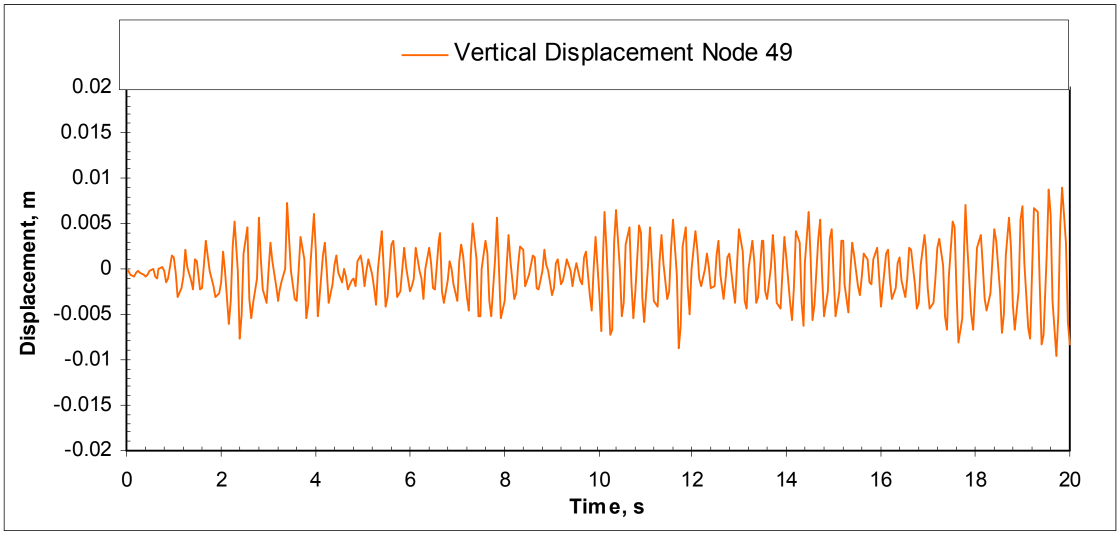

Figure D.225 - Span5, Imperial Valley 3D input, SCED k = 79.1MN/m$^{1.3}$, node 49 vertical displacement

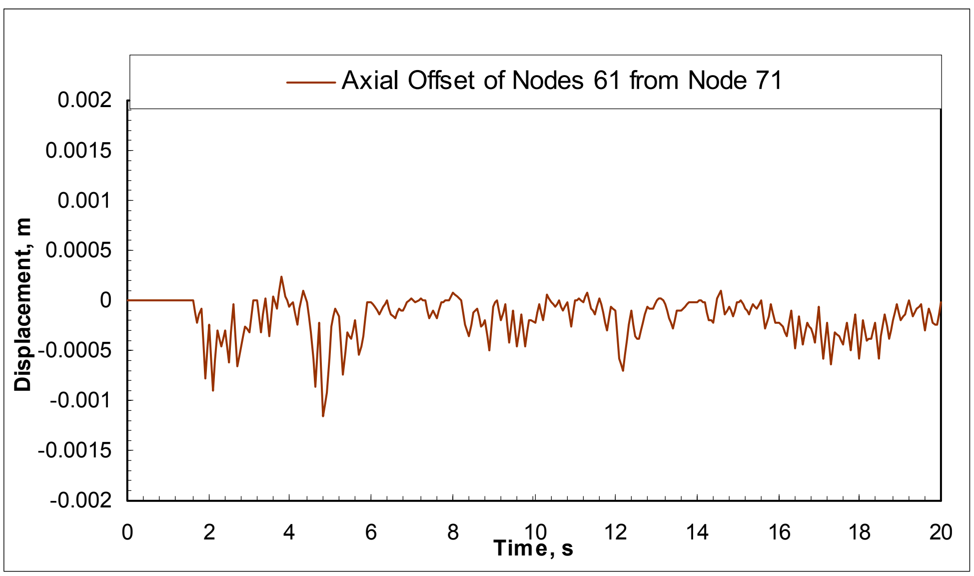

Figure D.226 - Span5, Imperial Valley 3D input, SCED k = 79.1MN/m$^{1.3}$, node 61 and 71 response

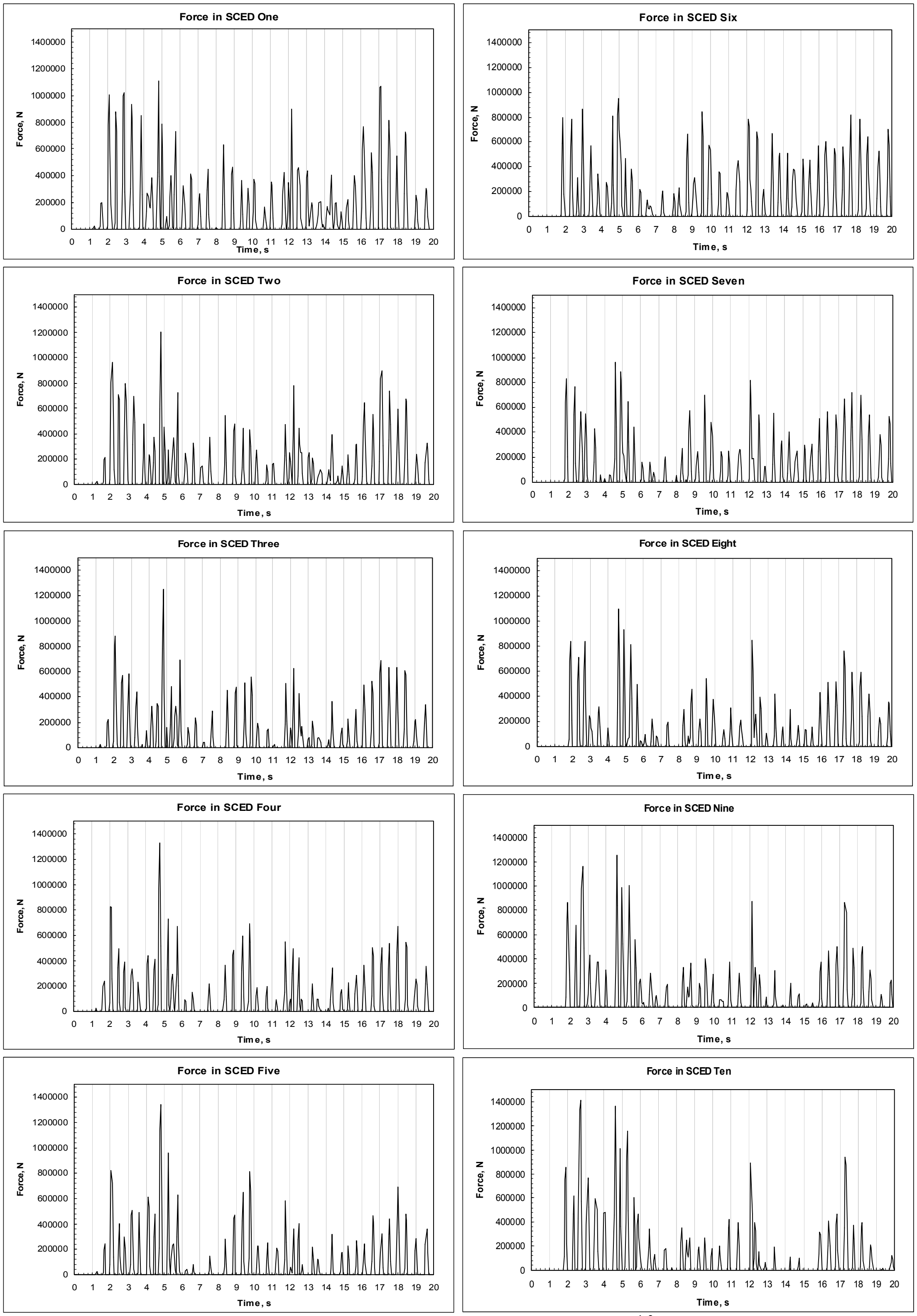

Figure D.227 - Span5, Imperial Valley 3D input, SCED k = 79.1MN/m$^{1.3}$, snap load histories

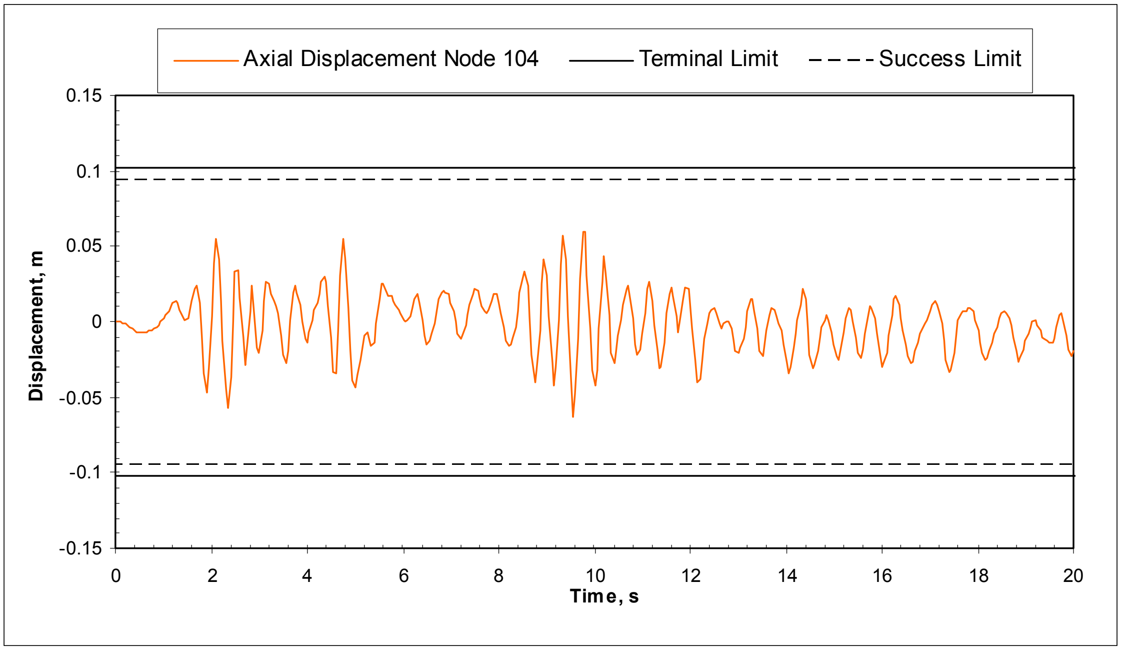

Figure D.228 - Span5, Imperial Valley 3D input, SCED k = 63.3MN/m$^{1.3}$, node 104 axial displacement

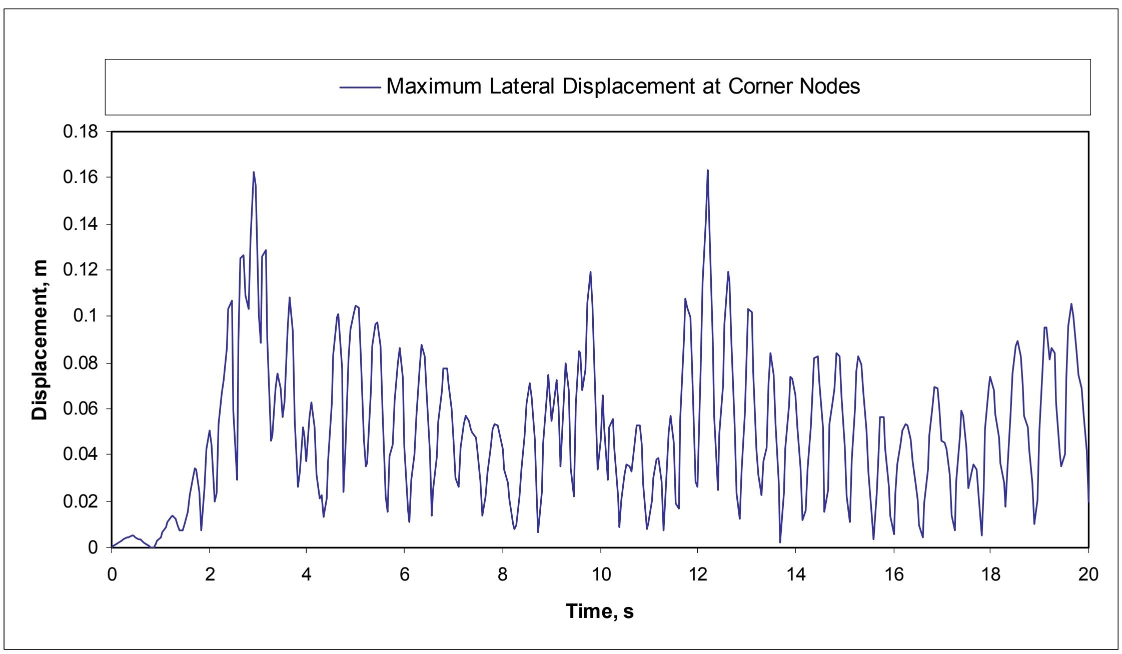

Figure D.229 - Span5, Imperial Valley 3D input, SCED k = 63.3MN/m$^{1.3}$, maximum axial displacement

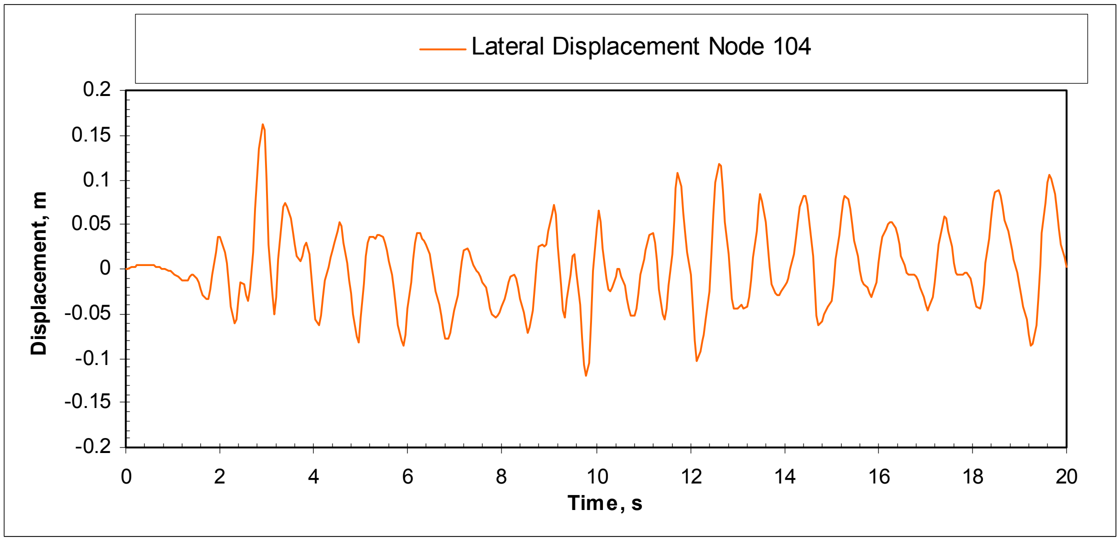

Figure D.230 - Span5, Imperial Valley 3D input, SCED k = 63.3MN/m$^{1.3}$, node 104 lateral displacement

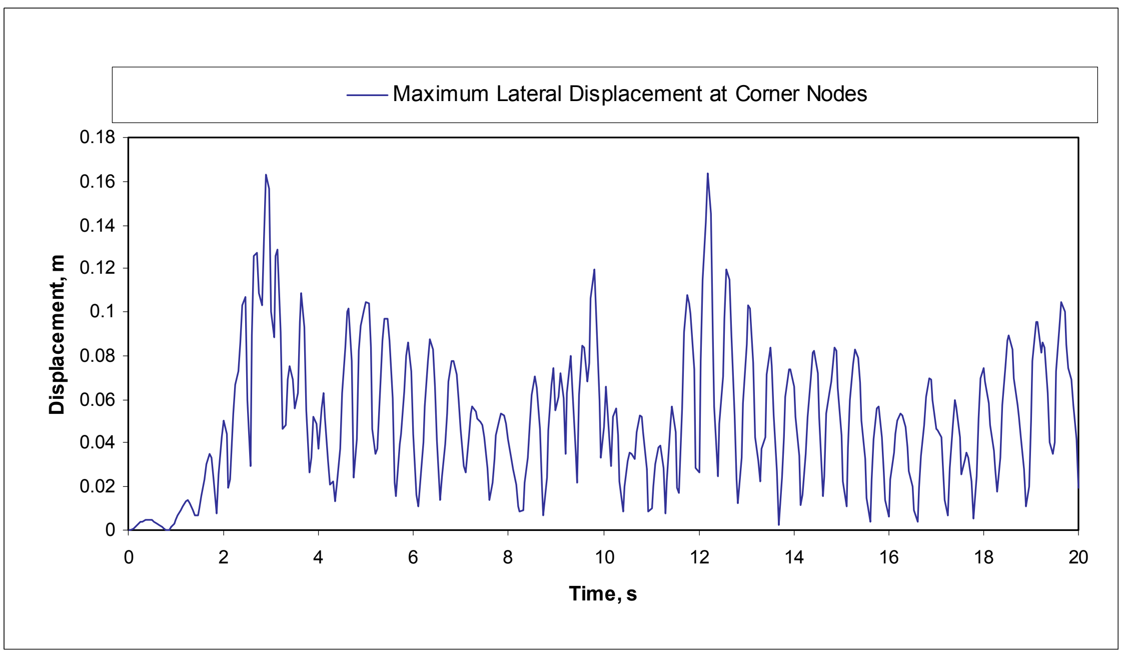

Figure D.231 - Span5, Imperial Valley 3D input, SCED k = 63.3MN/m$^{1.3}$, maximum lateral displacement

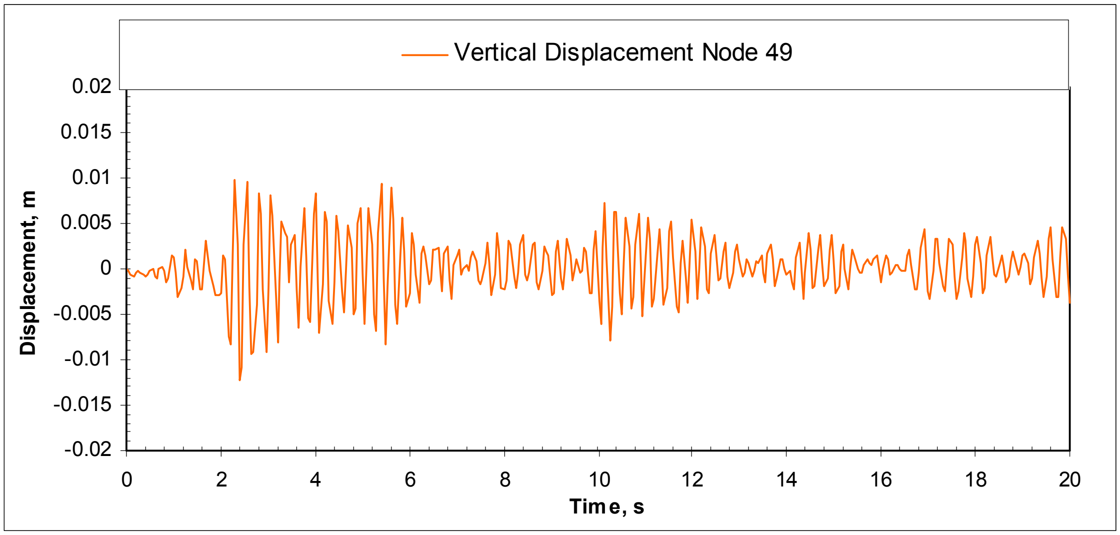

Figure D.232 - Span5, Imperial Valley 3D input, SCED k = 63.3MN/m$^{1.3}$, node 49 vertical displacement

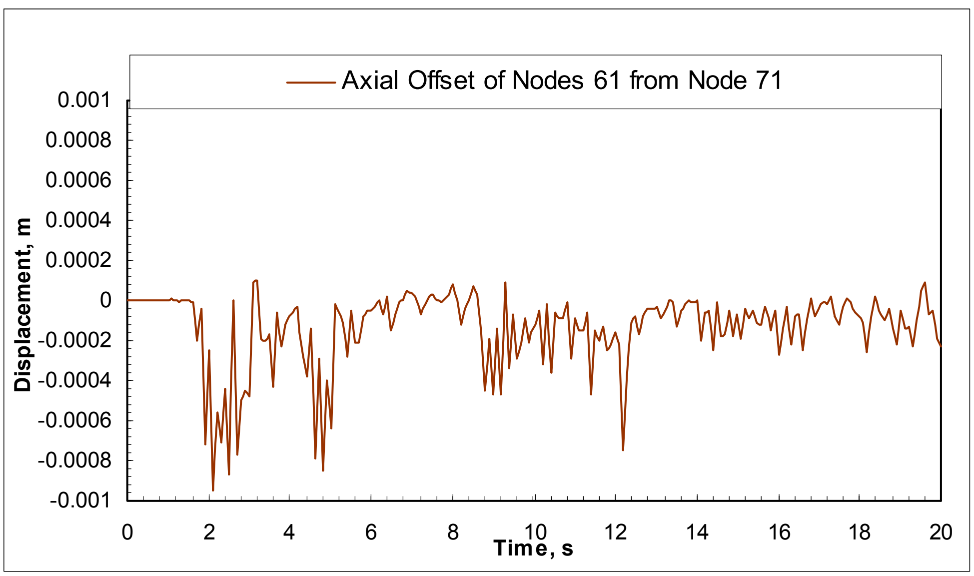

Figure D.233 - Span5, Imperial Valley 3D input, SCED k = 63.3MN/m$^{1.3}$, node 61 and 71 response

Figure D.234 - Span5, Imperial Valley 3D input, SCED k = 63.3MN/m$^{1.3}$, snap load histories

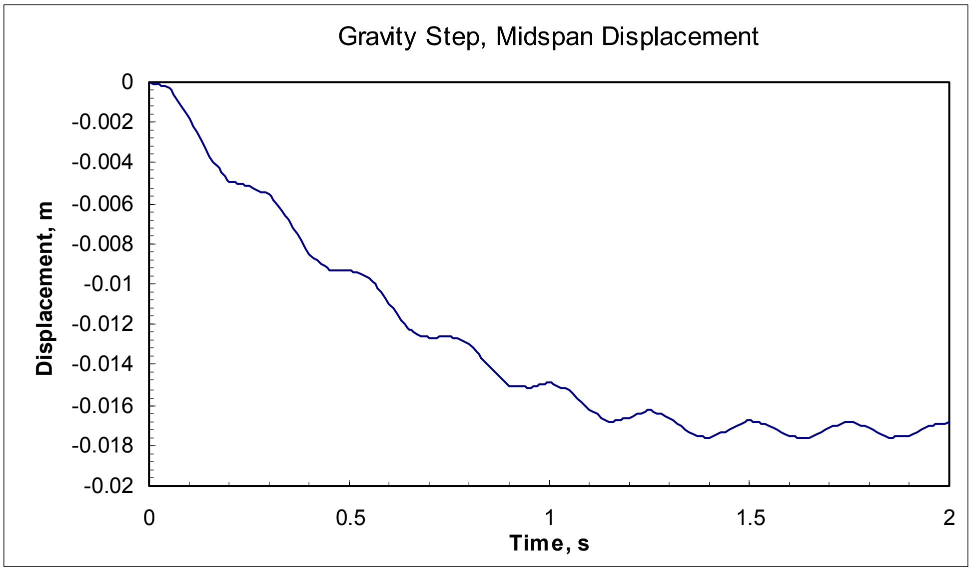

Figure D.235 - Span5, Northridge input, gravity step response

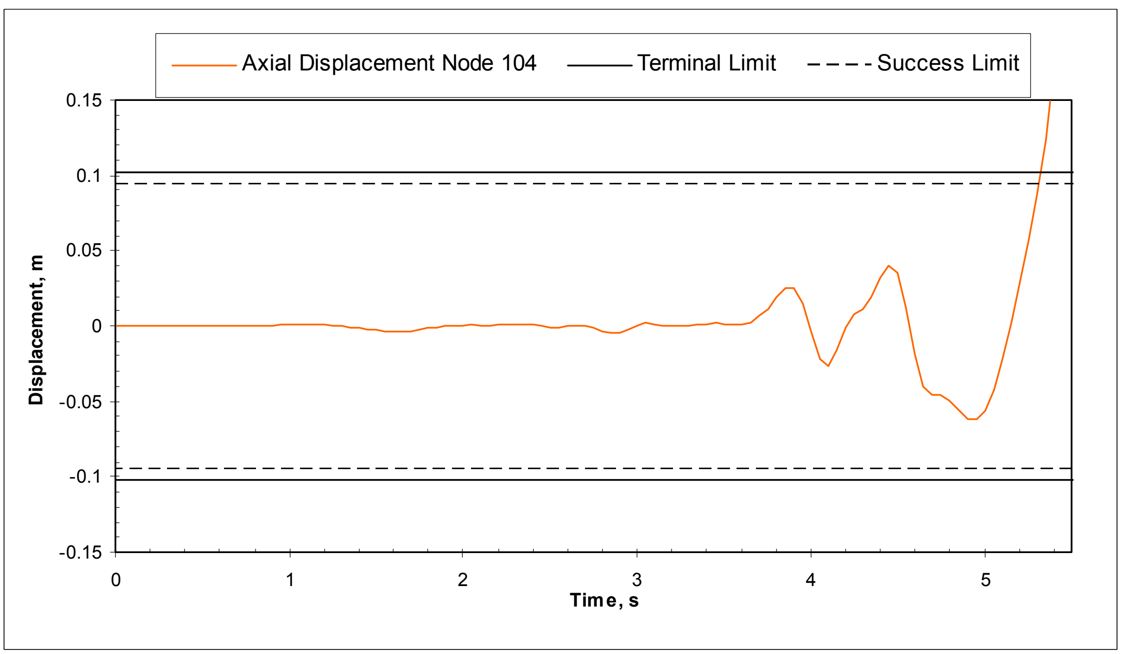

Figure D.236 - Span5, Northridge axial input only, node 104 axial displacement

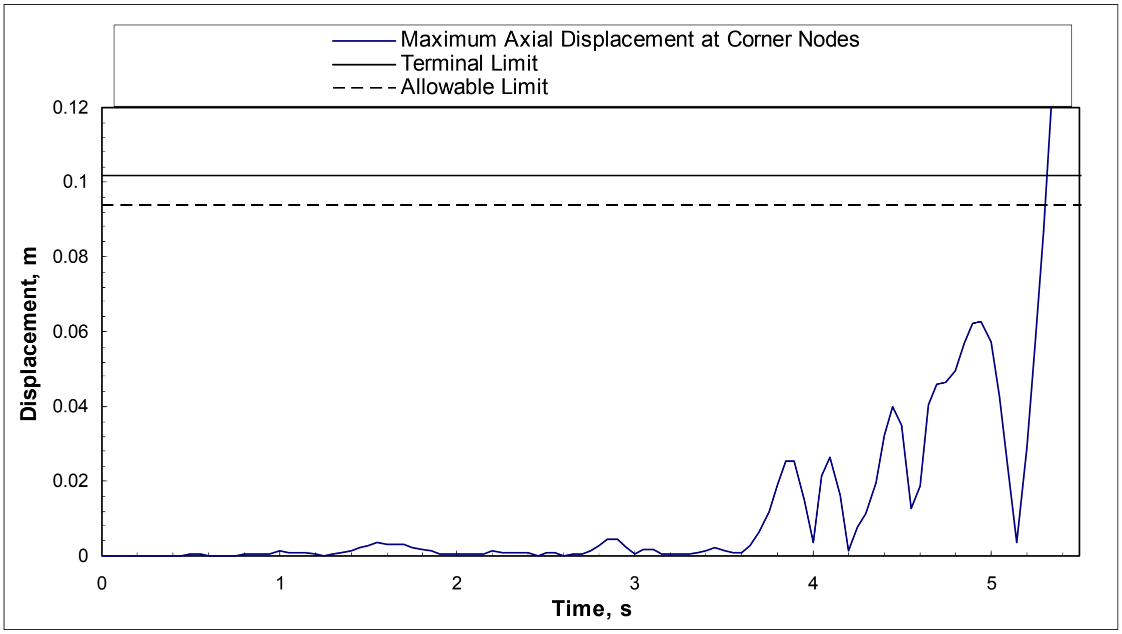

Figure D.237 - Span5, Northridge axial input only, maximum axial displacement

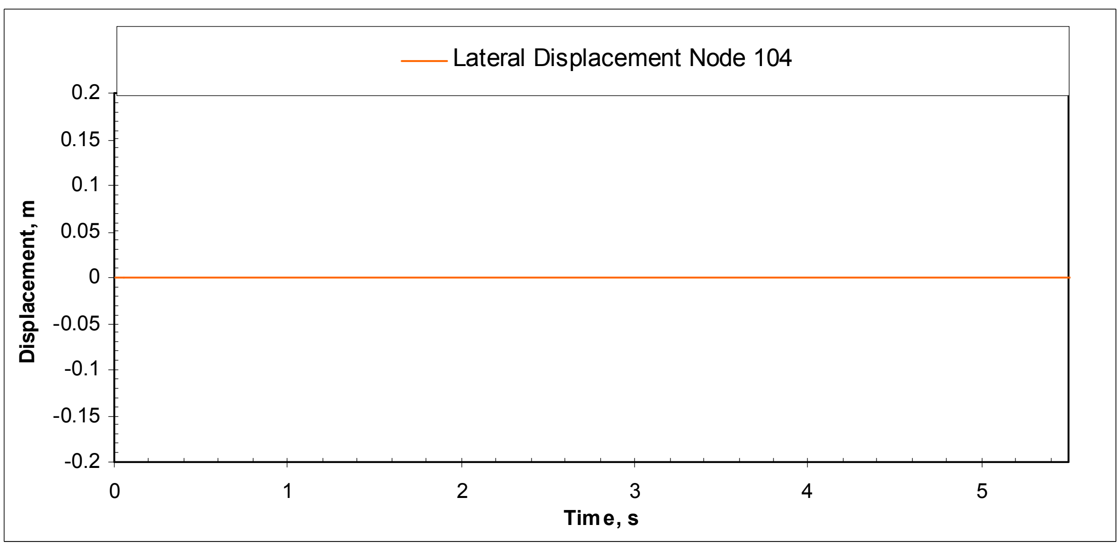

Figure D.238 - Span5, Northridge axial input only, node 104 lateral displacement

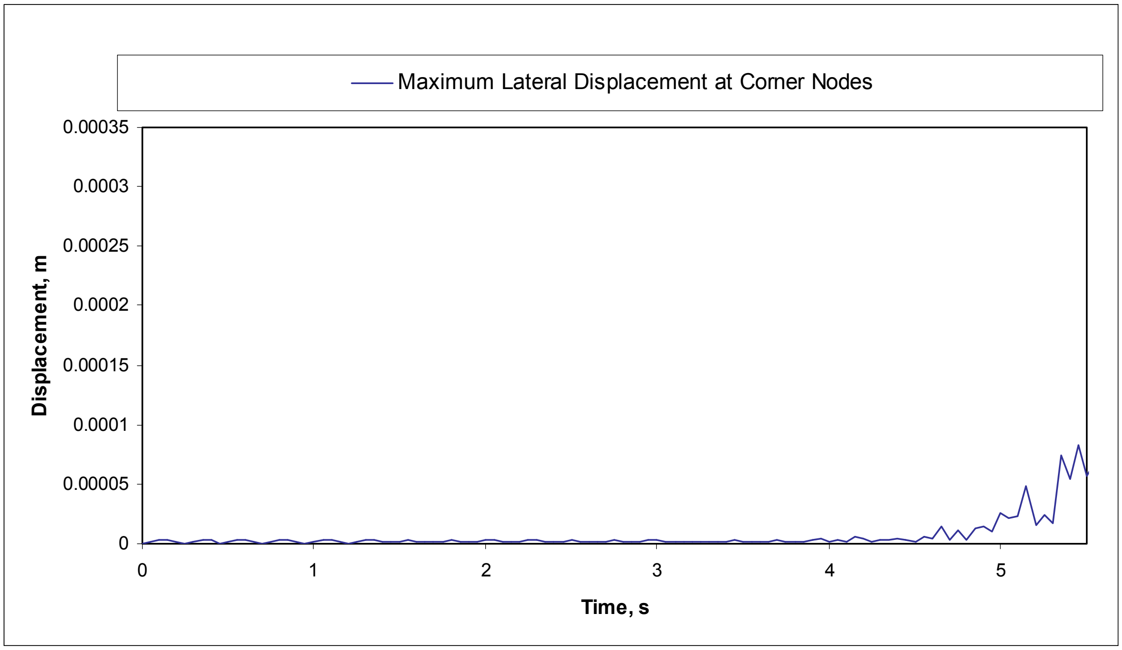

Figure D.239 - Span5, Northridge axial input only, maximum lateral displacement

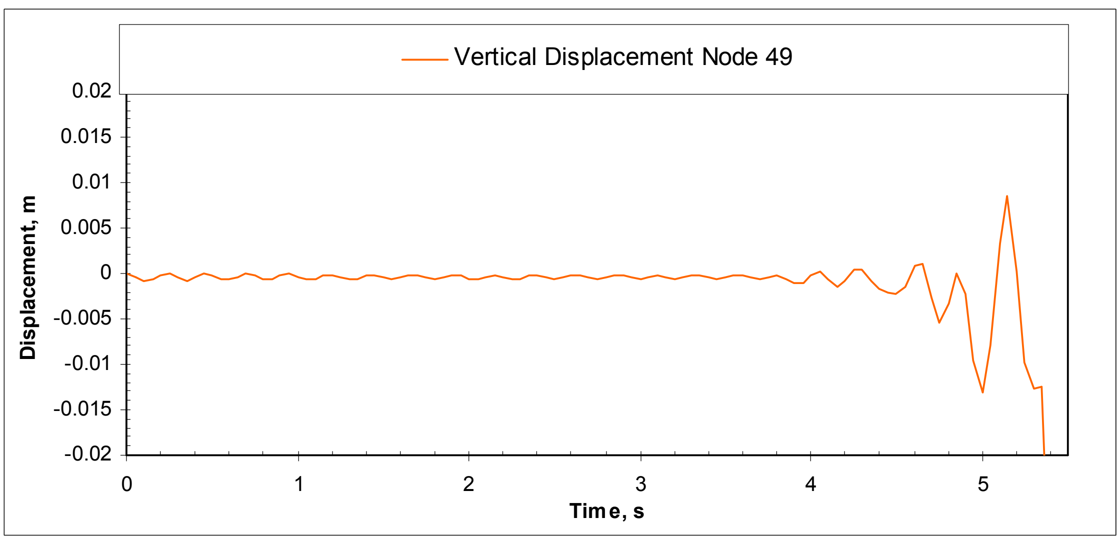

Figure D.240 - Span5, Northridge axial input only, node 49 vertical displacement

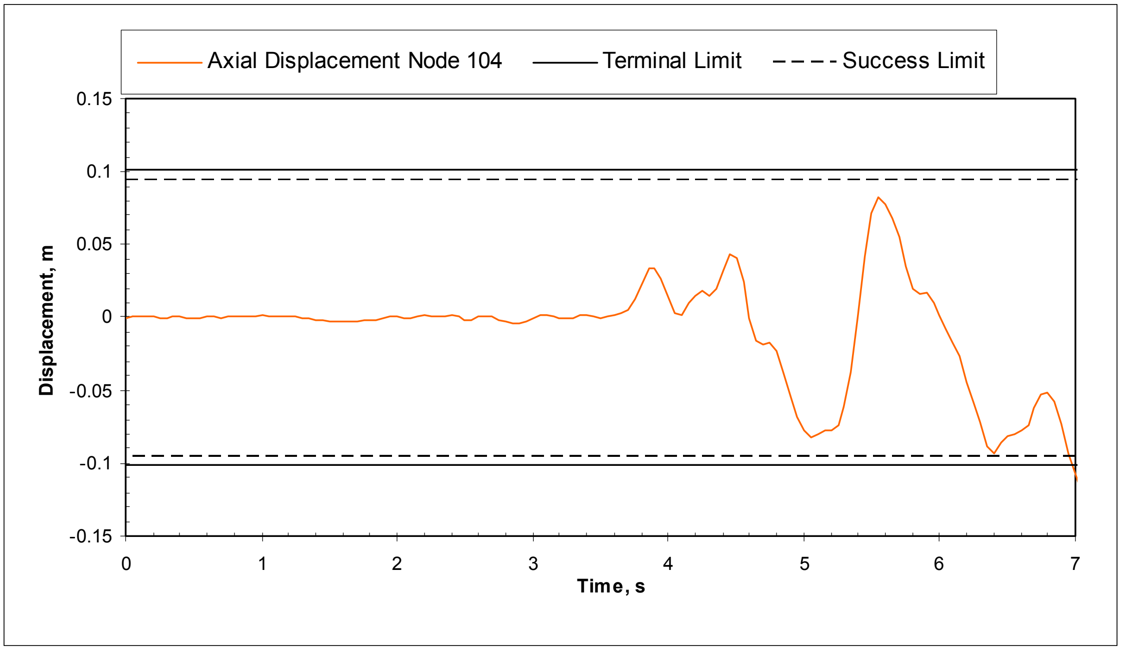

Figure D.241 - Span5, Northridge three-dimensional input, no SCEDs, node 104 axial displacement

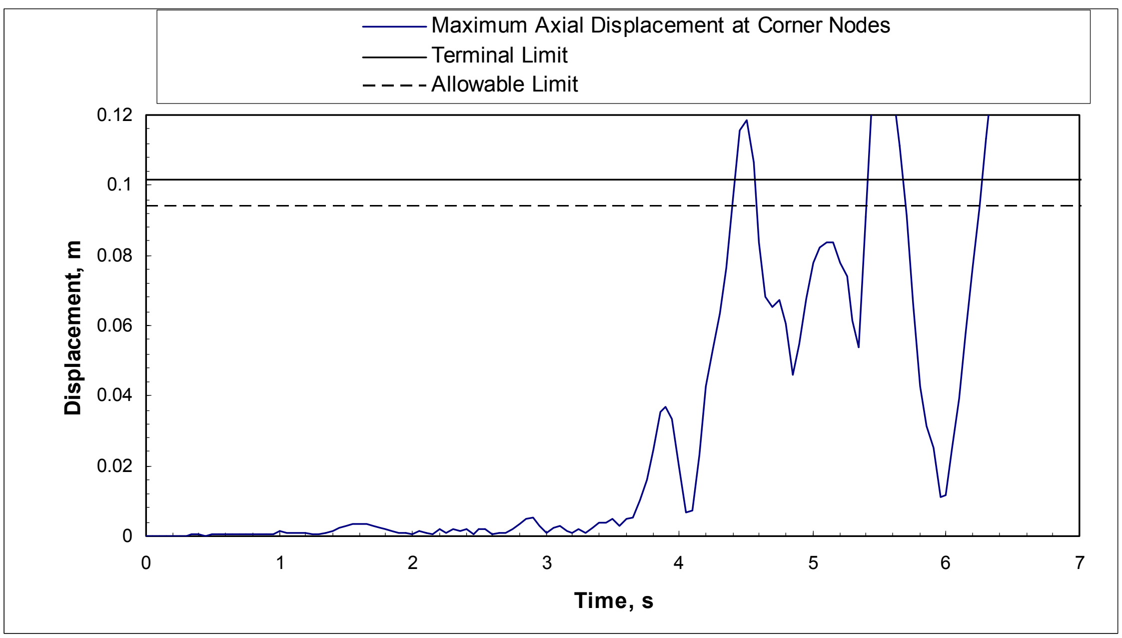

Figure D.242 - Span5, Northridge 3D input, no SCEDs, maximum axial displacement

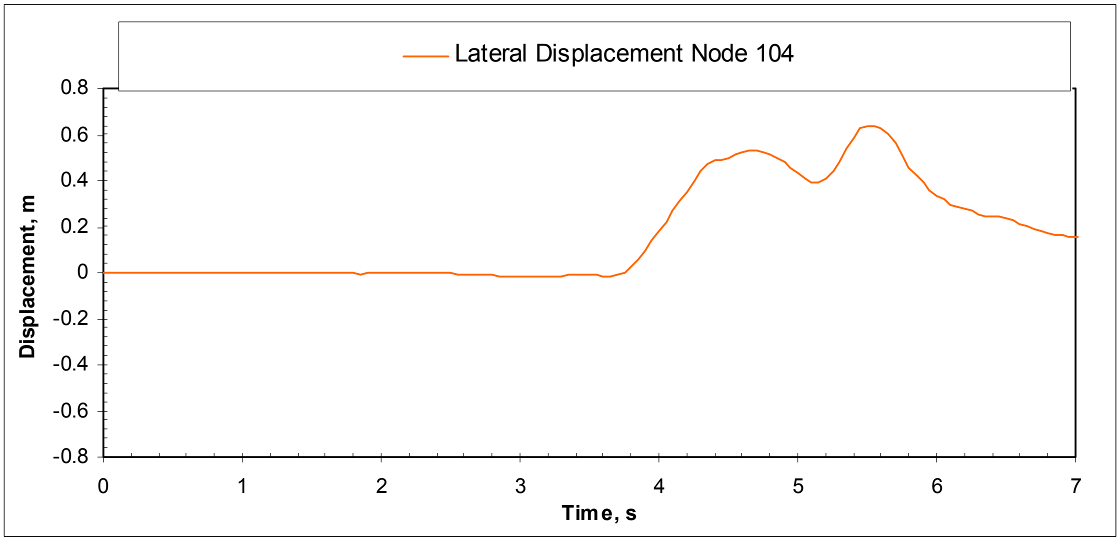

Figure D.243 - Span5, Northridge 3D input, no SCEDs, node 104 lateral displacement

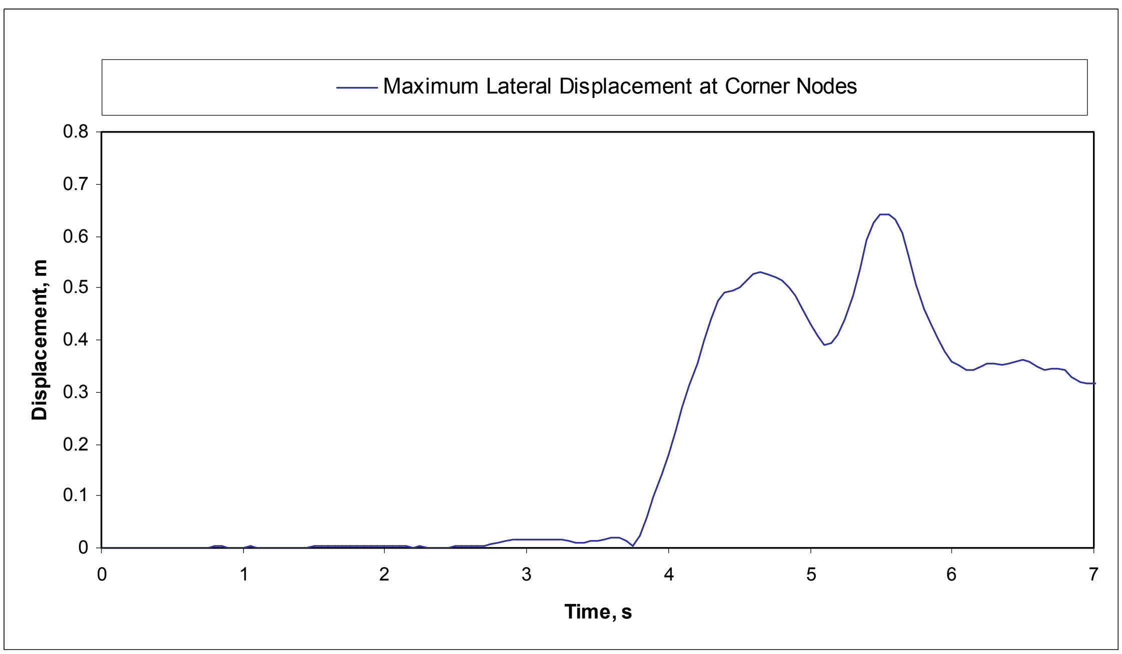

Figure D.244 - Span5, Northridge 3D input, no SCEDs, maximum lateral displacement

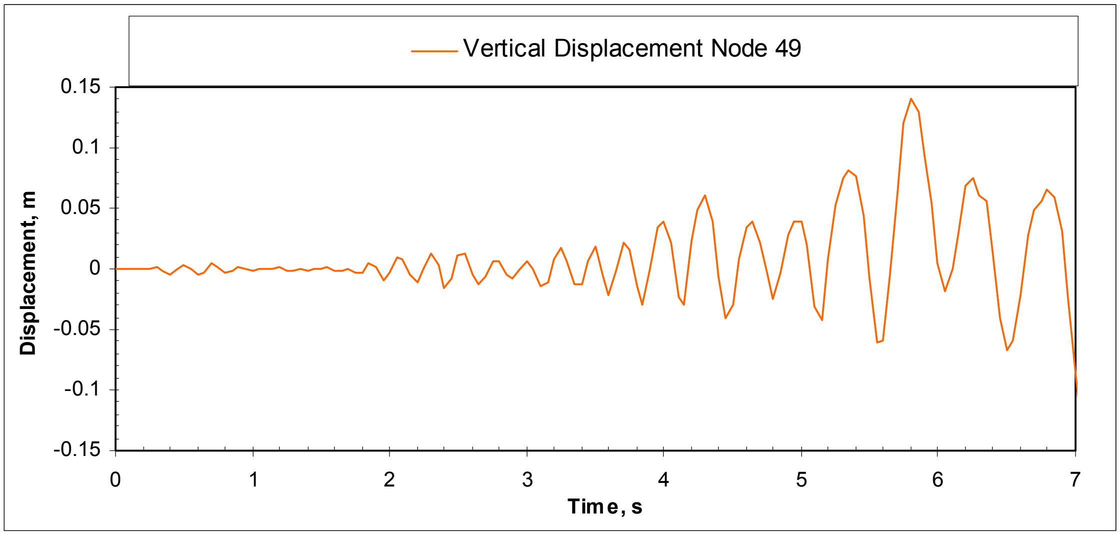

Figure D.245 - Span5, Northridge 3D input, no SCEDs, node 49 vertical displacement

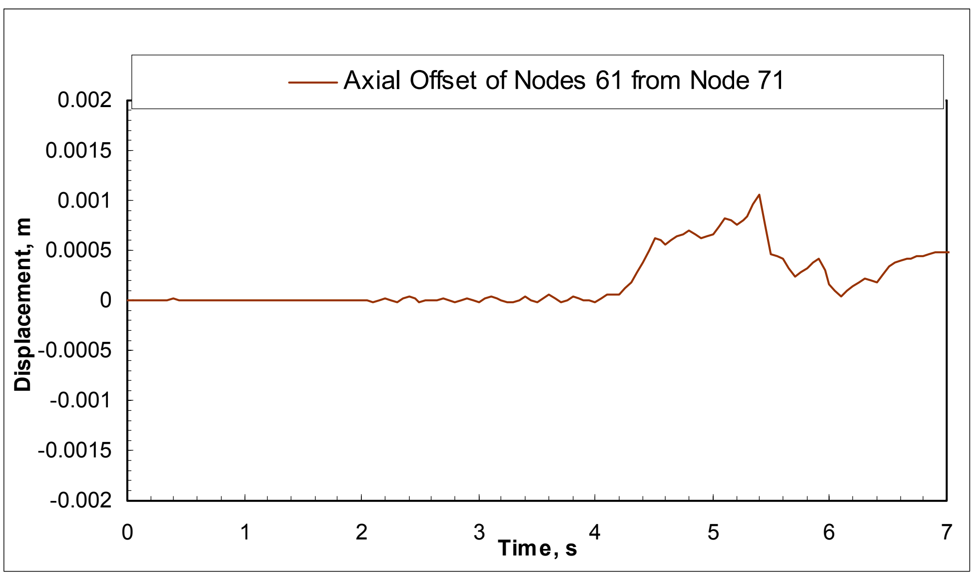

Figure D.246 - Span5, Northridge 3D input, no SCEDs, node 61 and 71 response

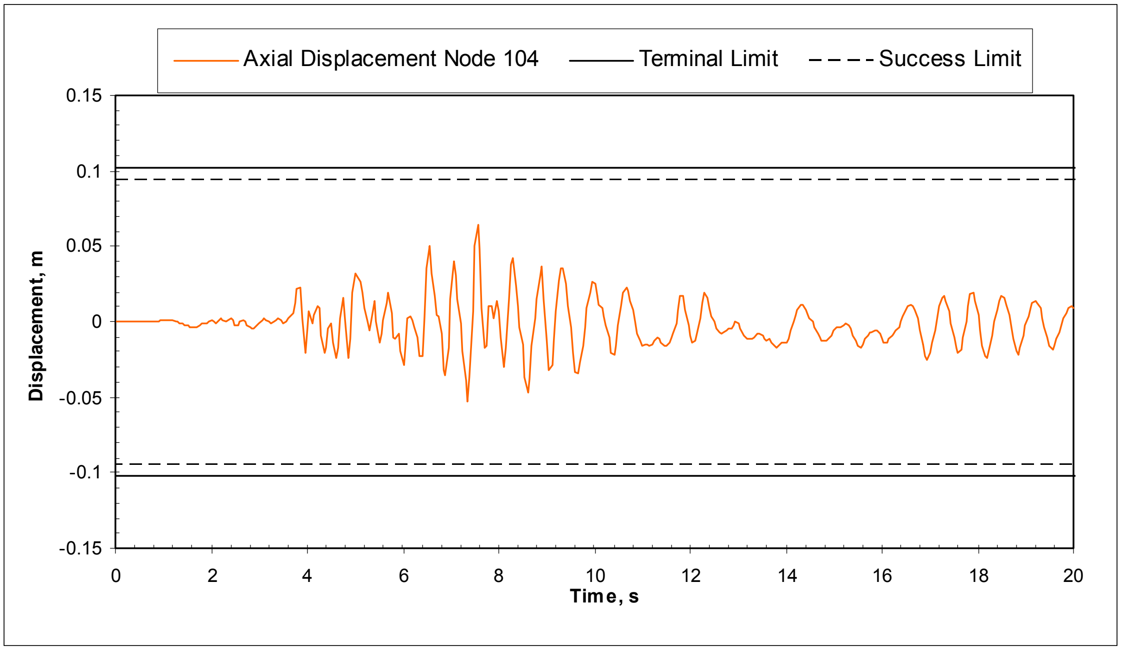

Figure D.247 - Span5, Northridge 3D input, SCED k = 79.1MN/m$^{1.3}$, node 104 axial displacement

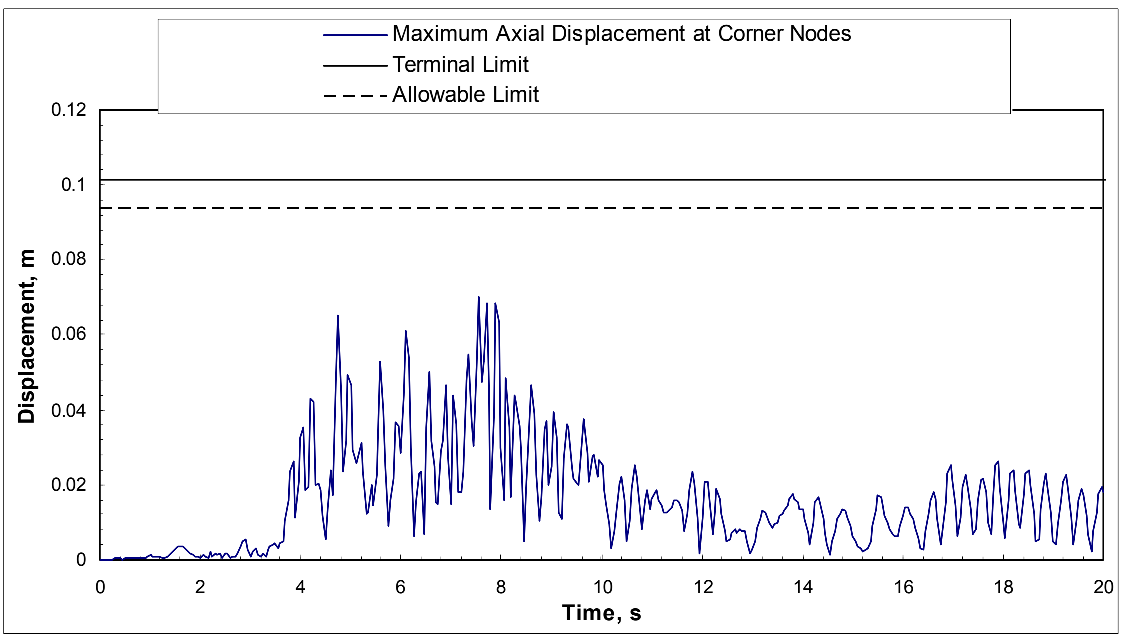

Figure D.248 - Span5, Northridge 3D input, SCED k = 79.1MN/m$^{1.3}$, maximum axial displacement

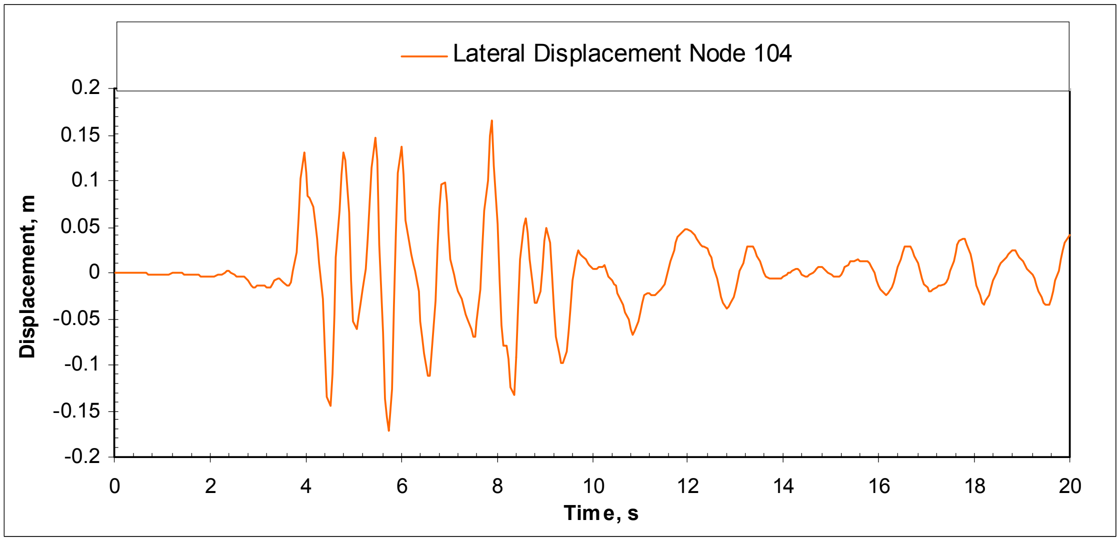

Figure D.249 - Span5, Northridge 3D input, SCED k = 79.1MN/m$^{1.3}$, node 104 lateral displacement

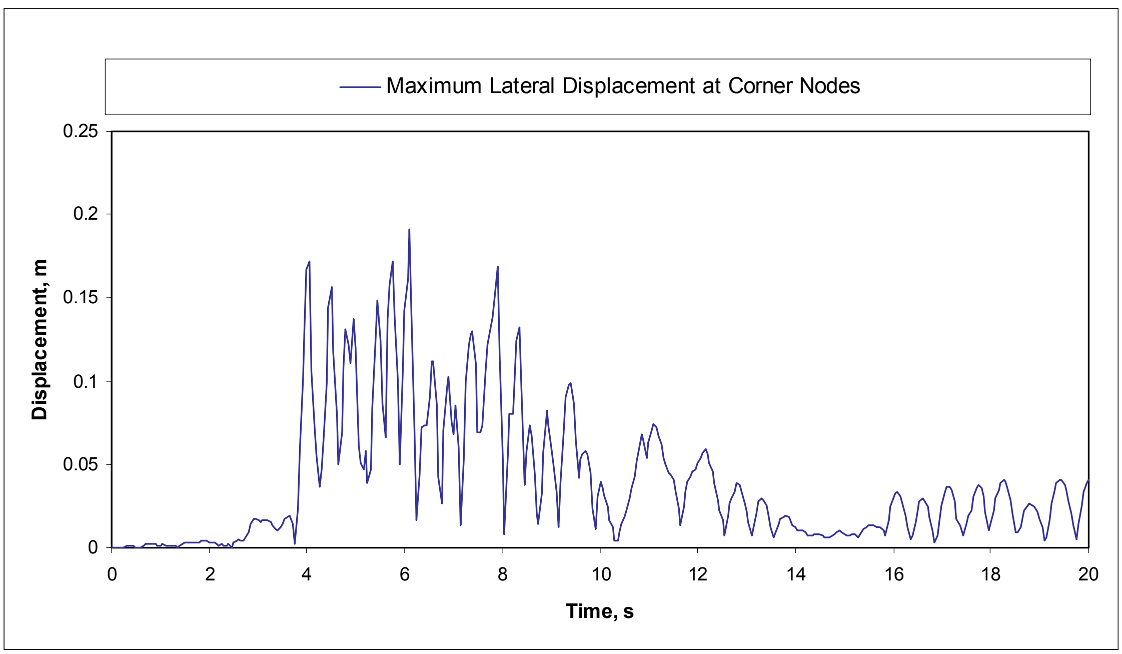

Figure D.250 - Span5, Northridge 3D input, SCED k = 79.1MN/m$^{1.3}$, maximum lateral displacement

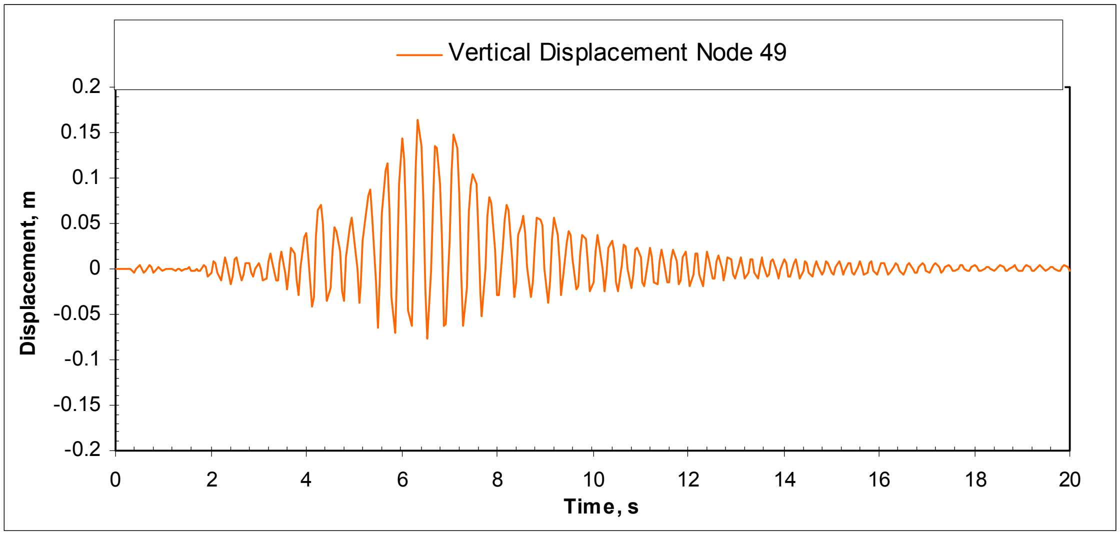

Figure D.251 - Span5, Northridge 3D input, SCED k = 79.1MN/$m^{1.3}$, node 49 vertical displacement

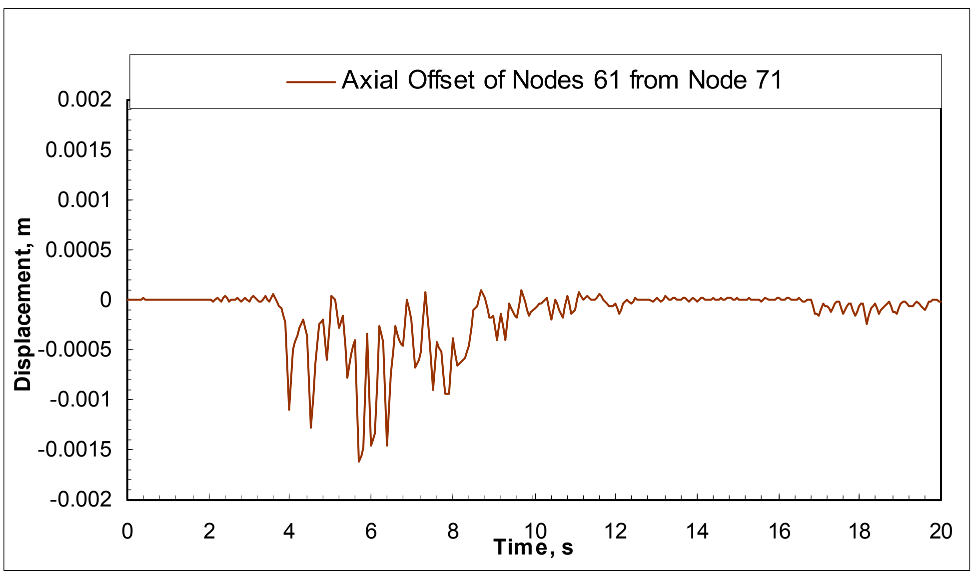

Figure D.252 - Span5, Northridge 3D input, SCED k = 79.1MN/$m^{1.3}$, node 61 and 71 response

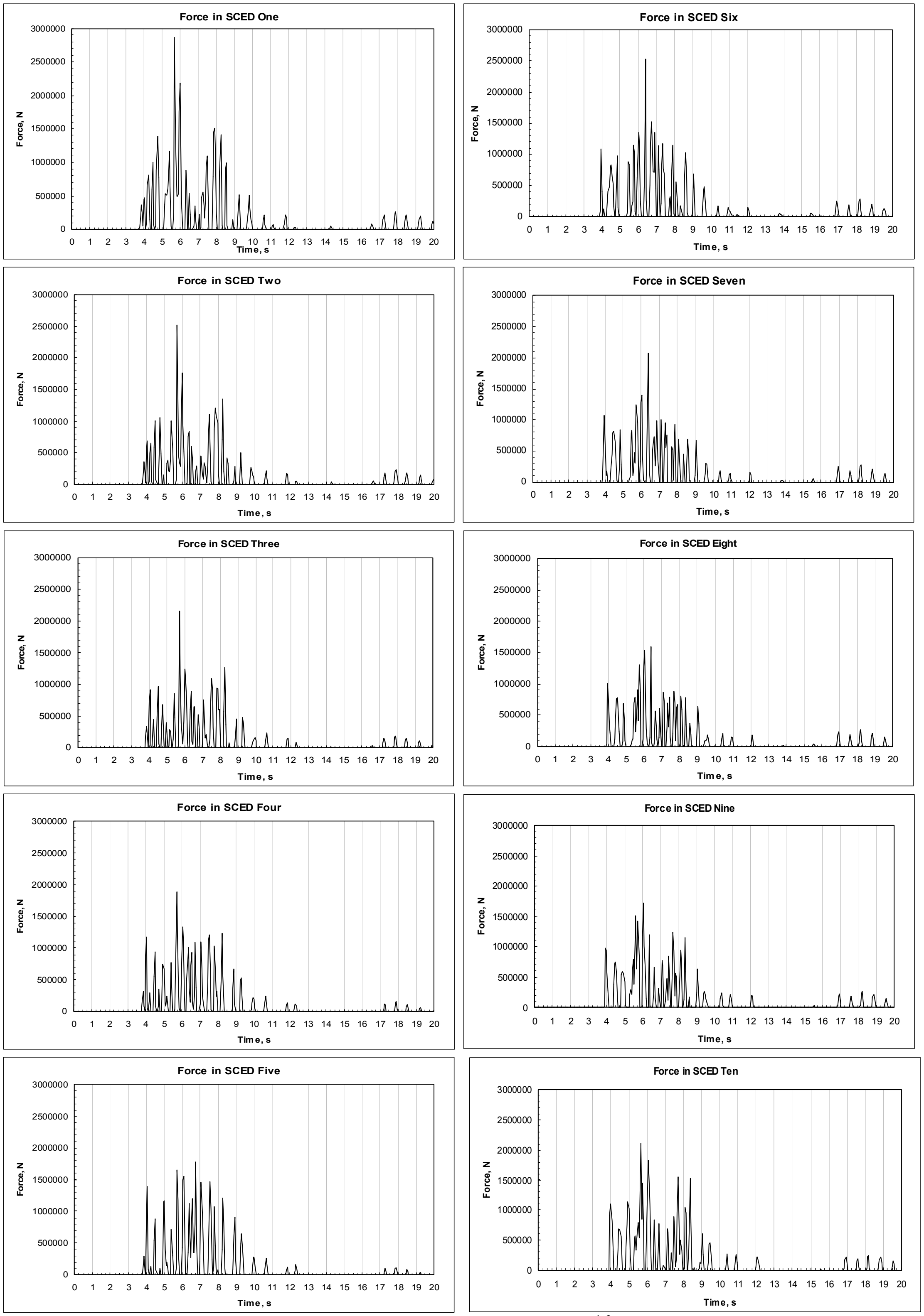

Figure D.253 - Span5, Northridge 3D input, SCED k = 79.1MN/$m^{1.3}$, snap load histories

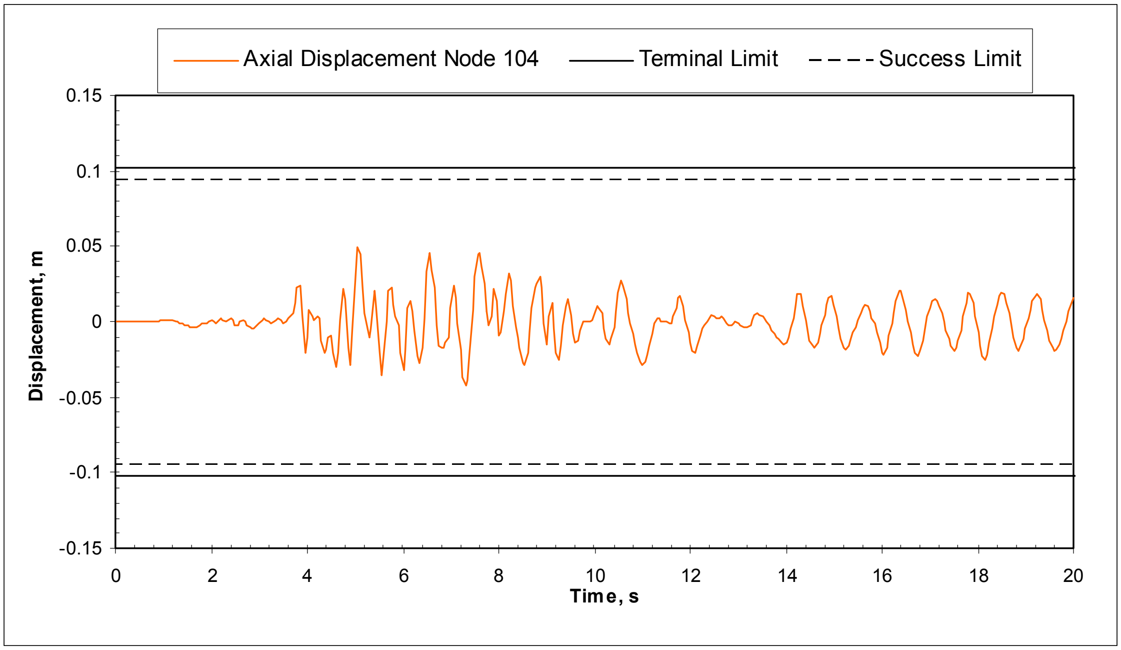

Figure D.254 - Span5, Northridge 3D input, SCED k = 68.5MN/m$^{1.3}$, node 104 axial displacement

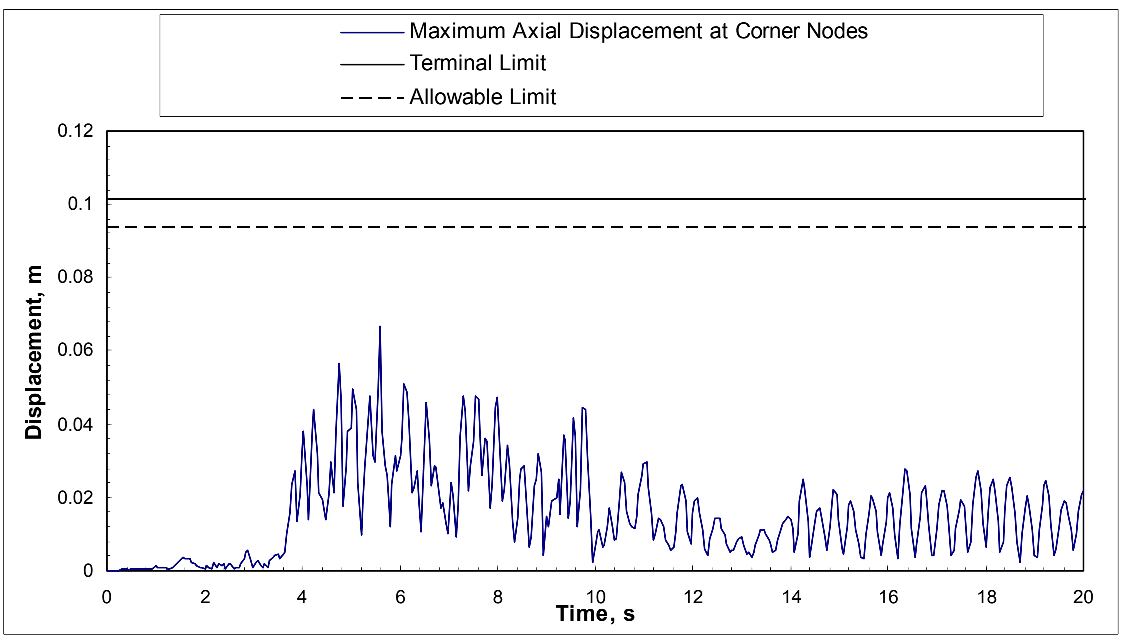

Figure D.255 - Span5, Northridge 3D input, SCED k = 68.5MN/m$^{1.3}$, maximum axial displacement

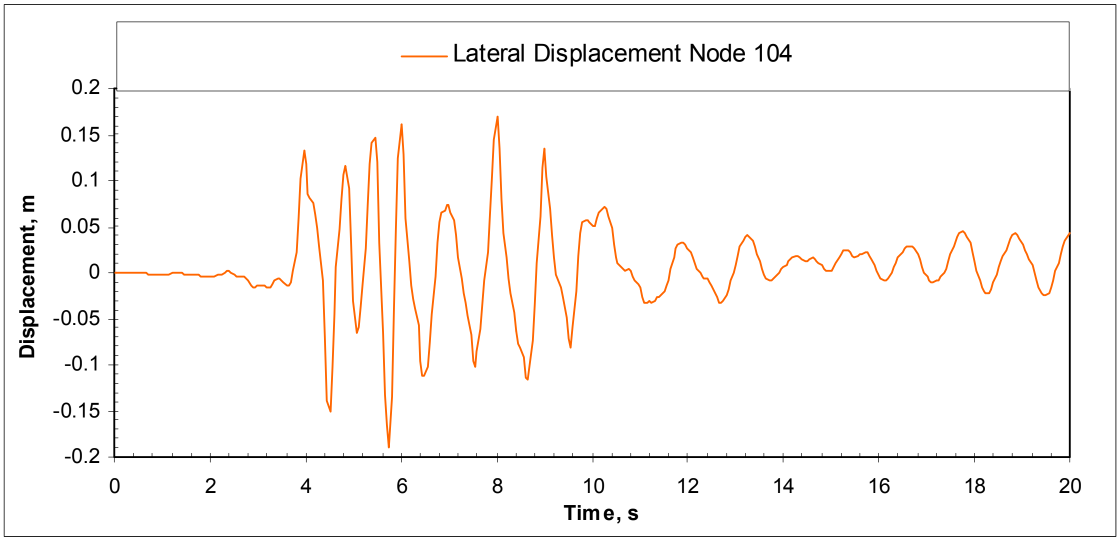

Figure D.256 - Span5, Northridge 3D input, SCED k = 68.5MN/m$^{1.3}$, node 104 lateral displacement

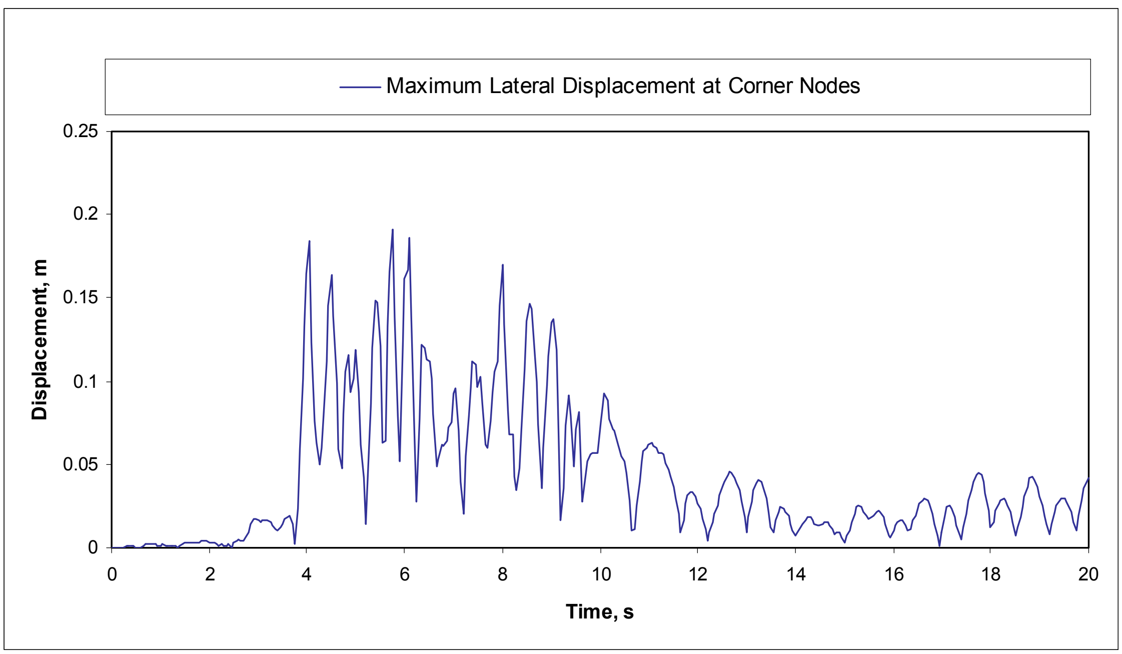

Figure D.257 - Span5, Northridge 3D input, SCED k = 68.5MN/m$^{1.3}$, maximum lateral displacement

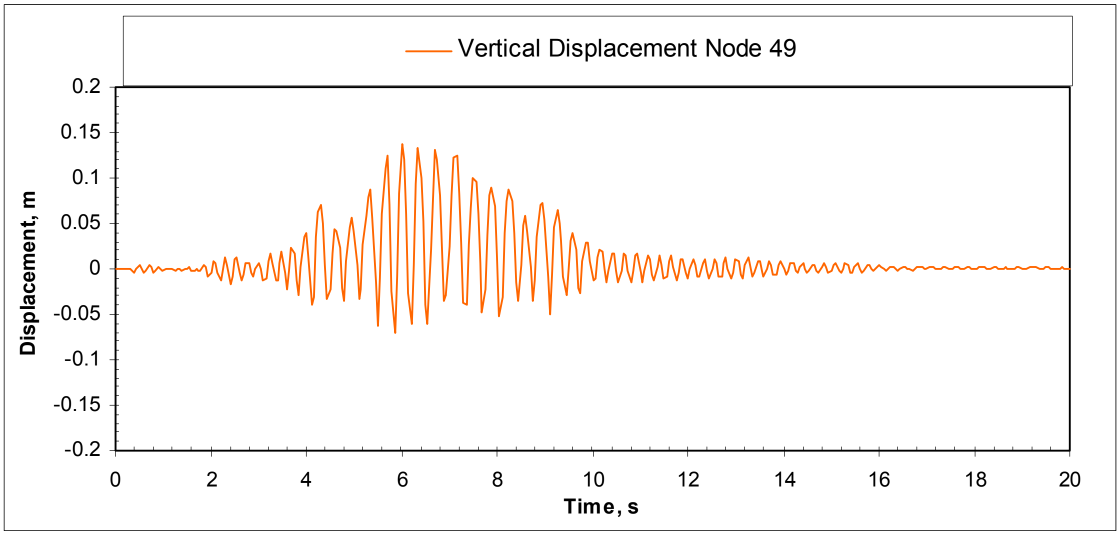

Figure D.258 - Span5, Northridge 3D input, SCED k = 68.5MN/m$^{1.3}$, node 49 vertical displacement

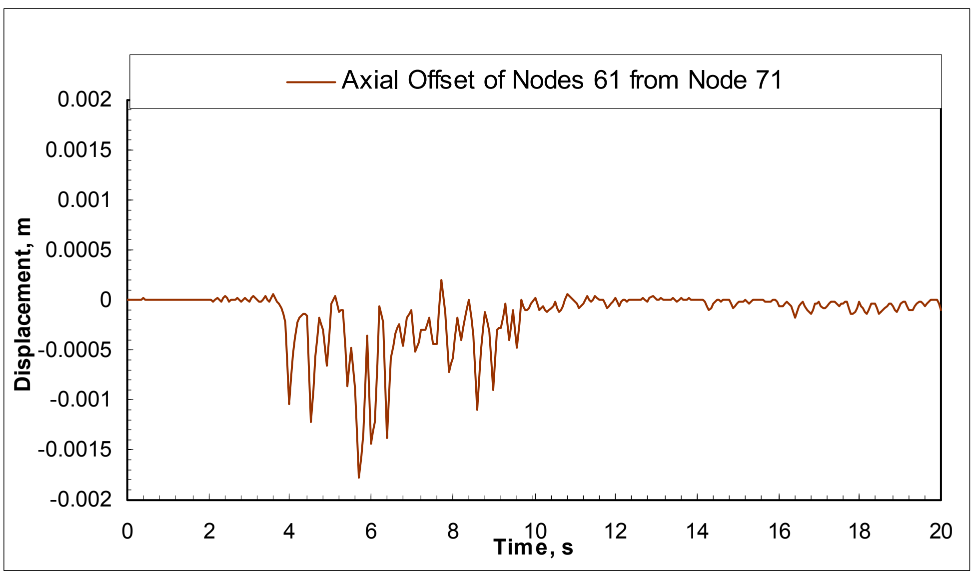

Figure D.259 - Span5, Northridge 3D input, SCED k = 68.5MN/m$^{1.3}$, node 61 and 71 response

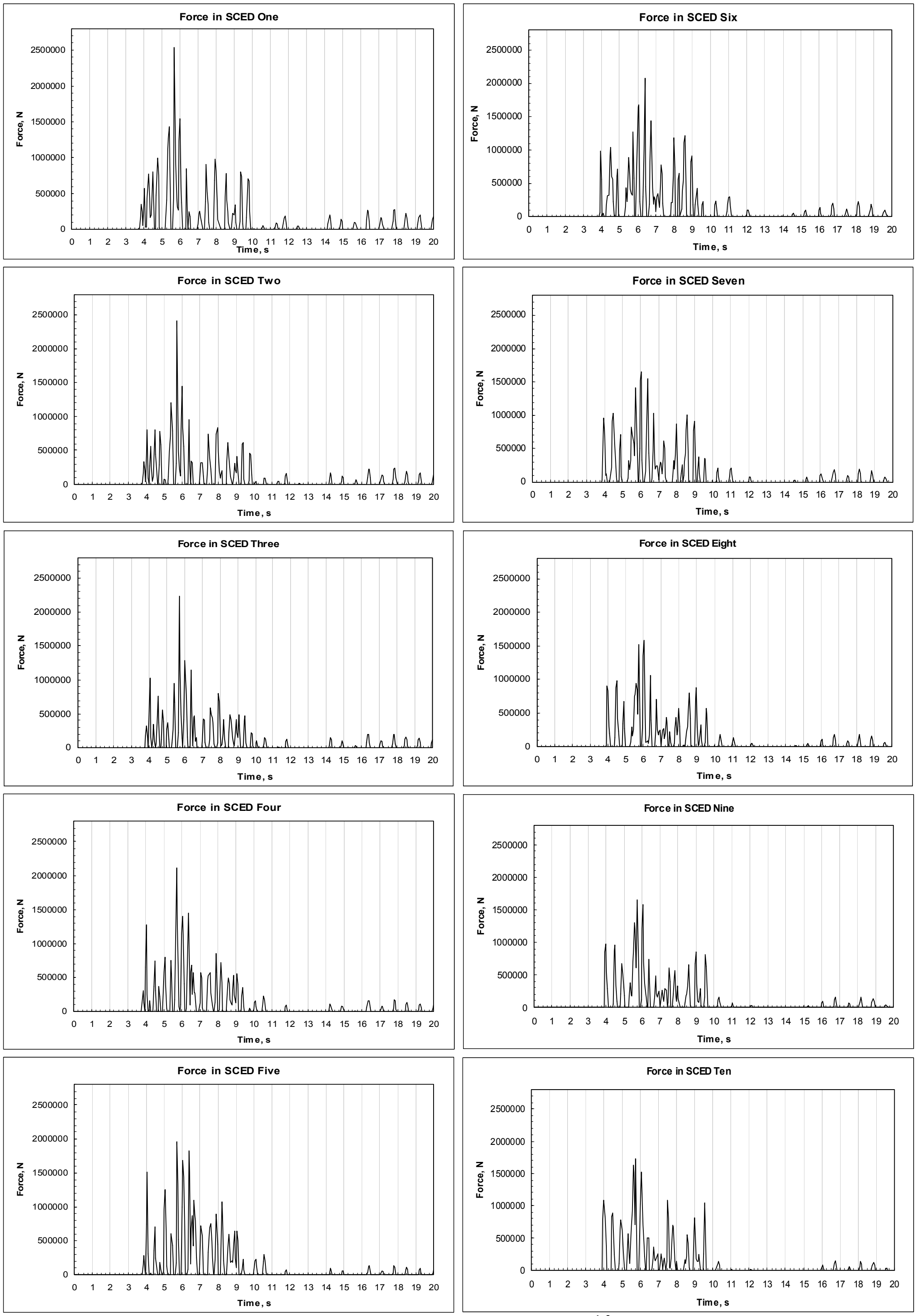

Figure D.260 - Span5, Northridge 3D input, SCED k = 68.5MN/m$^{1.3}$, snap load histories

D.6 Span6 Figures

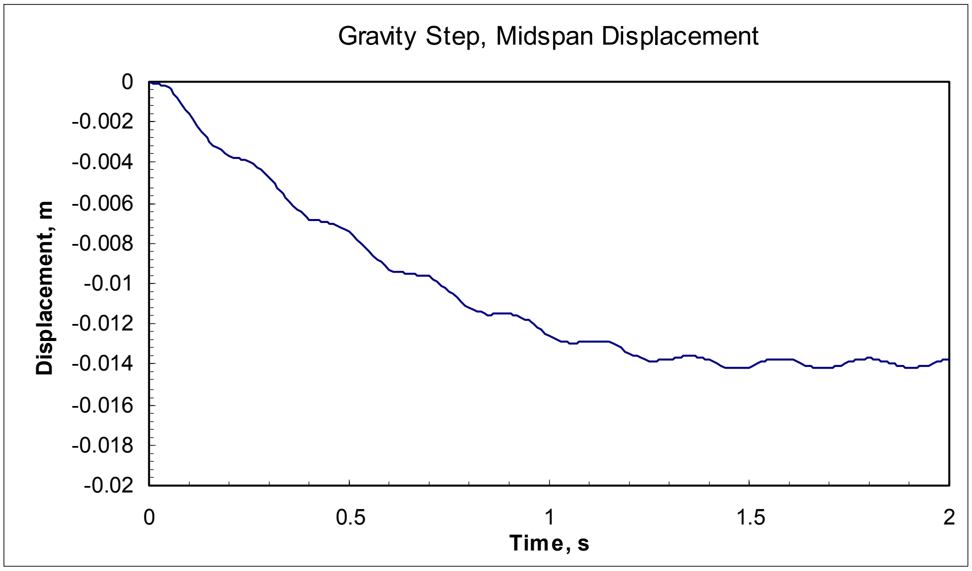

Figure D.261 - Span6, Imperial Valley input, gravity step response

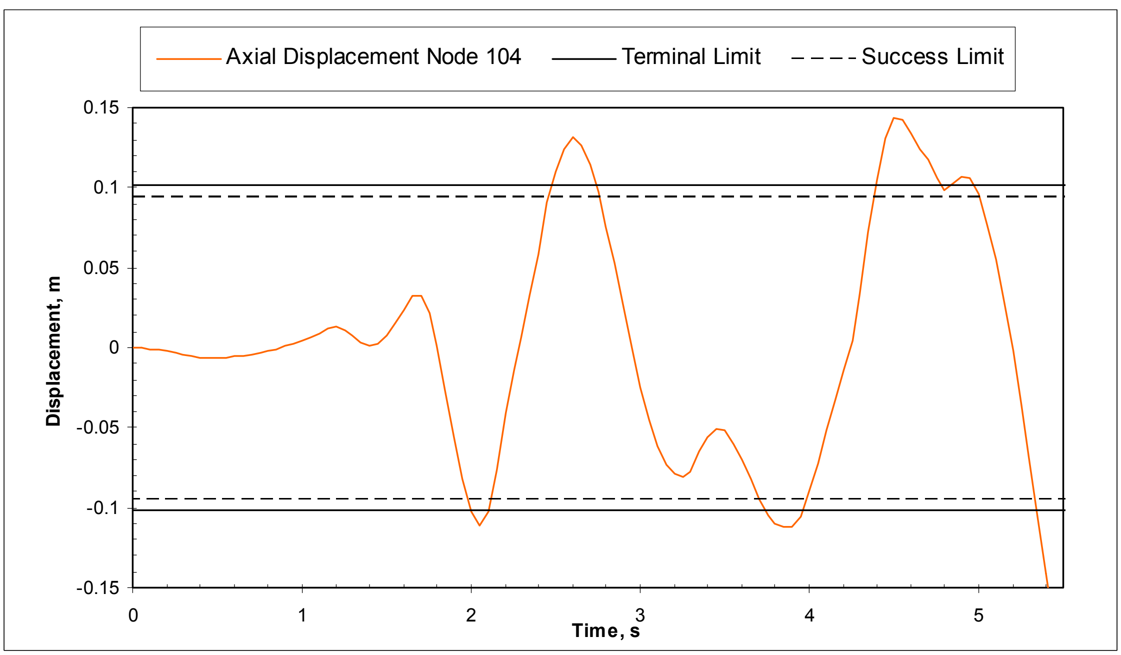

Figure D.262 - Span6, Imperial Valley axial input only, node 104 axial displacement

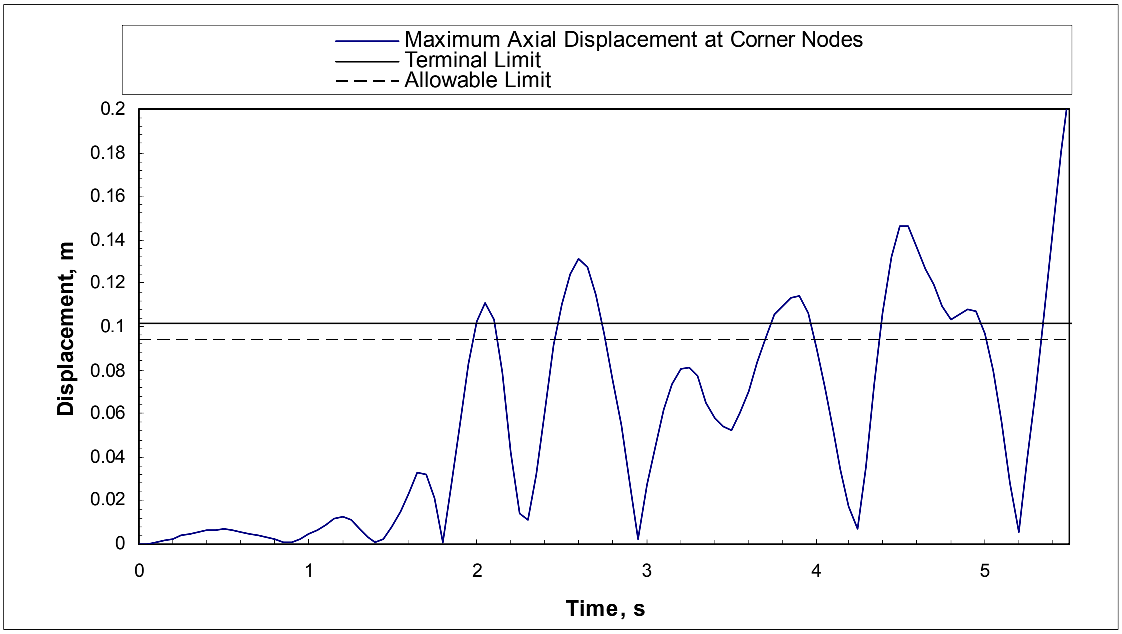

Figure D.263 - Span6, Imperial Valley axial input only, maximum axial displacement

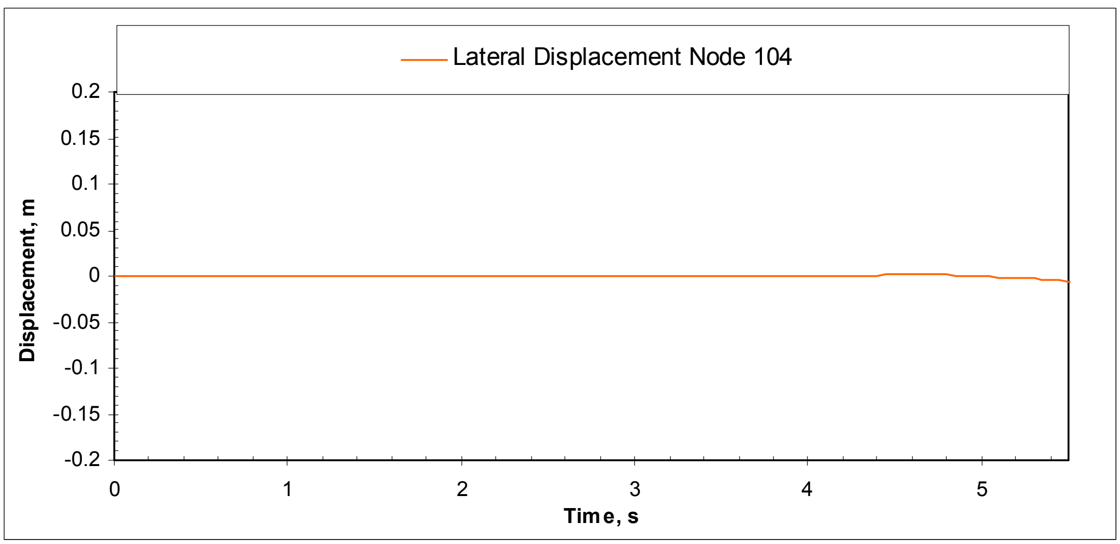

Figure D.264 - Span6, Imperial Valley axial input only, node 104 lateral displacement

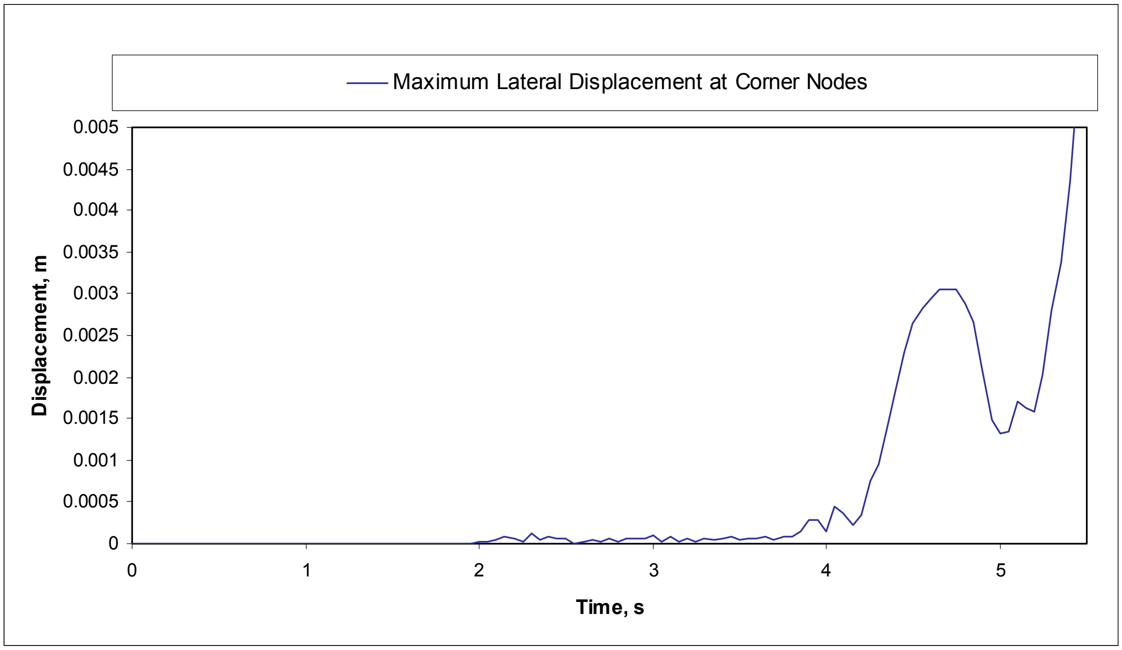

Figure D.265 - Span6, Imperial Valley axial input only, maximum lateral displacement

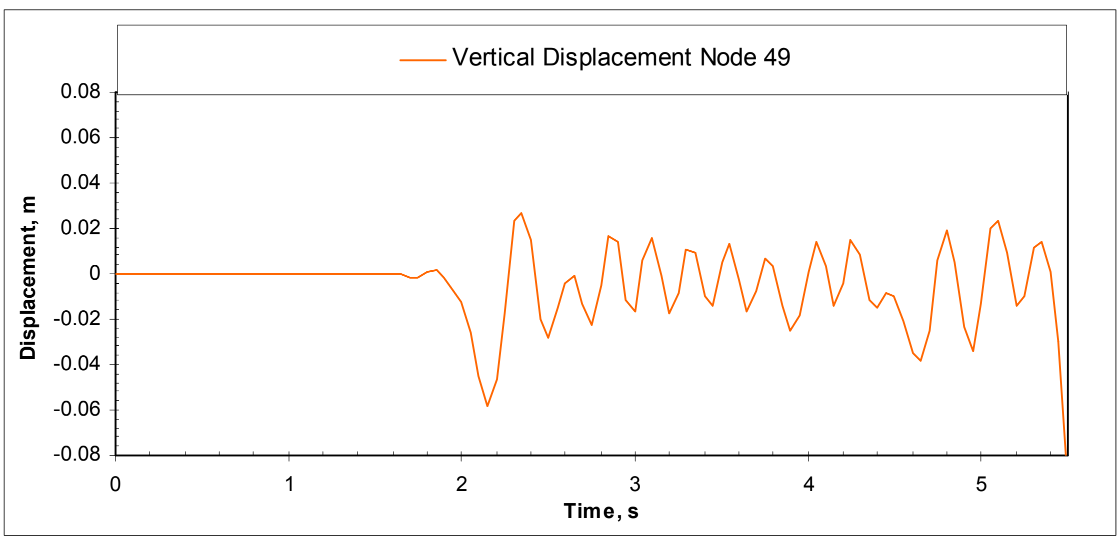

Figure D.266 - Span6, Imperial Valley axial input only, node 49 vertical displacement

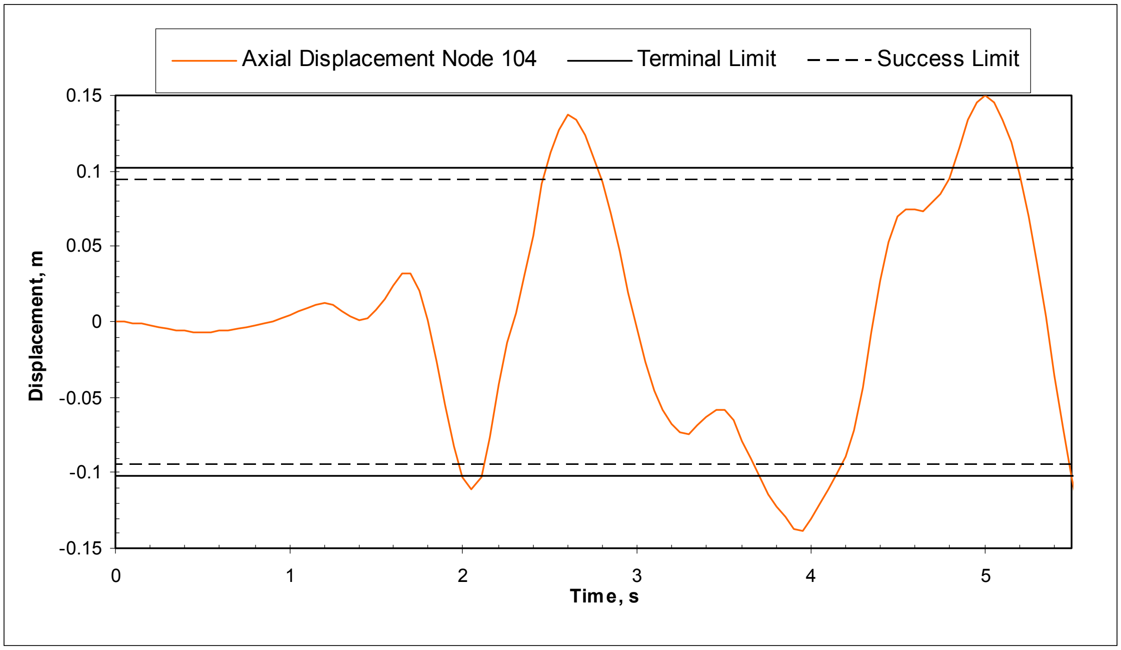

Figure D.267 - Span6, Imperial Valley three-dimensional input, no SCEDs, node 104 axial displacement

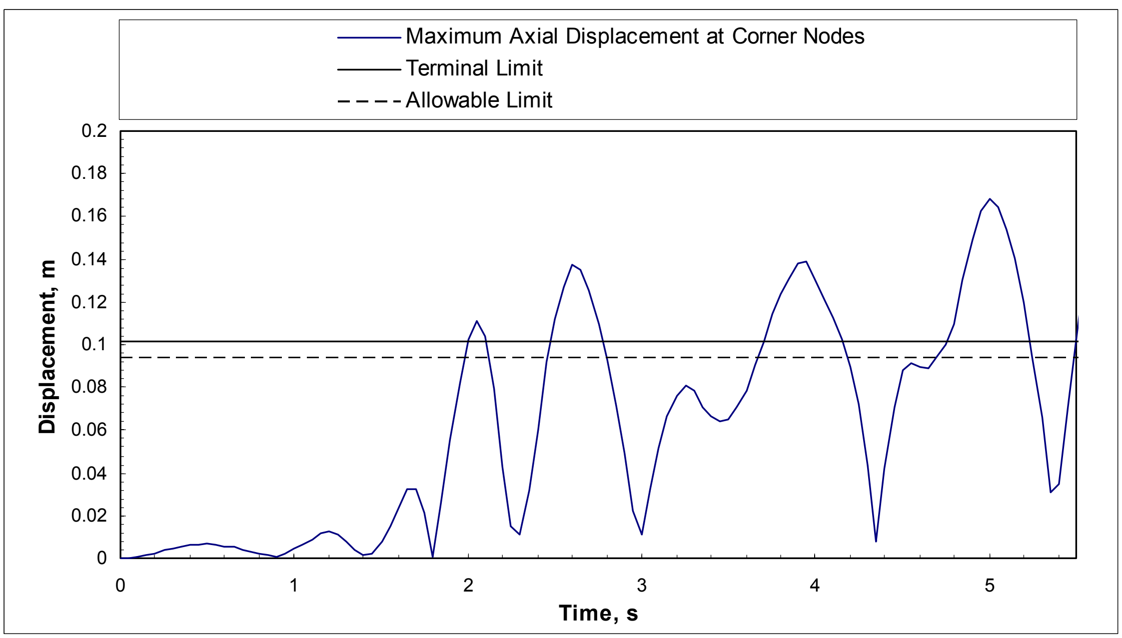

Figure D.268 - Span6, Imperial Valley three-dimensional input, no SCEDs, maximum axial displacement

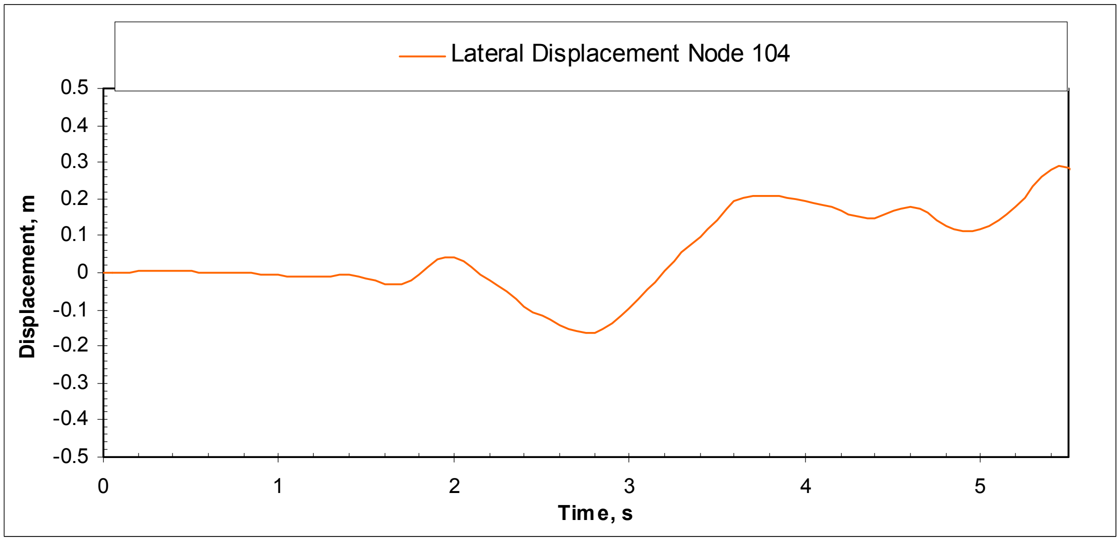

Figure D.269 - Span6, Imperial Valley 3D input, no SCEDs, node 104 lateral displacement

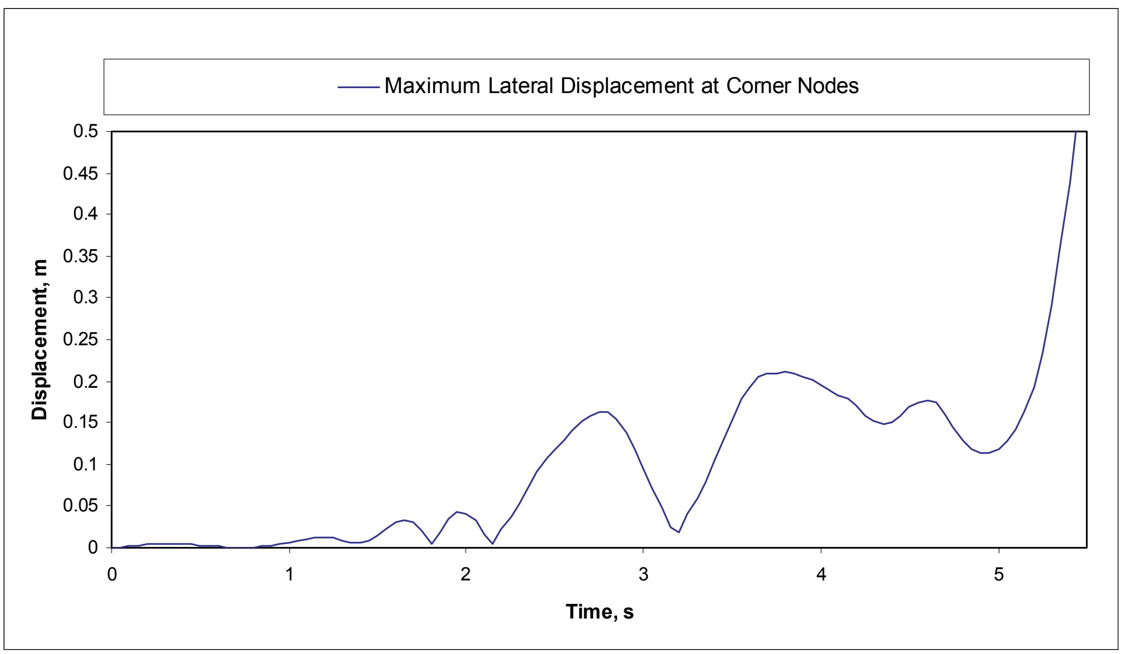

Figure D.270 - Span6, Imperial Valley 3D input, no SCEDs, maximum lateral displacement

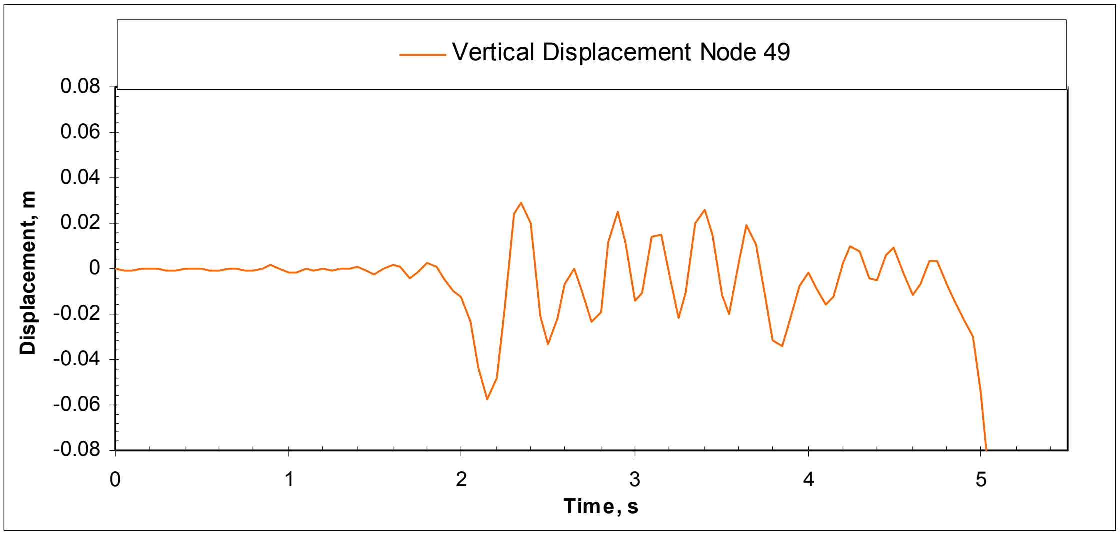

Figure D.271 - Span6, Imperial Valley 3D input, no SCEDs, node 49 vertical displacement

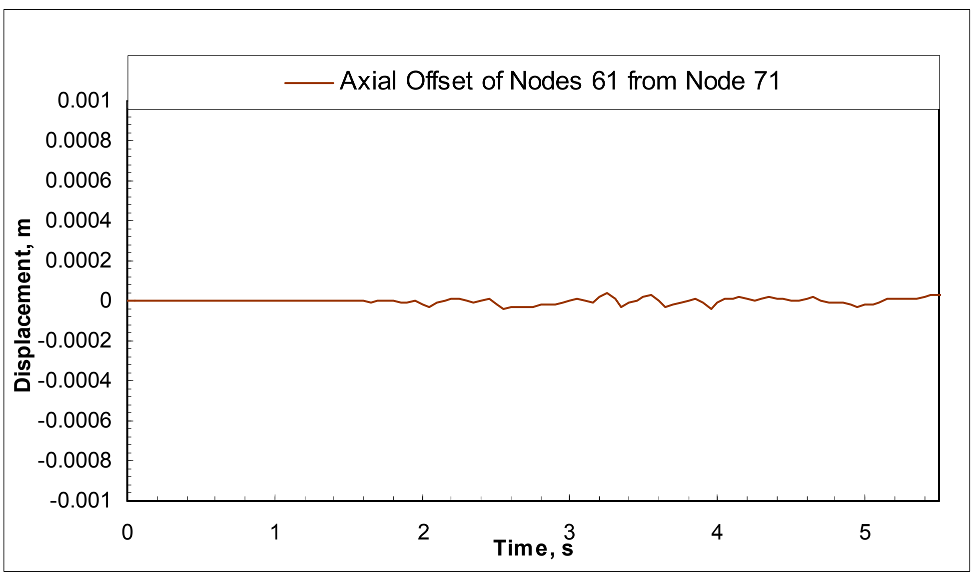

Figure D.272 - Span6, Imperial Valley 3D input, no SCEDs, node 61 and 71 response

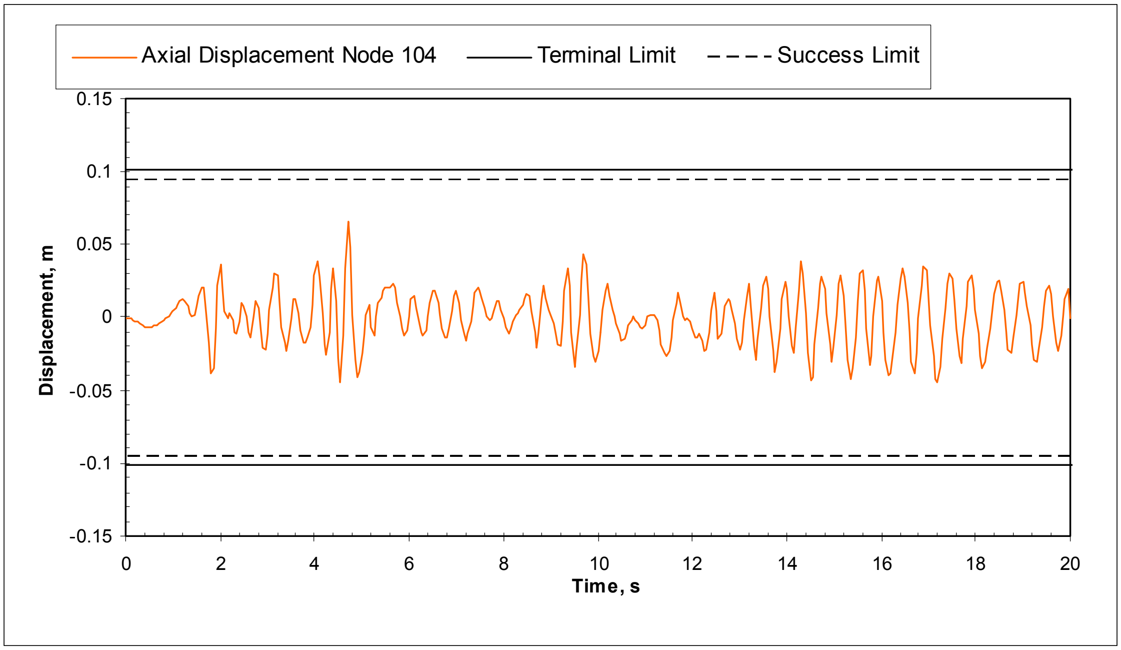

Figure D.273 - Span6, Imperial Valley 3D input, SCED k = 105.4MN/m$^{1.3}$, node 104 axial displacement

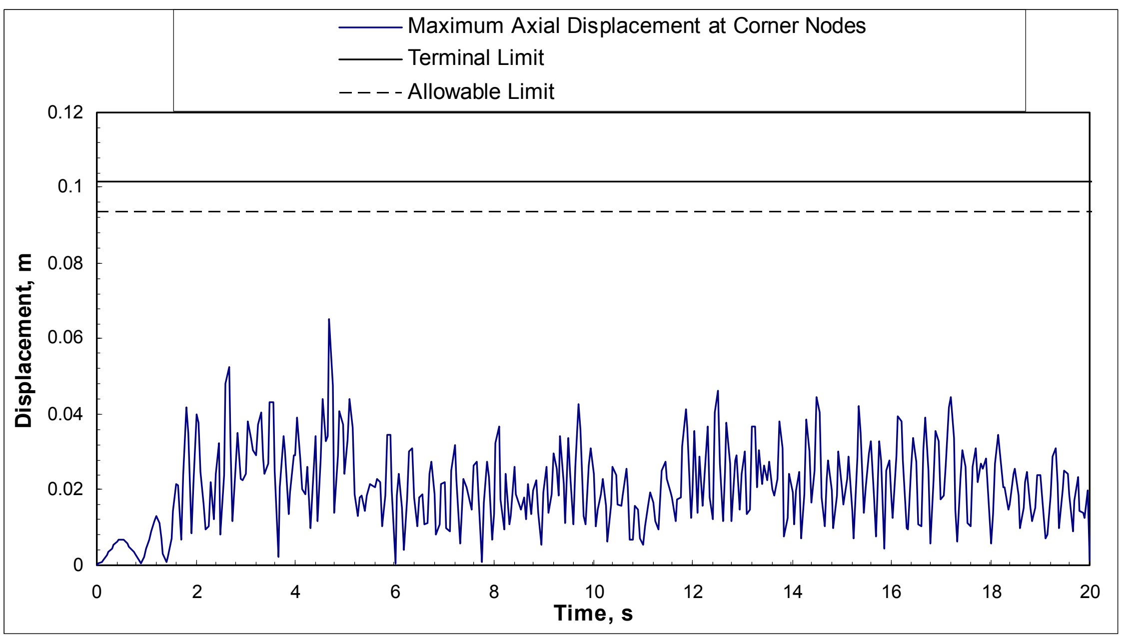

Figure D.274 - Span6, Imperial Valley 3D input, SCED k = 105.4MN/m$^{1.3}$, maximum axial displacement

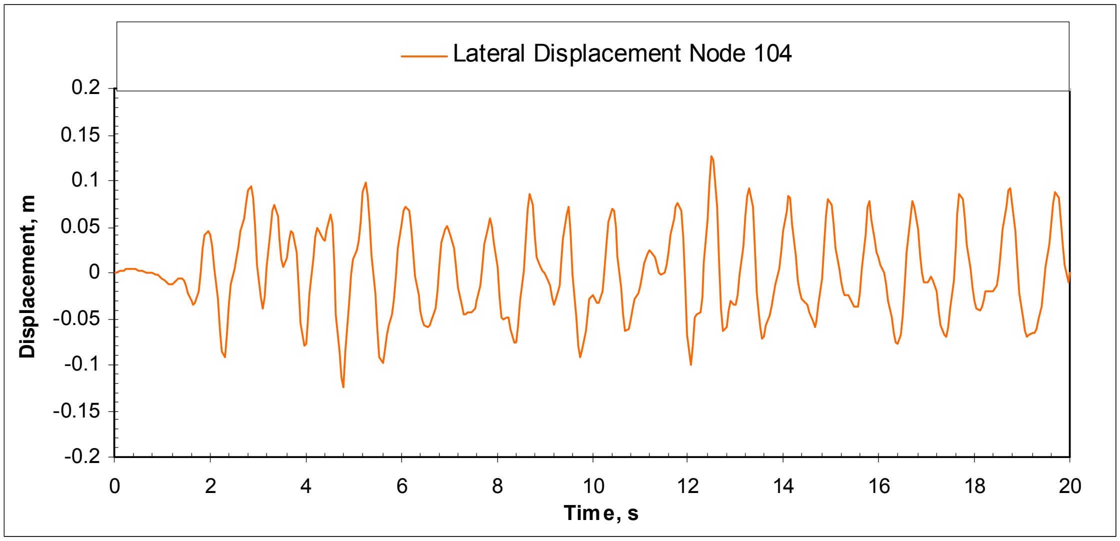

Figure D.275 - Span6, Imperial Valley 3D input, SCED k = 105.4MN/m$^{1.3}$, node 104 lateral disp.

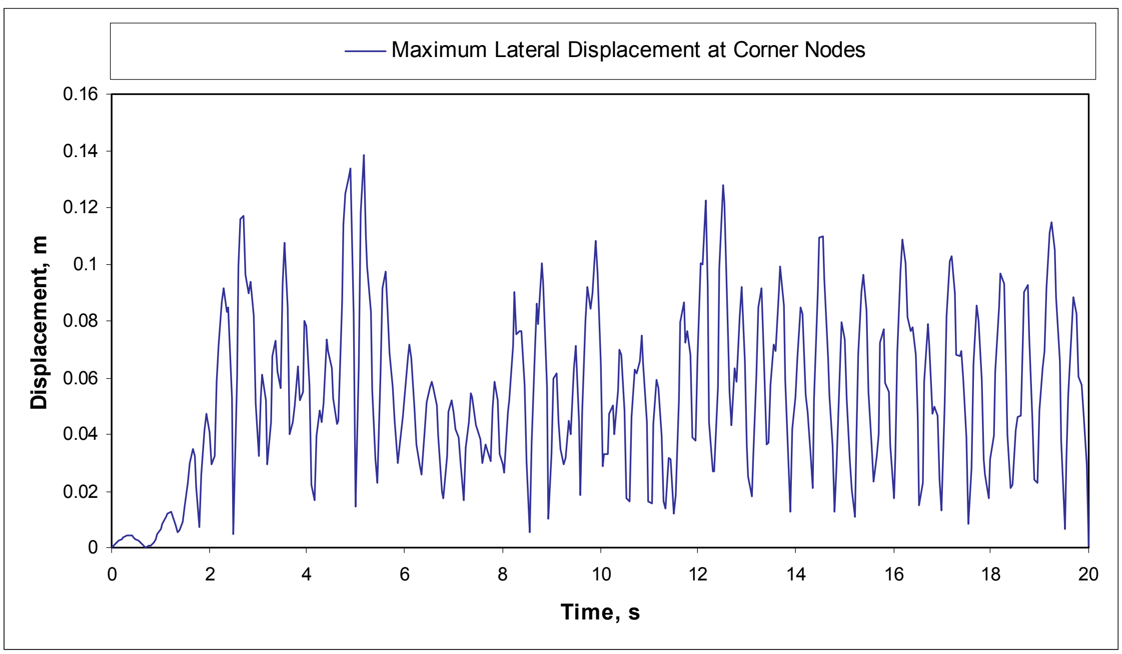

Figure D.276 - Span6, Imperial Valley 3D input, SCED k = 105.4MN/m$^{1.3}$, maximum lateral disp.

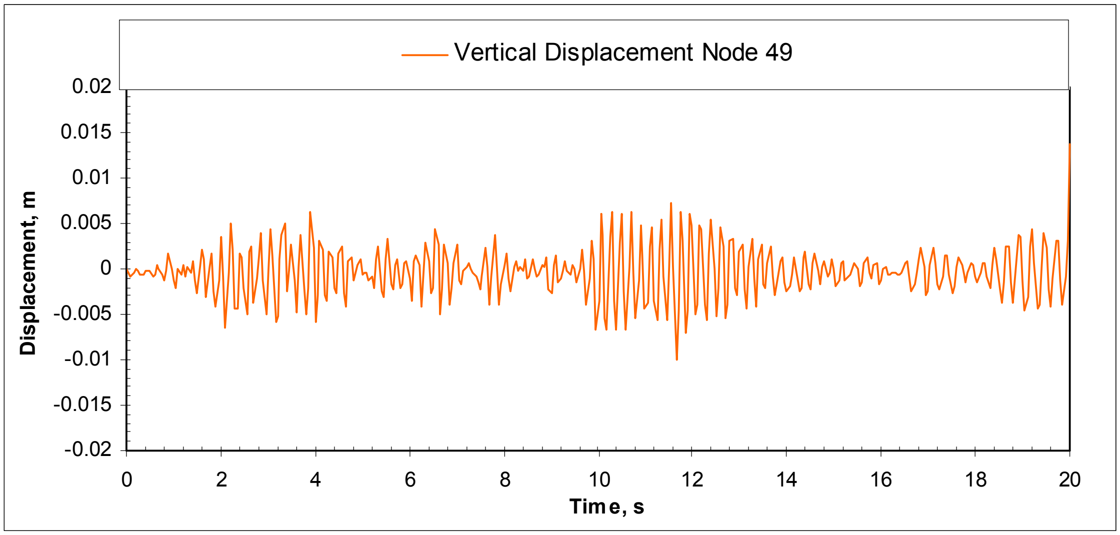

Figure D.277 - Span6, Imperial Valley 3D input, SCED k = 105.4MN/$m^{1.3}$, node 49 vertical disp.

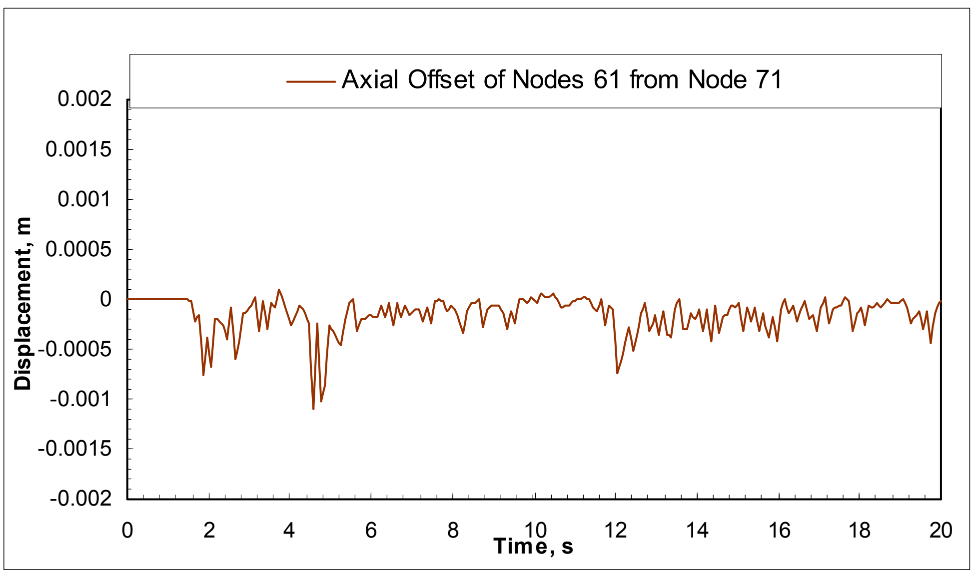

Figure D.278 - Span6, Imperial Valley 3D input, SCED k = 105.4MN/$m^{1.3}$, node 61 and 71 response

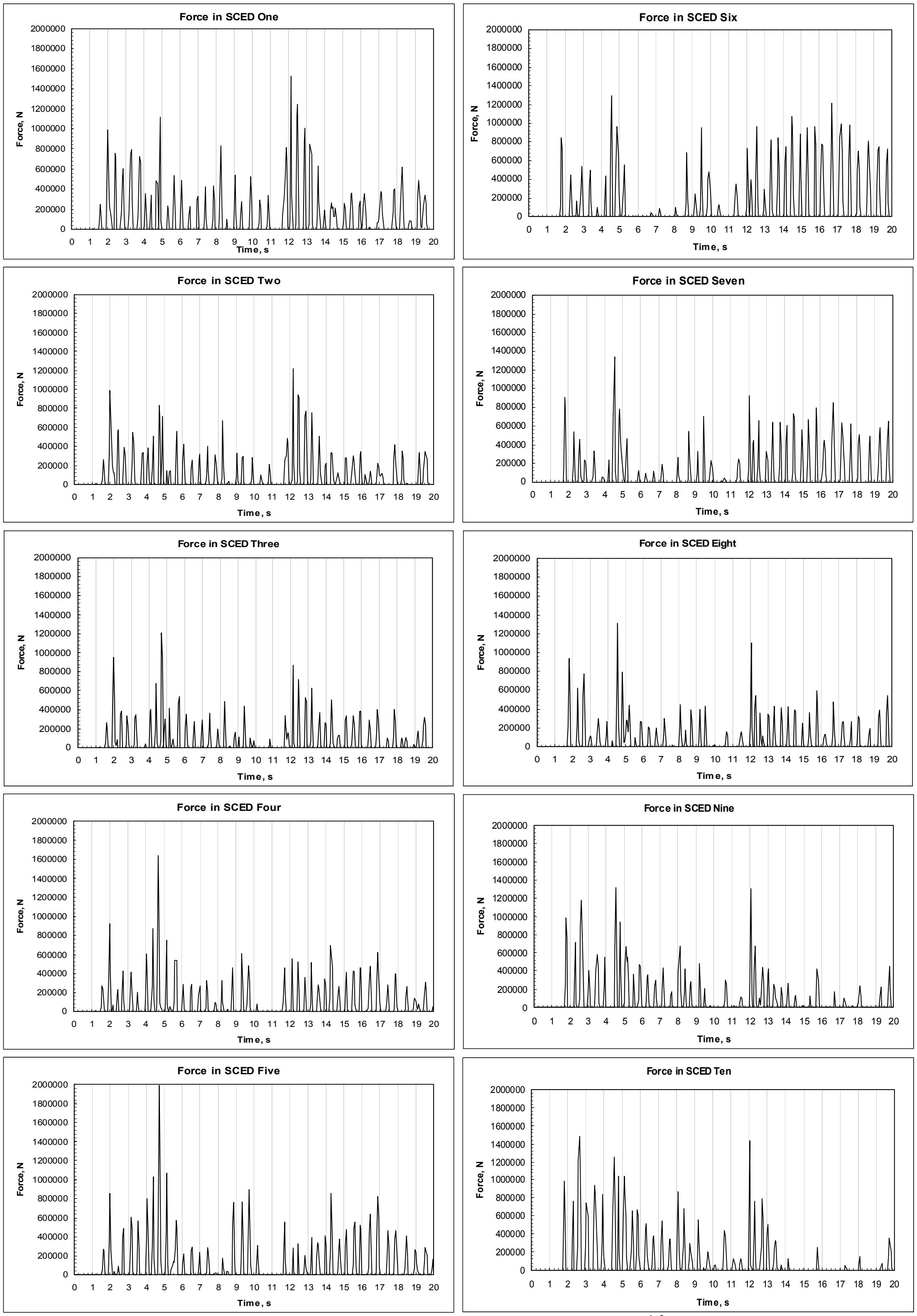

Figure D.279 - Span6, Imperial Valley 3D input, SCED k = 105.4MN/m$^{1.3}$, snap load histories

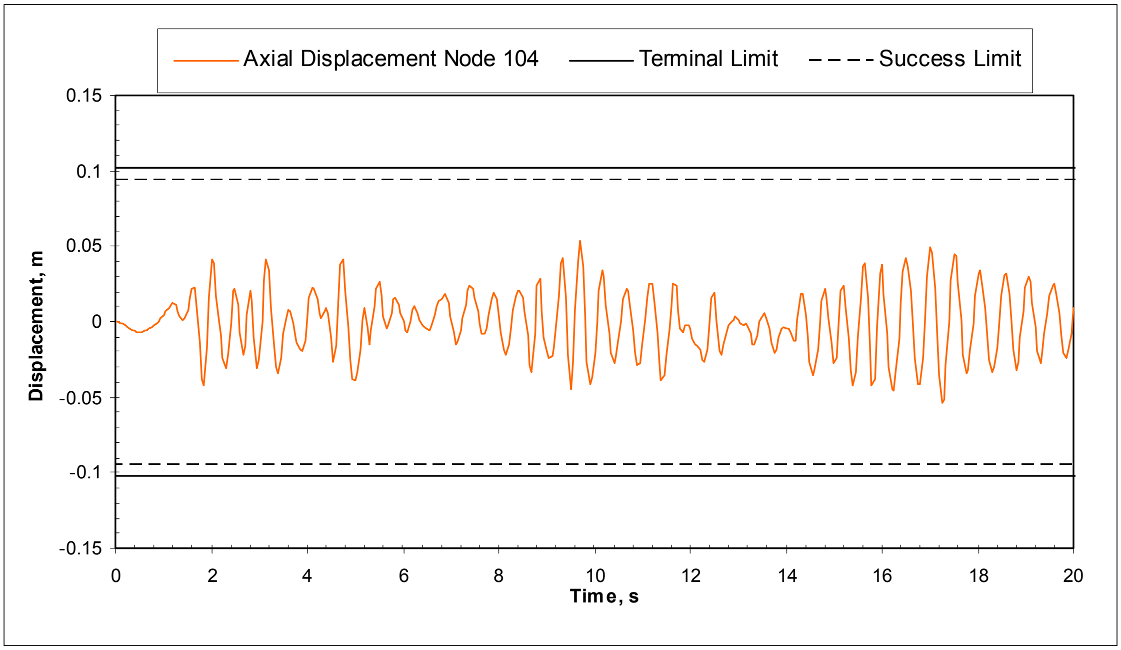

Figure D.280 - Span6, Imperial Valley 3D input, SCED k = 84.3MN/m$^{1.3}$, node 104 axial displacement

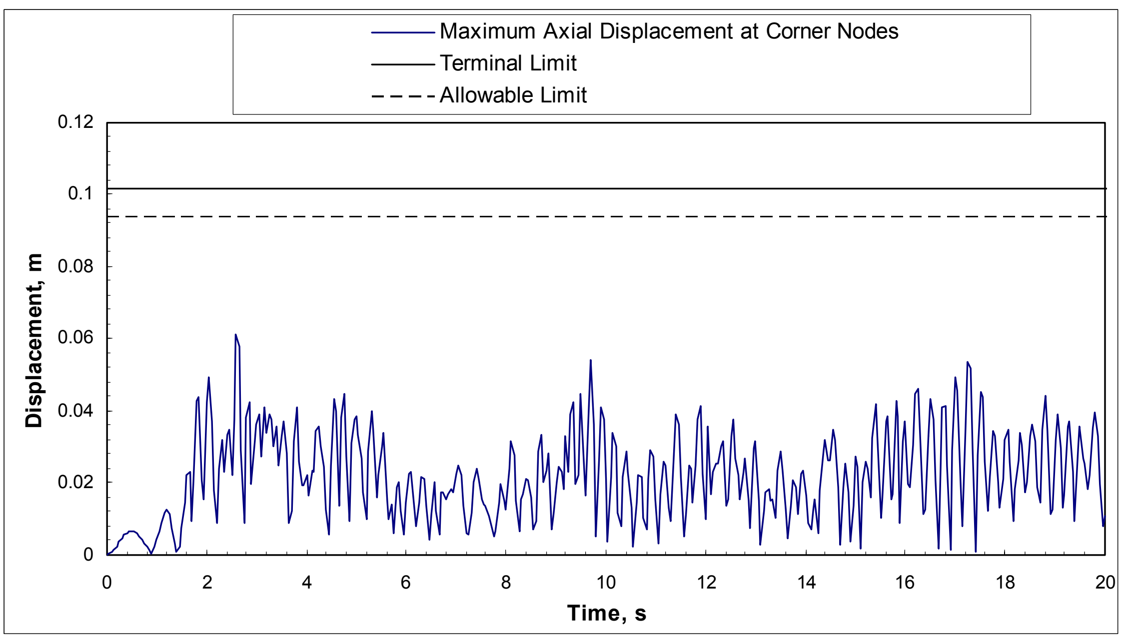

Figure D.281 - Span6, Imperial Valley 3D input, SCED k = 84.3MN/m$^{1.3}$, maximum axial displacement

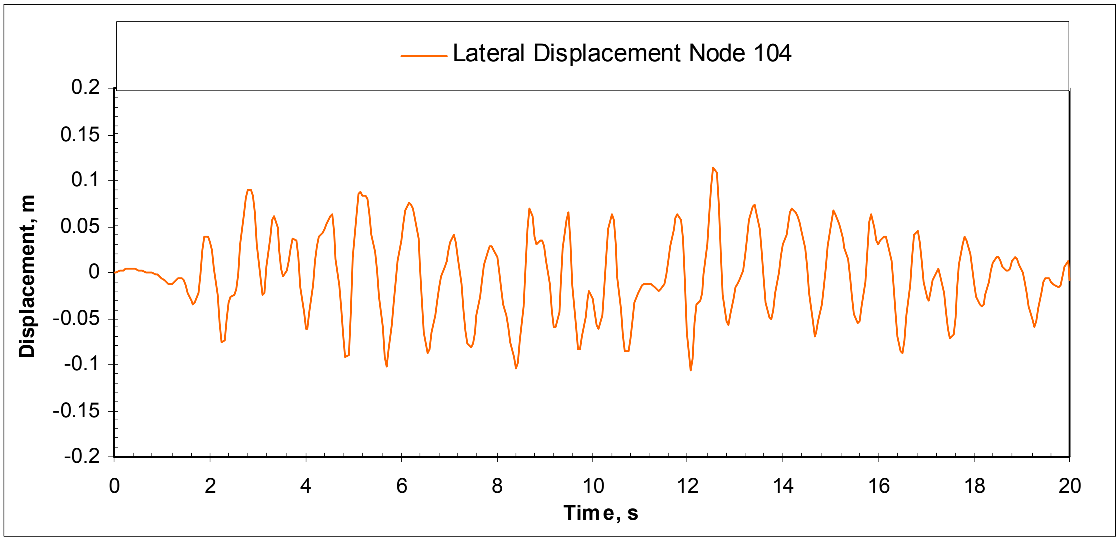

Figure D.282 - Span6, Imperial Valley 3D input, SCED k = 84.3MN/m$^{1.3}$, node 104 lateral displacement

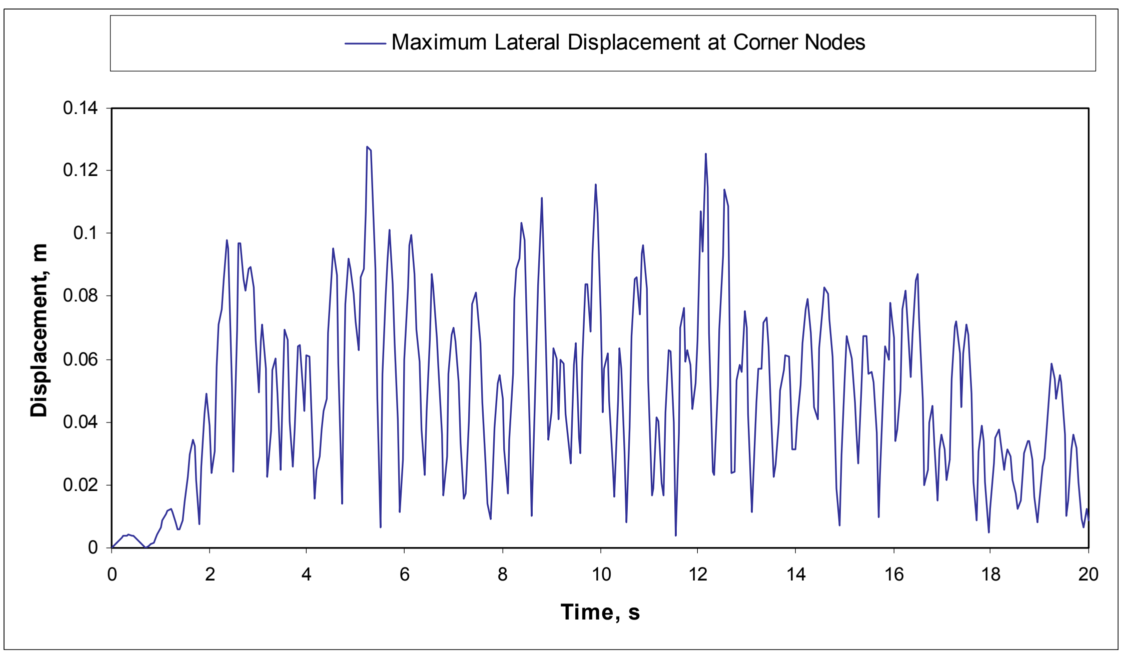

Figure D.283 - Span6, Imperial Valley 3D input, SCED k = 84.3MN/m$^{1.3}$, maximum lateral displacement

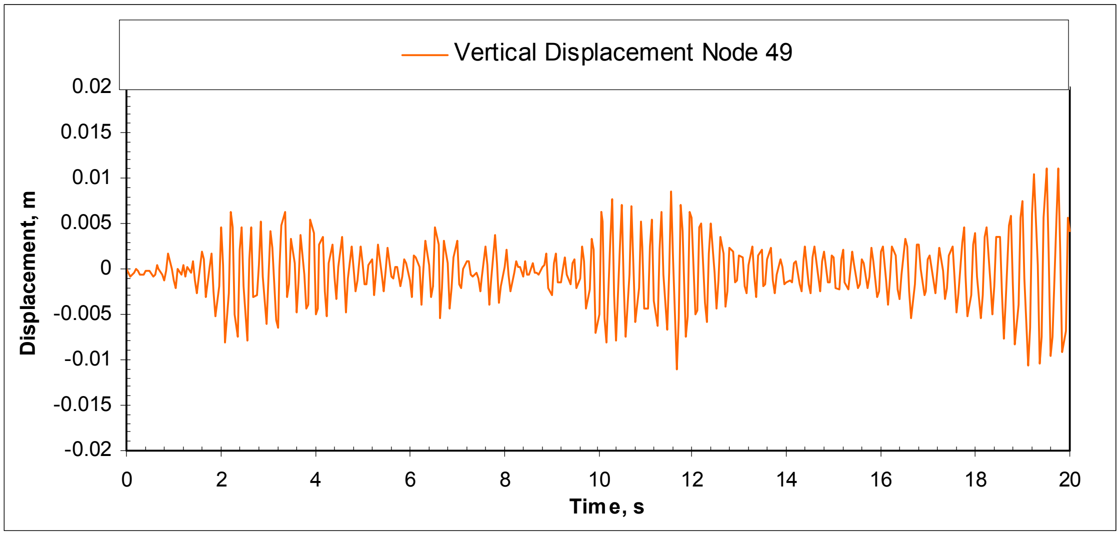

Figure D.284 - Span6, Imperial Valley 3D input, SCED k = 84.3MN/m$^{1.3}$, node 49 vertical displacement

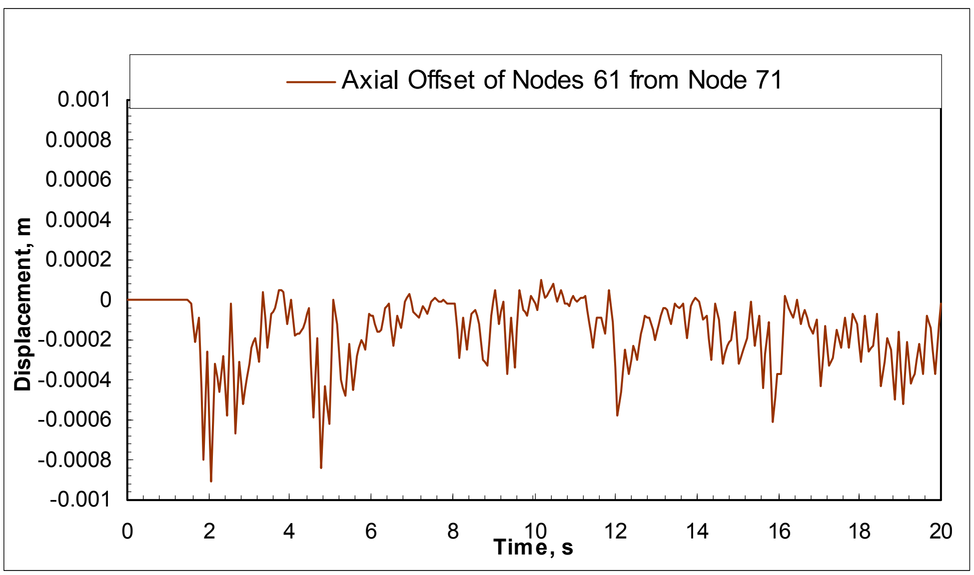

Figure D.285 - Span6, Imperial Valley 3D input, SCED k = 84.3MN/m$^{1.3}$, node 61 and 71 response

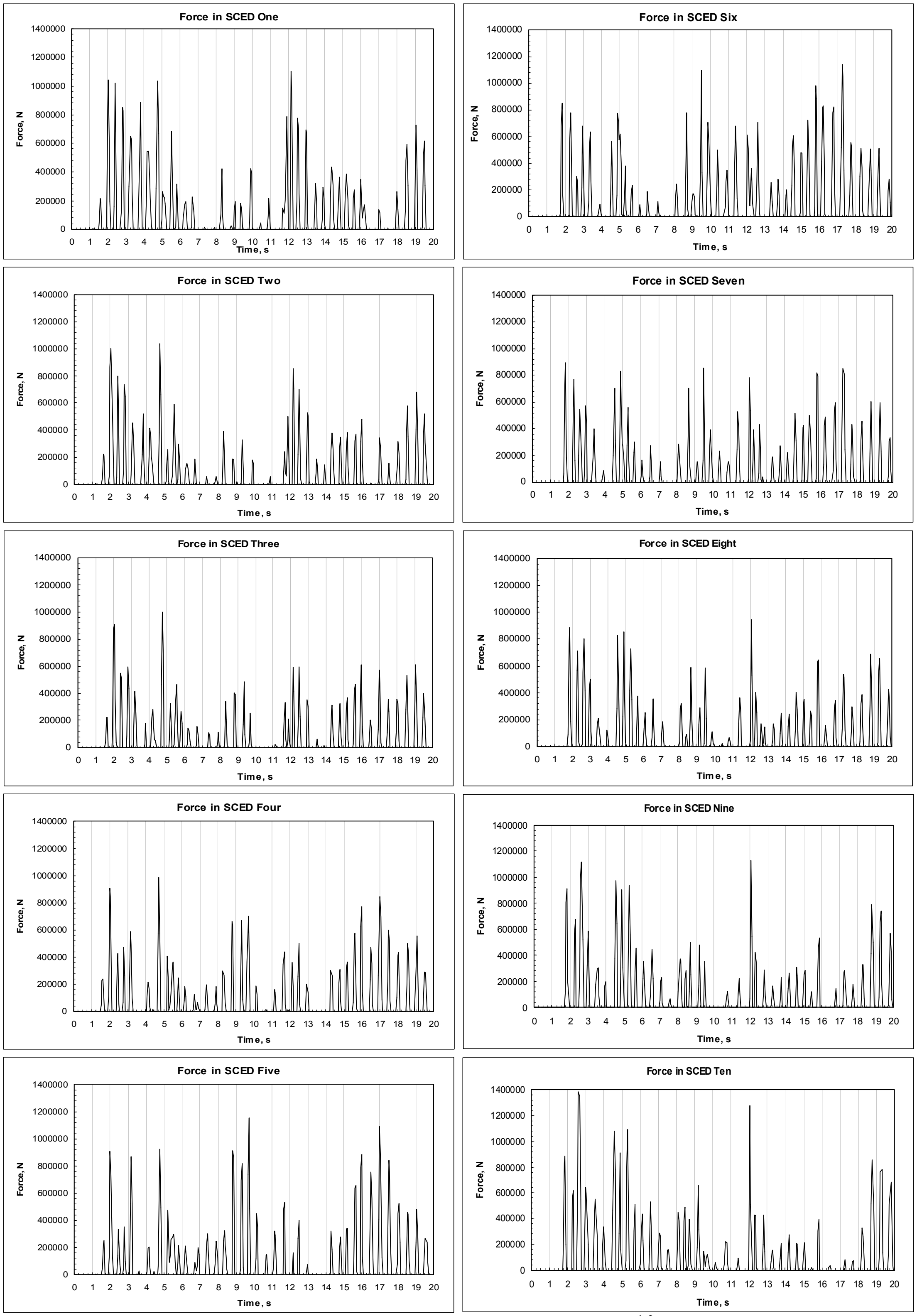

Figure D.286 - Span6, Imperial Valley 3D input, SCED k = 84.3MN/m$^{1.3}$, snap load histories

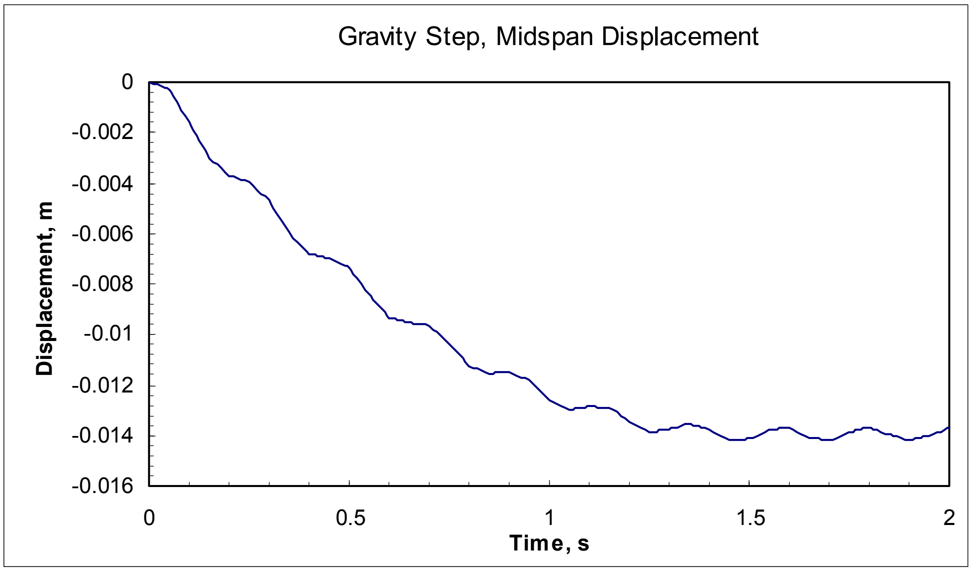

Figure D.287 - Span6, Northridge input, gravity step response

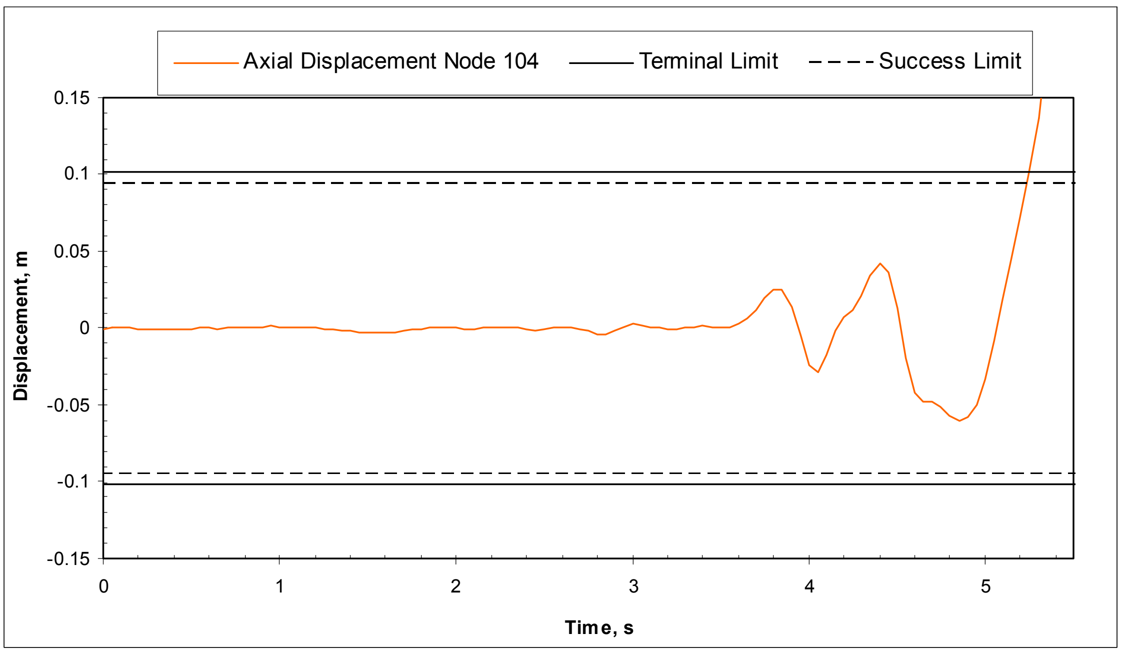

Figure D.288 - Span6, Northridge axial input only, node 104 axial displacement

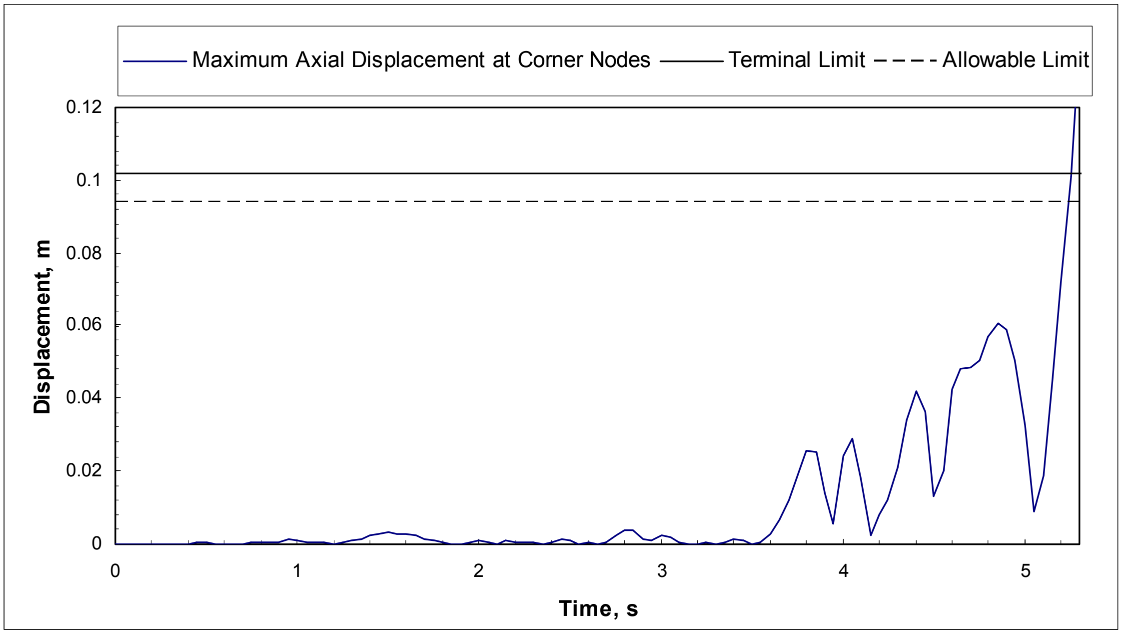

Figure D.289 - Span6, Northridge axial input only, maximum axial displacement

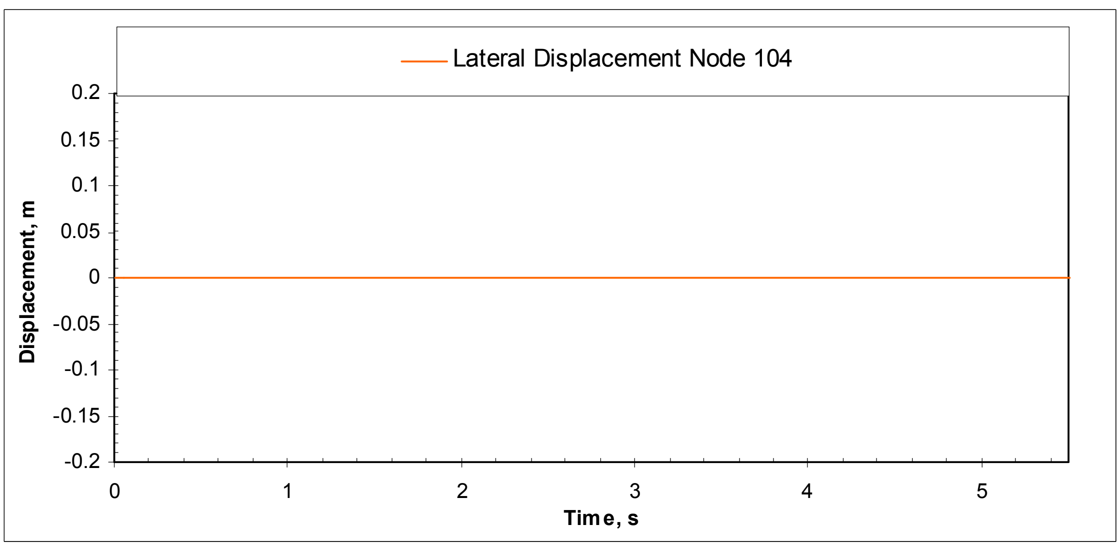

Figure D.290 - Span6, Northridge axial input only, node 104 lateral displacement

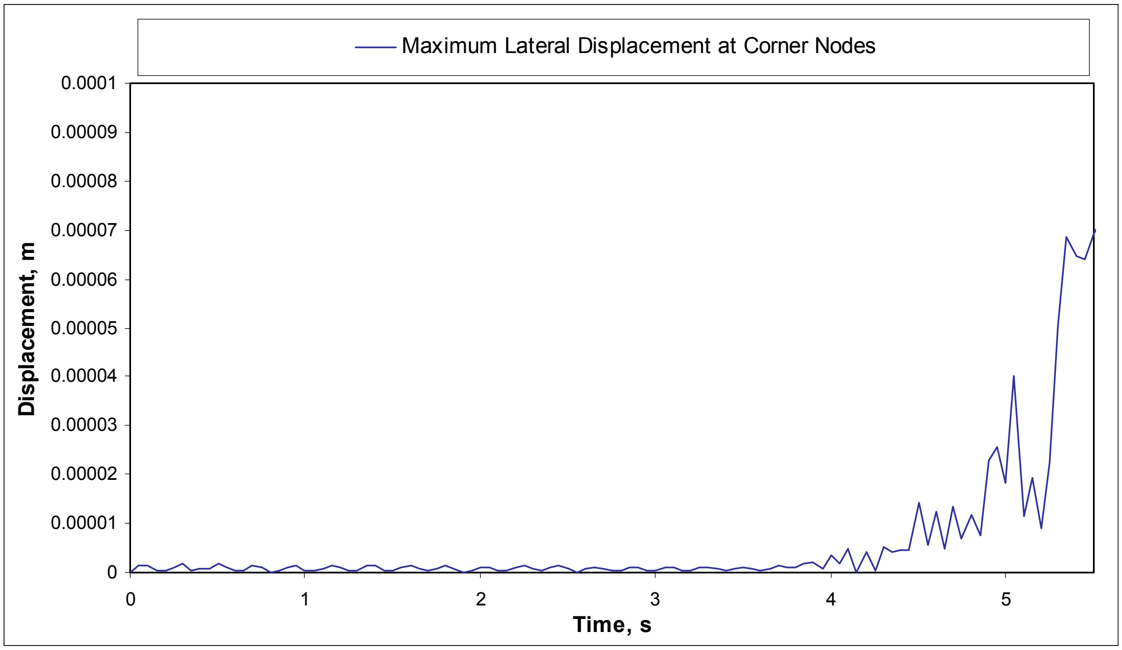

Figure D.291 - Span6, Northridge axial input only, maximum lateral displacement

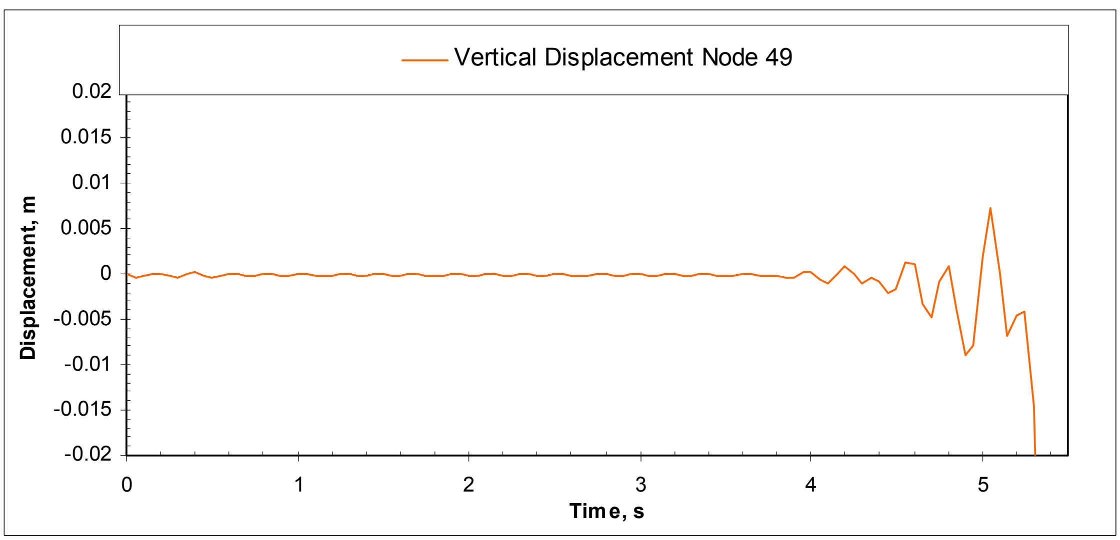

Figure D.292 - Span6, Northridge axial input only, node 49 vertical displacement

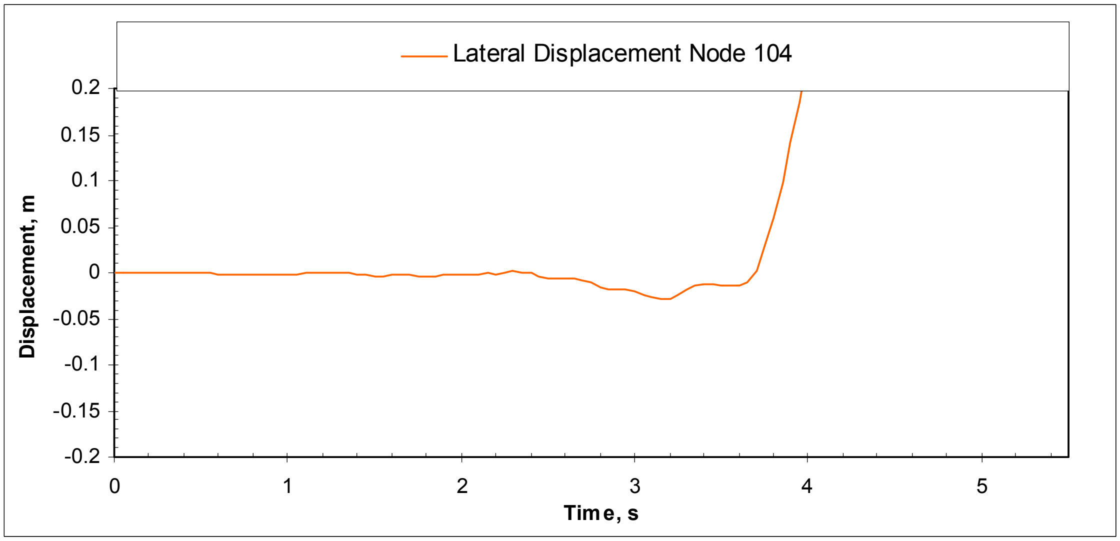

Figure D.293 - Span6, Northridge 3D input, no SCEDs, node 104 axial displacement

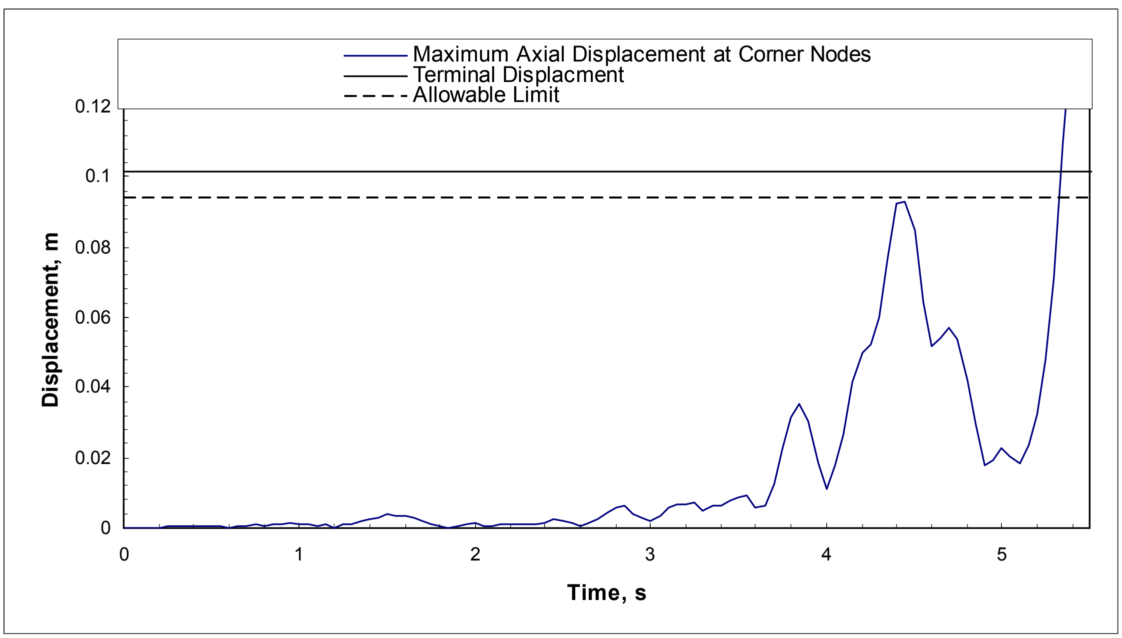

Figure D.294 - Span6, Northridge 3D input, no SCEDs, maximum axial displacement

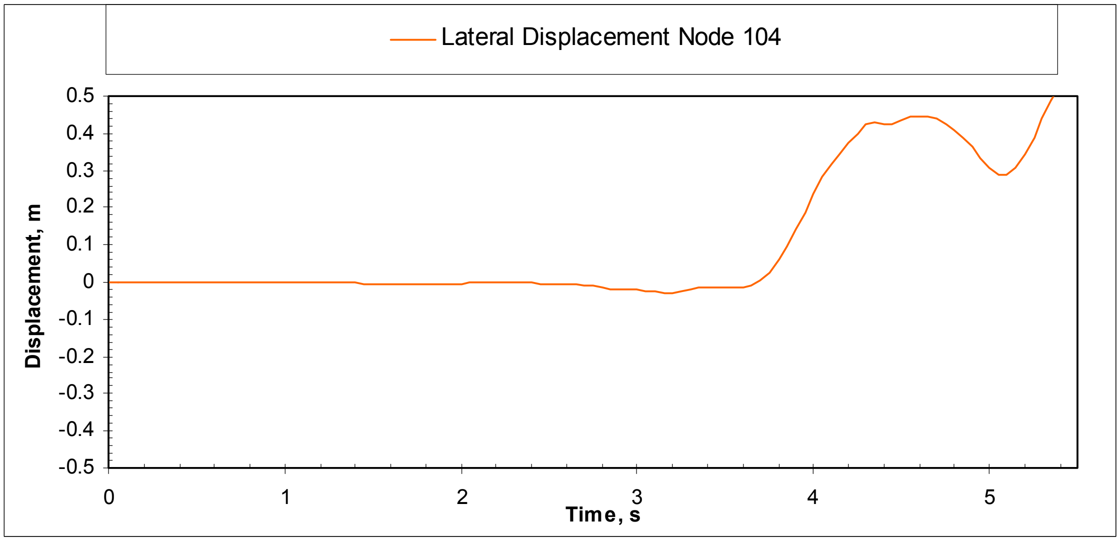

Figure D.295 - Span6, Northridge 3D input, no SCEDs, node 104 lateral displacement

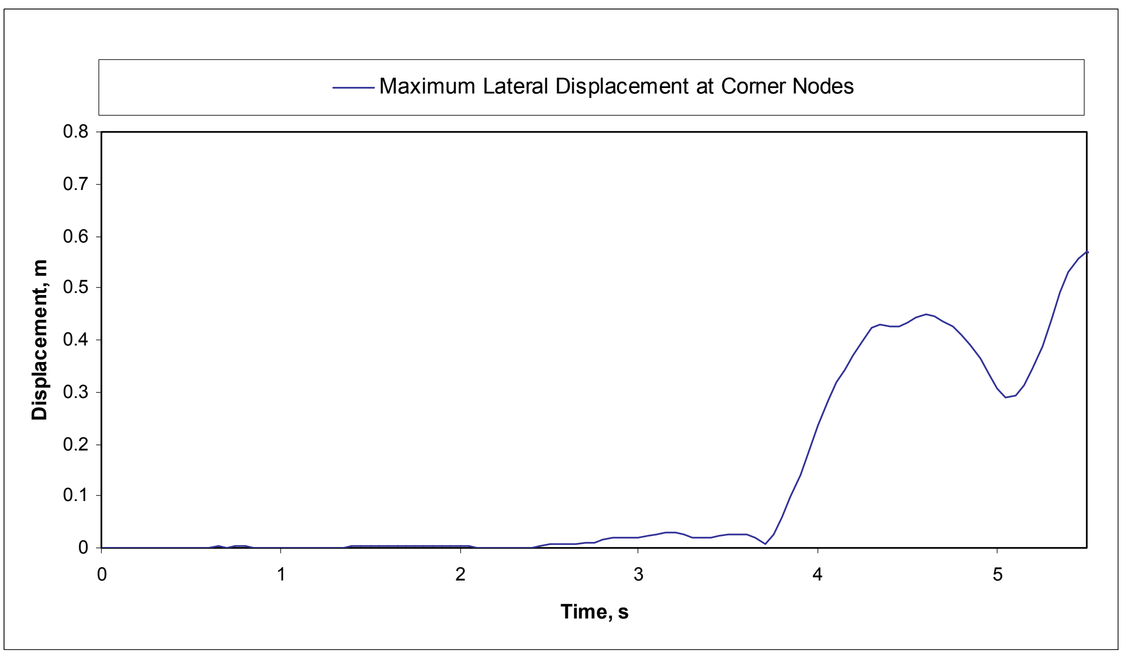

Figure D.296 - Span6, Northridge 3D input, no SCEDs, maximum lateral displacement

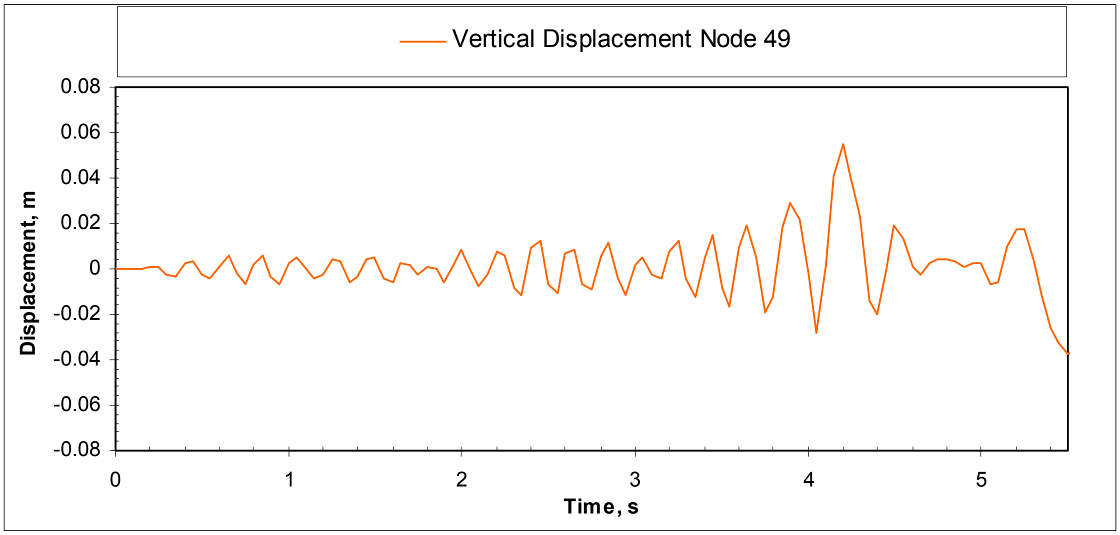

Figure D.297 - Span6, Northridge 3D input, no SCEDs, node 49 vertical displacement

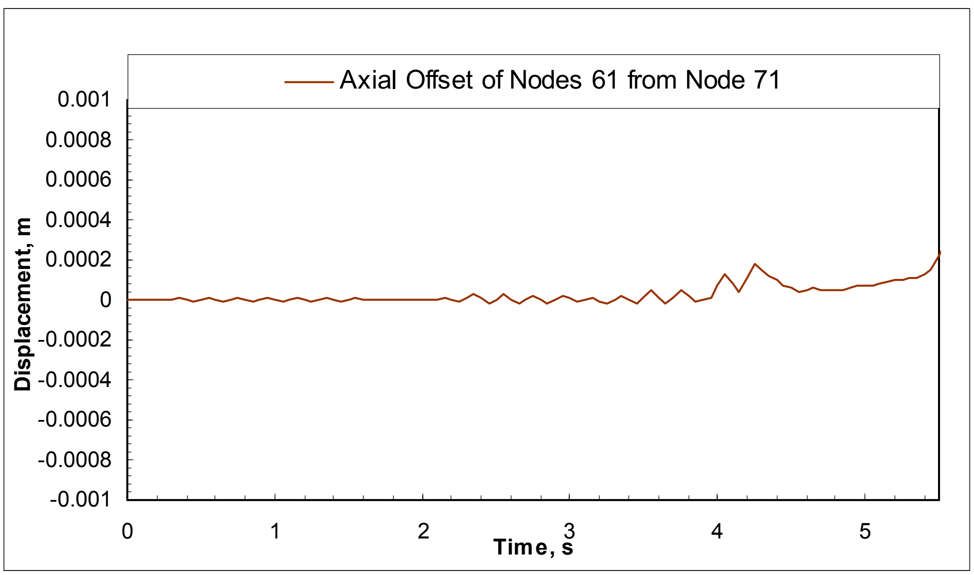

Figure D.298 - Span6, Northridge 3D input, no SCEDs, node 61 and 71 response

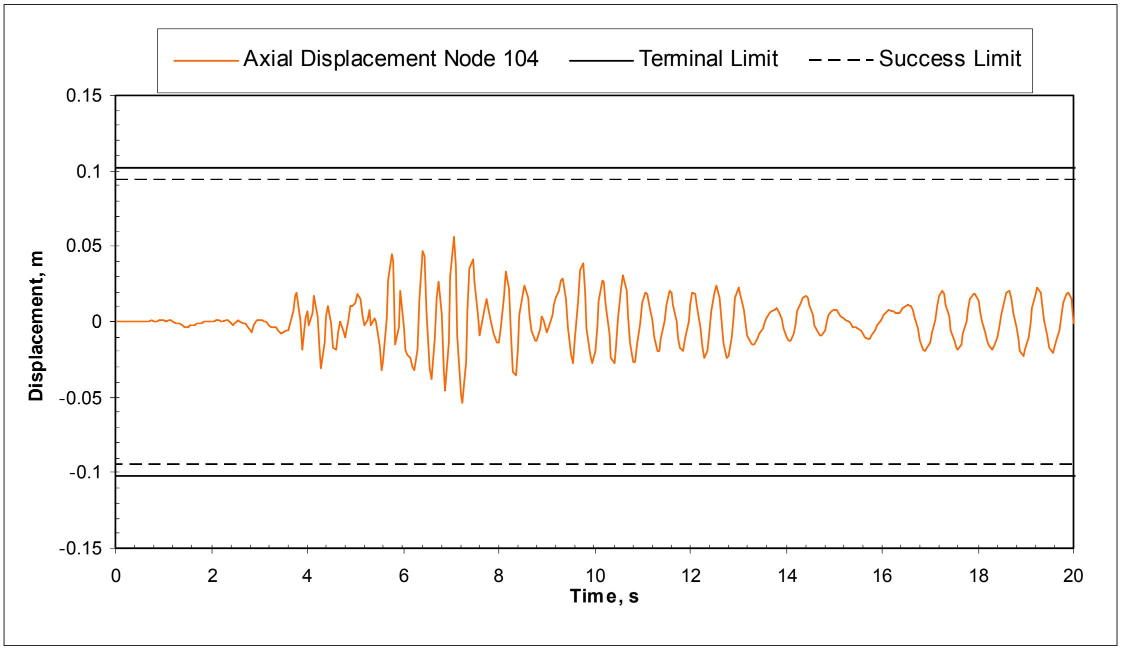

Figure D.299 - Span6, Northridge 3D input, SCED k = 105.4MN/m$^{1.3}$, node 104 axial displacement

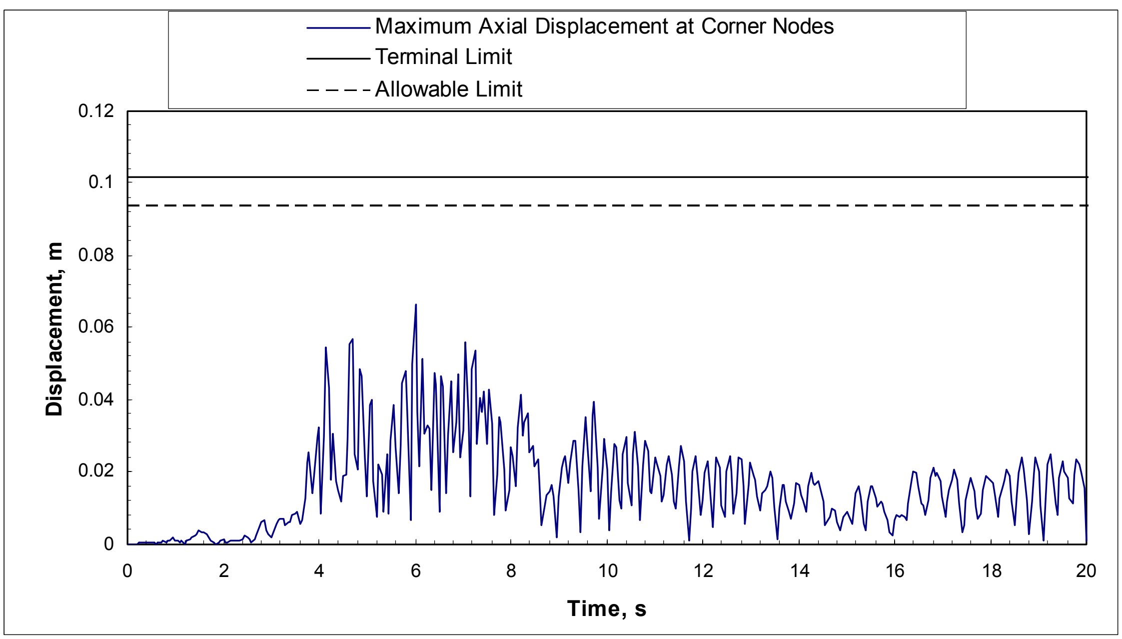

Figure D.300 - Span6, Northridge 3D input, SCED k = 105.4MN/m$^{1.3}$, maximum axial displacement

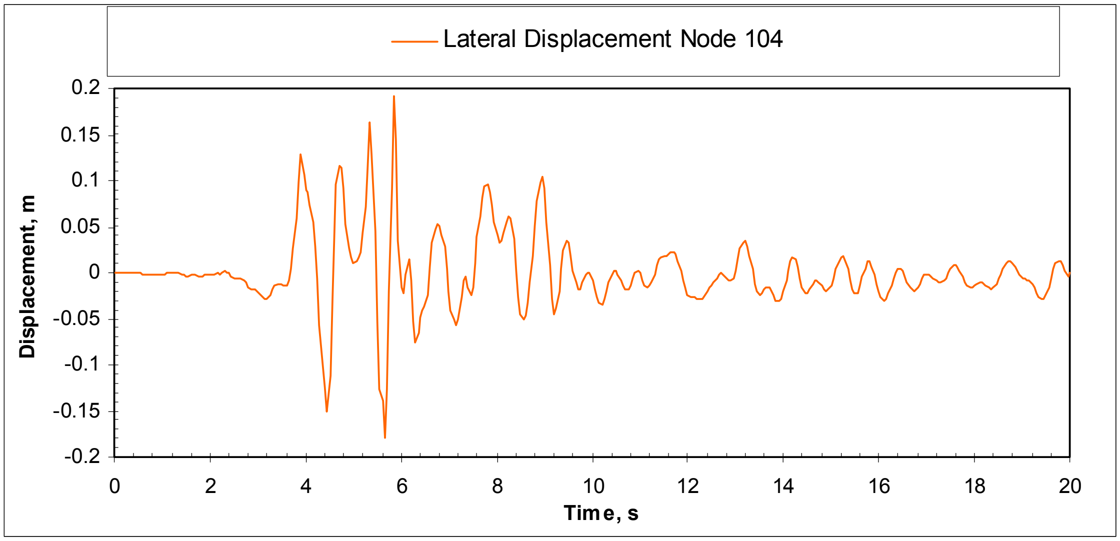

Figure D.301 - Span6, Northridge 3D input, SCED k = 105.4MN/m$^{1.3}$, node 104 lateral displacement

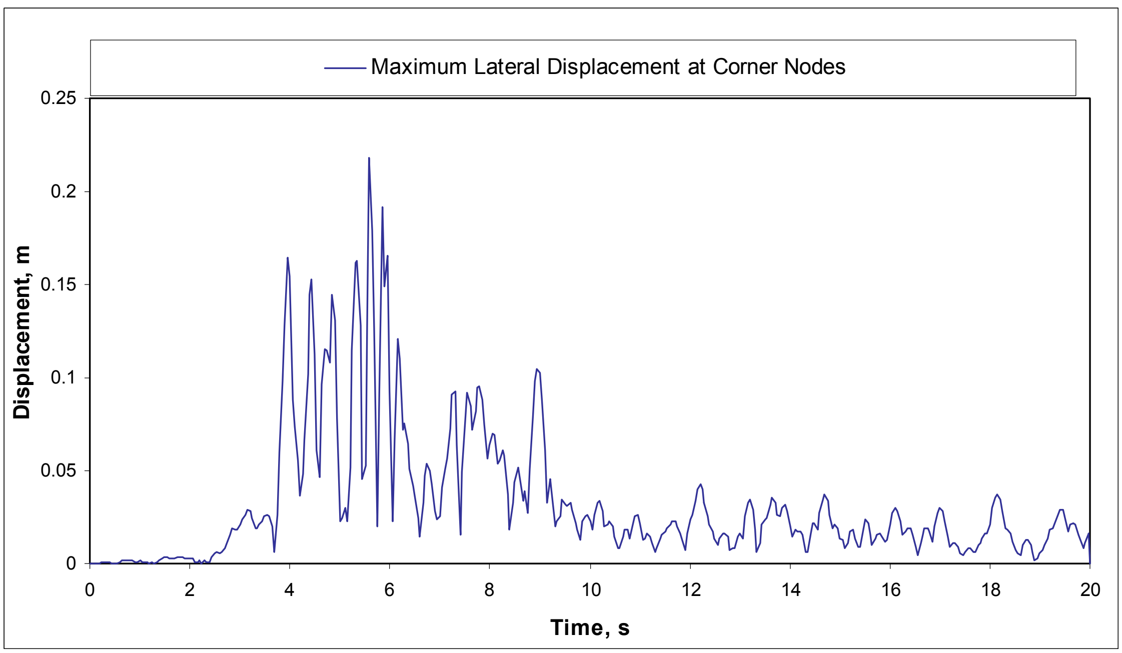

Figure D.302 - Span6, Northridge 3D input, SCED k = 105.4MN/m$^{1.3}$, maximum lateral displacement

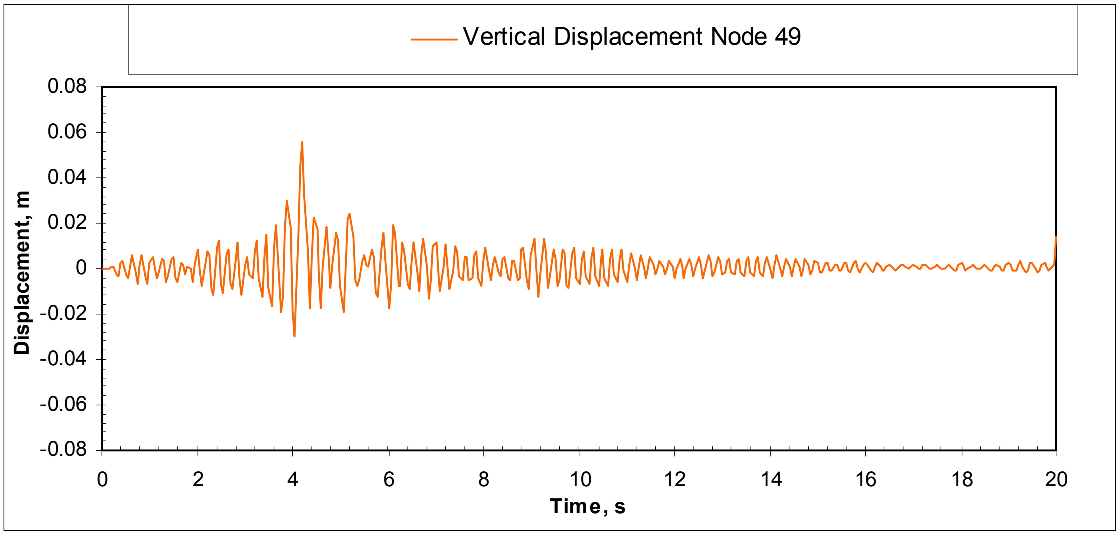

Figure D.303 - Span6, Northridge 3D input, SCED k = 105.4MN/m$^{1.3}$, node 49 vertical displacement

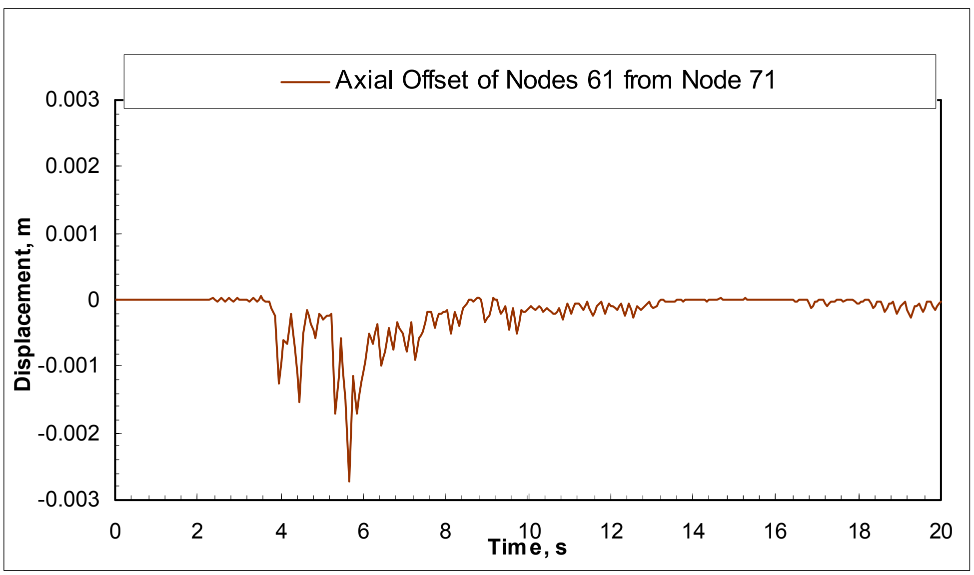

Figure D.304 - Span6, Northridge 3D input, SCED k = 105.4MN/m$^{1.3}$, node 61 and 71 response

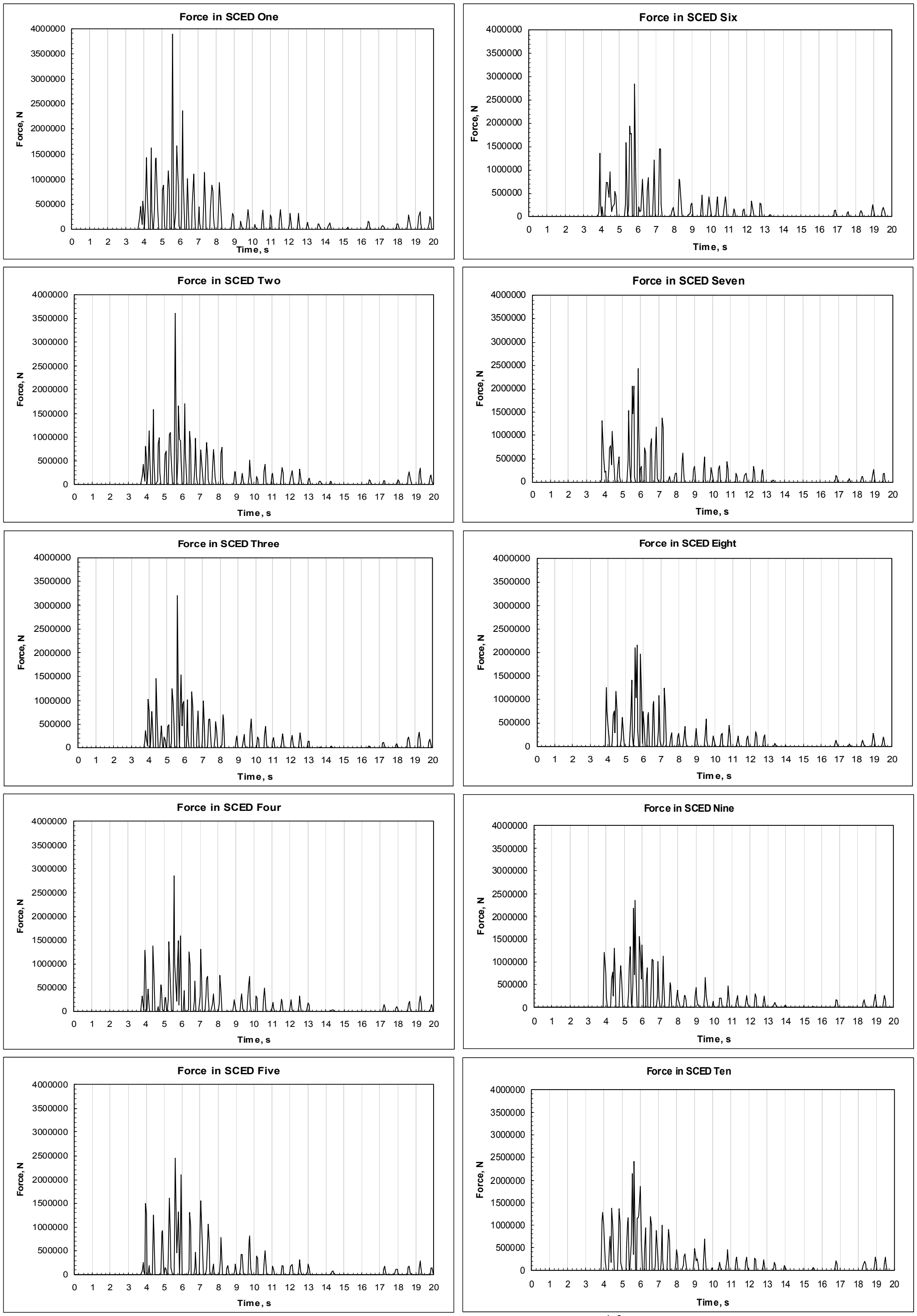

Figure D.305 - Span6, Northridge 3D input, SCED k = 105.4MN/m$^{1.3}$, snap load histories

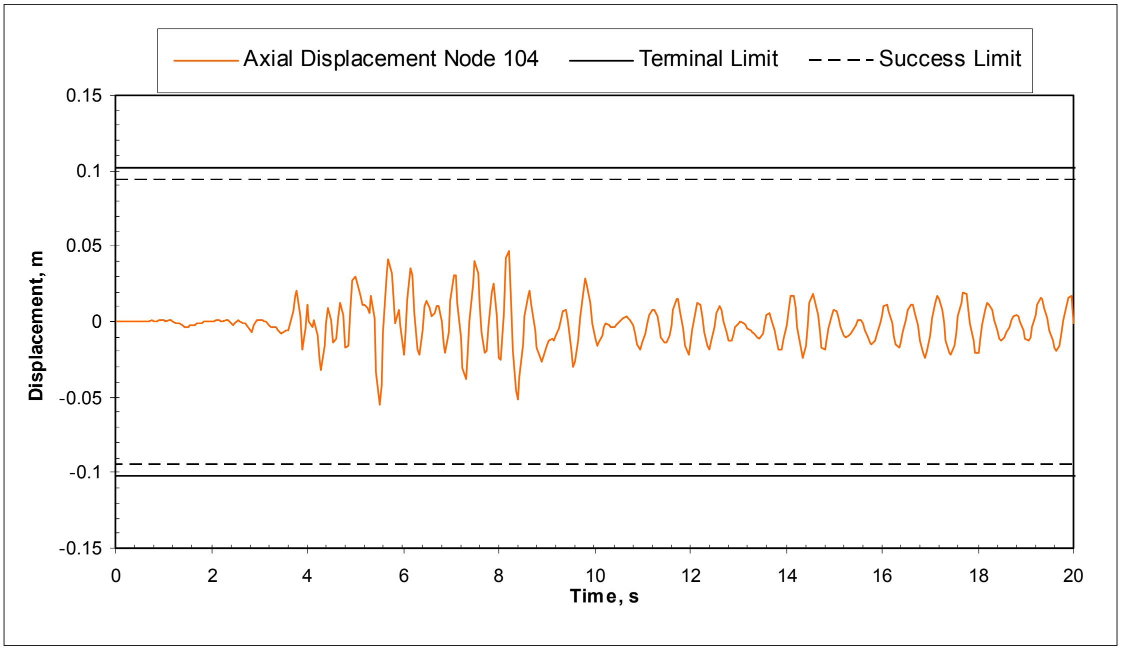

Figure D.306 - Span6, Northridge 3D input, SCED k = 84.3MN/m$^{1.3}$, node 104 axial displacement

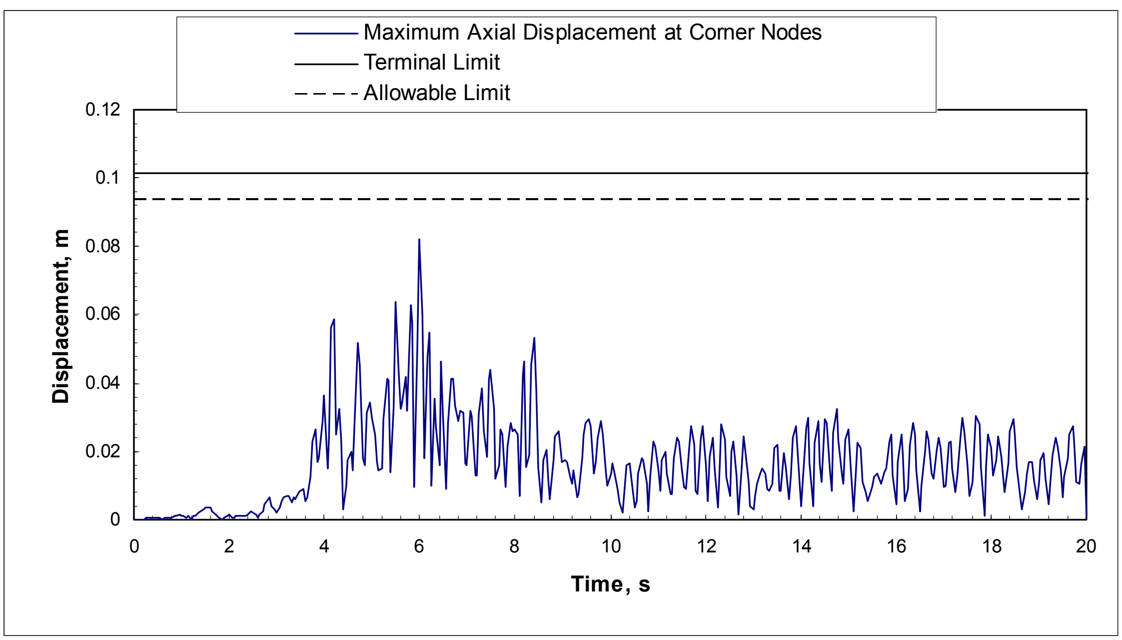

Figure D.307 - Span6, Northridge 3D input, SCED k = 84.3MN/m$^{1.3}$, maximum axial displacement

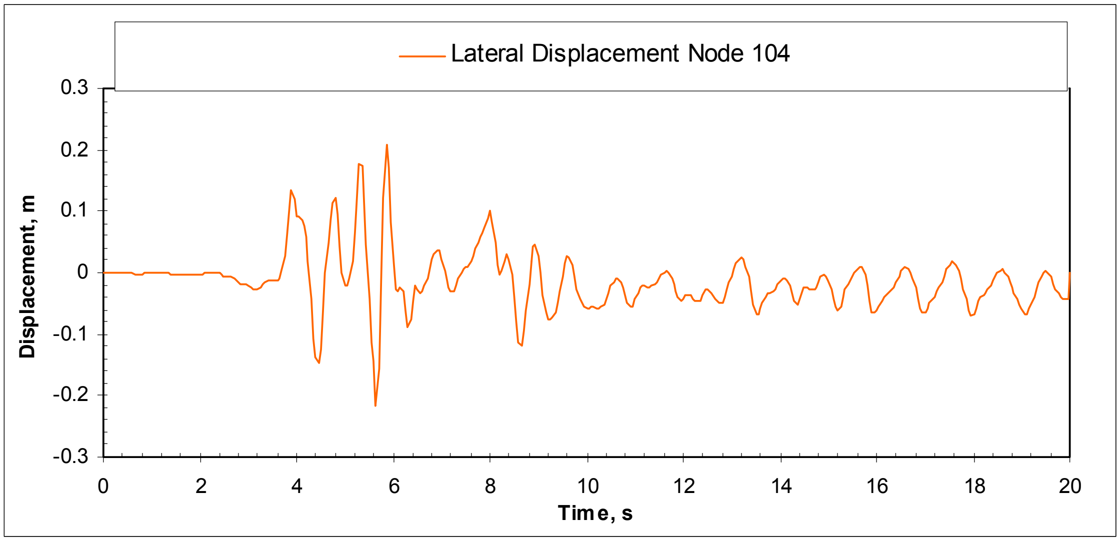

Figure D.308 - Span6, Northridge 3D input, SCED k = 84.3MN/m$^{1.3}$, node 104 lateral displacement

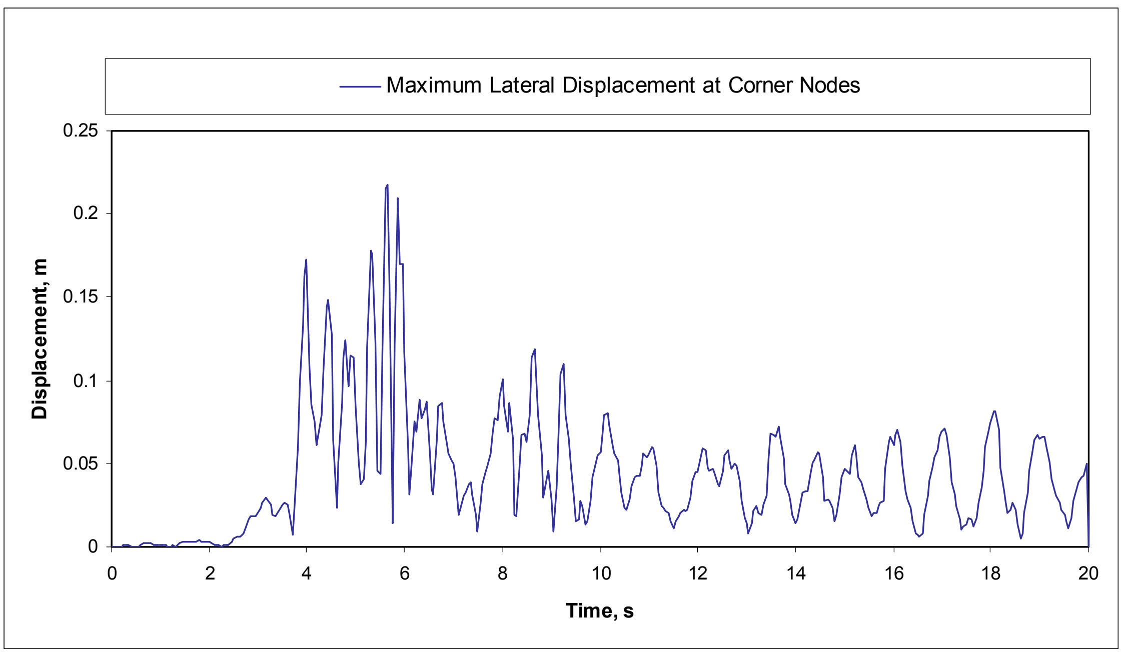

Figure D.309 - Span6, Northridge 3D input, SCED k = 84.3MN/m$^{1.3}$, maximum lateral displacement

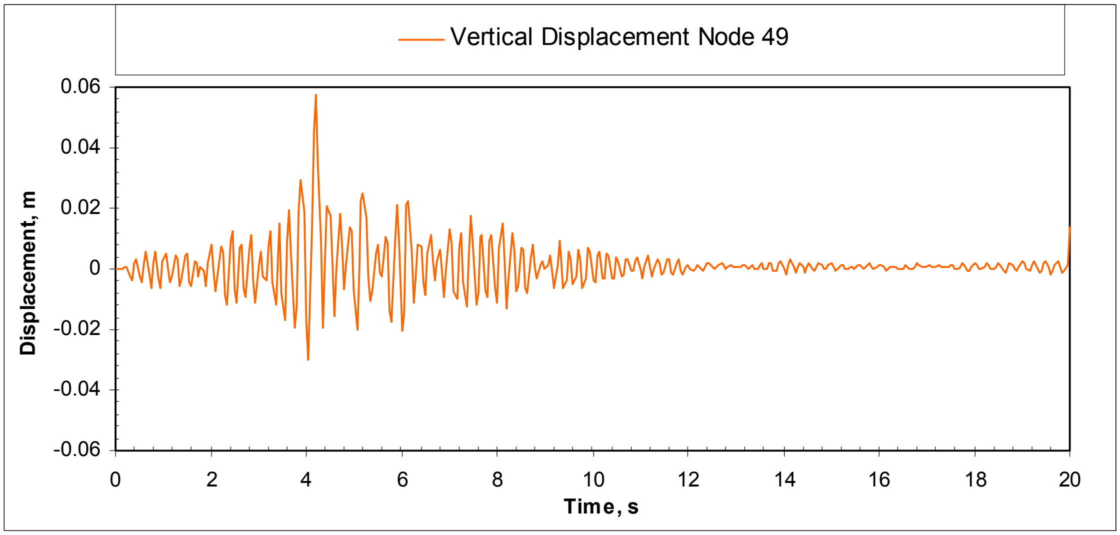

Figure D.310 - Span6, Northridge 3D input, SCED k = 84.3MN/m$^{1.3}$, node 49 vertical displacement

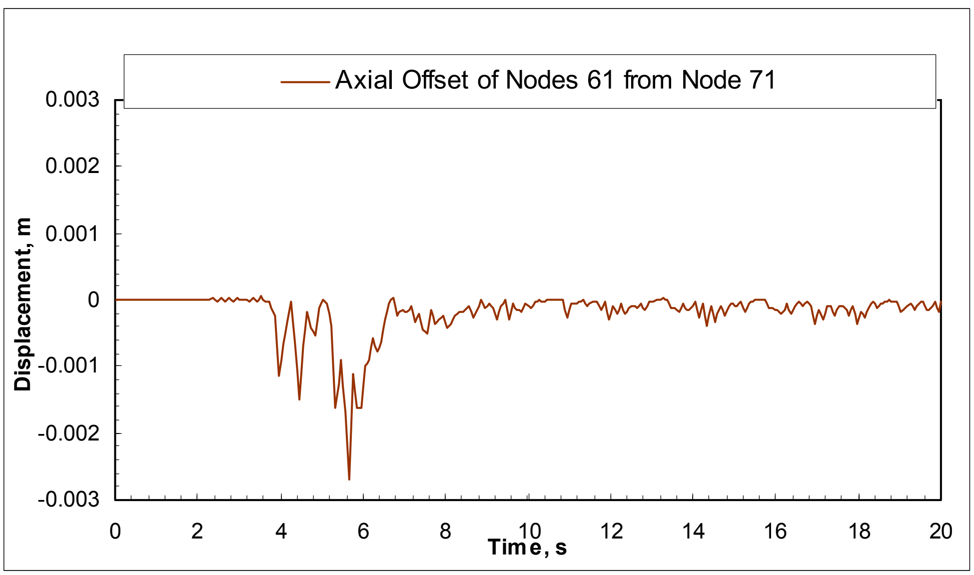

Figure D.311 - Span6, Northridge 3D input, SCED k = 84.3MN/m$^{1.3}$, node 61 and 71 response

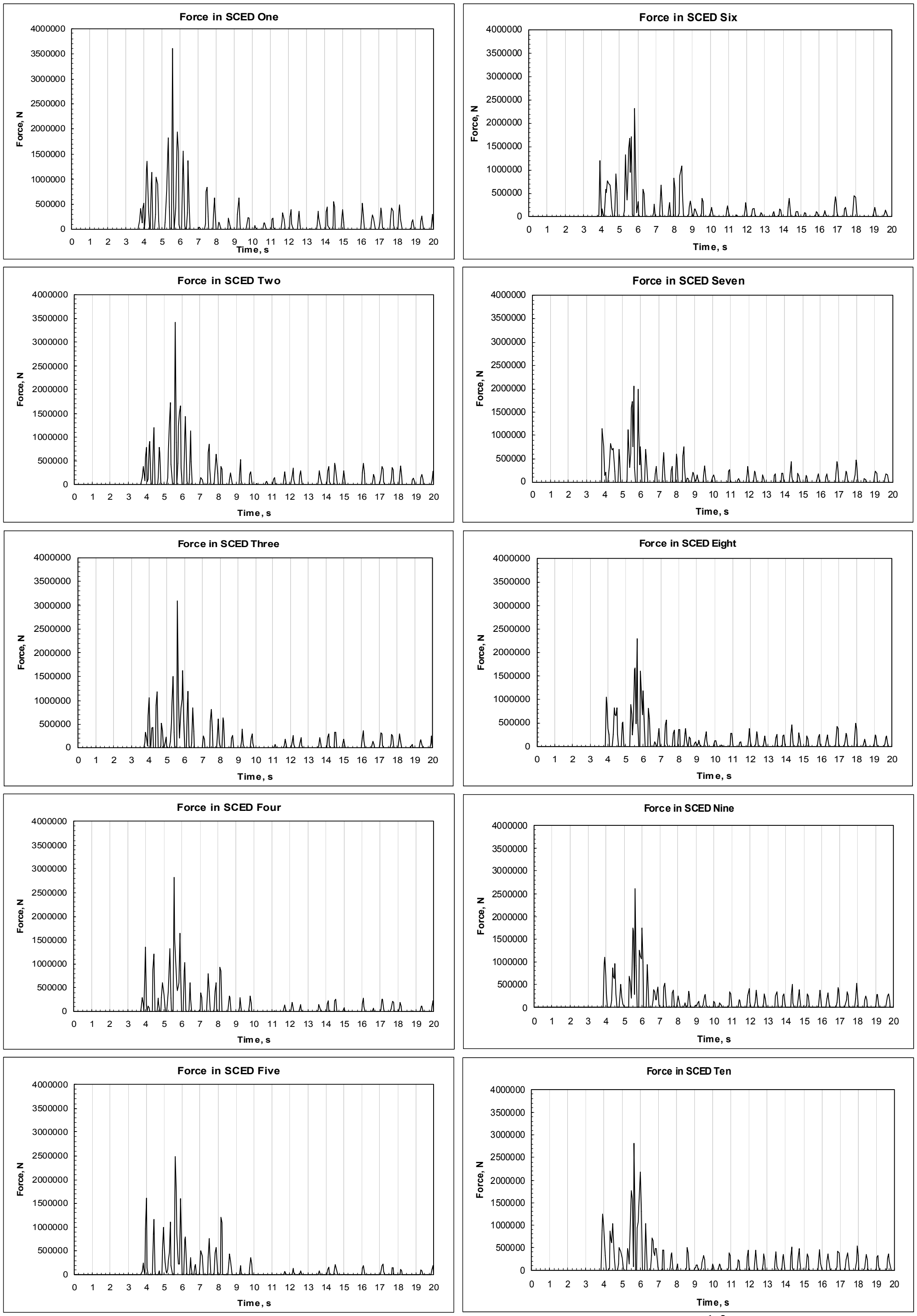

Figure D.312 - Span6, Northridge 3D input, SCED k = 84.3MN/m$^{1.3}$, snap load histories

Vita

Robert Paul Taylor was born in Radford, Virginia on September 15, 1981. He lived in Dublin, Virginia, until he graduated from Pulaski County High School in June 2000. Later that year, he began his attendance at Virginia Polytechnic Institute and State University (Virginia Tech) in Blacksburg, Virginia, where he received his Bachelor of Science Degree in Civil Engineering in 2004. Paul continued his education at Virginia Tech, pursuing a Master of Science Degree in Structural Engineering from the Via Department of Civil and Environmental Engineering. He completed his Master's Degree in August of 2005 and accepted a position with the Upstream Research Company of the ExxonMobil Corporation in Houston, Texas, where he began his career as an engineer in September 2005.

R. Paul Taylor